DECEMBER 15, 1992

Analytical CHEMISTRY

Digital Filtering
and Multivariate Regression
1155 A

FT-IR down-time?

No Problem!

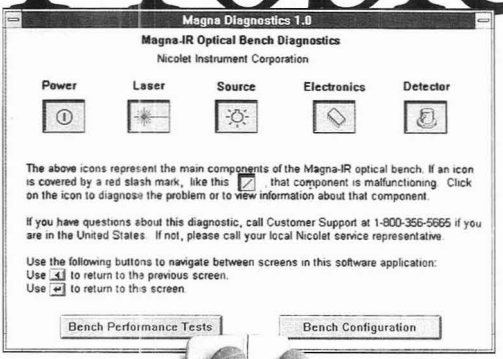

Nicolet's new Magna-IR™ and Impact™ spectrometers with OMNIC™ software will change the way you think about FT-IR technology.

You can easily replace the source, laser, detectors, and power supply–without getting in over your head. The only tool kit you'll ever need is a screwdriver.

Nicolet offers the first FT-IR systems with user-changeable components. Each is pinned-in-place, eliminating complicated alignment adjustments and a service call. This saves you time and money.

Plus, you are ensured of reliable FT-IR performance through Nicolet's advanced diagnostics program. With a click of the mouse, you are instantly updated on the system's operating status.

Magna-IR 750

No guessing.
No waiting.
No problem!

Contact Nicolet at 800-356-8088 for an eye opening demonstration or circle the reader service number to receive more information.

Nicolet

INSTRUMENTS OF DISCOVERY

The intelligent FT-IR choice!

5225 Verona Road / Madison, WI 53711-4495 / TEL: 608/271-3333 / FAX: 273-5046

CIRCLE 80 ON READER SERVICE CARD

DECEMBER 15, 1992
VOLUME 64
NUMBER 24

ANCHAM
64(24) 1141A–1180A/3069–3260 (1992)
ISSN 0003-2700

Analytical CHEMISTRY®

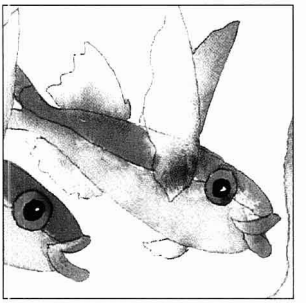

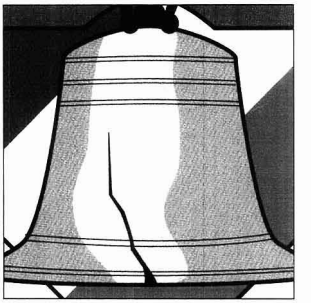

Matheson and the Environment

Special gas mixtures for environmental compliance, emissions monitoring, safety and industrial hygiene.

Backed by Matheson's more than 65 years of experience.

The 1990 revision of the Clean Air Act places increasing restrictions on the discharge of pollutants into the atmosphere and demands more proof of compliance. Penalties for noncompliance will increase. Compliance requires verification by accepted analytical procedures. Analytical data is acceptable only if instrumentation is calibrated with reliable standards. Questionable quality of calibration mixtures is intolerable. Accuracy and consistency must be assumed and verified.

Matheson, the world leader in specialty gases, has successfully prepared accurate calibration gas mixtures of every variety for over 65 years. With greater emphasis on pollution abatement and more demanding compliance requirements, analytical reliability becomes increasingly critical. Matheson's experience is your guarantee that the calibration mixture you receive will meet the requirement.

If you are involved with compliance testing, air quality monitoring or industrial hygiene - insist on reliability and consistency. Insist on Matheson.

VERIFIED

Matheson Gas Products
World Leader in Specialty Gases & Equipment

30 Seaview Drive,
Secaucus, NJ 07096-1587

Calibration Gas Mixtures Available from Matheson

EPA Protocol and NBS Traceable Calibration Mixtures in all Allowable Concentration Ranges

Pollutant	Balance Gas
Carbon Dioxide	Nitrogen or Air
Carbon Monoxide	Nitrogen or Air
Hydrogen Sulfide	Nitrogen or Air
Methane	Nitrogen or Air
Nitric Oxide	Nitrogen
Nitrogen Oxide	Nitrogen or Air
Oxygen	Nitrogen
Propane	Nitrogen or Air
Sulfur Dioxide	Nitrogen or Air
SO_2/O_2	Nitrogen
SO_2/NO	Nitrogen
SO_2/CO_2	Nitrogen
$SO_2/NO/CO$	Nitrogen

Certified Calibration Gas Mixtures for Industrial Hygiene

Pollutant	Balance Gas	Concentration Ranges
Carbon Dioxide	Air	2000 ppm - 2.5%
Carbon Monoxide	Air	20 - 4000 ppm
Ethylene Oxide	Nitrogen	1 -100 ppm
n-Hexane	Air	500 ppm
Hydrogen	Air	0.8 - 2%
Hydrogen Sulfide	Nitrogen	10 - 95 ppm
Methane	Air	1 - 3%
Nitric Oxide	Nitrogen	5 - 30 ppm
Oxygen	Nitrogen	5%
Pentane	Air	1000 ppm - 0.75%
Pentane and O_2	Nitrogen	0.75%/15%
Pentane, O_2 and CO	Nitrogen	0.75%/15%/60 ppm
Propane	Air	0.5 - 1.0%

Toxic Organic Mixtures (allowable combinations of the following components in Nitrogen in ***ppm or ppb*** concentrations)

Acetone	cis-1,2-Dichloroethylene
Acetonitrile	1,2-Dibromoethane
Benzene	Halocarbon 11
Benzyl Chloride	Methyl Ethyl Ketone
1,3-Butadiene	Tetrachloroethylene
Carbon Tetrachloride	Toluene
Chlorobenzene	1,1,1-Trichloroethane
Chloroform	o-Xylene
Dichlorobenzenes	Vinyl Chloride
1,1-Dichloroethane	Vinylidene Chloride
1,2-Dichloroethane	

CIRCLE 72 ON READER SERVICE CARD

Analytical CHEMISTRY

ANALYTICAL CHEMISTRY (ISSN 0003-2700) is published semimonthly by the American Chemical Society, 1155 Sixteenth St., N.W., Washington, DC 20036. Second-class postage paid at Washington, DC, and additional mailing offices. Postmaster: Send address changes to ANALYTICAL CHEMISTRY, Member & Subscriber Services, P.O. Box 3337, Columbus, OH 43210.

Canadian GST Reg. No. R127571347.

Subscription and Business Information

1992 subscription rates include air delivery outside the U.S., Canada, and Mexico. Canadian subscriptions are subject to 7% GST.

	Members	Nonmembers (personal)	Nonmembers (institutional)
U.S.	$ 33	$ 76	$ 373
Canada and Mexico	69	112	409
Europe	117	233	457
Other countries	150	266	490

Nonmember rates in Japan: Rates above do not apply to nonmember subscribers in Japan, who must enter subscription orders with Maruzen Company Ltd., 3–10. Nihonbashi 2-chrome, Chuo-ku, Tokyo 103, Japan. Tel: (03) 272-7211.

For multi-year and other rates, call toll free 800-227-5558 in the U.S. and Canada; in the Washington, DC, metropolitan area and outside the U.S., call 202-872-4363; fax 202-872-4615.

Single issues, current year, $16.00 except review issue, $40.00, and LabGuide, $50.00; **back issues and volumes and microform editions** available by single volume or back issue collection. For information or to order, call the number listed for subscription orders by phone; or write the Microform & Back Issues Office at the Washington address.

Subscription orders by phone may be charged to VISA, MasterCard, or American Express. Call toll free 800-333-9511 in the continental U.S.; in the Washington, DC, metropolitan area and outside the continental U.S., call 202-872-8065. Mail orders for new and renewal subscriptions should be sent with payment to American Chemical Society, Department L-0011, Columbus, OH 43268-0011.

Changes of address must include both old and new addresses with ZIP code and a recent mailing label. Send all address changes to the ACS Columbus address. Please allow 6 weeks for change to become effective. **Claims for missing numbers** will not be allowed if loss was due to failure of notice of change of address to be received in the time specified; if claim is dated (a) North America—more than 90 days beyond issue date, (b) all other foreign—more than 180 days beyond issue date. Hard copy claims are handled at the ACS Columbus address.

ACS membership information: Lorraine Bowlin (202-872-4567)

Articles

*Corresponding author

continued on p. 1149 A

EM SEPARATIONS
CHROMATOGRAPHY
1993

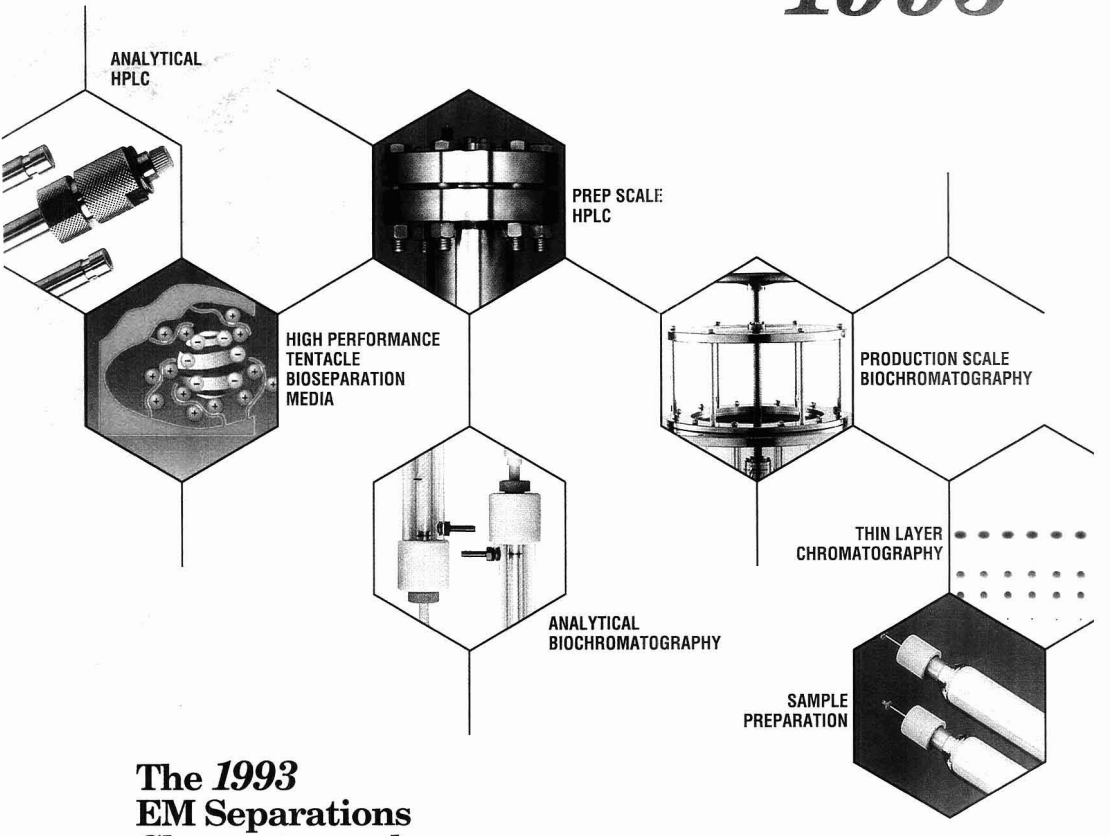

The *1993* EM Separations Chromatography Products Catalog Is Available Now.

Order Your Free Copy Today 1-800-922-1084

EM® US associate of E. Merck Darmstadt, Germany

EM SEPARATIONS

A Division of EM Industries, Inc.

480 Democract Road • Gibbstown, New Jersey 08027
(609) 224-0742 • (800) 922-1084 • FAX: (609) 423-4389

CIRCLE 30 ON READER SERVICE CARD

Analytical CHEMISTRY

Editorial Information

Instructions for authors of AC RESEARCH are published in the January 1 issue, p. 107. Guidelines for the INSTRUMENTATION, REPORT, ANALYTICAL APPROACH, and A/C INTERFACE features are available from the Washington editorial office. Please consult these instructions and guidelines prior to submitting a manuscript for consideration for publication.

Manuscripts for publication in AC RESEARCH (4 copies of text and illustrative material) should be submitted to the Editor at the University of North Carolina address. Please include a signed copyright status form; a copy of this document appears on p. 111 of the January 1 issue. Manuscripts for publication in the A-page section should be submitted to the Washington editorial staff.

For individual reprints of AC RESEARCH or A-page articles, please contact the authors directly. Bulk reprints of individual articles are available from ACS. For information, write or call the Distribution office at the ACS Washington address (202-872-4539; fax 202-872-4615).

ACS Division of Analytical Chemistry
Chair, Joseph L. Glajch (508-671-8413)
Secretary, Sarah Rutan (804-367-1298)

ACS Information

Library Services	202-872-4515
Education Division	202-872-4388
Meetings Dept.	202-872-4397
Member Services	202-872-4414
Employment Services	202-872-6120
Public Outreach	202-872-4091

Supplementary material is noted in the table of contents with a ■. It is available as photocopy ($10.00 for up to 3 pages and $1.50 per page for additional pages, plus $2.00 for foreign postage) or as 24X microfiche ($10.00, plus $1.00 for foreign postage). Canadian residents should add 7% GST. See supplementary material notice at end of journal article for number of pages. Orders *must* state whether for photocopy or for microfiche and give complete title of article, names of authors, journal, issue date, and page numbers. Prepayment is required and prices are subject to change. Order from Microforms & Back Issues Office at the ACS Washington address.

The paper used in this publication meets the minimum requirements of American National Standard for Information Sciences—Permanence of Paper for Printed Library Materials, ANSI Z39.48-1984.

Journals Department
American Chemical Society
2540 Olentangy River Road
P.O. Box 3330
Columbus, OH 43210
614-447-3600, Ext. 3171
TELEX 6842086; Fax 614-447-3745

Member & Subscriber Services
American Chemical Society
P.O. Box 3337
Columbus, OH 43210
614-447-3776
800-333-9511

Metrohm Karl Fischer titrators have always saved you time and money.

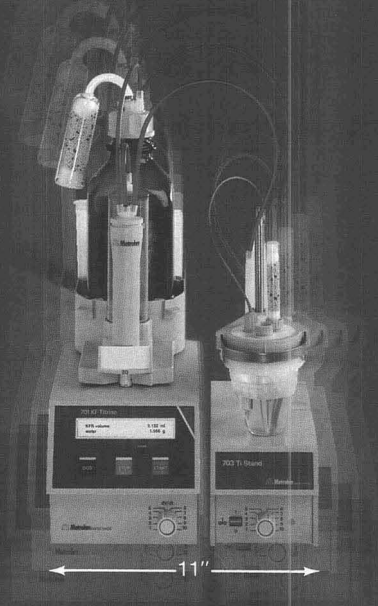

Now they save you space.

Introducing the smallest Karl Fischer titrator ever.

Greater work-station efficiency, more productivity.

When the people at Metrohm made the world's smallest Karl Fischer titrator, they also made it the optimum work station. The new Model 701 is equipped for true two-way communication... computer via RS232C and operator via alphanumeric display.

It's faster, too. It automatically determines the titer, blank, drift, or sample water in just 30 seconds, then aspirates the titrated sample at the touch of a button.

Traditional Metrohm accuracy.

A buret resolution of 10,000 pulses coupled with drift compensation makes the new Model 701 the most accurate yet simplest Karl Fischer titrator ever. Pure and simple, Metrohm *means* titration.

Metrohm Ltd.
CH-9101 Herisau/Switzerland
Phone 071/53 11 33
Telefax 071/52 11 14
Telex 88 27 12 metr ch

In U.S. and Canada:
Call 800-645-3050 for more information, or write Brinkmann Instruments, Inc., One Cantiague Road, P.O. Box 1019, Westbury, NY 11590-0207.

Metrohm

BRINKMANN Quality products for research and control.

AD 131

CIRCLE 70 ON READER SERVICE CARD

UPCOMING RESEARCH

Structure-Specific Collision-Induced Fragmentations of Ceramides Cationized with Alkali-Metal Ions

Complete information about structures of ceramides are obtained from collision-induced decompositions of cationized species. The detection limit for structural determination of *N*-palmitoyl-DL-sphinganine is 8 pmol.

Qinghong Ann and Jeanette Adams*, Department of Chemistry, Emory University, Atlanta, GA 30322

Experimental Determination of the Number of Trapped Ions, Detection Limit, and Dynamic Range in Fourier Transform Ion Cyclotron Resonance Mass Spectrometry

The theory and experimental protocol for determining the number of ions that contribute to the detected time domain signal in FT-ICRMS are presented.

Patrick A. Limbach, Peter B. Grosshans, and Alan G. Marshall*, Department of Chemistry, 120 West 18th Avenue, The Ohio State University, Columbus, OH 43210

Self-Assembled Monolayers in Electroanalytical Chemistry: Application of ω-Mercapto Carboxylic Acid Monolayers for the Electrochemical Detection of Dopamine in the Presence of a High Concentration of Ascorbic Acid

Self-assembled ω-mercapto carboxylic acid monolayers on gold electrodes are used to introduce an electrochemical differentiation between positively charged dopamine and negatively charged ascorbic acid.

Franck Malem and Daniel Mandler*, Department of Inorganic and Analytical Chemistry, The Hebrew University of Jerusalem, Jerusalem 91904, Israel

Heat-Induced Conformational Changes in Proteins Studied by Electrospray Ionization Mass Spectrometry

Electrospray ionization MS is used to investigate heat-induced denaturation of proteins and to improve the spectra of intractable proteins.

Urooj A. Mirza, Steven L. Cohen, and Brian T. Chait*, The Rockefeller University, New York, NY 10021

NMR Study of the State of Water in Ion-Selective Electrode Membranes

By using variable-temperature NMR, light-scattering centers formed in poly(vinyl chloride)-based ion-selective membranes immersed in water are shown to arise from water droplet formation.

Andy D. C. Chan and D. Jed Harrison*, Department of Chemistry, University of Alberta, Edmonton, Alberta, Canada T6G 2G2

These articles are scheduled to appear in AC RESEARCH in the near future.

*Corresponding author

pH–Metric log *P*. 3. Glass Electrode Calibration in Methanol–Water, Applied to pK_a Determination of Water-Insoluble Substances

A method for calibrating pH electrodes in methanol–water solutions, using a four-parameter equation that relates the operational pH scale to that based on concentration, p_cH, is developed and applied to determining aqueous pK_as of water-insoluble molecules.

Alex Avdeef*, John E. A. Comer, and Simon J. Thomson, Sirius Analytical Instruments Ltd., Manor House, Lewes Road, Forest Row, East Sussex, RH18 5AF, United Kingdom

Optimization of Waveforms for Pulsed Amperometric Detection of Carbohydrates Based on Pulsed Voltammetry

An automated procedure is described for optimization of all variables in PAD waveforms based on pulsed voltammetry at rotated disk electrodes.

William R. LaCourse and Dennis C. Johnson*, Department of Chemistry, Iowa State University, Ames, IA 50011

Determination of Atrazine in Water at Low- and Sub-Parts-per-Trillion Levels by Using Solid-Phase Extraction and Gas Chromatography/High-Resolution Mass Spectrometry

Mass profile monitoring is incorporated into a method for trace determination of atrazine. The precision of the method is 15% and the accuracy is > 85% at the 1-pptr level.

Zongwei Cai, V. M. Sadagopa Ramanujam, Daryl E. Giblin, and Michael L. Gross*, Midwest Center for Mass Spectrometry, Department of Chemistry, University of Nebraska, Lincoln, NE 68588-0304 and **Roy F. Spalding,** Water Center, University of Nebraska, Lincoln, NE 68588-0844

Matrix-Assisted Laser Desorption of Biological Molecules in the Quadrupole Ion Trap Mass Spectrometer

Biological molecules are introduced directly into a quadrupole ion trap mass spectrometer via matrix-assisted laser desorption. Single-unit femtomole detection limits and tandem MS structural analysis are demonstrated for small polypeptides.

David M. Chambers, Douglas E. Goeringer*, Scott A. McLuckey, and Gary L. Glish, Analytical Chemistry Division, Oak Ridge National Laboratory, Oak Ridge, TN 37831-6365

Effects of Buffer pH on Electroosmotic Flow Control by an Applied Radial Voltage for Capillary Zone Electrophoresis

Variation of pH for electronic electroosmotic flow control is examined theoretically and experimentally. Control is greatest at low pH and is least at high pH. Associated band broadening is also examined.

Mark A. Hayes, Indu Kheterpal, and Andrew G. Ewing*, Department of Chemistry, Penn State University, 152 Davey Laboratory, University Park, PA 16802

Jorgenson and Markides Receive Chromatographic Society Awards

James W. Jorgenson and Karen E. Markides received the Martin Award and the Jubilee Medal, respectively, on Sept. 14 at the 19th International Symposium on Chromatography in Aix-en-Provence, France.

The Martin Award, established in 1978, honors A.J.P. Martin, the first president of the Chromatographic Society. It recognizes achievements in all aspects of separations science, including newly emerging techniques. Jorgenson was recognized for his work in capillary electrophoresis (CE).

The Jubilee Medal was established in 1982 to celebrate the 25-year anniversary of the founding of the Chromatographic Society. It is intended to honor scientists who show outstanding promise in their careers in separations science. Markides was recognized for her work in capillary supercritical fluid chromatography (SFC).

Jorgenson, professor of chemistry at the University of North Carolina, Chapel Hill, and Associate Editor for separations for ANALTYICAL CHEMISTRY, received his B.S. degree in 1974 from Northern Illinois University and his Ph.D. in 1979 from Indiana University. He joined the faculty of the University of North Carolina, Chapel Hill, in 1979 and was appointed professor in 1987.

Jorgenson is credited with the critical early work in establishing CE as a viable microanalytical technique. His research interests include high-sensitivity single-cell analysis and multidimensional separations based on LC/CZE and CZE/MS.

Markides, chair of the department of analytical chemistry at Uppsala University (Sweden), received her B.S. degree and her Ph.D. from the University of Stockholm in 1978 and 1984, respectively. As a postdoctoral fellow at Brigham Young University working with Milton Lee, she developed instrumentation and columns for open tubular column SFC. She also developed stationary phases for the separation of enantiomers and instrumentation for SFE/SFC.

CAALS Associates

NIST has announced a new program for small businesses that want to get involved in the Consortium on Automated Analytical Laboratory Systems (CAALS). The consortium, started in 1990, is a collaboration among government agencies and businesses in the private sector interested in advancing automation in analytical chemistry.

For a $5000 fee, members in the CAALS Associates Program participate in the modularity and control communications aspect of the program by helping devise specifications and standards for laboratory automation, attending workshops, and receiving reports and newsletters. Additional benefits include interaction with individuals and organizations shaping laboratory automation and access to the broad-based expertise of NIST. The program is open to small businesses, individuals, not-for-profit and trade organizations, and universities. By contrast, general or research membership in CAALS costs $30,000. General or research members are entitled to participate in all three components of the program (the organic and inorganic demonstration projects, in addition to the modularity project described above); have voting rights; have access to all reports, newsletters, workshops, and the like; and have the right to use CAALS methods and technology within their own organizations. In addition, research members have options for co-exclusive license on intellectual property developed by the consortium. For more information, contact CAALS, A343 Chemistry Bldg., NIST, Gaithersburg, MD 20899 (301-975-4142).

For Your Information

NIST recently recertified two **SRMs for lead measurements**. Powdered Lead-Based Paint SRM 1579a is intended for calibrating lab equipment used to determine lead in paint scrapings. The standard contains 35 g of finely ground paint powder with a certified lead concentration; cost is $131. Lead in Blood SRM 955a, designed in conjunction with the Centers for Disease Control, is for laboratories measuring lead at < 50 ppb. The standard contains four vials of frozen cow blood, each of which has a lead concentration of between 5 and 55 μg/dL. Cost is $261. To order, contact the Standard Reference Materials Program, Rm. 204, Bldg. 202, NIST, Gaithersburg, MD 20899 (301-975-6776).

The American Society for Testing and Materials Committee E-13 on Molecular Spectroscopy is currently working on **three methods of interest to spectroscopists:** a procedure for calibrating photodiode arrays, a major revision of the existing standard for the measurement of stray radiant energy from spectrophotometers by the opaque filter method (E-387-84), and the first draft of "Standard Practices for General Techniques of Gas Chromatography/IR Analysis." For information on this particular document, contact Davis Compton, Bio-rad, Digilab Division, Cambridge, MA 02139 (617-868-4330). For information on the other methods, committee activities, or ways to volunteer, contact Eric F. Mooney, Tytronics, Inc., 224 Calvary St., P.O. Box 590, Waltham, MA 02254-0590 (617-894-0550; fax 617-894-9934).

35th ROCKY MOUNTAIN CONFERENCE ON ANALYTICAL CHEMISTRY

July 25 - 29, 1993

Hyatt Regency Denver
Denver, Colorado

Rocky Mountain Section
Society for Applied Spectroscopy

American Chemical Society
Colorado Section

Exhibits Chair
Vanessa Fishback
7578 Aberdeen Way
Boulder, CO 80301
(303) 530-5274

Conference Chair
Robert Wershaw
U.S.G.S.
P.O. Box 25046 MS408
Denver, CO 80225
(303) 467-8280

Program Chair
Christine White
Coors Brewing Company CC288
Golden, CO 80401
(303) 277-2275

SYMPOSIA

ATOMIC SPECTROSCOPY

Gary Rayson
New Mexico State University
Chemistry Department
Las Cruces, NM 88003
(505) 646-5839
Fax: (505) 646-2649

CHROMATOGRAPHY

Denise Kent
11671 Baca Road
Conifer, CO 80433
1-800-632-2708 ext. 2168

CLINICAL CHEMISTRY

Christine White
Coors Brewing Company CC288
Golden, CO 80401
(303) 277-2275
Fax: (303) 277-6670

COMPOSTING

Cal Kuska
8547 E. Arapahoe Rd. J221
Greenwood Village, CO 80112
(303) 791-8639
Fax: (303) 850-0623

ELECTROCHEMISTRY

Dan Buttry
University of Wyoming
Department of Chemistry
Laramie, WY 82071-3838
(307) 766-6677
Fax: (307) 766-2807

ENVIRONMENTAL CHEMISTRY

Maria Tikkanen
Association of California Water Agencies
910 "K" Street, Suite 250
Sacramento, CA 95814
(916) 441-4545
Fax: (916) 441-7893

EPR

Gareth Eaton
University of Denver
Chemistry Department
Denver, CO 80208
(303) 871-2980
Fax: (303) 871-2254

Sandra Eaton
University of Denver
Chemistry Department
Denver, CO 80208
(303) 871-3102
Fax: (303) 871-2254

FTIR/NIR/RAMAN SPECTROSCOPY

Abdul Chughtai
University of Denver
Chemistry Department
Denver, CO 80208
(303) 871-4404
Fax: (303) 871-2932

GENERAL POSTERS

Mary Cast
U.S. Geological Survey
QMG National Water Quality Lab
P.O. Box 25046 MS407
Denver, CO 80225
(303) 467-8044
Fax: (303) 467-9598

HAZARDOUS WASTE

Carlos Arozarena
U.S. Geological Survey
P.O. Box 25046 MS407
Denver, CO 80225
(303) 467-8035
Fax: (303) 467-9598

ICP/MS

Howard Taylor
U.S. Geological Survey
P.O. Box 25046 MS458
Denver, CO 80225
(303) 541-3007
Fax: (303) 447-2505

LABORATORY SAFETY

Marvin Goldberg
U.S. Geological Survey
P.O. Box 25046 MS424
Denver, CO 80225
(303) 236-4728
Fax: (303) 236-4418

LUMINESCENCE

DeLyle Eastwood
Lockheed Engineering
1050 East Flamingo Road, Suite 242
Las Vegas, NV 89119
(702) 897-3287
Fax: (702) 897-6641

Robert Hurtubise
University of Wyoming
Department of Chemistry
Box 3838 University Station
Laramie, WY 82071
(307) 766-6241
Fax: (307) 766-2807

MASS SPECTROMETRY

Joseph Zirrolli
Department of Pediatrics K923
National Jewish Center
Denver, CO 80206
(303) 398-1853
Fax: (303) 398-1694

NMR

Hellmut Eckert
University of California, Santa Barbara
Department of Chemistry
Santa Barbara, CA 93106
(805) 893-8163
Fax: (805) 893-4120

PHARMACEUTICAL ANALYSIS

Mike Cutrera
Marion Merrell Dow
10236 Marion Park Drive
Kansas City, MO 64137
(816) 966-7386
Fax: (816) 966-5222

Robert Lantz
Rocky Mountain Instrumental Labs
456 South Link Lane
Fort Collins, CO 80524
(303) 530-1169

Patricia Sulik
Rocky Mountain Instrumental Labs
456 South Link Lane
Fort Collins, CO 80524
(303) 530-1169

QUALITY ASSURANCE

William Shampine
U.S. Geological Survey
P.O. Box 25046 MS401
Denver, CO 80225
(303) 236-1940
Fax: (303) 236-1420

RADIOCHEMISTRY

Ann Mullin
U.S. Geological Survey/NWQL
P.O. Box 25046 MS407
Denver, CO 80225
(303) 467-8235
Fax: (303) 467-8240

ROBOTICS

Robert L. Wershaw
U.S. Geological Survey
P.O. Box 25046 MS408
Denver, CO 80225
(303) 467-8280
Fax: (303) 467-9598

ABSTRACT DEADLINE - MARCH 15, 1993

☐ Please send a preliminary program and pre-registration information. (To be published in May). AC

Name _____
Company _____
Address _____
_____

Return to: Robert L. Wershaw
U.S. Geological Survey
P.O. Box 25046 MS 408
Denver, CO 80225

REPORT

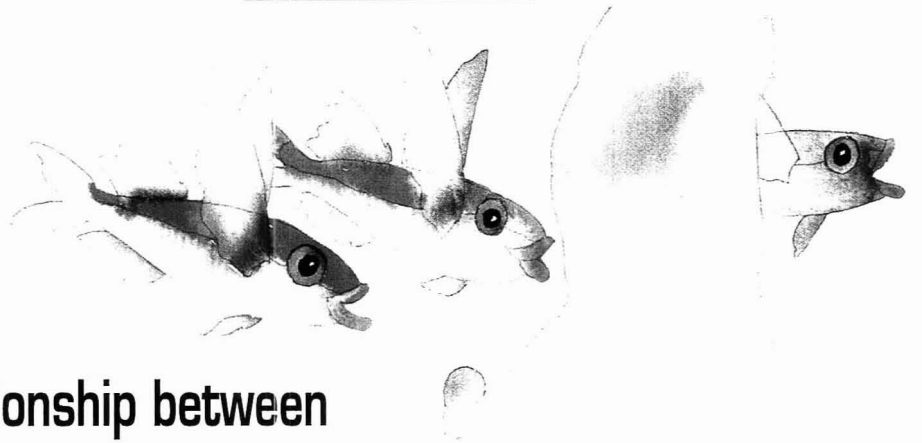

TRACY TAYLOR

Relationship between Digital Filtering and Multivariate Regression in Quantitative Analysis

Chris L. Erickson, Michael J. Lysaght[1], and James B. Callis
Center for Process Analytical Chemistry
Department of Chemistry, BG-10
University of Washington
Seattle, WA 98195

Analytical chemistry can be defined as the science dealing with the identification and quantitation of a sample's physical and chemical properties (state variables). The analytical variable most commonly probed is chemical concentration. An obvious way to determine chemical concentrations is to isolate all analytes and then determine their masses. Unfortunately, this type of analysis procedure can be time-consuming, laborious, or even impossible to perform. Therefore a great deal of effort in analytical chemistry has been expended on the development of automated electronic instrumentation capable of measuring analytical state variables by some indirect means.

Generally this involves performing an experiment on the sample in which a physical or a chemical stimulus is applied to the system. The analytical response to this perturbation is then measured. Unfortunately, the analytical measurement thus obtained is not a direct measure of the state variable(s) of interest, for the following reasons: the measurement process itself disturbs the system; the measurement scheme is not perfectly selective, and therefore interferences can contaminate the signal arising from the analyte; random noise in the system corrupts the measurement; or a theoretical relationship must be employed to obtain the state variable(s) of interest from the signal. Such a relationship may not be known in advance, or it may be complex. As a result, analytical measurements are generally processed in some way to remove interferences, reduce noise, and extract the information related to the desired state variables.

The common approach to developing an instrument for quantitative analysis is univariate and linear in nature (i.e., the sensing means is designed to be as selective as possible so that only a single measurement is needed to estimate the concentration of the analyte of interest). This minimizes postexperimental signal processing. An example of such a system would be an ion-selective electrode. Unfortunately, the perfectly selective sensing system has yet to be developed, because all methods are plagued to some degree by interferences. Obviously, interferences can be avoided or minimized by adequate sample cleanup, but this approach generally requires time-consuming manual operations.

An alternative approach is to use multichannel instruments that incorporate multiple sensors, each of which is characterized by its partial selectivity toward a particular analyte. The response then becomes multivariate in nature, and a pattern that allows correction for interferences and drift, and even permits simultaneous multicomponent analysis, can be developed. An example of an analytical method based on this approach is the near-IR spectroscopic analysis of grain for protein, starch, and moisture content (*1*).

Over the past decade two approaches have emerged for processing multivariate measurements contaminated by noise and interferences: digital filtering and multivariate regression. Bialkowski has reviewed the applicability of digital filter theory for this purpose (*2, 3*), whereas Beebe and Kowalski (*4*) as well as others (*5, 6*) have discussed the merits of multivariate regression-based calibration and predic-

[1] Current address: Department of Chemistry, U.S. Air Force Academy, USAFA, CO 80840

0003-2700/92/0364-1155A/$03.00/0

tion. Because these seemingly disparate approaches, which use different terminologies and mathematical notations, possess the identical goal of optimally deriving state variables from analytical measurements, the question naturally arises as to what relationship exists between the two. Accordingly, the purpose of this REPORT is to quantitatively explain and compare digital filtering and multivariate regression.

Before proceeding, we will outline the scope of this article and introduce a contemporary problem in chemical analysis, which will later serve as an experimental means of illustrating and comparing digital filtering and regression methodologies. As regards scope, the techniques discussed here apply primarily to quantitation of deterministic variables. Also, we limit the discussion of digital filtering to finite impulse response-type filters, and the discussion of multivariate regression to classical least-squares and principal components regression. Readers interested in studying other interesting connections between digital filter theory and multivariate regression should consult References 7–11. Although we will use the independent variable time in our equations, other domains such as wavelength, voltage, and space can be substituted as long as the domains meet the minimal stipulations described later.

The chemical analysis problem we will examine is the quantitation of the *o*-, *m*-, and *p*-xylene isomers in xylene mixtures. Traditionally, GC has been used to analyze xylene (*12*). This technique, however, has certain disadvantages: somewhat lengthy analysis times are required, carrier gas is consumed, columns deteriorate, and the sample generally is not preserved.

Short-wavelength near-IR spectroscopy appears to be an excellent alternative method for xylene analysis because analyses can be done rapidly; no materials are consumed; the instrumentation (a photodiode array spectrograph) is relatively inexpensive and highly reliable; and noninvasive, automated analysis is possible (*13*). However, as can be seen in Figure 1, the near-IR spectra of the three xylene isomers are very similar; thus, a measured spectrum of a xylene mixture must be extensively processed to recover the concentration estimates of the isomers.

Impulse response filter

A time-dependent measurement $x(t)$ can be represented as the sum of the pure analyte signal $s(t)$ and the noise $v(t)$ associated with that signal

$$x(t) = s(t) + v(t) \qquad (1)$$

The magnitude of $s(t)$ is influenced by the state variable initiating the signal. Noise can be defined as any disturbance in the measurement that obscures observance of the pure signal. The noise may be random (white) and/or cyclic in nature. Cyclic noise, sometimes called cyclostationary or periodic noise, is defined as noise that, if present, repeats itself consistently through each experimental cycle. The primary source of cyclic noise encountered in the xylene experiment is spectral interference. In spectroscopically quantifying *o*-xylene, for example, the *m*-xylene and *p*-xylene "signals" interfere with the *o*-xylene signal each time the experiment is done, and therefore they constitute cyclic noise (*2, 14*).

A filter generally can be designed to extract $s(t)$ from $x(t)$, reducing both random and cyclic noise to acceptable levels. Ideally, this filter will also derive from $s(t)$ the related property of interest. For a shift-invariant linear system, the time-dependent filtering process can be mathematically expressed as the convolution of the impulse response filter $h(t)$ with the input measurement $x(t)$ (*15, 16*)

$$y(t) = x(t) * h(t) = \int_{-\infty}^{\infty} x(\tau)\, h(t-\tau)\, d\tau \qquad (2)$$

The * symbol signifies convolution, τ is the delay variable or the time variable of integration, and $y(t)$ is the filter output, which we will later relate to desired state variables. The function $h(t)$ is called the impulse response function of the system because, given an impulse input (delta function), the output is described by $h(t)$.

For the usual analytical experiment, further simplifications of Equation 2 can be made. First, integration need only be done from τ equals 0 to t if the system is one-sided (*15, 16*), that is, if both $x(t)$ and $h(t)$ and thus $y(t)$ only have physical meaning for $t \geq 0$. Second, digital data acquisition makes the discrete form of Equation 2 a better description of the experiment. Equation 3 depicts this discrete convolution, which uses a digital impulse response function $h[n]$ to filter the digital input measurement $x[n]$ to yield the estimated signal $y[n]$

$$y[n] = \sum_{k=0}^{n} x[k]\, h[n-k] \qquad (3)$$

Square brackets denote discrete functions; parentheses are reserved for continuous functions (*15*). Continuous time variables t and τ have been replaced with incremental time variables n and k, respectively. The variable t, which has units of time, and n, which has no dimension, are related by a proportionality factor equal to the time between each discrete increment. The variables τ and k are similarly related. Because of this proportionality, n and k will continue to be referred to as "time" variables.

Figure 2 illustrates the measurement/filtering model described thus far. In Figure 2, three state variables or properties p give rise to three signals (e.g., three chemical concentrations give rise to three instrumental signals). In the measurement process, symbolized by the summation, the pure signals are added to the random and the cyclic noise to generate the measurement. In addition to the cyclic noise labeled v_c, the signals

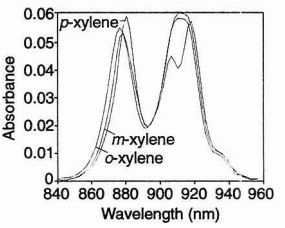

Figure 1. Pure near-IR spectra of *o*-xylene, *m*-xylene, and *p*-xylene isomers.

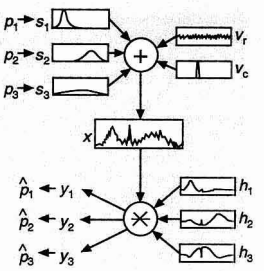

Figure 2. Measurement/filtering scheme.

In the measurement process, the pure signals s_1–s_3, which are induced by the state variables p_1–p_3, are summed with random and cyclic noise v_r and v_c to give the measurement x. Filters h_1–h_3 extract from x, via convolution, the three state variable estimates $\hat{p}_1$–$\hat{p}_3$. The filter outputs y_1–y_3 are directly related to $\hat{p}_1$–$\hat{p}_3$.

hinder quantitation of one another because of their overlapping responses and therefore constitute cyclic noise with respect to each other.

The lower half of Figure 2 depicts the filtering process in which three filters, whose design and implementation will be discussed below, extract the three state variables from the measurement. By convolving each filter with the measurement, an output y is obtained. For some experiments, obtaining the entire output function $y[n]$ with a high signal-to-noise ratio (S/N) is the primary goal. This may be the case, for example, in qualitative analysis, where the entire filtered output spectrum or chromatogram is used to identify distinctive features. However, this article focuses on quantitative analysis in which specific analytical properties such as analyte concentrations are derived from measurements. A key issue, which will be treated later, is the manner by which a property estimate $\hat{p}$, which is a scalar, can be optimally derived from the filtered output $y[n]$ obtained in Equation 3, which is a sequence or a vector.

We have introduced a filter function that can transform an input function to an output function that contains the desired state variable information. In the next sections we explain how a scalar property is estimated from a filter output vector. Systems in which the noise is exclusively random are examined first, followed by a more general and analytically relevant case in which both random and cyclic noise exist.

Matched filtering

Matched filtering is designed to optimally estimate a state variable in the case where the signal arises solely from that state variable, the signal is linearly related to the state variable amplitude, and the noise is random (*2, 14, 17, 18*). The impulse response filter can be shown as

$$h[n] = c\, s[-n] \qquad (4)$$

where c is a constant and $s[-n]$ represents the time-reversed signal unadulterated by noise. The filter is said to be matched because it equals the time-reversed pure signal uncorrupted by noise; thus, when $h[n]$ or $s[-n]$ is convolved with $x[n]$, a cross-correlation is effected between $s[n]$ and $x[n]$

$$y[n] = x[n] * h[n] = x[n] * c\, s[-n] = c\, s[n] \star x[n] \qquad (5)$$

The $\star$ symbol signifies cross-correlation. Equation 6 shows the discrete representation of cross-correlation

$$y[n] = c \sum_{k=0}^{n} s[k]\, x[n+k] \qquad (6)$$

We will justify the above form of the impulse response filter and show how it leads to a simplification of Equations 3 and 6, changing a convolution or a cross-correlation, which technically is a vector/matrix multiplication, to a simple dot product of vectors.

The optimal estimate of an analytical state variable can be derived from the filtered output if the quantitative experiment is deterministic, which means that each experiment takes place over an identical incremental range (of time, frequency, or wavelength). For such experiments the deterministic signal consistently repeats itself

$$s[k] = s[mN + k] \qquad (7)$$

Here N is the experimental cycle time, and the whole number m is the cycle number. The noise, meanwhile, varies randomly. For deterministic experiments the cross-correlation function in Equation 6 reaches a maximum value when $n = N$ (*17*). This cross-correlation maximum $y[N]$ (a scalar) is described by the equation

$$y[N] = c \sum_{k=0}^{N} s[k]\, s[k] + c \sum_{k=0}^{N} s[k]\; v[N+k] \qquad (8)$$

which is obtained by substituting Equations 1 and 7 into Equation 6. Equation 8 is essentially the sum of two dot products. The first dot product is between the signal and itself, which results in a positive squared estimate of the true signal. Because the signal and the random noise are orthogonal, the second dot product approaches zero as N becomes large. Thus it becomes apparent why the maximum cross-correlation occurs at $n = N$: At this time the cross-correlation function approaches a noise-free squared estimate of the pure signal. Any segment of the random noise function should be orthogonal to the signal; therefore, this second dot product approaches zero regardless of the incremental time offset inside the brackets. To simplify Equation 8, $v[k]$ is substituted for $v[N + k]$ to give

$$y[N] = c \sum_{k=0}^{N} s[k]\, s[k] + c \sum_{k=0}^{N} s[k]\, v[k] = c \sum_{k=0}^{N} s[k]\, x[k] = p \qquad (9)$$

Because the cross-correlation is maximum when $n = N$, the signal estimate, which results from the single cross-correlation at $n = N$, has a maximum S/N. This cross-correlation maximum $y[N]$ provides the optimum property estimate p (*19*); the entire cross-correlation summation for all values of $y[n]$ need not be solved.

At this stage it is important to remember that although the previous derivations were performed in the time domain, analogous representations can be formulated in any pertinent domain. This is made possible by the minimal restrictions imposed, which require the system to be linear, shift-invariant, one-sided, and deterministic. For systems that obey these constraints, complicated convolutions and cross-correlations (Equations 3 and 6) can be simplified to dot products.

These constraints may take on slightly different meanings under different domains. The xylene example considers spectral data in the wavelength domain. The one-sidedness argument is satisfied in this domain because the signal at any wavelength is independent of the signal at another wavelength, and the spectrum always starts at some initial wavelength. The deterministic condition is equivalent to requiring that spectra be taken over identical wavelength regions, which is typically the case in quantitative analysis.

When $s[n]$ and therefore $h[n]$ are not precisely known beforehand, the matched filter $h[n]$ can be experimentally derived by ensemble-averaging numerous measurements (*17*). Because we have assumed that noise is random in this case, the noise cancels upon ensemble-averaging while the signals add coherently. If a sufficient number of measurements are averaged, $h[n]$ will closely resemble the time-reversed pure signal and the convolution of $x[n]$ and $h[n]$, or the cross-correlation of $s[n]$ and $x[n]$, will render the optimal property estimate.

Kalman innovation filtering

Matched filtering is inadequate if cyclic noise exists in addition to the random noise (i.e., if the $v(t)$ term in Equation 1 includes both cyclic and random components). Recall that chemical interferences constitute a form of cyclic noise. A Kalman innovation filter (KIF) has been recommended for state variable estimation in this case (*2, 14, 17*). The KIF should not be confused with the Kalman filter, an infinite impulse re-

sponse filter (*3, 8, 20*). The KIF removes the effects of interfering noise by creating an impulse response function that is independent of, and orthogonal to, all cyclic noise components. Thus, when the impulse response filter operates on the measurement, it cancels the cyclic interferences while accurately estimating the signal. To create a KIF, the pure signal and the cyclic noise components must be known.

The first step in designing a KIF for one signal component is to "whiten" $x[n]$, which now possesses random and cyclic noise, thus creating an innovation $i[n]$. The function $i[n]$ is similar to $x[n]$ in that it contains separate signal and noise components $i_s[n]$ and $v[n]$

$$i[n] = i_s[n] + v[n] \quad (10)$$

but $i[n]$ is different from $x[n]$ in that the signal and noise parts of $i[n]$ are orthogonal to each other. In other words, the effect of "whitening" is to make the signal component orthogonal to the cyclic interfering noise, so that the interferences are removed from $x[n]$ upon application of the filter. The term "whitening" arises from the fact that because cyclic noise is eliminated, only white noise remains. The advantages of this "whitening" process will soon become apparent.

Once the noise components of $i[n]$ have been made random with respect to the signal component, the innovation simply becomes an extension of the matched filter. For $i[n]$ the matched KIF is

$$h[n] = c\, i_s[-n] \quad (11)$$

where c again is a constant. The function $h[n]$ is merely the time-reversed part of $i[n]$ that "matches" the desired signal yet is orthogonal to the noise (*14, 17*). Therefore, when cyclic noise exists, Equation 5 becomes

$$y[n] = x[n] * c\, i_s[-n] = c\, i_s[n] \star x[n] \quad (12)$$

An argument similar to that developed for the matched filter case above can be made that the best property estimate occurs at $n = N$, resulting in

$$p = c \sum_{k=0}^{N} i_s[k]\, x[k] \quad (13)$$

The rationale for creating the orthogonal innovation becomes evident when Equation 1 is substituted into Equation 13 to give

$$p = c \sum_{k=0}^{N} i_s[k]\, s[k] + i_s[k]\, v[k] \quad (14)$$

In Equation 14 a large correlation exists between i_s and s, whereas the cross-correlation or dot product between the orthogonal functions i_s and v approaches zero as N goes to infinity. Recall that $v[n]$ in this situation is both random and cyclic noise. Hence, the state variable p is optimally estimated from the signal, whereas both random and cyclic noise are largely disregarded.

However, as with matched filtering, the individual signal being estimated in the presence of cyclic and random noise must contain all the information necessary to compute p. For example, if concentration were the property being estimated, a spectrum, chromatogram, or voltammogram of each pure analyte and interfering species would be required to formulate the KIF. These pure signals independently contain all the information necessary to determine analyte concentrations. If, however, the desired state variable were gasoline octane number (*21*) or some other complex property, matched filters and KIFs could not be used to directly estimate the property. Gasoline octane number depends, in a complex manner, on several pure chemical components (e.g., branched and aromatic hydrocarbons or additives). Without knowing what a pure octane number signal looks like, and which interfering species are present and how they influence octane number, a KIF cannot be prepared. Quantitative analysis of such properties necessitates the use of calibration-based regression methods, which will be discussed later.

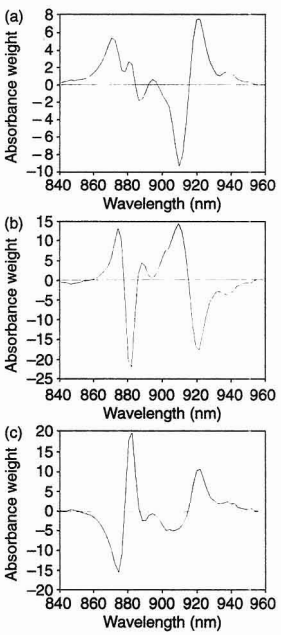

Figure 3. KIFs for (a) *o*-xylene, (b) *m*-xylene, and (c) *p*-xylene.

Experimental formation of the KIF is straightforward if the pure analyte and interfering species' signal features are known and if they interact linearly. In this situation the analyte signal $s[n]$ is made orthogonal to the cyclic noise $v[n]$, yielding $i_s[n]$. The Gram–Schmidt algorithm is generally used (*2, 22*). Although most descriptions of the KIF are limited to the case of a signal in the presence of one type of interfering species, the KIF can handle multiple known signals and interfering species.

To do so, an innovation filter is required for each property being quantified. Each component's KIF must be orthogonal to all cyclic noise components, which include interfering component signals and systematic cyclic noise. This means that the Gram–Schmidt orthogonalization process must be repeated for each component. In other words, simply forming one orthogonal basis set, as most orthogonalization algorithms do, is not sufficient; each basis vector (KIF) must be mutually orthogonal to all other interferences. In addition to this constraint, each basis vector must be properly scaled (*17*).

In dealing with multicomponent mixtures or systems wherein several properties are desired, it is convenient to expand the summations of discrete sequences (which are equivalent to vector dot products) to matrix/vector multiplications. In the following notation, vectors and matrices are represented by boldface lowercase and boldface uppercase symbols, respectively. By lumping c into i_s, Equation 13, which shows how the KIF extracts state variables from measurements, can be written as

$$p = \boldsymbol{x}\, \boldsymbol{i}_s \quad (15)$$

Here, $\boldsymbol{x}$ is the measurement vector with dimensions of one by N; $\boldsymbol{i}_s$ is the KIF, which is N by one in size; and p is the scalar property estimated by the KIF. Equation 15 can be expanded for multicomponent systems by incorporating an orthogonal filter for each component property to be estimated. Accordingly,

$$\boldsymbol{p} = \boldsymbol{x}\, \boldsymbol{I}_s \quad (16)$$

where the columns of the $\boldsymbol{I}_s$ matrix contain the KIF of each component; $\boldsymbol{I}_s$ has dimensions N by the number of components; and $\boldsymbol{p}$ becomes the property vector, which is one by number of components in size.

At this stage it is instructive to return to the xylene analysis example introduced earlier. Recall that only slight shifts in the wavelength and the relative intensity of the two primary peaks discriminate the pure spectra. Because the spectra are so closely correlated (because each xylene isomer acts as cyclic noise when quantifying the other isomers), matched filtering is not able to accurately estimate the isomer concentrations. Because the KIF can extract information when both random and cyclic noise are present, quantitation of each xylene isomer in the multicomponent mixture is possible.

KIFs were calculated for the three xylene isomers by orthogonalizing and properly scaling each pure component spectrum with respect to the others. These filters are shown in Figure 3. The KIFs were used to quantify the xylene isomer concentrations of 20 different mixtures whose spectra are shown in Figure 4. To evaluate the efficacy of filters in general, a standard error of prediction (SEP) is often calculated as

$$\mathrm{SEP} = \sqrt{\frac{\sum_{a=1}^{q} (p_a - \hat{p}_a)^2}{q}} \qquad (17)$$

where q is the number of samples; a is the sample index; p_a represents the true state variable (isomer concentration) in the ath sample, which is determined by a reference method; and $\hat{p}_a$ signifies the state variable predicted by the KIF. A SEP for each isomer concentration, calculated using the KIF, is listed in Table I. As Equation 17 shows, the SEP is similiar to a standard deviation. It is a root-mean-square error estimate of how well a filter estimates a state variable. In Table I, therefore, the numbers reported are absolute error estimates that reflect the amount of uncertainty associated with predicted xylene isomer concentrations. Because the xylene concentrations are measured in volume percent, these SEPs also have the units of volume percent.

A major disadvantage of the KIF via Gram–Schmidt orthogonalization is that the analyte and the interfering species' signals must be exactly known to compute $\boldsymbol{I}_s$. For example, if we supposed that only two components were present in the xylene mixture, the KIF would fail miserably. This assumption might naively be made because the *m*-xylene and *p*-xylene spectra are so similar. Table I indicates that the SEP values for the KIF using only an *o*-xylene and *m*-xylene model are unacceptable, particularly for *m*-xylene. Hence, the KIF is useful only when all the pure signals are known.

Unfortunately, exact aspects of the signal and the cyclic noise are frequently unknown. Under these circumstances multivariate regression provides a means for deriving the filter functions. In the following sections we will explore classical and inverse least-squares regression as well as the relationship between regression and the filtering concepts developed thus far.

Classical least squares

The classical least-squares (CLS) model for a multicomponent system assumes that a measurement is made up of linearly independent signals, each multiplied by a factor representing the degree to which that signal contributes to the overall measurement. The CLS model, also known as the K-matrix model (*23*), may be written as

$$\boldsymbol{x} = \boldsymbol{p}\,\boldsymbol{S} \qquad (18)$$

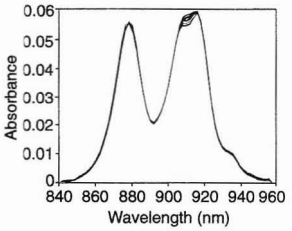

Figure 4. Near-IR spectra of xylene mixtures.

$\boldsymbol{S}$ contains the independent untainted signals of each component and the cyclic noise, and it has dimensions of number of components by number of time increments (or whatever measurement domain is being employed). The vectors $\boldsymbol{x}$ and $\boldsymbol{p}$ were defined in Equations 15 and 16, respectively. When signal and noise characteristics are known (when S is known), the desired properties of an unknown sample can be determined by solving Equation 18 for the least-squares estimate of $\boldsymbol{p}$

$$\boldsymbol{p} = \boldsymbol{x}\,\boldsymbol{S}^{+} \qquad (19)$$

$\boldsymbol{S}^{+}$ represents the pseudo-inverse of $\boldsymbol{S}$ and in this case equals $\boldsymbol{S}^{\mathrm{T}}(\boldsymbol{S}\boldsymbol{S}^{\mathrm{T}})^{-1}$, where $\boldsymbol{S}^{\mathrm{T}}$ denotes the transpose of $\boldsymbol{S}$ and $(\boldsymbol{S}\boldsymbol{S}^{\mathrm{T}})^{-1}$ signifies the inverse of $\boldsymbol{S}\boldsymbol{S}^{\mathrm{T}}$. The pseudo-inverse of a matrix is often derived by performing a singular value decomposition (SVD) on the matrix to be inverted (*24*). This decomposition and its effects will be described in the following section.

Although the CLS and the KIF approaches use different algorithms to produce $\boldsymbol{S}^{+}$ and $\boldsymbol{I}_s$, the columns of $\boldsymbol{S}^{+}$ are equivalent to the mutually orthogonal signal(s) and the cyclic noise that make up the innovation filters $\boldsymbol{I}_s$ (*25*). Multiplication of $\boldsymbol{S}$ by $\boldsymbol{S}^{+}$ ($\boldsymbol{S}\,\boldsymbol{S}^{+}$) ideally yields the identity matrix, as does $\boldsymbol{S}\,\boldsymbol{I}_s$. This is the same as saying that the jth column of $\boldsymbol{S}^{+}$ or $\boldsymbol{I}_s$ is orthogonal to all the rows of $\boldsymbol{S}$ (i.e., each signal and cyclic noise component, except for the jth row of $\boldsymbol{S}$, which is the signal whose state variable is being estimated). Because of the virtual equivalence of the CLS and the KIF methods, it is not surprising that their prediction abilities are identical. Table I shows the SEP values for each xylene isomer derived via CLS.

CLS can be used to fit linear combinations of pure component signals to measurements (i.e., curve fitting). For example, from one of the xylene

Table I. Comparison of standard error of prediction for xylene isomers computed using the KIF, the KIF two-component model, CLS, and PCR[a]

Method	SEP (vol %)		
	o-xylene	*m*-xylene	*p*-xylene
KIF	1.49	0.85	0.62
KIF (two-component model)	2.49	31.55	
CLS	1.49	0.85	0.62
PCR	1.14	2.45	1.87

[a]Actual concentration ranges were as follows: *o*-xylene, 12–28 vol %; *m*-xylene, 38–68 vol %; and *p*-xylene, 12–36 vol %. Individual volume percents for a given sample equal 100%.

mixture spectra shown in Figure 4, it is possible to estimate how much of the measurement arises from *o*-xylene, *m*-xylene, and *p*-xylene. The unknown spectral measurement can be decomposed into its pure component spectra if they are known. $\boldsymbol{S}^+$ is calculated from the pure spectra $\boldsymbol{S}$, then multiplied by the unknown spectrum $\boldsymbol{x}$ to give $\boldsymbol{p}$, the state variables (concentrations) of each isomer (Equation 19).

Figure 5a shows an example of a mixed xylene measurement. Underneath the measurement lie the pure spectra multiplied by their appropriate concentrations, which were derived from Equation 19. The sum of the three weighted spectra approximates the measurement. Figure 5b shows the difference between the overall measurement and the sum of the three properly weighted pure spectra. Residual analysis reveals whether random noise is the sole discrepancy between the measurement and the model, as it seems to be here, or whether some other component—perhaps cyclic noise not modeled—contributes to the measurement.

A disadvantage of CLS, as with the KIF, is that it is limited in the types of properties it can estimate. Because the CLS model assumes that pure signals are multiplied by separable state variables to give a measurement, each state variable must originate from one and only one pure component signal. Properties influenced by several components in an unknown manner cannot be estimated. Another drawback to which we have already alluded is that CLS, like the KIF and matched filtering, requires knowledge of and access to the pure signals as well as the cyclic noise before the filters can be generated. Frequently, however, the exact aspects of the signal and cyclic noise are not known.

Principal components regression (PCR), an inverse least-squares method, is introduced in the next section. We will show that PCR and similar techniques provide a means for deriving filters when signal and noise characteristics are inaccessible, and that PCR can predict complex state variables that are related to the pure chemical components in some way not known beforehand.

Inverse least-squares regression

Inverse least-squares regression models such as PCR assume that a regression vector $\boldsymbol{b}$ maps a measurement to a scalar property

$$p = \boldsymbol{x}\ \boldsymbol{b} \qquad (20)$$

Before Equation 20 can be used to estimate state variables, $\boldsymbol{b}$ must be derived through calibration, a process whereby measurements of several chemical mixtures containing varying amounts of analyte and cyclic noise components are acquired. These measurements ($\boldsymbol{x}$ row vectors) form a measurement matrix $\boldsymbol{X}$. In addition to experimentally measuring $\boldsymbol{X}$, the state variable of interest for each individual measurement $\boldsymbol{x}$ must be independently measured by an accurate reference method. These property data form the vector $\boldsymbol{p}$. The model for calibrating a single state variable is

$$\boldsymbol{p} = \boldsymbol{X}\ \boldsymbol{b} \qquad (21)$$

where $\boldsymbol{p}$ has dimensions of number of samples by one, $\boldsymbol{X}$ has dimensions of number of samples by number of time increments (or whatever domain is used), and $\boldsymbol{b}$ has dimensions of number of time increments by one. If several state variables are of interest, separate regression vectors can be determined for each. In this case, $\boldsymbol{b}$ and $\boldsymbol{p}$ become matrices instead of vectors.

Given the calibration model in Equation 21, $\boldsymbol{b}$ can be determined by

$$\boldsymbol{b} = \boldsymbol{X}^+\ \boldsymbol{p} \qquad (22)$$

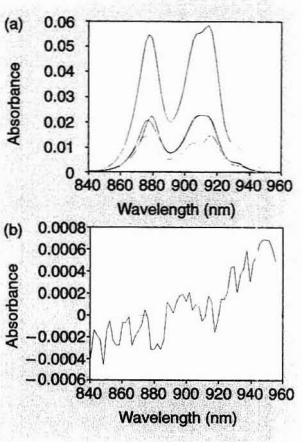

Figure 5. Curve-fitting the pure component xylene spectra to a measurement via CLS.

(a) Mixed xylene measurement (top) and pure spectra (bottom) multiplied by their appropriately estimated concentrations. Ideally, the three isomer spectra should add up to the mixture spectrum. (b) Difference between the overall measurement and the sum of the three properly weighted pure spectra. Ideally, residuals are random.

where $\boldsymbol{X}$ and $\boldsymbol{p}$ are measured experimentally. Derivation of $\boldsymbol{X}^+$ is what sets PCR apart from other inverse least-squares regression methods such as partial least-squares regression (*4*, *6*). In PCR the first step in determining $\boldsymbol{X}^+$ is to perform an SVD (*24*, *26*) on $\boldsymbol{X}$, which results in

$$\boldsymbol{X} = \boldsymbol{U}\,\Sigma\,\boldsymbol{V}^{\mathrm{T}} \qquad (23)$$

The purpose of decomposing $\boldsymbol{X}$ into $\boldsymbol{U}$, Σ, and $\boldsymbol{V}^{\mathrm{T}}$ is twofold. First, SVD yields column-orthogonal ($\boldsymbol{U}$ and $\boldsymbol{V}$) and diagonal (Σ) matrices; therefore, inversion of $\boldsymbol{U}$, Σ, and $\boldsymbol{V}$ is a stable, well-conditioned operation. Thus

$$\boldsymbol{X}^+ = (\boldsymbol{U}\,\Sigma\,\boldsymbol{V}^{\mathrm{T}})^+ = \boldsymbol{V}\Sigma^{-1}\boldsymbol{U}^{\mathrm{T}} \qquad (24)$$

In addition to making a stable inversion possible, SVD provides a means of reducing noise. At the heart of SVD and its noise reduction capabilities lies the concept of factors or principal components. A factor of $\boldsymbol{X}$ is a linear combination of the original sample or time variables that span $\boldsymbol{X}$ (*4*). Being consistent with the matrix dimensions assigned thus far, we see that the columns of $\boldsymbol{U}$ contain orthogonal factors that span the property variance of $\boldsymbol{X}$, whereas the columns of $\boldsymbol{V}$ constitute an orthogonal basis spanning the time variance of $\boldsymbol{X}$. Along the diagonal of Σ are weights associated with these factors. The weights represent the degree to which each factor contributes to the overall variance of $\mathbf{X}$.

The utility of SVD stems from the fact that the principal components are formulated in a way that the first principal component spans as much variance as possible (i.e., the first element of Σ is as large as possible, and so on with the second, third, etc.). By analyzing the magnitude of the elements along the diagonal of Σ, and, more importantly, the structure (or lack of structure) of the principal components, one can determine how many factors model signal or cyclic noise and how many model random noise. If it can be determined, for example, that the first three factors model the measurement space adequately, the remaining factors can be deleted. This reduces the number of columns in $\boldsymbol{U}$ and $\boldsymbol{V}$ as well as the number of rows and columns in Σ.

This reduction of the dimensionality of $\boldsymbol{U}$, Σ, and $\boldsymbol{V}$ precedes the inversion shown in Equation 24. Because the higher order principal components represent noise in the system, their removal reduces the overall noise, enhances the prediction ability of PCR, and reduces the chance of overfitting the data to noise (but also

adds bias to the model). Factor analysis, therefore, can be thought of as an information reduction process. Of course, one hopes that only the noise information is reduced, and not the signal.

Equipped with the noise-reduced $\boldsymbol{X}^+$ and the experimental $\boldsymbol{p}$, we can derive $\boldsymbol{b}$ from Equation 22. The regression vector $\boldsymbol{b}$ represents the optimal way to filter or multiply an input measurement vector $\boldsymbol{x}$ (i.e., a row of $\boldsymbol{X}$, such that a desired scalar property $\boldsymbol{p}$ can be estimated when random and/or cyclic noise are present) when one does not know the signal and noise characteristics beforehand. Connecting the notations of filter theory and multivariate regression, $\boldsymbol{b}$ is equivalent to the KIF $i_s[n]$ or $\boldsymbol{i}_s$, the part of $x[n]$ or $\boldsymbol{x}$ that matches the signal yet is simultaneously orthogonal to the noise and other signal components. A single cross-correlation summation at $n = N$ of $i_s[n]$ with $x[n]$, or the dot product of $\boldsymbol{b}$ with $\boldsymbol{x}$, produces the optimal property estimate for the single component.

To illustrate how a calibration-based PCR experiment generates regression vectors and then predicts properties by using these regression vectors, consider the xylene example. The spectra of the 20 xylene mixtures in Figure 4 form the calibration measurement matrix $\boldsymbol{X}$. The $\boldsymbol{p}$ vector for each xylene isomer is equivalent to the volume percent concentration of that isomer in each mixture. The SVD of $\boldsymbol{X}$, followed by analysis of the principal components, reveals that three linearly independent components span $\boldsymbol{X}$. This is not surprising, because the mixtures are composed of three isomers.

More than 99% of the variance in $\boldsymbol{X}$ is spanned by these three factors. Additional factors derived from the matrix decomposition are assumed to model random noise in the system; therefore, these factors are removed. The dimension-reduced matrices $\boldsymbol{U}$, Σ, and $\boldsymbol{V}$ are inverted and reconstructed to give $\boldsymbol{X}^+$ (Equation 24), and $\boldsymbol{X}^+$ is multiplied by each isomer's $\boldsymbol{p}$ to give a regression vector for each isomer. These regression vectors are shown in Figure 6.

To quantify the efficacy of calibration-based PCR, leave-one-out cross-validation was performed (*6*). In cross-validation a regression vector for each isomer is calculated with one calibration sample's spectrum and with concentration values omitted from $\boldsymbol{X}$ and $\boldsymbol{p}$, respectively. A regression vector for each isomer is derived, and each resulting $\boldsymbol{b}$ is then used to predict the concentration of the sample omitted from $\boldsymbol{p}$, using the spectrum of the sample omitted from $\boldsymbol{X}$. Cross-validation tests the method's ability to predict properties of samples not specifically included in the calibration set.

The SEP generated from cross-validation can be calculated from Equation 17 by defining $\hat{p}_a$ as the concentration predicted from the cross-validation experiment with the ath sample omitted from the calibration set. SEP values for each xylene isomer derived using the PCR calibration model are listed in Table I. As can be seen, the PCR performance is a bit inferior to that of CLS or the KIF. However, in designing the filter, PCR only requires knowledge of the component(s) of interest to accurately quantify the analyte's concentration. If a two-component model were assumed in the xylene example, PCR (unlike CLS or the KIF) would still accurately predict the *o*-xylene and *m*-xylene isomer concentrations as long as the model spanned the variance of the *p*-xylene isomer in the data.

A visual comparison of the PCR vectors with those of the KIF (see Figures 3 and 6) reveals that both methods generate similar filters. The calibration-based PCR filters appear to possess more noise than the KIFs, and the SEP values for the KIF are, in general, better than those of PCR. This apparent experimental superiority of the KIF over PCR may stem from two reasons.

First, from a numerical analysis standpoint, some experimental calibration designs are statistically superior to others. It is desirable to choose an experimental design that poses the calibration equation in the best conditioned manner. It can be shown that the KIF or CLS methods incorporate the best possible experimental design (i.e., they use pure known signals to derive the filters). Experimental designs based on calibration (methods that attempt to span a large measurement space by using many different mixtures) inherently are more poorly conditioned.

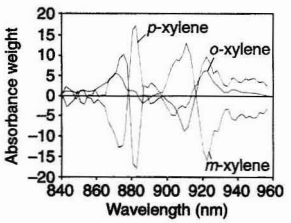

Figure 6. Regression vectors calculated via PCR for *o*-xylene, *m*-xylene, and *p*-xylene.

The second factor favoring the KIF and CLS is related to experimental uncertainty. For the xylene analysis, the experimental uncertainty in each $\boldsymbol{p}$ for the KIF is extremely low because the concentrations are pure. However, to experimentally determine each $\boldsymbol{p}$ via calibration, each isomer concentration in each mixture must be measured either by preparing the volumetric mixtures or by using some other independent reference method. Obviously, because calibration-based methods will incorporate more measurement uncertainty into the $\boldsymbol{p}$ vectors, they will induce more error in the predicted state variable. For the above reasons, when the pure signals are well known and the system is well understood, the KIF or CLS using pure signals should provide improved prediction ability over that of calibration-based methods.

PCR can estimate a vast range of properties that the KIF and CLS cannot evaluate. The inverse model allows properties to depend on any chemical component contributing to the measurement. For example, inverse regression methods have been coupled with near-IR spectroscopy to predict complex state variables such as hydroxide ion concentration (*27*), intrinsic viscosity of polymer blends (*28*), and gasoline octane number (*21*). These properties cannot be directly determined from the pure spectral signals, for various reasons. The problem with determining the hydroxide ion concentration is that it is impossible to directly measure the pure spectrum of hydroxide in solution because of the interfering presence of water. Spectroscopic analysis of polymer viscosity is hindered by the fact that it is not obvious how polymer viscosities are related to polymer spectra.

The difficulty with spectroscopic octane number determination is understanding the correlation between octane number and the numerous signals of the chemical components. To perform octane number analysis spectroscopically using CLS, one would need to independently determine the concentration of the hundreds of pure components that make up gasoline and then see how these components were correlated to the octane number. Spectroscopic octane number analysis by PCR requires only one independent reference measurement (the octane number) for

each gasoline sample. Much work, however, should be done to verify that the calibration step uses a valid experimental design. Ideally, each chemical component should vary independently over a broad range within the calibration model. PCR, then, can determine how many principal components are necessary to span the measurement space and accurately predict the octane number. When done definitively, this experimental design phase can be nearly as laborious as the CLS method.

We should point out that preprocessing data using mean-centering (*4*, *13*) or derivative (*1*, *13*) methods often results in improved SEP values. In particular, for xylene quantitation using PCR, the SEP for all isomers can be reduced to below 0.50% if one takes the second derivative of the xylene measurements prior to principal components analysis and regression. The second derivative removes irreproducible instrumental baseline offsets and slopes from the spectra. Because our purpose here was to explain and critically compare digital filtering and multivariate regression, rather than to estimate xylene concentrations with minimal error, we have omitted further discussion of data preprocessing.

Summary

We have described the similarities and differences between finite impulse response digital filtering and multivariate regression as they pertain to quantitative property estimation. These techniques formulate a filter that operates on an input measurement to give a desired state variable estimate as an output. Bialkowski has shown that selection of the correct filter is based on one's knowledge of the signal and noise characteristics (*2*). He showed that if the signal and the noise are precisely known, either matched filtering (random noise only) or the KIF (both random and cyclic noise) methodologies optimally filter the data. Although this is true, caution should be used when following this logic. If something in the system is not perfectly understood and modeled when the filter is constructed, errors may result in property estimation. Furthermore, these filtering methods are not useful for the case commonly encountered in quantitative analysis in which a complete understanding of the system is not at hand.

We have shown that multivariate regression provides a powerful recipe for designing finite impulse response filters, which accurately extract properties from data contaminated with both random and cyclic noise. PCR uses a statistically designed calibration experiment to create property extraction filters and therefore does not require a full understanding of the signals and noise a priori. The calibration step of PCR requires only that an independent reference method determine the properties of the component(s) of interest, but great care must be taken to assure that the calibration model spans the variance of the other components in the data.

Unlike the KIF and CLS, inverse regression techniques can predict properties that depend on multiple components in the system. Xylene concentrations, properties that depend only on the individual component signals, were estimated to compare the methods. The KIF, CLS, and PCR methods were all capable of es-

timating concentrations with a few percent error. However, were we to quantify some other property that depended on multiple signal components, the KIF and CLS would have failed. Therefore, calibration-based inverse regression methods offer improved methods of filter design when the signal and noise characteristics of a system are not totally known and when complex properties are being estimated.

The authors acknowledge the Center for Process Analytical Chemistry and the National Science Foundation for financial support. M. B. Seasholtz, B. M. Wise, N. L. Ricker, and the anonymous reviewers are thanked for their valuable critiques of this article.

References

(1) Williams, P. C.; Norris, K. H. *Near-Infrared Technology in the Agricultural and Food Industries*; American Association of Cereal Chemists: St. Paul, MN, 1987.
(2) Bialkowski, S. E. *Anal. Chem.* **1988**, *60*, 355 A–361 A.
(3) Bialkowski, S. E. *Anal. Chem.* **1988**, *60*, 403 A–413 A.
(4) Beebe, K. R.; Kowalski, B. R. *Anal. Chem.* **1987**, *59*, 1007 A–1017 A.
(5) Martens, H.; Naes, T. *Multivariate Calibration*; Wiley: New York, 1989.
(6) Kowalski, B. R.; Seasholtz, M. B. *J. Chemom.* **1991**, *5*, 129–45.
(7) Wise, B. M.; Ricker, N. L.; Veltkamp, D. F.; Kowalski, B. R. *Process Control Qual.* **1990**, *1*, 41–51.
(8) Brown, R. G. *Introduction to Random Signal Analysis and Kalman Filtering*; Wiley: New York, 1983.
(9) Brown, S. D. *Chemom. Intell. Lab. Syst.* **1991**, *10*, 87–105.
(10) Vanslyke, S. J.; Wentzell, P. D. *Anal. Chem.* **1991**, 2512–19.
(11) Small, G. W.; Harms, A. C.; Kroutil, R. T.; Ditillo, J. T.; Loerop, W. R. *Anal. Chem.* **1990**, 1768–77.
(12) *1989 Annual Book of ASTM Standards*; American Society for Testing and Materials: Philadelphia, PA, 1989.
(13) Lysaght, M. J. Ph.D. Dissertation, University of Washington, Seattle, 1991.
(14) Papoulis, A. *Probability, Random Variables, and Stochastic Processes*, 2nd ed.; McGraw-Hill: New York, 1984.
(15) Jackson, L. B. *Signals, Systems, and Transforms*; Addison-Wesley: Reading, MA, 1991.
(16) Papoulis, A. *The Fourier Integral and Its Applications*; McGraw-Hill: New York, 1962.
(17) Bialkowski, S. E. *Rev. Sci. Instrum.* **1987**, *58*, 687–95.
(18) Dyer, S. A.; Hardin, D. S. *Appl. Spectrosc.* **1985**, *39*, 655–62.
(19) Bialkowski, S. E. *Appl. Spectrosc.* **1988**, *42*, 807–11.
(20) Candy, J. V. *Signal Processing—The Model-Based Approach*; McGraw-Hill: New York, 1986.
(21) Kelly, J. J.; Barlow, C. H.; Jinguji, T. M.; Callis, J. B. *Anal. Chem.* **1989**, *61*, 313–20.
(22) Anton, H. *Elementary Linear Algebra*, 4th ed.; Wiley: New York, 1984.
(23) Brown, C. W.; Lynch, P. F.; Obremski, R. J.; Lavery, D. S. *Anal. Chem.* **1982**, *54*, 1472–79.
(24) Golub, B. H.; Van Loan, C. F. *Matrix Computations*, 2nd ed.; Johns Hopkins University: Baltimore, 1989.
(25) Brown, C. W.; Obremski, R. J.; Anderson, P. *Appl. Spectrosc.* **1986**, *40*, 734–42.
(26) Wold, S. *Chemom. Intell. Lab. Syst.* **1987**, *2*, 37–52.
(27) Phelan, M. K.; Barlow, C. H.; Kelly, J. J.; Jinguji, T. M.; Callis, J. B. *Anal. Chem.* **1989**, *61*, 1419–24.
(28) Zhu, C.; Hieftje, G. M. *Appl. Spectrosc.* **1992**, *46*, 69–72.

Chris L. Erickson (left) is pursuing his Ph.D. in analytical chemistry at the University of Washington. He earned his B.S. and M.S. degrees in 1987 and 1989, respectively, from Utah State University. His research interests include chemical analysis using visible and near-IR interferometry, digital filtering, multivariate analysis, and photothermal spectroscopy.

James B. Callis (right) is professor of chemistry and adjunct professor of bioengineering at the University of Washington. He received his B.S. degree in 1965 from the University of California at Davis and his Ph.D. in physical chemistry in 1970 from the University of Washington. His research focuses primarily on improving instrumentation for optical spectroscopy, including studies in phosphorescence, near-IR spectroscopy, imaging, and noninvasive reaction monitoring.

Michael J. Lysaght is assistant professor of chemistry at the U.S. Air Force Academy. He received his B.S. degree from George Mason University (VA) in 1979 and his Ph.D. from the University of Washington in 1991. His research interests focus on instrumentation, fundamentals, and applications of near-IR spectroscopy.

MEETINGS

The 44th Pittsburgh Conference and Exposition on Analytical Chemistry and Applied Spectroscopy will be held at the Georgia World Congress Center, Atlanta, GA, March 8–12. The technical program will feature approximately 46 symposia and a number of poster sessions. The Exposition of Modern Laboratory Equipment, showing the latest instruments and related chemicals, equipment, and publications, will include 1000 companies in 2900 booths. The following symposia are scheduled as part of the technical program:

MONDAY MORNING

Bomem–Michelson Award Symposium
Arranged by D. M. Haaland, Sandia National Laboratories

Modern Techniques in GC
Arranged by H. M. McNair, Virginia Polytechnic Institute & State University, and C. Cramers, Eindhoven Technical University

New Frontiers in MS
Arranged by F. W. McLafferty, Cornell University

Nonmedical Applications of NMR Imaging
Arranged by M. Gordon, ATI Instruments, and H. L. Retcofsky, U.S. Department of Energy—PETC (retired)

Recent Advances in Imaging Techniques for Surface Analysis: How Small Can We Go?
Arranged by B. R. Strohmeier, Aluminum Company of America Technical Center

MONDAY AFTERNOON

Inside the Single Cell
Arranged by J. V. Sweedler, University of Illinois

Microwave Sample Preparation: The State of the Art
Arranged by H. M. Kingston, Duquesne University

Promising Analytical Techniques on the Horizon (dedicated to the memory of L. B. Rogers)
Arranged by A. J. Bard, The University of Texas, and J. F. Coetzee, University of Pittsburgh

Step-Scan Fourier Transform Spectroscopy
Arranged by R. A. Palmer, Duke University, and C. Marcott, The Procter & Gamble Company

SFC: Solutions to Real-World Problems
Arranged by T. L. Chester, The Procter & Gamble Company

James L. Waters 4th Annual Symposium Recognizing Pioneers in the Development of Analytical Instrumentation: NMR
Arranged by S. Manocha, PPG Industries, Inc.

TUESDAY MORNING

Dal Nogare Award Symposium: Future Perspectives of Microseparation Methods
Arranged by M. E. McNally, E. I. du Pont de Nemours & Co.

Frontiers in Forensic Science
Arranged by W. L. Hearn, Dade County Medical Examiner Department

Immunoanalytical Chemistry
Arranged by L. G. Bachas, University of Kentucky, and G. S. Sittampalam, Lilly Research Laboratories

Industrial Hygiene: A Chemist's Perspective
Arranged by R. S. Danchik, Aluminum Company of America

Pittsburgh Spectroscopy Award and the Maurice F. Hasler Award Symposium
Arranged by N. R. Dando, Aluminum Company of America

TUESDAY AFTERNOON

Advances in Raman Spectroscopy
Arranged by S. A. Asher, University of Pittsburgh

Immunoanalysis in Food Safety
Arranged by R. A. Durst, Cornell University

New Approaches for Rapid Sample Analysis
Arranged by M. V. Buchanan, Oak Ridge National Laboratory

Pittsburgh Analytical Chemistry Award Symposium
Arranged by R. J. Carlson, Consol Inc.

WEDNESDAY MORNING

Atmospheric Chemistry I
Arranged by J. W. Birks, University of Colorado

Comparability and Traceability: An Aid to International Trade
Arranged by B. King, LGC

Keene P. Dimick Award in Chromatography Symposium: Chromatography, MS, Electrophoresis, and Biomedicine
Arranged by G. A. Bello, PPG Industries, Inc.

Near-IR Spectroscopy: Industrial and Clinical Trials and Tribulations
Arranged by N. R. Dando, Aluminum Company of America, and R. Lodder, University of Kentucky Medical Center

New Approaches to Selectivity in (Bio)Sensors
Arranged by S. G. Weber, University of Pittsburgh

Science and Scientists: Image Shaping in the Mass Media
Arranged by R. L. Garrell, University of California, Los Angeles

WEDNESDAY AFTERNOON

Array Detectors in Spectroscopy
Arranged by R. McCreery, The Ohio State University

Atmospheric Chemistry II
Arranged by J. W. Birks, University of Colorado
New Developments and Applications in Electrospray Ionization MS
Arranged by R. D. Smith, Pacific Northwest Laboratory
Quality in the United States
Arranged by H. Hertz, NIST
Charles N. Reilley Award and Young Investigator Award Symposium
Arranged by A. Brajter-Toth, University of Florida
Spectroscopy in Process Analytical Chemistry
Arranged by B. R. Kowalski, University of Washington

THURSDAY MORNING

ICPMS: The 10th Anniversary of the 1st Commercial Instrumentation (1983–1993)
Arranged by V. B. Conrad, Consol Inc.
Laser Desorption MS of Biomolecules
Arranged by B. T. Chait, The Rockefeller University
Modern Methods of Analysis for Xenobiotics and Natural Toxins
Arranged by H. M. Stahr, Iowa State University
Nondestructive Characterization of Materials Using NMR
Arranged by N. R. Dando, Aluminum Company of America
Selectivity Control in Reversed-Phase LC
Arranged by J. G. Dorsey, University of Cincinnati
Williams–Wright Award Symposium
Arranged by B. J. Streusand, Applied Analytical, Inc.

THURSDAY AFTERNOON

Analytical Aspects of New Drug Analysis
Arranged by L. Wong, Biovail/IWF Research
Electrochemical Characterization of Electronic Materials
Arranged by J. G. Osteryoung, North Carolina State University
The Future of Laboratory Information Management Systems (LIMS)
Arranged by D. R. Balya, Aluminum Company of America Technical Center
Environmental Monitoring with FT-IR Spectroscopy
Arranged by R. J. Combs and R. T. Kroutil, U.S. Army
Managing the Analytical Laboratory in the '90s: Industry and the University
Arranged by P. LaFleur, Eastman Kodak Company

FRIDAY MORNING

The Condition of Planet Earth
Arranged by S. H. Peterson, Westinghouse STC
40th Anniversary of the Coblentz Society: Historical Perspectives and Current State of the Art in Vibrational Spectroscopy
Arranged by L. A. Nafie, Syracuse University, and D. M. Haaland, Sandia National Laboratory

Eleven scientists will be honored at award presentations.

Jack L. Koenig of Case Western Reserve University will receive the Bomem–Michelson Award from the Coblentz Society. This award will recognize his work elucidating the structure of polymers by spectroscopic techniques.

Jacques A. Rijks of Technische Universiteit Eindhoven, The Netherlands, will receive the Dal Nogare Award from the Chromatography Forum of the Delaware Valley. Rijks is being honored for his contributions to fast GC at the femtogram level and for his efforts to expand the application of chromatography in Third World countries.

Egil Jellum of the University of Oslo, Norway, has been selected as the Keene P. Dimick awardee. This award recognizes an analytical chemist for accomplishments in GC or SFC and is administered by the Society for Analytical Chemists of Pittsburgh (SACP). Jellum is being honored for his work in analytical separation technology for the diagnosis of diseases.

Brian Osborne of Flour Milling and Baking Research Association, U.K., will receive the Tomas Hirschfeld Award for his contributions to the advancement of near-IR spectroscopy. This award, which commemorates Hirschfeld's work in spectroscopy, is sponsored by Bran + Luebbe Analyzing Technologies.

Dennis H. Evans of the University of Delaware will receive the Charles N. Reilley Award from the Society for Electroanalytical Chemistry. His research involves the characterization of the role of conformational change and isomerism in electrode reactions.

Edward S. Yeung of Ames Laboratory, Iowa State University has been chosen to receive the Pittsburgh Analytical Chemistry Award, sponsored by the SACP. Yeung is being recognized for his work on laser-based detectors for LC and capillary zone electrophoresis (CZE).

Catherine Fenselau of the University of Maryland Baltimore County will receive the 1993 Pittsburgh Spectroscopy Award, presented by the Spectroscopy Society of Pittsburgh. Fenselau is being honored for her work in MS, protein chemistry, and the chemistry of conjugated drug metabolites.

Robert S. Houk of Ames Laboratory, Iowa State University will receive the Maurice F. Hasler Award, sponsored by Applied Research Laboratories and administered by the Spectroscopy Society of Pittsburgh. Given in alternate years, the award recognizes contributions to the field of spectroscopy that have resulted in applications of broad utility. Houk is being honored for his work in the fundamental studies and applications of plasma ion sources for MS.

Curtis Marcott of the Procter & Gamble Company has been selected to receive the Williams–Wright Award from the Coblentz Society for his pioneering work in 2D mid-IR spectroscopy.

In addition, the Society for Electroanalytical Chemistry has initiated the Young Investigators Award to recognize scientists in the early stages of their careers who have made outstanding contributions to the field of electroanalytical chemistry. The 1993 award is being given jointly to **Leonidas G. Bachas** of the University of Kentucky and **Werner G. Kuhr** of the University of California at Riverside. Bachas is being recognized for his contributions in the areas of competitive binding immunoassay, ion-selective electrodes, and fiber-optic sensors. His work focuses on the incorporation of new ionophores and polymeric materials into novel sensor designs. Kuhr is being recognized for his work in the area of analytical neurochemistry, which has resulted in contributions to the areas of in vivo voltammetry using microelectrodes, CZE, modified carbon surfaces, and fluorescence imaging of surface activity.

The following scientists will be recognized at the James L. Waters Symposium (Monday afternoon): James Shoolery, Varian Associates (retired); John Waugh, Massachusetts Institute of Technology; Ray Freeman, Cambridge University; and Paul Lauterbur, University of Illinois.

The following short courses are tentatively scheduled as part of the continuing education program: A Basic Introduction to Chirality and Its Impact on Industrial Analytical Separations; Advanced Statistics; Analysis of Proteins; Basic Statistics; Biomedical Sample Preparation, Including Derivatization; Buying Instruments; Career Development and/or Selling Oneself; Cultural Differences in Technical Management; Effective and Practical Presentation Strategies for Scientists; FABMS; FFF; GC Troubleshooting; Getting

Started with a PC in Your Lab; Headspace GC; HPLC Method Validation with Computer-Aided Diode Array Detection; Interpretation of Dynamic Mechanical Spectra; Laboratory PC Applications: Combining the Power of the Spreadsheet and Data Management Programs; LC and GC for Technicians; LIMS for Laboratory Managers: Strategy and Tactics; Managing for Quality within the Analytical Laboratory; Mathematical Calculations for Sampling and Analyte Concentration for Gas, Liquid, and Solid Samples; Microwave Sample Preparation; Near-IR Spectroscopy: An Overview; Practical MS/MS Analysis; Precontrol as an Effective Method of Process Control; Principles and Applications of 2D NMR; Principles and Applications of Step-Scan FT-IR; Professional Analytical Chemists in Industry; Public Speaking for Scientists; Searching and Using Chemical Information; Spreadsheets and Sail Away!: A Motto to Teach Analytical Chemistry By; SFE: Practical Considerations and Applications in Environmental Analysis; Teaching Approaches to Laboratory Automation; The Art of Sample Preparation; The Write Way to Success; TOFMS; and Understanding Chemical Reactions: The Key for Developing Automated Chemical Methods. Registration information will be available in the preliminary program.

Advance registration is urged. Fees are $50 for advance and $100 for on-site registration, $25 for advance exposition-only registration, $50 for on-site exposition registration, $15 for advance or on-site student registration, $40 for advance spouse registration, and $75 for on-site spouse registration. Preregistration forms will be provided in the preliminary program and should be sent to Registration Control Systems, 2368 Eastman Ave., Suite 11, Ventura, CA 93003. The Pittsburgh Conference *Update* will also contain registration forms as well as housing and travel information. All preregistration forms should be postmarked by Feb. 1, 1993.

An employment referral service will be provided during the conference. For more information, contact Beth Kirol, The Pittsburgh Conference, Suite 332, 300 Penn Center Blvd., Pittsburgh, PA 15235-5503 (412-825-3220 or 800-825-3221; fax: 412-825-3224). The technical program will appear in the Feb. 1 issue of ANALYTICAL CHEMISTRY, along with additional details about the conference.

BOOKS

Chemometrics and QA

Data Fitting in the Chemical Sciences. Peter Gans. 258 pp. John Wiley & Sons, 605 Third Ave., New York, NY 10158. 1992. $75

Reviewed by Barry Wythoff, Inorganic Analytical Research Division, Chemical Science and Technology Laboratory, National Institute of Standards and Technology, Gaithersburg, MD 20899

A textbook cannot be all things to all people, and *Data Fitting* is not for everyone. It is not a volume for chemometrics voyeurs, or even for meat-and-potatoes users of scientific statistics. This book does, however, represent a valuable addition to the library of those who are or want to become involved in the use of regression methods for modeling scientific data.

My suggestions for the audience would be persons with good mathematics backgrounds or a fair amount of experience in statistics and/or "numerical methods." The prospective reader should have a healthy appetite for derivations involving differential calculus and matrix algebra methods. Such methods would not, of course, be considered complex by a mathematician; however, most scientists do not use such tools on a regular basis.

Readers who become nervous or queasy at the sight of equation-filled pages may want to consider passing up this book. I must confess to feeling a bit light-headed when the phrase "Cholesky decomposition" leapt from the pages when I first scanned the book. Comforting myself with the notion that prior knowledge of all of a book's secrets would obviate any need to read it, I flipped on . . . .

Having said all that, I would recommend that if you are a scientist who already uses numerical methods for data fitting and you want to learn more about the theoretical underpinnings, as well as possible alternatives for doing so, this book definitely deserves a read. Although Gans does have a fondness for derivations, they are not the sole or even the major element of the book.

There are also numerous instructive illustrations and examples. These user-friendly portions represent an important distinction between *Data Fitting* and more theoretical texts that might be favored by a mathematician or a statistician. The fact that the latter are often devoid of qualitative discussion often renders their presentation of similar material alien to the scientist. Readers who are not intimidated by derivations will likely find the ones in this book a valuable way to satisfy yearnings to know more about the foundations underlying the expressions used in practice.

"A valuable addition to the library of anyone seriously involved in using regression methods."

Notable by their exclusion from the book are so-called "latent variable" methods, such as factor analysis, principle components regression, and partial least squares. Although the cognoscenti may argue about the virtues and vices of these techniques, they have become quite popular in the research literature for analytical chemistry and have found their way into the data packages of many modern instruments.

Data Fitting thoroughly examines the concepts and formulas involved in regression analysis, from estimation of population means to analytic nonlinear equation fitting and beyond. There is impressive coverage of alternative numerical methods for locating the minimum on a general (nonquadratic) error surface. Methods range from the more assumptive Levenberg–Marquardt method to the little-constrained Simplex method.

The author rightly places strong emphasis on the processes of formulation, evaluation, and selection of models by devoting two chapters to these topics. In real-world applications of regression, these procedures are often the most difficult part of the analysis and constitute the "real science" in the work. Unfortunately, these topics are frequently given short shrift in articles or texts on data fitting, but this is not the case here.

The more empirical topics of fitting orthogonal polynomials, smoothing and differentiation by convolution, and fitting smoothing splines are tackled in detail in the next couple of chapters. Following this, the topic of peak fitting is presented, albeit with little discussion of so-called Voigt fitting, which is popular with many theorists. Instead, the emphasis is placed on more empirical (but more easily solved) methods of mixing Gaussian and Lorentzian functions for peak fitting, such as a linear additive model.

The penultimate chapter is a very readable and insightful discussion of the Fourier transform, its properties, and some commonly associated calculations such as convolution and deconvolution. Gans then closes with a chapter that is a sort of case study in regression analysis, involving potentiometric titrations.

As noted at the start, this is not a book for someone with a casual interest in data fitting. If you have some prior knowledge and experience and want to become more seriously involved with this subject, however, the book will be a worthy addition to your bookshelf.

Practical Guide to Chemometrics. Stephen John Haswell, Ed. ix + 324 pp. Marcel Dekker, 270 Madison Ave., New York, NY 10016. 1992. $100

Reviewed by Bruce Kowalski, Center for Process Analytical Chemistry, University of Washington, BG-10, Seattle, WA 98195

Nine research chemometricians contributed to this book, edited by Haswell (University of Hull, Hull, U.K.). The stated purpose is to offer a

practical guide and general text to the scientist—principally, the analytical chemist—interested in chemometrics. The preface also states that "the text restricts itself to the mathematics considered necessary for the basic understanding of the various techniques covered . . . ." This is indeed the case and properly qualifies the book as a guide to the subject—even as a practical guide—because several applications of the tools of chemometrics can be found in its pages.

As a general text, the book falls somewhat short; the state of the art in some of the topics covered is never reached. Also, only a small number of problems appear, and not all chapters have them. For use in a graduate course, the book would have to be supplemented heavily with advanced texts. However, if an instructor could add several problem sets to the chapters and use some commercially available chemometric software, the book would make an excellent undergraduate textbook.

The 10 chapters cover a wide range of topics. The first two chapters introduce the book and provide the reader with some basic statistics. Chapter 3 is a good introduction to nonparametric and robust statistics. These methods are not commonly practiced in chemistry, but this chapter could facilitate their application. Chapter 4 covers the important topic of calibration and is followed by a chapter on nonlinear regression.

In keeping with the title of the book, the authors guide the reader through the subjects but do not attempt to be users' manuals for the tools they cover. My choice for Chapter 6 would be to have it appear earlier in the book, because experimental design is fundamental to an experimental science. The next two chapters cover the important topic of signal processing (spectrum and waveform analysis) and multivariate data enhancement and analysis (pattern recognition); they complement each other nicely. The book concludes with a chapter on computer hardware and laboratory information management systems software as well as a look into the future. Although predicting the future is, of course, associated with some uncertainty, this last chapter should be read by all analytical chemists, especially those associated with instrument companies.

One goal of chemometrics is to make every chemist part chemometrician. This book goes a long way toward achieving that goal.

Quality at Work in Research and Development. George J. Kidd, Jr. 152 pp. QR Press, One Water Street, White Plains, NY 10601. 1992. $30

Reviewed by R. A. Nadkarni, Exxon Chemical Co., P.O. Box 536, Linden, NJ 07036

Statistical quality assurance (SQA) tools have been applied to manufacturing for many years, and recently the service industry has paid more attention to such tools. However, in R&D, little attention has been given to SQA. This book is an attempt to fill this void by an author with considerable experience in R&D as both a researcher and a manager.

There is a certain belief (erroneous, in my view) among those in the R&D community that QC activities will stifle their creative efforts. This book tries to demonstrate how SQA will help a research group to achieve its goals. This is not a how-to handbook, as the author readily admits; R&D cannot be done by using a cookbook. It is written in a straightforward fashion with simple language and not a lot of jargon. The references are quite up to date; 1990 is the best that can be expected for a book published in early 1992.

The book is divided into seven chapters that define the ideas of quality, discuss the costs and benefits of a QA program, review available quality tools, and discuss the place of R&D in industry. Finally, what the author terms "a complete quality model" (CQM) is described and used to develop examples in the R&D organization.

In Chapter 3 the author distinguishes between research and development but does not develop this discussion fully. Chapter 6 is a review of what in the quality community is called the seven basic quality tools. These are well described in many other books, and I found this author's treatment sketchy. The book would have benefited considerably by the inclusion of more details, examples, and how-to information. Similarly, Chapter 4, which discusses costs and benefits, could have been improved by including industrial examples of such a program.

The author's proposed CQM model is a system that includes functions of preparation, execution, evaluation, reward, improvement, and correction. The model is applied to R&D situations in the last chapter. However, to successful R&D groups in established organizations, the steps are not innovative. Most researchers already follow the system given in the book for getting a research paper published—it should be second nature to them by now. The CQM system is essentially a more detailed approach of Edwards Deming's well-known plan/do/check/act cycle, which has been in vogue for years.

Overall, this is a good effort to introduce quality principles to the R&D community, but the specific model proposed here has more to do with efficient administration than with quality activities.

Books Received

Target Sites for Herbicide Action. Ralph C. Kirkwood, Ed. xiv + 339 pp. Plenum Press, 233 Spring St., New York, NY 10013. 1991. $80

The major target sites of herbicides, the effects of synergists or antagonists as modifiers of herbicide action, and aspects of efficient target site delivery are discussed in 10 chapters. Primary target sites include photosynthesis; lipid and carotenoid synthesis; respiration; and the biosynthesis of chlorophyll, isoprenoids, cellulose, proteins, nucleic acids, and folic acid. The fate of soil-applied herbicides, the pathways and mechanisms of the uptake of foliage-applied herbicides (including the role of surfactants), herbicide transport pathways and mechanisms in plants, and herbicide metabolism as a basis for selectivity are also discussed. The book lists authors and their affiliations as well as chemical names of the herbicides. A subject index is also included.

Spectroscopic Properties of Inorganic and Organometallic Compounds. Volume 24. E. G. Davidson, Senior Reporter. xiv + 493 pp. Royal Society of Chemistry, Distribution Center, Blackhorse Rd., Letchworth, Herts SG6 1HN, U.K. 1991. $300

The eight chapters of this volume of the Specialist Periodical Reports review the literature on the spectroscopy of inorganic and organometallic compounds up to late 1990. Topics include NMR spectroscopy, nuclear quadrupole resonance spectroscopy, rotational spectroscopy, characteristic vibrations of compounds of main group elements, vibrational spectra of transition element compounds and of some coordinated ligands, Mössbauer spectroscopy, and gas-phase molecular structure determination using electron diffraction methods. A list of conversion factors appears at the beginning of the book.

FOCUS

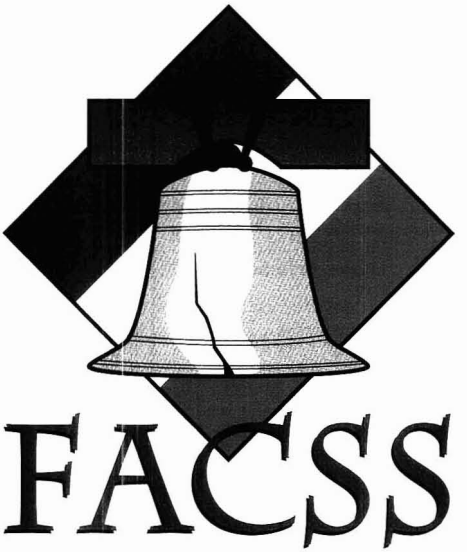

FACSS

1992 CONFERENCE HIGHLIGHTS

Nancy J. Miller-Ihli
U.S. Department of Agriculture
Nutrient Composition Laboratory
Beltsville, MD 20705

The 19th annual meeting of the Federation of Analytical Chemistry and Spectroscopy Societies (FACSS) was held Sept. 20–25 at the Adams Mark Hotel in Philadelphia, PA. Designed to bring together scientists who share an interest in problem solving, FACSS is considered by many to be one of the most important technical analytical meetings held annually. This year's program of expanded coverage, which emphasized emerging technologies in the analytical, spectroscopic, chemical, and biochemical sciences, confirmed this opinion. More than 1700 persons attended the conference, and approximately 800 papers and posters were presented throughout the week in parallel sessions. This FOCUS is intended to highlight conference events of interest to the analytical audience.

FACSS is perhaps best known for its impressive spectroscopy program; the more than 50 symposia related to spectroscopy this year substantiated this reputation. The sessions devoted to MS, focusing on ion trapping, FT-MS, and high mass analysis, were of particular interest to conferees. The historic prominence of a strong program in plasma spectroscopy was continued with symposia on ICP, ICPMS, plasma diagnostics, and sample introduction strategies. Graphite furnace AAS symposia focused on fundamentals, applications, and solid and slurry sampling.

The chromatography field was also well represented. A variety of sessions covered topics such as separation scientists of the 21st century, chromatography in the Delaware Valley, size exclusion, advances in preparative chromatography, and SFE. Milos Novotny of Indiana University, who received the 1992 ANACHEM award, discussed microcolumn separation systems during a symposium held in his honor. Chromatographers and spectroscopists joined forces for a symposium on element-specific detection in chromatography using plasmas.

Three excellent poster sessions contributed to the success of the program. The Tuesday evening poster session focused on a wide range of spectroscopic techniques, including glow discharges, ICP, electrothermal vaporization ICPMS, atomic fluorescence, and graphite furnace AAS. Wednesday evening's poster session included presentations on ion chromatography, HPLC, FT-IR and laser spectroscopy, NMR and ^{13}C NMR spectroscopy, and liquid adsorption chromatography. A third poster session devoted to general topics was held Thursday evening and included thermosonimetry of polymers, comparison of methods for determining cyanide, bone lead analysis, and submicrometer optical fiber chemical and biological sensors. The poster sessions were well attended and sparked many interesting discussions.

Several special symposia were highlighted in the program. One of these honored the late Peter Keliher, a professor at Villanova University who was closely involved in the FACSS organization. Through the years, Keliher served the group in a variety of capacities, including governing board chair, exhibits chair, and assistant program chair. Many of his friends and colleagues from around the world participated in the symposium, which was organized by Julian Tyson of the University of Massachusetts at Amherst.

FACSS also serves as the forum for recognizing outstanding young scientists pursuing graduate degrees. This year, three Hirschfeld award winners were named: Vasilis Gregoriou of Duke University for his work on FT-IR spectroscopy, Patrick Limbach of The Ohio State University for his work on Fourier transform ion cyclotron resonance, and Jeff Mazzeo of Northeastern University for his work on capillary isoelectric focusing. The FACSS Student Award went to Evelyn Guizhen Su, a graduate student at the University of Connecticut working under the direction of Robert Michel. Cheryl Bye, a graduate student at the University of Illinois working under the direction of Alexander Scheeline, received the SAS student award.

As is traditional with FACSS, several short courses and workshops were held in conjunction with the meeting. FACSS workshops historically have been well attended, and this year spectroscopists found the chemometrics, statistics, and sample preparation courses of particular interest. SAS short courses held on the weekend before the conference also attracted a number of participants. The employment bureau, available to employers and conferees from Monday through Thursday, was a popular place for employers and potential employees to review work opportunities.

Conferees enjoyed one of the largest instrument exhibits in the history of FACSS, which was kicked off with a well-attended wine and cheese reception on Monday evening. More than 100 booths occupied the sold-out exhibition area, and nearly all major suppliers of spectroscopic instruments and equipment were represented. Manufacturers displayed their latest offerings and had a good number of technical support people on hand to answer questions. Catalog, optical, and chemical companies were also well represented, as were publishing companies and many specialty companies whose custom services support research efforts.

The 1992 FACSS conference was indeed a success. Please mark your calendar with dates for FACSS XX, to be held Oct. 17–22, 1993, in Detroit. The deadline for title submission is Feb. 1, 1993. If you would like to place your name on the FACSS mailing list or if you need additional information about the meeting, send your request to FACSS, P.O. Box 278, Manhattan, KS 66502-0003 or call the Frederick, MD, office at (301) 846-4797.

Nancy J. Miller-Ihli served as publicity chair for FACSS in 1991 and 1992. A research chemist in the Nutrient Composition Laboratory at the USDA, she received her B.A. degree in chemistry from Shippensburg University (PA) and her Ph.D. in analytical chemistry from the University of Maryland.

NEW PRODUCTS

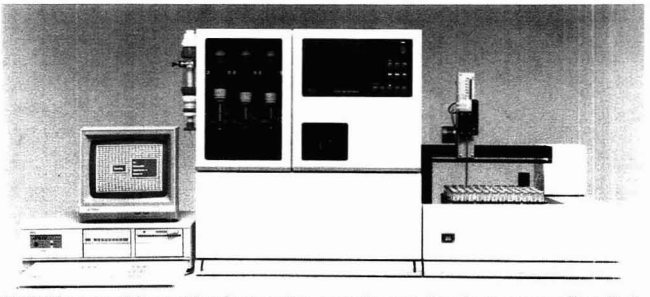

9050 Plus peptide synthesizer, a Fmoc continuous-flow instrument, offers flexibility in incorporating activation chemistries, dual-syringe activation, menu-driven software, synthesis cycles as rapid as 16 min, and the ability to prepare quantities of peptides ranging from 0.05 to 5 mmol. Millipore **412**

Instrumentation

Probe. T-176R temperature probe can convert a strip chart or a potentiometric recorder into a temperature recorder. The thermistor-based probe plugs directly into recorder input terminals and has a range of 0–120 °C with a readability of 0.1 °C. Lazar Research Laboratories **401**

Controller. Hastings model HPC-222 low-flow mass flow controller uses a piezoelectric valve actuator to simplify valve construction and reduce power supply current requirements. Applications include GC, pollution monitoring, and low-flow gas blending. Ranges are available from 0–10 SCCM to 0–1000 SCCM of air; accuracy and linearity are ± 2%. Teledyne Hastings-Raydist **402**

Cyanide analyzer. Model PS1214 automates sample preparation and cyanide analysis. Disposable microdistillation columns, used in a 30-min preparation procedure, snap apart after sample preparation; the sample container can then be transferred directly to the 42-position autosampler. Leeman Labs **403**

Total sulfur. TS-XVI, a computerized, lead acetate tape-based analyzer that measures total sulfur in liquids and gases to low-ppb levels, has a typical analysis time of 120 s. It features a multisampling carousel that can hold up to 40 samples for continuous sampling in the automatic mode or a computer-directed syringe drive for single samples in the manual mode. Houston Atlas **405**

ATR. VariMax in-compartment variable-angle horizontal ATR accessory permits users to vary the angle of incidence from 25° to 80° while maintaining alignment of the accessory at all angles. Applications include depth-profiling studies as well as analysis of liquids and pastes. International Crystal Laboratories **406**

Thermal analysis. DTA 7 differential thermal analyzer provides direct quantitative measurement of the endothermic and exothermic behavior of a variety of samples from ambient to elevated (1600 °C) temperatures. Designed to operate as part of the multianalyzer 7 series/Unix thermal analysis system, the DTA 7 can be used simultaneously with other thermal analyzers such as the TGA 7, the DSC 7, the DMA 7, and the TMA 7. Perkin Elmer **407**

FID. Organic-fueled remote FID for GC/SFC is based on the discovery that organic compounds containing Pb, Sn, P, or Si form stable, long-lived ion species in flame combustion, whereas hydrocarbon ions are rapidly neutralized by ion–ion recombination processes. Detection levels of 1 pg/s for Pb, Sn, and P are achieved, and selectivities exceed 5×10^5 g C/g for Pb, Sn, and P. Detector Engineering and Technology **408**

Reflectance. VRMS-600 visible reflectance measurement system is designed to measure the total reflectance from samples over the 0.4–0.7-μm spectral range. Applications include measurement of light reflectance of acoustic materials or the measurement of haze and luminescence transmittance of transparent plastics. Labsphere **409**

Freezer. Model U85-25 laboratory freezer is designed for medical research applications; storage of biological products; and the preservation of tissue, plasma, blood cells, and microbiology specimens. An indicating temperature control provides an adjustable temperature range from –18 °C to –85 °C. So-Low Environmental Equipment **410**

Software

Scientific graphics. PlotIT, designed to transform complex data into charts and graphs for more effective analysis, is available for DOS, Windows, and a variety of mini- and mainframe operating systems. All versions of the program provide a choice of more than 60 2D, 3D, and QC graph types and include command, menu, mouse, function key, or batch interface options. An on-line worksheet simplifies most spreadsheet operations and provides statistical analysis functions. Scientific Programming Enterprises **411**

Chromatography/spectroscopy. Peakfit, a chromatography/spectros-

P/ACE 2100 system for CE/MS requires only a few nanoliters of sample to produce high-resolution separations of pharmaceuticals, carbohydrates, proteins, peptides, and nucleic acids. Analytes eluting from the CE column are ionized by ESI, producing charged molecules that can be readily analyzed with a single or triple quadrupole MS system. Beckman Instruments **404**

copy analysis package for PC-compatibles, uses nonlinear curve fitting to reduce noise and to separate and characterize unresolved peaks in overlapping peak data. Analysis includes all model parameters and statistics as well as system suitability information (peak area, asymmetry, resolution) and characterization of data useful in spectroscopy (peak amplitude, area, center, width). Jandel Scientific **413**

Statistics. Standard and enhanced versions of release 9 of Minitab statistical software are available for VAX/VMS computers. The standard version offers new multivariate analysis features and a powerful macro programming language that can be used to customize and extend the scope of Minitab operations and to automate repetitive tasks. The enhanced version includes presentation-quality graphics, quality control capabilities, and all features of the standard version. Minitab Statistical Software **414**

Manufacturers' Literature

Lab Reporter. Fall issue features a cover story on ISO 9000 that explains quality system guidelines and their effect on laboratories. The tabloid also lists new products, including a disposable IR card for qualitative IR in the 4000–400 cm^{-1} range and an electronic burette with a continuous range of 0.01–9999.99 mL. 24 pp. Fisher Scientific **415**

Separations. Product guide describes instruments and systems for preparative and analytical chromatography, SFE, CE, and gel electroelution. Several new instruments are introduced, including an expanded line of automated SFE systems. 12 pp. Isco **416**

Preparative chromatography. "Separation Solutions," Vol. 1, No. 2 features an article describing the Kiloprep 100 Prep-LC system, which can be used to optimize synthetic organic separations. The newsletter also includes information on radial compression cartridges and LC software control strategy. 6 pp. Biotage **417**

Injector. Brochure details the low-volume injector, a GC accessory configured for GC/MS determination of volatile compounds with purge-and-trap sample introduction. The injector uses standard septa and allows direct injection for troubleshooting while minimizing the dead volume in the inlet. 4 pp. J&W Scientific **418**

Oscilloscopes. Technical Note ATS-2023 describes five capability areas of the 7200 series modular oscilloscope system: acquisition, processing, display, internal programmability, and mass storage. The modular architecture of the series allows full digitizing speed and memory to be maintained as more channels are added. 48 pp. LeCroy **419**

Chromatography. Guide highlights more than 30 instruments for isocratic and gradient elution LC and sample preparation applications. Detailed information is presented on detectors, including models for UV, UV–vis, fluorometric, electrochemical, and RI detection, and fraction collectors suitable for analytical, semipreparative, and preparative LC. 12 pp. Gilson Instruments **420**

Mass flow measurement. Design/selection guide details the benefits of mass flow measurements in the pharmaceutical and biotech industries. Schematics and photographs describe typical installations of thermal gas flow monitors in fermenters, reactors, fluid bed dryers, and pill coaters. 4 pp. Sierra Instruments **421**

Catalogs

Research chemicals. Alfa Catalog for 1993–1994 offers a large analytical section with more than 10 new product lines, including aqueous and matrix modifier solutions as well as asbestos, environmental, and IC and ICP standards. More than 4000 inorganic compounds, 3000 organic compounds, and 1000 pure elements and fabricated metals impurities, ranging from technical grade to high purity, are available. 1200 pp. Alfa/Johnson Matthey **422**

Chemicals. Catalog for 1993–94 lists more than 15,500 organic and inorganic chemicals as well as biochemicals. Structural formulas and literature references describing new applications are included. 1512 pp. Fluka **423**

Water purification. WaterPro systems catalog contains information on WaterPro workstations, RO stations, and PS stations as well as a guide to determine the appropriate system for a particular application. An overview of water purification and a discussion of NCCLS water types and applications, contaminants, and water testing and purification methods are included. 28 pp. Labconco **424**

Lab equipment. Illustrated catalog covers a wide range of laboratory equipment and glassware for biotechnology as well as industrial, research, and pharmaceutical applications. Features, benefits, and specifications of thousands of products comprising approximately 90 product lines are included. 300 pp. Bellco Glass **425**

Environmental analysis. *Catalog of Hazardous Waste Testing Equipment* features products for EPA's toxicity characteristic leaching procedure, including rotary extractors, hazardous waste filtration units, gas-tight syringes, and zero-headspace extractors. Other products include an auto-volatile organic composite water sampler and equipment for purge-and-trap procedures. Associated Design and Manufacturing **426**

Glassware. Fiftieth anniversary edition describes more than 6000 standard laboratory glassware products for chemistry and the life sciences. New items developed for use in environmental sampling and testing, NMR, HPLC, column chromatography, filtration, and cell culture are included. 400 pp. Kontes **427**

For more information, please circle the appropriate numbers on one of our Readers' Service Cards.

LABORATORY SERVICE CENTER

LABORATORY SERVICE CENTER

(Equipment, Materials, Services, Instruments for Leasing), Maximum space — 4 inches per advertisement. Column width, 2-3/16″; two column width, 4-9/16″. Artwork accepted. No combination of directory rates with ROP advertising. Rates based on number of inches used within **12** months from first date of first insertion.

Per inch: **1″ — $185; 12″ — $180; 24″ — $175; 36″ — $170; 48″ — $165.**

CALL OR WRITE JANE GATENBY

ANALYTICAL CHEMISTRY
1599 Post Road East
P.O. Box 231
Westport, CT 06881
203-256-8211
FAX: 203-256-8175

USE LABORATORY SERVICE CENTER

FREE DATA, FAST

To quickly amass data on all of the products you need, consult the Lab Data Service section on our *Analytical Chemistry* reader reply card insert.

HELP WANTED ADS

ROP display at ROP rates. Rate based on number of insertions within contract year. Cannot be combined for frequency.

Unit	1-TI	6-TI
1″ (25 mm)	$210	$190
	12-TI	24-TI
	$180	$170

CALL OR WRITE JANE GATENBY

ANALYTICAL CHEMISTRY
1599 Post Road East
P.O. Box 231
Westport, CT 06881
203-256-8211
FAX: 203-256-8175

ACS Congressional Fellowship

Available Fall 1993

The Fellowship places an ACS member in a staff position in Congress to

- Gain firsthand knowledge of the operation of the legislative branch of the federal government,
- Make scientific and technical expertise available to the government, and
- Forge links between the scientific and government communities.

Applications due January 1,1993.

For more information contact:
Department of Government Relations and Science Policy
American Chemical Society
1155 Sixteenth Street, N.W.
Washington, DC 20036,
(202) 872-4467.

Applications consist of a letter of intent, and two letters of reference. Arrangements should be made to send the letters of reference directly to ACS. Candidates should contact ACS prior to submitting an application to determine the type of information needed in the letter of intent.

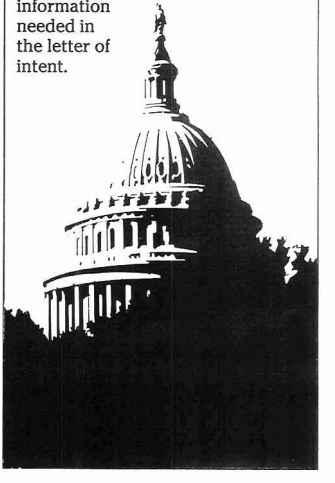

INDEX TO ADVERTISERS IN THIS ISSUE

Directory section, see page 1176A.
** See ad in ACS LabGuide.*

Advertising Management for the American Chemical Society Publications

CENTCOM, LTD.

President
James A. Byrne
Executive Vice President
Benjamin W. Jones

Robert L. Voepel, *Vice President*
Joseph P. Stenza, *Production Director*

1599 Post Road East
P.O. Box 231
Westport, Connecticut 06881-0231
(Area Code 203) 256-8211
Fax No. 203-256-8175

DIRECTOR, ADVERTISING SALES, LABORATORY PRODUCTS
Bruce E. Poorman

ADVERTISING PRODUCTION MANAGER
Jane F. Gatenby

SALES REPRESENTATIVES

Philadelphia, Pa. . . . Matthew J. McCloskey, CENTCOM, LTD. GSB Building, Suite 405, 1 Belmont Ave., Bala Cynwyd, PA. 19004. Telephone: 215-667-9666, FAX: 215-667-9353

New York/New Jersey . . . Dean A. Baldwin, John F. Raftery, CENTCOM, LTD., Schoolhouse Plaza, 720 King Georges Post Road, Fords, NJ 08863, Telephone: 908-738-8200, FAX: 908-738-6128

Westport, CT./Boston, MA. . . . Edward M. Black, CENTCOM, LTD., 1599 Post Road East, P.O. Box 231, Westport, CT 06881-0231. Telephone: 203-256-8211, FAX: 203-256-8175

Cleveland, OH./Atlanta, GA. . . . Bruce E. Poorman, CENTCOM, LTD., 325 Front St., Suite 2, Berea, OH 44017. Telephone: 216-234-1333, FAX: 216-234-3425

Chicago, IL./Houston, TX. . . . Michael J. Pak, CENTCOM, LTD., 540 Frontage Rd., Northfield, IL. 60093. Telephone: 708-441-6383, FAX: 708-441-6382

West Coast/Denver, CO. . . .Paul M. Butts, Jay S. Francis, CENTCOM, LTD., Suite 808, 2672 Bayshore Parkway, Mountain View, CA 94043. Telephone: 415-969-4604, FAX: 415-969-2104

United Kingdom, Scandinavia and Europe (Except: Germany, Switzerland, Austria) . . . Malcolm Thiele, Technomedia Ltd., Wood Cottage, Shurlock Row, Reading RG10 OQE, Berkshire, England. Telephone: 0734-343302, FAX: 0734-343848

Germany, Switzerland, Austria . . . InterMedia Partners, GmbH, Deutscher Ring 40, 5600 Wuppertall 11, Germany. Telephone: (0202) 711091, FAX: (0202) 712431

Tokyo, Japan . . . Sumio Oka, International Media Representatives Ltd., 1-11-5-502, Tamazutsumi, Setagaya-ku, Tokyo 158 Japan. Telephone: 502-0656, Telex #22633, FAX: 5706-7349

Asia (Except Japan) . . . Bruce E. Poorman, CENTCOM, LTD., 325 Front St., Suite 2, Berea, OH 44017. Telephone: 216-234-1333, FAX: 216-234-3425

South America . . .Bruce E. Poorman, CENTCOM, LTD., 325 Front St., Suite 2, Berea, OH 44017. Telephone: 216-234-1333, FAX: 216-234-3425

AC RESEARCH

Effects of Film Morphology on the Frequency and Attenuation of a Polymer-Coated SAW Device Exposed to Organic Vapor

David S. Ballantine, Jr.

Chemistry Department, Northern Illinois University, DeKalb, Illinois 60115

The frequency and attenuation of PIB polymer-coated SAW devices were monitored during exposure to isooctane vapor as the coating thickness on the SAW was varied incrementally up to film thicknesses of about 300 kHz. Airbrush-coated devices exhibited significantly different response behavior compared to drop evaporation coated devices, most notably in attenuation of the acoustic wave. The drop evaporated films exhibited periodic, large attenuation with concurrent decreases in observed frequency shifts. These results are consistent with the film resonance model of Martin and Frye. In this work, we demonstrate how this model can also be used to estimate the shear modulus of polymer films exposed to vapors. For the PIB films used in this work exposed to isooctane vapor the resonance thickness is calculated to be 0.0082 μm (before swelling), with a calculated modulus of 2.7 × 10⁵ dynes/cm². This represents a significant decrease in modulus compared to a neat PIB film (not exposed to vapor) and supports recent reports on the importance of polymer swelling in SAW responses.

INTRODUCTION

Surface acoustic wave devices are under increasing development for a variety of analytical applications, including chemical sensing and the characterization of thin films.[1,2] The frequency response behavior of these devices has been theoretically derived by several investigators,[3-6] with sensor frequency perturbations arising due to changes in mass loading, viscoelasticity, or conductivity of the thin film overlay. When the film is a nonconducting, viscoelastic polymer the frequency of the sensor can be described by the familiar Wohltjen equation[3]

$$\Delta f_s = (k_1 + k_2)f^2h\rho - k_2f^2h\left(\frac{4\mu}{v_R^2}\left(\frac{\lambda + \mu}{\lambda + 2\mu}\right)\right) \quad (1)$$

where Δf_s is the frequency shift due to the applied coating (in hertz), k_1 and k_2 are material constants dependent on the substrate having units of $m^2 \cdot s/kg$, f is the resonant frequency of the device (in hertz), h is the film thickness in meters, ρ is the film density (kg/m^3), v_R is the Rayleigh wave velocity in the substrate in meters per second, and μ and λ are the shear modulus (N/m^2) and the Lame constant for the coating, respectively. A similar relationship can be derived for the frequency shift of a coated device upon sorption of vapor. In such cases the h, ρ, μ, and λ values change to reflect the state of the polymer in equilibrium with the vapor. The first term in the eq 1 relates to mass loading effects while the second term deals with viscoelastic effects. It was previously assumed that, for a polymer well above its glass transition temperature (T_g), the second term was negligible and that the frequency response was dominated by the mass loading term. At the high operating frequencies of these devices, however, this assumption may not be valid. Coupling between the polymer film and the acoustic wave acts to increase the apparent modulus of the film by as much as 2–4 orders of magnitude. Recent investigations have provided substantial evidence that viscoelastic effects are not negligible and may, in fact, represent the major contribution to the frequency response.[6] Grate et al. proposed that the observed frequency decreases of a polymer-coated SAW are the combined result of mass loading due to vapor sorption *and* decreases in the modulus due to subsequent swelling of the polymer. The frequency shift due to vapor sorption was represented as

$$\Delta f_v = \left(\frac{\Delta f_s C_v K_{GLC}}{\rho_s}\right) + \left(\frac{\Delta f_s C_v K_{GLC}}{\rho_L}\right)\left(\frac{A_{SAW}}{\alpha}\right) \quad (2)$$

where Δf_v is the frequency shift of the SAW exposed to a vapor of concentration C_v, K_{GLC} is the partition coefficient for the vapor/polymer system determined by gas chromatography, Δf_s is the frequency shift caused by the deposition of the polymer coating, ρ_s is the density of the polymer coating when in equilibrium with sorbed vapor, ρ_L is the density of the vapor in the liquid state, α is the polymer thermal expansion coefficient, and A_{SAW} represents the frequency change of a polymer-coated SAW due to thermally induced swelling. As in the case of the eq 1, the two terms in eq 2 deal with mass loading and elastic effects. The first term estimates the increase in mass due to the equilibrium distribution of vapor into the polymer film. The second term in eq 2 estimates the magnitude of the frequency shift accompanying a change in volume due to swelling. The underlying assumption in this case is that the frequency shifts observed upon vapor-induced swelling, represented by (C_vK_{GLC}/ρ_L), are comparable

(1) Ballantine, D. S.; Wohltjen, H., *Anal. Chem.* **1989**, *61*, 704A.
(2) Frye, G. C.; Martin, S. J. *Appl. Spectrosc. Rev.* **1991**, *26*, 73.
(3) Wohltjen, H. *Sens. Actuators* **1984**, *5*, 307.
(4) Ricco, A. J.; Martin, S. J.; Zipperian, T. E. *Sens. Actuators* **1985**, *8*, 319.
(5) Bartley, D. L.; Dominguez, D. D. *Anal. Chem.* **1990**, *62*, 1649.
(6) Grate, J. W.; Klusty, M.; McGill, R. A.; Abraham, M. H.; Whiting, G.; Andonian-Haftvan, J. *Anal. Chem.* **1992**, *64*, 610.

0003-2700/92/0364-3069$03.00/0

in magnitude to the frequency shifts observed due to thermal swelling, represented by (A_{SAW}/α). This relationship was not intended to provide an quantitative model of SAW response behavior, yet it provides very good qualitative agreement with observed results and establishes the importance of viscoelastic effects.

While eq 1 provides an adequate theoretical framework for the prediction of SAW responses, it is limited by the fact that exact values for the modulus of the polymers, both in the presence and absence of vapor, are not always easily obtained. In addition, the underlying assumption in the derivation of eq 1 is that the surface film overlay is of uniform thickness covering the entire active surface of the device. Most of the SAW studies performed to date, however, have utilized airbrush films for which this assumption is clearly not valid. The effects of differing film morphology on SAW device response behavior have yet to be investigated. Clearly, more thorough analyses of SAW response behavior are required to adequately describe the dependence of SAW frequency on the many film parameters. More specifically, the nature of film morphology and viscoelastic effects on observed response must be clarified. In addition, the viscoelastic properties of polymeric materials used as sensor coatings need to be determined. Such information is critical if the potential of these devices as sensors and as tools for materials characterization is to be fully realized.

Recently, Martin and Frye presented a novel approach to modelling the behavior of a polymer-coated thickness-shear resonator device, the quartz crystal microbalance (QCM).[7] One advantage of this model is that it provides a framework for interpreting the acoustic sensor response in terms of both film mass (thickness, density) and modulus. The development of an analogous model for SAW-type sensors would address some of the limitations of the previously discussed predictive relationships (eqs 1 and 2). Due to the operational similarities between the QCM and the SAW devices, it should be possible to interpret SAW sensor data in terms of this model.

In this work the response of a polymer-coated SAW observed upon exposure to organic vapor is reported. Specifically, we will do the following:

1. Investigate both the frequency and attenuation response of a polymer-coated SAW upon exposure to an organic vapor. These investigations will be carried out while systematically varying the thickness of the polymer film.

2. Perform these investigations using films deposited by two different coating techniques, airbrushing and solvent evaporation, to determine the effects of film morphology on sensor response behavior.

3. Interpret the results in terms of the existing response models, with special emphasis on the film resonance model. The ramifications of these results are discussed in terms of sensor applications.

THEORETICAL CONSIDERATIONS

According to the film resonance model presented by Martin and Frye,[7] the oscillating QCM acts as a shear micromotor; a film bonded to the surface of a resonating device is subjected to an oscillatory driving force. The base of the film is usually sufficiently bonded to the surface so that it moves synchronously with the oscillating surface. The motion of the remainder of the film depends on the operating frequency of the device and the density, shear modulus, and thickness of the film. For rigid films the phase shift, ϕ, is very small and the entire film moves synchronously with the surface. In such cases shear deformation is negligible and the device

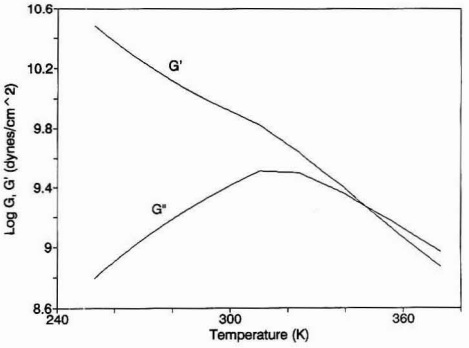

Figure 1. Plot of loss modulus (G'') and storage modulus (G') as a function of temperature. Data are extracted from literature values.[9]

responds only to surface mass changes. For a nonrigid or rubbery film there is an appreciable phase shift, and the upper region of the film tends to lag behind the oscillator surface. The resulting shear deformation causes elastic energy to be stored. The storage of acoustic energy in the film results in attenuation of the acoustic wave; this attenuation reaches a maximum when the phase shift across the film is an odd multiple of $\pi/2$. In addition, the frequency of the device decreases rapidly at ϕ just below $\pi/2$ and then increases dramatically at ϕ just above $\pi/2$. The relationship between phase shift across the film and the various film and device parameters is described as

$$\phi = \omega h_f(\rho_f/G)^{1/2} \quad (3)$$

where ϕ is the phase shift across a film of thickness h_f, ρ_f is the film density, G is the complex shear modulus of the polymer, and ω is the angular oscillation frequency (note: $\omega = 2\pi f$, where f is the resonant frequency of the device). The behavior of the polymer-coated QCM was described by way of an equivalent circuit model. By increasing the temperature of the coated device, the film modulus was decreased to the point where resonance damping occurred.

In so far as longitudinal particle displacement occurs at the SAW device surface, it is conceivable that SAW propagation may also cause shear deformation within a compliant film, and similar resonance phenomena may be observed. The polymer selected for study was polyisobutylene. Polyisobutylene (PIB) is an elastomer with a T_g of −76 °C; it was one of the polymers used in the previously cited work on QCM polymer film resonance. In addition, the modulus behavior of PIB as a function of both frequency and temperature is well documented.[8] The storage and loss moduli (G' and G'', respectively) for PIB at 157.9 MHz, the operational frequency of the SAWs used in this study, are given in Figure 1 as a function of temperature.[9] At the temperature range for this work, 25–29 °C, the PIB shear modulus determined from Figure 1 is (8.2–8.9) × 10^9 dynes/cm^2 (or 10^8 N/m^2). These values should be accepted with some reservation, since they are extracted from literature values having an upper limit of only 1 × 10^9 dynes/cm^2. Using eq 3 we can calculate the film thickness that would be sufficient to induce film resonance at a standard temperature of 25 °C. Setting $\phi = \pi/2$, for an operating frequency of 157.9 MHz, G = 8.9 × 10^9 dynes/cm^2, and ρ = 0.918 g/cm^3 yields a film thickness of 1.56 μm.

(7) Martin, S. J.; Frye, G. C. *Proc. 1991 IEEE Utrason. Symp.* **1991**, 393.

(8) Ferry, J. D. *Viscoelastic Properties of Polymers*, 3rd ed.; Wiley: New York, 1980.

(9) Calculated using data extracted from ref 8, p 606, and extrapolation algorithm developed by S. J. Martin, Sandia National Labs.

By way of comparison, typical film thicknesses for a 158-MHz device are on the order of 0.10 μm. Using eq 1, for example, a 0.10-μm PIB film having a shear modulus of 8.9 $\times 10^8$ N/m^2, a density of 918 kg/m^3, values for k_1 and k_2 of -8.7×10^{-8} and -3.9×10^{-8} m^2·s/kg respectively, and an acoustic velocity of 3300 m/s (in quartz) will produce a frequency decrease due to mass loading of −288 kHz, and a frequency *increase* of 27 kHz due to modulus effects for a net frequency shift of ca. −261 kHz. A 1.5-μm film would produce a 4-MHz shift, which is well beyond the operational range of these sensors. Using eq 3, the modulus value (G) needed to observe resonance effects for the 0.10-μm PIB film is about 4×10^7 dynes/cm^2 (log G = 7.6). From Figure 1 it is seen that to lower the film modulus to this level would require heating the coated device to a temperature well above 100 °C. Thus, observation of film resonance effects via thermally induced changes in modulus, as was accomplished by Martin and Frye for a 5-MHz QCM,[7] is not practical for the 158-MHz SAW devices.

Alternatively, absorption of vapor produces slight swelling of the polymer with a concurrent reduction in the shear modulus. On the basis of the conclusions of Grate et al., this reduction in modulus may be substantial. Thus, it should be possible to identify film resonance effects for vapor-saturated polymer films using SAW devices. Decreases in the modulus of the film will produce decreases in the resonant frequency of the coated device, as predicted by eq 1. Furthermore, if the modulus change is sufficient to make the film more lossy, then attenuation of the surface wave should also be observed. Monitoring both the frequency and attenuation of the SAW during vapor exposure should provide verification of the role of elasticity effects in observed SAW responses. In addition, correlation of the attenuation response with film thickness will provide verification of the applicability of the film resonance model of Martin and Frye to SAW sensors.

EXPERIMENTAL SECTION

Materials. The polyisobutylene polymer was obtained from Aldrich. The average MW of the PIB is reported as 420 000, with a density of 0.918 g/cm^3. The polymer was dissolved in HPLC solvent-grade toluene obtained from Baker. The toluene–PIB solutions were used in coating the SAW devices following the procedures described below. The isooctane (2,2,4-trimethylpentane) used for vapor testing was obtained from Aldrich (99.9% purity) and was used as received.

Instrumentation. The SAW sensors and rf electronics used during this study were 158-MHz dual delay line devices obtained from Microsensor Systems, Inc. (Lexington, KY) which have been described previously.[10] In normal practice, the coated devices are sealed with a nickel-plated lid with inlet and outlet tubes attached to allow for introduction of test vapors. This configuration was unacceptable for this study, since the experimental approach called for varying the thickness of the PIB coating in small increments over a broad thickness range. To eliminate potential error due to minor device-to-device variation, it was desirable to use the same device for the entire study. This required that the device be placed in a sample cell that would allow for vapor testing and subsequent removal of the sensor for additional coating application. A suitable sensor cell was constructed, consisting of a plug of phenolic resin–linen composite material that was machined to accommodate the sensor TO-8 package. Two holes were drilled, and $^1/_8$-in. copper tubing was cemented in place to act as vapor inlet/outlet lines. The TO-8 package fit snugly into the machined cavity; three set screws were situated on the base of the cell to ensure that the sensor was held firmly in place during testing. Bevelling of the cell was needed to permit insertion of the cell (with sensor) into the rf electronics board. The bevelled edges also provided a lip for easy grasping, facilitating removal of the cell after testing. Use of this cell permitted evaluation of sensor responses while varying coating thickness on a single device.

Vapor generation and dilution were performed by the VG-400 vapor generation system, also obtained from Microsensor Systems, Inc. The bubbler containing the isooctane was maintained at 15.0 °C (±0.05). Vapor and clean air flow rates were adjusted to 100 mL/min. The vapor generation system was calibrated, and flow rates were balanced following procedures reported previously.[11] The flow rates were routinely checked at the beginning of every set of experiments, and adjustments were made as needed.

Both the frequency and the amplitude of the polymer-coated SAW were monitored during vapor exposure. The frequency of a single delay line was monitored using a Fluke-Phillips PM-6674 universal frequency counter interfaced to a Hyundai 286 computer via an IEEE-488 bus. The SAW amplitude was monitored using a Hewlett-Packard 54600 A dual channel digital oscilloscope, interfaced to the computer system via an RS-232 communications port.

The temperature of the sensor during a typical experiment was monitored with a YSI series 400 temperature probe (Yellow Springs Instrument Co., Yellow Springs, OH), which was placed in contact with the sensor cell. The temperature during a given experiment was fairly constant; the temperature during the entire study, however, varied between 26 and 29 °C. In order to minimize the effects of temperature on the data set the frequency response data were corrected to a standard temperature of 25 °C following procedures described below.

Coating Procedures. The adhesion and morphology of SAW coatings has been observed to be affected by prior cleaning of the device.[6] All devices used in this study had been previously treated with silanizing reagents to "deactivate" the quartz/SiO_2 surfaces. Prior to application of polymer coatings the devices were cleaned by immersion in appropriate solvents (toluene, methanol, and acetone) and subjected to ultrasonication for 2–5 min. After drying, the surfaces were visually inspected for residue. The wettability of the surface was evaluated by application of a small drop (1 μL) of toluene. If the droplet spread smoothly over the surface, the device was deemed sufficiently clean and wettable to obtain a good film. In some cases, the droplet did not spread evenly but appeared to pool on the surface. Such devices were not considered acceptable for this study.

Polyisobutylene polymer films were applied using two different techniques. The first technique was an airbrush method, in which a dilute solution of the polymer in a volatile solvent was aspirated to produce a fine mist, which was directed onto the surface of the SAW device while the device frequency was monitored to determine the amount of coating deposited. It was relatively easy to deposit small increments of coating material via this technique. Each successive application produced between 8 and 15 kHz of frequency shift. After each coating increment, the sensor was exposed to isooctane vapor of varying concentrations.

The second technique was a drop-coating method, in which a drop of PIB solution was placed on the surface of the SAW. The volatile solvent evaporated leaving a thin film of PIB on the surface of the SAW. As expected, it was not as easy to control the amount of coating applied by this method. By trial and error it was possible to obtain coatings of varying thicknesses (represented as kilohertz of frequency shift) over the range of 8–250 kHz.

The morphology of the coating films differed significantly between the two techniques. For the airbrush films, the PIB appeared as overlapping plates of varying thickness dispersed over the entire surface of the device. For the drop evaporation method, the film thickness was typically more uniform over the SAW surface, with minor ripples and thickness variations near the edges of the device. Of the two, the drop evaporation method produced a more contiguous, uniform film, whereas the airbrush film surface was more undulating. The errors associated with coating thickness (kHz) from the drop evaporation method were larger than those associated with the airbrush method, but are still estimated to be within ±5 kHz.

Normalization of Frequency Data. The frequency response of the PIB-coated sensor is entirely dependent on the amount

(10) Grate, J. W.; Snow, A. W.; Ballantine, D. S., Jr.; Wohltjen, H.; Abraham, M. H.; McGill, R. A.; Sasson, P. *Anal. Chem.* 1988, *60*, 869.

(11) Grate, J. W.; Klusty, M. *NRL Memorandum Report #6762*, 1990.

of vapor sorbed into the film. This partitioning phenomenon, which is defined quantitatively by the coefficient K, is sensitive to variations in temperature. Minor fluctuations in ambient temperature during our experiments would be expected to produce fluctuations in the observed sensor responses as well. To eliminate this potential source of error, it was necessary to normalize all frequency data to a standard temperature. The temperature dependence of a PIB-coated SAW sensor response to isooctane vapor was determined by Grate et al.[6] The frequency response (Hz) can be converted to a partition coefficient (K_{SAW}) by the following relationship:

$$K_{SAW} = \frac{\Delta f_v \rho_s}{\Delta f_s C_v} \quad (4)$$

where Δf_s is the frequency shift (kHz) due to coating deposition, Δf_v is the frequency shift (Hz) observed upon sorption of vapor, and ρ_s is the density of the coating (kg/m^3) in equilibrium with a vapor concentration of C_v (g/L). It should be stressed that the value of K_{SAW} is not equivalent to partition coefficients determined from gas chromatography studies, K_{GLC}. The latter values are derived from dynamic equilibrium between two phases and are based on solubility interactions. The former values are also partially dependent on the relative strength of these interactions, but the magnitude of K_{SAW} values are the net result of both mass loading due to sorption of vapor *and* concurrent changes in viscoelastic properties of the polymer, as discussed by Grate et al.[6]

The frequency responses of a 280-kHz PIB airbrush film to isooctane vapor, reported by Grate et al., were converted to K_{SAW} values and plotted vs inverse temperature (K^{-1}). The plot of log K_{SAW} vs $1/T$ is linear and, within the temperature range of the study, the value of K_{SAW} increases by 6% for every 1.0 °C decrease in temperature. Thus, frequency response data Δf_v, which are directly proportional to K_{SAW}, can be corrected by multiplying by the appropriate factor. For our purposes, all frequency data were corrected to a standard temperature of 25 °C. It should be noted that the correction discussed above have been made to permit direct comparison with previously reported results[6] and to minimize temperature effects on the data set as a whole. The results discussed below were readily observable both before and after the temperature corrections were applied.

RESULTS

The frequency shifts and attenuation of PIB-coated SAWs were monitored as a function of film thickness and isooctane vapor concentration for both airbrush and drop evaporation films. The response behavior for airbrush and drop evaporated films are summarized below. It should be noted that, although representative data from only one device are presented in each case, these effects were observed to be reproducible for other similarly coated devices.

Airbrush Films. The frequency responses for PIB airbrush films exposed to three different concentrations of isooctane vapor are plotted in Figure 2. The concentrations of 201 000, 80 400, and 50 250 mg/m^3 correspond to dilution factors of 1.0, 2.5, and 4.0, respectively, for the VG-400 vapor generation system. As discussed above, all data have been corrected to a reference temperature of 25 °C. For the most part the initial portions of the curves are linear, although there is a pronounced steep initial slope for the highest isooctane concentration that levels off for film thicknesses greater than 60 kHz. Above about 190 kHz there appears to be a sinusoidal variation in the frequency response. This is most easily observed at 201 000 mg/m^3 but is also present at the other concentrations. A possible explanation for this behavior will be discussed later.

We can calculate K_{SAW} values using eq 4 for comparison with previous studies. Using response data for the 271-kHz PIB film, summarized in Table I, we obtain K_{SAW} values of 3.190, 3.125, and 3.116 for the three concentrations studied. The latter two values are in excellent agreement with the

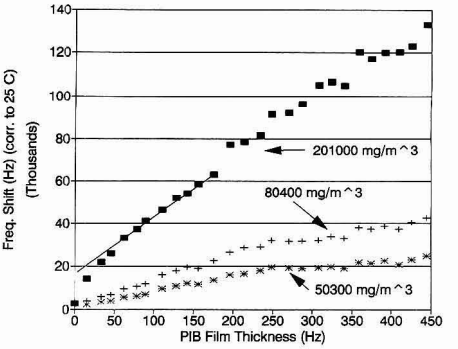

Figure 2. Frequency responses of PIB-coated SAW (airbrush film) exposed to different concentrations of isooctane vapor. Responses are plotted as a function of PIB film thickness (kHz).

Table I. Calculation of K_{SAW} Values for PIB-Coated SAWs Exposed to Isooctane Vapor

isooctane concn (mg/m^3)	freq shift (Hz) (271 kHz PIB film)	K_{SAW}[a]	slope (Hz shift/kHz coating)[b]	K_{SAW}
201 000	92 000	3.190	265.7	3.084
80 400	31 680	3.125	106.9	3.087
50 300	19 380	3.116	63.6	3.065

[a] Calculated from single frequency response for 271-kHz PIB film using eq 4. [b] Calculated from initial slopes in Figure 2, as discussed in text.

value calculated by Grate et al. of 3.12. The calculated K_{SAW} values increase as the vapor concentration increases. It is obvious from the curves in Figure 2 that the response curves have nonzero intercepts, a situation which is not accounted for when using eq 4. The nonzero intercepts are most likely due to interfacial or surface adsorption effects; this phenomenon may also explain the steep initial slope at the highest isooctane concentration, since adsorption effects for nonpolar vapors would be more pronounced at higher concentrations.[12] Such effects introduce errors into the calculated value of K_{SAW}, which is intended to be a measure of the intrinsic response of the coating alone.

An alternative for calculating K_{SAW} values is from the slope of the response vs film thickness plot. The slope of the curve represents the change in response to vapor (Δf_v) as a function of changes in film thickness (Δf_s) and can be substituted into eq 4 in place of the ratio ($\Delta f_v/\Delta f_s$). The slopes for the initial portions of the curves in Figure 2 were calculated and are also included in Table I. It should be noted that the slope at the highest concentration was taken from the region indicated by the dashed line in the figure. In this region interfacial or surface adsorption effects have leveled off, and further changes in the frequency response are due to the intrinsic absorptive properties in the coating. Using this approach yields K_{SAW} values of 3.084, 3.087, and 3.065, which are in better agreement from top to bottom than values calculated from a single response. These values are still significantly greater than the K_{GLC} of 2.28 reported by Grate et al.[6] because of modulus effects as discussed previously. The fact that these values are comparable at the three concentrations studied, however, is a strong indication that both the modulus responses and sorption responses increase linearly with vapor concentration. It is suggested that using the slope method to calculate K_{SAW}

(12) Martin, S. J., Ricco, A. J.; Ginley, D. S.; Zipperian, T. E. *IEEE Trans. Ultrason. Ferro. Freq. Control* 1987, *UFFC-34* (2), 142.

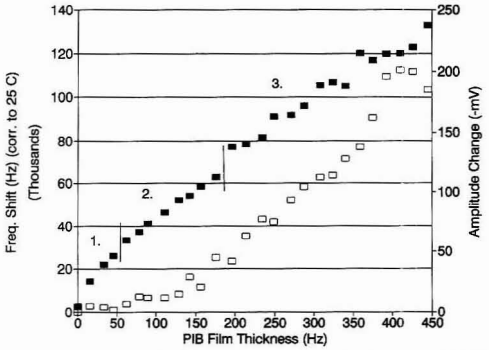

Figure 3. Frequency (solid square) and attenuation (open square) of SAW signal for PIB airbrush film exposed to 201 000 mg/m^3 isooctane vapor. Response behavior for regions identified as 1, 2, and 3 are discussed in the text.

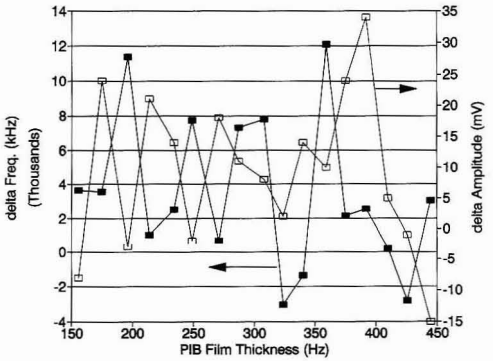

Figure 4. Differential frequency and attenuation response for PIB airbrush film exposed to 201 000 mg/m^3 isooctane vapor for film thicknesses above 150 kHz. Data represent the change in frequency and attenuation at different film thicknesses.

values provides a more accurate assessment of the intrinsic response behavior of the coating and also provides a means to determine the linearity of the modulus and sorption responses.

Attenuation of the surface wave was also monitored during vapor exposure experiments. The initial amplitude of the polymer-coated SAW was generally about 600–800 mV. Changes in film properties, i.e. modulus, that result in attenuation of the surface wave are observed as a decrease in the SAW amplitude. A comparison of the attenuation, reported as decrease in SAW amplitude (mV), and frequency response for airbrush films exposed to 20 100 mg/m^3 isooctane is given in Figure 3. Attenuation is slight for film thicknesses below about 150 kHz and then increases steadily as film thickness increases. The increase in attenuation appears to coincide with the onset of sinusoidal variation in frequency response. From Figure 3 we can identify three different response regions labeled numerically as 1, 2, and 3. In the following discussion we will interpret both the frequency and attenuation response behavior within these regions.

Region 1 is characterized by essentially zero attenuation and a steep slope in the frequency response. In this region it is postulated that the amount of coating deposited by the airbrush technique does not yet completely cover the device surface. Because of the irregular shape and distribution of the coating droplets on the surface, the total surface area of coating is steadily increasing in this region. As surface area increases, frequency shifts due to adsorption of vapor would also expect to increase.

In region 2 (above 60 kHz) the airbrush film now completely covers the device surface. Incremental additions of coating will increase the mass on the surface but will not increase coating surface area. In this region increases in frequency response will be related to the intrinsic properties of the coating (sorptive or modulus properties). There is a slight attenuation response in this region, but it is still relatively small, i.e. less than 50 mV.

In region 3 (>190 kHz of coating) there is an increase in the attenuation response and nonlinear behavior in the frequency response. This effect is also seen for sensor responses at lower vapor concentrations; while attenuation increases significantly in this region, it is generally much smaller than that observed at the highest vapor concentration. The frequency response appears to vary sinusoidally with a periodicity of approximately 50 kHz. Such periodic variation in the frequency response is consistent with the film resonance model, which predicts that the frequency response (negative hertz shift) should first increase and then decrease as the phase shift across the film approaches and then exceeds an odd multiple of $\pi/2$. The fact that this behavior coincides with an increase in attenuation further supports the assumption that this behavior is due to film resonance effects.

This point is more clearly seen by calculating the differential frequency and attenuation at different film thicknesses. A simple method for doing so is to determine the point-to-point change in frequency shift or attenuation as coating thickness is increased. Linear behavior would be translated into a straight line of zero slope, whereas nonlinear variations in response would appear as peaks and valleys. A peak in this point-to-point differential plot would correspond to a large increase in response, whereas a valley would correspond to a small increase or, in some cases, a decrease in response. A differential plot of the frequency and attenuation response for region 3 is given in Figure 4. From 150 to 300 kHz of film thickness it is clear that the frequency response (filled square/solid line) and attenuation response (open square/dashed line) vary systematically. More specifically, when there is a maximum in the attenuation there is a minimum in the frequency response, consistent with the resonance model. Again, the periodicity of this variation is about 50 kHz. Above 300 kHz this behavior is not as consistently observed. This may be due in part to a lack of data points to adequately describe this effect in this region.

The question arises as to why this phenomenon is not observed in region 2, but only appears above about 190 kHz. The answer may lie in the morphology of the airbrush film. As noted earlier, microscopic inspection of the airbrush films reveals that they appear as small, overlapping platelets of varying size distributed over the surface of the device. Thus the film thickness varies from one location on the device surface to another. This lack of uniform thickness may be sufficient to prevent film resonance from occurring when the film is sufficiently thin. For thicker films, swelling of the film when exposed to vapor may produce a smoother surface so that film resonance may occur. The fact that there are localized minima and maxima in the attenuation supports this conclusion. The attenuation response does not decrease to nominal levels, however, which would be expected once film thickness increases beyond the region where resonance effects are observed. It is possible that, for the airbrush films, there are localized areas on the device surface that are in resonance and give rise to attenuation of the SAW signal regardless of the average thickness, even though the film as a whole exhibits some small systematic variations due to resonance effects.

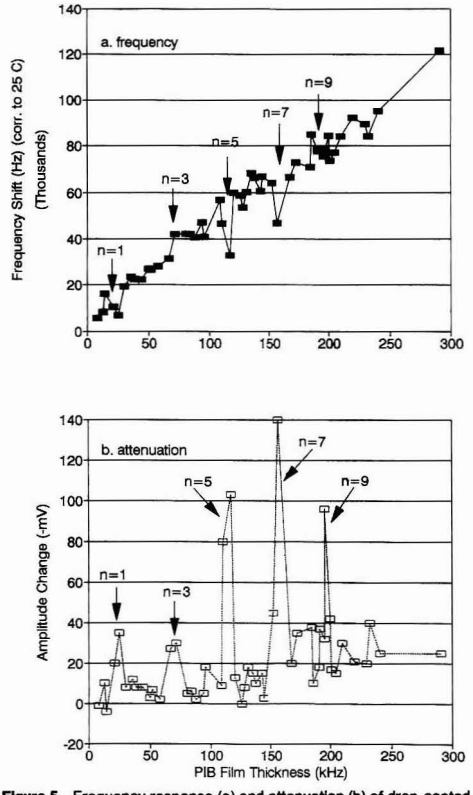

Figure 5. Frequency response (a) and attenuation (b) of drop-coated SAW device exposed to isooctane vapor (201 000 mg/m^3) as a function of PIB film thickness (kHz). Regions identified as n = 1, 3, 5, 7, 9 refer to film thicknesses corresponding to phase shifts that are odd multiples of $\pi/2$.

Drop Evaporation Films. A similar methodology was followed for the drop evaporation films. PIB coatings were applied as discussed previously, and the coated device(s) were exposed to isooctane vapors of varying concentrations while the frequency and attenuation response of the device were monitored. The frequency and attenuation responses were then plotted vs PIB film thickness (kHz). The results for a PIB-coated SAW exposed to isooctane vapor of 201 000 mg/m^3 are summarized in Figure 5a,b.

In general, it should be noted that the average frequency responses between airbrush and drop-coated devices are comparable. The frequency shifts for 50 kHz of coating are on the order of 25 kHz in both cases, for 100 kHz of coating are on the order of 45 kHz, and for 200 kHz of coating are on the order of 80 kHz. From Figure 5 it is obvious, however, that there is much greater overall variation in both the frequency and the attenuation response of the drop-coated SAW device compared to the airbrush-coated device data in Figure 3. Some of this variation is due to the coating technique as noted earlier, but some of the variations are too large to be explained in terms of small errors in the amount of coating deposited. These data can very readily be interpreted in terms of the film resonance model, and the systematic variations in both frequency and attenuation responses can be assigned to film thicknesses corresponding to phase shifts of $n\pi/2$, where n = 1, 3, 5, 7, etc., as indicated in Figure 5. Film thicknesses corresponding to these phase shifts were estimated as the midpoint between the thicknesses which produced the two largest attenuation responses in that thickness region. These average thicknesses are listed in Table II, along with the corresponding phase shift n value.

Table II. Determination of Film Thickness at Resonance Modes for PIB Exposed to 201 000 mg/m^3 Isooctane Vapor

n	thickness (kHz)	difference	thickness (μm)
1	43		0.0088
		46	
3	69		0.0264
		45	
5	114		0.0436
		41	
7	155		0.0594
		43	
9	198		0.0758
		av = 43.8	

For most cases where significant attenuation is observed there are also easily observable variations in the frequency response. These are most notable for thicknesses corresponding to n = 1, 5, and 7. At these film thicknesses there are obvious, dramatic decreases in the frequency response that coincide with maxima in the attenuation response. In addition, for film thicknesses between those where film resonance effects are observed the attenuation response is generally small, on the order of 20 mV or less. This is in contrast to the airbrush film results where attenuation increased steadily and dramatically above a thickness of 150 kHz. These results are wholly consistent with the film resonance model proposed by Martin and Frye and are related to film morphology. Whereas the airbrush film exhibited nonuniform thickness over the device surface, the drop evaporation films are more contiguous with more uniform thickness. Some variations in thickness were noted at the edges of the device which could explain some of the baseline noise in the attenuation response.

Unfortunately, it was not possible to readily identify unique attenuation peaks for the isooctane vapor concentrations below 210 000 mg/m^3. There were instances of significant attenuation, but these coincided very closely with those observed for 201 000 mg/m^3; at the lowest concentrations, attenuation effects were generally very slight which made identification of attenuation maxima even more difficult. These difficulties may be due, in part, to the film application method. While the drop evaporation films are more uniform than the airbrush films, there may still be enough variation in film thickness to hinder the observation of unique resonance effects at different vapor concentrations. In retrospect, spin-coating techniques which provide very uniform films would have been a more favorable technique. Such techniques, however, are not without disadvantages in terms of time and cost. The results presented above still strongly suggest that film resonance effects play a significant role in observed SAW responses for these films and warrant further study.

DISCUSSION

Using the data in Table II we can calculate the resonance thickness for a PIB coating that is in equilibrium with 201 000 mg/m^3 isooctane vapor. The differences between film thicknesses corresponding to n = 1, 3, 5, and 7 yield an average of difference of 43.8 kHz between each resonance mode. This value agrees well with the estimated sinusoidal periodicity of the frequency response (50 kHz) discussed earlier for the airbrush film (see Figure 3, region 3, and related discussion in text). Since this difference corresponds to a phase shift of $\Delta n\pi/2$, where Δn = 2, the resonance thickness is actually about 23 kHz. This thickness in kilohertz can be converted

to a thickness in meters using eq 1. Upon rearrangement to solve for film thickness, h, the following relationship is yielded:

$$h = \frac{\Delta f}{f^2}\left(\frac{1}{(k_1 + k_2)\rho - k_2\left(\frac{\mu}{\nu^2}\right)\left(\frac{\lambda + \mu}{\lambda + 2\mu}\right)}\right) \quad (5)$$

where Δf_s is the coating thickness (23 kHz), f is operating frequency of the device (157.9 MHz), ρ is the density of the coating (918 kg/m^3), μ is the shear modulus of the polymer at the SAW operating frequency (8.9×10^8 kg/m·s^2), and ν is the Rayleigh acoustic wave velocity in quartz (3300 m/s). Values for the materials constants, k_1 and k_2, are -8.7×10^{-8} and -3.9×10^{-8} m^2 s/kg, respectively. The last term in the denominator, $(\lambda + \mu)/(\lambda + 2\mu)$, is constrained between 0.5 and 1, with 0.85 serving as a reasonable value for our purposes. Upon solving the above equation, we obtain a PIB film thickness of 0.0082 μm. It should be stressed that the above thickness was calculated using both terms in eq 1; i.e. modulus effects are not considered negligible for this film, since the modulus of PIB at a frequency of 158 MHz is on the order of 10^9 dynes/cm^2. If this term were neglected, calculated film thicknesses would be consistently lower by 12%.

To determine the modulus of the PIB film upon exposure to isooctane vapor we can now use eq 3. Corrections must first be applied, however, to account for changes in the thickness and density of the film due to swelling. These corrections can be made by following the method of Grate et al.[6] From eq 2, the term C_vK/ρ_L provides an estimate for the volume fraction increase of the sorbent phase due to vapor sorption. For a vapor concentration of 0.201 g/L, a liquid density of 692 g/L, and a K value of 190 from GC studies,[6] we obtain an estimated volume increase of 5.5%. The expansion of a polymer film on the surface of a SAW device is likely to be constrained in length and width, so that the swelling will be manifested entirely as an increase in film thickness. The density of the swelled film can be calculated as the sum of the volume fractions of PIB and isooctane, each at their given densities, divided by the total volume

$$\rho_{\text{swelled}} = \left(\frac{918\ \text{g/L} + (0.055)692\ \text{g/L}}{1.055}\right)$$

which yields a density of 906 g/L (0.906 g/cm^3). We can now determine the modulus of the swelled PIB film using eq 3 by setting $\phi = \pi/2$, $h_f = 8.65 \times 10^{-7}$ cm (corrected for swelling), and $\rho_f = 0.906$ g/cm^3 and solving for G. The calculation yields a value of 2.7×10^5 dynes/cm^2. This value is more than 4 orders of magnitude lower than the modulus of the original, unswelled PIB film which has a modulus value 8.9×10^9 dynes/cm^2. Such a dramatic reduction in modulus supports the conclusions of Grate et al. and further implicates swelling-induced modulus changes as an important response mechanism for polymer-coated SAWs. Furthermore, the results presented here demonstrate the utility of the film resonance model in estimating the mechanical properties of polymer films upon exposure to vapor.

The observed effects discussed above have been preliminarily assigned to film resonance modes corresponding to $n = 1, 3, 5, 7$, etc. It is possible that the drop evaporation films are of less-than-uniform thickness and that a portion of each of the films for which resonance effects were observed are of the same thickness. If this is the case, then the possibility must be considered that these effects are actually multiple observations of a single resonance mode (i.e. film thickness, $n = 1$). Several factors prompt consideration of this possibility. First, the attenuation maxima appeared at very nearly the same film thicknesses for all vapor concentrations. Second, the attenuation maxima appeared as rather sharp peaks in contrast to the broad maxima observed during the thermal studies cited previously.[7] Third, the magnitude of the effect on the frequency response must be considered. During thermal studies, the frequency of a PIB-coated 5-MHz QCM device increased by as much as 60 kHz (12 000 ppm) as the phase shift increased beyond $\phi = \pi/2$.[7] In contrast, the largest differences in the expected frequency response of the PIB-coated SAW during vapor exposure (at $n = 1, 5, 7$ in Figure 5) were only about 10–15 kHz (60–100 ppm).

Finally, the modulus for the PIB polymer film exposed to isooctane vapor calculated using eq 3, assuming a resonance film thickness of 8.2×10^{-7} cm is on the order of 10^5 dynes/cm^2. In contrast, polymers in the elastomer region are characterized by moduli on the order of 10^7 dynes/cm^2. While sorption of vapor and the subsequent swelling of the polymer would be expected to decrease the polymer modulus somewhat, a decrease of 2 orders of magnitude might be larger than would reasonably be expected.

On the other hand an argument can be made to support the assignment of multiple resonance modes. First, the odds of such phenomena being observed at such reproducible periodic intervals purely at random by the application of drop evaporated films are rather slim. In addition, the periodicity of the observed effects for the airbrush films (50 kHz) is of the same order of magnitude as that observed for the drop evaporation film. In any event, the observations of increased attenuation concurrent with decreased frequency response clearly support the film resonance model, although the assignment of specific resonance modes may be in doubt.

FINAL REMARKS

The results presented above strongly suggest that film resonance effects can be observed for polymer-coated SAW sensors. While a comprehensive film resonance model has yet to be developed for SAWs, these results indicate that such a model could provide a more fundamental understanding of the response behavior of these devices. To summarize the significant results presented above:

1. Plotting SAW frequency (and attenuation) responses to vapor as a function of film thickness provides a more accurate assessment of the intrinsic properties of the coating material than calculating K values from a single response at only one coating thickness.

2. For drop evaporation films, significant attenuation of the surface acoustic wave occurs at periodic film thicknesses. At these film thicknesses there are also dramatic decreases in the frequency response. Both of these observations are consistent with film resonance effects.

3. For airbrush films, film resonance effects are not readily observable below about 200 kHz and produce only minor variations in frequency above this thickness. In terms of sensor applications, airbrush techniques are still the most easily utilized and produce highly reproducible results. The response is both linear and predictable for relatively thin films (<200 kHz) with only minor fluctuations in frequency response for thicker films.

4. For the PIB films used here, resonance effects were only observed at high vapor concentrations. The extent of modulus change occurring in polymer films upon sorption of organic vapors has not yet been quantitatively studied. The possibility of observing such resonance effects under low vapor concentration conditions cannot, therefore, be adequately evaluated.

Film resonance effects might be successfully utilized, however, in a number of ways. For chemical sensing, this effect is well suited for threshold sensors. A film having a well-defined thickness can be applied; subsequent swelling upon exposure to a critical vapor concentration reduces the modulus to the point where film resonance occurs, with a

subsequent increase in attenuation and decrease in frequency response. For materials characterization applications, the film resonance model would be useful in estimating the modulus changes in thin films both as a function of temperature and/or vapor-induced swelling.

It should be noted that the film resonance model discussed above was developed for the QCM; an analogous model has yet to be fully developed for the SAW device, although the results presented here indicate that such a model is appropriate. The quantitative aspects of the model are of particular importance. For example, calculations presented above yielded a film thickness of 0.0082 μm (0.00865 swelled), corresponding to a frequency shift of 23 kHz of coating. Upon exposure to isooctane vapor of 210 000 mg/m^3, the modulus of the film decreases from an initial value of 8.9×10^9 to 2.7×10^5 dynes/cm^2. The predicted frequency response using eq 2 and data from ref 6 is −8.2 kHz, with 90% (7.3 kHz) of this response arising from modulus effects. The frequency shift due to modulus effects can be estimated by the magnitude of the second term in eq 1, or by using some other appropriate equation such as eq 12 from ref 6. In both cases, a modulus-induced frequency shift of ca. −2.2 kHz is calculated, considerably less than that calculated above. Some of the discrepancies between various predicted and observed results may be due to the initial value for G used above which, as was discussed previously, was obtained by extrapolation from literature values. In addition, the average thicknesses of the drop evaporation films are estimated using eq 1. Actual film thicknesses may vary somewhat depending on location on the device surface. As noted earlier, spin-coated films would provide a more quantitative measure of these effects. Still, future studies should attempt to reconcile the various models for SAW response behavior.

ACKNOWLEDGMENT

The author wishes to thank Mr. Larry Gregerson of the NIU machine shop for the design and construction of the SAW sample cells and Mr. Dan Edwards and Mr. Ed Hyland of the NIU glass shop for the airbrush coating nozzles. A special thanks to Dr. S. J. Martin of the Sandia National Labs for his invaluable assistance in providing an algorithm for the extraction of PIB modulus values, as well as lengthy discussions on the film resonance model. Acknowledgment is made to the donors of the Petroleum Research Fund, administered by the American Chemical Society, for partial support of this research.

RECEIVED for review August 13, 1992. Accepted October 7, 1992.

Analysis of Diffusional Broadening of Vesicular Packets of Catecholamines Released from Biological Cells during Exocytosis

Timothy J. Schroeder, Jeffrey A. Jankowski, Kirk T. Kawagoe, and R. Mark Wightman*

Department of Chemistry, University of North Carolina at Chapel Hill, Chapel Hill, North Carolina 27599-3290

Christine Lefrou and Christian Amatore

Ecole Normale Superieure, Departmente de Chimie URA CNRS 1110, 24 Rue Lhomond, 75231 Paris, France

Secretion of catecholamines is observed as a series of current spikes when measured at the surface of a bovine adrenal medullary cell in culture with a carbon-fiber microelectrode operated in the amperometric mode. Prior work has shown that these spikes are due to detection of concentrated packets of catecholamines which are released from individual vesicles after their fusion with the cell membrane, a process known as exocytosis. The shape of the individual current spikes, detected with a 5-μm spacing between the hemispherical cell and the electrode, has been compared to the shape generated by a theoretical model. The model consists of an instantaneous point source of material on a surface which subsequently diffuses to a disk that consumes the emitted material. The pertinent diffusion conditions have been evaluated with finite difference and random walk digital simulations. The two methods give identical results when the point source is located on a plane. The more realistic simulation geometry, emission from a hemispherical surface, was evaluated with the random walk method. The simulations allow a set of criteria to be established to evaluate diffusion-controlled broadening of spike shape. The broad range of spike widths observed experimentally and their individual shapes measured with 5-μm cell–electrode spacing are consistent with diffusion from point sources randomly distributed across a hemispherical surface. The data can be described with the diffusion coefficient for catecholamines in free solution. The model enables evaluation of signal-to-noise losses and correction for diffusional losses which are dependent on electrode radius. Through evaluation of spike areas and correction for diffusive losses, an apparent vesicular concentration of catecholamines can be determined.

INTRODUCTION

One useful feature of microelectrodes is that they can be used to measure local concentrations in very small spaces. This feature is being exploited in the technique of scanning electrochemical microscopy.[1–5] Microelectrodes have also been used to probe concentrations inside[6–8] and at the surface[9–14] of biological cells. Our research has been directed at real time monitoring of the exocytotic secretion of the catecholamines norepinephrine and epinephrine from bovine adrenal medullary cells in culture. Catecholamines are easily oxidized compounds, and their secretion can be detected with a microelectrode placed adjacent to an individual cell. The use of cyclic voltammetry has established that catecholamines are the only electroactive substances secreted from individual cultured cells when stimulated under a variety of conditions.[10,12,13] With the electrode used in the amperometric mode, much greater time resolution can be obtained, and secretion is observed in the form of a rapid succession of current spikes of variable amplitude which have a duration of a few milliseconds.[9,12,14] The spikes are a consequence of exocytosis, a secretion mechanism employed by these cells in which vesicles within the cell fuse with the plasma membrane, and their contents, including the catecholamines, are extruded into the extracellular space.[12] In previous work various features of the spikes have been examined to establish that they are of vesicular origin.[12,14] Thus, the opportunity exists to probe the biochemical steps associated with exocytosis in real time. This result is of considerable interest because this secretory mechanism is also believed to be used by neurons.[15]

In this paper we address the question of information contained within the spike shape. The issues to be addressed can affect all chemical measurements in microenvironments.[1] The observed concentration changes contain information about events which occur at the source and transport of species to the electrode surface. For biological cells, the observed current spikes may reflect diffusion, convection, or kinetic processes associated with exocytosis. The hypothesis to be tested in this paper is that the shapes are diffusion controlled. This implies that convection does not occur and that fusion of the vesicle is rapid compared to the time scale of diffusional mass transport. Under these conditions the secretion event will appear to be an instantaneous point source on the cell surface, a condition that can be simulated.

* To whom correspondence should be addressed.

(1) Engstrom, R. C.; Pharr, C. N. *Anal. Chem.* 1989, *61*, 1099A–1104A.
(2) Bard, A. J.; Fan, F.-R.; Kwak, J.; Leo, O. *Anal. Chem.* 1989, *61*, 132–138.
(3) Bard, A. J.; Denault, G.; Lee, C.; Mandler, D.; Wipf, D. O. *Acc. Chem. Res.* 1990, *23*, 357–363.
(4) Bard, A. J.; Fan, F. F.; Pierce, D. T.; Unwin, P. R.; Wipf, D. O.; Zhou, F. *Science* 1991, *254*, 68–73.
(5) Lee, C.; Wipf, D. O.; Bard, A. J.; Bartels, K.; Bovik, A. C. *Anal. Chem.* 1991, *63*, 2442–2447.
(6) Meulemans, A.; Poulain, B.; Baux, G.; Tauc, L.; Henzel, D. *Anal. Chem.* 1986, *58*, 2088–2091.
(7) Chien, J. B.; Wallingford, R. A.; Ewing, A. G. *J. Neurochem.* 1990, *54*, 633–638.
(8) Chen, T. K.; Lau, Y. Y.; Wong, D. K. Y.; Ewing, A. G. *Anal. Chem.* 1992, *64*, 1264–1268.
(9) Leszczyszyn, D. J.; Jankowski, J. A.; Viveros, O. H.; Diliberto, E. J., Jr.; Near, J. A.; Wightman, R. M. *J. Biol. Chem.* 1990, *265*, 14736–14737.
(10) Leszczyszyn, D. J.; Jankowski, J. A.; Viveros, O. H.; Diliberto, E. J., Jr.; Near, J. A.; Wightman, R. M. *J. Neurochem.* 1990, *56*, 1855–1863.
(11) Kawagoe, K. T.; Jankowski, J. A.; Wightman, R. M. *Anal. Chem.* 1990, *63*, 1589–1593.
(12) Wightman, R. M.; Jankowski, J. A.; Kennedy, R. T.; Kawagoe, K. T.; Schroeder, T. J.; Leszczyszyn, D. J.; Near, J. A.; Diliberto, E. J., Jr.; Viveros, O. H. *Proc. Natl. Acad. Sci. U.S.A.* 1991, *88*, 10754–10758.
(13) Ciolkowski, E. L.; Cooper, B. R.; Jankowski, J. A.; Jorgenson, J. W.; Wightman, R. M. *J. Am. Chem. Soc.* 1992, *114*, 2815–2821.
(14) Chow, R. L.; von Ruden, L.; Neher, E. *Nature* 1992, *356*, 60–63.
(15) Valtarta, F.; Fesce, R.; Grohovaz, F.; Haimann, C.; Hurlbut, W. P.; Iezzi, N.; Torri Tarelli, F.; Villa, A.; Ceccarelli, B. *Neuroscience (Oxford)* 1990, *35*, 477–489.

0003-2700/92/0364-3077$03.00/0

The diffusion-based models developed here are based on the physical characteristics of the experimental system. Bovine adrenal medullary cells in culture have a hemispherical shape with an average radius of 8 μm.[16] The vesicles in which the catecholamines are stored have an average radius of approximately 0.15 μm in epinephrine-containing cells.[17] The diffusion coefficient of catecholamines in free solution is $D = 6 \times 10^{-6}$ cm^2 s^{-1}.[18] However, the concentration of catecholamines in these vesicles is on the order of 0.5 M,[19] and they contain greater than 0.1 M ATP and significant amounts of chromogranin, vesicular proteins.[16] The possibility exists that this concentrated milieu may alter the diffusion coefficient; a much lower value has been reported to explain the spike shapes.[14] In this work we compare results from a diffusion-based model with experimental data. The results agree, and they are consistent with the diffusion coefficient of catecholamines in free solution when measurements are made 5 μm from the cell surface.

EXPERIMENTAL SECTION

Electrochemistry. Carbon fibers (5-μm radius, Thornell P-55, Amoco Corp., Greenville, SC, and 16-μm radius, Textron Specialty Material, Lowell, MA) were used to prepare electrodes.[20] The larger fiber was sealed with epoxy in a glass micropipette, and the tip was polished on a micropipette beveller (Model BV-10, Sutter Instrument Co., Novato, CA) at a 45° angle. The smaller fiber was also sealed in glass, but with a 100-μm length of fiber exposed at the tip. The protruding fiber was encapsulated by electrochemical deposition of 2-allylphenol,[11] and an elliptical surface was exposed by polishing at a 45° angle. The surface area was 1.1×10^{-6} cm^2 and is equivalent in area to that of a disk with a radius of 6 μm. Similarly, the larger electrode has an equivalent radius of 20 μm. The reference electrode employed throughout was a sodium saturated calomel electrode (SSCE).

Amperometry (E_{app} = 0.65 V) employed a potentiostat (EI-400, Ensman Instrumentation, Bloomington, IN) used in a two-electrode mode. The signal was filtered at 16 kHz, digitized with a VCR adapter (digitization rate, 44.1 kHz, Model PCM-2, Medical Systems Corp., Greenvale, NY), and recorded on videotape.

Single-Cell Secretion Experiments. Primary cultures of bovine adrenal medullary cells were prepared from fresh tissue.[10] The cells employed were enriched in epinephrine and cultured as previously described (6×10^5 cells per 35-mm diameter plate[13]). Experiments were performed at room temperature (23.0 ± 0.1 °C) between days 4 and 10 of culture. For release studies, the culture media was replaced with a solution containing 150 mM NaCl, 4.2 mM KCl, 1.0 mM Na_2HPO_4, 11.2 mM glucose, 0.7 mM $MgCl_2$, 2 mM $CaCl_2$, and 10 mM HEPES (pH 7.4).

The culture plates were viewed with an inverted-stage microscope (Axiovert 35, Zeiss, Thornwood, NY). The carbon-fiber microelectrodes with the exposed surface parallel to the cell plate were positioned above the pole of a single cell with a piezo-electric device (PCS-250 Patch Clamp Driver, Burleigh Instruments, Fishers, NY). For the smaller electrode, the cell and electrode could be visualized simultaneously. The electrode–cell spacing was determined by lowering the electrode onto the top of the cell until the cell membrane was visually, elastically deformed. The electrode was then raised and lowered in increasingly small increments to determine the position at which the cell membrane just began to be deformed. This location was defined as the cell surface, and the value of the digital readout of the piezo-electric positioner was noted. The electrode was raised to the desired position above the cell using the calibration of the positioner. The larger electrode blocked the view of the cell when positioned directly over it. Therefore, the vertical position was adjusted with the electrode displaced laterally, and the electrode was moved over the cell after the vertical position was established.

Solutions were locally applied to the cells from micropipettes (≈10-μm o.d. at the tip) by pressure ejection (Picospritzer, General Valve Corp., Fairfield, NJ). The micropipettes were positioned 40–50 μm from the cell surface with a mechanical, three-dimensional micromanipulator (Narishige Japan, Tokyo, Japan). Typical ejection pressures were 5–10 psi. Rates of delivery of air into mineral oil with these pipettes and pressures was determined by microscopic observation to be approximately 1 nL/s.

Data Analysis. Recorded data were replayed through a fourth-order, low-pass filter (Krohn-Hite Model 3750, Avon, MA) and captured on a digital oscilloscope. The low-pass filter (100 Hz) was used to remove noise with minimal distortion of the spike shape. Locally written software was used to find and extract the spike amplitude, area, and half width. Signals were designated as spikes if the amplitude was five times greater than the rms noise measured over a baseline of 83 ms. The routines employed a multiple-pass algorithm to determine each peak position and its beginning and end. Thus, spike identification was objective rather than subjective as might occur with visual spike identification.

Finite Difference Simulation. Digital simulations of diffusion from a point source into a semiinfinite media were performed using an explicit finite difference method. Secretion was modeled as an instantaneous point source on a flat planar surface located a distance l under a solid cylinder of radius r whose end served as the electrode. A two-dimensional, cylindrical geometry (grid size: 129 × 129) was employed when the point source was located on the symmetry axis of the system. The dimensionless variable employed was $\tau^* = Dt/l^2$ with dimensionless coordinates: $u = d/r$; $v = z/l$ (d is the off-axis coordinate, z is the vertical coordinate). To ensure stability, $\Delta\tau^*/\Delta l^2$ ($\Delta l = \Delta u = \Delta v$, the dimensionless space increment; $\Delta\tau^*$, the dimensionless time increment) was kept at 0.1; an increase in the time increment led to a corresponding increment in Δl. At initial times (diffusion profile smaller than 0.1v) the analytical solution for point-source, spherical diffusion was used to describe diffusion from the planar surface to avoid instability caused by discontinuities in the concentration profiles. The size of the grid elements was increased stepwise as a function of distance to ensure that at any time, the concentration at the outer limits of the space grid was less than 10^{-5} of the initial concentration.

To evaluate diffusion from a point source that is displaced from the symmetry axis, a three-dimensional grid with cartesian coordinates (32 space elements in each direction) was used. The dimensionless coordinates were $X = x/r$; $Y = y/r$; $Z = z/r$ with $\Delta l = \Delta x = \Delta y = \Delta z$ as the dimensionless space increment.

The simulations were run with two different boundary conditions at the electrode surface. To simulate amperometric detection the surface concentration of the diffusing species was set to zero. The computed flux into the surface was converted to current by $i = nFA\,(dC/dx)_{x=0}$. Simulations were also run without consumption at the electrode surface, and the electrode-surface concentration was monitored as a function of time.

Random Walk Simulation. Diffusion into semiinfinite media from a point source to a disk-shaped electrode of radius r was also simulated with a three-dimensional random walk technique.[21] To replicate the finite difference simulations, the point source was located on a plane at a distance l beneath the electrode and at the center of symmetry. Alternatively, the point source was confined to the surface of a hemisphere of radius R_h located on an infinite plane, with the electrode positioned parallel to the plane. With this geometry the point source was located at the pole or base of the hemisphere or on one of the grid lines shown in Figure 1. The electrode contained an insulating surface around its circumference with a thickness w (w = 1 and 10 μm for r = 6 and 20 μm, respectively, corresponding to the experimental conditions used in this work). Initially, the particles were placed on the secreting surface and, in each subsequent time interval, particles were allowed to move ±1 unit length in each of the Cartesian coordinates. Typically 50 000 particles were used, and the simulations were normalized to the experi-

(16) Winkler, H.; Westhead, E. *Neuroscience (Oxford)* **1980**, *5*, 1803–1823.
(17) Coupland, R. E. *Nature* **1968**, *217*, 384–388.
(18) Gerhardt, G.; Adams, R. N. *Anal. Chem.* **1982**, *54*, 2618–2620.
(19) Hillarp, N.-A. *Acta Physiol. Scand.* **1959**, *47*, 271–279.
(20) Wightman, R. M.; Wipf, D. O. *Electroanalytical Chemistry*; Bard, A. J., Ed.; Marcel Dekker: New York, 1988; Vol. 15, pp 267–353.
(21) Berg, H. C. *Random Walks in Biology*; Princeton University Press: Princeton, NJ, 1983; pp 5–12.

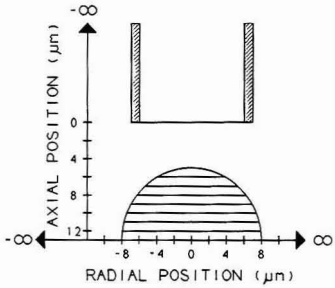

Figure 1. Geometry for the three-dimensional random walk simulations of semiinfinite linear diffusion. Point sources are located on the surface of the hemisphere at the base, the pole, or on the horizontal lines. The flux is measured at a disk surface which is at the end of a cylinder surrounded by an insulator (hatched region). The disk is positioned symmetrically above the hemisphere and parallel to the insulating plane at an axial distance (l) above the pole of the cell. The zero point on the radial axis is the axis of symmetry for the system, and in the axial direction is the disk surface. In this drawing $R_h = 8$ μm, $r = 6$ μm, $l = 5$ μm, $w = 1$ μm, and the horizontal lines are 1 μm apart.

mental data. The dimensionless length of each step was optimized for accuracy and was always less than one-tenth of l. The direction of movement was determined by a random number generator for each particle. Attempted movement into the cell membrane, the infinite plane, or the insulation of the electrode resulted in no movement for that time interval. Movement to the surface of the electrode resulted in consumption of the particle (amperometric mode) and was counted as a measurement event. The simulation was continued until all particles were consumed or for 3000 time iterations. Longer simulations did not alter the results for the distances involved.

The simulation and experimental geometry differ in that the shank of the electrode is at an angle (45°) with respect to the plate surface. Since the surface of the experimental electrodes is elliptical, this geometry was incorporated in the random walk simulations used for comparison with the experimental data. Because an ellipitical surface centered over a hemisphere is not a symmetrical system, the point sources were placed below the minor and major axes, and the reported values are the average of these two.

Reagents. The culture medium, Dulbecco's Modified Eagle's Medium/Ham's F12 Medium, was obtained from Gibco Laboratories (Grand Island, NY). Collagenase (Type I) for digestion of glands was obtained from Worthington Chemicals (Freehold, NJ). Renografin-60 was purchased from Squibb Diagnostics (New Brunswick, NJ). All other chemicals were reagent grade from Sigma (St. Louis, MO), and solutions were prepared with doubly distilled water.

RESULTS AND DISCUSSION

Point Source Diffusion from a Planar Surface. Diffusion from a point source located on an infinite, inert plane to a disk-shaped electrode symmetrically located above the source and parallel to the plane was simulated for different vertical separations between the electrode and the plane. The finite difference method, which uses the integrated form of Fick's laws, gave smoother curves for the electrode flux than the random walk method which uses a finite number of particles (compare the noise in Figures 2B and 3A). However, the spike shape, its maximal current (i_m), its width at half-maximal amplitude ($t_{1/2}$), and the integrated area (Q) were identical with both methods, thus confirming the utility of the random walk method.

Finite difference simulations of the amperometric current are shown in Figure 2A for different distances between the electrode and the point source. Normalization of the time axis of the individual spikes by $t_{1/2}$ and normalization of the current by i_m leads to curves which closely overlap (Figure 2B). Thus the distance of the electrode from the secreting surface does not affect the normalized shape of the spikes within the precision of the experimental measurements. The value of Q decreases with increasing vertical displacement of the electrode from the point source and can be seen as a decrease in the coulometric-collection efficiency (Q/Q_{ves}, where Q_{ves} is the charge which corresponds to the molecules originally in the point source ($Q_{ves} = nFN_{ves}$) (Table I)).

Empirically, the values for i_m, given in dimensionless form, follow eq 1 for different values of the electrode radius (r) at a distance l from the point source:

$$\log [(4\pi^{3/2}r^2/nFDN_{ves})i_m] = 1.52 - 2.70 \log [l/r] - 0.959\{\log [l/r]\}^2 \quad (1)$$

Similarly, the dependence of $t_{1/2}$ is given by

$$\log [(D/r^2)t_{1/2}] = -0.539 + 1.80 \log [l/r] + 0.217\{\log [l/r]\}^2 \quad (2)$$

These expressions are valid for values of l/r from 0.25 to 4.0.

Simulations of the surface concentration profile for the case where the electrode does not consume the diffusing species are shown in Figure 2C. This case corresponds to an electrode sampling technique such as repetitive chronoamperometry or fast-scan cyclic voltammetry in which the concentration is sampled rapidly and with sufficient time between measurements that diffusion from the point source is not perturbed by a concentration gradient at the electrode. Again, the curves superimpose when normalized (Figure 2D). Although the spikes have shapes similar to those in amperometry, the spikes are broader at small values of l/r. This difference is a result of the additional diffusion gradient induced by the electrode in amperometry. The values for the average maximal, surface concentration, C_m, given in dimensionless form, were found to be a function of l/r for values of this ratio between 0.25 and 4 according to

$$\log [(4\pi^{3/2}r^3/N_{ves})C_m] = 1.03 - 2.17 \log [l/r] - 1.06\{\log [l/r]\}^2 \quad (3)$$

The values of $t_{1/2}$ are given by

$$\log [(D/r^2)t_{1/2}] = -0.235 + 1.17 \log [l/r] + 0.924\{\log [l/r]\}^2 \quad (4)$$

Whereas $t_{1/2}$ varies approximately with the square of l/r in the amperometric mode, it varies approximately linearly with this ratio when the concentration at the electrode surface is not perturbed.

Diffusion from the Pole of a Hemispherical Surface. Random walk simulations from a point source at the pole of a hemispherical surface ($R_h = 8$ μm) to a 6-μm radius electrode with the geometry shown in Figure 1 were generated. As the vertical distance between the pole and the electrode is increased, i_m and $t_{1/2}$ alter in a way similar to that for the planar geometry, and the normalized spikes closely overlap. The collection of particles as a function of the vertical displacement between the electrode and point source decreases to a greater degree than with the planar model. For example, for a 6-μm radius electrode located 5 μm from the pole of the hemisphere, 64% of the quantity of the point source is collected, whereas 75% is collected from a source on a planar surface (Table I).

To examine whether the finite size of the vesicle alters the point source approximation, random walk simulations were constructed in which the initial concentration source occupied a volume of inverted hemispherical geometry ($r_{ves} = 0.15$ μm) at the pole of the hemisphere ($R_h = 8$ μm), and the electrode ($r = 6$ μm) was located 1 μm away with $D = 6 \times 10^{-6}$ cm^2 s^{-1}.

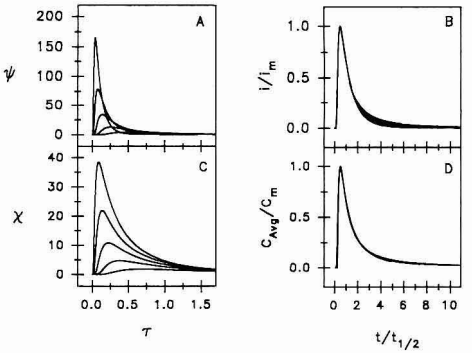

Figure 2. Finite difference simulations of diffusion from a point source located on a plane in semiinfinite media. (A) Dimensionless plots of amperometric current simulated for l/r ratios of 0.5 (largest trace), 0.71, 1, 1.4, and 2. Abscissa: $\tau = tD/r^2$, ordinate: $\psi = I(4\pi^{3/2}r^2/nFDN_{ves})$. (B) Normalized curves from A (see text). (C) Dimensionless surface concentrations (electrode does not consume material) for the same values of l/r as in A. Ordinate: $\chi = (4\pi^{3/2}r^3/N_{ves})C_{avg}$, where C_{avg} is the average surface concentration. (D) Normalized curves from C.

The value of $t_{1/2}$ increased from 0.75 ms with the point source to 0.86 ms. Thus, the effect of finite vesicle size is small and is negligible with 5-μm spacing between the electrode and hemisphere.

Effect of Location of the Point Source. With the planar configuration, the characteristics of the spikes are virtually insensitive to the radial position of the point source with respect to the axis of symmetry as long as it originates within the projection of the electrode circumference on the plane. However, simulations of secretion from the hemispherical source (Figure 3) show that the results depend upon the electrode size and the axial position of the point source on the hemisphere. Amperometric curves were simulated for two different electrode sizes and for point sources located at the pole, the base, and at lines spaced equally apart in the axial direction on the hemisphere (Figure 1). These lines separate the surface into equal surface area segments and provide a way to simulate random release sites distributed over the surface.

As before, the shape of the normalized curves overlap (Figure 3A). The value of $t_{1/2}$ increases (Figure 3B) and i_m decreases (Figure 3C) as the axial position of the point source is moved toward the base of the hemisphere. These changes are greater than for an increased axial separation with the planar geometry. The similarity of the last three values of $t_{1/2}$ is because the particles are not allowed to enter the plane at the base of the hemisphere, and are reflected from this region. Note that the larger electrode has a more uniform value of Q/Q_{ves} (Figure 3D). Inspection of Figure 1 shows that particles from a point source located near the base have a circuitous route to reach an electrode which is smaller than the hemisphere from whose surface secretion occurs. Thus, broad, diffusionally controlled spikes detected with the smaller electrode will contain only a partial quantity of the amount present in the original source.

In summary, the simulations show that the diffusion-controlled current spikes that arise from concentration packets which originate at a hemispherical surface will have the following characteristics when detected amperometrically. First, spikes should superimpose when normalized as in Figure 2B. Second, the values of $t_{1/2}$ will reflect the diffusional distance and diffusion coefficient at a fixed electrode–cell spacing. Third, the coulometric-collection efficiency depends on the size of the electrode as well as the cell–electrode spacing.

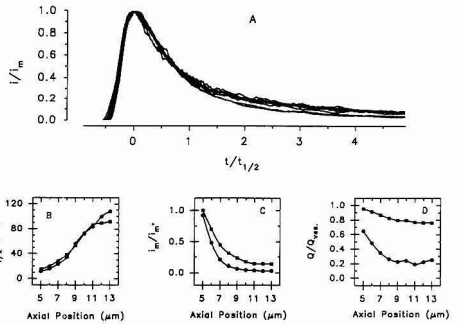

Figure 3. Characteristics of spikes simulated by the random walk procedure for the geometry shown in Figure 1 (5-μm hemisphere–electrode spacing, $D = 6 \times 10^{-6}$ cm^2 s^{-1}). The axial positions of the point sources on the surface of the hemisphere are 5 μm (pole), 13 μm (base), or at the axial positions shown by the horizontal lines in Figure 1. (A) Spikes normalized to their respective maximum currents (i_m) and width at half heights ($t_{1/2}$) for simulations with the dimensions shown in Figure 1. To remove noise caused by the finite number of particles employed, curves were smoothed with a moving average employing $2n + 1$ points, where n is the number of volume elements between the initial point source and the electrode surface. (B) Width at half height. Solid circles: $r = 6$ μm. Solid squares: $r = 20$ μm. (C) Normalized maximum currents for $r = 6$ μm (solid circles) and $r = 20$ μm (solid squares). The normalization factor, i_m^* is the current detected with $r = 20$ μm and the point source located at the pole of the hemisphere. (D) Coulometric-collection efficiency (Q/Q_{ves}) for $r = 6$ μm (solid circles) and $r = 20$ μm (solid squares).

Table I. Coulometric-Collection Efficiencies (Q/Q_{ves}) for a 6-μm-Radius Electrode as a Function of Source–Electrode Spacing Evaluated at 10 $t_{1/2}$ Values after Point Source Occurance[a]

axial position, μm	planar geometry	hemi-spherical geometry	axial position, μm	planar geometry	hemi-spherical geometry
0.1	1.00	1.00	5.0	0.75	0.64
0.2	1.00	1.00	6.0	0.67	0.55
0.5	1.00	1.00	9.0	0.52	0.43
1.0	1.00	0.99	12.0	0.39	0.31
2.0	0.98	0.93	20.0	0.21	0.17
3.0	0.92	0.83	30.0	0.12	0.09
4.0	0.82	0.71			

[a] Point sources were placed on the axis of symmetry of a planar or hemispherical surface, and diffusion was simulated with $D = 6 \times 10^{-6}$ cm^2 s^{-1}.

Characteristics of Spikes Measured with an $r = 6$ μm Electrode. A representative trace recorded with a carbon-fiber electrode ($r = 6$ μm) placed 5 μm from a bovine adrenal medullary cell is shown in Figure 4. Secretion was induced by 100 μM nicotine introduced onto the cell surface from a pressure-ejection pipet. Spikes of variable amplitude and width are clearly resolved from the baseline noise. When the spikes are superimposed, a wide range of i_m and $t_{1/2}$ values are apparent. However, when normalized by i_m and $t_{1/2}$, the curves superimpose and have the same shape as predicted for diffusion from a point source on a hemispherical surface. The normalized shape of 684 randomly selected spikes measured with the $r = 6$-μm electrode were correlated with the diffusion based model. The average correlation coefficient was 0.9074 when the data and model were compared over a width of four $t_{1/2}$ values beginning with one $t_{1/2}$ value before the spike maximum.

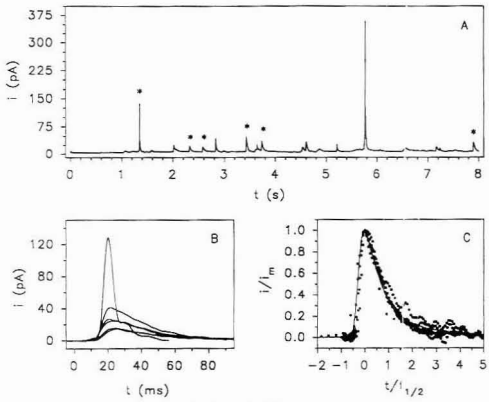

Figure 4. Amperometrically detected (E_{app} = 0.65 V vs SSCE) spikes measured with a 6-μm-radius electrode, 5 μm from the pole of bovine adrenal medullary cell during exposure of the cell to 100 μM nicotine. (A) Amperometric recordings. (B) Spikes marked by asterisks in A superimposed. (C) Spikes from B normalized by i_m and $t_{1/2}$ superimposed. The solid line is a spike simulated as in Figure 3A.

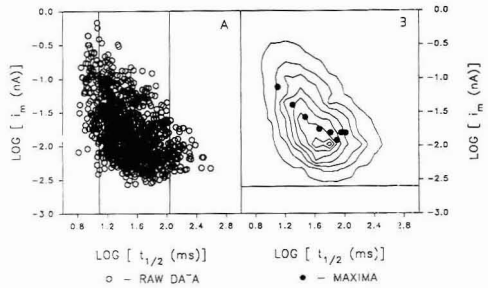

Figure 5. Logarithm of the maximum amperometric currents (i_m) plotted as a function of logarithm of their widths at half height ($t_{1/2}$) for 1044 spikes measured at seven cells during exposure to 100 μM nicotine with a 6-μm radius electrode located 5 μm from the pole of the cells. (A) Each circle represents an individual spike, and the vertical lines are the upper and lower bounds simulated for $t_{1/2}$ using the conditions in Figure 1 and $D = 6 \times 10^{-6}$ cm^2 s^{-1}. (B) Contour plot of the same data. Horizontal line: average rms noise in the current measurements. Closed circles: average maximum currents for the data which lies between the points given in Figure 3B for this geometry.

Evaluation of the experimental spikes in terms of the simulated curves is complicated by variability of biological origin. This is illustrated in Figure 5A where the logarithm of i_m for all spikes detected from seven cells during three successive exposures to 100 μM nicotine is plotted versus the logarithm of its $t_{1/2}$. These data were obtained with a 6-μm-radius electrode positioned 5 μm from the cell pole. The solid lines on the $t_{1/2}$ axis (at 12 and 108 ms) represent the limits for diffusion-controlled transport of the catecholamines as determined from the simulations using the diffusion coefficient of catecholamines in free solution (6×10^{-6} cm^2 s^{-1}). Of the 1044 spikes, only 8.5% have $t_{1/2}$ values less than 12 ms, and 5.4% have values greater than 108 ms.

When evaluated as a contour plot (Figure 5B) the wide distribution of i_m values at each value of $t_{1/2}$ is more readily evaluated. This range of amplitudes is not unexpected because the vesicles have a broad distribution of radii[17] and would be expected to contain a broad range of catecholamine contents. The closed circles in this figure are the average i_m values determined between values of $t_{1/2}$ obtained from the simulations of this geometry (Figure 3B) using the solution

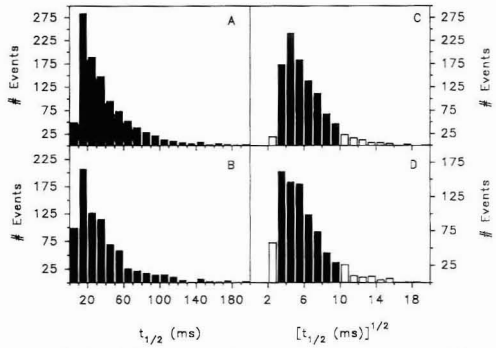

Figure 6. (A, B) Histograms of the widths at half height ($t_{1/2}$) from experiments with the electrodes located 5 μm above the pole of the cell. The cells were exposed to 100 μM nicotine, detection was amperometric, and the bin size is 10 ms. (A, C) Measurements with 6-μm-radius electrode. (B, D) Measurements with 20-μm-radius electrode. (C, D) Histograms of the same data in A and B, respectively, but with the bin size determined by the square root of $t_{1/2}$. The unfilled bars indicate data which falls outside the limits predicted by random walk simulation with the appropriate dimensions and $D = 6 \times 10^{-6}$ cm^2 s^{-1}.

diffusion coefficient. At small values of $t_{1/2}$ the average i_m decreases in a manner consistent with the simulations (Figure 3C). However, at values of $t_{1/2}$ greater than 55 ms the average i_m values become independent of $t_{1/2}$, inconsistent with the simulated results. Inspection of the contour plot shows that truncation of the distribution of spikes occurs at larger values of $t_{1/2}$ because the current amplitudes for some spikes become comparable to the cutoff of the spike-finding program determined by the noise level (horizontal line) of the measurements. For this reason, the distribution of current amplitudes at small values of $t_{1/2}$ is taken as more representative of the range of events which occur at the cell surface.

Characteristics of Spikes Measured with an $r = 20$ μm Electrode. As with the smaller electrode, spikes measured with the $r = 20$-μm electrode have widths at half height varying from 5 to 250 ms. Correlation of the normalized shape of 733 randomly chosen spikes with the diffusion-based model gave a correlation coefficient of 0.8737. Of the total of 825 spikes measured at four cells (each stimulated three times), 24% have a $t_{1/2}$ value less than 15 ms, the value obtained by simulation for this geometry and the free solution diffusion coefficient, whereas 9% had $t_{1/2}$ values greater than 92 ms, the maximum spike width expected. Thus, the fit with the diffusion-based model is not as good, but the error in positioning is greater with the larger electrode since it blocks the view of the cell. Plots of the data obtained with the larger electrode similar to Figure 5 show that the distribution of spikes identified is also truncated at larger values of $t_{1/2}$ because of the signal-to-noise ratio. The noise was greater (7 times larger than the small electrode) because of the larger capacitance associated with the increased electrode area.[22] When the data was purposely overfiltered (20 Hz) to look for additional spikes with $t_{1/2}$ values greater than 92 ms, only 10% more were found.

Distribution of Spike Widths. Histograms of the values of $t_{1/2}$ determined at several cells with a 5-μm cell–electrode spacing are shown in Figure 6A,B for electrodes of two different radii. Histograms with bins determined by $(t_{1/2})^{1/2}$ are shown in Figure 6C,D. This approach was chosen because the simulated data in Figure 3B are approximately linear

(22) Howell, J. O.; Kuhr, W. G.; Ensman, R. E.; Wightman, R. M. *J. Electroanal. Chem. Interfacial Electrochem.* **1986**, *209*, 77–90.

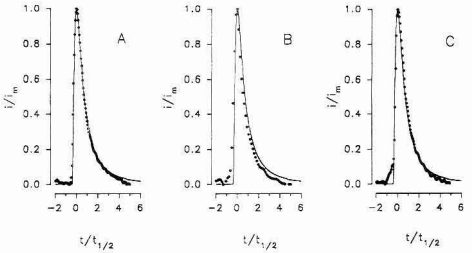

Figure 7. Experimental spikes measured with r = 6-μm electrode and normalized by $t_{1/2}$ and i_m and superimposed on the normalized diffusion-based model. Points: experimental data. Line: diffusion-based model. (A) i_m = 65 pA, $t_{1/2}$ = 38 ms, r = 0.9908. (B) i_m = 72 pA, $t_{1/2}$ = 15 ms, r = 0.9054. (C) i_m = 78 pA, $t_{1/2}$ = 35 ms, r = 0.9880.

when $(t_{1/2})^{1/2}$ is plotted against axial position. Since the region between each simulated $t_{1/2}$ point describes a region of equal surface area, such a plot should show bins equally filled if the concentration spikes originate uniformly over the surface. Previous immunofluorescence studies suggests random sites of exocytosis,[23,24] and our measurements with dual electrodes support this view.[9,11] Within experimental error these expectations seem to be met for small values of $t_{1/2}$ at both sizes of electrode. At larger values, both electrodes have fewer events in each bin. However, as already noted, some spikes with large values of $t_{1/2}$ are lost in the noise. From these considerations it appears that less than 50% of the number of spikes which originate on the hemispherical surface of the cell are detected with both sizes of electrodes. Although simulated results suggest more efficient detection of spikes with the larger electrode, its increased noise negates this advantage.

Correlation coefficients of the normalized spikes which lie within the range of $t_{1/2}$ values expected with the diffusion-based model were determined. The values were 0.9151 for the smaller electrode (n = 601 spikes evaluated) and 0.8992 for the larger electrode (n = 602 spikes evaluated). Three spikes measured with the smaller electrode are given in Figure 7 and illustrate the quality of fit of these spikes. An excellent fit is obtained in Figure 7A; a fit representative of the average is shown in Figure 7B. Some spikes showed an increase in current before the main spike (Figure 7C), a feature that has been reported previously.[14]

In view of the uncertainty in the electrode position and the variability in cell radii, the data obtained with 5-μm cell–electrode spacing show a reasonable fit with the diffusion-based model. Thus, it appears that the spike shape is predominantly determined by transport of a packet of catecholamines released at random locations on the cell surface to the electrode with a rate determined by the free solution diffusion coefficient. Because the half-widths are linearly dependent on the diffusion coefficient (eq 2), its value can be determined quite readily.

The spikes with $t_{1/2}$ values greater than 100 ms (unshaded bars, Figure 6C,D) do not agree with the model. They were individually examined and have the shape expected for diffusion, similar correlation coefficients to the narrower spikes, and do not appear to be the result of overlapping, coincident spikes. Their presence in these histograms may reflect geometrical errors in the placement of the electrodes. Alternatively, there may be slow events associated with exocytosis that precede diffusion to the electrode. Preliminary data suggest that there is much poorer agreement with a diffusion-based model when the electrode is placed closer to the cell surface. Indeed, such features should be more apparent with closer spacing where diffusional broadening plays less of a role.

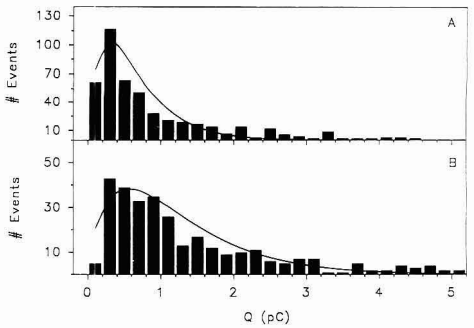

Figure 8. Histograms of spike charge (Q) detected in the two experiments described in Figure 6. Only spikes with $t_{1/2}$ values between 10 and 30 ms are included. The bin size is 0.2 pC. (A) Charge measured with 6-μm-radius electrode. (B) Charge measured with 20-μm electrode. In each histogram, the solid line is a nonlinear least-squares fit of the probability density function previously derived for this type of histogram.[12] The correlation coefficient for A is 0.908 and is 0.885 for B.

Interpretation of the Spike Areas. The integral of an individual spike gives by Faraday's law the quantity of material detected per spike. Histograms of the spike areas of spikes with $t_{1/2}$ values between 10 and 30 ms are given in Figure 8 for measurements made with a 5-μm electrode–cell spacing at the 6- and 20-μm-radius electrodes. The histograms both show the skewed shape we have reported earlier.[12] The shape is that expected when the variation is due to the range of volumes of vesicles.[25] The solid line superimposed on the histograms is a probability density function based on a constant concentration in each vesicle, a two-electron oxidation process, and a gaussian distribution of vesicle radii.[12] With the use of the mean and standard deviation of the vesicle radii,[17] the best-fit line shown was obtained with only the vesicular concentration as an adjustable parameter. Values of 0.17 and 0.33 M are obtained for the 6- and 20-μm-radii electrodes, respectively.

Note, however, that these values, and those we reported earlier,[12] are not corrected for the coulometric-collection efficiency. For the bins employed, simulations show that on average 48% of the material secreted is detected for the 6-μm-radius electrode, whereas 90% is detected with the 20-μm-radius electrode. With these corrections the values for the estimated vesicular concentration is 0.36 M at each size of electrode, close to a previous estimate.[19] The success of this approach further supports the validity of the diffusion controlled model to describe the measured events at the cell–electrode spacing employed.

CONCLUSIONS

Fusion of vesicles with the cell surface results in the extrusion of the vesicle contents into the extracellular space. In this paper we have modeled this phenomenon as an instantaneous point source at the surface of a hemisphere which diffuses to the electrode. The individual spike shapes and their range of half-widths measured with two different electrode sizes are consistent with the model when the free solution diffusion coefficient is employed. Thus, we conclude

(23) Hesketh, J. E.; Ciesielski-Treska, J.; Aunis, D. *Cell Tissue Res.* 1981, *218*, 331–343.
(24) Phillips, J. H.; Burridge, K.; Wilson, S. P.; Kirshner, N. *J. Cell Biol.* 1983, *97*, 1906–1917.
(25) Beckers, J. M.; Richerson, G. B.; Stevens, C. F. *Proc. Natl. Acad. Sci. U.S.A.* 1990, *79*, 5359–5362.

that the temporal spike characteristics measured with a 5-μm cell pole–electrode spacing is a result of mass transport of a concentration packet from the cell surface to the electrode by diffusion. Analysis of the data suggests that spikes originating far from the electrode are lost in the noise. In addition the modeling shows that diffusive losses are quite extensive with the smaller electrode. Correction for these losses allows a more accurate estimate of the vesicle concentration to be made.

Despite the overall agreement of the data and the diffusion-based model, there are suggestions in the data that factors involved in the exocytotic process may also be evident. The prespike feature (Figure 7C) has been attributed to formation of a preexocytotic state formed between the vesicle and cell membrane.[14] We have observed that the average area of all detected spikes remains constant with cell–electrode spacings of 1, 3, and 5 μm,[11] whereas the diffusion-based theory predicts an increase in coulometric-collection efficiency with decreased spacing (Table I). Future experiments with smaller cell–electrode separations will be required to clarify these issues.

ACKNOWLEDGMENT

This research was supported by the Office of Naval Research (R.M.W.), a travel grant from NATO, and CNRS-Utimatech (C.A.). Helpful discussions with B. L. Schroeder are gratefully acknowledged.

RECEIVED for review June 22, 1992. Accepted September 28, 1992.

Registry No. Norepinephrine, 51-41-2; epinephrine, 51-43-4.

Hydrogen Peroxide and β-Nicotinamide Adenine Dinucleotide Sensing Amperometric Electrodes Based on Electrical Connection of Horseradish Peroxidase Redox Centers to Electrodes through a Three-Dimensional Electron Relaying Polymer Network

Mark Vreeke, Ruben Maidan, and Adam Heller*

Department of Chemical Engineering and Materials Science and Engineering Center, The University of Texas at Austin, Austin, Texas 78712-1062

Hydrogen peroxide is efficiently electroreduced at an electrode modified with a hydrophilic, permeable film of horseradish peroxidase (HRP) covalently bound to a 3-dimensional epoxy network having polyvinyl pyridine (PVP)-complexed $[Os(bpy)_2Cl]^{3+/2+}$ redox centers. The sensitivity of the resulting H_2O_2 cathode at 0.0 V (SCE) is 1 A cm^{-2} M^{-1}. Its current increases linearly with H_2O_2 concentration in the 1×10^{-7}–2×10^{-4} M range. Related NAD(P)H cathodes are based on stoichiometric homogeneous reduction of O_2 to H_2O_2 by NADH or NAD(P)H. The reduction involves two known steps. In the first step, NAD(P)H transfers two electrons and a proton to a dissolved quinoid. The quinoids are typically derived of phenazines; however phenothiazine and phenoxazine derivatives are also useful. In the second step, two electrons and a proton are transferred from the reduced quinoid to O_2. This reaction produces H_2O_2 and the original quinoid. Because the two reactions are quantitative, the sensitivity and the linear range of the resulting NADH and NADPH electrodes are identical with those of the H_2O_2 electrode, 1 A cm^{-2} M^{-1} and 1×10^{-7}–2×10^{-4} M, respectively.

INTRODUCTION

Selective electrooxidation of NADH and NADPH cofactors (reaction 1) of enzymes allows, in principle, amperometric assay of a substantial number of biochemicals. When the

$$\mathrm{NAD(P)H} \rightarrow \mathrm{NAD(P)^+} + 2e^- + \mathrm{H^+} \qquad (1)$$

electrooxidation products are the cofactors NAD^+ or $NADP^+$, these can be enzymatically rereduced and electrocatalytic enzyme electrodes can be made. The reversible potential of the $NADH/NAD^+$ couple is −0.56 V (SCE) at pH 7.[1] Because, the reaction involves the concerted transfer of two electrons and a proton, it is usually slow, proceeding at practical rates on most electrodes only at high overpotentials. At these high overpotentials reaction products of NADH and other constituents of biological fluids that are also electrooxidized interfere with the amperometric assays of NAD(P)H.[2,3] Following Elving's definition of this problem,[4-6] several groups, particularly those of Miller,[7-10] Gorton,[11] and Kulys,[12,13] developed electrodes on which reaction 1 proceeds rapidly at low overpotentials. The most successful electrodes, of which Gorton's phenoxazine-derivative and Kulys' phenazine-based electrodes are examples,[11-16] utilize electrode-bound, electrode-adsorbed, or freely diffusing mediators having quinoid structures in their oxidized state. The quinoids effectively catalyze reaction 1 at potentials near 0.0 V (SCE).

Here we consider a more complex but nevertheless very fast and efficient set of coupled reactions for the amperometric assay of NAD(P)H. The first is a homogeneous solution reaction, exemplified by (2), where, as in the electrode

$$\mathrm{PMS^+} + \mathrm{NADH} \rightarrow \mathrm{PMSH} + \mathrm{NAD^+} \qquad (2)$$

reactions of Miller, Kulys, and Gorton, two electrons and a proton are transferred from NAD(P)H to a quinoid mediator. A particularly effective mediator is the water-soluble 5-methylphenazonium cation (PMS^+) which is quantitatively reduced by NAD(P)H to 5-methylphenazine (PMSH). PMSH is next reoxidized to PMS^+ by dissolved molecular oxygen which is, in turn, reduced to H_2O_2 (reaction 3). With reactions

$$\mathrm{PMSH} + \mathrm{O_2} + \mathrm{H^+} \rightarrow \mathrm{PMS^+} + \mathrm{H_2O_2} \qquad (3)$$

2 and 3 being quantitative, each mole of NAD(P)H produces 1 mol of H_2O_2. H_2O_2 is then assayed through electroreduction on the "wired" peroxidase electrode (reaction 4). Several

$$\mathrm{H_2O_2} + 2e^- + 2\mathrm{H^+} \rightarrow 2\mathrm{H_2O} \qquad (4)$$

previously reported detection schemes for NADH and NADPH have utilized reactions 2 and 3, amperometrically sensing the depletion of oxygen[17,18] or spectrophotometrically mea-

(1) Clark, W. M. *Oxidation-Reduction Potentials of Organic Systems*; William and Wilkins: Baltimore, 1960.
(2) Moiroux, J.; Elving, P. J. *Anal. Chem.* **1979**, *51*, 346–50.
(3) Blaedel, W. J.; Jenkins, R. A. *Anal. Chem.* **1975**, *47*, 1337–43.
(4) Samec, Z.; Elving, P. J. *J. Electroanal. Chem. Interfacial Electrochem.* **1983**, *144*, 217–34.
(5) Elving, P. J.; Bresnahan, W. T.; Moiroux, J.; Samec, Z. *Bioelectrochem. Bioenerg.* **1982**, *9*, 365–78.
(6) Moiroux, J.; Elving, P. J. *J. Am. Chem. Soc.* **1980**, *102*, 6533–8.
(7) Degrand, C.; Miller, L. L. *J. Am. Chem. Soc.* **1980**, *102*, 5728–32.
(8) Kitani, A.; So, Y. H.; Miller, L. L. *J. Am. Chem. Soc.* **1981**, *103*, 7636–41.
(9) Fukui, M.; Kitani, A.; Degrand, C.; Miller, L. L. *J. Am. Chem. Soc.* **1982**, *104*, 28–33.
(10) Lau, N. K.; Miller, L. L. *J. Am. Chem. Soc.* **1983**, *105*, 5271–84.
(11) Gorton, L.; Csoregi, E.; Domingues, E.; Emneus, J.; Jonsson-Petterson, G.; Marko-Varga, G.; Persson, B. *Anal. Chim. Acta* **1991**, *250*, 203–48.
(12) Cenas, N. K.; Kanapieniene, J. J.; Kulys, J. J. *J. Electroanal. Chem. Interfacial Electrochem.* **1985**, *189*, 163–9.
(13) Kulys, J. J. *Biosensors* **1986**, *2*, 3–13.
(14) Gorton, L.; Torstensson, A.; Jaegfeldt, H.; Johansson, G. *J. Electroanal. Chem. Interfacial Electrochem.* **1984**, *161*, 103–20.
(15) Persson, B.; Gorton, L. *J. Electroanal. Chem. Interfacial Electrochem.* **1990**, *292*, 115–38.
(16) Bremle, G.; Persson, B.; Gorton, L. *Electroanalysis* **1991**, *3*, 77–86.
(17) Polster, J.; Schmidt, H.-L. *Talanta* **1989**, *36*, No. 8, 864–6.

0003-2700/92/0364-3084$03.00/0

Table I. Amperometric H_2O_2 Sensors Based on HRP-Modified Electrodes

electrode surface	mediator or redox matrix	electrode potential[a]	sensitivity (A cm^{-2} M^{-1})	linear range (μM)	comments	ref
glassy carbon	none	0.0	10^{-2}		HRP covalently bound to a hydrophilic epoxy network; polyvinylpyridine-derived polyamine cross-linked with PEGDGE	this work
glassy carbon	polymer I	0.0	1	0.1–100	HRP covalently bound to hydrophilic epoxy network; polymer I crosslinked with PEGDGE	this work
spectrographic graphite	none[c]	0.05	0.175	0.1–500	BSA with glutaraldehyde cross-linking	36
carbon paste	*o*-phenylenediamine[d]	−0.15	NA[b]	3.1–200	butanone peroxide used as the substrate	37
Pt	hexacyanoferrate (0.01 M)[d]	−0.05	*e*	5–1700	HRP immobilized onto a Nylon net	38
NMP^+TCNQ^-	none[f]	0.05	0.168		HRP entrapped with dialysis membrane	39
SnO_2	ferrocenecarboxylic acid[d]	0.2	0.04	0.01–1	HRP immobilized with glutaraldehyde	40
carbon paste	ferrocene[d]	0.05	NA[b]	0.1–10	Nafion coating applied to the electrode to prevent loss of mediator	41
graphite foil	potassium hexacyanoferrate(II)[d]	−0.02[a]	0.03	<600	electrolyte was dioxane with 15% aqueous buffer	42
carbon fiber[g]	none	*h*		40–5000	biotin/avidin complex used to obtain a surface layer of HRP	43
Pt, organic metal, or glassy carbon	potassium ferrocyanide	*i*			membrane with albumin and glutaraldehyde	44
spectrographic graphite or carbon film	hexacyanoferrate(II)[d]	0.0	*e*	0.1–1000	HRP immobilized on arylamino-derivatized controlled-pore glass, packed into a flow-through reactor	45
aminosilylated glassy carbon	hexacyanoferrate(II)[d]	0.0	*i*		glycerophosphate oxidase, HRP, and BSA covalently cross-linked on the glassy carbon surface	46
glassy carbon	hexacyanoferrate(II)[d]	0.0	*i*		albumin, glutaraldehyde, HRP, and oxidase (xanthine, uricase, glucose) matrix held close to the electrode with a dialysis membrane	47
gold or graphite	several[k]	*k*	2.0[j]	0.05–6[j]	HRP free in solution	48

[a] Potential vs SCE. [b] Macroporous electrode. The true surface area is unknown. [c] Uncertainty as to whether the surface species created during electrode pretreatment are mediating. [d] Freely diffusing mediator. [e] Flow system. [f] Probably mediated by the soluble component of the organic metal or the reaction product of the organic metal. [g] Microelectrode. [h] Cyclic voltametry used to provide selective detection of oxygen generated by autocatalytic decomposition of hydrogen peroxide. [i] HRP incorporated into a bienzyme system. [j] Best reported result for ferrocenemonocarboxylic acid. [k] mediators used and redox potential: $[Ru(NH_3)_5py](ClO_4)_3$ = +28, $CpFeC_2B_9H_{11}$ = −8.0, 1,1′-dimethyl-3-(2-aminoethyl)ferrocene = +75, (2-aminoethyl)ferrocene = +185, ferrocenemonocarboxylic acid = +275, (aminomethyl)ferrocene = +309 mV.

suring the H_2O_2 generated.[19-21] We now add to these amperometric reduction of H_2O_2 on peroxidase, electrically connected (wired) through a permeable 3-dimensional redox polymer network to an electrode. Several horseradish peroxidase modified diffusionally mediated and mediatorless type electrodes have been earlier described. Their characteristics are compared with the wired HRP electrode in Table I.

In the wired HRP electrodes electrons from the electrode are relayed to the enzyme through a redox epoxy network to which the enzyme (HRP) is covalently bound. The centers consist of $[Os(bpy)_2Cl]^{3+/2+}$, complexed to polyvinylpyridine. The HRP and the redox polymer are cross-linked into a 3-dimensional epoxy network with a water-soluble diepoxide. In earlier papers we showed that the resulting redox epoxy accepts electrons from substrate-reduced enzymes, relaying these to electrodes.[22,23] Here we show that the network also relays electrons in the reverse direction from the electrode to a bound enzyme. Network-bound HRP is efficiently electroreduced at 0.0 V (SCE), and H_2O_2 is detected with 1 A cm^{-2} M^{-1} sensitivity. Because NAD(P)H concentrations are stoichiometrically translated to H_2O_2 through reactions 2 and 3, these cofactors are also detected at the same potential with the same sensitivity.

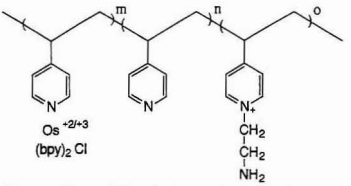

Figure 1. Composition of the electron-relaying redox polymer (m = 1; n = 3.35; o = 0.6). After cross-linking with PEGDGE, it forms a 3-dimensional network that is able to relay electrons to covalently bound HRP. The polymer is referred to as polymer I.

EXPERIMENTAL SECTION

Reagents. Horseradish peroxidase (HRP) E.C. 1.11.1.7 (Sigma P-8375 Type VI, 260 units/mg) was used. Poly(ethylene glycol 600 diglycidyl ether), technical grade (PEGDGE) was purchased from Polysciences (Catalog No. 8211). The osmium redox polyamine (polymer I, Figure 1) was synthesized as described previously.[24] NADH and NADPH were purchased from Sigma (340–110 and N-1630, respectively). 5-Methylphenazonium methyl sulfate was from Aldrich. Other mediators were from Aldrich or Sigma. All chemicals were used as received.

Electrode Construction and Preparation. Rotating disk electrodes were made of a 1-cm length of 3-mm-diameter vitreous

(18) Huck, H.; Schelter-Graf, A.; Danzer, J.; Kirch, P.; Schmidt, H.-L. *Analyst* **1984**, *109*, 147–50.
(19) Williams, D. C., III; Seitz, W. R. *Anal. Chem.* **1976**, *48*, 1478–81.
(20) *Eur. Pat. Appl.* EP 317070, 1989.
(21) *Eur. Pat. Appl.* EP 285998, 1988.
(22) Gregg, B. A.; Heller, A. *J. Phys. Chem.* **1991**, *95*, 5976–80.
(23) Pishko, M. V.; Katakis, I.; Lindquist, S.-E.; Heller, A. *Mol. Cryst. Liq. Cryst.* **1990**, *190*, 221–49.
(24) Gregg, B. A.; Heller, A. *J. Phys. Chem.* **1991**, *95*, 5970–5.

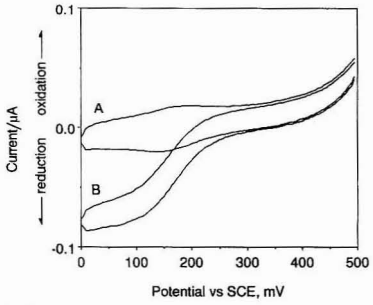

Figure 2. Cyclic voltammogram of a vitreous carbon electrode modified with the Schiff base formed of polyaldehyde–HRP and polymer I *without* $[Os(bpy)_2Cl]^{3+/2+}$ electron-relaying centers, additionally cross-linked with PEGDGE: (A) no H_2O_2; (B) 0.1 mM H_2O_2. Conditions: aerated pH 7 physiological phosphate buffer (PBS) solution; scan rate 2.5 mV s^{-1}; 500 rpm.

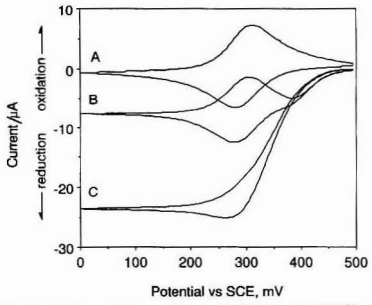

Figure 3. Electrode as in Figure 2, but *with* $[Os(bpy)_2Cl]^{3+/2+}$ electron-relaying centers (polymer I) (1:5 enzyme to polymer I ratio): (A) no H_2O_2; (B) 0.1 mM H_2O_2; (C) 0.5 mM H_2O_2. Conditions for A and B are as in Figure 2. For C the scan rate is 2.5 mV s^{-1}; 2000 rpm.

carbon rods from Atomergic Chemicals Corp. These were press-fitted into one end of a Teflon sleeve. The opposite end of the sleeve had a press-fitted stainless steel rod threaded to match a Pine rotator. Electrical contact between the vitreous carbon and stainless steel rods was made with a silver epoxy Epo-tek H2OE from Epoxy Technology Inc. The electrodes were polished first with 6-μm then with 1-μm diamond suspension, followed by 0.3-μm alumina. The polishing compounds were from Buehler. After each polishing step, the electrodes were sonicated 3–6 min in deionized water.

Enzyme Immobilization. HRP (2 mg) was dissolved in 100 μL of 0.1 M sodium bicarbonate solution. After the addition of 50 μL of 12 mg/mL sodium periodate, the enzyme solution was incubated in the dark for 2.3 h. A 10 mg/mL solution of polymer I was used to dilute aliquots of the enzyme solution to make enzyme: polymer I solutions of various ratios (1:5, 1:10, 1:50, 1:100). A 1-μL loading of enzyme: polymer I solution was applied to the polished vitreous carbon surface. The electrodes were allowed to partially dry for 5–15 min, after which, 1 μL of a 1 mg/mL solution of PEGDGE was applied. The electrodes were then cured in water-saturated air at room temperature for >4 h.

Electrodes were also made by coimmobilizing the $NaIO_4$-oxidized HRP with a polyamine that had no redox centers. This polyamine was obtained by reacting polyvinylpyridine (PVP) (MW 60 000) with 2-bromoethylamine to form the pyridinium-*N*-ethylamine derivative. It is thus similar to polymer I but has no $[Os(bpy)_2Cl]^{3+/2+}$ redox centers. The HRP was cross-linked to the polyamine using PEGDGE through the above described process.

Buffers, Electrodes, and Electrochemical Equipment. The electrodes were operated at room temperature in modified Dulbecco's buffer (PBS) at pH 7.4. Unless otherwise indicated, the solutions were well aerated. All mediator solutions were made daily and protected from light until used. Potentials were referenced to a saturated calomel electrode from EG & G, Catalog No. K0077. A platinum wire was used as the counter electrode. The chronoamperometric experiments were performed on an EG & G potentiostat/galvanostat Model 173 and recorded on a Kipp & Zonen XY recorder Model BD91. The cyclic voltammograms were run on an EG & G potentiostat/galvanostat Model 273A and recorded on a PC with software developed in this lab. The rotator used was a Pine Instruments AFMSRX with the ACMDI 1906C shaft.

RESULTS

H_2O_2 Sensing Electrodes. Electroreduction of H_2O_2 is observed on electrodes modified with HRP immobilized in the epoxy network formed of either the polyamine without $[Os(bpy)_2Cl]^{3+/2+}$ redox centers (Figure 2) or with $[Os(bpy)_2Cl]^{3+/2+}$ redox centers (Figure 3). When there are no $[Os(bpy)_2Cl]^{3+/2+}$ centers in the polymer, reduction takes place at potentials negative of 0.2 V (SCE). In 1×10^{-4} M H_2O_2 a ~1 μA cm^{-2} plateau is reached near 0.1 V (SCE). In the redox epoxy network formed by PEGDGE cross-linking of polymer I containing $[Os(bpy)_2Cl]^{3+/2+}$ centers, the current density at 0.0 V (SCE) increases by 2 orders of magnitude to about 100 μA cm^{-2}. Furthermore, H_2O_2 electroreduction is observed already at +0.45 V (SCE) and the steady-state current plateaus at +0.3 V (SCE) (Figure 4).

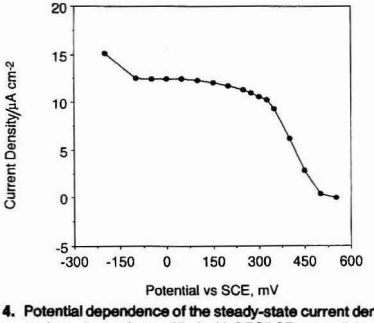

Figure 4. Potential dependence of the steady-state current density for a vitreous carbon electrode modified with PEGDGE-cross-linked HRP–polymer I at 1:5 ratio. Conditions: PBS; 1000 rpm; 1×10^{-5} M H_2O_2.

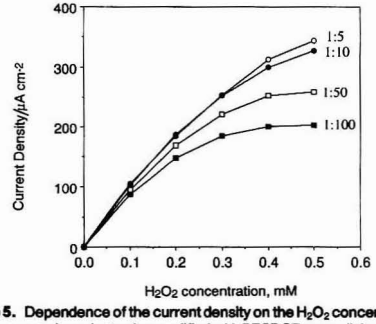

Figure 5. Dependence of the current density on the H_2O_2 concentration for vitreous carbon electrodes modified with PEGDGE-cross-linked HRP–polymer I films. The HRP:polymer I ratios are indicated. Conditions: PBS; 0.0 V (SCE); 1000 rpm.

The dependence of the catalytic H_2O_2 electroreduction current density on the HRP:polymer I ratio in PEGDGE cross-linked films is seen in Figure 5. The current density is nearly independent of the HRP:polymer ratio at low ($<1 \times 10^{-4}$ M) H_2O_2 concentration. At higher ($>1 \times 10^{-4}$ M) H_2O_2 concen-

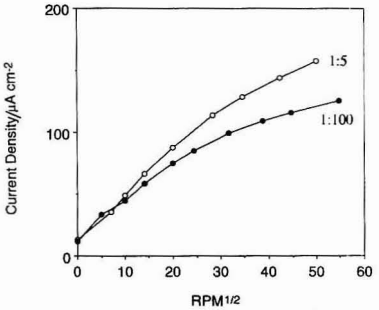

Figure 6. Dependence of the current density on the square root of the angular velocity of PEGDGE-cross-linked 1:5 and 1:100 HRP:polymer I electrodes. Conditions: PBS; 0.0 V (SCE); 0.1 mM H_2O_2.

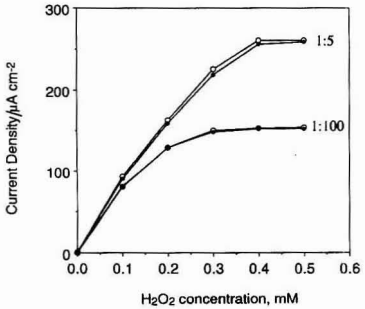

Figure 7. Steady-state calibration curves for PEGDGE-cross-linked 1:5 and 1:100 HRP:polymer I electrodes in air (solid circles) and nitrogen (open circles). Conditions: 0.0 V (SCE); PBS; 500 rpm.

tration the current density increases as the film becomes richer in HRP up to a ratio of 1:5 (Figure 5); the current density then decreases upon further increasing the enzyme content (not shown). The current densities of electrodes with 1:10 and 1:5 (HRP:polymer I) film ratios do not differ greatly. For electrodes with the 1:5 (HRP:polymer I) films the sensitivity in the (0–1) $\times 10^{-4}$ M H_2O_2 concentration range is 1 A cm^{-2} M^{-1}; i.e. the current density at 1×10^{-4} M H_2O_2 is 100 μA cm^{-2}. When the H_2O_2 concentration exceeds 0.25 mM, the current is time dependent and decays because of (slow) substrate inhibition of HRP. Control electrodes, made with PEGDGE cross-linked films of polymer I without HRP show no measurable H_2O_2 response.

Figure 6 shows Levich plots for 1:100 and 1:5 (HRP:polymer I) electrodes in 1×10^{-4} M H_2O_2. Linear dependence of the current density on the square root of the angular velocity is observed only up to about 400 rpm. At higher angular velocities the current densities increase with the HRP content of the films but are not proportional to the HRP content. At 2500 rpm increasing the HRP concentration from 1:100 to 1:5 increases the current density by only 30%.

The insensitivity of the electrodes to the partial pressure of oxygen is seen in Figure 7. There is no measurable difference between the calibration curves of the 1:100 (HRP: polymer I) electrode in nitrogen-purged or air-saturated solutions. For the 1:5 (HRP:polymer I) electrode there appears to be a marginal difference, with the readings in air exceeding those in nitrogen by less than 2%.

The dynamic range of the 1:5 (HRP:polymer I) electrode is seen in Figure 8. The current density increases linearly with H_2O_2 concentration over a range of 3 orders of magnitude from about 1×10^{-7} to 1×10^{-4} M (correlation coefficient

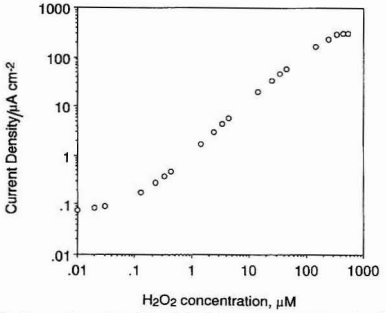

Figure 8. Dynamic range of the 1:5 HRP:polymer I electrode. Steady-state measurements were at 0.0 V (SCE) and 1000 rpm with PBS.

0.997; slope 1 A cm^{-2} M^{-1}). At 10^{-5} M H_2O_2 the 0–95% rise time is 2 min. At lower concentrations the rise times are longer. Following an H_2O_2 injection raising the concentration from 0.0 to 1×10^{-7} M, the rise time is about 10 min. The noise equivalent H_2O_2 concentration is 3 nM; i.e. at 1×10^{-8} M H_2O_2 the signal to noise ratio is 3. The background current, measured after the electrode was allowed to stabilize for 30 min, is 70 nA cm^{-2}.

NAD(P)H Sensing Electrodes Derived of HRP Wired to a 3-Dimensional Redox Polymer Network. The wired HRP electrodes are insensitive to NAD(P)H; i.e. the background current at 0.0 V (SCE) does not change when either cofactor is added. However, if 1-methoxy-5-methylphenazonium methyl sulfate (I, cation), 5-methylphenazonium methyl sulfate (II, cation), Meldola's blue (III, cation), Nile blue (IV, cation), toluidine blue O (V, cation), methylene blue (VI, cation), thionine (VII), flavin mononucleotide (VIII), 4,5-dihydro-4,5-dioxo-1*H*-pyrrolo[2,3-*f*]quinoline-2,7,9-tricarboxylic acid (PQQ) (IX), or methylene violet (Bernthsen) (X) is added, an NAD(P)H concentration dependent cathodic current is observed. The structures of these heterocyclic quinoids are shown in Figure 9. The relative effectiveness of these mediators in the H_2O_2-forming reaction is in the order of their listing, the phenazonium derivatives and Meldola's blue being the most effective and flavin mononucleotide, PQQ, and methylene violet the least. Addition of any of the mediators at <1.0 μM concentration does not produce a current response.

The dependence of the steady-state current density on the NADH concentration for aerated solutions containing 1.6 μM 5-methylphenazonium methyl sulfate is seen in Figure 10. The dependence is linear through the 1–100 μM NADH concentration range and the slope, i.e. sensitivity, is 1 A cm^{-2} M^{-1}, similar to that for H_2O_2. Corresponding results for NADPH are seen for the 1:5 electrode in Figure 11. The linear range for NADPH is from 1 to 200 μM, and the sensitivity is again 1 A cm^{-2} M^{-1}. The equilibration times for steady-state measurements depend on the concentration of the mediator; a higher mediator concentration results in acceleration of the H_2O_2 production. Typically, the 0–95% rise time of the current following an NADH injection was 5–7 min at 3.3 μM 5-methylphenazonium methyl sulfate concentration.

As expected from reaction 3, electroreduction currents were observed only in aerated or oxygenated solutions. The current did not increase when O_2 rather than air was bubbled through the solution. When the solutions were purged of oxygen by bubbling with N_2, the current reversed; i.e. an electrooxidation current was observed in the PMSH (PMS^+ and NADH) containing solution. Electrooxidation of PMSH proceeded on glassy carbon electrodes whether or not these were modified

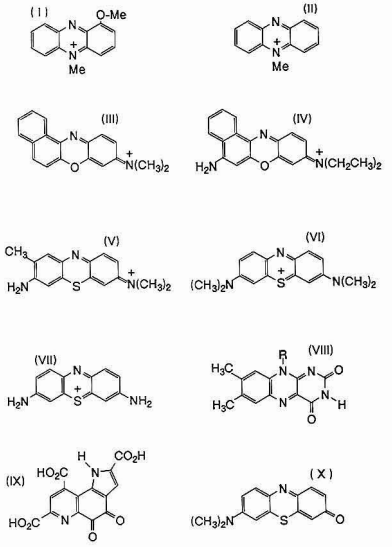

Figure 9. Structures of the mediators which are able to catalytically cycle through reactions 2 and 3. Note the central quinoidal structure stabilized by the adjacent aromatic rings: cation of 1-methoxy-5-methylphenazonium methyl sulfate (I); cation of 5-methylphenazonium methyl sulfate (II); cation of Meldola's blue (III); cation of Nile blue (IV); cation of toluidine blue O (V); cation of methylene blue (VI); thionine (VII); flavin mononucleotide (VIII); 4,5-dihydro-4,5-dioxo-1*H*-pyrrolo[2,3-*f*]quinoline-2,7,9-tricarboxylic acid (PQQ) (IX); methylene violet (Bernthsen) (X).

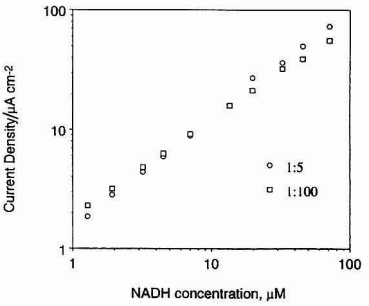

Figure 10. Dependence of the steady-state electrocatalytic reduction current density on the NADH concentration for PEGDGE-cross-linked 1:5 and 1:100 HRP:polymer I film-modified vitreous carbon electrodes. Conditions: 0.0 V (SCE), 1000 rpm, 1.6 μM 5-methylphenazonium methyl sulfate (PMS^+); PBS.

with HRP-containing films. Even minimal aeration of the PMSH solutions reversed the current, but only on HRP-modified electrodes.

Light Effects. PMS^+ solutions strongly absorb $\lambda < 480$ nm light. It has been reported that the mechanism of reduction of heterocyclic quinoid dyes by NADH can involve their excited states.[17,25] Furthermore, the oxidant of the NADH-reduced quinoid dye may not be ground-state (triplet) oxygen but excited (singlet) oxygen, formed through energy transfer from the excited dye in its triplet state. Thus, as a precaution, the effect of 0.2 mW cm^{-2} 4100 K color temperature "cool-white" fluorescent on the rise time of the current

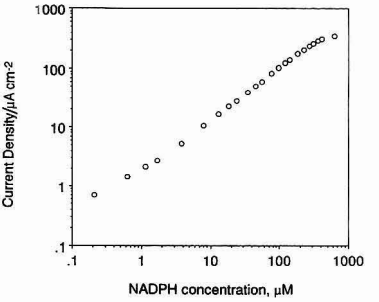

Figure 11. Dependence of the steady-state electrocatalytic reduction current density on the NADPH concentration for the 1:5 electrode of Figure 10. Conditions were as in Figure 10, except that the 5-methylphenazonium methyl sulfate concentration was 4.7 μM.

was checked. Control experiments with PMS^+ (1×10^{-5} M) show that the current is not changed when the electrode is operated in the dark or with the above ambient irradiance. It was also noted, however, that PMS^+ measurably photodecomposed even at low irradiance by the ambient light.

DISCUSSION

HRP-Based Hydrogen Peroxide Sensing Electrodes. Table I compares H_2O_2 electrodes based on direct, diffusionally mediated, and redox polymer-relayed electroreduction of HRP. Comparison of the electrodes shows that the wiring of HRP to an electrode, i.e. its covalent binding to a hydrophilic 3-dimensional electron-relaying redox network, increases sensitivity. In the absence of osmium-complex relays the observed sensitivity, 1×10^{-2} A cm^{-2} M^{-1}, is 2 orders of magnitude lower than that in their presence (Figures 2 and 3). In the first case only redox centers of HRP molecules actually contacting the electrode surface may be electroreduced. These redox centers produce the redox wave in Figure 2. In contrast, most HRP molecules in the films, the thickness of which is $\simeq 10^{-4}$ cm, are electrically accessible when electrons are relayed through $[Os(bpy)2Cl]^{3+/2+}$ centers complexed to the polyvinylpyridine backbone in polymer I. Electrooxidation of HRP in the electron-relaying epoxy network starts at +0.45 V, i.e. 0.18 V positive of the +0.27-V redox potential of the $[Os(bpy)_2Cl]^{3+/2+}$ centers. This implies that oxidized HRP accepts electrons from the network even when the ratio of the reduced to oxidized centers is only about 1:1000.

The optimal HRP:polymer I ratio in the film (Figure 5) is near 1:5. At higher enzyme content, the electron-relaying capacity of the films is diminished by the nonrelaying HRP in the network. The network, with an electron diffusion coefficient below 10^{-8} cm^2 s^{-1},[24] does not transport or transfer electrons to the bound enzyme molecules fast enough to match their turnover rate at optimal (10^{-4} M) substrate concentration. Had the electron transport through the polymer been faster, still higher current densities might have been realized. That the electrodes are limited by the rate of electron transfer either through the network or from the network to the enzyme is seen in the Levich plots of Figure 6. These show normal solution mass transfer limited kinetics of the substrate, characterized by linear dependence of the current density on the square root of the angular velocity, only at low angular velocities. At high angular velocities where the kinetics does not depend linearly on substrate mass transport and depends only weakly on enzyme content, the characteristics are dominated by transport of either electrons or substrate through the film. Previous work with glucose oxidase

(25) Julliard, M.; Le Petit, J. *Photochem. Photobiol.* **1982**, *36*, 283–90.

containing redox epoxy films suggests electron transfer or transport limitation.[24]

Reduction of Heterocyclic Quinoids by Two Electron Plus Proton Transfer from NAD(P)H. The earlier results of Miller, Gorton, Kulys, and their colleagues[26-31] show that NAD(P)H is rapidly and cleanly oxidized to $NAD(P)^+$ by transferring two electrons plus a proton to any of a variety of dissolved or electrode-surface-bound quinoids, including native quinoids on oxidized graphite (reaction 5). 5-Meth-

$$\text{quinoid}_{ox} + \text{NAD(P)H} \rightarrow \text{quinoid}_{red} + \text{NAD(P)}^+ \quad (5)$$

ylphenazonium derivatives and Meldola's blue and its derivatives are particularly fast two electron plus proton acceptors from NAD(P)H. The homogeneous bimolecular two electron proton transfer rate from NADH to PMS^+ (reaction 2) is $3.8 \times 10^3\ M^{-1}\ s^{-1}$ at 25 °C.[32]

Oxidation of PMSH by O_2 (reaction 3), whereby PMS^+ is recovered and H_2O_2 is produced, has a bimolecular homogeneous rate constant of $1.8 \times 10^2\ M^{-1}\ s^{-1}$ in water at 25 °C.[32] Thus in an aqueous solution in equilibrium with air ($\cong 2.5 \times 10^{-4}$ M O_2), the oxidation of PMSH is rapid. Indeed, the related reaction of dihydrophenazine and O_2 in an organic solvent (reaction 6) has been considered as an industrial process for the production of H_2O_2.[33]

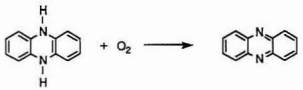

(6)

The rates of reactions 2 and 3 and H_2O_2 diffusion may all slow the response, i.e. rise time, of the NAD(P)H sensor. At low NADH concentration (0.1 μM) the calculated rate from reaction 2 and inherent diffusion-controlled transport of H_2O_2 are limiting factors of the electrode's kinetics. At higher NADH concentration (100 μM) and at low PMS^+ concentrations (1.6 μM) reaction 3 limits the electrode's response. The calculated H_2O_2 formation rates through reaction 3 and experimental sensor rise times are of the same order of magnitude.

The variation of current with concentration, and the 1 A $cm^{-2}\ M^{-1}$ sensitivity, for NADH (Figure 10) and NADPH (Figure 11) through their 1×10^{-7} to 2×10^{-4} M concentration range are identical to those of H_2O_2 (Figure 8). We infer from the identical sensitivities and dynamic ranges that the homogeneous two electron and proton transfer reactions proceed either at or very close to unit current efficiency, i.e. that NAD(P)H produces a stoichiometric amount of H_2O_2 through reactions 2 and 3. The actual mechanism of H_2O_2 production involves more steps than represented by equations 2 and 3.

Interferences. Schmidt et al. suggested that "Reduction of the oxygen proceeds by a complex sequence of reactions, producing among other intermediates the superoxide radical ion, which leads to hydrogen peroxide and this in turn is capable of oxidizing methylene blue and so a stoichiometric production of hydrogen peroxide is not observed".[17] The disparity probably results from the higher dye concentrations employed by Schmidt et al. At a high dye concentration the rates of side reactions, particularly between the reduced dye and H_2O_2, are increased. At the NAD(P)H and mediator concentrations employed here we observe only the stoichiometric reaction 7. As is evident from reaction 3, the assay

$$\text{NAD(P)H} + H^+ + O_2 \rightarrow \text{NAD(P)}^+ + H_2O_2 \quad (7)$$

requires that the solutions be aerated. A decrease in O_2 partial pressure will slow reaction 3. Nevertheless, even in this case the ultimate steady-state current will not change, because reaction 3 is irreversible. The high bimolecular rate constant ($1.8 \times 10^2\ M^{-1}\ s^{-1}$) for PMSH oxidation by O_2 usually ensures a rapid reaction in air-exposed solutions. When the oxygen concentration is only $^1/_{10}$th of that in a well-aerated solution (a typical value at 25 °C being 0.25 mM), the half-life of PMSH is 154 s, assuming a pseudo-first-order reaction in PMSH.

HRP-catalyzed reactions may cause severe interference by a number of interferants. H_2O_2-oxidized HRP may be reduced by any of a number of hydrogen donors. Such reduction will cause loss of catalytic current. Addition of 0.1 mM ascorbate, a common component of biological samples, will reduce the cathodic current by over 50%. Current will also be lost if NAD(P)H directly reduces H_2O_2-oxidized HRP. This reaction is actually observed in our experiments as a dip in the current from the electrodes when NAD(P)H is initially injected into a solution with a substantial H_2O_2 concentration already present. Once the NAD(P)H reacts to form H_2O_2 and $NAD(P)^+$, the current recovers. The ultimate current is not lowered, because reactions occurring at the electrode surface do not change the bulk solution concentrations, the bulk H_2O_2 concentration being reached through the homogeneous solution reactions 2 and 3. Beyond organic hydrogen donors, H_2O_2 itself is oxidized by HRP to O_2 and water.[34] Fortunately, the latter reaction is not fast.

CONCLUSIONS

In contrast with redox centers of flavoprotein enzymes like glucose oxidase, that do not communicate directly with carbon electrodes on which the enzymes are adsorbed, redox centers of directly absorbed horseradish peroxidase do communicate electrically with carbon electrodes.[35,36] The maximum current

(26) Murray, R. W. In *Electroanalytical Chemistry*; Bard, A. J., Ed.; Marcel Dekker: New York; Vol. 13, pp 191–238.
(27) Albery, W. J.; Bartlett, P. N.; Cass, A. E. G. *Phil. Trans. R. Soc. London B* **1987**, *316*, 107–19.
(28) Albery, W. J.; Bartlett, P. N. *J. Chem. Soc., Chem. Commun.* **1984**, 234–6.
(29) Itoh, S.; Kinugawa, M.; Mita, N.; Ohshiro, Y. *J. Chem. Soc., Chem. Commun.* **1989**, 694–5.
(30) Yabuki, S.; Mizutani, F.; Asai, M. *Biosensors Bioelectron.* **1991**, *6*, 311–5.
(31) Kimura, Y.; Niki, K. *Anal. Sci.* **1985**, *1*, 271–4.
(32) Halaka, F. G.; Babcock, G. T.; Dye, J. L. *J. Biol. Chem.* **1982**, *257*, No. 3, 1458–61.
(33) *Encyclopedia of Chemical Technology*, 3rd ed.; Kirk, J. R., Othmer, D. F., Eds.; John Wiley and Sons: New York, 1981; Vol. 13, pp 16–22.
(34) Brill, A. S. *Comprehensive Biochemistry*; Elsevier: Amsterdam, 1966; pp 447–79.
(35) Yaropolov, A. I.; Malovik, V.; Varfolomeev, S. D.; Berezin, I. V. *Dokl. Akad. Nauk. USSR* **1979**, *249* (6), 1399–401.
(36) Jonsson, G.; Gorton, L. *Electroanalysis* **1989**, *1*, 465–8.
(37) Wang, J.; Frieha, B.; Naser, N.; Romero, E. G.; Wollenberger, U.; Ozsoz, M.; Evans, O. *Anal. Chim. Acta* **1991**, *254*, 81–8.
(38) Cosgrove, M.; Moody, G. J.; Thomas, J. D. R. *Analyst* **1988**, *113*, 1811–5.
(39) Kulys, J. J.; Samalius, A. S.; Svirmickas, G.-J. S. *FEBS Lett.* **1980**, *114*, 7–10.
(40) Tatsuma, T.; Okawa, Y.; Watanabe, T. *Anal. Chem.* **1989**, *61*, 2352–5.
(41) Sanchez, P. D.; Ordieres, A. J. M.; Garcia, A. C.; Blanco, P. T. *Electroanalysis* **1991**, *3*, 281–5.
(42) Schubert, F.; Saini, S.; Turner, A. P. F. *Anal. Chim. Acta* **1991**, *245*, 133–8.
(43) Pantano, P.; Morton, T. H.; Kuhr, W. G. *J. Am. Chem. Soc.* **1991**, *113*, 1832–3.
(44) Kulys, J. J.; Pesliakiene, M. V.; Samalius, A. S. *Bioelectrochem. Bioenerg.* **1981**, *8*, 81–8.
(45) Lundback, H.; Olsson, B. *Anal. Lett.* **1985**, *18* (B7), 871–89.
(46) Kojima, J.; Morita, N.; Takagi, M. *Anal. Sci.* **1988**, *4*, 497–500.
(47) Kulys, J. J.; Laurinavicius, V.-S. A.; Pesliakiene, M. V.; Gureviciene, V. V. *Anal. Chim. Acta* **1983**, *148*, 13–8.

density does not exceed, however, in the absence of a diffusional mediator or of nondiffusing electron-relaying centers, the current density associated with the turnover of the enzyme layer directly contacting the electrode surface. Oxidized horseradish peroxidase molecules, that are remote from the electrode surface, do not accept electrons from electrodes unless the electrons are relayed through redox centers in the polymer. The current density is increased by 2 orders of magnitude when the HRP molecules bound throughout the thick film are connected to the electrode through its 3-dimensional electron-relaying network. The sensitivity of the resulting amperometric H_2O_2 sensor is 1 A cm^{-2} M^{-1} at 0.0 V (SCE), and its dynamic range is 1×10^{-7}–2×10^{-4} M H_2O_2.

Two electron plus proton transfer from NAD(P)H to quinoids produces stoichiometric concentrations of H_2O_2. With NADH and NAD(P)H stoichiometrically translated to H_2O_2, their concentrations can be amperometrically assayed at wired horseradish peroxidase cathodes poised at 0.0 V (SCE) (Figure 12). The sensitivities and dynamic ranges of these cathodes are identical with those of H_2O_2 cathode, 1 A cm^{-2} M^{-1} through the 1×10^{-6}–10^{-4} M concentration range.

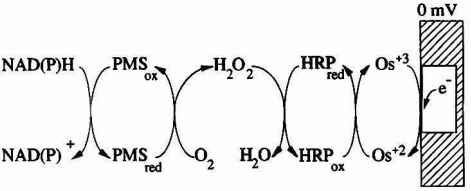

Figure 12. Cycles of the proposed NADH (and NADPH) cathodes.

Although the assay of these cofactors requires molecular oxygen, the electrodes are not excessively sensitive to variations in O_2 partial pressure because the quinoid-catalyzed NAD(P)H reactions with O_2 are irreversible.

ACKNOWLEDGMENT

The work described was supported by the Office of Naval Research, by the National Science Foundation, and by the Welch Foundation.

RECEIVED for review April 21, 1992. Accepted September 28, 1992.

(48) Frew, J. E.; Harmer, M. A.; Allen, H.; Hill, O.; Libor, S. I. *J. Electroanal. Chem. Interfacial Electrocem.* **1986**, *201*, 1–10.

In Situ UV–Visible Reflection Absorption Wavelength Modulation Spectroscopy of Species Irreversibly Adsorbed on Electrode Surfaces

Sunghyun Kim and Daniel A. Scherson*

Department of Chemistry, Case Western Reserve University, Cleveland, Ohio 44106

A method is herein described for the in situ detection of species adsorbed on electrode surfaces which employs a vibrating grating to modulate the wavelength of the incident light. This technique denoted as reflection absorption wavelength modulation spectroscopy (RAWMS) has made it possible to obtain at *a fixed electrode potential* normalized, differential UV–visible spectra of a single, *irreversibly* adsorbed monolayer of cobalt tetrasulfonated phthalocyanine ($Co^{II}TsPc$) on the basal plane of highly oriented pyrolytic graphite (HOPG(bp)) and of methylene blue (MB) on graphite. The (wavelength) integrated difference RAWMS spectra for these adsorbed species were remarkably similar to those observed for the same compounds in aqueous solutions when present in the monomeric form. Complementary wavelength modulation experiments involving a conventional transmission geometry have shown that the instrument involved in the in situ RAWMS measurements is capable of resolving absorbance changes on the order of 0.002 units.

INTRODUCTION

Reflectance spectroscopy in the UV–visible range provides a versatile means of probing a variety of phenomena at metal–electrolyte interfaces, such as ionic and molecular adsorption and the formation and removal of superficial oxide films at coverages well below a monolayer.[1]

Of particular interest to the field of electrocatalysis is a better understanding of the mode of bonding of *irreversibly* adsorbed species on electrode surfaces, including orientation and electronic overlap.[2] Insight into these issues can be gained by determining the optical constants of the *adsorbed phase*. Such information can be obtained, in principle, from measurements of the interfacial reflectivity in the absence and in the presence of the adsorbate under otherwise identical conditions[3] *provided that the optical properties of the substrate and the electrolyte solution immediately adjacent to the substrate (or to the adsorbed layer) are not affected by the presence of the adsorbed phase.* Regardless of whether these stringent conditions are met, the acquisition of such conceptually simple data for species irreversibly adsorbed on electrode surfaces has proven to be exceedingly difficult. Far less demanding from an experimental viewpoint are UV–vis reflectance spectroscopic techniques which are based on the modulation of the applied potential across the electrode–electrolyte interface.[4–7] Despite their extraordinary sensitivity (10^{-4}–10^{-5} relative absorption units), the interpretation of results obtained with these fairly popular methods must be performed with great care, as the measured signals are derived from changes in the spectral properties of the interface generated by the applied potential and not from the (static) interface itself.

The present work introduces the use of reflection absorption wavelength modulation spectroscopy (RAWMS) for the in situ detection of species irreversibly adsorbed on electrode surfaces at a *fixed electrode potential*. This specific technique has been used earlier by other workers to investigate ex situ highly detailed aspects of the reflectivity of semiconductors and metals at the solid–air interface.[8–10]

Two fairly well-documented adsorbate/substrate systems were selected in this study to assess the advantages and limitations of in situ RAWMS: cobalt tetrasulfonated phthalocyanine (CoTsPc) adsorbed on the basal plane of highly oriented pyrolytic graphite (HOPG(bp)[7,11] and methylene blue (MB) on graphite.[5] Both these adsorbates exhibit well-defined voltammetric peaks in a readily accessible potential range, and hence the absolute coverages can be calculated by straightforward integration. It may be noted that CoTsPc is a powerful electrocatalyst for the 2-e reduction of dioxygen to hydrogen peroxide in aqueous electrolytes.[12]

As will be shown, in situ RAWMS in its present stage of development is capable of detecting spectra for the adsorbate/substrate systems involved in this study at coverages on the order of a single monolayer.

The overall sensitivity of the WMS instrument was established by conducting experiments in the conventional transmission mode using very dilute solutions of CoTsPc in aqueous media.

THEORETICAL CONSIDERATIONS

The optical response of a three-layer system consisting of a noninteracting homogeneous film of finite thickness (adsorbate layer) interposed between two semiinfinite phases (electrode and electrolyte) can be represented in terms of the normalized reflectivity, defined as $\Delta R/R = (R - R_o)/R_o$, where R_o and R are the reflectivities observed in the absence and

(1) Kolb, D. In *Spectroelectrochemistry: Theory and Practice*; Gale, R. J., Ed.; Plenum Press: New York, 1988.
(2) Murray, R. W. In *Electroanalytical Chemistry*; Bard, A. J., Ed.; Marcel Dekker: New York, 1984; Vol. 13.
(3) McIntyre, J. D. E. In *Advances in Electrochemistry and Electrochemical Engineering*; Delahay, P., Tobias, C. W., Eds.; John Wiley & Sons; New York, 1973; Vol. 9.
(4) Ngameni, E.; Laouenan, A.; L'Her, M.; Hinnen, C.; Hendricks, N. H.; Collman, J. P. *J. Electroanal. Chem. Interfacial Electrochem.* **1991**, *301*, 207.
(5) Sagara, T.; Iizuka, J.; Niki, K. *Langmuir* **1992**, *8*, 1018.
(6) Lezna, R. O.; de Tacconi, N. R.; Hahn, F.; Arvia, A. J. *J. Electroanal. Chem. Interfacial Electrochem.* **1991**, *306*, 259.
(7) Kim, S.; Xu, X.; Bae, I. T.; Wang, Z.; Scherson, D. A. *Anal. Chem.* **1990**, *62*, 2647.
(8) Fong, C. Y.; Cohen, M. L.; Zucca, R. R. L.; Stokes, J.; Shen, Y. R. *Phys. Rev. Lett.* **1970**, *25*, 1486.
(9) Zucca, R. R. L.; Shen, Y. R. *Phys. Rev. B.* **1970**, *1*, 2668.
(10) Balslev, I. *Phys. Rev.* **1966**, *143*, 636.
(11) Nikolic, B.; Adzic, R. R.; Yeager, E. B. *J. Electroanal. Chem. Interfacial Electrochem.* **1979**, *103*, 281.
(12) Zagal, J.; Bindra, P.; Yeager, E. B. *J. Electrochem. Soc.* **1980**, *127*, 1506.

0003-2700/92/0364-3091$03.00/0

in the presence of the adsorbate layer. Explicit expressions for $\Delta R/R$ for s- and p-polarized light in terms of the optical constants of the three phases (ϵ_i, $i = 1$–3), the thickness of the adsorbate layer (d), the angle of incidence (ϕ_1), and the wavelength of the incident light (λ) can be derived from Fresnel's equations. These relationships can be greatly simplified for $d/\lambda \ll 1$, a condition that is universally fulfilled for layers of atomic or molecular dimensions in the UV–visible and infrared regions.[3]

From a purely formal viewpoint, the derivative of the normalized reflectivity with respect to λ can be written as

$$\partial(\Delta R/R)/\partial\lambda = (R/R_o)[1/R(\partial R/\partial\lambda)_\lambda - 1/R_o(\partial R_o/\partial\lambda)_\lambda] \quad (1)$$

The technique described in this work enables the two terms on the right-hand side of eq 1 to be determined with a great degree of accuracy, making it possible to obtain (within an additive constant) $\Delta R/R$ as a function of wavelength by a simple numerical integration.

EXPERIMENTAL SECTION

Unlike other approaches reported in the literature which employ either a vibrating mirror[8,9] or a moving (entrance) slit[10] to modulate the wavelength, the present strategy involves the application of a mechanical perturbation to the galvanometer-driven grating/mirror assembly of a rapid scanning RSS Harrick unit to achieve the same goal. In this arrangement, the torsion of the galvanometer or, equivalently, the deflection of the grating is proportional to the dc current (I_{dc}) and therefore to λ. A linear relationship between I_{dc} and λ was indeed found for the Harrick instrument in the range between 400 and 800 nm, yielding a slope of about 0.875 mA/V. For the RAWMS measurements, the galvanometer was driven by a sinusoidal ac current, $\Delta I \sin \omega t$, where ΔI is directly proportional to the amplitude of the wavelength modulation, or $\Delta\lambda$, superimposed on I_{dc}, or a fixed λ. The input signal to the galvanometer, $I_{dc} + \Delta I \sin \omega t$, was generated by adding an (sinusoidal) ac voltage from a stable source to a dc voltage (obtained from a programmable Metrabyte DAC-02 board) and feeding the resulting signal into a PAR Model 173 potentiostat operated in the galvanostatic mode. All experiments were conducted using $\Delta\lambda = 3.5$ nm (ΔI ca. 3 mA) and $\omega = 10$ Hz. Average values of the dc and ac components at a fixed (average) wavelength λ_o, i.e. $R(\lambda_o)$ and $(\Delta R/\Delta\lambda)_{\lambda_o}$, were obtained with a lock-in amplifier (Stanford Research Instruments, Model 510) and stored in a computer for further processing. For small modulation amplitudes, such as those used in this work, $\Delta R/\Delta\lambda \approx \partial R/\partial\lambda$. Data were acquired over the desired spectral range at 2-nm intervals. The WMS unit was fully controlled by a personal computer using routines developed in this laboratory.

In situ RAWMS spectra (or $1/R(\partial R/\partial\lambda)_\lambda$ vs λ curves) were recorded first in the absence and then in the presence of the adsorbate on the surface, denoted as s and r, respectively. Similar data were also collected after polarizing the electrode at potentials at which most of the adsorbed material would be expected to desorb from the surface followed by repeated rinsing with neat electrolyte.

For the spectroscopic measurements, the adsorption of CoTsPc and MB was effected (after the in situ RAWMS spectra of the bare surface had been recorded) by injecting (with a syringe) a solution of the material in the base electrolyte, i.e. 1.0×10^{-6} M CoTsPc in 0.05 M H_2SO_4 and 1.8×10^{-4} M MB in 0.5 M KNO_3, 0.1 M phosphate buffer (pH = 7.9), respectively, with the electrode at open circuit. After a few minutes, the adsorbate-containing solution was removed and neat electrolyte was injected into and then withdrawn from the cell. This rinsing procedure was repeated at least 10 times to ensure that no nonadsorbed material was left in the cell. During all these operations the position of the cell was maintained fixed, a factor found to be crucial to the success of the measurements. After the cell was filled with neat electrolyte, a series of voltammograms were recorded to determine the surface coverage.

Potential modulation experiments at properly selected wavelengths were performed only for the CoTsPc/HOPG(bp) system using techniques and procedures described in detail elsewhere.[7]

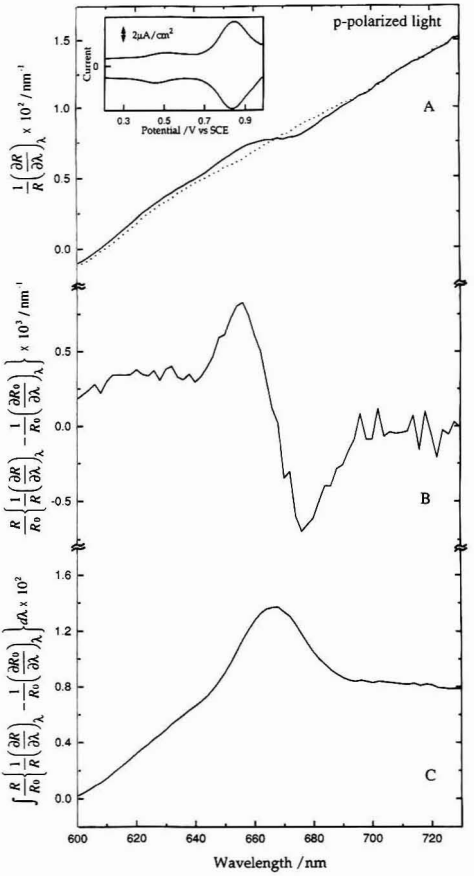

Figure 1. (A) In situ p-polarized RAWMS spectra of HOPG(bp) in 0.05 M H_2SO_4 before (dotted curve) and after (solid curve) adsorption of about 18 pmol/cm² of CoTsPc. Both spectra were obtained with the electrode polarized at 0.5 V vs SCE (see text for details). Insert: Cyclic voltammogram for a single monolayer of CoTsPc on HOPG(bp) obtained in the base electrolyte. Scan rate: 100 mV s⁻¹. Electrode area: 3 cm². (B) Normalized difference RAWMS spectra, $R/R_o[1/R(\partial R/\partial\lambda)_\lambda - 1/R_o(\partial R_o/\partial\lambda)_\lambda]$ for CoTsPc adsorbed on HOPG(bp) obtained from the data in (A) in this figure. R_o represents the reflectivity spectrum of the bare HOPG(bp) surface before CoTsPc was admitted into the cell. (C) Integrated $R/R_o[1/R(\partial R/\partial\lambda)_\lambda - 1/R_o(\partial R_o/\partial\lambda)_\lambda]$ vs λ, for CoTsPc on HOPG(bp) obtained from the data shown in (B) in this figure.

RESULTS AND DISCUSSION

1. Irreversibly Adsorbed Monolayers. A. CoTsPc on HOPG(bp). The in situ RAWMS spectrum of bare HOPG-(bp) obtained in 0.05 M H_2SO_4 at a potential of 0.5 V (prior to introducing the CoTsPc solution into the cell), using p-polarized light, is shown in Figure 1A (see dotted curve). The voltammogram recorded in the neat electrolyte after adsorption (and subsequent rinsing with the macrocycle-free solution) displayed a characteristic peak at 0.84 V vs SCE ascribed to the $Co^{II}TsPc/Co^{III}TsPc$ couple (see insert in Figure 1A).[7,13] The coverage of CoTsPc, as determined by integration of (either one of) the peak(s) was about 18 pmol/cm² and thus

(13) Zagal, J.; Sen, R. K.; Yeager, E. B. *J. Electroanal. Chem. Interfacial Electrochem.* **1977**, *83*, 207.

somewhat smaller than that usually observed for this adsorbate/substrate system, ca. 30 pmol/cm^2. The electrode was then polarized at 0.5 V and a new RAWMS spectrum recorded yielding a rather shallow bipolar peak in the region between 640 and 690 nm (see solid line in Figure 1A). This feature, attributed to the irreversibly adsorbed $Co^{II}TsPc$ monolayer, can be more clearly observed by subtracting the two curves in Figure 1A and multiplying the difference by the factor R/R_o, as prescribed by the right-hand side of eq 1). The resulting normalized difference RAWMS spectra, i.e. $R/R_o[1/R(\partial R/\partial\lambda)_\lambda - 1/R_o(\partial R_o/\partial\lambda)_\lambda]$ vs λ, is shown in B, Figure 1.

According to eq 1, the wavelength dependence of the normalized reflectivity can be determined (within an additive constant) by integrating the curve in Figure 1B, yielding in this case the $\Delta R/R$ vs λ plot depicted in Figure 1C. The peak position (668 nm) is in good agreement with that of CoTsPc in dilute enough solutions for the species to be predominantly in the monomeric form.[14] Furthermore, the width at half-height (ca. 33 nm) is also in harmony with reflection absorption data reported much earlier by Nikolic et al. (ca. 27 nm) for this same system, who obtained a height for the absorption peak larger than that observed here (ca. 0.01).[11] The sloping background observed in the region extending from 600 to 640 nm originates from the small difference (3×10^{-4}) in the values of $1/R(\partial R/\partial\lambda)_\lambda$ between the bare and CoTsPc-covered HOPG-(bp) surface in that same spectral range (see Figure 1A). It is conceivable that this integrated spectra represents the true optical interfacial response of the system. However, the possibility of this background to be derived from instrumental artifacts, such as long-term drifts or other sources, cannot be ruled out.

In independent measurements, in situ RAWMS data for the $Co^{II}TsPc$/HOPG(bp) system were acquired with s-polarized light, yielding (except for the sloping background) very similar results (see Figure 2A). Unlike the experiments performed with p-polarized light, the RAWMS spectra in this case were first acquired for HOPG(bp) after adsorbing the CoTsPc (solid curve in Figure 2). Subsequently, the electrode was polarized at 1.0 V to desorb the CoTsPc from the surface and the cell then thoroughly rinsed with neat electrolyte. A cyclic voltammogram was then performed to ensure that the amount of macrocycle left on the surface was minimal. A second RAWMS spectrum was then acquired with the electrode polarized at 0.5 V (see dotted curve, Figure 2). As shown in B and C of Figure 2, exceptionally good results were obtained using this last specific RAWMS spectrum as a reference. This affords further confirmation that the spectra shown in A of Figures 1 and 2 (solid curves) are indeed derived from the adsorbed monolayer and not from solution-phase material. Some indication that the electrochemically-induced desorption was not complete was provided by the presence of a very small peak in the normalized difference spectra of the surface obtained after CoTsPc desorption using as a reference the corresponding spectra for the same substrate before CoTsPc was introduced into the cell.

It is interesting to note that the potential-modulated spectrum of the same interface obtained with p-polarized light (see Figure 3) also displays a positive-going peak centered at about the same wavelength as that in Figure 1C. This implies that the negative-going feature in the potential-modulated spectrum can be attributed almost entirely to the $Co^{III}TsPc$ species.

It should be stressed that despite repeated attempts no *direct* normalized spectra could ever be detected with the

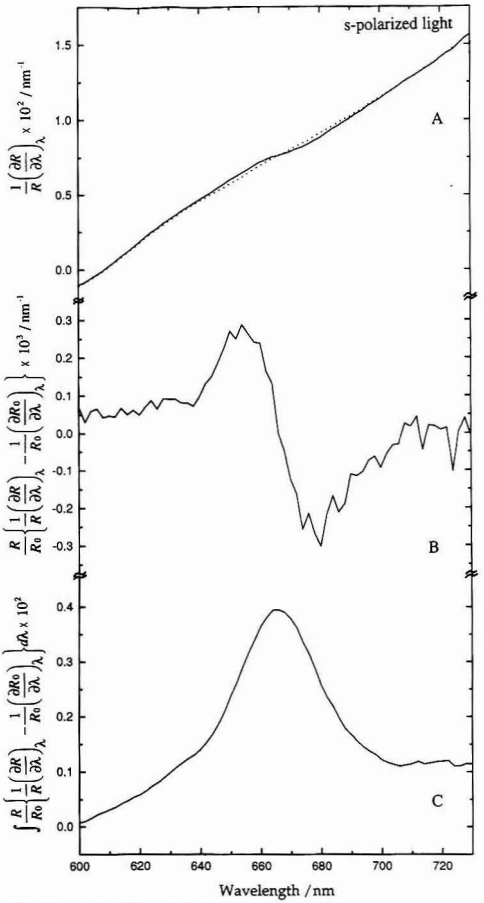

Figure 2. (A) In situ s-polarized RAWMS spectra of HOPG(bp) in 0.05 M H_2SO_4 in the absence (dotted curve) and in the presence (solid curve) of about 20 pmol/cm^2 of adsorbed CoTsPc. Both spectra were obtained with the electrode polarized at 0.5 V. Electrode area: 3 cm^2. (B) Normalized difference RAWMS spectra, $R/R_o[1/R(\partial R/\partial\lambda)_\lambda - 1/R_o(\partial R_o/\partial\lambda)_\lambda]$ of CoTsPc/HOPG(bp) obtained from the data in (A) in this figure. R_o in this case represents the reflectivity spectrum of HOPG-(bp) after desorption of CoTsPc from the surface (see text for details). (C) Integrated $R/R_o[1/R(\partial R/\partial\lambda)_\lambda - 1/R_o(\partial R_o/\partial\lambda)_\lambda]$ vs λ, for CoTsPc on HOPG(bp) obtained from the data shown in (B) in this figure.

Harrick instrument working in the conventional rapid scanning mode using signal averaging techniques to improve the signal-to-noise ratio.

B. MB on OG. The interfacial capacity per unit cross-sectional area for the OG specimen used in these studies, as determined from cyclic voltammetry, was found to be about 1 mF/cm^2 and thus much larger than that observed for HOPG-(bp)[15,16] (ca. 3 μF/cm^2 at the point of zero charge) or glassy carbon (ca. 15 μF/cm^2).[16] Although the edge plane of HOPG is known to exhibit much larger capacity values than those of HOPG(bp) (50–70 μF/cm^2),[16] the differences observed in this work appear too large to be explained solely on this basis. This suggests that the surface roughness of this OG specimen

(14) Nevin, W. A.; Liu, W.; Melnik, M.; Lever, A. B. P. *J. Electroanal. Chem. Interfacial Electrochem.* **1986**, *213*, 217.

(15) Randin, J. P.; Yeager, E. B. *J. Electrochem. Soc.* **1971**, *118*, 711.

(16) Randin, J. P.; Yeager, E. B. *J. Electroanal. Chem. Interfacial Electrochem.* **1972**, *36*, 257.

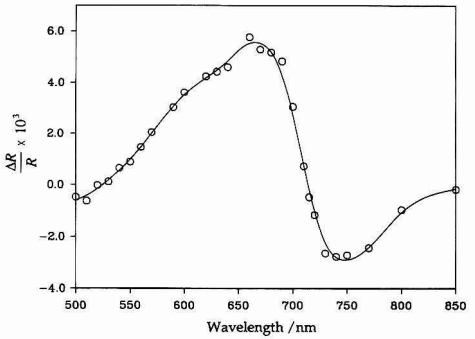

Figure 3. Potential-modulated spectra of CoTsPc/HOPG(bp) in 0.05 M H_2SO_4 at 0.9 V normalized by reflectivity at 0.5 V. These measurements were obtained with p-polarized light, and the potential was scanned from 0.1 to 0.9 V at 300 mV/s (see ref 7 for further details).

is rather high. Further evidence in support of this view was obtained from cyclic voltammetry curves for MB adsorbed on graphite following thorough rinsing with base electrolyte (see insert, Figure 4). As would be expected for a surface-confined species, the peak currents in this case were found to be directly proportional to the scan rate. The MB coverage was on the order of 2.9 nmol/cm^2 and thus about 1 order of magnitude larger than those reported by other authors on pyrolytic graphite (0.40 nmol/cm^2)[5] or sulfide-modified gold (0.15–0.26 nmol/cm^2) substrates.[6,17,18]

RAWMS spectra recorded at 0.0 V vs SCE for graphite before (dotted line) and after (solid line) adsorption of MB are shown in Figure 4. These measurements were performed with unpolarized light to offset the very small reflectivity of the carbon substrate. The peculiar peaks observed in both spectra in the region between 615 and 675 nm appear to be intrinsic to this particular graphite specimen. As indicated in Figure 4B, the normalized difference RAWMS spectrum displayed a prominent negative-going peak with a maximum at 680 nm, which can be clearly associated with adsorbed MB, and much smaller features at higher energies. Integration of this latter curve (see Figure 4C) produced a peak with a maximum at 664 nm and a small shoulder at higher energies. Essentially identical features have been observed for MB in the solution phase and attributed to monomeric (peak) and dimeric (shoulder) forms of the species.[19] It must be stressed, however, that the optical properties of the substrate can be modified by the presence of the adsorbate, and therefore the occurrence of small features in a spectral region where the substrate exhibits peaks of its own (such as the shoulder in Figure 4C) cannot be readily ascribed to the adsorbate. These results are somewhat different than those reported by Corn et al.[20] who observed a substantial blue shift in the peak maximum for monolayers of MB adsorbed on silica from MB aqueous solutions at a concentration of 2.5×10^{-4} M or higher.

The electrode was then polarized at −0.55 V vs SCE in an attempt to desorb the material from the surface. This procedure, however, was found to be only partially successful, as even after repeated rinsing with base electrolyte, both the voltammetry and the optics produced much smaller, albeit still detectable signals associated with adsorbed MB.

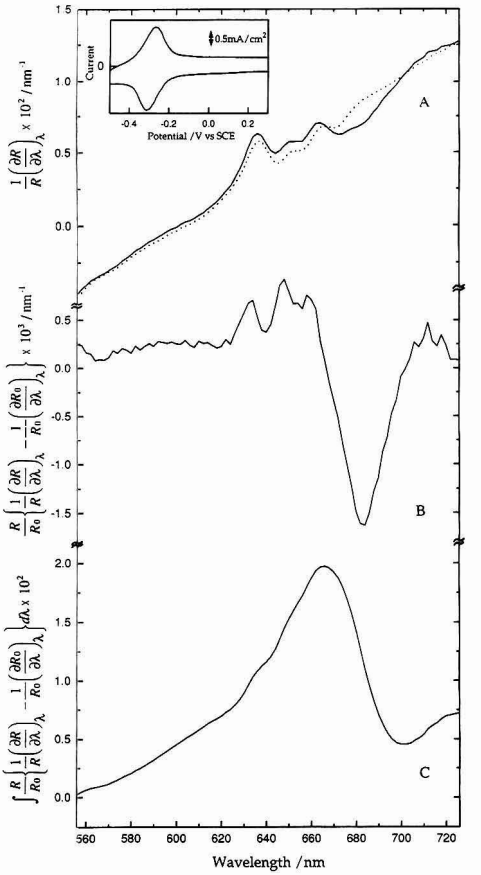

Figure 4. (A) In situ RAWMS spectra obtained with unpolarized light for OG before (dotted curve) and after (solid curve) adsorption of MB in 0.5 M KNO_3, 0.1 M phosphate buffer (pH = 7.9) obtained at 0.0 V vs SCE. Insert: Cyclic voltammogram for a single monolayer of MB on OG. Scan rate: 200 mV/s. Electrode area: 3 cm^2. (B) Normalized difference RAWMS spectra, $R/R_o[1/R(\partial R/\partial\lambda)_\lambda - 1/R_o(\partial R_o/\partial\lambda)_\lambda]$ vs λ, for a monolayer of MB irreversibly adsorbed on OG based on the data shown in (A) in this figure. (C) Integrated $R/R_o[1/R(\partial R/\partial\lambda)_\lambda - 1/R_o(\partial R_o/\partial\lambda)_\lambda]$ vs λ spectra for MB on OG based on the data shown in (B) in this figure.

2. Wavelength Modulation Spectra in the Transmission Mode. A number of experiments were conducted in which the wavelength modulation instrument was employed to record spectra of solution-phase $Co^{II}TsPc$ in the transmission mode using conventional cuvettes. As indicated in Figure 5, highly defined derivative-like curves could be observed down to a concentration of 14 nM, corresponding to ca. 0.0014 absorption units. This regime is not easily accessible with conventional spectrophotometers which illustrates the very high sensitivity of wavelength modulation compared to more popular spectroscopic techniques in this spectral range.

CONCLUSIONS

The results of this investigation have shown that RAWMS in its present stage of development provides a very sensitive

(17) Barner, B. J.; Corn, R. M. *Langmuir* **1990**, *6*, 1023.
(18) Svetlicic, V.; Clavilier, J.; Zutic, V.; Chevalet. J. *J. Electroanal. Chem. Interfacial Electrochem.* **1991**, *312*, 205.
(19) Mckay, R. B. *Trans. Faraday Soc.* **1965**, *61*, 787.
(20) Higgins, D. A.; Byerly, S. K.; Abrams, B.; Corn, R. M. *J. Phys. Chem.* **1991**, *95*, 6984.

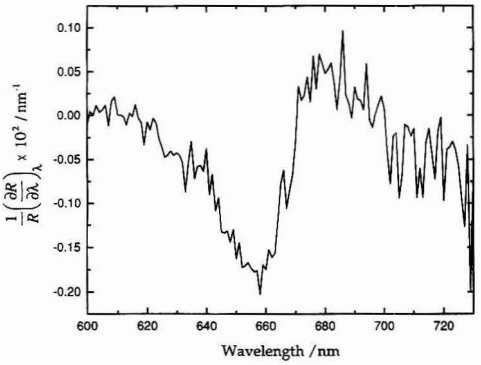

Figure 5. Transmission wavelength modulation spectra of a 14 nM $Co^{II}TsPc$ aqueous solution obtained using the same instrument involved in the in situ RAWMS measurements.

means of observing in situ species irreversibly adsorbed on graphite electrodes at a fixed electrode potential. It should be noted that the reflectivity of graphite in the visible region is much lower than that of common metals; hence, further gains in sensitivity can be expected to be obtained for RAWMS studies involving, for example, gold, platinum, or silver as electrode substrates. Such experiments are currently in progress in this laboratory and will be reported in due course. The uncertainties associated with the background reflectivity may not be regarded as very restrictive since most often only peak positions are used for spectral identification. Far more critical are questions regarding the actual interpretation of the data because the assumptions regarding the optical properties of the substrate referred to in the Introduction may be expected to be only rarely satisfied.

Despite these shortcomings, however, a combination of RAWMS and potential-modulated reflection spectroscopy may become a powerful tool for studying various structural and electronic properties of a wide variety of both reversibly and irreversibly adsorbed species on various types of electrode surfaces.

ACKNOWLEDGMENT

This work was supported in part by IBM, Yorktown Heights. Additional funding was provided by the Gas Research Institute.

RECEIVED for review August 17, 1992. Accepted October 9, 1992.

Voltage-Scan Fluorometry of Rose Bengal Ion at the 1,2-Dichloroethane–Water Interface

Takashi Kakiuchi,* Yoko Takasu, and Mitsugi Senda

Department of Agricultural Chemistry, Faculty of Agriculture, Kyoto University, Sakyo-ku, Kyoto 606, Japan

A new approach to ion sensing has been presented. Transfer of Rose Bengal (RB) anions from the aqueous phase (W) to the 1,2-dichloroethane (DCE) phase accompanied by the linear sweep of the voltage across the interface is monitored as an increase in fluorescence intensity (F) from RB dianions transferred to the DCE phase. RB in W can be detected down to 20 nM as a peak on a F vs time curve. The peak height (ΔF_p) is proportional to the concentration of the dye anion (${}^{b}c_{RB}^{W}$) up to 2 μM. At higher concentrations, ΔF_p vs ${}^{b}c_{RB}^{W}$ plot gradually deviates from the straight line. ΔF_p is inversely proportional to the square root of the scan rate. The Lambert–Beer's law in conjunction with the concentration profile of transferred ions in the DCE phase accounts for the salient features of the F vs t curves.

INTRODUCTION

Ion transfer across the interface between two immiscible electrolyte solutions is a fundamental process in selective detection of ions, e.g. solvent extraction and ion-selective electrodes.[1,2] In electrochemistry at liquid–liquid interfaces, the transfer of ions across the interface is measured as an electrical current passing through the interface. A residual current due to nonideal polarizability of the liquid–liquid interface and noise current, particularly amplified in the positive feedback mode, usually limit the lower bound of analyte ion concentration to 0.01–0.1 mM in conventional electrochemical measurements. Fluorescence is in principle much more sensitive than electrical current and has been used in detecting ions based on optode techniques.[3-5] Liquid–membrane attached optodes[3,6-10] have been proposed as a promising approach since the specific extraction of ions into the membrane gives rise to the change in optical properties of the bulk membrane rather than the change in monolayer level, which is common to receptor-immobilized optodes. A crucial step in detecting ions with membrane-attached optodes is the distribution of ions from a sample solution to the membrane. External control of the potential drop across the membrane–solution interface enables us to select ions on the basis of their relative lipophilicity. In the present study, we have applied fluorometry to detect the transfer of fluorescent Rose Bengal (RB) dianion through the 1,2-dichloroethane (DCE)-water (W) interface accompanied by the linear scan of the potential drop across the interface. When the excitation light was introduced from DCE to the interface so that the condition of total reflection is satisfied, the fluorescence from dye ions transferred from the aqueous to DCE phase can be measured with high sensitivity. The present system can be seen as a simple model of membrane-solution interfaces in optodes equipped with a thin membrane for specific extraction of ions.

THEORETICAL CONSIDERATION

We consider the combination of voltage-dependent transfer of dye ions across the DCE–W interface and the fluorescence from ions transferred into the DCE phase.

Prior to the quantitative consideration, it would be useful to qualitatively consider the properties of fluorescence intensity ($F(t)$) vs time (t) curves, which we call voltfluorograms. If all dye ions transferred to the DCE phase are equally excited and concentration quenching is negligible, $F(t)$ should be proportional to the total amount of dye ions in the DCE phase, i.e., $F(t)$ is proportional to the integral of the current with respect to time. By integrating the current for linear sweep voltammetry, it can be shown that the total charge transferred into the DCE phase is proportional to the bulk concentration of i in the aqueous phase, ${}^{b}c_i^{W}$, and is inversely proportional to the square root of the scan rate, $v^{1/2}$. Since in real systems excitation light is attenuated by absorption and all dye ions are not equally excited, this proportionality holds only in infinite dilution or at a very fast scan rate. Nevertheless, a voltfluorogram should resemble the corresponding total charge transferred vs t curve, or its derivative should be similar to the corresponding cyclic voltammogram; a single peak will appear on a voltfluorogram at the potential where the sign of the current is reversed in the reverse scan and the steepest rise and fall of $F(t)$ will correspond to the potential around the peak for the forward scan and that in the reverse scan, respectively, in a cyclic voltammogram.

To calculate the fluorescence intensity, we neglect, for simplicity, the fluorescence from the aqueous phase. In the present system the concentration of dye ions is a function of t and distance normal to the interface, x. The intensity of excitation light also is hence a function of t and x. When the angle of incident light is not in parallel with x-axis, the calculation of the intensity of excitation light is fairly involved. Here we simplify the treatment by supposing that the excitation light comes from the bulk of DCE phase in the direction normal to the interface and is absorbed at the interface.

Lambert–Beer's law has the form[11]

$$d \ln I = -\kappa c_i^{DCE}(t,x)\, dx \qquad (1)$$

where κ is the molar absorption coefficient of ion i and

(1) Girault, H. H.; Schiffrin, D. J. *Electroanalytical Chemistry*; Bard, A. J., Ed.; Marcel Dekker: New York, 1989; Vol. 15, pp 1–144.
(2) Senda, M.; Kakiuchi, T.; Osakai, T. *Electrochim. Acta* **1991**, *36*, 253–262.
(3) Bright, F. V.; Piorier, G. E.; Hieftje, G. M. *Talanta*, **1988**, *35*, 113–118.
(4) Suzuki, K.; Tohda, K.; Tanda, Y.; Ohzora, H.; Nishihara, S.; Inoue, H.; Shirai, T. *Anal. Chem.* **1989**, *61*, 382–383.
(5) Kawabata, Y.; Kamichika, T.; Imasaka, T.; Ishibashi, N. *Anal. Chem.* **1990**, *62*, 1528–1531.
(6) Kawabata, Y.; Kamichika, T.; Imasaka, T.; Ishibashi, N. *Anal. Chem.* **1990**, *62*, 2054–2055.
(7) Seiler, K.; Morf, W. E.; Rusterholz, B.; Simon, W. *Anal. Chem.* **1989**, *5*, 557–561.
(8) Morf, W. E.; Seiler, K.; Lehmann, B.; Behringer, C.; Hartman, K.; Simon, W. *Pure Appl. Chem.* **1989**, *61*, 1613–1618.
(9) Tan, S. S. S.; Hauser, P. C.; Chaniotakis, N. A.; Suter, G.; Simon, W. *Chimia* **1989**, *43*, 257–261.
(10) Hauser, P. C.; Périsset, P. M. J.; Tan, S. S. S.; Simon, W. *Anal. Chem.* **1990**, *62*, 1919–1923.
(11) Atkins, P. W. *Physical Chemistry*, 4th ed.; Oxford University Press: Oxford, 1990; Chapter 17.

0003-2700/92/0364-3096$03.00/0

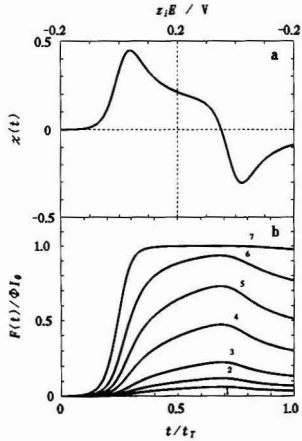

Figure 1. A cyclic voltammogram of the reversible ion transfer (a) and voltfluorograms (b) at $\epsilon({}^{b}c_i^{W})/v^{1/2}$ = 0.005 (1), 0.010 (2), 0.020 (3), 0.050 (4), 0.100 (5), 0.200 (6), and 0.500 (7) calculated from eq 5.

$c_i^{DCE}(t,x)$ is the concentration of i in DCE. By integrating this equation, we obtain

$$I(t,x) = I_0 \exp[-\kappa \int_{\infty}^{x} c_i^{DCE}(t,\zeta)\, d\zeta] \quad (2)$$

On the other hand, fluorescence intensity from a thin layer of thickness dx, $dF(t,x)$, is given by

$$dF(t,x) = \kappa\Phi I(t,x) c_i^{DCE}(t,x)\, dx \quad (3)$$

where Φ is the quantum yield of fluorescence at a given wavelength. Combining these two equations and assuming the absence of concentration quenching, we may write for the total fluorescence intensity

$$F(t) = \kappa\Phi I_0 \int_0^{\infty} c_i^{DCE}(x,t)[\exp\{-\kappa \int_{\infty}^{x} c_i^{DCE}(t,\zeta)\, d\zeta\}]\, dx \quad (4)$$

$c_i^{DCE}(x,t)$ is given by solving the diffusion equation with appropriate initial and boundary conditions. To obtain $c_i^{DCE}(x,t)$, we assumed that the diffusion of ion i follows the semiinfinite linear conditions both in DCE and W phases and that the transfer of i is reversible. Since the analytical form of $c_i^{DCE}(t,x)$ is not available, we first calculated $c_i^{DCE}(t,x)$ and then $F(t)$ numerically using a finite difference method. $F(t)$ is then expressed as

$$F(t) = \epsilon\Phi I_0 \frac{{}^{b}c_i^{W}}{v^{1/2}} \sum_{i=1}^{\infty} \left[f^0(i,t) \exp\left\{ -\epsilon \frac{{}^{b}c_i^{W}}{v^{1/2}} \sum_{k=\infty}^{i} f^0(k,t) \right\} \right] \quad (5)$$

where

$$\epsilon = \kappa \left(\frac{D_i^{DCE}}{\mathbf{D}_i^{DCE}} \frac{1}{L} \frac{RT}{z_iF} \right)^{1/2} \quad (6)$$

and $f^0(i,t) = c_i^{DCE}/{}^{b}c_i^{W}$. Here D_i^{DCE} is the diffusion coefficient of i in DCE, $\mathbf{D}_i^{DCE}$ is the dimensionless diffusion coefficient defined by $\mathbf{D}_i^{DCE} = D_i^{DCE}\Delta t/(\Delta x)^2$, Δx and Δt are discretized distance and time, and L is the number of iteration per RT/z_iF. In eq 6, ${}^{b}c_i^{W}$ and $v^{1/2}$ appear as a combined parameter, ${}^{b}c_i^{W}/v^{1/2}$, ${}^{b}c_i^{W}$ and $1/v^{1/2}$ is equivalent in determining the magnitude of $F(t)$. $F(t)$ is not linear with respect to ${}^{b}c_i^{W}/v^{1/2}$.

$F(t)/\Phi I_0$ vs t/t_T plots at several values of $\epsilon({}^{b}c_i^{W})/v^{1/2}$ are shown in Figure 1b, where t_T is time needed for one measurement. At lower values of $\epsilon({}^{b}c_i^{W})/v^{1/2}$, the peaks are located at the potential where the dimensionless current, $\varkappa(t)$, crosses the line of $\varkappa(t) = 0$ (Figure 1a). With increasing $\epsilon({}^{b}c_i^{W})/v^{1/2}$, the peak potential shifts to the right by a few millivolts (smaller E). The peak becomes broader and eventually shows a plateau when $\epsilon({}^{b}c_i^{W})/v^{1/2} > 0.5$. The peak height ($F_p/\Phi I_0$) in Figure 1b is plotted against $\epsilon({}^{b}c_i^{W})/v^{1/2}$ in Figure 2. $F_p/\Phi I_0$ is approximately a linear function of $\epsilon({}^{b}c_i^{W})/v^{1/2}$ up to $\epsilon({}^{b}c_i^{W})/v^{1/2}$ = 0.05 (inset of Figure 2) and becomes saturated above $\epsilon({}^{b}c_i^{W})/v^{1/2}$ = 0.2.

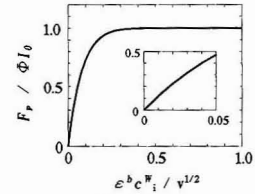

Figure 2. Peak height vs $\epsilon({}^{b}c_i^{W})/v^{1/2}$ curve corresponding to the calculated $F(t)/\Phi I_0$ vs t/t_T curves in Figure 1. The inset shows the magnified view at smaller $\epsilon({}^{b}c_i^{W})/v^{1/2}$ values.

EXPERIMENTAL SECTION

Materials. Reagent-grade RB was used without further purification. Methods of the purification of water and tetrabutylammonium chloride (TBACl) and of the preparation of tetrabutylammonium tetraphenylborate (TBATPB) have been described elsewhere.[12] Other chemicals used were of reagent grade.

Methods. Cyclic voltammograms were recorded using a computer-controlled voltammetry system.[13] The positive feedback method was used for the compensation of potential drop due to solution resistance.[12] The electrochemical cell is represented by

I	II	III	IV	V	VI	VII
		0.01 M	0.01 M	0.01 M LiCl		
Ag	AgCl	TBACl	TBATPB	Phosphate–Borate	AgCl	Ag
				Buffer at pH9.0		
				α M Rose Bengal		
		(water)	(DCE)	(water)		

To make sure that Rose Bengal takes a divalent anionic form, the pH of the phase V was adjusted to 9.0 using 0.01 M phosphate–borate buffer. The interface between IV and V is the polarized interface. The potential of the right-hand side terminal of the cell with respect to the left is denoted as E. The current was taken to be positive when positively charged species pass through the interface from W to DCE. Figure 3 illustrates the cell used for fluorescence measurements. A cylindrical sample vial of 2-cm diameter and 3.5-cm length was modified to accommodate another inlet and used for the outer cell (Figure 1). The polarized DCE–W interface between phases IV and V was made at the end of the inner glass tube, whose inner diameter was 4.6 mm. The location of the interface was adjusted at the central axis of the cylindrical outer cell. The orifice and outer surface of the tube was made hydrophobic by applying dimethyldichlorosilane vapor. After the interface was adjusted to be as flat as possible, the stopcock connected to the inner tube was closed to maintain the location and shape of the interface as is. Light from a 150-W xenon lamp was led to the vicinity of the outer glass wall of the cell through an optical wave guide equipped with a convex lens. The diameter of the lens was 7 mm and its focal length was 2 cm. Light was impinged to the interface from the DCE phase through the outer glass wall of the cell. The angle of incidence to the DCE–W

(12) Kakiuchi, T.; Senda, M. *Bull. Chem. Soc. Jpn.* **1983**, *56*, 1322–1326.
(13) Osakai, T.; Nuno, T.; Yamamoto, Y.; Saito, A.; Senda, M. *Bunseki Kagaku* **1989**, *38*, 479–485.

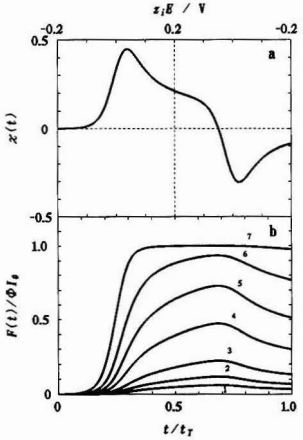

Figure 1. A cyclic voltammogram of the reversible ion transfer (a) and voltfluorograms (b) at $\epsilon({}^{b}c_i^{W})/v^{1/2}$ = 0.005 (1), 0.010 (2), 0.020 (3), 0.050 (4), 0.100 (5), 0.200 (6), and 0.500 (7) calculated from eq 5.

$c_i^{DCE}(t,x)$ is the concentration of i in DCE. By integrating this equation, we obtain

$$I(t,x) = I_0 \exp[-\kappa \int_{\infty}^{x} c_i^{DCE}(t,\zeta)\, d\zeta] \quad (2)$$

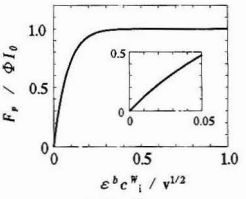

Figure 2. Peak height vs $\epsilon({}^{b}c_i^{W})/v^{1/2}$ curve corresponding to the calculated $F(t)/\Phi I_0$ vs t/t_T curves in Figure 1. The inset shows the magnified view at smaller $\epsilon({}^{b}c_i^{W})/v^{1/2}$ values.

located at the potential where the dimensionless current, $\kappa(t)$, crosses the line of $\kappa(t) = 0$ (Figure 1a). With increasing $\epsilon({}^{b}c_i^{W})/v^{1/2}$, the peak potential shifts to the right by a few millivolts (smaller E). The peak becomes broader and eventually shows a plateau when $\epsilon({}^{b}c_i^{W})/v^{1/2} > 0.5$. The peak height ($F_p/\Phi I_0$) in Figure 1b is plotted against $\epsilon({}^{b}c_i^{W})/v^{1/2}$ in Figure 2. $F_p/\Phi I_0$ is approximately a linear function of $\epsilon({}^{b}c_i^{W})/v^{1/2}$ up to $\epsilon({}^{b}c_i^{W})/v^{1/2}$ = 0.05 (inset of Figure 2) and becomes saturated above $\epsilon({}^{b}c_i^{W})/v^{1/2}$ = 0.2.

EXPERIMENTAL SECTION

Materials. Reagent-grade RB was used without further purification. Methods of the purification of water and tetrabutylammonium chloride (TBACl) and of the preparation of tetrabutylammonium tetraphenylborate (TBATPB) have been described elsewhere.[12] Other chemicals used were of reagent

CORRECTION

Voltage-Scan Fluorometry of Rose Bengal Ion at the 1,2-Dichloroethane–Water Interface

Takashi Kakiuchi,* Yoko Takasu, and Mitsugi Senda (*Anal. Chem.* 1992, *64*, 3096–3100).

Since the origin of the x-axis is taken at the interface, $-\kappa$ in eqs 1, 2, and 4 should be read as κ and in eq 5 $-\epsilon$ should be read as ϵ.

form of $c_i^{DCE}(t,x)$ is not available, we first calculate [illegible] (t,x) and then $F(t)$ numerically using a finite difference method. $F(t)$ is then expressed as

$$F(t) = \epsilon\Phi I_0 \frac{{}^{b}c_i^{W}}{v^{1/2}} \sum_{i=1}^{\infty} \left[f^0(i,t) \exp\left\{ -\epsilon \frac{{}^{b}c_i^{W}}{v^{1/2}} \sum_{k=\infty}^{i} f^0(k,t) \right\} \right] \quad (5)$$

where

$$\epsilon = \kappa \left(\frac{D_i^{DCE}}{\mathbf{D}_i^{DCE}} \frac{1}{L} \frac{RT}{z_iF} \right)^{1/2} \quad (6)$$

and $f^0(i,t) = c_i^{DCE}/{}^{b}c_i^{W}$. Here D_i^{DCE} is the diffusion coefficient of i in DCE, $\mathbf{D}_i^{DCE}$ is the dimensionless diffusion coefficient defined by $\mathbf{D}_i^{DCE} = D_i^{DCE}\Delta t/(\Delta x)^2$, Δx and Δt are discretized distance and time, and L is the number of iteration per RT/z_iF. In eq 6, ${}^{b}c_i^{W}$ and $v^{1/2}$ appear as a combined parameter, ${}^{b}c_i^{W}/v^{1/2}$; ${}^{b}c_i^{W}$ and $1/v^{1/2}$ is equivalent in determining the magnitude of $F(t)$. $F(t)$ is not linear with respect to ${}^{b}c_i^{W}/v^{1/2}$.

$F(t)/\Phi I_0$ vs t/t_T plots at several values of $\epsilon({}^{b}c_i^{W})/v^{1/2}$ are shown in Figure 1b, where t_T is time needed for one measurement. At lower values of $\epsilon({}^{b}c_i^{W})/v^{1/2}$, the peaks are

[illegible] interface. The potential of the right-hand side terminal of the cell with respect to the left is denoted as E. The current was taken to be positive when positively charged species pass through the interface from W to DCE. Figure 3 illustrates the cell used for fluorescence measurements. A cylindrical sample vial of 2-cm diameter and 3.5-cm length was modified to accommodate another inlet and used for the outer cell (Figure 1). The polarized DCE–W interface between phases IV and V was made at the end of the inner glass tube, whose inner diameter was 4.6 mm. The location of the interface was adjusted at the central axis of the cylindrical outer cell. The orifice and outer surface of the tube was made hydrophobic by applying dimethyldichlorosilane vapor. After the interface was adjusted to be as flat as possible, the stopcock connected to the inner tube was closed to maintain the location and shape of the interface as is. Light from a 150-W xenon lamp was led to the vicinity of the outer glass wall of the cell through an optical wave guide equipped with a convex lens. The diameter of the lens was 7 mm and its focal length was 2 cm. Light was impinged to the interface from the DCE phase through the outer glass wall of the cell. The angle of incidence to the DCE–W

(12) Kakiuchi, T.; Senda, M. *Bull. Chem. Soc. Jpn.* **1983**, *56*, 1322–1326.

(13) Osakai, T.; Nuno, T.; Yamamoto, Y.; Saito, A.; Senda, M. *Bunseki Kagaku* **1989**, *38*, 479–485.

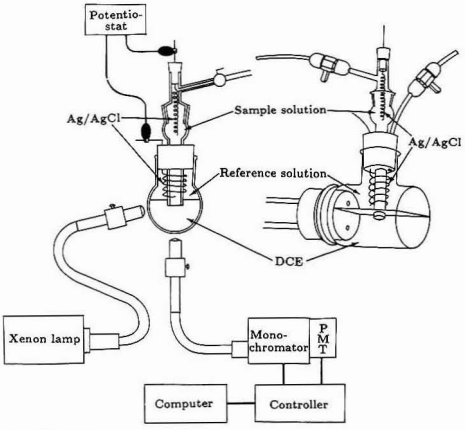

Figure 3. Schematic representation of the cell at two different views.

interface was adjusted so that the excitation beam focused at the interface was totally reflected. The refractive index is greater in DCE ($n^{20}_D = 1.4421$) than in water ($n^{20}_D = 1.3330$). The critical angle for the DCE–water interface is then 67.56° when both phases consist of pure solvents. The angle of incidence was set at about 75°.

The reflection of the light at the interface was monitored visually by using a piece of black paper placed at the opposite side of the cell. In fact, mainly due to the incomplete focusing of light and the dispersion of light when passing through the outer glass wall of the cell, it was difficult to achieve the complete reflection of incident light at the DCE–W interface; a certain portion of the light inevitably leaked through the interface into the aqueous phase. Filtering of excitation light with a monochromator or a filter did not appreciably improve the penetration of light into the aqueous phase. Emitted light normal to the interface was monitored through another optical waveguide which was set beneath the cell (Figure 3) and was connected to a photon-counting apparatus (Unisoku, Japan) via a monochromator. The depth of the DCE phase beneath the interface was about 10 mm. Time-dependent fluorescence was monitored usually at the maximum emission, 590 nm. Triggering signal for starting a photon-counting measurement with time scan mode at a given wavelength was also fed to the computer-controlled voltammetry system for enabling the voltage scan. All measurements were made at room temperature, 23 ± 2 °C.

RESULTS AND DISCUSSION

Properties of Fluorescence Intensity vs Time Curves. Voltfluorograms recorded at a scan rate (v) = 10 mV s^{-1} are shown in Figure 4b for ${}^{b}c^{W}_{RB}$ = 0.5 mM (curve 1) and 0.5 μM (curve 2). E was applied in a cyclic voltammetry mode between the initial potential (E_{init}) at 400 mV and the switching potential (E_S) at 75 mV. Transfer of RB anions from W to DCE was detected as an increase in F. In the reverse scan of E, F decreased as RB ions went back to the aqueous phase. After each scanning, E was kept at 400 mV. Continued decrease in F with time at this potential indicates that RB in the DCE phase was gradually redistributed into the W phase.

Curve 1 showed characteristic features which are predicted in the theoretical treatment described above (Figure 1). The peak appeared at the E value on the reverse scan. The rate of the increase in F in the forward scan was significantly reduced before reaching the E_S. When E returned to the initial potential, the F decreased to only 20% of the maximum value of F.

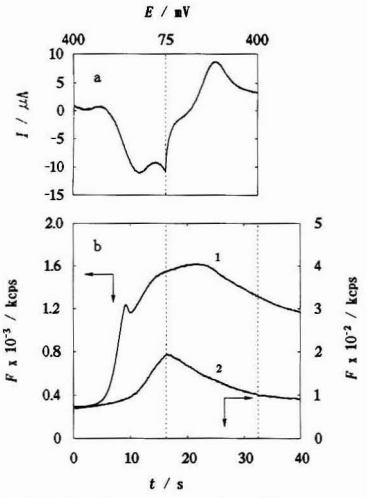

Figure 4. A cyclic voltammogram and a voltfluorogram (curve 1) simultaneously recorded at ${}^{b}c^{W}_{RB}$ = 0.5 mM in W and at v = 20 mV s^{-1}. Curve 2 is a voltfluorogram at ${}^{b}c^{W}_{RB}$ = 2 μM.

A small reproducible peak appearing in the forward scan cannot, however, be interpreted within the framework of the model discussed above and suggests the participation of other factors not directly related to the ion transfer current, e.g. movement of the interface due to the change in surface tension, convective motion of the DCE solution, or small emulsion particle formed in the vicinity of the interface.

A cyclic voltammogram simultaneously recorded during the fluorescence measurement at ${}^{b}c^{W}_{RB}$ = 0.5 mM is shown in Figure 4a. It is seen that the peak in curve 1 in Figure 4b appeared at the potential where the current became zero in Figure 4a. The position of the peak in the reverse scan of the cyclic voltammogram corresponds to the steepest decrease in the voltfluorogram in Figure 4b. Similar correspondence for the peak in the cyclic voltammogram in the forward scan was not observed probably due to the small peak in the voltfluorogram in Figure 4b.

When ${}^{b}c^{W}_{RB}$ was lowered, the peak in voltfluorograms shifted to around E_S, as exemplified by the trace at ${}^{b}c^{W}_{RB}$ = 2 μM (curve 2 in Figure 4b). Thus the peak appeared much earlier than that predicted from eq 5. The decrease in F in the reverse scan was more rapid than expected in the above model (Figure 2). After one cycle of the voltage scanning, F decreased to less than half of the peak height. The point of inflection in the forward scan corresponds to the forward peak of the cyclic voltammogram in Figure 4b.

When ${}^{b}c^{W}_{RB} < 10\ \mu$M, the residual current mainly due to the transfer of supporting electrolytes far exceeds the current corresponding to RB ion transfer.[14,15] The observed shift of the peak in the voltfluorogram at lower RB concentrations may be associated with the disturbance of the interface due to the transfer of supporting electrolyte ions.

Concentration Dependence of Fluorescence Intensity. Voltfluorograms at several different values of ${}^{b}c^{W}_{RB}$ between 50 nM and 5 μM at v = 10 mV s^{-1} are shown in Figure 5. In

(14) Kakiuchi, T.; Senda, M. *Bull. Chem. Soc. Jpn.* **1983**, *56*, 1322–1326.

(15) Kakiuchi, T.; Senda, M. *Collect. Czech. Chem. Commun.* **1991**, *56*, 112–129.

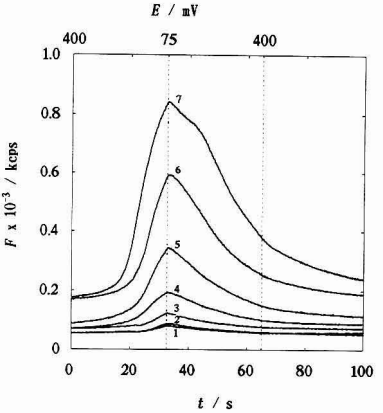

Figure 5. Voltfluorograms ${}^{b}c_{RB}^{W}$ = 0.05 (1), 0.10 (2), 0.2 (3), 0.50 (4), 1.00 (5), 2.00 (6), and 5.00 (7) μM recorded at v = 10 mV s^{-1}.

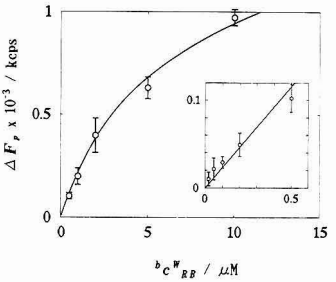

Figure 6. Peak height vs ${}^{b}c_{RB}^{W}$ curve. Experimental conditions are the same as those in Figure 5. The inset shows the magnified view at lower ${}^{b}c_{RB}^{W}$ values.

the concentration range shown in Figure 5, all peaks were located at about E_S and the position was independent of ${}^{b}c_{RB}^{W}$.

The fluorescence increased with ${}^{b}c_{RB}^{W}$. The concentration dependence of the peak height (ΔF_p) on voltfluorograms corrected for the background fluorescence is shown in Figure 6. Error bars in the figure indicate the standard deviation for two independent sets of measurements, a total five runs. In the lower concentration range, F increased linearly with ${}^{b}c_{RB}^{W}$ as shown in the inset in Figure 5. In the lower limit, the peak was detectable down to ${}^{b}c_{RB}^{W}$ = 20 nM. Deviation from the straight line becomes appreciable when ${}^{b}c_{RB}^{W} > 2$ μM.

The background fluorescence, i.e. F at $E = E_{init}$ before the voltage scan, increased with ${}^{b}c_{RB}^{W}$. This increase is probably attributable to three factors. First is the fluorescence from RB excited by an evanescent wave in the aqueous side of the interface. Second is the fluorescence from RB in W excited by the light passed through the interface due to incomplete reflection at the interface. Third is the fluorescence from RB in DCE. When a new DCE–W interface was formed without applying the potential across the two Ag–AgCl electrodes, a certain amount of RB spontaneously dissolved into the DCE phase. Although RB went back to the W phase after setting the potential at 400 mV, a certain portion of RB spread over the DCE phase remained to contaminate the DCE phase.

Effect of Scan Rate. The effect of scan rate is illustrated in Figure 7 between v = 5 and 100 mV s^{-1} at ${}^{b}c_{RB}^{W}$ = 2 μM. With increasing scan rate, F decreased as predicted above. The

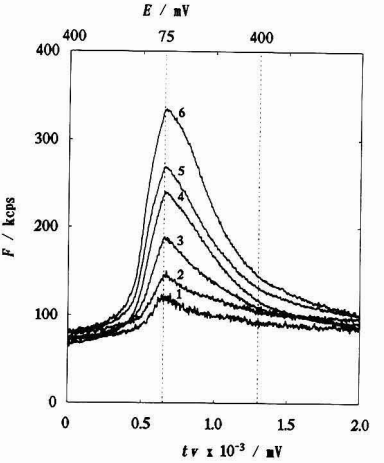

Figure 7. Effect of scan rate on voltfluorogram at ${}^{b}c_{RB}^{W}$ = 2 μM and at v = 100 (1), 50 (2), 20 (3), 10 (4), 8 (5), and 5 (6) mV s^{-1}. tv was taken as the abscissa so that voltfluorograms at different scan rates can be compared with each other.

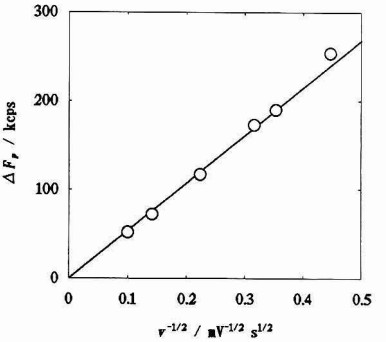

Figure 8. Dependence of the peak height of voltfluorograms on scan rate. Data were taken from Figure 7.

peak potential remained constant at $E = E_s$ over the range of v between 5 and 100 mV s^{-1}. The ΔF_p was inversely proportional to $v^{1/2}$ as shown in Figure 8. According to eq 5, the increase in scan rate is equivalent to the decrease in ${}^{b}c_{RB}^{W}$. Since the ΔF_p vs ${}^{b}c_{RB}^{W}$ plot at v = 10 mV s^{-1} in Figure 6 is almost linear at ${}^{b}c_{RB}^{W}$ = 2 μM, observed linearity in Figure 8 is in harmony with the linear variation in the inset in Figure 6.

When $\epsilon({}^{b}c_i^{W})/v^{1/2}$ is small enough to neglect higher terms of the series expansion of the exponential term in eq 5, we have

$$F(t) = \epsilon\Phi I_0 \frac{{}^{b}c_i^{W}}{v^{1/2}} \sum_{i=1}^{\infty} f^0(i,t) + \epsilon^2 \Phi I_0 \left(\frac{{}^{b}c_i^{W}}{v^{1/2}}\right)^2 \sum_{i=1}^{\infty} [f^0(i,t) \sum_{k=\infty}^{i} f^0(k,t)] \quad (7)$$

Further, if $\epsilon({}^{b}c_i^{W})/v^{1/2}$ is so small that the second term of the right-hand side of eq 7 is negligible, the linear variation of $F(t)$ with respect to either ${}^{b}c_i^{W}$ or $v^{1/2}$ is expected. The observed linear variations of $F(t)$ in Figures 6 and 8 assure that $\epsilon({}^{b}c_i^{W})/v^{1/2}$ is small enough in the experimental range of ${}^{b}c_i^{W}$ and $v^{1/2}$.

CONCLUSIONS

Fluorometric detection of ion transfer is 3 orders of magnitude more sensitive than conventional electrochemical techniques. The potential drop across the interface as a new parameter in optical detection of ionic substances enables separate detection of ions having different degree of lipophilicity, which augments the selectivity inherent to optical techniques based on excitation or fluorescence spectrum of analytes. The fluorescence technique has been applied to obtain partition coefficient of fluorescent dyes between the oil and water phases.[16,17] The present results show the possibility that the partition coefficients or transfer free energies between an oil and water phases can be determined based on voltfluorograms. Another advantage of the present method is that the presence of nonfluorescent ions transferred within the potential window, even in large quantity, does not interfere with the determination of analyte ions. The present study has been concerned with the detection of fluorescent ions. However, the method can be extended to the detection of nonfluorescent ions by using fluorescent ionophores.

(16) Wiegand, D. H.; Vanýsek, P. *Appl. Spectrosc.* **1988**, *42*, 958–961.
(17) Wiegand, D. H.; Vanýsek, P. *J. Colloid Interface Sci.* **1990**, *135*, 272–282.

RECEIVED for review August 11, 1992. Accepted October 6, 1992.

Determination of Chromium(III) and Chromium(VI) in Water Using Flow Injection On-Line Preconcentration with Selective Adsorption on Activated Alumina and Flame Atomic Absorption Spectrometric Detection

Michael Sperling, Shukun Xu,† and Bernhard Welz*

Department of Applied Research, Bodenseewerk Perkin-Elmer GmbH, W-7770 Überlingen, Germany

A rapid and sensitive method for the species-selective determination of chromium(III) and chromium(VI) in water samples by flame atomic absorption spectrometry using on-line preconcentration on a microcolumn packed with activated alumina (acidic form) has been developed. Sequential species-selective sorption was possible by using the Clark–Lubs buffer systems with pH 7 for Cr(III) and pH 2 for Cr(VI). The preconcentrated species were eluted directly from the column to the nebulizer–burner system using 1.0 mol/L nitric acid and 0.5 mol/L ammonia for Cr(III) and Cr(VI), respectively. The retention efficiency was better than 80% for Cr(III) and better than 90% for Cr(VI), giving a sensitivity enhancement of 25 for a 3-mL sample loading. The effect of concomitant species was investigated, and satisfactory recovery of 90–106% could be obtained from natural water samples. Linear calibration for both species was established over the concentration range 10–200 μg/L with detection limits (3 s) of 1.0 and 0.8 μg/L for Cr(III) and Cr(VI), respectively.

INTRODUCTION

There is a rapidly increasing demand for fast and reliable analytical methods for the determination of chemical forms of elements in environmental samples. The interest in chromium is governed by the fact that its toxicity depends critically on its oxidation state: While chromium(III) is considered essential for mammals for the maintenance of glucose, lipid, and protein metabolism,[1] chromium(VI) is known to be toxic to humans.[2] Cr(III) and Cr(VI) enter the environment as a result of effluent discharge from steel works, electroplating, tanning industries, oxidative dyeing, chemical industries, and cooling water towers. The metal may also enter drinking water supply systems from the corrosion inhibitors used in water pipes and containers or by contamination of the underground water from sanitary landfill leaching. Therefore it is of major concern to understand the behavior of chromium in natural aquatic systems. In view of the difference between the oxidation states, and in order to follow the pathways for interconversion in the environment, it is increasingly important to monitor the concentration of the individual chemical species as well as the total concentration of chromium in the environment. Traditional methods for the speciation of inorganic chromium, are, however relatively time-consuming, involving species separation based on solvent extraction,[3] coprecipitation,[4] electrochemical separation,[5] ion exchange,[6,7] solid-phase extraction,[8,9] or selective volatilization in combination with graphite furnace atomic absorption spectrometry (GFAAS).[10]

Many methods are based on the determination of Cr(VI) and total chromium because Cr(III) is kinetically inert, calling for a conversion step. The conversion of metal species from one form to another can have serious drawbacks including incomplete conversions (particularly at low concentrations), introduction of contamination by the oxidation/reduction agents, interferences from other metals present, and generally, complex and time-consuming sample pretreatment procedures. Of the numerous methods developed for chromium speciation, those which physically separate the individual species followed by direct quantitation are preferred because they are relatively fast and require only minimal sample pretreatment. This last factor is particularly important because prolonged sample manipulation may affect the chromium species distribution significantly.[11] During the past decade, problems inherent in manual sample manipulation could be overcome, at least in part, by hyphenated techniques such as HPLC or FIA coupled to photometric or spectrometric detection techniques, which are summarized in Table I.[12–26] Detection limits given in Table I are based on 3 s and were

* To whom correspondence should be addressed.

† On leave from the Flow Injection Analysis Research Center, Institute of Applied Ecology, Academia Sinica, Shenyang, 110015, China.

(1) Ottaway, J. M.; Fell, G. S. *Pure Appl. Chem.* **1986**, *58*, 1707.
(2) Nriagu, J. O.; Nieboer, E. *Chromium in the Natural and Human Environment*; Wiley: New York, 1988.
(3) Sugiyama, M.; Fujino, O.; Kihara, S.; Matsui, M. *Anal. Chim. Acta* **1986**, *181*, 159.
(4) Lan, C.-R.; Tseng, C.-L.; Yang, M.-H.; Alfassi, Z. B. *Analyst* **1991**, *116*, 35.
(5) Issa, R. M.; Abdel-Nabey, B. A.; Dadek, H. *Electrochim. Acta* **1968**, *13*, 1827.
(6) Johnson, C. A. *Anal. Chim. Acta* **1990**, *238*, 273.
(7) Mazzucotelli, A.; Minoia, C.; Pozzoli, L.; Ariati, L. *At. Spectrosc.* **1983**, *4*, 182.
(8) Miyazaki, A.; Barnes, R. M. *Anal. Chem.* **1981**, *53*, 364.
(9) Morocco, M. T.; Newman, G. P.; Syty, A. *J. Anal. Atom. Spectrom.* **1990**, *5*, 29.
(10) Dungs, K.; Fleischhauer, H.; Neidhart, B. *Fresenius' Z. Anal. Chem.* **1985**, *322*, 280.
(11) Florence, T. M.; Batley, G. E. *CRC Crit. Rev. Anal. Chem.* **1980**, *9*, 219.
(12) de Andrade, J. C.; Rocha, J. C.; Baccan, N. *Analyst* **1985**, *110*, 197.
(13) de Andrade, J. C.; Rocha, J. C.; Baccan, N. *Analyst* **1984**, *109*, 645.
(14) Ruz, J.; Rios, A.; Luque de Castro, M. D.; Valcárcel, M. *Fresenius' Z. Anal. Chem.* **1985**, *322*, 499.
(15) Lynch, T. P.; Kernoghan, N. J.; Wilson, J. N. *Analyst* **1984**, *109*, 839.
(16) Syty, A.; Christensen, R. G.; Rains, T. C. *J. Anal. Atom. Spectrom.* **1988**, *3*, 193.
(17) Krull, I. S.; Panaro, K. W.; Gersheim, L. L. *J. Chromatogr. Sci.* **1983**, *21*, 460.
(18) Urasa, I. T.; Nam, S. H. *J. Chromatogr. Sci.* **1989**, *27*, 30.
(19) Shah, A.; Devi, S. *Anal. Chim. Acta* **1990**, *236*, 469.
(20) Milosavljevic, E. B.; Solujic, L.; Nelson, J. H.; Hendrix, J. L., *Microchim. Acta* **1985**, III, 353.
(21) Syty, A.; Christensen, R. G.; Rains, T. C. *At. Spectrosc.* **1986**, *7*, 89.
(22) Hirata, S.; Umezaki, Y.; Ikeda, M. *Anal. Chem.* **1986**, *58*, 2603.
(23) Cox, A. G.; Cook, I. G.; McLeod, C. W. *Analyst* **1985**, *110*, 331.
(24) Cox, A. G.; McLeod, C. W. *Anal. Chim. Acta* **1986**, *179*, 487.
(25) Ahmad, S.; Murthy, R. C.; Chandra, S. V. *Analyst* **1990**, *115*, 287.
(26) Sperling, M.; Yin, X.; Welz, B. *Analyst* **1992**, *117*, 629.

0003-2700/92/0364-3101$03.00/0

Table I. Comparison of Published Methods for the Selective Determination of Chromium(III) and/or Chromium(VI) by On-Line Separation Techniques[a]

Cr species	technique	sorbent	F_s, 1/h	V_s, mL	RSD, %	DL, μg/L	range, μg/L	ref
Cr(VI)	FI–UV	DPC	ng	0.164	3.0 (100 μg/L)	18	20–2000	13
Cr(T)	FI–UV	oxidat, Ce(IV)	ng	0.164	2.0 (200 μg/L)	55	50–4000	
Cr(VI)	FI–UV	DPC	ng		<3	ng	100–1250	14
Cr(T)	FI–UV	oxidat, Ce(IV)	ng	30–100	<1	ng	500–5000	
Cr(VI)	FI–UV	DPC	120	0.03	ng	ng	100–20000	15
Cr(T)	FI–FAAS		120	0.03	ng	ng	1000–50000	
Cr(III)	HPLC–FAAS	RP	30?	0.2	8.9 (1240 μg/L)	60	100–2000	16
Cr(VI)		RP	30?	0.2	7.5 (1280 μg/L)	120	200–2000	
Cr(III)	HPLC–DCP-AES	C_{18}-RP	5	0.1	ng	5–10	10–5000	17
Cr(VI)								
Cr(III)	HPLC–DCP-AES	ion exchanger	1–8	1.0	<1	ng	ng	18
Cr(VI)								
Cr(III)	FI–FAAS	PHXA	1	100	ng	ng	20–100	19
Cr(III)	FI–FAAS	CPG-8HOQ	120	0.2	1.0 (600 μg/L)	ng	70–2000	20
Cr(VI)		direct			0.5 (1000 μg/L)	ng	100–5000	
Cr(III)	FI–FAAS	CPG-8HOQ	60	1.0	0.67 (100 μg/L)	16	20–400	
Cr(VI)		direct			0.52 (500 μg/L)	85	100–5000	
Cr(VI)	FI–FAAS	RP	2–4	10–14	ng	1.2	5–100	21
Cr(III)	FI–ICP-AES	Muromac-1 ion-exchange	17	18	<5 (10 μg/L)	0.21	0.2–100	22
Cr(III)	FI–ICP-AES	alumina, acidic	20	2.0	2.2 (10 μg/L)	2.1	5–1000	23
Cr(VI)			20	2.0	1.1 (10 μg/L)	0.3	5–1000	
Cr(III)	FI–ICP-AES	alumina, basic	5–20	0.2–10	12 (10 μg/L)	1.4	10–1000	24
Cr(III)	FI–DCP-AES	alumina, acidic	ng	0.5	2.32 (200 μg/L)	40	100–500	25
Cr(VI)			ng	0.5	1.34 (200 μg/L)	20	100–500	
Cr(T)	FI–ETAAS	oxidation	22	3.0	9.1 (0.1 μg/L)	0.018	0.05–0.5	26
Cr(VI)		DDTC/C_{18}-RP	22	3.0	9.1 (0.1 μg/L)	0.016	0.05–0.5	

[a] F_s, sample rate; V_s, sample volume; DL, detection limit (3 s); RSD, relative standard deviation; ng, not given; Cr(T), total chromium; CPG-8HOQ, quinolin-8-ol immobilized on controlled-pore glass; DPC, diphenyl carbazide; DDTC, diethyl dithiocarbamate; PHXA, polyhydroxamic acid; RP, reversed phase; FI, flow injection; HPLC, high performance liquid chromatography; IC, ion chromatography; ICP-AES, inductively coupled plasma atomic emission spectrometry; DCP-AES, direct current plasma atomic emission spectrometry; FAAS, flame atomic absorption spectrometry; ETAAS, electrothermal atomic absorption spectrometry; UV, UV photometry.

recalculated from original data if necessary in order to allow direct comparison.

In photometric methods,[12–15] which are traditionally used for the determination of Cr(VI), several conditions such as temperature and amount of reagent must be kept strictly constant in order to achieve good reproducibility. Generally these methods have problems in handling complex sample matrices and they have to be combined with a conversion step. Conversion by on-line oxidation of Cr(III) with Ce(IV) at elevated temperature[12–14] has the disadvantages of introducing serious contamination and hence impairing detection limits.

Separation of chromium species using chromatographic techniques[16–18] often results in inadequate sensitivity for trace concentrations of Cr in real samples because of low sample loading. Syty et al.[16] used a reversed-phase polymeric C_{18} material for chromium speciation. Trivalent Cr was essentially not retained on the column while Cr(VI) emerged after 70 s. On-line determination by flame atomic absorption spectrometry (FAAS) gave detection limits of 60 μg/L for Cr(III) and 120 μg/L for Cr(VI), which was inadequate for most natural water samples. Krull and co-workers[17] have separated Cr(III) and Cr(VI) by means of a reversed-phase C_{18} HPLC column coupled directly to DCP-AES. A wide linear range, detection limits of a few micrograms per liter Cr, and good recovery of Cr(III)/(VI) added to distilled water were reported. However, they were not able to recover Cr(VI) added to a variety of environmental or biological samples nor detect any Cr species in NIST SRM 1643a (trace elements in water). In order to achieve adequate detection limits some preconcentration, preferentially on-column, has to be performed. Preconcentration of Cr(III) is not as straightforward as for Cr(VI) because the kinetic inertness of Cr(III) hinders efficient complexation resulting in poor sensitivity, low sampling frequency,[15,19] and incomplete recovery.[15]

When FI techniques are used for separation, the objective is to separate a single analyte or group of analytes from interfering sample components or matrices, often simultaneously achieving some degree of preconcentration and therefore gaining sensitivity at the expense of separation power. The FI separation process is quite similar to batch filtration or solvent extraction procedures, and no chromatographic processes are involved, despite the fact that some chromatographic equipment like HPLC pumps and on-line columns might be used for this purpose. Different solid sorbents[19–26] were used for FI preconcentration and separation of Cr(III) and Cr(VI). Shah and Devi[19] used a poly(hydroxamic acid) resin for the preconcentration of Cr(III). Sample throughput was very low, achieving a 50-fold preconcentration by loading 100 mL of sample in 50 min, and complete recovery of Cr(III) from the resin was not possible even after prolonged elution. Hirata et al.[22] used a chelating ion exchanger (Muromac A-1) and achieved a maximum 113-fold preconcentration of Cr(III) with a loading time of 180 s. However, besides the availability of the material, its low selectivity caused problems giving rise to spectral interferences by coeluted cations such as magnesium and competition on the column for example by aluminum. Cox et al.[23] used a minicolumn of activated alumina in the acidic form in combination with inductively-coupled plasma atomic emission spectrometry (ICP-AES) for rapid sequential determination of Cr(III) and Cr(VI). While preconcentration for Cr(VI)

was straightforward, Cr(III) could not be retained on the column and therefore only detected with greatly reduced sensitivity. Later the same group of authors reported the preconcentration of Cr(III) on an basic alumina column.[24] Retention of both chromium species on an acidic alumina column and sequential elution by changing the elution conditions was reported by Ahmad et al.[25] However, no information was given on the flow conditions or on results for samples, and detection limits were not adequate for real samples (see Table I).

In spite of that, however, activated alumina offers the principal possibility for preconcentration of both chromium species since it can function both as an anion and a cation exchanger depending on the pH of the solution. Under acidic conditions alumina exhibits a high affinity for oxyanions whereas it strongly retains cations under basic conditions. We therefore investigated the possibility of using acidic activated alumina for the sequential preconcentration of Cr(III) and Cr(VI) using carefully selected pH conditions. Flow injection (FI) techniques were used with FAAS detection which, as a single-element technique, is ideally suited for the speciation of a single element. Compared to ICP-AES it has the advantages of less spectral interferences by concomitants and less running costs.

EXPERIMENTAL SECTION

A Perkin-Elmer Model 2100 atomic absorption spectrometer with deuterium arc background correction was used throughout. The hollow cathode lamp for chromium was operated at 25 mA, and the spectrometer was set to 357.9 nm with a spectral bandwidth of 0.7 nm. A standard air–acetylene nebulizer-burner system without any impact system (impact bead and flow spoiler removed) was operated at an acetylene flow rate of 3.1 L/min and an air flow rate of 5.0 L/min in order to produce a fuel-rich flame. The burner height was adjusted to about 3.5 mm for optimum sensitivity. The nebulizer uptake rate was adjusted to give optimum response for conventional sample aspiration. No provision was taken to compensate for the lower flow rates delivered by the FI system; however, the transfer capillary to the nebulizer (PTFE, 0.3-mm i.d.) restricted the uptake rate to values close to the flow rate provided by the FI system. Running the nebulizer under this restricted sample flow rate will not reduce the sensitivity proportional to the flow reduction because of better nebulizer efficiency under starved conditions. The reduction of sample flow in the FI mode in comparison to conventional free uptake of the nebulizer is also beneficial for the droplet diameter distribution, which is shifted to smaller droplets and therefore less prone to vaporization interferences. The impact bead and flow spoiler could therefore be removed from the spray chamber, resulting in an additional gain in sensitivity. Time-resolved absorbance signals of the elution peaks for Cr(III) and Cr(VI) were displayed on the monitor and printed together with peak height and integrated absorbance values using an Epson Model FX-80+ printer. For peak height absorbance evaluation the spectrometer was operated with a time constant of 0.5 s.

A Perkin-Elmer Model FIAS-200 flow injection system connected to the spectrometer was used for the on-line preconcentration of chromium(III) and chromium(VI). The automatic operation of the injector valve and the two multichannel peristaltic pumps was programmed using the spectrometer software. Tygon pump tubes were used to propel all sample and reagent solutions. A minimum length of PTFE tubing with an i.d. of 0.3 mm was used for all connections in order to minimize the dead volume. A conically shaped microcolumn of 50-μL capacity (Perkin-Elmer, Überlingen, Germany), packed with alumina, was used in the manifold for selective sorption of Cr(III) and Cr(VI) species. Aluminum oxide 90, acidic activated for column chromatography (Merck, Darmstadt, Germany), was sieved, and the fraction in the range 56–170 μm was used for the packing, providing minimum dispersion, and acceptable backpressure.

Reagents, Standard Solutions, and Samples. All reagents were of at least analytical reagent grade purity, and ultrapure water (18 MOhm/cm, Nanopure System, Barnstedt) was used

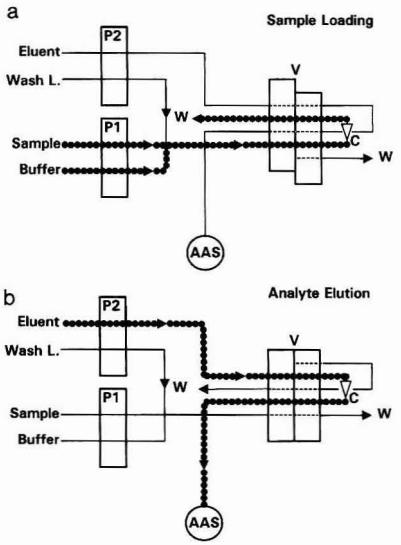

Figure 1. Flow injection manifold for on-line preconcentration of Cr(III) and Cr(VI). V, injector valve; P1, P2 peristaltic pumps; C, microcolumn packed with activated alumina (acidic form); W, waste; AAS, flame atomic absorption spectrometer: (a) sample loading sequence, (b) elution sequence.

throughout. The Clark–Lubs buffer solution with pH 2.0, used for the sorption of Cr(VI), was prepared by mixing 88.1 mL of 0.2 mol/L potassium chloride solution with 11.9 mL of 0.2 mol/L hydrochloric acid and diluting to 200 mL with water. The Clark–Lubs buffer solution with pH 7.0, used for the sorption of Cr(III), was prepared by mixing 50 mL of 0.2 mol/L potassium hydrogen phosphate solution with 29.5 mL of 0.2 mol/L sodium hydroxide solution and diluting to 200 mL with water; 1.0 mol/L nitric acid and 0.5 mol/L ammonia were used for the elution of Cr(III) and Cr(VI) species, respectively.

Standard solutions of Cr(III) and Cr(VI) were prepared by appropriate dilution from 1000 mg/L stock solutions, made up from commercially available concentrates, Titrisol (Merck) for Cr(III) and Fixanal (Riedel-de-Haën, Seelze, Germany) for Cr(VI). Synthetic mixtures of both species were produced by appropriate mixing of these standard solutions for the investigation of selectivity and recovery.

Water samples were filtered if necessary and acidified to pH 4 with nitric acid. Lake and tap water samples were provided by the Lake Constance Water Supply (BWV, Sipplingen, Germany). Because of the lack of standard reference materials certified for chromium species, standard reference materials "trace elements in water" SRM 1643b and SRM 1643c (NIST, USA) and "river water" SLRS-1 (National Research Council Canada) were used for recovery experiments and comparison of the chromium species concentration with certified values for total chromium.

Procedure. The FI manifold for on-line preconcentration and elution is shown in Figure 1, and the optimized operating parameters are given in Table II. Sample and buffer solutions were pumped simultaneously and mixed on-line. The preconcentration time was usually 35 s. Preconcentration and determination of Cr(III) and Cr(VI) were performed sequentially by selecting the appropriate buffer and eluent solutions. During the preconcentration of one species, the other species just passed the column without being retained. However, during the selective preconcentration of one species, column and connecting tubes to the valve acted as a sample loop for the other species. During the elution stage, the nonsorbed species would run in front of the sorbed species. By carefully optimizing the flow rates and the peak evaluation time windows, both species could be determined sequentially in one run (Figure 2), giving low sensitivity for the

Table II. Sequence of Operation for Selective On-Line FI Preconcentration of Cr(III)/Cr(VI) for Determination by FAAS

step	time, s	flow rate, mL/min pump 1	flow rate, mL/min pump 2	medium	valve position	function
1	5	4.8		sample	inject	prefill tubes with sample
		0.6		buffer[a]		
			3.5	eluent[b]		elute residual Cr
2	35	4.0		sample	fill	load Cr onto alumina column
		0.5		buffer[a]		
3	10		3.5	wash solution[c]	fill	wash column
4	15		3.5	eluent[b]	inject	elute Cr to flame

[a] Buffer solution: pH 2 for Cr(VI), pH 7 for Cr(III). [b] Eluent: 0.5 mol/L ammonia for Cr(VI), 1 mol/L HNO_3 for Cr(III). [c] Wash solution: water for Cr(VI), 0.5 mol/L ammonia for Cr(III).

nonsorbed species (direct determination) and high sensitivity for the sorbed species (preconcentration). However, this procedure would have added complexity and deteriorated selectivity in cases of big differences in concentration between the two species. A wash cycle was therefore introduced before the elution in order to flush the residual sample from the interstitial spaces of the column. Water was used for that purpose in the determination of Cr(VI) and 0.5 mol/L ammonia solution in the determination of Cr(III). During that wash cycle the eluent was pumped to the FAA spectrometer in order to record the baseline. To avoid any carry over between samples and replicate measurements, a prefill cycle was used in front of the preconcentration step, in which the sample tube was filled with the next sample and the column washed with the eluent.

A linear calibration graph was obtained over the concentration range 10–200 μg/L for both species, using aqueous standard solutions, performing the same procedure as for the samples.

RESULTS AND DISCUSSION

Calculation of the Distribution of Chromium Species. The method is based on the possibility of influencing the surface charge of activated alumina by conditioning through selection of the pH value of the buffer system (see Figure 3A). In order to have a rational basis for the optimization of the procedure and further discussion, the distribution of chromium species in relation to pH was calculated by using published thermodynamic data.

Chromium(III) is reported to form several hydroxo species, including $CrOH^{2+}$, $Cr(OH)_2^+$, $Cr(OH)_3^0$, $Cr(OH)_4^-$, $Cr_2(OH)_2^{4+}$, and $Cr_3(OH)_4^{5+}$. Polynuclear species were ignored because their contribution under the present conditions (trace concentration, room temperature) are considered insignificant.[27] The chromium(III) distribution was calculated by using the following equations:

$$Cr(OH)_3(s) + 3H^+ \rightleftharpoons Cr^{3+} + 3H_2O \quad \log K_1 = 9.76 \quad (1)$$

$$Cr(OH)_3(s) + 2H^+ \rightleftharpoons CrOH^{2+} + 2H_2O \quad \log K_2 = 5.96 \quad (2)$$

$$Cr(OH)_3(s) + H^+ \rightleftharpoons Cr(OH)_2^+ + H_2O \quad \log K_3 = -0.44 \quad (3)$$

$$Cr(OH)_3(s) \rightleftharpoons Cr(OH)_3^0 \quad \log K_4 = -6.84 \quad (4)$$

$$Cr(OH)_3(s) + H_2O \rightleftharpoons Cr(OH)_4^- + H^+ \quad \log K_5 = -18.25 \quad (5)$$

Under the assumption that the chromium species represented by eqs 1–5 are the only species present in significant amounts in solution, the total concentration of Cr in equilibrium with $Cr(OH)_3$ (s) can be expressed as

$$[Cr]_{total} = [Cr^{3+}] + [Cr(OH)^{2+}] + [Cr(OH)_2^+] + [Cr(OH)_3^0] + [Cr(OH)_4^-] \quad (6)$$

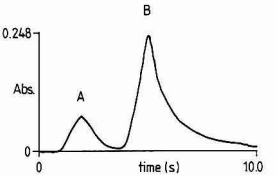

Figure 2. Detection of both Cr(III) and Cr(VI) in presence of each other during a single elution sequence without a preceding washing step following 30-s sample loading: A, unretained Cr(III); B, retained Cr(VI).

The contribution of each species was calculated by using the thermodynamic equilibrium constants given by Rai et al.[27] with the help of a spreadsheet program (LOTUS 1-2-3, Ver. 3.1) running on an Epson AX2 AT-compatible computer. The result of this calculation is shown in Figure 3B.

Chromium(VI) may be present in aqueous solutions as chromate, dichromate, hydrogen chromate, chromic acid, hydrogen dichromate, trichromate, and tetrachromate.[28] The last three ions have been detected only in strongly acidic solutions, however, and only for very high concentrations of chromium(VI) which do not apply here. Equilibrium and stoichiometric relationships for the three species considered here are presented in eqs 7–10.

$$H_2CrO_4 \rightleftharpoons H^+ + HCrO_4^- \quad \log K_7 = -0.74 \quad (7)$$

$$HCrO_4^- \rightleftharpoons H^+ + CrO_4^{2-} \quad \log K_8 = -6.49 \quad (8)$$

$$2HCrO_4^- \rightleftharpoons H_2O + Cr_2O_7^{2-} \quad \log K_9 = 1.52 \quad (9)$$

The concentration of chromic acid in relationship to pH and total chromium concentration was obtained by solving the equation:

$$[Cr]_{total} = [H_2CrO_4] + [HCrO_4^-] + [CrO_4^{2-}] + 2[Cr_2O_7^{2-}] \quad (10)$$

The concentrations of the chromium(VI) species were obtained by solving eq 10 for a total chromium concentration of 10^{-6} mol/L and using the above given thermodynamic data for eqs 7–9.[29] The result obtained by using a spreadsheet program (Lotus 1-2-3, Ver.3.1 with BackSolver) is shown in Figure 4.

(27) Rai, D.; Sass, B. M.; Moore, D. A. *Inorg. Chem.* 1987, *26*, 345.

(28) Tandon, R. K.; Crisp, P. T.; Ellis, J.; Baker, R. S. *Talanta* 1984, *31*, 227.

(29) Richard, F.; Bourg, A. C. M. *Wat. Res.* 1991, *25*, 807.

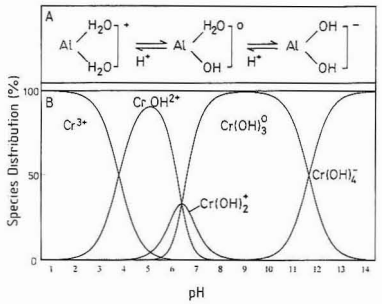

Figure 3. (A) Surface charge of alumina in relationship to pH. (B) Calculated distribution of inorganic chromium(III) species as a function of pH (solution in equilibrium with $Cr(OH)_3$ precipitate).

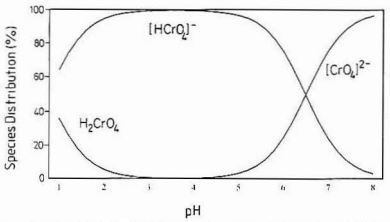

Figure 4. Calculated distribution of inorganic chromium(IV) species as a function of pH (10^{-6} mol/L total chromium concentration; data taken from ref 37).

Optimization of Flame Conditions. The determination of chromium by FAAS using the air–acetylene flame is subject to many interferences,[30-32] which can be avoided in part by using the hotter nitrous oxide–acetylene flame,[31,32] but at the expense of a significantly reduced sensitivity.[33] In addition, sensitivity and interferences in the air–acetylene flame are related in a complex manner to the oxidation state of chromium,[31,33] the flame gas composition,[34,35] and the burner position.[34] A significantly different sensitivity can be observed for the two oxidation states, whereby Cr(III) generally gives the higher values.[31,33] This effect can also be observed in the nitrous oxide–acetylene flame.[31] While this species-related problem has to be accounted for in the determination of total chromium, it is not a real problem in the determination of the individual species. As the selective preconcentration also separates the chromium species under investigation, at least in part, from other matrix components, it was expected that some of the interference problems reported in the literature would be reduced or eliminated. In contrast to recommendations to use the nitrous oxide–acetylene flame for interference-free determination of chromium, the air-acetylene flame was chosen and operated under moderately reducing conditions in order to obtain high sensitivity and good linearity of the analytical curve. The burner position was adjusted automatically by an optimization routine performed by the spectrometer. Best conditions were found for 3.1 L/min acetylene and 5.0 L/min air and an observation height of approximately 3.5 mm, giving a characteristic concentration better than 76 μg/L. Compensation of the nebulizer free-

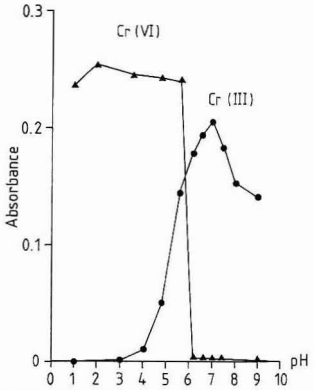

Figure 5. Effect of the pH of various buffer solutions (see text) on the peak height absorbance of 200 μg/L Cr(III) and Cr(VI) (for FI parameters see the Experimental Section).

uptake rate and the FI flow rate by air[36] cannot be recommended, because sensitivity and precision were degraded significantly. Background correction, used during method development, was found to be unnecessary as the separation by sorption and the wash cycle were effective in eliminating any nonspecific absorption by concomitant species.

Optimization of the Buffer System. Activated alumina can act as an anion or a cation exchanger depending on solution pH. Under acidic conditions it exhibits a high affinity for oxyanions whereas it strongly sorbs cations under basic conditions. The effect of various buffer solutions on the sorption behavior of Cr(III) and Cr(VI) was investigated over the range pH 1–9. The different buffer systems examined in this study were potassium chloride/hydrochloric acid for pH 1.0–2.0, sodium acetate/acetic acid for pH 3.6–5.6, sodium hydroxide/potassium dihydrogen phosphate for pH 6.2–7.4, and ammonia/ammonium chloride for pH 8.0 and 9.0. The buffer solutions were added to the standard solutions of Cr(III) and Cr(VI), on-line, followed by preconcentration, elution, and determination. The results, which are presented in Figure 5 show that the optimum value for the sorption of Cr(III) is pH 7. From the equilibrium graph of the different Cr(III) species (see Figure 3), this behavior can be explained by the sorption of the uncharged $Cr(OH)_3$ species on an uncharged alumina surface (see Figure 3A) whereas the anionic Cr(VI) species is not sorbed at all under these conditions. The observed sensitivity loss for Cr(III) at pH values higher than 7 could be explained by the formation of a negatively charged species such as $[Cr(OH)_4]^-$ (amphoteric character of Cr(III)) which cannot be retained on the negatively charged alumina surface. Interestingly, the buffer solution with pH 7.0 enhanced the signals of Cr(III) in comparison to the unbuffered system at the same pH as is shown in Figure 6a. This effect might be due at least in part to analyte loss by sorption on container walls which was reported to be most pronounced at pH 6.95.[37]

The Cr(VI) species can be sorbed on the column at pH values 1.0–5.6 using the Clark–Lubs buffer. This can be best explained by the sorption of the predominant species $[HCrO_4^-]$ on the acidic alumina having a positive surface charge under these conditions (see Figure 3A). The dichromate ion concentration as calculated from thermodynamic data is negligible as is shown in Figure 4. Interestingly Cr-

(30) Rubeska, I.; Musil, J. *Anal. Spectrosc.* **1979**, *2*, 309.
(31) Maruta, T.; Suzuki, M.; Takeuchi, T. *Anal. Chim. Acta* **1970**, *51*, 381.
(32) Knecht, J. *Fresenius' Z. Anal. Chem.* **1983**, *316*, 409.
(33) Kraft, G.; Lindenberger, D.; Beck, H. *Fresenius' Z. Anal. Chem.* **1976**, *282*, 119.
(34) Steglich, F.; Stahlberg, R. *Fresenius' Z. Anal. Chem.* **1983**, *315*, 329.
(35) Steglich, F.; Stahlberg, R.; Grossmann, O. *Fresenius' Z. Anal. Chem.* **1984**, *318*, 309.
(36) Garcia, I. L.; Córdoba, M. H.; Sánchez-Pedreno, C. *Analyst* **1987**, *112*, 276.
(37) Shrendrikar, A. D.; West, P. W. *Anal. Chim. Acta* **1974**, *72*, 91.

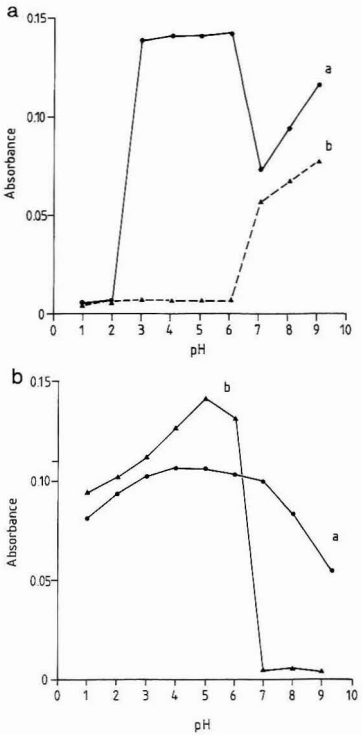

Figure 6. (a) Effect of the acidity of sample solution on the peak height absorbance of 100 μg/L Cr(III) obtained (a) with and (b) without adding buffer solution of pH 7, as described in the Experimental Section. (b) Effect of sample solution acidity on the peak height absorbance of 100 μg/L Cr(VI) obtained (a) with and (b) without adding buffer solution of pH 2, as described in the Experimental Section.

(VI) could be sorbed neither at pH 4.0 using the Clark–Lubs buffer solution made from potassium hydrogen phthalate and sodium hydroxide nor at pH 5.7 using the Britton–Robinson buffer made from phosphoric acid, acetic acid, and boric acid. Cox et al.[23] have shown that acidic activated alumina has a high affinity for oxyanion species such as arsenate, molybdate, phosphate, and vanadate. The sorption of Cr(VI) will hence be affected by other oxyanions, which should therefore be avoided, particularly in the buffer system. In the presence of the Clark–Lubs buffer for pH 2.0, the efficiency of the Cr(VI) retention was about 10% lower than under nonbuffered conditions at the same pH as can be seen in Figure 6b.

From these results it is clear that the buffering solution not only plays a role in controlling the pH and hence the Cr species present, but also in controlling the affinity of the sorbent material for these species. In general, cation sorption enhances the positive surface charge and therefore favors electrostatic adsorption of anions.[29] The Clark–Lubs buffer systems of pH 2.0 and 7.0 were chosen for all future work, giving high selectivity and robust conditions in the case of varying sample acidity. No significant influence on retention efficiency was observed for buffer concentrations in the range of 0.1–0.25 mol/L, and a buffer concentration of 0.2 mol/L was therefore used for all determinations. No influence of sample pH in the range of pH 2.5–6 was observed in the preconcentration of Cr(III) (see Figure 6). For Cr(VI), less than 5% relative change in absorbance was observed with

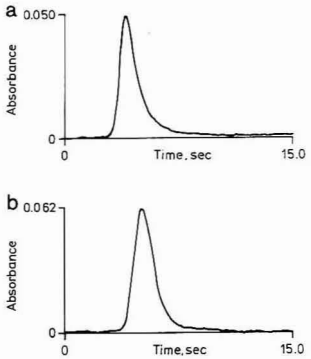

Figure 7. Transient signals for 50 μg/L of both Cr(III) and Cr(VI) in presence of each other. (a) Transient signal for 50 μg/L Cr(III) in the presence of 50 μg/L Cr(VI). (b) Transient signal for 50 μg/L Cr(VI) in the presence of 50 μg/L Cr(III).

samples in the range of pH 3–6 and less than 10% in the pH range of 2–7 (see Figure 6b). In order to avoid losses of Cr(III) by sorption onto container walls during sample processing as well as a reduction of Cr(VI) under strongly acidic conditions, the samples were kept at approximately pH 4.

Optimization of FI Flow Conditions. High sample loading flow rates are important for an efficient preconcentration and high sample throughput. In general FI sample flow rates are limited by the back-pressure produced by the column and/or the sorption efficiency which decreases with increasing flow rate. No degradation in sorption efficiency was observed up to a loading flow rate of 4 mL/min for both Cr species, which is the highest flow rate that can be handled accurately and reproducibly by the peristaltic pump with the type of column used in this work. The buffer solution flow rate adds to the total loading flow rate and hence calls for a proportional reduction of the sample flow rate. The buffer flow rate should not be too low to guarantee good mixing of buffer and sample solutions. No influence of the buffer flow rate on the absorbance was detectable in the range 0.4–0.8 mL/min, and a flow rate of 0.5 mL/min was used for all future work.

The effect of eluent concentration and eluent flow rate on the absorbance of 200 μg/L Cr(III) and 100 μg/L Cr(VI) was investigated for the concentration range 0.2–1.0 mol/L and for flow rates ranging from 1.0 to 3.5 mL/min. A 1.0 mol/L nitric acid concentration was found optimum for Cr(III) as it eluted about 95% of the sorbed chromium within 5 s. Higher concentrations of nitric acid, hydrochloric acid, or mixtures of both acids did not improve the recovery and were not used because of their possible side effects on column lifetime. In order to avoid any carry over between samples, the residual chromium was eluted during the prefill sequence. 0.5 mol/L ammonia was used for the elution of Cr(VI); higher concentrations were avoided because they would attack the alumina solid sorbent. For both species an elution flow rate of 2.2 mL/min was selected, giving optimum sensitivity and elution peaks with minimum tailing (Figure 7).

Performance of the On-Line Preconcentration System. Characteristic data for the performance of the on-line preconcentration system are summarized in Table III. The efficiency of sorption was investigated by analyzing the previously collected column effluent of a standard solution containing 200 μg/L chromium using the same solid-sorbent preconcentration technique. From the results obtained by this repeated preconcentration a retention efficiency of 80% for Cr(III) and 92% for Cr(VI) was calculated. The sorption/

Table III. Performance Data for On-Line Preconcentration of Chromium by Sorption on Alumina with a Loading Time of 35 s

	Cr(III)	Cr(VI)
working range, μg/L	10–200	10–200
sensitivity enhancement (EF)[a]	25	25
concentration efficiency, EF/min	23	23
characteristic concentration		
μg/L (peak height absorbance)	3.9	3.2
μg/L (integrated absorbance)	2.2	1.8
detection limit, μg/L (3 s)	1.0	0.8
precision[b]		
(200 μg/L)	1.1	1.3
(100 μg/L)	1.0	1.1
(50 μg/L)	1.7	
sample consumption, mL	3.0	3.0
sample frequency, 1/h	55	55

[a] Compared to conventional continuous nebulization. [b] Integrated absorbance, $n = 11$, within run.

Table IV. Influence of Potential Concomitants on the Peak Height Absorbance Signal Produced by 100 μg/L Cr(III)

ion	concn, mg/L	interference, %	ion	concn, mg/L	interference, %
SO_4^{2-}	1000	<±5	Zn^{2+}	10	<±5
NO_3^-	1000	+20	Fe^{3+}	40	−64
	500	<±5		10	−60
Mo(VI)	10	+25	Fe^{2+}	10	−60
	2	<±5		2.5	−40
PO_4^{3-}	20	<±5		0.5	<±5
Cl^-	1000	<±5	Al^{3+}	5	−47
Pb^{2+}	1	<±5		1	−40
Cu^{2+}	5	−25		0.5	−15
	2	<±5		0.2	<±5
Cd^{2+}	0.1	−30	Fe^{2+} [a]	2.0	−43
	0.05	<±5	Fe^{3+} [a]	2.0	−50
Ni^{2+}	0.5	−50	Fe^{2+} [b]	2.0	−18
	0.25	−20	Fe^{3+} [b]	2.0	−20
	0.1	<±5	Fe^{2+} [c]	2.0	<±5
Mn^{2+}	5.0	−15	Fe^{3+} [c]	2.0	<±5
Cr(VI)	0.2	<±5			

[a] 0.1% (w/v) NH_4F added to buffer. [b] 0.5% (w/v) NH_4F added to buffer. [c] 1.0% (w/v) NH_4F added to buffer.

elution is highly reproducible giving an overall precision better than 2% (for details see Table III). Using 200 μg/L chromium standard solutions a linear relationship was observed between loading time and enrichment factor up to 1-min preconcentration time. With a loading time of 35 s a sensitivity enhancement of 25 was obtained for both species, allowing a sample frequency of 55/h. For the determination of chromium concentrations below 10 μg/L the method can be modified by using a longer preconcentration period at the expense of a reduced sample throughput. If concentrations below 1 μg/L have to be determined, a method with higher sensitivity using flow injection coupled with graphite furnace atomic absorption spectrometric detection[26] is more advisable.

Interferences. Cr(III) exhibits a typical cationic sorption behavior. Its adsorption increases with pH but decreases when competing cations are present because of the low selectivity of alumina. The effects of common coexisting ions on the determination of Cr(III) are summarized in Table IV. From these results it can be concluded that there is no obvious interference to be expected from normal concomitant levels found in natural waters, but higher concentrations of iron and aluminum do interfere. The concomitant cations are retained on the column and coeluted, causing an interference in the air–acetylene flame, which is well documented.[38–44] It could be overcome in the usual manner[45–47] by adding ammonium fluoride or ammonium chloride as a releasing agent to the buffer solution (see Table IV).

Table V. Influence of Potential Concomitants on the Peak Height Absorbance Signal Produced by 100 μg/L Cr(VI)

ion	concn, mg/L	interference, %	ion	concn, mg/L	interference, %
SO_4^{2-}	1000	−88	Zn^{2+}	10	<±5
	500	<±5	Pb^{2+}	5.0	<±5
NO_3^-	1000	−15	Cu^{2+}	5.0	<±5
	500	<±5	Cd^{2+}	0.5	<±5
Mo(VI)	10	−45	Ni^{2+}	1.0	<±5
	2	<±5	Mn^{2+}	5.0	<±5
PO_4^{3-}	100	−45	Al^{3+}	5.0	<±5
	20	−18	Fe^{3+}	5.0	<±5
	10	<±5			
Cl^-	1000	−10	Cr(III)	2.0	<±5
	500	<±5			

Cr(VI), on the other hand, exhibits a typical anionic sorption behavior. Its adsorption decreases with increasing pH and in the presence of competing dissolved anions. Millimolar concentrations of major cations such as K^+, Ca^{2+}, and Mg^{2+} have only a very minor influence on Cr(VI) adsorption, shifting the adsorption edge to a slightly higher pH. Cation sorption enhances the positive surface charge and hence favors electrostatic adsorption of anions.[29] Competing anions, however, have a significant effect on Cr(VI) adsorption, which depends on the concentrations of the competing anion and of $[CrO_4]^{2-}$, on their relative affinities for the solid surface and on the number of available surface sites. A shift of the adsorption edge toward lower pH values was generally observed in sorption experiments[29] for competing anions such as Cl^-, NO_3^-, SO_4^{2-}, HCO_3^-, HPO_4^{2-}, and MoO_4^{2-}.

The effect of concomitant species on the determination of Cr(VI) is summarized in Table V. From these results it can be deducted that oxyanions are in fact the most serious interferents. However, the alumina column makes possible the determination of Cr(VI) in natural water, tolerating nitrate, sulfate, phosphate, and molybdate at a 5000-, 1000-, 100-, and 20-fold excess, respectively, compared to chromate, under the conditions used here.

Recovery. Recovery experiments were carried out with spiked water samples and reference materials because certified reference materials for chromium(III) and/or chromium(VI) species are not available. The results are shown in Table VI. A small influence of the signal evaluation procedure on recovery was observed, integrated absorbance signals giving in some cases better recovery and also slightly better precision than peak height absorbance. No systematic error could be found in the added concentration range of 20–100 μg/L of chromium. The Cr(III) concentration found in two NIST standard reference materials was in good agreement with the certified value for total chromium as can be seen in Table VII. No Cr(VI) was detected in these samples, which is in close agreement with results of other groups[18,23] and most probably a result of the sample conservation used by NIST.

(38) Beccaluva, L.; Venturelli, G. *At. Absorpt. Newsl.* **1971**, *10*, 50.
(39) Cobb, W. D.; Foster, W. W.; Harrison, T. S. *Analyst* **1976**, *101*, 255.
(40) Pandey, L. P.; Ghose, A.; Dasgupta, P.; Rao, A. S. *Talanta* **1978**, *25*, 482.
(41) Aggett, J.; O'Brian, G. *Analyst* **1981**, *106*, 497.
(42) Aggett, J.; O'Brian, G. *Analyst* **1981**, *106*, 506.
(43) Miller, D. B. *At. Spectrosc.* **1988**, *9*, 43.
(44) Kitagawa, K.; Yanigisawa, M.; Takeuchi, T. *Anal. Chim. Acta* **1980**, *115*, 121.
(45) Agemian, H.; Chau, A. S. Y. *Anal. Cim. Acta* **1975**, *80*, 61.
(46) Roos, J. T. H. *Spectrochim. Acta* **1972**, *27B*, 473.
(47) Arpadjan, S.; Chadjiivanov, K.; Tsalev, D. *Spectrochim. Acta* **1985**, *40B*, 697.

Table VI. Recovery of Cr(III) and Cr(VI) Added to Water Samples

sample	spiked concn, μg/L	% recovery[a] Cr(III)	Cr(VI)
drinking water	100	97 ± 2	99 ± 3
	50	92 ± 5	98 ± 5
	20	91 ± 6	95 ± 6
river water	100	94 ± 3	101 ± 5
(SLRS-1)	50	102 ± 8	96 ± 5
	20	93 ± 9	106 ± 3
lake water	100	100 ± 1	95 ± 4
	50	99 ± 9	102 ± 9
	20	93 ± 6	90 ± 3

[a] Average and standard deviation of three determinations based on peak height absorbance.

CONCLUSION

One of the characteristics of flow injection is that this technique can work accurately and reproducibly under nonequilibrium conditions through the accurate control of time. This often results in a great reduction of the analysis time and allows the possibility of working reliably with unstable analyte species and reagents. In the procedure described in this work the water samples were kept at a "safe" pH of 4 prior to analysis. The pH of 2 and 7, which was found optimum for the selective sorption of Cr(VI) and Cr(III), respectively, at which, however, the chromium species were not stable, was adjusted by adding a buffer on-line only fractions of a second before the corresponding chromium species was sorbed onto the column. In this way, any risk of analyte loss and/or shift in equilibrium between the species was minimized. This is in contrast to chromatographic procedures which are orders of magnitude slower and hence much more subject to shifts in equilibrium. On-line separation of the two chromium species also avoids the disadvantages of conversion methods which include the risk for incomplete conversion, introduction of contamination, and complexity of the procedure.

Table VII. Determination of Chromium Species in Two NIST Standard Reference Materials "Trace Elements in Water"

sample	certificate, μg/L	found,[a] μg/L Cr(III)	Cr(VI)
NIST-1643b	18.6 ± 0.4	18.0 ± 0.5	nd
NIST-1643c	19.0 ± 0.6	19.5 ± 0.5	nd

[a] Average and standard deviation of three determinations based on peak area is given. nd, not detected.

The preconcentration efficiency, particularly for Cr(III), was improved significantly by optimizing the buffer systems with respect to pH and composition. As a result, both species, Cr(III) and Cr(VI), could be preconcentrated in the same system and determined with comparable sensitivity.

RECEIVED for review June 23, 1992. Accepted September 18, 1992.

Registry No. H_2O, 7732-18-5; Cr, 7440-47-3.

World Health Organization International Intercalibration Study on Dioxins and Furans in Human Milk and Blood

Robert D. Stephens,*,† Christoffer Rappe,‡ Douglas G. Hayward,† Martin Nygren,§ James Startin,⊥ Annette Esbøll,‖ Jørgen Carlé,# and Erkki J. Yrjänheikki@

Hazardous Materials Laboratory, California Department of Health Services, Berkeley, California 94704, Institute for Environmental Chemistry, University of Umeå, Umeå, Sweden, National Defense Research Establishment, Umeå, Sweden, Food Science Laboratory, MAFF, Norwich, UK, Danish Institute of Plant and Soil Science, Lyngby, Denmark, National Environment Research Institute, Søborg, Denmark, and WHO/EURO, Copenhagen, Denmark

Under the sponsorship of the World Health Organization (WHO), an interlaboratory calibration on the analysis of PCDD/PCDFs in human milk and blood was carried out which included 19 laboratories from 14 countries. The study design involved the analysis of three samples of each matrix in triplicate. Selected samples were spiked with native standards of certain 2,3,7,8-substituted congeners at concentrations known only to WHO staff. The study design resulted in approximately 4000 individual pieces of PCDD/PCDF data generated by a variety of analytical methods, at various concentrations, and by laboratories of widely different experience. This was, by considerable margin, the largest study which allowed for the direct comparison of laboratory and method performance. The results of statistical analysis of this data base addresses the effect on data quality of clean up methods, instrumental methods, analyte concentration, laboratory QA programs, and laboratory experience. The study has shown that the laboratory is the single most important determinant of data precision and accuracy. The method of analyte enrichment (sample clean up), analyte measurement [gas chromatography/mass spectrometry (GC/MS) protocol], and analyte concentration have weaker correlations with data quality.

INTRODUCTION

The characterization of exposure and attendant risk to human health from polychlorinated dibenzo-*p*-dioxins (PCDDs) and polychlorinated dibenzofurans (PCDFs) demands the availability of reliable data on the concentration of these compounds in human tissues and fluids. Previous studies have evaluated the performance of available methods and existing laboratories to produce quality data on PCDD/PCDFs in adipose tissue.[1] The difficulties in obtaining human adipose samples limit the routine use of this tissue in assessing human exposure. Consequently, researchers have turned to the analysis of blood and breast milk as indicators of exposure.[2,3] Although blood and milk are more readily obtained through the use of less invasive procedures, they present significant analytical challenges. Within this context, the World Health Organization Regional Office for Europe (WHO/EURO) has been conducting interlaboratory quality control studies on levels of PCDF/PCDDs in human milk and blood within its overall project on the health effects of these chemicals.[4,5] The goal of this effort is to ensure that reliable and comparable data on these compounds can be obtained.

The results of the first round of studies, on human milk only, were evaluated by a WHO experts group and subsequently published.[6,7] At completion of this first round, it was recommended that the studies be continued and that a new round should be organized every second year from 1988 onward. Based on that recommendation, a series of meetings were held by WHO/EURO to design the study protocol that would encompass the analysis of both human blood and milk.

The intercalibration study began in 1989 with the distribution of human milk and blood samples to 19 participating laboratories. The final reports of data on the last of the three pools of milk and blood were submitted to the study coordinators in 1990. The results from all of the participating laboratories were collected by WHO staff, and preliminary statistical calculations were carried out. A meeting was held in June of 1990 in Rovaniemi, Finland, and attended by 22 experts from 15 countries representing the 19 participating laboratories as well as representatives from WHO/EURO. Discussions were held at this meeting regarding the interlaboratory study plan, laboratory methodologies, and data quality. During these discussions, participating laboratories were unaware of the scoring of their own results. A preliminary report evaluating the observations of the 19 participating laboratories was presented at Dioxin 90 in Bayreuth, Germany.[8]

The purpose of this paper is to identify, principally through statistical means, which factors contributed most to data quality. We also wanted to identify analytes or procedures that gave laboratories the most difficulty and to estimate minimum detection and quantitation limits in these matrices. The study design allows for a statistical examination of trends across laboratories and pools (repeat measures) and made possible a more rigorous assessment of agreement that can

* To whom correspondence should be sent.
† California Department of Health Services.
‡ University of Umeå.
§ National Defense Research Establishment.
⊥ Food Science Laboratory.
‖ Danish Institute of Plant and Soil Science.
National Environment Research Institute.
@ WHO/EURO.

(1) Albro, P. W.; Crummett, W. B.; Dupuy, A. E., Jr.; Gross, M. L.; Hanson, M.; Harless, R. L.; Hileman, F. D.; Hilker, D.; Jason, C.; et al. *Anal. Chem.* **1985**, *57*, 2717–25.
(2) Lindstrom, G.; Rappe, C.; Sjoestroem, M. *Chemosphere* **1989**, *19* (1–6), 745–50.
(3) Needham, L. L.; Patterson, D. G., Jr.; Pirkle, J. L.; Henderson, L. O.; Burse, V. W.; *Chemosphere* **1989**, *18* (1–6), 425–30.
(4) WHO Regional Office for Europe. *Environment Health Series 29*; WHO: Copenhagen, 1988.
(5) WHO Regional Office for Europe. *Environmental Health Series 34*; WHO: Copenhagen, 1989.
(6) Rappe, C.; Tarkowski, S.; Yrjanheikki, E. *Chemosphere* **1989**, *18* (1–6), 883–9.
(7) Tarkowski, S.; Yrjanheikki, E. *Chemosphere* **1989**, *19*, (1–6), 995–1000.
(8) Ersboell, A.; Nygren, M.; Yrjanheikki, E. Dioxin 90 Abstract of Papers, Vol. 4, pp 169–174.

0003-2700/92/0364-3109$03.00/0

be expected from highly capable laboratories analyzing human milk and blood.

STUDY DESIGN

The design of the present study was developed at the consultation held in Copenhagen in February 1988 and was intended to facilitate the use of statistical methods of analysis of PCDD and PCDF data described by Pallesen.[9] The coordination of the studies and preparation of samples for analysis was carried out by Drs. Nygren and Yrjänheikki.

The study was designed to take into account both the short-term and the long-term variation of the data, which was described as the repeatability and the reproducibility, respectively. For each of the two matrices, human milk and human plasma (hereafter referred to as blood), a single homogeneous pool was prepared and divided into three subpools. The blood pool was prepared from blood which had exceeded its shelf life and was no longer suitable for medical purposes. Prior to the division into three subpools, a quantity of ^{14}C-labeled [1-^{14}C]polychlododecane was added to allow homogeneity to be checked. The radioactivity present in the three pools agreed within 10%. For each matrix, two of the subpools were fortified by the addition of a certain amount of the PCDD and PCDF congeners having a substitution pattern including the 2,3,7-, and 8-positions which are normally found in human samples. The third subpool was unfortified. The exact fortification schema had been agreed to between the study coordinators and WHO/EURO in accordance with the requirements for a full statistical analysis and was not known to the participating laboratories. Initially, samples of two subpools of each matrix were sent to participants. Samples of the final subpool were distributed after results for the first two had been submitted to WHO. Each participant was required to make three separate analyses of each subpool. All participating laboratories were requested to use common $^{12}C_{12}$ and $^{13}C_{12}$ standards which were supplied by the coordinating laboratory. All samples were shipped frozen.

Laboratories were free to choose their own analytical methods for either blood or milk. Laboratories generally used similar but not always identical methods. The method variable we define is a class variable with two levels. We grouped all the extraction and isolation procedures into two broad classes. The first class includes all laboratories using a method described by Smith and Stalling[10] or minor modifications of this method. The method uses AX21 carbon as the primary PCDD and PCDF isolation step followed by alumina. The second class includes all other procedures, most used sulfuric acid first followed by alumina. Nearly all methods used some type of carbon chromatography step as well. Two laboratories used GPC instead of sulfuric acid for either milk or blood and two used solid-phase extraction followed by alumina and carbon. In addition, two laboratories used Florisil in place of alumina. Most laboratories used high-resolution sector instruments operating in electron impact at 2000–10 000 resolution (all but one were manufactured by the same company). Three laboratories used low-resolution quadrupole instruments operating in a negative chemical ionization mode and two laboratories did not report their cleanup or separation and detection methods.

(9) Pallesen, L. *Waste Manage. Res.* **1987**, *5* (3), 367–79.
(10) Smith, L. W.; Stalling, D. L.; Johnson, J. L. *Anal. Chem.* **1984**, *56*, 1830–42.

STATISTICAL METHODS

Calculations for reproducibility and repeatability were carried out according to Youden and Steiner and ISO.[11,12] The coefficient of variation for reproducibility (CV_{repro}) was computed according to eq 1

$$CV_{repro} = \frac{\bar{Z}_{ijk}}{Y^*_{ij}} \quad (1)$$

where $\bar{Z}_{ijk}$ is the standardized average deviation from the median value for congener i, pool j, laboratory k and Y^*_{ij} is the median value for congener i, pool j. The CV_{repro} reflects the closeness of agreement between individual results obtained on the same material but under different conditions (e.g. time). CV_{repro} is not a true measure of accuracy for there was no "true value" for each analyte. The true value was taken as the median of all measurements for a given analyte.

The CV for repeatability (CV_{repeat}) is computed as the standard deviation between the three determinations for each laboratory, congener, and pool using eq 2 divided by the mean value of the three determinations for each laboratory (eq 3). The CV_{repeat} was taken as a measure of the closeness of agreement between the same measurements on identical materials under the same conditions (e.g. time)

$$S^2_{ijk} = 1/\{n_1 - 1\}\sum_l (Y_{ijkl} - \bar{Y}_{ijk})^2 \quad (2)$$

$$CV_{repeat} = \frac{S_{ijk}}{Y_{ijk}} \quad (3)$$

Our analysis of the data used a standardized data set. All observations of any congener were standardized to a mean of zero and a standard deviation of one for all reported values in each pool and matrix. This allowed an evaluation of the effects of pool across all congeners and made comparisons between laboratories easier. In the analysis, laboratory identification (A–S), pool (a, b, or c), replicate (1, 2, or 3) and analytical method (0 or 1) were considered as possible explanatory variables. The relationships between the congeners reported and laboratory identification were investigated first using principal components analysis. A multivariate analysis of variance, modeling lab, pool, and replicate as random or fixed effects was used to examine the relative importance of the explanatory variables. Laboratory and pool means, by congener, were tested for significant differences.

For purposes of the principal component analyses only, missing data, which resulted from laboratories not reporting data on specific congeners, were assigned values equal to the mean standardized value reported for all other congeners in the observation with the missing value. It was necessary to replace missing values in the PCA analysis, otherwise an entire observation would be deleted by the SAS program running the PCA calculations. Missing values were replaced with the mean standardized value for a given observation of all other dioxin or furan values reported in that observation.

Laboratories E, I, J, and M had missing values on HxCDD1,2 and sometimes HxCDD3 in milk and blood. In the case of laboratories E and I, HxCDD1 and -2 were not chromatographically separated and were reported as one number. Laboratories J and M had four missing HxCDD1 values for probably the same reason as well as four and one missing HxCDD3 value, respectively. In addition, laboratory J had HxCDF1,2 and -4 missing from two observations that had missing HxCDD1, and M had HxCDF1,2,4 and HpCDF1

(11) Youden, W. J.; Steiner, E. H. *J. Assoc. Off. Anal. Chem.* **1975**, 88.
(12) ISO, 5725; 1976.

Table I. WHO Qualified Laboratories[a]

principal	organization	milk	blood
de Jong, A.	RIVM Bilthoven, NL	yes	yes
Ende, M.	Staat. Chem. Unters. Oldenberg, FRG	yes	yes
Fürst, P.	Chem. Landes. Nord. Westf., FRG	yes	yes
Gross, M.	U. of Nebraska Lincoln, NE, USA	yes	NP
Hannah, D.	DSIR, Lower Hutt New Zealand	yes	yes
Mathar, W.	FHO Berlin, FRG	yes	NP
Needham, L.	CDC Atlanta, GA, USA	NP	yes
Oehme, M.	NILU Lillistrøm, Norway	yes	NP
Olie, K.	U. of Amsterdam Amsterdam, NL	yes	yes
Päpke, O.	ERGO Hamburg, FRG	NP	yes
Rappe, C.	U. of Omeå Umeå, Sweden	yes	yes
Ryan, J. J.	H&W Canada Ottawa, Canada	yes	yes
Startin, J.	MAFF Norwich, UK	yes	yes
Stephens, R.	DHS Berkeley, CA, USA	yes	yes

[a] NP = not participating.

values missing from one observation. Laboratory S had missing TCDD values in both blood and milk due to exclusive use of negative chemical ionization, and laboratories F and L were missing six values for PeCDF1 in blood probably due to the spiking error. Laboratory R was missing five HxCDF4 values in blood and one each of TCDF, PeCDF1, HxCDF1, HxCDF2, HxCDD1 and HxCDD2. R had three HxCDF4 values and two TCDD values missing from milk. No missing values were replaced in an observation where all values of the analytes were not reported. The substitution of values did not effect the general PCA mapping of a laboratory's observations significantly. Assigned values for missing data were not used in either the multivariate analysis or the descriptive data.

This statistical treatment differs from that used by WHO in the initial evaluation of the data where the CVs for reproducibility and repeatability for the different congeners were weighted according to their Nordic toxic equivalent factors (Nordic TEF).[13,14] The Nordic TEFs differ from the more commonly used International TEFs only in use of the factor of 0.01 for 1,2,3,7,8-PeCDF whereas the ITEF for this congener is 0.05. Laboratories were then ranked (classified) according to their weighted and summed CV values. Missing values for specific congeners were assigned CV values equal to the largest CV value of the reporting laboratories. The rational for using the TEF weighing factors and assigning high CV values (scores) to missing values relates to the objective of WHO of evaluating the use of laboratories which produce PCDD/PCDF data for health risk assessment.[4,5] This scoring led to a listing by WHO of laboratories qualified to conduct analysis of PCDD/PCDFs in human blood and in human milk for the purpose of providing data for health risk assessments. This listing of qualified laboratories is presented in Table I. The objective of this current paper is to evaluate the analytical performance of the participating laboratories, the different analytical methods used, and the effect of concentration on the two matrices studied. As a result, TEF weighing was not considered.

(13) Ahlborg, U. G. *Chemosphere* **1989**, *19* (1–6), 603–608.
(14) Yrjanheikki, E. *Environment and Health in Europe 37*; WHO: Copenhagen, 1991.

Table II. Median Values for PCDDs and PCDFs (Unfortified and Fortified, pg/g wet wt)

	milk pool[a]			blood pool[a,b]		
congener	a	b	c	a	b	c
TCDD (TD)	0.05	0.06	0.22*	0.02	0.07*	0.02
PeCDD(PD)	0.12	0.12	0.45*	0.21*	0.04	0.03
HxCDD(Hx1)	0.15*	0.07	0.07	0.02	0.05*	0.02
HxCDD2(Hx2)	1.0*	0.53	1.1*	0.16	0.47*	0.16
HxCDD3(Hx3)	0.15	0.13	0.13	0.04	0.04	0.03
HpCDD(Hp)	4.04*	1.3	2.49*	1.40*	1.25*	0.40
OCDD(OD)	13.6*	5.6	15.9*	3.15	10.4*	3.10
TCDF(TF)	0.19*	0.04	0.04	n/c	n/c	0.01
PeCDF1(PF1)	0.02	0.02	0.02	n/c	n/c	0.005
PeCDF2(PF2)	0.28	0.26	1.1*	n/c	n/c	0.12
HxCDF1(HF1)	0.13	0.09	0.08	0.03	0.03	0.03
HxCDF2(HF2)	0.13*	0.08	0.07	0.03	0.05*	0.02
HxCDF3(HF3)	0.02	0.02	0.01	0.01	0.01	0.01
HxCDF4(HF4)	0.04	0.03	0.03	0.03*	0.01	0.01
HpCDF1(Hp1)	0.30*	0.13	0.32*	0.20*	0.10	0.10
HpCDF2(Hp2)	0.03	0.03	0.02	0.01	0.01	0.01
OCDF(OF)	0.10*	0.04	0.11*	0.032	0.011	0.029

[a] * = fortified congener. [b] n/c = not calculated.

RESULTS

The study produced a substantial PCDD/PCDF data base upon which assessments of laboratory and analytical method performance could be made. In all, 16 laboratories submitted complete, or near complete, data on PCDD/PCDFs in the human milk samples, and 15 laboratories submitted data on the human blood samples. This represents approximately 4000 separate measurements. As a result, this study represents, by far, the largest controlled interlaboratory calibration for PCDD/PCDFs. The concentration of the PCDD/PCDF analytes on a volume basis ranged from 0.02 to 18 ppt in milk and from 0.01 to 10 ppt in blood serum.

Table II presents the target analytes of the study and the median reported values and their ranges for both the unfortified (unspiked) and fortified (spiked) congeners for blood and milk.

One of the measures of method and laboratory performance is the recovery of spiked analytes. The experimental design allowed for the estimation of recovery by summing the mean determined concentration of a given analyte by a laboratory in an unfortified sample and the known amount of the spike for that analyte and comparing this sum with the concentration determined by that laboratory for the analyte in a fortified sample. Using this approach, the recoveries were calculated for all data reported by a laboratory. Means and ranges for the recovery data from each laboratory are presented in Table III. Negative recoveries are sometimes calculated because a laboratory may report less in the fortified pool than in an unfortified pool.

The coefficients of variation for repeatability and reproducibility, as defined in eqs 1 and 3 were calculated for each analyte, pool, and laboratory. The average CV values for all analytes and pools for each laboratory were calculated. The results for both blood and milk are presented in Figures 1 and 2.

The results reported were also examined by congener. Figures 3 and 4 present the range of the 2nd and 3rd quartile (25th to 75th percentile) measured as a relative percent difference from the median (the value at the 50th percentile). The distance between the 25th and the 75th percentiles is divided by the median for each analyte. These bar graphs show the range of half the reported values that are closest to the median for unfortified milk and blood determinations,

Table III. Recovery Figures[a]

	milk		blood	
lab	pool a	pool c	pool a	pool b
A	71 (58–77)	81 (61–102)	87 (66–112)	87 (77–108)
B	18 (–25–108)	155 (76–219)	*	*
C	99 (68–143)	113 (36–212)	79 (71–88)	77 (62–87)
D	96 (82–114)	82 (46–114)	*	*
E	88 (82–90)	86 (70–112)	93 (82–102)	87 (67–106)
F	89 (68–122)	104 (77–138)	81 (53–100)	105 (82–141)
G	77 (50–138)	99 (45–163)	75 (60–94)	78 (34–116)
H	89 (146–149)	36 (–148–79)	65 (–2–94)	80 (30–108)
I	89 (57–109)	55 (29–87)	90 (78–105)	85 (50–105)
J	*	*	0.5 (–42–60)	922 (–25–2176)
K	37 (–34–73)	119 (62–247)	50 (3–91)	429 (–98–2416)
L	95 (78–140)	66 (–15–119)	–329 (–1041–75)	–176 (–762–82)
M	76 (62–96)	75 (49–113)	*	*
N	*	*	72 (68–77)	73 (39–114)
O	*	*	107 (67–138)	109 (78–171)
P	73 (59–89)	89 (68–112)	*	*
Q	68 (69–86)	91 (69–104)	76 (59–89)	86 (51–132)
R	91 (60–140)	136 (108–168)	112 (101–123)	163 (112–242)
S	63 (30–91)	90 (61–143)	104 (91–115)	106 (76–113)

[a] Recoveries for fortified pools of blood and milk for all participating laboratories. Mean values for all congeners as well as ranges of reported values are given (in parentheses). Negative recoveries signify that some labs reported lower values for fortified samples than the corresponding unfortified sample. *Not participating.

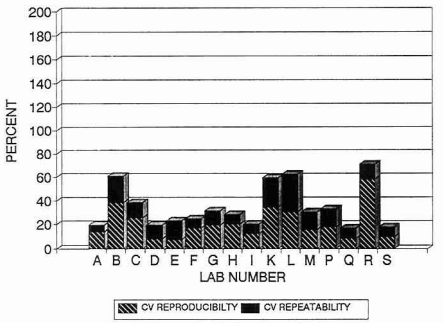

Figure 1. CV_{repro} (%) and CV_{repeat} (%) in milk for each laboratory.

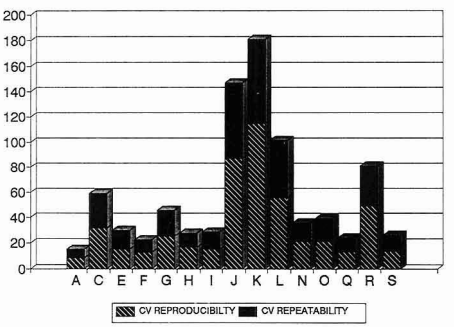

Figure 2. CV_{repro} (%) and CV_{repeat} (%) in blood for each laboratory.

respectively. The results shown exclude outliers and reflect the range of measurements that are closest to the median. The congeners median values ranged over 2 orders of magnitude, therefore making it difficult to plot the actual medians. The purpose is to identify differences in precision for the congeners that may reflect difficulties that most laboratories experienced. It is possible to see a trend toward high results for most analytes. Analytes showing less agreement between laboratories can be identified (PeCDF1 and OCDF for milk and TCDF, PeCDF1, TCDD, HxCDD1, and OCDD for blood).

There are a number of possible reasons why a laboratory may report high or low results on dioxins or furans. These compounds are ubiquitous and are known to contaminate laboratories. The resulting contamination will affect these very low level quantitations differently depending upon the patterns of high and low congeners in the source. In addition, random and systematic artifacts do occur in the multistep process of doing these low-level measurements. The source of these anomalies can be difficult, if not impossible, to identify. A laboratory may handle the labeled internal standards incorrectly and allow solutions to evaporate or be diluted. Since unlabeled furans and dioxins were sent in separate ampoules, then incorrect amounts of either furans or dioxins could have been mixed, producing systematically high or low results. All laboratories experienced difficulty with TCDF, PeCDF1, and PeCDF2 in pools a and b in blood which resulted from an inadvertent fortification of PeCDF2 at a very high level. The PeCDF2 which was spiked at an excessive level contained TCDF and PeCDF1 as impurities, which precluded accurate quantitation of these congeners in pools a and b. A principal components analysis was performed on the standardized data set to further examine the interrelationships between the congeners and the laboratories reporting the congener quantitation.

The variables used in the PCA analysis are given in Table IV. They include all the analytes that were measurable and exclude values that reflect the reporting of detection limits. In addition PeCDF2 was excluded from the blood analysis due a spiking error. Table IV gives the eigenvectors and eigenvalues for principal component 1, 2 and 3 (PC1, 2 or -3). The eigenvalues for PC4 and PC5 were 0.98, 0.88 and 0.82, 0.77 for milk and blood, respectively. Although they are not greater than one (standardized variables will have a mean of zero and a variance of one), it could be argued that they should be considered, since only a relatively small part of the variance is accounted for by PC1 (less than 40%). The eigenvectors for the variables in PC1 are all about the same magnitude and direction for both milk and blood. This indicates that generally the values reported tracked with one another. If a laboratory reported high or low values, then they generally reported high or low results on many congeners. This is to be expected, since these compounds are analyzed together. The eigenvectors for the other PCs contrast certain groups of congeners with other groups. As will be discussed later these eigenvectors correlate with the standardized mean values of one or a few laboratories. All the variables had comparable weightings on at least two of the first three PCs except for PCDF2, HxCDF1, and HxCDF2 in milk and HxCDD2 and HxCDD3 in blood. These congeners are ones in milk, which very few or no laboratories had statistically significantly different mean standardized values.

The first five principal components (prin1–5 or PC1–5) explained 74% (81% for blood data) of the total variability, and the first principal component explained 39% (40% for blood data) in the milk data set. The remaining principal components explain very small amounts of the variability and were therefore considered the analytical noise. The first, second, third, and/or fourth principal components (prin) scores for each laboratory were plotted against one another. At a glance one can separate certain labortories's observations with respect to their agreement with other laboratories and their own repeated measures (Figures 5–8). The laboratories determined by the earlier WHO evaluation using Nordic TEF weighing factors to be performing less well than the consensus group also clearly separate from a consensus group of laboratories. In addition, laboratories falling outside the

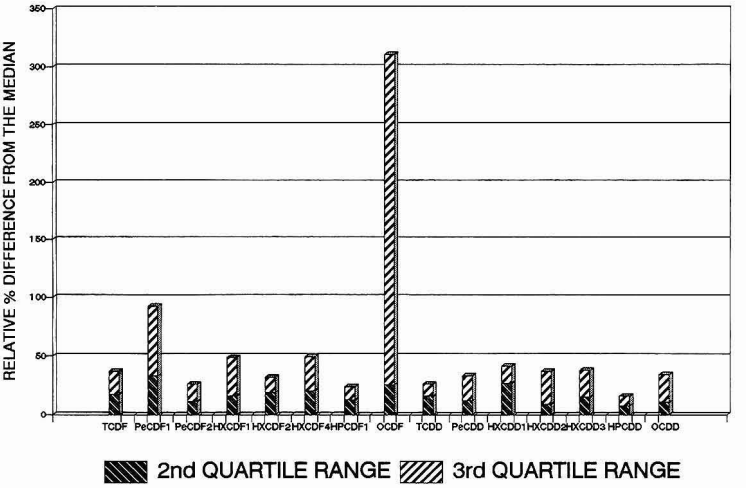

Figure 3. Range of the 2nd and 3rd quartile in relative percent difference from the median for each congener in milk.

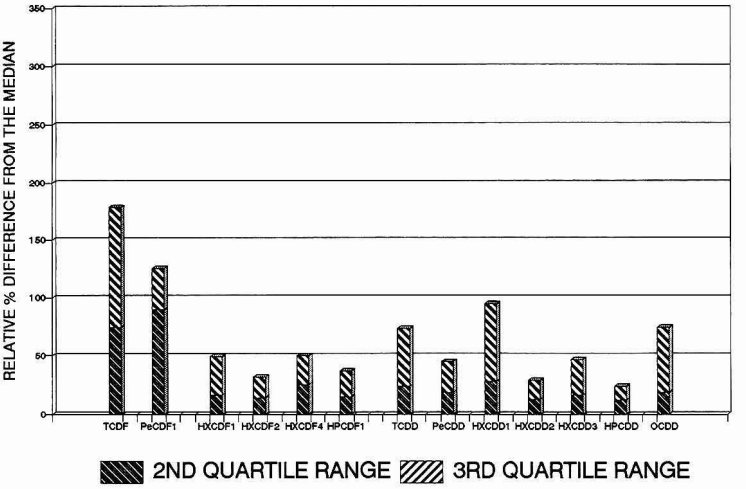

Figure 4. Range of the 2nd and 3rd quartile in relative percent difference from the median for each congener in blood.

consensus group separate from each other. The laboratories with the most consensus also showed closer agreement with their repeat measures than the laboratories with less consensus. It is also possible to group laboratories that fell between the extremes. The plotting of prins 2–5 against prin 1 separated out different laboratories from the origin. Prin 2 plotted against prin 3 (Figure 6) shows laboratories G, H, B, and K being separated from the laboratories with the closest scores. These plots (Figures 6–8) consistently show several laboratories mapping very near the origin (Q, D, E, A, S, P, F, I) while all other laboratories map away from the origin and away from each other (R, K, B, L, G, H, C, M), showing a range of progressively less agreement with the origin mapping labs and one another. A similar result is seen in the case of the principal components analysis for blood data. Many of the same laboratories map close to the origin, while others are easily separated.

The substitution of values did not affect the general PCA mapping of a laboratory's observations significantly. The PCA revealed that most observations mapped in one region, and certain observations mapped in separate regions. This did not change after values were substituted for missing values.

The absolute values of the principal component scores were summed for prins 1–5 for each laboratory. Figures 9 and 10 show bar graphs of summed scores by laboratory for milk and blood, respectively. It is interesting to note that the pattern of relative scores is very similar to the reported CVs for reproducibility (accuracy toward the median). The same 11 laboratories have similar sum scores. The minor differences are probably due to the changes made for missing values or the use of the means in the principal component analysis and not medians.

At this point it was useful to return to the original standardized data set to examine the individual laboratories further by exploring what was happening to individual analytes. Each laboratory could be examined individually at greater detail by taking the means by congener and laboratory and plotting them against the eigenvectors for an appropriate principal component (principal component 2 was chosen for the specific labs illustrated). Figures 11–14 give examples of

Table IV. Principal Components Variables and Their Eigenvectors and Eigenvalues for the First Three Principal Components in Milk and Blood

	PC1		PC2		PC3	
	milk	blood	milk	blood	milk	blood
TCDD	0.26	0.32	0.34	−0.002	0.27	−0.43
PeCDD	0.26	0.29	−0.15	0.19	−0.15	0.3
HxCDD1	0.25	0.3	−0.2	−0.13	−0.33	0.28
HxCDD2	0.26	0.28	−0.4	−0.11	0.05	0.12
HxCDD3	0.33	0.34	−0.02	−0.06	−0.25	0.12
HpCDD	0.24	0.18	−0.39	0.55	0.29	0.14
OCDD	0.08	0.16	−0.26	0.51	0.63	−0.21
TCDF	0.34	0.19	0.04	0.03	0.15	−0.26
PeCDF1	0.2	0.23	0.28	−0.22	−0.14	0.46
PeCDF2	0.32		−0.06		0.05	
HxCDF1	0.31	0.31	0.094	−0.22	−0.03	−0.39
HxCDF2	0.26	0.32	−0.05	−0.24	−0.13	−0.31
HxCDF4	0.29	0.32	0.096	−0.22	−0.25	0.14
HpCDF1	0.14	0.29	0.46	0.41	0.082	0.046
OCDF	0.18		0.36		0.36	
eigenvalues	5.8	5.2	1.98	2.2	1.5	1.7

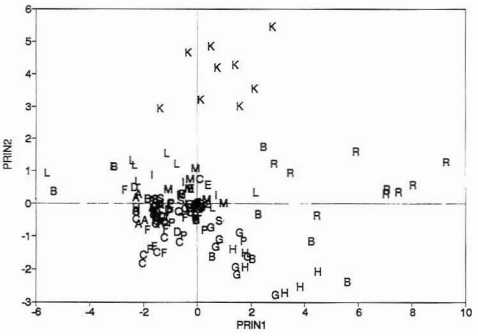

Figure 5. Principal component 1 plotted against principal component 2 for milk. Observations are designated with a letter refering to the laboratory of origin.

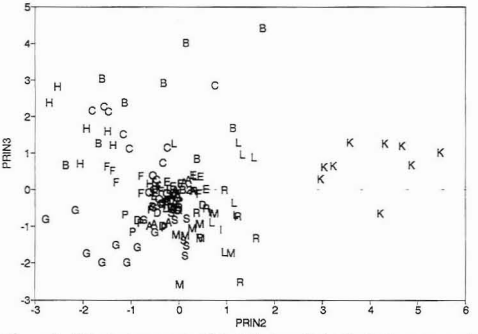

Figure 6. Principal component 2 plotted against principal component 3 for milk. Observations are designated with a letter refering to the laboratory of origin.

the poor performers and the best performers for both milk and blood. The particular congeners that on average were in the poorest agreement could be identified for any laboratory as well as the magnitude and direction from the mean. It is also interesting to note that laboratories with the poorest results correlate with the eigenvectors for the principal component. The congeners furthest from the mean are the ones given the largest weighting for principal component 2. PC2 explains the results of certain laboratories well (K, G,

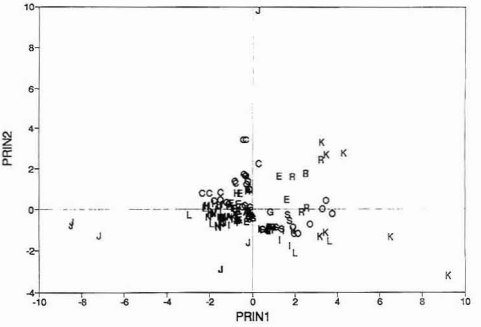

Figure 7. Principal component 1 plotted against principl component 2 for blood. Observations are designated with a letter refering to the laboratory of origin.

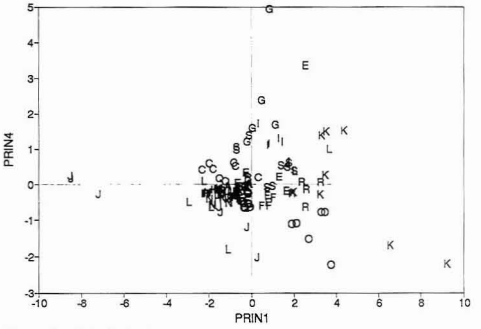

Figure 8. Principal component 1 plotted against principal component 4 for blood. Observations are designated with a letter refering to the laboratory of origin.

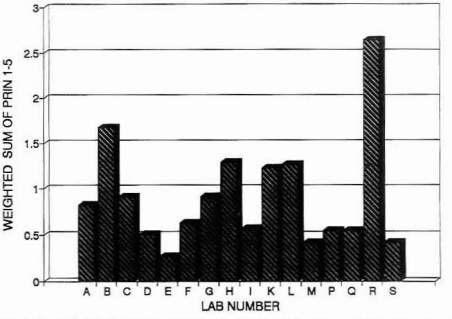

Figure 9. Principal component scores of milk data weighted by their fraction of the variance explained and the absolute values summed (prin 1–5).

and H in milk and L in blood). Laboratories with the highest consensus (A, Q, S, D, E, F, I, and P) show no correlation at all with any principal component eigenvectors, and when mapped with principal component 1 they mapped in the same region for all analytes demonstrating a high degree of consensus. In general, laboratories with most, if not all, of their mean results within zero and minus half a standard deviation of the mean had the highest consensus. This was not the case for eight laboratories, which had several analytes one or more standard deviations from the mean (R, L, K, B)

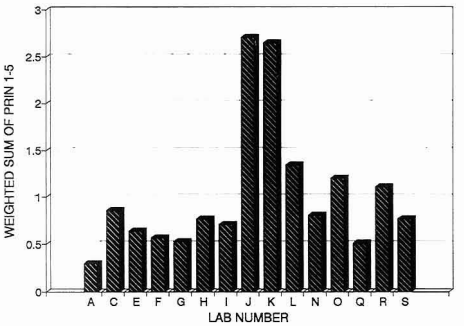

Figure 10. Principal component scores of blood data weighted by their fraction of the variance explain and the absolute value summed (prin 1–5).

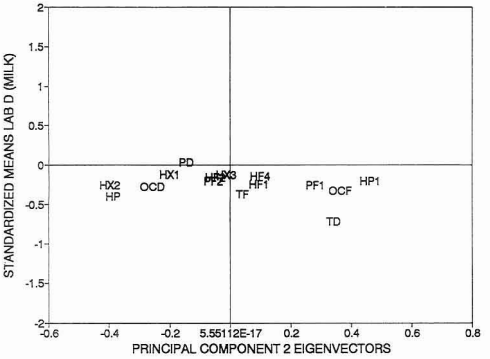

Figure 11. A consensus laboratory's (laboratory D) standardized mean milk level for each congener plotted against the principal component 2 eigenvectors for the entire group. (Dioxin and furan levels were standardized for each pool to a mean of 0 and a standard deviation of 1.)

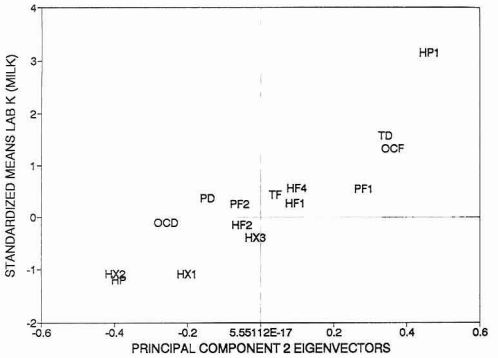

Figure 12. A nonconsensus laboratory's (laboratory K) standardized mean milk level for each congener plotted against the principal component 2 eigenvectors for the entire group. (Dioxin and furan levels were standardized for each pool to a mean of 0 and a standard deviation of 1.)

or had two or three congeners one or more standard deviations from the means (C, G, H, M). Although some of the laboratories reported biased results on the same congener, all nonconsensus laboratories had difficulties with a different subset of the congeners.

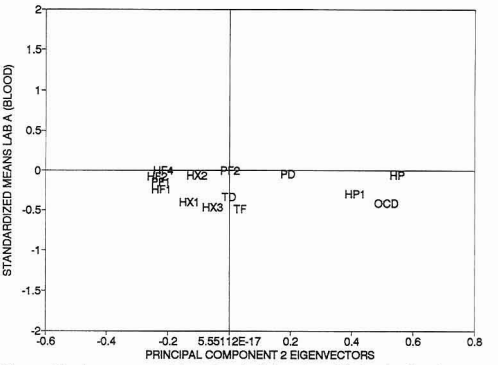

Figure 13. A consensus laboratory's (laboratory A) standardized mean blood level for each congener plotted against the principal component 2 eigenvectors for the entire group. (Dioxin and furan levels were standardized for each pool to a mean of 0 and standard deviation of 1.)

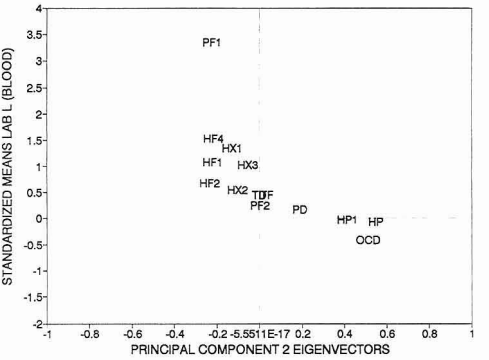

Figure 14. A nonconsensus laboratory's (laboratory L) standardized mean blood level for each congener plotter against the principal component 2 eigenvectors for the entire group. (Dioxin and furan levels were standardized for each pool to a mean of 0 and standard deviation of 1.)

A multivariate analysis of variance revealed, as had been suspected, that laboratory identification (A–S) explained most of the variability in the data set, while pool (a, b, and c) and replicate number (1, 2, or 3) made only small contributions to the variability which were not statistically significant. The model was run treating laboratory, pool, and replicate as fixed effects and examining interactions between laboratory and pool and then testing cell means. The analysis was run a second time, treating laboratory as a random effect. In both models laboratory identification was the most significant explanatory variable, while pool and replicate were almost always not significant. There was a significant interaction between laboratory identification and pool for all variables under both models. Apparently the performance of the laboratories changed in different ways as they analyzed the three pools. Method was examined separately in milk and blood by a one-way analysis of variance (ANOVA). There were no statistically significant differences detected in the results reported for any dioxin or furan using the two methods.

The means for all laboratories by congeners in milk were tested for significant differences. This testing showed that there was less agreement between some of the laboratories on the OCDF, OCDD, TCDD, PeCDF1, HxCDD2, and HpCDD values and on dioxins in general. These laboratories were from the nonconsensus group (R, L, K, B, G, H, M, and C).

The greatest agreement was achieved with the congeners PeCDF2, HxCDF1, HxCDF2, and HpCDF1 where only one or two laboratory means were significantly different from the others. In general standardized means were not statistically different if they were less than 0.75 standard deviations apart.

The magnitude of separation between means is obviously dependent on the size of the estimated standard error (even an estimate of this is usually not known). If one examines the standard error calculated for each dioxin and furan for all reported results for milk by pool with the grand mean for each congener and pool, one sees that all the standard errors are between 20% and 120% of the size of the mean (most are about 30%) with two notable exceptions, OCDF and PeCDF1, which are between 60% and 200% HxCDF4 and HpCDF1 were also higher, averaging 55% to 70% across the three pools. It seems likely that under these conditions two values could not a priori be considered different if they were within a factor of 2 of one another.

DISCUSSION

Several approaches were used to assess the principal determinants of the quality of data produced in this study. The variables that were potentially related to the data quality were laboratory identification, analytical methodology, analyte (some congeners may be more difficult than others), concentration of analyte, and pool (the effect of time on a replicate measure). In addition, we attempted to determine what data quality (precision, accuracy, and quantitation limits) could be expected for the 17 toxic congeners in human blood and milk. Figure 1, which presents the sum of the mean CVs for repeatability and reproducibility on milk data, indicates that 11 of the 16 laboratories have quite similar values, with means between 20–30%. Data from four laboratories have CVs in the range of 60–70%. Figure 2, which presents the CV data for blood, also shows a similar pattern of CVs. Nine of the laboratories produced data with mean CVs less that 30%. The remaining laboratories had CVs significantly higher, ranging from 55% to 130%.

The mean coefficient of variation for repeatability of the data reported by most laboratories was less than their mean coefficient of variation for reproducibility. This observation in itself does not necessarily indicate anything significant about data quality from a particular laboratory. Most labs had combined CVs of <30%. However, this difference can indicate the presence of some bias in the accuracy of the results. It is important to note that normally a laboratory only has current information on its CV for repeatability, which could quite easily give the incautious observer a misleading indication about the quality or lack of quality of any given result.

Although most laboratories which performed well in both blood and milk used a standard cleanup very similar to the Smith–Stalling method and HRMS, some laboratories which performed quite well used other cleanup methods combined with high- or low-resolution MS. Conversely, some of the laboratories which performed less well were using Smith–Stalling methods and HRMS as well as other methods. The analysis of variance for method showed no significant differences between methods and results for any congener. This result is interpreted to mean that the use of specific protocols was less important to the production of high quality data than were other factors related to laboratory, for example the experience of laboratory or the specific condition of a laboratory at the time of analysis or random errors. Figures 15 and 16 show the laboratories mapped against principal component 1 and identified by the method used for blood and milk, respectively. It can be seen that laboratories using both the Smith–Stalling method (designated by 0) and

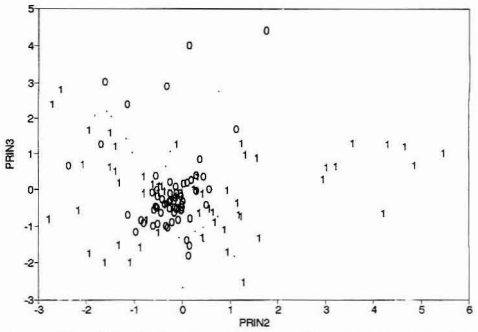

Figure 15. Milk principal component 2 plotted against principal component 3 showing observations using the Smith–Stalling method (designated by 0) and observations using other methods (designated by 1).

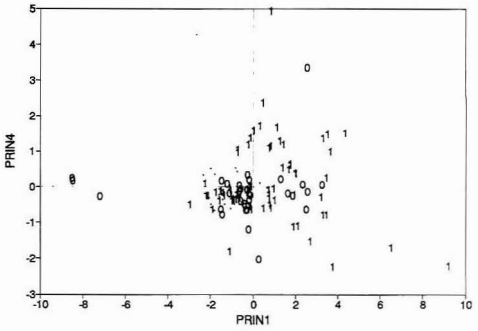

Figure 16. Blood principal component 1 plotted against principal component 4 showing observations using the Smith–Stalling method (designated by 0) and observations using other methods (designated by 1).

laboratories using other methods (designated by 1) for the clean up of blood samples are represented in the consensus group.

The data presented in Figures 3 and 4 show the relative agreement achieved for each of the target congeners. Two of the congeners, PeCDF1 and OCDF, showed a significantly larger quartile range. The relative percent difference from the median for PeCDF1 in the blood data was even larger than in the milk data. The problem with PeCDF1 may be related to the very large spiking error of PeCDF2 in two of the pools, making it more difficult than usual to measure that isomer. The determination of TCDF and PeCDF1 in blood appeared to cause difficulty and to a lesser extent TCDD, OCDD, and HxCDD1 as well. It is believed that much of the problem with the data on OCDF can be traced to a combination of very low levels (40–110 ppq) and the use of polar GC columns (SP 2330 or similar) by many laboratories. These columns are known to produce poor recoveries for OCDF. Additionally, no ^{13}C-OCDF internal standard was used. This necessitated the use of another ^{13}C internal standard for recovery estimation of OCDF.

There appeared to be some correlation between the concentration of an analyte and the relative percent difference (RPD) from the median as shown in Figures 17 and 18. However several congeners which were at a concentration of less that 0.1 ppt had CVs from the median in the 20–30% range which is quite comparable to that found for congeners at concentration in the 1–10 ppt range. Precision problems

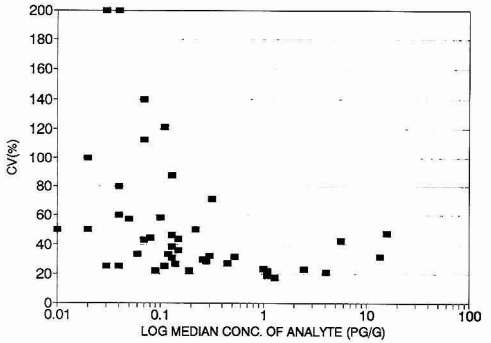

Figure 17. Coefficient of variation of the data for each congener in each milk pool plotted against congener concentration.

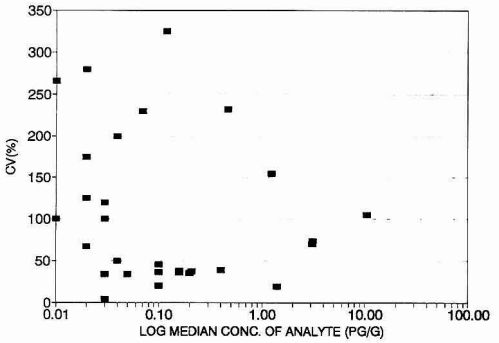

Figure 18. Coefficient of variation of the data for each congener in each blood pool plotted against congener concentration.

appeared to be at least in part related to congener-specific problems. The congeners with the largest variance from the median were at concentrations in the range of 0.02–0.04 ppt. OCDF appears to present particular difficulties for many laboratories. This is probably due to the reasons stated above.

The relationship between analyte concentration and CV is shown in Figures 17 and 18. Analytes at with large CVs (>50%) may be a result of data from a few of the participating laboratories which are not part of the consensus group and not identified as qualified by WHO. There appears to be no significant correlation of CV with analyte concentration either in blood or milk. In both matrices, analytes at concentrations below 100 ppq were reported with good precision (CV_{repeat}). As a result, it is difficult to assess the expected quantitation limits for an experienced, well-qualified laboratory. If the four laboratories with the largest average CVs are removed from the data set, satisfactory method performance (CVs <50%) is retained down to approximately 0.05 ppt or less.

Overall data quality has been affected to some extent by the use of a common set of ^{12}C and ^{13}C standards which was supplied by WHO. Interlaboratory comparison of data can be significantly influenced by the use of standards from different sources. The magnitude of this effect is difficult to assess. It has been suggested for future studies that laboratories calibrate their in house standards against a common set supplied by WHO.

CONCLUSIONS

A significant consensus was observed by a majority of the laboratories in the analysis of milk and blood plasma. The laboratories with the highest consensus produced accurate and precise results on congeners at concentration which ranged from 0.01 to 15 ppt. The mean results of the consensus laboratories were within 0.5 standard deviations of the ground mean. The standard error was largest for OCDF and PeCDF1. The coefficient of variation of the data from blood tended to be larger for a given congener than the data from milk. Although some bias could be easily observed in the laboratories with the highest consensus, it was largely insignificant to the development of an overall consensus (differences were not statistically significant and therefore may not indicate anything systematic in the analytical work).

Several factors which could potentially affect data quality were examined. There were analyte concentration, clean up method, use of high- or low-resolution mass spectrometry, pool number, replicate number, and sample matrix. In addition, information was collected on such factors as length of dioxin analytical experience and type of laboratory (academic, government, or private). None of these factors, taken as variables, were correlated with either accuracy or precision of the reported values. Some laboratories, with relatively less experience in the dioxin field, using low-resolution mass spectrometry, produced apparently good (consensus) data. Other laboratories, with substantial experience, using state of the art high-resolution mass spectrometers, produced poorer (nonconsensus) data. A few laboratories contributed the most to variability in the data set and usually introduced a general bias toward high results. One nonconsensus laboratory reported having significant laboratory contamination problems. The results of these few laboratories did not agree with other laboratories nor did they agree with one another. There was much less consensus between all labs on the level of OCDF in milk and PeCDF1 in blood. It did appear that laboratories that had well-established QA programs, which they followed carefully, produced superior results.

RECEIVED for review August 6, 1992. Accepted September 18, 1992.

Combined Effect of Coulombic and van der Waals Interactions in the Chromatography of Proteins

Jan Ståhlberg*

Astra Pharmaceutical Production AB, Quality Control, S-151 85 Södertälje, Sweden

Bengt Jönsson

Division of Physical Chemistry 1, Chemical Center, University of Lund, S-221 00 Lund, Sweden

Csaba Horváth

Department of Chemical Engineering, Yale University, New Haven, Connecticut 06520

We have recently proposed a theoretical framework for the effect of the eluting salt ionic strength of the eluent on the retention factor of proteins in ion-exchange chromatography of proteins. It is based on the solution of the linearized Poisson–Boltzmann equation for two oppositely charged planar surfaces in contact with a salt solution and describes the coulombic interaction between the protein and the oppositely charged stationary-phase surface. At sufficiently high salt concentrations in the mobile phase van der Waals interactions between the protein and the stationary phase become important. In this work we consider the effect of salt on the combined coulombic and van der Waals interactions by combining the electrostatic theory with the theory for van der Waals interactions. The combined theory describes the retention of proteins as a function of eluting salt concentration over a wide salt concentration range. The protein molecules are, according to the proposed theory, held in a diffuse layer close to the stationary phase and are not in a distinct layer, which is assumed in the traditional thermodynamic interpretation of the capacity factor. For this reason, we also examine the thermodynamic interpretation of the capacity factor when it is due to distant dependent interactions.

INTRODUCTION

Electrostatic interaction (ion-exchange) chromatography of proteins with high-performance columns and instrumentation is widely used in the analysis and purification of proteins. In this branch of chromatography the surface of the stationary phase bears fixed charges and the retention is modulated by varying the concentration and nature of the eluting salt in the mobile phase. The classical theory for the effect of salt concentration of protein retention is based on a stoichiometric ion-exchange model.[1,2] However, stoichiometric laws fail to account for electrostatic interactions of polyelectrolytes, and such treatment does not consider explicitly stationary-phase properties. Moreover, the stoichiometric approach does not explicitly take into account other phenomena, e.g., van der Waals interactions, which may affect concomitantly the magnitude of retention due to coulombic interactions.

In an attempt to construct a more realistic model for the retention in electrostatic interaction chromatography of proteins, two nonstoichiometric theories have been put forward by using the Manning counterion condensation model.[3,4] Furthermore, the retention of various proteins has been successfully correlated with their surface potential[5] and this finding also lends support to the nonstoichiometric nature of the "ion-exchange" process with proteins.

Recently, we have proposed[6] that the retention of a protein molecule by the charged chromatographic surface can be approximately described by considering coulombic interaction between two oppositely charged planar surfaces in contact with a buffered salt solution. For this simple geometry the linearized Poisson–Boltzmann equation was solved to evaluate the free energy change as a function of the distance between the two surfaces. The results predict that in the case of coulombic interactions the logarithmic capacity factor linearly depends on the reciprocal square root of the ionic strength of the mobile phase. Indeed, corresponding plots of retention data obtained over a wide range of experimental conditions yielded straight lines, and their slope allowed the estimation of the net charges on the proteins by using only independently measurable physicochemical parameters. In chromatographic practice, however, besides coulombic interactions, the retention of proteins is likely to entail also van der Waals interactions with nonpolar moieties at the stationary phase surface. Therefore, in describing the effect of the eluting salt on the retention over a wide range of salt concentration in the eluent, one has to account for both kinds of interactions, as shown previously.[3] The combined coulombic and van der Waals interaction is known from colloid chemistry to describe the long-range interaction (i.e. separation distances >1 nm) in this kind of system. At shorter separation distances the interaction becomes extremely complex, involving short-ranged solvation and steric forces. Because of this complexity, a rigorous treatment of the interaction at all separation distances cannot be made. We will describe the distance-dependent interactions as a sum of coulombic and van der Waals interactions, as is done in the DLVO theory for describing the interaction between colloidal particles.

In several theoretical treatments of interactions between a protein molecule and a surface in aqueous media, they are ascribed to van der Waals forces. Generally, they entail a combination of London, Debye, and Keesom forces, as well as desolvation forces which are related to the energy needed to dehydrate the surfaces in contact upon binding. In the

(1) Boardman, N. K.; Partridge, S. M. *Biochem. J.* **1955**, *59*, 543.
(2) Morris, C. J. O. R.; Morris, P. *Separation Methods in Biochemistry*, 2nd ed.; Wiley: New York, 1976; pp 86–87.
(3) Melander, W. R.; El Rassi, Z.; Horváth, Cs. *J. Chromatogr.* **1989**, *469*, 3.
(4) Mazsaroff, I.; Varady, L.; Mouchawar, G. A.; Regnier, F. E. *J. Chromatogr.* **1990**, *499*, 63.
(5) Haggerty, L.; Lenhoff, A. M. *J. Phys. Chem.* **1991**, *95*, 1472.
(6) Ståhlberg, J.; Jönsson, B.; Horváth, Cs. *Anal. Chem.* **1991**, *63*, 1867.

0003-2700/92/0364-3118$03.00/0

Lifshitz theory,[7] the van der Waals forces between large bodies are expressed in terms of dielectric constants and refractive indices, neglecting the atomic structure. Van Oss and co-workers[8,9] adopted the Lifshitz theory to treat the adsorption of proteins to noncharged surfaces. Combination of electrostatic repulsion and van der Waals attraction between charged particles of the same sign constitutes the classical DLVO theory that has been used by Ruckenstein et al.[10,11] to offer a qualitative description for protein retention in the so-called potential barrier chromatography. Following another approach, Horváth and co-workers[3,12,13] have adapted the solvophobic theory of Sinanoğlu[14] in their treatment of hydrophobic interactions.

Here we examine the effect of the ionic strength of the mobile phase on the interplay of coulombic and van der Waals forces in the chromatography of proteins by combining the above mentioned electrostatic theory with a first approximation of the Lifshitz treatment of van der Waals interactions. In both cases the magnitude of retention is determined by interactions that are distance dependent, and this prompted us to reexamine the concept of capacity factor and phase ratio of the chromatographic column. The results are expected to facilitate the interpretation of the physicochemical phenomena underlying the retention process in ion-exchange chromatography over a range of salt concentration.

THEORY

In the ensuing development of the theory for protein retention, involving both coulombic and van der Waals forces, first the fundamentals of the two kinds of interactions are treated individually, and then their combined effect is considered. We will examine the magnitude of the combined forces as a function of the distance between the protein and the surface of the stationary phase. It will be shown that, depending on the magnitude of the physical parameters involved, the minimum in free energy of the protein may occur at a certain distance from the stationary phase. This means that the protein molecules are held in a diffuse layer close to the surface. Subsequently, an interpretation of the retention factor appropriate for the chromatographic process based on such interactions is given. Finally, an expression is derived for the dependence of the retention factor on the salt concentration when the magnitude of protein retention is determined by both coulombic and van der Waals interactions.

Interaction of Proteins with the Chromatographic Surface. *van der Waals Interactions.* The theory of van der Waals interactions between macroscopic bodies is well developed and frequently used in colloid and surface chemistry.[7] For simplicity, we consider van der Waals interactions between two flat surfaces for which the free energy change per unit surface area can be approximated[7] as

$$\Delta G_{vdW}/A_p = -H/12\pi L^2 \quad (1)$$

where ΔG_{vdW} is the change in free energy when the two surfaces having areas of A_p are brought from infinity to a distance L

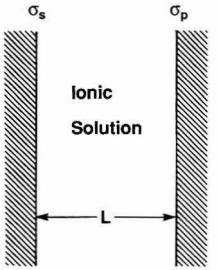

Figure 1. Schematic view of the geometry of the proposed model for the combined coulombic and van der Waals interaction between the oppositely charged protein and stationary-phase surface.

and H is the Hamaker constant that depends on the dielectric properties of the intervening medium and of the two plates. In our case, ΔG_{vdW} represents the energy of protein binding to the stationary phase from the eluent.

Electrostatic Interactions. The electrostatic interaction between the charged protein and the oppositely charged surface of the stationary phase has already been treated by a simple theory[6] based on a solution of the Poisson–Boltzmann equation. In order to use analytical solutions of the Poisson–Boltzmann equation, it is assumed that the oppositely charged surfaces of both the protein molecule and the stationary phase are planar and are in contact with a buffered salt solution, as shown in Figure 1. For this one-dimensional system the solution of the linearized Poisson–Boltzmann equation[6,15] yields for the electrostatic free energy per unit surface area, which is needed to move the surfaces from infinity to a seperation distance L, the following expression:

$$\frac{\Delta G_{es}}{A_p} = \frac{1}{\kappa\epsilon_0\epsilon_r}\left(\frac{(\sigma_p^2 + \sigma_s^2)e^{-\kappa L} + 2\sigma_s\sigma_p}{e^{\kappa L} - e^{-\kappa L}}\right) \quad (2a)$$

where ΔG_{es} is the free energy change due to electrostatic interactions, A_p is the appropriate protein surface area, σ_p and σ_s are the respective charge densities on the protein and the stationary phase surface, and ϵ_0 and ϵ_r are the permittivity of vacuum and the dielectric constant of the mobile phase, respectively. The inverse Debye length κ is defined by

$$\kappa = F(2I)^{1/2}/(\epsilon_0\epsilon_r RT)^{1/2} \quad (2b)$$

where F is the Faraday constant, I is the ionic strength of the bulk solution, i.e., that of the mobile phase, R is the gas constant, and T is the absolute temperature. The coulombic free energy change according to eq 2a has been illustrated previously for various conditions as far as the charge densities and ionic strength are concerned.[6] It has been shown that at sufficiently large separation distances ΔG_{es} is negative so that the plates are attracted to each other. With decreasing separation distance, however, ΔG_{es} may reach a minimum if the charge densities of the two surfaces not are the same. Thus, for plates carrying opposite charges, there is an equilibrium distance between the surfaces at which the free energy is minimum.

Combined Coulombic and van der Waals Interactions. As the protein approaches the oppositely charged surface, the combined effect of Coulombic and van der Waals interactions becomes important. Coulombic interactions are attractive at long distances, but as mentioned above, they may become repulsive at short distances. On the other hand, the van der Waals interactions are most often attractive and increasingly

(7) Israelachvili, J. N. *Intermolecular and Surface Forces*; Academic Press: London, 1985.
(8) Van Oss, C. J.; Good, R. J.; Chaudury; M. K. *J. Colloid Interface Sci.* **1986**, *111*, 378.
(9) Van Oss, C. J.; Good, R. J.; Chaudury; M. K. *Sep. Sci. Technol.* **1987**, *22*, 1.
(10) Lesins, V.; Ruckenstein, E. *Biotechnol. Prog.* **1988**, *4*, 12.
(11) Ruckenstein, E.; Chillakuru, R. *Sep. Sci. Technol.* **1990**, *25*, 27.
(12) Melander, W. R.; Corradini, D.; Horváth, Cs. *J. Chromatogr.* **1984**, *317*, 67.
(13) Katti, A.; Maa, Y.-F.; Horváth, Cs. *Chromatographia* **1987**, *24*, 646.
(14) Sinanoğlu, O. In *Molecular Associations in Biology*; Pullman, B., Ed.; Academic Press: New York, 1968; pp 427–445.
(15) Parsegian, V. A.; Gingell, D. *Biophys. J.* **1972**, *12*, 1192.

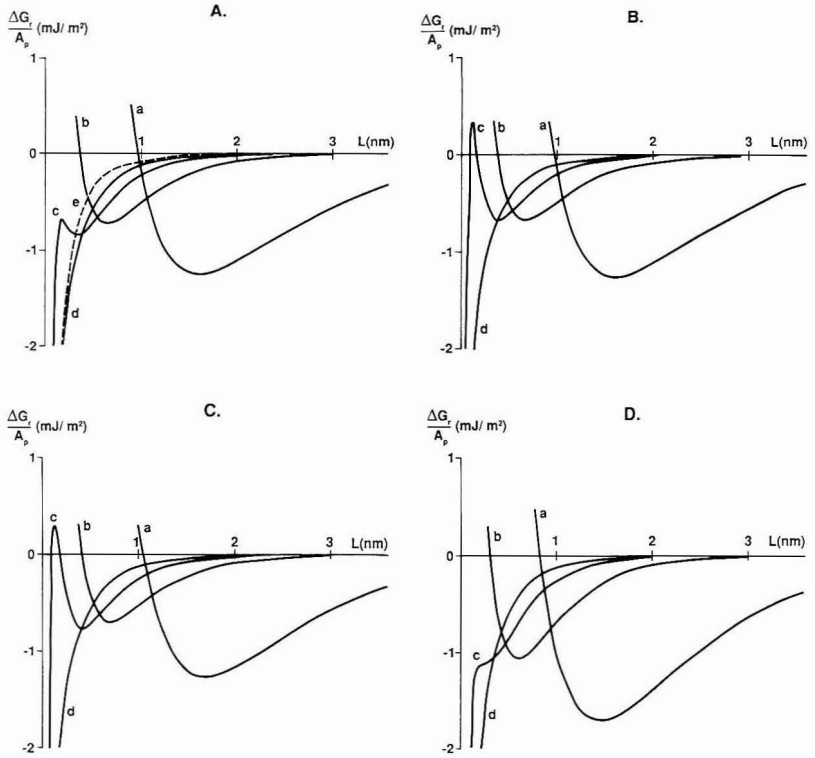

Figure 2. (A–D) Plots according to eq 3 of the Gibbs free energy per unit area, $\Delta G_r/A_p$, as a function of the distance between the two oppositely charged surfaces, L. In each figure the ionic strength is the parameter so that curves a–d represent ionic strength = 0.1, 0.5, 1.0, and 2.0 m. In Figure 2A curve e represents the ionic strength independent van der Waals interaction with the Hamaker constant H set to 3.0×10^{-21} J. In Figure 2A, $\sigma_s = 0.16$ C/m^2, $\sigma_p = -0.03$ C/m^2, and $H = 3.0 \times 10^{-21}$ J. In Figure 2B, $\sigma_s = 0.16$ C/m^2, $\sigma_p = -0.03$ C/m^2, and $H = 2.25 \times 10^{-21}$ J. In Figure 2C, $\sigma_s = 0.175$ C/m^2, $\sigma_p = -0.03$ C/m^2, and $H = 3.0 \times 10^{-21}$ J. In Figure 2D, $\sigma_s = 0.16$ C/m^2, $\sigma_p = -0.035$ C/m^2, and $H = 3.0 \times 10^{-21}$ J.

stronger the shorter the separation distance. It is known from measurements of the force acting between molecularly smooth surfaces that the two dominating forces at distances larger than around 1 nm are the van der Waals interaction described by eq 1 and the electrostatic interaction here described by eq 2a. Such measurements also show that at shorter separation distances between the two macroscopic bodies these two equations start to deviate from experimental values because of the structural behavior of the solvent molecules remaining between the two surfaces.[7]

In our case this means that when the protein reaches the proximity of the chromatographic surface, the intervening water between the two surfaces has to be removed, and the work required to do that depends in a complex way on the composition of the mobile phase as well as the properties of the protein and the stationary phase. The latter includes the pertinent molecular architectures and contact areas, the density and distribution of the surface charges as well as the structure of water near the interacting surfaces.

A detailed treatment of such a complex binding process is beyond the scope of the present work. In taking a simplified approach, we assume that all major features involved are implicit in eqs 1 and 2a; i.e. the numerical value for the Hamaker constant, H, is regarded as a formal or effective value for the considered system and is therefore not solely due to pure van der Waals interactions. We can therefore express the overall free energy change for chromatographic retention, ΔG_r, as the sum of the free energy changes associated with coulombic and van der Waals interactions. This leads to the following relationship

$$\frac{\Delta G_r}{A_p} = \frac{\Delta G_{es}}{A_p} + \frac{\Delta G_{vdW}}{A_p} = \frac{1}{\kappa\epsilon_0\epsilon_r}\left(\frac{(\sigma_p^2 + \sigma_s^2)e^{-\kappa L} + 2\sigma_s\sigma_p}{e^{\kappa L} - e^{-\kappa L}}\right) - \frac{H}{12\pi L^2} \quad (3)$$

The dependence of the retention free energy due to combined coulombic and van der Waals interactions on the separating distance, according to eq 3, is illustrated in Figure 2A–D for different values of the Hamaker constant and the charge densities. In each case calculations were made for ionic strengths of 0.1, 0.5, 1.0, and 2.0 m and the results obtained with these values are represented by the plots a–d, respectively.

The plots in Figure 2A show that when the ionic strength is low ($I = 0.1$ m) and the seperating distances are large, the free energy change is negative so that the surfaces attract each other. As the distance decreases to 1.6 nm, the free energy reaches a minimum, and at shorter distances, the surfaces repel each other. This behavior has been explained previously[6] by the decreasing entropy of the ions in the solution between the plates that more than offsets the gain

in electrostatic energy when they come closer than the equilibrium distance. When I is 0.5 m, the minimum free energy has a higher value and the equilibrium distance is smaller than shown for $I = 0.1$ m. In this case the surfaces also repel each other upon a further decrease in the separating distance. At higher ionic strength, $I = 1.0$ m, the equilibrium separating distance is further reduced and the value of the minimum free energy is lower than before due to the effect of the attractive van der Waals interactions. With a further decrease of the distance between the surfaces, the free energy reaches a maximum at about 0.2 nm, and at smaller distances van der Waals attraction dominates over electrostatic repulsion. Upon a further increase in ionic strength, as illustrated for $I = 2.0$ m, both electrostatic attraction and repulsion are attenuated to the extent that the free energy of interaction between the surfaces is dominated by van der Waals attraction. The distance dependence of the free energy solely due to van der Waals interactions, when the Hamaker constant equals 3.0×10^{-21} J, is also illustrated for the sake of comparison by the dotted line e in Figure 2A. It is seen that at sufficiently high ionic strength the interactions are almost exclusively due to short-range van der Waals forces and there is no equilibrium distance.

In Figure 2B,C the same parameters were used as a Figure 2A with the exception that the Hamaker constant is taken as 2.25×10^{-21} J in Figure 2B and σ_s is 0.175 C/m^2 in Figure 2C. Comparing these results to those shown in Figure 2A we can see that at ionic strengths of 0.1 and 0.5 m the influence of these changes is small except that the equilibrium distances in Figure 2C are slightly greater. We can conclude, therefore, that electrostatic interactions between the surfaces are not affected palpably by the value of the Hamaker constant and the charge density of the chromatographic surface at low or moderate ionic strengths. When the ionic strength is higher, as seen for the results with $I = 1.0$ m, the above change in the parameters results in a smaller influence of the van der Waals forces in Figure 2B,C compared to that shown in Figure 2A. As a result, the plots of the free energy against the separating distance for $I = 1.0$ m show a rather high energy barrier at the separation distance of 0.2 nm in Figure 2B,C. With a further increase of the ionic strength to $I = 2.0$ m, van der Waals attraction dominates the interaction again and gives rise to the same kind of behavior as seen in Figure 2A.

In calculating the results depicted in Figure 2D, we used the same parameters as in Figure 2A except for σ_p that was taken as 0.035 C/m^2. Comparing the reults to those illustrated in Figure 2A, we see that, at ionic strengths of 0.1 and 0.5 m, the retention free energy has a greater negative value at all separation distances due to stronger electrostatic attractions. With increasing σ_p, the charge density difference between the two surfaces decreases and, as a result, electrostatic attraction is more pronounced at smaller separation distances. The effect is shown for $I = 1.0$ m in Figure 2D where the potential barrier, which is at 0.2 nm in Figure 2A–C, has changed to a plateau. When the ionic strength increases above 1.0 m, the free energy change is dominated by van der Waals attraction in this case also.

Retention Factor with Distance-Dependent Interactions. The results in Figure 2A–D illustrate that the free energy change associated with the interaction between the oppositely charged surface of the protein and the stationary phase encompass different values depending on the separating distance. It follows then that, in the chromatographic process, retention occurs when the protein molecules are held in a *diffuse* layer close to the stationary-phase surface rather than at specific binding sites as postulated by the stoichiometric displacement model. Our treatment also departs from traditional retention models that assume that the bound protein molecules are uniformly confined to a *distinct* layer. For this reason, we shall examine the thermodynamic interpretation of the chromatographically measured retention factor when it is due to interactions whose strength varies with the distance between the retained molecules and the actual chromatographic surface. The approach presented here is applicable to all forms of chromatography where the interactions underlying the retention are distance dependent.

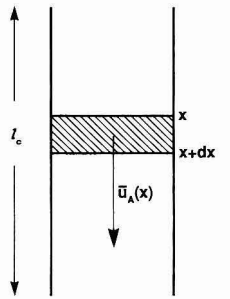

Figure 3. Schematic view of a zone of eluite A with the axial velocity $\bar{u}_A(x)$ eluting through a column of length l_c.

Let us consider a chromatographic column with a uniform cross-section and length l_c, as schematically shown in Figure 3. We assume that there is no axial dispersion and that chemical equilibrium is instantaneously attained in any point of the column. Since the local velocity of the mobile phase in the axial direction is different at different cross-sectional points, the eluite moves with a velocity given by the average of its point velocities. Our concern is a zone of eluite A that occupies the volume dV between the axial distances x and $x + dx$ in the column. The axial velocity, $\bar{u}_A(x)$ of the zone is given by the mean velocity of the eluite molecules within the zone as

$$\bar{u}_A(x) = \sum_{dV} u(x,y,z)\, n_A(x,y,z) / \sum_{dV} n_A(x,y,z) \qquad (4)$$

where $u(x,y,z)$ and $n_A(x,y,z)$ are the respective mobile-phase velocities in the axial direction and the number of moles of A, both at the point (x,y,z), and the summation is taken over all points within the volume dV. It follows from eq 4 that the more eluite molecules at points of low axial velocity the greater is the retention of the zone. Since $n_A(x,y,z)$ is equal to $c_A(x,y,z)$ dy dz, where c_A is the molar concentration of A, it is convenient to rewrite eq 4 and the corresponding integrals as

$$\bar{u}_A(x) = \int_{y,z} u(x,y,z)\, c_A(x,y,z)\, dy\, dz \Big/ \int_{y,z} c_A(x,y,z)\, dy\, dz \qquad (5)$$

With incompressible mobile and stationary phases the column properties are assumed to be independent of x. Thus the zone velocity has a constant value of $\bar{u}_A(x)$ and we can therefore integrate both the numerator and the denominator in the x direction to obtain $\bar{u}_A$. The retention time of A in a column of length l_c can be expressed as

$$t_A = \frac{l_c}{\bar{u}_A} = \frac{l_c \int_{x,y,z} c_A(x,y,z)\, dx\, dy\, dz}{\int_{x,y,z} u(x,y,z)\, c_A(x,y,z)\, dx\, dy\, dz} = \frac{l_c \int_V c_A(r)\, dV}{\int_V u_A(r)\, c_A(r)\, dV} \qquad (6)$$

where $c_A(r)$ and $u_A(r)$ are the point concentration and point velocities, respectively.

Within the moving zone there is an equilibrium distribution of A as a result of interaction with the chromatographic surface

and the concentration at any given point $c_A(r)$ is related to the concentration at a reference point, $c_A(0)$, by

$$c_A(r) = c_A(0)e^{-\Delta G(r)/RT} \quad (7)$$

where $\Delta G(r)$ is the change in free energy upon transferring 1 mol of A from the reference point to point r. Combination of eqs 6 and 7 yields for the retention time of A the expression

$$t_A = l_c \int_V c_A(0)\, e^{-\Delta G(r)/RT}\, dV / \int_V u(r)\, c_A(0)\, e^{-\Delta G(r)/RT}\, dV \quad (8)$$

Equation 8 is a general expression for the retention time in chromatography and is valid also when the eluite is retained by distance-dependent interactions with the stationary phase.

In the following we apply eq 8 to a chromatographic system comprising a column packed with porous particles with a retentive layer at the surface accessible to the eluite. Such stationary phases, for instance with a nonpolar layer, are widely used in reversed-phase chromatography. The total column volume V_{tot} is given by

$$V_{tot} = V_s + V_r + V_p + V_i \quad (9)$$

where V_s, V_r, V_p, and V_i are the respective volumes of the inert support, the retentive layer, the intraparticulate pores, and the interstitial space. The integral in eq 8 can be applied to each of the spaces and summation of the numerators and denominators yields the retention time as follows:

$$t_R = \{l_c c_A(0)[\int_{V_s} e^{-\Delta G_A(r)/RT}\, dV + \int_{V_r} e^{-\Delta G_A(r)/RT}\, dV + \int_{V_p} e^{-\Delta G_A(r)/RT}\, dV + \int_{V_i} e^{-\Delta G_A(r)/RT}\, dV]\} / \{c_A(0)[\int_{V_s} u(r) e^{-\Delta G_A(r)/RT}\, dV + \int_{V_r} u(r) e^{-\Delta G_A(r)/RT}\, dV + \int_{V_p} u(r) e^{-\Delta G_A(r)/RT}\, dV + \int_{V_i} u(r) e^{-\Delta G_A(r)/RT}\, dV]\} \quad (10)$$

For a nonretained eluite the chemical potential is the same throughout the spaces V_p and V_i and is infinitely high in spaces V_s and V_r. As the zone of such an eluite moves down the column, its concentration is uniform and equal in the spaces V_i and V_p but zero in V_s and V_r because it is excluded from these spaces. Such an eluite has the properties of an inert tracer used for the measurement of the mobile-phase space in a column. In light of the above discussion, the integrals over the volumes V_s and V_r in eq 8 vanish and the retention time of the tracer, t_o, can be expressed as

$$t_o = \frac{l_c c_A(0)[\int_{V_i} dV + \int v_p dV]}{c_A(0)[\int_{V_i} u(r)\, dV + \int_{V_p} u(r)\, dV]} = \frac{l_c(V_i + V_p)}{\int_{V_i} u(r)\, dV + \int_{V_p} u(r)\, dV} = \frac{l_c}{\bar{u}_o} \quad (11)$$

Now let us consider a retained eluite with the same properties as the unretained tracer, except that the change in free energy, ΔG_r, for its transfer between the spaces V_i and V_r is finite and constant throughout V_r. By applying these conditions to eq 10 we obtain the retention time of such an eluite:

$$t_R = \frac{l_c[\int_{V_i} dV + \int_{V_p} dV + \int_{V_r} e^{-\Delta G_r/RT}\, dV]}{[\int_{V_i} u(r)\, dV + \int_{V_p} u(r)\, dV + \int_{V_r} u(r) e^{-\Delta G_r(r)/RT}\, dV]} \quad (12)$$

If we further assume that the eluite in the space V_r is stationary so that $u(r)$ is zero at any point in V_r and that its velocity in V_i and V_p is equal to that of the unretained component, eq 12 can be further simplified to obtain the following relationship:

$$t_R = l_c(V_i + V_p + V_r e^{-\Delta G_r/RT})/\bar{u}_o(V_i + V_p) \quad (13)$$

In chromatographic practice the retention factor is evaluated from the relationship $k' = (t_R - t_o)/t_o$. Using the expressions obtained for t_o and t_R in eqs 11 and 13, we obtain for the retention factor

$$k' = \frac{t_R - t_o}{t_o} = \frac{V_r(e^{-\Delta G_r/RT})}{(V_i + V_p)} = \phi K \quad (14)$$

where $\phi = V_r/(V_i + V_p)$ is the phase ratio and $K = e^{-\Delta G_r/RT}$ is the equilibrium constant for the chromatographic process. It is seen that only when several simplifying assumptions are made does eq 8 reduce to the traditional expression for the retention factor as the product of the phase ratio and the equilibrium constant. In turn, this analysis leads to the conclusion that eq 14 cannot be used to express the retention factor when the interactions between the eluite and the chromatographic surface are distance dependent. This caveat gains particular significance in the chromatography of large polyelectrolyte molecules on stationary phases with fixed charges due to the long range of coulombic interactions.

Retention Factor of Proteins in Electrostatic Interaction Chromatography. It was shown above that the general expression for the retention time given in eq 8 leads to the traditional definition of the retention factor only in certain particular cases. In this section we will discuss the implications of eq 8 for the specific case of the chromatography of proteins on ion-exchanger stationary phases.

Let us consider a column of length l_c, that is packed with a porous stationary phase having a surface charge density of σ_s. In the column, the proteinaceous eluite explores the mobile-phase space that is given by the sum of V_i, the interstitial volume, and V_p, the intraparticulate pore volume. By applying eq 8, the retention time of the protein t_R can be expressed as

$$t_R = \frac{l_c c_A(0)[\int_{V_i} e^{-\Delta G(r)/RT}\, dV + \int_{V_p} e^{-\Delta G(r)/RT}\, dV]}{c_A(0)[\int_{V_i} u(r) e^{-\Delta G(r)/RT}\, dV + \int_{V_p} u(r) e^{-\Delta G(r)/RT}\, dV]} \quad (15)$$

Assuming that the mobile phase is stagnant in the pores, i.e. $u(r)=0$ in V_p, and that the protein concentration, $c_A(0)$, is the same throughout the interstitial space, we can simplify eq 15 to obtain the expression

$$t_R = l_c(V_i + \int_{V_p} e^{-\Delta G(r)/RT}\, dV) / \int_{V_i} u(r)\, dV \quad (16)$$

The pores of the stationary phase in protein chromatography have radii much larger than the Debye length in order to accommodate the protein molecules. Consequently, we can transform the integral in the numerator of eq 16 from a volume-dependent to a distance-dependent relationship. By using the relation $dV_p = A_s\, dL$, where A_s is the surface area of the stationary phase equiaccessible to the protein, we obtain for the retention time of the protein the following expression:

$$t_R = l_c(V_i + A_s \int_{L_{min}}^{L'} e^{-\Delta G(L)/RT}\, dL) / \int_{V_i} u(r)\, dV \quad (17)$$

The retention time of a marker molecule, which does not interact with the stationary phase and has the same size as the protein, is the holdup time of an inert tracer in the column, t_o. By using the same arguments as above in deriving eq 17, we obtain for t_o the relationship

$$t_o = l_c(V_i + A_s \int_{L_{min}}^{L'} dL) / \int_{V_i} u(r)\, dV \quad (18)$$

In the numerators of eqs 17 and 18 the value of L' is formally

chosen so that the numerical value of the integral equals that of the mobile-phase space in the pores V_p, i.e. $\int_{L_{min}}^{L'} A_s \, dL = V_p$. By combining eqs 17 and 18, we can express the retention factor of the protein as follows:

$$k' = \frac{t_R - t_o}{t_o} = \frac{A_s}{V_o}\int_{L_{min}}^{L'} (e^{-\Delta G(L)/RT} - 1)\, dL \qquad (19)$$

where the integral in the numerator is proportional to the surface excess of the protein. Equation 19 was already derived in another way and used in our previous paper.[6] By substituting the distance-dependent free energy change from eq 3 into eq 19, we can express the retention factor of a protein due to combined coulombic and van der Waals interactions as

$$k' = \frac{A_s}{V_o}\int_{L_{min}}^{L'} \left[\exp\left(-\frac{A_p}{RT\kappa\epsilon_0\epsilon_r}\frac{(\sigma_s^2 + \sigma_p^2)e^{-\kappa L} + 2\sigma_s\sigma_p}{e^{\kappa L} - e^{-\kappa L}} + \frac{A_p H}{RT(12\pi L^2)}\right) - 1\right] dL \qquad (20)$$

where A_p is the surface area of the protein molecule that interacts with the stationary phase and, as a first approximation it can be regarded as half of the total molecular surface area of the protein.[6]

RESULTS AND DISCUSSION

Protein retention in chromatography with ion-exchanger stationary phases is likely to involve both coulombic and van der Waals interactions. The expression for the corresponding retention factor is given by eq 20 which requires numerical integration. We used the Statgraphics software version 4.0 and a Compaq computer to carry out the calculations for certain cases of interest, and the results are discussed as follows.

Plots of the logarithmic retention factor against $1/\sqrt{I}$ for a hypothetical protein having a net charge +7 and an interacting molecular surface area of 2500 Å^2 are presented in Figures 4 and 5. At sufficiently high ionic strengths the numerical value of the integral in eq 20 is dependent on the lower integration limit L_{min}, which is arbitrarily set to 0.17 nm for all cases illustrated in Figures 4 and 5. The plots shown in Figure 4 were made with the Hamaker constant as the parameter by assuming a fixed charge density of the stationary-phase surface. The value of the Hamaker constant was varied in the range from 1.0 to 10.0 × 10^{-21} J or taken as zero. It is seen that when the ionic strength of the mobile phase is low, i.e., $1/\sqrt{I}$ is larger than 3, the influence of the Hamaker constant on the logarithmic retention factor is small. The limiting slope of the plots approaches that of the plot calculated with $H = 0$ in order to represent the hypothetical case when van der Waals interactions are absent.

This behavior at low ionic strength is readily understood by examining the results depicted in Figure 2A,B, which show that the effect of the Hamaker constant on the free energy change becomes negligible at sufficiently low ionic strengths and the magnitude of the retention factor is determined essentially by coulombic interactions. With increasing ionic strength, however, the magnitude of electrostatic interactions is attenuated and at short separating distances attractive van der Waals forces begin to dominate. As a result, at a certain value of the ionic strength, which depends on the magnitude of the Hamaker constant, van der Waals attraction dominates over electrostatic interactions. Thus the retention factor increases with a further increase in the ionic strength.

It should be noted that the retention free energy change due to van der Waals interactions can also be treated by a surface thermodynamic approach[7] and expressed by the

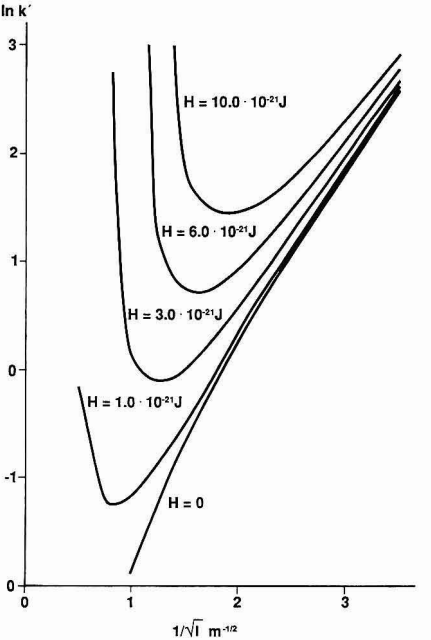

Figure 4. Theoretically calculated logarithmic retention factor as a function of the reciprocal square root of the ionic strength with the Hamaker constant as the parameter. The curves are calculated by numerical integration of eq 20 by setting A_p to 2500 Å^2/molecule, A_s/V_o to 135 × 10^6 m^2/m^3, and the charge densities σ_s and σ_p to 0.16 and −0.0224 C/m^2, respectively.

characteristic interfacial tensions of the system as

$$\frac{\Delta G_{vdW}}{A_p} = -\frac{H}{12\pi L_{min}^2} = \gamma_{sm} + \gamma_{pm} - \gamma_{ps} \qquad (21)$$

where γ_{ij} is the surface tension between phases i and j, and the subscripts s, m, and p denote the stationary, mobile, and protein phases, respectively. Adsorption data at high ion concentrations may therefore be used to estimate the value of L_{min} from the quotient H/L_{min}^2, if the effective Hamaker constant, H, is known.

The effect of the charge density at the stationary-phase surface on the plots of the logarithmic retention factor against $1/\sqrt{I}$ is illustrated in Figure 5 for the chromatography of a hypothetical protein when the retention is due to both coulombic and van der Waals interactions. The value of the Hamaker constant was taken as 6.0 × 10^{-21} J, and the size and net charge of the protein are assumed to be the same as in Figure 4. Figure 5 shows that at low ionic strengths the magnitude of the logarithmic retention factor and its dependence on $1/\sqrt{I}$ are rather insensitive to changes in the charge density of the stationary-phase surface so that the pattern is very similar to that depicted in Figure 4. This behavior is easily understood from a comparison of the plots in Figure 2A,C which shows that at ionic strengths of 0.1 and 0.5 m an increase in the surface charge density from 0.160 to 0.175 C/m^2 does not affect the value of free energy minimum and only slightly shifts its position in the direction of increasing ionic strength. Comparison of Figure 2A,C also shows that at sufficiently high ionic strengths, a higher surface charge density of the stationary phase engenders a higher potential barrier for the interaction, and this effect is responsible for the lower capacity factors in Figure 5. The

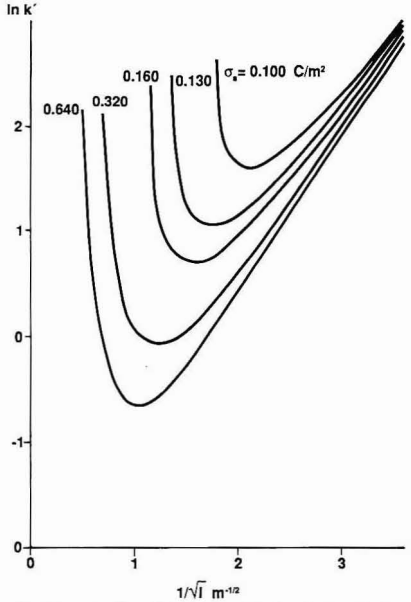

Figure 5. Theoretically calculated logarithmic retention factor as a function of the reciprocal square root of the ionic strength with the surface density of the stationary phase as the parameter. The curves are calculated by numerical integration of eq 20 by setting A_p to 2500 Å^2/molecule, A_s/V_o to 135 × 10^6 m^2/m^3, H to 6.0 10^{-21} J, and σ_p to −0.0224 C/m^2.

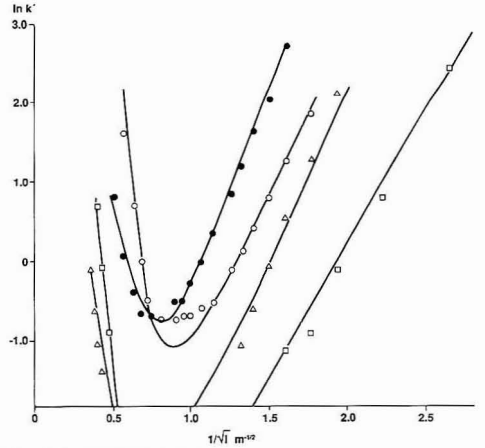

Figure 6. Comparison between the theoretically calculated and experimentally observed logarithmic retention factor as a function of the reciprocal square root of the ionic strength for four different proteins. The theoretical curves are calculated by numerical integration of eq 20 by setting the column parameter A_s/V_o to 3.4 × 10^6 m^2/m^3 and σ_s to −0.220 C/m^2. The theoretical parameters σ_p, A_p, and H, respectively, are for the respective proteins: lysozyme (●) 0.0500 C/m^2, 4410 Å^2, and 1.55 × 10^{-21} J; α-chymotrypsinogen (○), 0.0430 C/m^2, 4834 Å^2, and 2.11 × 10^{-21} J; cytochrome *c* (△) 0.0430 C/m^2, 4410 Å^2, and 0.94 × 10^{-21} J; ribonuclease (□) 0.0387 C/m^2, 4160 Å^2, and 1.24 × 10^{-21} J. The experimentally observed capacity factors are from ref 3.

greater the difference in the charge density of the two interacting surfaces, the higher the ionic strength required to make the potential barrier vanish.

As a test for the theory proposed here, the experimentally observed retention behavior of proteins in ion-exchanger columns over a wide range of salt concentrations in the eluent was simulated by numerical integration of eq 20. The theoretical results are compared to the experimental data for four proteins in Figure 6. The procedure for constructing the theoretical plots was as follows. First the values of A_s/V_o, σ_s, H, and σ_p were varied by trial and error in order to obtain the best fit of the calculated dependence of the logarithmic retention factor on $1/\sqrt{I}$ to the experimental data for the lysozyme. Then, by using the same column parameters, A_s/V_o and σ_s, found appropriate with lysozyme, the values of H and σ_p representing protein properties were varied to fit the calculated data to the experimental results obtained with the other three proteins. The lower integration limit, L_{min}, was 0.16 nm for lysozyme and α-chymotrypsinogen and 0.12 nm for cytochrome *c* and ribonuclease. In all four cases the surface area of the protein, A_p, which interacts with the stationary phase was taken to be half of the surface area of the spherical protein molecule.[6]

The results illustrated in Figure 6 shows a good agreement between plots of the experimental data and those calculated by the present theory as far as the dependence of the logarithmic retention factor on the reciprocal square root of the ionic stength is concerned. Because of the large number of variables involved in this procedure and their complex interdependence, the limited set of numerical values obtained by this analysis may not be accurate. Yet, the parameter values for the proteins and for the stationary phases are all physically reasonable. Further studies are required to examine closer the potential of this approach for the evaluation of various physicochemical parameters which can be used to characterize the chromatographic system and/or the proteins.

CONCLUSIONS

The simple theoretical framework presented here for the retention of proteins in chromatography due to both coulombic and van der Waals interactions is based on a macroscopic approach. Thus the neglect of interactions on the molecular level may entail certain oversimplifications. Nevertheless, the physicochemical basis of the theory is firm and the proposed approach can be useful for the organization, analysis, and interpretation of chromatographic data. Further experimental studies using well-characterized proteins and stationary phases are needed to explore in more detail the realm of applicability for this theory.

RECEIVED for review April 6, 1992. Accepted September 14, 1992.

Analytical SPLITT Fractionation: Rapid Particle Size Analysis and Measurement of Oversized Particles

Chwan Bor Fuh, Marcus N. Myers, and J. Calvin Giddings*

Field-Flow Fractionation Research Center, Department of Chemistry, University of Utah, Salt Lake City, Utah 84112

In SPLITT fractionation (SF), particles or molecules are separated rapidly by field-driven migration over a short (submillimeter) path lying across a ribbonlike flow cell having splitters at the ends. The outlet splitter separates components of high and low mobilities, directing the fractions to different outlet substreams for collection and measurement. The SF process, when run continuously, allows the scaleup of difficult separations. However, the rapid (often <1 min) division and measurement of injected sample pulses can provide useful and timely analytical information. When used this way SF becomes *analytical SPLITT fractionation* (ASF). Here we utilize a miniature gravity SPLITT cell for particle size analysis in the 5–75-μm size range. The measurement of "oversized" particles is particularly straightforward using ASF. Oversized particles (those exceeding a criterion diameter) have adverse effects on the performance or safety of such products as abrasives, polishers, coatings, and pharmaceutical emulsions. Oversized particle analysis is illustrated using starch granules, abrasive particles, and glass beads. Most run times are 0.3–2.0 min. By making a series of runs at different cutoff diameters, we show that entire size distribution curves can be constructed. This case is illustrated using quartz particles and glass beads. By using microscopy and published size distribution data, we show that our results are in good agreement with those expected theoretically.

Split-flow thin (SPLITT) cells are elongated unpacked flow cells resembling field-flow fractionation (FFF) channels, except that their operation requires the presence of one or more flow splitters at the outlet end of the channel and often at the inlet end as well.[1–4] The outlet splitter(s) serves to divide the sheet of liquid flowing through the channel into two (or more) laminae. A field or gradient applied over the cell's thin dimension (as in FFF) creates transverse concentration gradients such that the divided laminae have different contents, which means that separation has been realized (see Figure 1).

Although SPLITT fractionation (SF) and FFF are carried out in a similar thin channel flow system with an applied transverse field, the two separation processes are fundamentally different in nature. In FFF, separation is generated along the flow axis of the channel as a consequence of the different velocities of the stream filaments that different components are forced to occupy by the transverse field.[5–9] In SPLITT fractionation, by contrast, separation is generated along the short transverse axis as a direct consequence of the differential transport induced by the applied field or gradient.[1–4]

The primary advantage of SPLITT cell separation relative to FFF is that SF can be made to occur continuously, making it a strong candidate for small- and intermediate-scale preparative work on macromolecules and particles. In addition SF tends to be a faster separation process (typical separation time ~1 min or less) than FFF, although there are exceptions. The high speed of separation is due to the short separation path, equal to some fraction of the channel thickness and thus often lying in the 100-μm range. Although the resolving power generated over such a short path is obviously limited,[10] the resolution is often surprisingly high (particularly for particles) because of the uniformity of flow and the near absence of pathological flow effects in the SPLITT cell.

The high speed of SPLITT fractionation and the simplicity of the apparatus and the underlying process make this an attractive approach for certain analytical applications, particularly in the area of process analysis and quality control. However the separation and output would differ significantly from that of FFF, which is also promising for certain process control applications. FFF, which resembles chromatography, is capable of analyzing a series of discrete samples, producing typically a particle size or molecular weight distribution for each. The individual run times might range from 1 to 5 min for the high speed steric or hyperlayer FFF of particles >1 μm in diameter to 10–30 min for high-resolution colloid or polymer fractionation. Analytical SPLITT fractionation (ASF), by contrast, can report continuously on an unbroken stream of suspended or dissolved sample, although it too can be fed discrete sample pulses if desired. However, rather than yielding a complete size or mass distribution (as does FFF) for each volume element of the entering sample stream, ASF divides the distribution into a small number of finite elements or "channels", each corresponding to a separate outlet substream. The cutoff between elements is controllable. The simplest and often most effective SPLITT cells are binary systems that produce only two substreams, as shown in Figure 1.

The suitability of ASF for analysis depends in part on whether the analytical problem can be adequately treated by the limited informational content of the two or more channels. In many cases such information is adequate. In these cases the high speed and the possibility for continuous SPLITT analysis would constitute significant gains in analytical capabilities. Even in those cases for which the limited information of a single ASF run is inadequate, the high speed of ASF permits multiple runs in a short time period and thus the compounding of information as described below.

One promising area where SF might be useful at both analytical and preparative levels is in the production, cleanup, and characterization of particulate materials from which

* Corresponding author

(1) Giddings, J. C. *Sep. Sci. Technol.* **1985**, *20*, 749–768.
(2) Springston, S. R.; Myers, M. N.; Giddings, J. C. *Anal. Chem.* **1987**, *59*, 344–350.
(3) Giddings, J. C. *Sep. Sci. Technol.* **1988**, *23*, 931–943.
(4) Levin, S.; Giddings, J. C. *J. Chem. Tech. Biotechnol.* **1991**, *50*, 43–56.
(5) Giddings, J. C. *J. Chromatogr.* **1976**, *125*, 3–16.
(6) Giddings, J. C. *Anal. Chem.* **1981**, *53*, 1170A–1175A.
(7) Caldwell, K. D. *Anal. Chem.* **1988**, *60*, 959A–971A.
(8) Beckett, R.; Hotchin, D. M.; Hart, B. T. *J. Chromatogr.* **1990**, *517*, 435–447.
(9) Giddings, J. C. *Chem. Eng. News* **1988**, *66*, 34–45.
(10) Giddings, J. C. *Sep. Sci. Technol.* **1992**, *27*, 1489–1504.

0003-2700/92/0364-3125$03.00/0

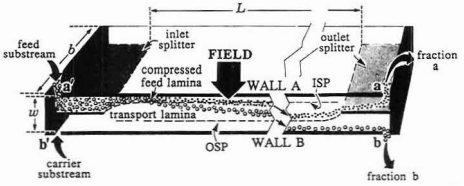

Figure 1. Schematic diagram of SPLITT cell. Thickness of cell is exaggerated to illustrate differential transport between wall A and wall B.

"oversized" particles (those exceeding a certain criterion diameter) must be rigorously excluded (or at least reduced to very low levels) because of the adverse effects they produce. Examples include abrasives,[11] polishers,[11,12] coatings,[12,13] aerosols,[12] and injectable emulsions.[14] By setting the cutoff diameter d_c of the SPLITT cell at this criterion diameter, the oversize particles are isolated from their numerous small diameter counterparts, thus simplifying their detection and quantitation. The removal (and if desired the measurement) of oversize particles is highly efficient, and thus scaleup of the SPLITT cell is also promising for small- and intermediate-scale preparative purposes.

An analytical SPLITT cell could be used flexibly in several different ways for the determination of oversized particles. First of all, the ASF process could be readily automated using an autoinjector, giving in many cases the capability of making one or more determinations per minute on an ongoing basis. Alternately, ASF could be run continuously by tapping into a process feed stream. In this case, ASF would provide a continuous report on the oversized content of the stream. Undesirable shifts would be detected almost immediately because of the rapid response of the SPLITT cell.

Another promising area where SF might be useful at the analytical level is in the determination of particle size distributions. The mass of sample above a specified size can be obtained by measuring the relative content of the two outlet streams providing the cutoff diameter is adjusted to equal the specified diameter. This step is identical to that required to measure the relative amount of oversized particles that exceed a specified criterion diameter. To obtain a full (cumulative) size distribution, this step must be repeated for a series of cutoff diameters. This multiple-step process is feasible because of the high speed of the individual steps.

The throughput of a SPLITT cell is proportional to its length L and breadth b but independent of thickness w.[10] Thus the area bL of the cell can be increased (within limits) to accommodate throughput requirements. For analytical SPLITT fractionation, where information rather than fractionated material is the desired product, area bL and thus the overall size of the device can be reduced to levels dictated more by convenience than throughput. Accordingly, for this work we have constructed and utilized a miniature split cell many times smaller than any previously reported (see Figure 2).

For the work reported here, fractionation is achieved through differential transport in a gravitational field. However, a number of other transport mechanisms that have been proposed and in some cases utilized for preparative SPLITT operation could also be harnessed for analytical purposes.

(11) Miller, B. V.; Lines, R. W. *CRC Crit. Rev. Anal. Chem.* **1988**, *20*, 75–115.
(12) Cadle, R. D. *Particle Size*; Reinhold Publishing: New York, 1965; Chapter 6.
(13) Rump, H. *Particle Technology*; Chapman and Hall: New York, 1991; pp 1–15.
(14) Hersey, J. A. In *Particle Characterization in Technology*; Beddow, J. K., Ed.; CRC: Boca Raton, FL, 1984; Vol. 1, pp 69–79.

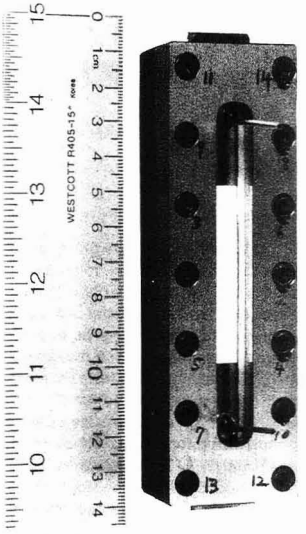

Figure 2. Photograph of analytical SPLITT cell used in these studies.

Alternate driving forces for transport include centrifugation, electrical forces,[15] hydrodynamic lift forces,[16] and concentration gradients.[4] Using the appropriate force it should be possible to achieve rapid analytical fractionation based on differences in sedimentation coefficient and size (as we report here), density, electrical mobility, isoelectric point, and diffusion coefficient.

THEORY

Figure 1 shows the principles underlying the operation of a simple binary SPLITT cell. Due to the action of the external field or driving force, particles or molecules are transported differentially across the thickness w of the cell, which in the experimental system reported here is only 0.38 mm. Rapidly migrating particles are separated from those undergoing slower transport by means of an outlet splitter that divides the channel laminae into two outlet substreams, a and b.

The effectiveness of the SPLITT process is enhanced by the active control of the positions of the inlet splitting plane (ISP) and the outlet splitting plane (OSP), a control gained by varying the flow rates of inlet and outlet substreams. As shown in Figure 1, the ISP divides the sample-containing lamina originating at inlet a′ from the sample-free lamina whose source is inlet b′. When the volumetric flow rate of the substream entering b′, $\dot{V}(b')$, exceeds that of the substream entering a′, $\dot{V}(a')$, then the ISP swerves upward from the inlet splitter, compressing the sample feed lamina into a thin band ideal for initiating separation. The degree of compression is arbitrary as dictated by the flow rate ratio. The only negative effect of increasing the compression is its association with a low rate of feed input, which is proportional to $\dot{V}(a')$, but this is of little concern for analytical SF.

The OSP, dividing the thin ribbon of flow in the cell into the two laminae that eventually emerge as substreams a and b, is likewise controlled by the ratio of the outlet volumetric flow rates $\dot{V}(a)$ and $\dot{V}(b)$. It is, of course, necessary that the sum of inlet flow rates equal the sum of outlet flow rates as

(15) Giddings, J. C. *J. Chromatogr.* **1989**, *480*, 21–33.
(16) Giddings, J. C. *Sep. Sci. Technol.* **1988**, *23*, 119–131.

expressed by

$$\dot{V}(a') + \dot{V}(b') = \dot{V}(a) + \dot{V}(b) \quad (1)$$

Sandwiched between the ISP and the OSP is a thin film of liquid termed the transport lamina. As the particles enter the cell and pass beyond the inlet splitter, they are gradually driven into this transport lamina by the applied field. However, as made clear by Figure 1, particles must be driven across the entire thickness of the transport lamina in order to emerge from outlet b. Particles whose field-driven migration is too slow to allow passage through the transport lamina in the course of their residence in the cell fail to penetrate through the OSP and thus emerge from outlet a. Because of the thinness of the compressed feed lamina and the uniformity of the transport lamina, a fairly sharp cutoff in migration velocity distinguishes the particles emerging from outlets a and b. If the field-induced velocity depends upon particle size, as is the case for sedimentation, this cutoff velocity can be translated into a unique value of the cutoff diameter d_c.

The theory defining the cutoff diameter has been described in previous publications.[2,10] It is assumed that particles are driven at constant velocity U from wall A to wall B during their residence in the SPLITT cell. As a consequence of this uniform transport, the particles are driven across a thin filament of the flowing liquid. The volumetric flowrate of the filament traversed by the particles is given simply by[2]

$$\Delta\dot{V} = bLU \quad (2)$$

where b is the breadth of the cell and L is its length as measured between the inlet and outlet splitting edges.

When transport is driven by gravity or a centrifuge, U is given by

$$U = sG \quad (3)$$

where s is the sedimentation coefficient and G is the field strength measured as acceleration. For spherical particles of diameter d, s is given by

$$s = \frac{(\rho_p - \rho)d^2}{18\eta} = \frac{\Delta\rho d^2}{18\eta} \quad (4)$$

where ρ_p is the particle density, ρ is the carrier density, $\Delta\rho$ is the density difference, and η is the carrier viscosity. The substitution of eqs 3 and 4 into 2 shows that for sedimenting particles

$$\Delta\dot{V} = bLsG = \frac{bLG}{18\eta}\Delta\rho d^2 \quad (5)$$

Of critical importance is the relative magnitude of $\Delta\dot{V}$ and $\dot{V}(t)$, the latter being the volumetric flow rate of the transport lamina. For present purposes, we assume that all particles for which $\Delta\dot{V} > \dot{V}(t)$ will emerge from outlet b. Particles of lesser $\Delta\dot{V}$, such that $\Delta\dot{V} < \dot{V}(t)$, will emerge from outlet a. Therefore the cutoff value of $\Delta\dot{V}$ is given by

$$\Delta\dot{V}_c = \dot{V}(t) \quad (6)$$

The cutoff value $\Delta\dot{V}_c$ specifies the cutoff particle diameter d_c. Thus from eqs 5 and 6

$$\dot{V}(t) = \Delta\dot{V}_c = \frac{bLG}{18\eta}\Delta\rho d_c^2 \quad (7)$$

and d_c is therefore expressed by

$$d_c = \left(\frac{18\eta\dot{V}(t)}{bLG\Delta\rho}\right)^{1/2} \quad (8)$$

The volumetric flowrate of the transport lamina $\dot{V}(t)$ is given by (see Figure 1)

$$\dot{V}(t) = \dot{V}(a) - \dot{V}(a') \quad (9)$$

The use of eq 1 gives the alternate expression

$$\dot{V}(t) = \dot{V}(b') - \dot{V}(b) \quad (10)$$

The substitution of eq 9 (or one can use eq 10 if prefered) into eq 8 yields

$$d_c = \left\{\frac{18\eta[\dot{V}(a) - \dot{V}(a')]}{bLG(\rho_p - \rho)}\right\}^{1/2} \quad (11)$$

In principle, all particles smaller than d_c exit outlet a while larger particles exit b. Clearly, d_c depends upon particle density ρ_p because of the influence of ρ_p on sedimentation velocities. Thus a unique value of d_c can only be established for particles of uniform density.

As shown by eq 11, the cutoff diameter can be readily adjusted or altered by changing the volumetric flow rates of substreams a and a′. Somewhat less flexible means for controlling d_c include altering the SPLITT cell dimensions b and L, changing the field strength G (through tilting the cell on end or applying a centrifugal force), using an additive to change ρ, or varying the temperature to change viscosity. In addition, we note that the same basic methodology can be used both for floating particles as for sinking particles except in the former case the feed substream a′ would be introduced adjacent to the wall of lowest gravitational potential.

While eq 11 gives a unique value for the cutoff diameter, there will actually be a small range in diameters that divide between outlets a and b.[10] This range is introduced by imperfections in the system, particularly in the splitters, and sometimes in the measurable displacement caused by Brownian motion. In addition, we note that eq 11 slightly underestimates the true cutoff diameter because in reality particles must migrate somewhat further than the distance between the ISP and the OSP to gain outlet b. The additional distance depends upon the initial position of a given particle within the compressed feed lamina. Since particles sediment toward the inlet splitter between the time of their entrance at inlet a′ and the time that they reach the splitter edge, conditions can be adjusted such that particles in the critical diameter range sediment to the surface of the splitter before the two inlet substreams are merged. (Such conditions apply in the present experiments.) In this case the incremental migration distance is only slightly larger than a single particle radius, leading generally to only a small perturbation in the cutoff diameter relative to the value given by eq 11.

Although eq 11 fixes the flow rate difference $\dot{V}(t) = \dot{V}(a) - \dot{V}(a')$ once d_c is chosen, the four constituent flow rates (two in and two out) are not rigidly fixed by the above equations, leading to additional flexibility in operation. Some criteria for choosing these flow rates has been discussed in a recent paper on the optimization of SPLITT operation.[10] Briefly, we require $\dot{V}(a') \ll \dot{V}(t)$ for maximum resolution, but reducing $\dot{V}(a')$ excessively will delay particle elution and will risk particle deposition on the inlet splitter. A ratio of $\dot{V}(a')/\dot{V}(t)$ of 0.1–0.3 is generally suitable. The value of $\dot{V}(b')$ is also chosen by compromise. A high $\dot{V}(b')$ hastens elution but causes unwanted sample dilution. Its value must be high enough to supply the flowstream represented by $\dot{V}(t)$ with enough flow left over to flush particles out of outlet b (see eq 10). In most cases $\dot{V}(b')/\dot{V}(t)$ is best chosen in the range 1.5–3.0. Once the inlet flow rates $\dot{V}(a')$ and $\dot{V}(b')$ are set as above, the outlet flow rates $\dot{V}(a)$ and $\dot{V}(b)$ are determined by eqs 9 and 10.

EXPERIMENTAL SECTION

The working dimensions of the SPLITT channel are 5-cm length, 1-cm breadth, and 381-μm thickness. The cell void volume is thus 0.19 mL. The channel thickness w is determined by the combined thickness of two Mylar spacers (0.005 in. or 127 μm

each) and a stainless steel splitter layer (127 μm). All these components are sandwiched between two glass plates in much the same way as larger SPLITT cells are assembled.[2] Finally, these layers are held together firmly by two stainless steel plates and clamped evenly with bolts. The finished cell, whose overall external length is only 12.5 cm, is shown in Figure 2.

One Minipuls peristaltic pump (Gilson, Middleton, WI) and one Kontron 410 pump (Kontron Electrolab, London, UK) provided the independent flows to inlets a′ and b′, respectively, for the wheat starch experiments. Two QD-0 pumps (FMI, Oyster, NY) provided the inlet flows for the potato starch experiments. For most experiments two Model 153 UV absorbance detectors (Altex, Berkeley, CA), both operated at 254 nm, were connected to outlets a and b to monitor the particulate content of the emerging streams. (However, for the particle counting experiments (see Figure 8) a Model 757 UV detector from Applied Biosystems (Ramsey, NJ) with a shorter response time was used.) Samples were injected using a Valco (Houston, TX) injection valve with a 17-μL loop. The two detectors were temporarily connected in series to determine their sensitivity ratio for each type of experiment. Results from the detectors were supplemented by scanning electron microscopy using a Hitachi (Tokyo, Japan) Model S-450 instrument.

The carrier fluid was an aqueous solution of 0.002% (w/v) FL-70 (Fisher Scientific, Fair Lawn, NJ) and 0.005% (w/v) sodium azide (Sigma Chemical Co., St. Louis, MO). Samples consisted of suspensions of 0.1% (w/v) wheat starch, 1% potato starch, 0.3% and 1% glass beads, 0.3% polystyrene latex beads, 0.5% BN abrasive, and 1% quartz (BRC 67) prepared in the carrier fluid. Both starch samples were obtained from Sogetal Inc. (San Francisco, CA). One glass bead sample specified as SRM 1003 from NIST (Washington, DC) had bead diameters between 5 and 30 μm. Samples of 1–5-μm- and 10-μm-diameter glass beads were obtained from Duke Scientific (Palo Alto, CA). The glass beads were centrifuged in 1,4-diiodobutane (Aldrich, Milwaukee, WI) before the ASF experiments to remove those beads with bubbles inside. The quartz powder is a Commision of the European Communities Standard (BCR 67) obtained from Duke Scientific (Palo Alto, CA). The cubic boron nitride (BN) abrasive was obtained from GE Superabrasives (Worthington, OH).

The fraction of sample emerging from outlet b (and thus the fraction with diameter $d > d_c$) was calculated from the equation

$$F_b = A(b)\dot{V}(b)/[A(b)\dot{V}(b) + A(a)\dot{V}(a)] \quad (12)$$

where $A(a)$ and $A(b)$ are the peak areas of the detector response curves at outlets a and b, respectively, and $\dot{V}(a)$ and $\dot{V}(b)$ are the volumetric flow rates from the two outlets, respectively. The same equation applies to the fraction F_a if $A(b)\dot{V}(b)$ in the numerator is replaced by $A(a)\dot{V}(a)$. Clearly

$$F_a + F_b = 1 \quad (13)$$

For the size distribution experiments, all flow rates were kept constant during each run. The outlet flow rates $\dot{V}(a)$ and $\dot{V}(b)$ were then changed, corresponding to different cutoff sizes, for each experiment in the series. New samples were injected for each set of outlet flow rate conditions selected. The retrieval factor F_a for each flow condition corresponds to a point on the cumulative size distribution curve located at the cutoff size as explained in the next section.

RESULTS AND DISCUSSION

In the first experiments, glass beads, wheat starch, potato starch, and the cubic boron nitride abrasive were used to demonstrate, with preparative as well as analytical implications, the successful removal of particles above a selected cutoff diameter. In the final part, the glass beads and quartz samples were used to illustrate the application of SF for determining the particle size distribution.

The performance of the miniature SPLITT cell was evaluated by its application to a variety of particulate samples using different flow and cutoff conditions. Most important initially was testing its capability to split a particulate sample into two subpopulations divided around a designated cutoff diameter d_c. Figure 3 shows the results obtained for wheat starch. In this figure the two detector response curves for the two outlets are shown along with micrographs of the material collected from each outlet. The figure shows that the fractionation into large and small size ranges is largely completed in just over 1 min.

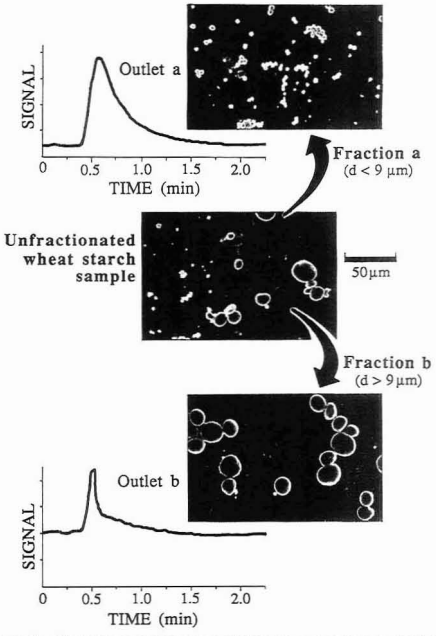

Figure 3. Simultaneous responses of detectors at outlets a and b for wheat starch with $d_c = 9$ μm. The micrographs serve to compare the fractionated particle subpopulations collected from these two outlets with those found in the unfractionated wheat starch sample.

For the wheat starch run shown in Figure 3, a critical diameter of $d_c = 9$ μm was chosen in order to divide the bimodal size distribution (as shown by sedimentation/steric FFF) into its two major components. By applying eq 7 and assuming $\Delta\rho = 0.5$ g/mL and $\eta = 0.01$ poise along with the other known parameters, we calculate that the required $\dot{V}(t) = 0.66$ mL/min. This value was provided in accordance with eq 10 by adjustments giving $\dot{V}(b') = 1.57$ and $\dot{V}(b) = 0.91$ mL/min. The volumetric flow rate of the feed stream was $\dot{V}(a') = 0.52$ mL/min while $\dot{V}(a) = 1.18$ mL/min. Examination of a large set of micrographs shows that the separation is very clean; only a minor population of particles cross over to emerge from the wrong outlet. Most importantly for the analysis (or removal) of oversized particles, larger particles (>9 μm) are recovered from outlet b at virtually 100%.

An experimental study similar to that reported above was carried out for the glass bead sample consisting of particles that are more truly spherical. The size distribution for the sample is known to be monomodal as confirmed by sedimentation/steric FFF with a peak in the distribution at about 16 μm.[17] For the ASF experiment, the cutoff diameter was set at $d_c = 15$ μm. Based on $\Delta\rho = 1.41$ g/mL, this cutoff was obtained using the substream flow rates $\dot{V}(a') = 3.0$, $\dot{V}(b') = 13.0$, $\dot{V}(a) = 8.0$, and $\dot{V}(b) = 8.0$ mL/min. Because of the higher density and the larger cutoff diameter, these flow rates are considerably larger than those applied to the wheat starch. Consequently, the run is completed in less than 0.5 min. This is shown by the detector response curves in Figure 4. This

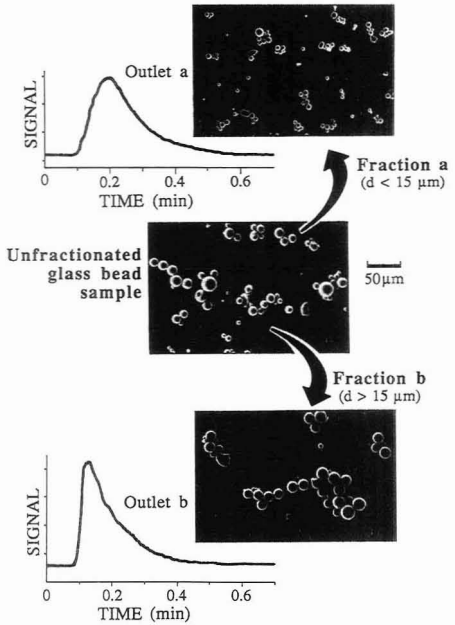

Figure 4. Detector responses and micrographs for NIST glass bead sample. For this run flow rates were adjusted to give d_c = 15 μm.

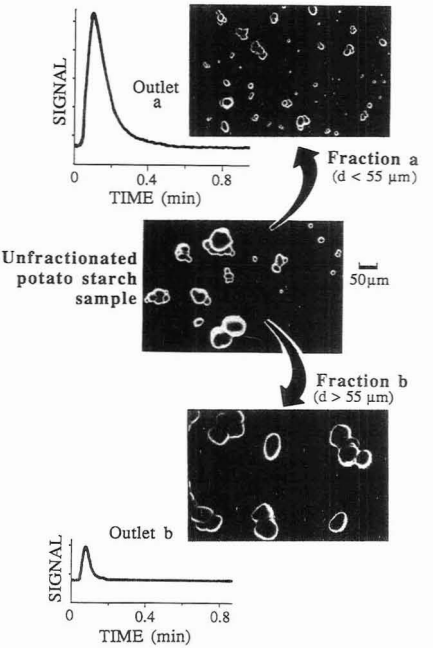

Figure 5. Measurement of oversized potato starch particles, considered as those with diameters above d_c = 55 μm. The small peak observed for the b outlet represents the relative amount of these larger particles. The fractionation around the 55-μm cutoff is confirmed by the electron micrographs.

figure also shows the micrographs of unfractionated and fractionated material. These micrographs again confirm the efficacy of the particle separation.

Oversized particles are almost always those at the extreme upper end of the particle size distribution. In order to examine the effectiveness of fractionation of oversized particles from a wide size distribution, we have adjusted the cutoff diameter to lie near the upper extreme of the size distribution of two quite different particulate materials. The first is a potato starch sample which sedimentation/steric FFF shows to have particles ranging from 8- to 75-μm diameter with a mode at 38 μm. The cutoff diameter for the ASF run was set at 55 μm, which entailed using the flow rates $\dot{V}(a') = 5.0$, $\dot{V}(b') = 30$, $\dot{V}(a) = 30$, $\dot{V}(b) = 5.0$ mL/min. The results are shown in Figure 5. The run is observed to be effectively completed in ~0.3 min.

As expected, the detector response curves show that only a minor portion of the sample, corresponding to the oversized particles constituting the tail of the distribution, emerge from outlet b. The area of the outlet b peak relative to the total area of outlet a and b peaks when corrected for differences in flow rates and detector sensitivity is 6.1%. Interestingly, if one looks at the detector response curve from a sedimentation/steric FFF run, the percent of the peak area corresponding to a diameter larger than 55 μm is 5.8%, in reasonable agreement with the ASF results. The micrographs shown in Figure 5 (and others not shown) confirm that virtually all of the oversized particles are eluted in substream b.

The second material we have examined for oversized particles is cubic boron nitride abrasive with particles much smaller, more angular, and considerably higher in density (3.45 g/cm^3) than the potato starch sample described above. Microscopic examination shows that the size distribution lies between about 0.5 and 7.0 μm. Accordingly, we have set the cutoff diameter at 5 μm using the flow rate $\dot{V}(a') = 0.4$, $\dot{V}(b') = 2.0$, $\dot{V}(a) = 1.4$, and $\dot{V}(b) = 1.0$ mL/min. The results are shown in Figure 6. The run in this case is completed in approximately 2 min. Once again, particles with a size larger than the cutoff diameter are found to be removed completely from the finer material. In this case, the weighted fraction of oversized material, as obtained from peak areas, is 3.9%.

Since oversized particles should constitute a minor fraction of any particular product, it is important to examine the sensitivity and accuracy of ASF for the measurement of low levels of oversized particles. Two factors are especially important here. First is the intrinsic sensitivity of the detector used to monitor outlet substream b, which contains the oversized particles. The present studies were done using commercial UV detectors designed for HPLC work. The sensitivity of such detectors could probably be improved by using a detector that measures scattered light directly rather than indirectly.

The second factor is the possibility that a small fraction of particles below diameter d_c will "leak" across the transport lamina and exit outlet b, thereby interfering with the measurement of the oversized particles. Although larger particles rarely cross over to exit outlet a, as noted above, a few smaller particles can make their way to outlet b along the edges of the SPLITT cell where the flow of the transport lamina is reduced over a short distance due to frictional drag at the edge walls. This leakage is somewhat amplified by the reduced aspect ratio (breadth/thickness = 26) of the small analytical SPLITT cell used here.

We note that for a well-designed SPLITT cell, only a minor fraction of small particles should leak into the large (oversized) fraction. However, when determining the content of oversized particles, which constitute a lesser component at the tail end of a distribution, the leakage of a small fraction of the dominant small particle population will constitute a relatively large contamination of the oversized particles. This is borne

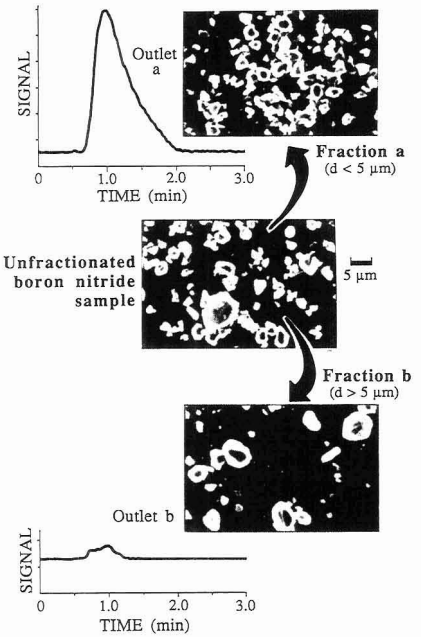

Figure 6. Measurement of oversized particles (those above d_c = 5 μm) in a cubic boron nitride abrasive material.

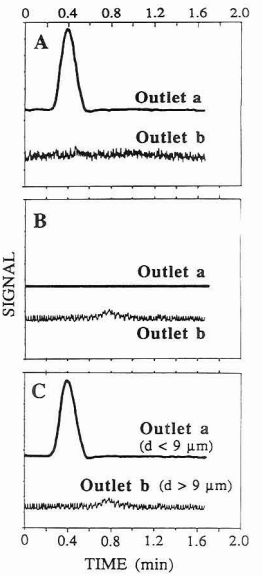

Figure 7. Detector responses at outlets a and b for (A) the injection of 45 μg of 1–5-μm glass beads, (B) 0.25 μg of 10-μm glass beads, and (C) a mixture of the two.

out by comparing Figures 3–6. The electron micrographs for the large particle fractions in Figures 3 and 4 show relatively little small particle contamination because the cutoff diameters are relatively close to the center of the distribution. However, when the extreme tail of the distribution is examined for oversized particles as shown in Figures 5 and 6, the relative contamination level of small particles increases for the reason just described. Although the *number* of small particle contaminants in the latter cases is significant, it is clear from the figures that the relative *mass* or *scattering intensity* contributed by small particle contaminants would be quite negligible compared to that of the true oversized particles. Thus only in rare cases will the leakage of small particles significantly perturb the measurement of oversized particles.

In assessing the meaning and accuracy of oversize measurements, it is important to keep in mind the nature of the detector response. Since in the present case this response is proportional to scattered light intensity, and since in the particle size range under investigation the intensity of scattered light is proportional to the surface area of the particles in the detector cell, the integrated response (i.e., peak area) represents an area-weighted distribution.[17] (For larger particles, these detectors can be used to count particle numbers as discussed below.) In order to convert these area-weighted measurements to relative mass, a correction factor would be necessary. The correction factor, if considered necessary, could be obtained from empirical calibration.

Several sets of experiments were carried out to evaluate sensitivity. In the first set, the detection limit of 10-μm glass beads mixed with a larger population of 1–5-μm glass beads was examined using $\dot{V}(a') = 0.8$, $\dot{V}(b') = 2.8$, $\dot{V}(a) = 2.7$, and $\dot{V}(b) = 0.9$ mL/min, conditions for which $d_c = 9$ μm. It was found that the 10-μm glass beads could be reduced to a level around 0.25 μg (0.5% of the sample mass) before the oversized (outlet b) peak became too noisy for measurement. This is illustrated in Figure 7. In Figure 7A the detector responses for outlets a and b are shown for the injection of 45 μg of 1–5-μm glass beads. We observe that there is no detectable signal for outlet b. Figure 7B shows the two detector responses for the injection of 0.25 μg of 10-μm glass beads. In this case a meaningful (but noisy) peak emerges from outlet b while the detector response from outlet a is quiet. (Since a 0.25-μg sample consists of only ~200 individual beads, the signal at outlet b is expected to be noisy.) Figure 7C shows the two detector responses when a mixture of the above specified quantities of the two glass bead samples is injected into the system. Again the oversized peak is readily discernible, although noisy. These preliminary results show that oversized particles can be measured using our present experimental system down to 0.25 μg, constituting 0.5% by weight of the sample, without significant interference from the smaller particles.

Very similar sensitivity results were obtained using a 50-μg sample of 21-μm polystyrene latex beads and 0.2-μg sample of 28-μm latex with d_c = 25 μm. The oversized (28-μm) particles were detected without measurable interference for the mixture of these two latexes, thus confirming the ability of the present system to measure oversized particles down to the 0.4% level.

The sensitivity to oversized particles exceeding 20 μm diameter can be further enhanced using the Applied Biosystems detector whose response is sufficiently rapid and sensitive to detect single particles passing through the detector cell. This modified system was tested using polystyrene latex beads of 10- and 28-μm diameter. The 28-μm beads could be individually detected as small pulses as shown in Figure 8. However, without fractionation, the signal from 800 of the smaller beads totally obscured the signal from individual larger beads as shown by elution through a 50-cm length of Teflon tubing (0.08-cm inside diameter) immediately pre-

(17) Giddings, J. C.; Moon, M. H.; Williams, P. S.; Myers, M. N. *Anal. Chem.* **1991**, *63*, 1366–1372.

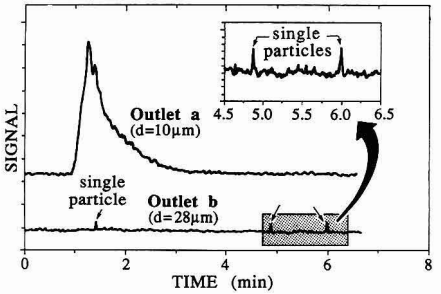

Figure 8. Detector responses for an injection of 60 000 10-μm polystyrene latex beads and three 28-μm beads using the rapid response detector at outlet b. The three individual 28-μm beads can be observed as separate pulses at outlet b.

ceding the detector inlet. However, by using the SPLITT cell, 65 000 beads of 10-μm diameter could be injected without interfering with the individual 28-μm pulses as shown in Figure 8. For this injection, in which three of the larger beads are observed to elute from outlet b, the mass ratio of 10 to 28-μm beads is $\sim 10^3$. This ratio could undoubtedly have been increased further, but no effort was made in this direction. Thus the oversized (28-μm) spheres are detectable at levels at least as low as 0.1% by mass. This result was achieved with flow rate settings $\dot{V}(a') = 0.2$, $\dot{V}(b') = 1.0$, $\dot{V}(a) = 0.7$, and $\dot{V}(b) = 0.5$ mL/min, giving $d_c = 25$ μm.

We noted earlier that size distribution curves could be obtained from gravitational ASF data providing successive runs are made using different cutoff diameters. Size distributions are frequently represented by cumulative distribution curves.[18] A point on the cumulative distribution curve represents the fraction of particles (or of particle mass) with diameters less than that specified on the abscissa scale of the plot. Consequently the ordinate value of a point on such a plot is simply equal to F_a, the fraction of sample emerging from outlet a; the abscissa value is the corresponding cutoff diameter d_c. Thus by carrying out a series of experiments at different flow rate increments $\dot{V}(a) - \dot{V}(a')$ that correspond to different d_c values as expressed by eq 11, a plot of F_a versus d_c can be generated that is equivalent to the cumulative distribution curve.

The type of cumulative distribution measured depends upon the detector response. For a detector that simply counts particles, the ordinate scale of the plot would become the fraction of the total *number* of particles having a diameter less than the specified value. If the detector responds to particle mass (that is, if the peak areas A in eq 12 are proportional to mass), then the plot of F_a versus d_c becomes a cumulative *mass* distribution curve. However, the detectors used here, while capable of providing particle counts for larger particles as noted above, respond primarily to particle surface area,[17] yielding a cumulative *area* distribution curve. For particles of similar geometry, relative area can be converted to relative mass through multiplication by particle diameter (or other size parameter). This correction will provide a cumulative mass distribution curve.

The above approach has been applied to two particulate samples. Results for the NIST glass bead material (SRN 1003) are reported in Figure 9. Both the raw data plot (F_a versus d_c) and the plot corrected to yield cumulative mass distribution show good agreement with the cumulative mass

(18) Allen, T. *Particle Size Measurement*, 4th ed.; Chapman and Hall: New York, 1990; pp 124–169.

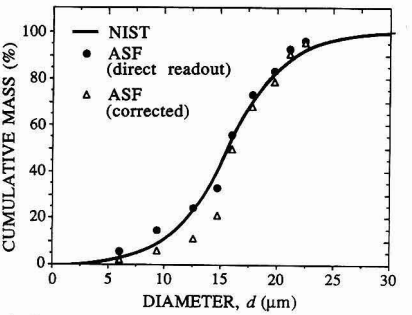

Figure 9. Cumulative size distribution data for NIST glass beads based both on the direct readout of F_a from ASF operation and on corrections to the above accounting for light scattering. The NIST reference curve is shown for comparison.

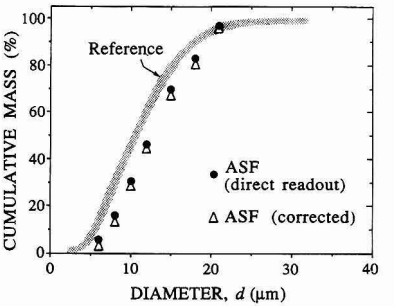

Figure 10. Cumulative mass distribution data for quartz particles (BCR 67) compared to reference curve.

distribution curve provided by NIST. For the more blocky quartz particles of the second sample (BCR 67), the departure of the ASF results from the reference curve is somewhat greater than for the glass beads as shown in Figure 10. However, the agreement is still quite satisfactory.

While each data point in Figures 9 and 10 represents a discrete measurement of F_a under different flow (and thus cutoff) conditions, the cumulative distribution curve could be generated in a single experiment in which the flow rate $\dot{V}(a)$ is varied gradually but continuously (with $\dot{V}(a')$ held constant) in order to "scan" across the diameter range of interest. The F_a value accumulated from the detector signals at any given time would be ascribed to the flow conditions (and the corresponding d_c calculated from eq 11) applicable a brief period before the measurement is made in order to account for the short time lag between the separation and the detector response. Further work would be needed to establish a value for the time lag.

CONCLUSIONS

While SPLITT fractionation (SF) was conceived as a method for the clean preparative fractionation of particulate and molecular materials,[1–4] the high intrinsic speed of this technique gives it considerable analytical potential for certain applications. This study demonstrates the efficacy of analytical SPLITT fractionation (ASF) for the rapid determination of oversized particles and, to a lesser degree, for the construction of particle size distribution curves. The results for the particle populations examined are encouraging. The two most important features of these results are that the observed run times, as predicted, are very short, lying for the

most part (except as shown in Figure 8) in the range from 0.3 to 2.0 min and, second, that the fractionation is relatively clean and in good agreement with the calculated cutoff diameter. There is virtually no contamination of the small particle fraction by oversized particles (which is perhaps most significant for preparative applications) whereas there is a small leakage of small particles into the oversized fraction. The latter leakage does not appear sufficient to perturb the measurement of oversized particles.

The fast separations achieved here are more a consequence of the intrinsic high speed of the method than of any special effort to maximize speed. However, our results show clearly that separation speed is correlated with channel flow rate which, in turn, is adjusted to the particle population being examined. More specifically, the flow rate of the transport lamina is specifically tied to particle density and cutoff diameter as shown by eq 7. This relationship suggests that this specific flow rate, and thus the speed of separation, will increase in proportion to $\Delta\rho d_c^2$. The time of separation will thus be roughly proportional to $1/\Delta\rho d_c^2$. (Other flow rates in the SPLITT cell including $\dot{V}(a')$ and $\dot{V}(b)$ can also be adjusted to influence separation time but once optimized these usually increase in proportion to $\dot{V}(t)$.) This predicted dependence of analysis time on particle parameters is confirmed qualitatively by our results. Thus the run time is shortest (0.3 min) for the larger potato starch particles using a cutoff diameter of 55 μm (Figure 5). The analysis time is longer (>1 min) for wheat starch where a cutoff diameter of 9 μm was used (Figure 3). The separation time is also relatively long (2 min) for the boron nitride abrasive, where the cutoff diameter is 5 μm, although this small cutoff diameter is somewhat offset by the higher density (3.45 g/cm^3) of this material. By extrapolation of the above results, we conclude that high-speed operation could no longer be maintained as particle diameters dropped to a few μm and/or as particle densities approach those of the carrier liquid. In this case it would be necessary to amplify the driving force by using a centrifugal SPLITT system in order to maintain timely analysis.

ACKNOWLEDGMENT

This work was supported by Grant CHE-9102321 from the National Science Foundation.

GLOSSARY

a	outlet at cell wall A
a′	feed inlet
A	cell wall adjacent to feed inlet
b	cell breadth
b	outlet at cell wall B
b′	carrier inlet
B	cell wall adjacent to carrier inlet
d	particle diameter
d_c	cutoff diameter
F_a	fraction of component exiting outlet a
F_b	fraction of component exiting outlet b
G	sedimentation field strength
L	cell length
s	sedimentation coefficient
U	velocity induced by field
$\dot{V}$	volumetric flow rate through SPLITT cell
$\dot{V}(a)$	volumetric flow rate exiting outlet a
$\dot{V}(a')$	volumetric flow rate of feed inlet substream a′
$\dot{V}(b)$	volumetric flow rate exiting outlet b
$\dot{V}(b')$	volumetric flow rate entering inlet b′
$\dot{V}(t)$	volumetric flow rate of transport lamina
w	cell thickness
$\Delta\dot{V}$	volumetric flow rate of filament traversed by particles
$\Delta\dot{V}_c$	cutoff value of $\Delta\dot{V}$
$\Delta\rho$	density difference of particles and carrier
η	carrier viscosity
ρ	carrier density
ρ_p	particle density

RECEIVED for review April 20, 1992. Accepted September 23, 1992.

Improvements in the Computerized Analysis of 2D INADEQUATE Spectra

Reinhard Dunkel,† Charles L. Mayne,† Ronald J. Pugmire,‡ and David M. Grant*,†

Departments of Chemistry and Fuels Engineering, University of Utah, Salt Lake City, Utah 84112

The carbon skeleton of a molecule can be determined by using the powerful 2D INADEQUATE experiment, but the method suffers from very poor sensitivity at natural carbon-13 abundance. A computer program, described previously, has been significantly improved in its ability to recognize AB spectral patterns corresponding to carbon–carbon bonds which makes it possible to evaluate reliably spectra with rms S/N ratio as low as 2.5, i.e., nearly 1 order of magnitude below the level required for routine manual interpretation. Application of the INADEQUATE experiment to samples containing as little as 20 μmol of a compound of interest is now possible. The method is described in detail and critically evaluated by means of examples and simulations.

INTRODUCTION

Two-dimensional (2D) nuclear magnetic resonance (NMR) spectroscopy has become a prominent technique for the determination of molecular structure. While computerization has dramatically increased the amount and variety of data obtainable from such spectroscopic measurements, comparatively little effort has been expended to use computers to improve and accelerate the data interpretation process. Previous research aimed at using computer-assisted or automated techniques to interpret 2D NMR spectra have consisted mainly of the application of direct techniques[1,2] (e.g., cluster analysis and peak picking), linear prediction or maximum entropy methods,[3] or least-squares parameter optimization[4] in cases of severe overlap and/or strong coupling. Such techniques have been applied almost exclusively to chemical shift correlation spectra.

The 2D version of the incredible natural abundance double quantum transfer experiment (INADEQUATE)[5,6] is one of the most elegant 2D structure elucidation techniques. A single spectrum has the potential to reveal the complete carbon skeleton of a molecule. The method depends on creation of double quantum coherence in a spin system consisting of two bonded ^{13}C nuclei. At natural abundance for ^{13}C (1.1%) about one molecule in ten thousand will have two ^{13}C nuclei participating in a particular bond. Thus, the method will be very insensitive compared to the more routine experiments observing carbon in molecules with only one ^{13}C nucleus. To take advantage of this elegant experiment, some have synthetically enriched the compound of interest or used large amounts of material. For example, Oh et al.[7] used 2D INADEQUATE spectra in conjunction with a "semiautomated graphics package" to identify individual peptides in proteins uniformly labeled to 26% in ^{13}C. In many cases, however (natural products are a particularly good example), neither of these solutions to the problem of sensitivity is practical.

In previous publications[8,9] we described a computer program capable of extracting bond information from low signal-to-noise ratio (S/N) 2D INADEQUATE spectra in a fully automated fashion. The well-defined structural complexity of 2D INADEQUATE spectra can be exploited to define a parametric model, the use of which significantly improves the detection limit of an automated bond extraction algorithm. In this paper we describe substantial improvements to the technique permitting data with modest digital resolution and a S/N as low as 2.5 to be analyzed. (In this paper, signal-to-noise ratios will be given as the ratio of peak signal intensity to root-mean-square, rms, noise. A S/N of three means that the signal is about the same amplitude as the peak-to-peak noise in a spectrum.) The reliability of the method is carefully explored by means of computer simulations and analysis of a known compound. With the discussed improvements the routine determination of the carbon backbone of 20 μmol of a compound is possible at natural abundance of ^{13}C.

AUTOMATED SPECTRAL ANALYSIS

At first consideration a dataset of sufficient size to adequately digitize a 2D INADEQUATE spectrum would seem to preclude the use of compute-intensive modeling techniques for spectral analysis. A typical 2D carbon spectrum at magnetic fields above 11 T, would have peaks with line widths of about 0.5 Hz dispersed over as much as 25 kHz in both dimensions. Digitization of a hypercomplex 2D spectrum to take full advantage of the available spectral resolution would require 100 GB of data. This number clearly shows the amazing resolution obtainable by 2D NMR spectroscopy, but useful spectra may be acquired with the digitization reduced by 3 or more orders of magnitude. These practical adjustments bring total data acquisition time and requirements for processing and storage within reasonable limits. However, truncation and underdigitization of the spectrum must then be dealt with in the data analysis.

Modeling of the hundreds of megabytes of data still cannot be accomplished in a reasonable time using currently available computer systems. Figure 1 illustrates, for the molecular fragment $>CHCH_2CH_3$, the approach taken to bring the problem within the capability of readily available computer workstations. From a proton-decoupled one-dimensional carbon spectrum, the chemical shifts of all ^{13}C nuclei are known. For every pair of bonded carbon atoms, the 2D

* To whom correspondence should be addressed.
† Department of Chemistry.
‡ Department of Fuels Engineering.

(1) Glaser, S.; Kalbitzer, H. R. *J. Magn. Reson.* **1987**, *74*, 450.
(2) Meier, B. U.; Mádi, Z. L.; Ernst, R. R. *J. Magn. Reson.* **1987**, *74*, 565.
(3) Gesmar, H.; Led, J. J. *J. Magn. Reson.* **1989**, *83*, 53.
(4) Mádi, Z. L.; Ernst, R. R. *J. Magn. Reson.* **1988**, *79*, 513.
(5) Bax, A.; Freeman, R.; Kempsell, S. P. *J. Am. Chem. Soc.* **1980**, *102*, 4849.
(6) Bax, A.; Freeman, R.; Frenkiel, T. A. *J. Am. Chem. Soc.* **1981**, *103*, 2102.
(7) Oh, B. H.; Westler, W. M.; Darba, P.; Markley, J. L. *Science* **1988**, *240*, 908.
(8) Dunkel, R.; Mayne, C. L.; Curtis, J.; Pugmire, R. J.; Grant, D. M. *J. Magn. Reson.* **1990**, *90*, 290.
(9) Dunkel, R. Ph.D. Thesis, University of Utah, December 1990.

0003-2700/92/0364-3133$03.00/0

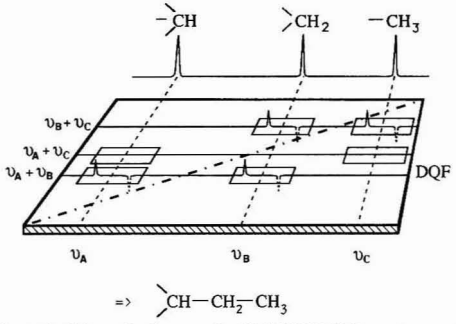

Figure 1. Schematic diagram of a 2D INADEQUATE spectrum and the corresponding 1D carbon-13 spectrum for a three carbon molecular fragment.

spectrum contains a four-line pattern restricted to two small regions[10] that we will call the "fitting window" symbolized by a pair of rectangles as shown in Figure 1. Each rectangle contains two of four transitions comprising the spectrum of a coupled two-spin system. The spectral lines are derived from a double quantum coherence and are antiphase rather than both positive as in normal 1D spectra. Each doublet encloses the chemical shift frequency of one of the bonded carbons on the horizontal chemical shift axis. In the second dimension, the double quantum frequency (DQF) axis, all four transitions appear at a frequency that is the sum of the two chemical shifts. In Figure 1 four transitions can be found, two with shift frequencies of the methine carbon at approximately $\nu_A \pm J/2$, where J is the carbon–carbon scalar coupling constant, and two at approximately $\nu_B \pm J/2$ for the methylene carbon. All four transitions have a DQF of approximately $\nu_A + \nu_B$. A similar bond pattern between the methylene (ν_B) and methyl (ν_C) carbons also exists, but no bond pattern is found between the methine (ν_A) and methyl (ν_C) carbons.

The strategy, then, is to search for bond patterns only in those areas of the 2D spectrum where bond patterns could exist consistent with a pair of resonances in the 1D spectrum. The area to be searched for a bond pattern typically comprises only about 0.03% of the total dataset. For n carbon atoms there are $n(n-1)/2$ possible pairs of carbon atoms, and the time required for an exhaustive search of all potential bond regions is proportional to n^2. A spectroscopist is able to interpret only fairly simple spectra using this tedious approach precluding the application of this visual method to more complex spectra. Fortunately, the approach is well structured for computer analysis in that only a fairly small dataset (a few kilobytes) must be examined for each potential bond. Consequently, a relatively large number of bond regions can be processed with reasonable computing resources.

The smallest dataset described in this and the accompanying paper contains more than 33 million floating point numbers. For each bond pattern to be identified about 10 of the numbers will contain appreciable signal amplitude. The traditional approach is to acquire spectra with sufficient S/N to be able to manually phase the dataset and to identify all signals from carbon–carbon couplings by examining the pure absorption quadrant of the data. This will only be possible if the peaks protrude well above the noise in the spectrum. The detection limit of the program CCBOND (Carbon–Carbon BOND) described in this paper lies well below the S/N at which a spectroscopist can detect bond patterns. It will be shown subsequently that this increased sensitivity can be achieved by examination of a parameter response surface associated with the least-squares fitting process. The least-squares fitting process filters the data in such a way that the effective S/N for bond detection is markedly increased.

CONSTRUCTION OF THE PARAMETRIC MODEL

The model equation used previously[8] to describe the 2D INADEQUATE spectrum incorporated only the absorption mode spectrum of a system of two coupled spins. Purely Lorentzian line shapes were assumed in both spectral dimensions. While it has proven very useful, this earlier model had certain limitations:

(1) By restricting the previous model to the pure absorption mode, the other three quadrants of the experimental hypercomplex dataset are ignored. Since the noise in these other quadrants is at least partially uncorrelated to the noise in the pure absorption mode, independent information about the spins is being discarded.

(2) Truncation of the data acquisition in the time domain caused the spectrum to be convolved with a sinc function; the more severe the truncation, the more the sinc function will dominate the line shape causing a Lorentzian model to fit the data poorly. Also, manual phasing of the spectrum is difficult for reasons to be discussed later. In order to keep data acquisition time and mass storage requirements reasonable, both dimensions of a 2D INADEQUATE FID usually are truncated, and the DQ dimension is normally severely distorted. Apodization of the time domain data has been used to limit the effects of truncation, but this only partially solves the problem and often degrades the resolution of the spectrum unacceptably.

(3) In the previous pure absorption mode model, it was necessary to phase correctly the spectrum for a pure absorption presentation in both dimensions. An application of the first-order phase correction is inappropriate because the lines are usually aliased in the double quantum direction to minimize the size of the data set. This can be done without reducing the information content of the spectrum, but the phase correction must then be applied to the lines true position and not its apparent position. Heretofore this phasing has been done manually using the software supplied by the spectrometer vendor. Since only a linear phase correction was available, the best solution to this problem was often a compromise that was found to be unsatisfactory in many cases.

Removal of these three limitations, while simple in principle, adds considerable complexity to the required computer simulations. One simply extends the model to include all four quadrants of the hypercomplex spectrum and uses a line shape consisting of a Lorentzian convolved with a sinc function. Parameterization of the full hypercomplex line shape leads naturally to the inclusion of the phases of the lines in both dimensions as parameters. Once this is done, the need to phase the spectrum for pure absorption is eliminated, and the spectrum is simply simulated for the experimental phases appropriate for any one quadrant. The equations for a model incorporating these features will be described below.

In both our previous and present models the scalar coupling terms in the Hamiltonian were included in a full quantum mechanical treatment so as to correctly predict the frequencies and intensities of the four transitions for all values of coupling constants and shifts. Thus, complete generality is preserved for both AB cases, where second-order effects become important, but also for AX cases. Because our treatment is totally general and not limited to first-order cases, we have

(10) Bernassau, J. M.; Boissiere, F.; Thomas, J. F. *Comput. Chem.* **1986**, *10* (4), 253.

chosen to designate our coupled two-spin system with the unrestricted AB designation even though it is exact also for AX cases. If not stated otherwise, time parameters are stated in seconds, frequency parameters in hertz, and phase angles in radians.

The spectral response of an AB spin system in the 2D INADEQUATE spectrum, S, is a function of positions ν_1 along the DQ-axis and ν_2 along the chemical shift axis and can be expressed as a product of the line shapes in the single quantum, S^{SQ}, and the double quantum, S^{DQ}, directions:

$$S(\nu_1,\nu_2) = S^{DQ}(\nu_1)S^{SQ}(\nu_2) \quad (1)$$

provided the line shape in the DQ dimension, S^{DQ}, is the same for all four transitions. The line shape of these transitions in both shift and DQ dimension is nominally Lorentzian due to transverse relaxation and dephasing due to magnetic field inhomogeneity during the acquisition time. This shape is then convolved with a sinc function as a consequence of limited data acqusition. The equation in one dimension for a Lorentzian convolved with a sinc lineshape is[11]

$$S_{abs}{}^{1D}(\Delta\nu,T_2,T_A) = \frac{T_2}{1+[2\pi T_2\Delta\nu]^2}\Big[1 + \exp\Big(-\frac{T_A}{T_2}\Big)\{2\pi T_2\Delta\nu \sin[2\pi T_A\Delta\nu] - \cos[2\pi T_A\Delta\nu]\}\Big] \quad (2)$$

for the absorption mode, $S_{abs}{}^{1D}$, and

$$S_{disp}{}^{1D}(\Delta\nu,T_2,T_A) = \frac{T_2}{1+[2\pi T_2\Delta\nu]^2}\Big[2\pi T_2\Delta\nu - \exp\Big(-\frac{T_A}{T_2}\Big)\{2\pi T_2\Delta\nu \cos[2\pi T_A\Delta\nu] + \sin[2\pi T_A\Delta\nu]\}\Big] \quad (2')$$

for the dispersion mode, $S_{disp}{}^{1D}$, where T_2 and T_A are the relaxation and acquisition times, respectively, and $\Delta\nu$ is the deviation of the independent frequency variable, ν_1 or ν_2, from the center of the line. For an arbitrarily phased line, the observed real spectrum will consist of a linear combination of absorption and dispersion mode dictated by the phase angle, ϕ

$$S^{1D}(\Delta\nu,T_2,T_A,\phi) = S_{abs}{}^{1D}(\Delta\nu,T_2,T_A)\cos\phi + S_{disp}{}^{1D}(\Delta\nu,T_2,T_A)\sin\phi \quad (3)$$

The imaginary part of the spectrum will have the same functional form, but ϕ must be replaced by $\phi + \pi/2$. All four satellite signals of the ^{13}C–^{13}C coupling are assumed to possess, in the DQ-direction, the same line shape; and, hence, S^{DQ} is equal to S^{1D} with $\Delta\nu = \nu_1 - \nu_{DQ}$, $T_2 = T_2{}^{DQ}$, $T_A = T_A{}^{DQ}$ and $\phi = \phi_{DQ}$: so that

$$S^{DQ} = S^{1D}(\nu_1 - \nu_{DQ},T_2{}^{DQ},T_A{}^{DQ},\phi_{DQ}) \quad (4)$$

The shift direction contains the four satellite signals belonging to an AB spin system, described by the scalar coupling constant J and the chemical shifts ν_A and ν_B of the two relevant carbons. The transition frequencies for the A1, A2, B1 and B2 transitions are given by

$$\nu_{A1} = \frac{\nu_A + \nu_B + J + R}{2}$$

$$\nu_{A2} = \frac{\nu_A + \nu_B - J + R}{2}$$

$$\nu_{B1} = \frac{\nu_A + \nu_B - J - R}{2}$$

$$\nu_{B2} = \frac{\nu_A + \nu_B + J - R}{2}$$

$$R = \sqrt{(\nu_A - \nu_B)^2 + J^2} \quad (5)$$

The relative intensities of A1 and B1 transitions, $I_{A1,B1}$, and the A2 and B2 transitions, $I_{A2,B2}$, can be obtained from the quantum mechanical description of a generalized AB spin system:[12]

$$I_{A1,B1} = 1 - J/R$$

$$I_{A2,B2} = 1 + J/R \quad (6)$$

The INADEQUATE pulse sequence suppresses the strong signals of isolated ^{13}C spins by producing double quantum coherence, which cannot be formed by isolated spins. When the double quantum coherence is transformed back into the observable single quantum coherence, the net magnetization is theoretically zero, and the doublet components are antiphase.[13] The pulse sequence used produces the downfield member of each doublet in positive and the upfield member in negative absorption for $J > 0$. To reduce the number of parameters, the phases as well as the relaxation times of both transitions of a doublet are assumed to be identical. The expectation function for the shift direction then becomes

$$S^{SQ} = I_1I_{A1,B1}S^{1D}(\nu_2 - \nu_{A1},T_{2,A}{}^{SQ},T_A{}^{SQ},\phi_A) - I_2I_{A2,B2}S^{1D}(\nu_2 - \nu_{A2},T_{2,A}{}^{SQ},T_A{}^{SQ},\phi_A) + I_3I_{A2,B2}S^{1D}(\nu_2 - \nu_{B2},T_{2,B}{}^{SQ},T_A{}^{SQ},\phi_B) - I_4I_{A1,B1}S^{1D}(\nu_2 - \nu_{B1},T_{2,B}{}^{SQ},T_A{}^{SQ},\phi_B) \quad (7)$$

where I_1–I_4 are the factors needed to convert the relative intensities to observed intensities for each transition, ϕ_A and ϕ_B are the phase angles, $T_{2,A}{}^{SQ}$ and $T_{2,B}{}^{SQ}$ are the transverse relaxation times for each doublet, and $T_A{}^{SQ}$ is the acquisition time.

Equations 1–7 describe the spectral response expected from each carbon–carbon bond in one of the four datasets of a phase-sensitive 2D INADEQUATE spectrum. The remaining three datasets then differ only in their relative phase angles and can also be calculated from these equations by shifting the phase angles of imaginary datasets by $\pi/2$. So if eqs 1–7 are taken to describe the real/real dataset with phase angles ϕ_A, ϕ_B, and ϕ_{DQ}, then the phase angles for the real/imaginary dataset are ϕ_A, ϕ_B, and $\phi_{DQ} + \pi/2$, for the imaginary/real dataset they are $\phi_A + \pi/2$, $\phi_B + \pi/2$, and ϕ_{DQ}, and finally for the imaginary/imaginary data the phase angles are $\phi_A + \pi/2$, $\phi_B + \pi/2$ and $\phi_{DQ} + \pi/2$. The sign of the factor $\pi/2$ depends on the phase shift between the normal and quadrature components in the INADEQUATE pulse program and can be negative for one or both dimensions.

A dataset acquired from a mixture of 56% 1,2,3,4-tetrahydro-1,1-dimethylnaphthalene (1,1-dimethyltetralin)

(11) Marshall, A. G.; Comisarow, M. B.; Parisod, G. *J. Chem. Phys.* **1979**, *71* (11), 4434.

(12) Corio, P. L. *Structure of High-Resolution NMR Spectra*; Academic: New York, 1966; p 192.

(13) Bax, A. *Two-Dimensional Nuclear Magnetic Resonance in Liquids*; Delft University: Delft, Holland, 1982; p 160.

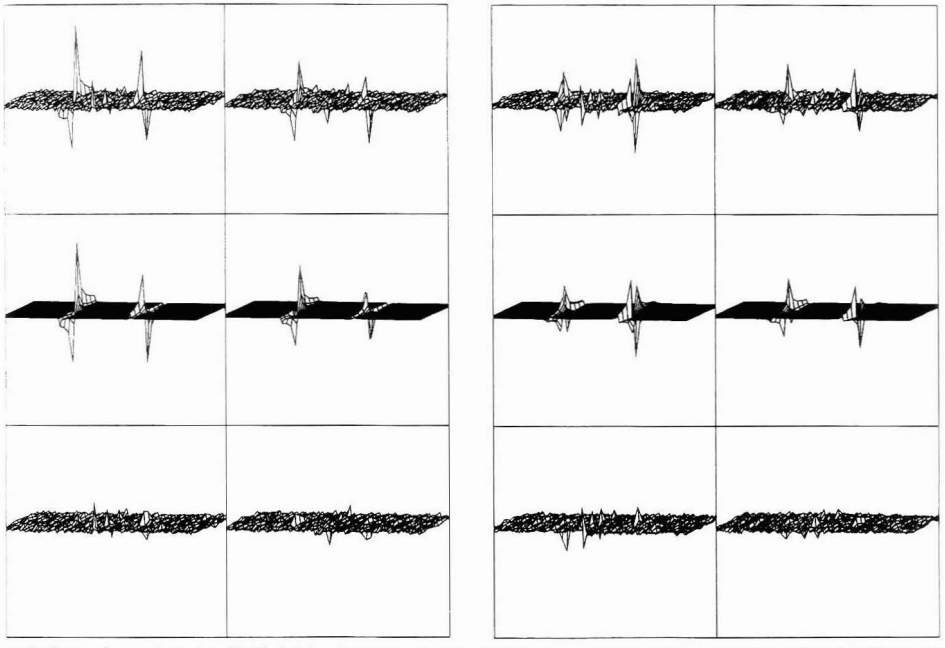

Figure 2. Regression results for bond 2–3 in 1,1-dimethyltetralin. From top to bottom are shown the unphased experimental, the best-fit calculated, and the residual spectrum. The real/real and real/imaginary quadrants of the hypercomplex dataset are shown on the left and right, respectively.

and 6% of the isomeric 2-ethyl-1,2,3,4-tetrahydronaphthalene (2-ethyltetralin) in $CDCl_3$ was described in a previous publication[8] and will be used here to illustrate the computerized analysis of 2D INADEQUATE spectra. Figures 2 and 3 show the spectrum of bond 2–3 of 1,1-dimethyltetralin with small second-order effects, to illustrate the agreement between experimental data and the best-fit model. The rows from top to bottom show the unphased experimental spectrum, the best-fit spectrum calculated from the equations above, and the difference between experimental and simulated spectra. Most of the nonrandom residuals are due to incompletely suppressed single quantum magnetization appearing close to the chemical shifts of each carbon. The remaining residuals near each line are due primarily to slightly non-Lorentzian line shapes caused by magnet inhomogeneity.

Figures 4 and 5 show a comparison of experimental and simulated bond patterns with prominent second-order effects. This larger spectral region contains the partly overlapping signals of bond 6–7 in the upper right of the spectrum and bond 7–8 at the left side of the spectrum, both with prominent second-order effects. The B doublet of bond 5–6 appears in the lower right of the region shown. The simulation was calculated as the sum of the three individually determined bond signals mentioned above without any correction for signal overlap. The experimental data contain additional signals, both from 1,1-dimethyltetralin and 2-ethyltetralin, that are not caused by these three bonds and are not included in the simulation. In summary, Figures 2–5 have been given to show that the model equation captures all the main features in 2D INADEQUATE spectra using all four quadrants of the hypercomplex data. The next sections will show how bond information may be extracted from the data and establish criteria for the reliability of the method.

RESPONSE SURFACE MAPPING

The previous section described how a bond signal is a function of 16 parameters. It is possible, at least in principle, to refine initial parameter estimates to describe the spectral pattern in the fitting window, to estimate the errors in the parameter values, and to base the identification of a bond pattern on these values. This process was shown[8] to work well if the initial estimates are sufficiently accurate for convergence to the spectral pattern and if signal overlap is not present in the fitting window that could cause convergence to an unwanted spectral pattern. However, compliance with these two conditions can be difficult in some cases, and this section describes a way to overcome these limitations.

A suitable estimate of the one-bond carbon–carbon coupling constant,[14–18] usually unavailable from prior knowledge, is especially crucial for convergence to the correct spectral pattern. The initial estimate of J used by CCBOND is based on the hybridization of each carbon atom suggested by its chemical shift.[8] Since the correlation between chemical shift and coupling constant is only approximate, these estimates can be inaccurate by 10 Hz or more. The initial values of

(14) Wasylishen, R. E. Spin-Spin Coupling Between Carbon-13 and the First Row Nuclei. In *Annual Reports on NMR Spectroscopy*; Webb, G. A., Ed.; Academic Press: New York, 1977; Vol. 7, pp 245–291.

(15) Wray, V. Carbon-Carbon Coupling Constants: A Compilation of Data and a Practical Guide. In *Progress in NMR Spectroscopy*; Pergamon Press: New York, 1979; Vol. 13, pp 177–256.

(16) Wray, V.; Hansen, P. E. Carbon-Carbon Coupling Constants: Data. In *Annual Reports on NMR Spectroscopy*; Webb, G. A., Ed.; Academic Press: New York, 1981; Vol. 11A, pp 99–181.

(17) Marshall, J. L. *Carbon-Carbon and Carbon-Proton NMR Couplings: Applications to Organic Stereochemistry and Conformational Analysis*; VCH: New York, 1983; Methods in Stereochemical Analysis, Vol. 2.

(18) Kluge, H. Dissertation zur Erlangung des Grades eines Doktors der Naturwissenschaften; Technische Universität Braunschweig, 1984.

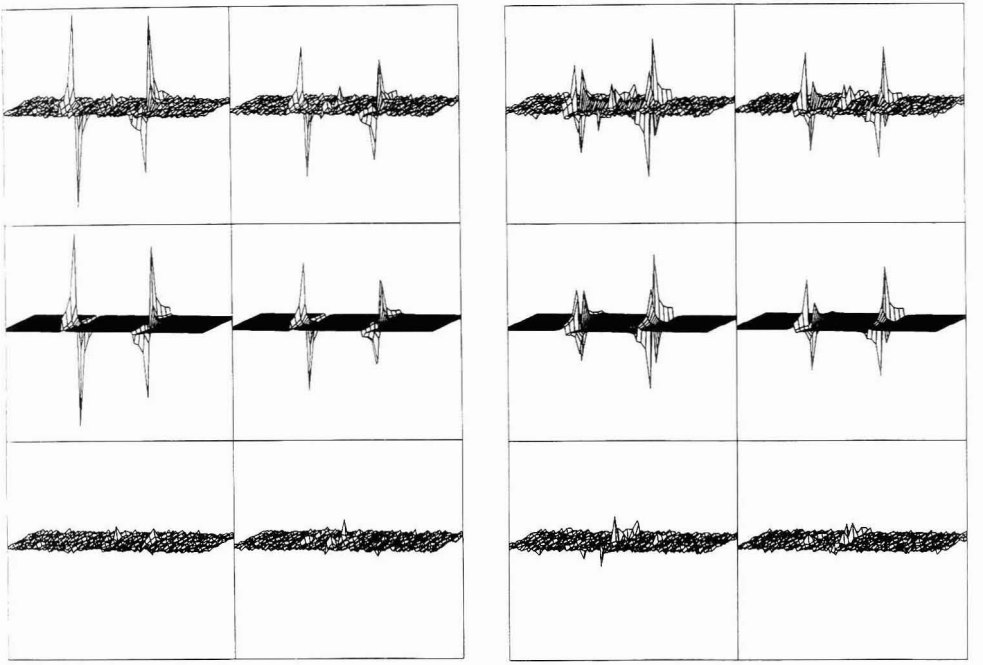

Figure 3. Regression results for bond 2–3 in 1,1-dimethyltetralin. From top to bottom are shown the unphased experimental, the best-fit calculated, and the residual spectrum. The imaginary/real and imaginary/imaginary quadrants of the hypercomplex dataset are shown on the left and right, respectively.

chemical shift frequencies are obtained from the 1D spectrum where the adjacent nuclei are ^{12}C, and the accuracy of these values is limited by isotope shifts induced when these ^{12}C nuclei are replaced by ^{13}C in the INADEQUATE spectrum. ^{13}C versus ^{12}C isotope shifts of up to 0.027 ppm have been observed.[19]

When the signals of more than one bond pattern appear in a given fitting window, ambiguities may arise. These overlap situations are aggravated by the acquisition of 2D INADEQUATE spectra with severe underdigitization for reasons explained above. Consider, for example the eight lines shown schematically in Figure 6. This represents a slice from a fitting window parallel to the chemical shift direction. The eight transitions are resolved in the shift direction but are unresolved in the orthogonal DQ direction, due in part to less than optimal digitization. For example, such a pattern might occur for bonded carbons at ν_A and ν_B and bonded carbons at $\nu_A + \epsilon$ and $\nu_B + \epsilon'$. If ϵ and ϵ' are of the order of the expected isotope shift and the scalar couplings are similar for the two bonds, then searching for a bond in this eight-line pattern could yield as many as four different assignments shown in Figure 6a. Since all the DQ frequencies differ by a term of order ϵ, more accurate knowledge of the DQ frequency independent of the values of the chemical shifts would remove the ambiguities not resolvable in a severely under-digitized DQ spectrum. If, in addition to the ambiguity created by similar coupling constants, ϵ is within a line width equal to ϵ' as shown in Figure 6b, two additional interpretations expand the number of possible assignments to a total of six. Furthermore, interpretations 2, 3, 5, and 6 have the same DQ frequency and would be indistinguishable even for better DQ resolution.

A regression analysis with a one-bond model is not capable of correctly analyzing such overlap situations. For the four carbon atoms involved, there are $(n-1)n/2 = 6$ bond regions to be considered. This overlap region could contain a bond between two carbons on the left side and a bond between two carbons on the right side of Figure 6. Should such bonds exist, they would yield strongly second-order AB patterns with quite different DQ frequencies than those shown. Each of the remaining four searches may yield any one of the potential four or six bond patterns shown in Figure 6. In each of these cases the result obtained in the convergence could depend on the initial parameters used in the analysis and may not necessarily be correct.

Other overlap situations leading to ambiguous results are also possible, and a way to deal with this problem is important to the automated procedure. Since a correct interpretation is not always guaranteed, an automated algorithm for extracting connectivity is needed, at least, to detect and to enumerate all possible bond interpretations. Such a suitable algorithm is used to explore all plausible interpretations of the data in a specific fitting window, and an exhaustive search of all fitting windows then completes the enumeration of all possible interpretations of spectral signals. When all four resonances of an identified pattern are not part of any other interpretation, a valid bond pattern has been identified that can be assigned unambiguously to a specific pair of carbon resonances in the 1D spectrum. The remaining cases must be resolved using additional information not contained in the INADEQUATE spectrum. Examples of these ambiguous

(19) Hansen, P. E. *Isotope Effects on Nuclear Shielding*, in *Annual Reports on NMR Spectroscopy*; Webb, G. A., Ed.; Academic Press: New York, 1983; Vol. 15, pp 105–234.

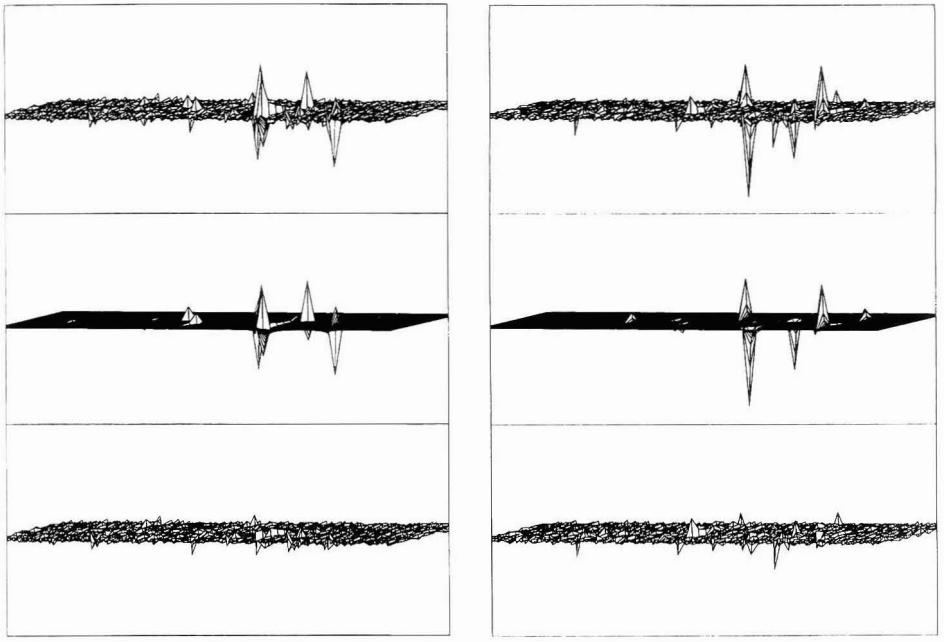

Figure 4. Regression results for 1,1-dimethyltetralin showing overlapping and highly second order patterns. The strong doublet at the right front of the spectrum is the B part of bond 5–6. At the rear on the right is bond 6–7 and on the left is bond 7–8. From top to bottom are shown the unphased experimental, the best-fit calculated, and the residual spectrum. The real/real and real/imaginary quadrants of the hypercomplex dataset are shown on the left and right, respectively.

situations are described in the accompanying application paper for a cholesterol sample.[20]

It is noteworthy that all possible interpretations of the spectral patterns encountered in Figure 6 differ at least in one of the two transition frequencies, ν_A or ν_B, arising from the two relevant carbon atoms or in the magnitude of the $^{13}C-^{13}C$ coupling constant, J. Only a change in one of these three parameters (ν_A, ν_B, J) can lead to different bond patterns as illustrated in Figure 6b. None of the remaining parameters in the model equation or even any combination of these parameters can lead to more than one valid bond pattern even though variations in these parameters may produce local minima on the response surface. Exploration of such minima is unnecessary when only a bond test is required. The response surface terminology is used here to describe the functional dependence of the sum-of-squared residuals on the 16 adjustable parameters in the model equation. Even though all of these parameters are not generally included in the regression, to be discussed in detail later, the response surface potentially may have up to 16 dimensions, making the full surface impractical to compute and impossible to display. Thus, the alternative ambiguous interpretations differ at least in one of the two chemical shift frequencies or in the coupling constant, and these three parameters form a special three-dimensional subspace of the 16 dimensional parameter space that is critical in determining all local minima important to bond identification.

The model equation can be used to calculate the sum-of-squared residuals between a low S/N 2D INADEQUATE spectral region and the corresponding simulation as a function of the two chemical shift frequencies and the scalar coupling constant. While a bond signal in the 2D spectrum consists of four transitions, it becomes a single minimum in the sum-of-squared-residuals function. Every valid interpretation of a spectral pattern has a unique combination of chemical shift frequencies and a coupling constant, and each minimum in the sum-of-squared residuals for the 3D parameter subspace corresponds to an alternative interpretation of the spectral data. Enumeration of all such minima will catalog all possible interpretations of the spectral signals in the 2D spectrum. It is evident from Figure 6 that a dataset with these properties has to include the coupling constant as well as the two shifts since bond patterns 5 and 6 are only resolved by the J parameter. Thus, ambiguous signal assignments can, at times, be directly identified from the position of the minima. Every signal in the real-valued 3D parameter space comprises the information from all four quadrants of the hypercomplex dataset for both halves of the fitting window filtered through the model equation. Use of the response surface function results in an increase in the S/N ratio of about one order of magnitude.

Figure 7 shows a simulated signal overlap corresponding to the graphical illustration in Figure 6b, calculated from parameters similar to those of bond 2–3 in 1,1-dimethyltetralin with a separation of $\epsilon = 2$ Hz between the two overlapping patterns. Normally distributed pseudorandom noise is added to correspond to a S/N of 10. To enhance the visual presentation of response surfaces it is better to show the negative sum-of-squared residuals as a way to portray the agreement between simulated and experimental spectral patterns. Figure 8 shows for this spectral region a typical

(20) Dunkel, R.; Mayne, C. L.; Foster, M. P.; Ireland, C. M.; Du, L.; Owen, N. L.; Pugmire, R. J.; Grant, D. M. *Anal. Chem.*, following paper in this issue.

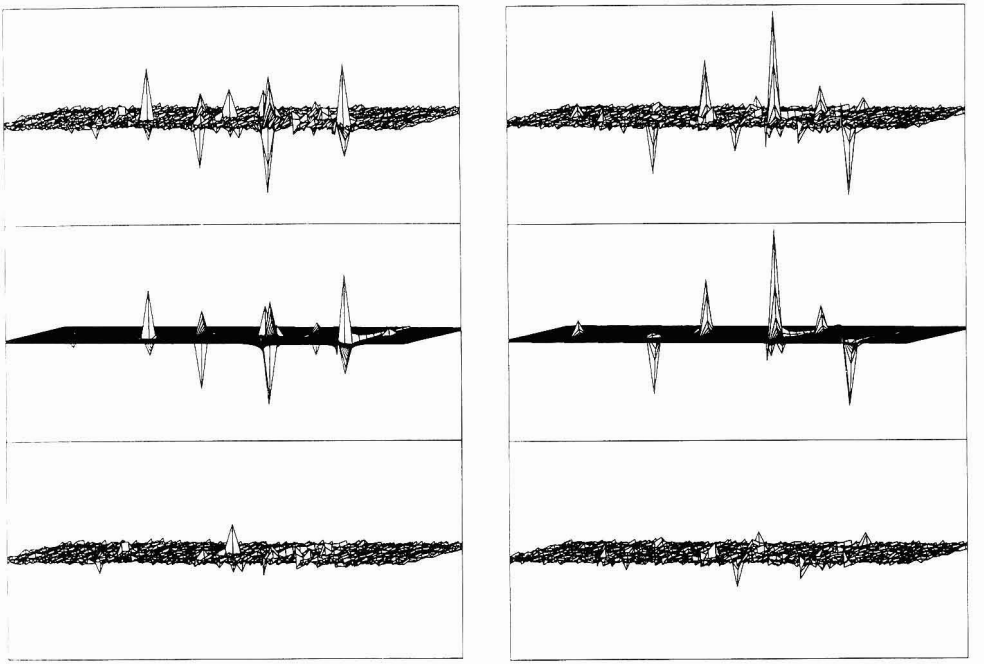

Figure 5. Regression results for 1,1-dimethyltetralin showing overlapping and highly second order patterns. The strong doublet at the right front of the spectrum is the B part of bond 5–6. At the rear on the right is bond 6–7 and on the left is bond 7–8. From top to bottom are shown the unphased experimental, the best-fit calculated, and the residual spectrum. The imaginary/real and imaginary/imaginary quadrants of the hypercomplex dataset are shown on the left and right, respectively.

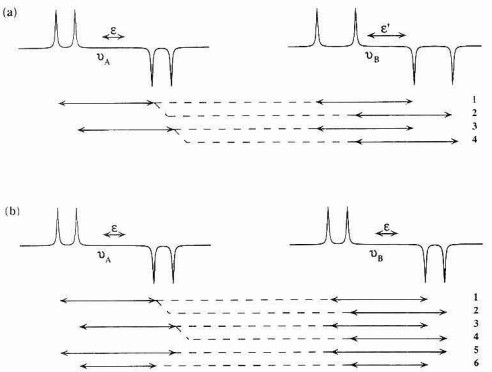

Figure 6. Two overlapping bond patterns are shown schematically. The two patterns are resolved in the chemical shift dimension, but due to severe data truncation, they are not resolved in the double quantum dimension. The scalar coupling constants are presumed equal, a common occurrence when the chemical shifts are pairwise nearly equal as shown. (a) The chemical shifts of two carbons in the A part of the spectrum differ by ϵ while those of the B part differ by ϵ'. Four different interpretations of the data are possible as indicated. (b) If $\epsilon = \epsilon'$ then six different interpretations of the overlapping patterns are possible.

three parameter (ν_A, ν_B, and J) contour surface of constant agreement at 67% of the maximum value. All six interpretations that are indicated in Figure 6b are fully resolved and visible at this level. Additional surfaces at 50% and 3% are shown as partially transparent shells. Refer to the color and opacity maps given for details of the rendering. For the volume rendering in this picture the agreement function is sampled with a grid density of 30 points in both shift directions and 60 points in the coupling constant dimension. At each grid point the coupling constant and both transition frequencies are locked to the grid values while optimizing the intensity values and possibly other parameter values (see the next section) to maximize the agreement function. The dimensions of the displayed region are 3 Hz in the two shift axes and 6 Hz in the scalar coupling axis. The 54 000 regression analyses of the fitting window required for such a plot can be computed in about 40 min using eqs 12 and 13 (described later). The volume rendering of the resulting data matrix such as the one shown in Figure 8 is based on a ray-tracing algorithm and takes several minutes to complete. The timing information in this paper is given in wall-clock time for an IBM RS/6000-320 workstation.

For the numerical analysis of such a 3D agreement function the resolution of the grid can be significantly reduced below that necessary to produce an acceptable figure. Any signal measured in the time domain will influence at least one point in the frequency spectrum; thus, it is unnecessary to use a grid point density greater than the digital resolution. A grid density corresponding to half the digital resolution has been found to give satisfactory results for the data analyzed to date. A simple peak picking algorithm is used to identify the local maxima of the grid values. Parameter values corresponding to a grid point with maximum agreement can be further refined by allowing the coupling constant and shift frequencies to be adjusted as described later. Such a grid search can easily consume 2 orders of magnitude more computer time than a single optimization process, but it assures that all possible interpretations of the data even for overlapping lines are identified and reported.

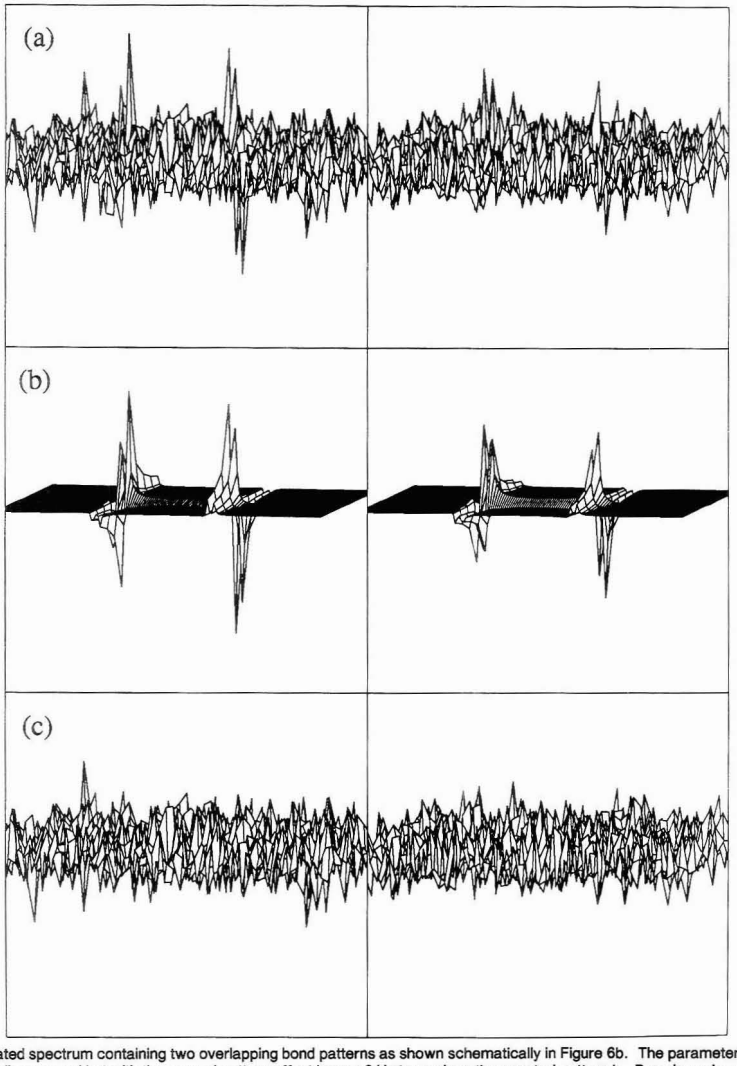

Figure 7. A simulated spectrum containing two overlapping bond patterns as shown schematically in Figure 6b. The parameters of the 2–3 bond in 1,1-dimethyltetralin are used but with the second pattern offset by ϵ = 2 Hz to produce the spectral pattern b. Pseudorandom noise (c) is added to produce a spectrum (a) with S/N of 10. The real/real quadrant of the hypercomplex dataset is shown with the A part of the AB pattern on the left and the B part on the right.

PARAMETER CORRELATION AND PRECISION

The equation describing an AB spin system in a hypercomplex 2D INADEQUATE spectrum contains 16 parameters, namely four intensities (I_1–I_4), three frequencies (ν_A, ν_B, ν_{DQ}), three phase values (ϕ_A, ϕ_B, ϕ_{DQ}), three transverse relaxation times ($T_{2,A}^{SQ}$, $T_{2,B}^{SQ}$, T_2^{DQ}), two acquisition times (T_A^{DQ}, T_A^{SQ}), and a coupling constant (J). All of these parameters represent physical features underlying and influencing the spectral response of the coupled spin system. Fortunately, prior knowledge is available to estimate reliably many of these parameters with sufficient accuracy that further refinement is not needed in the compute-intensive regression analysis. In some cases independent estimates are much more accurate than those obtainable from the 2D dataset, so these parameters should never be included in the regression under normal circumstances. We have found it informative, however, to obtain a regression of these parameters to verify the results with known values and to assure that the computer program is working correctly. The acquisition times in both spectral dimensions, T_A^{DQ} and T_A^{SQ}, are determined by times in the pulse sequence that are known very precisely. With compatible referencing of both spectral axes, the double quantum frequency is the sum of chemical shifts ($\nu_{DQ} = \nu_A + \nu_B$). On occasion ν_{DQ} is regressed independently in an attempt to resolve ambiguities. For example, if the double quantum frequency is found to differ significantly for the

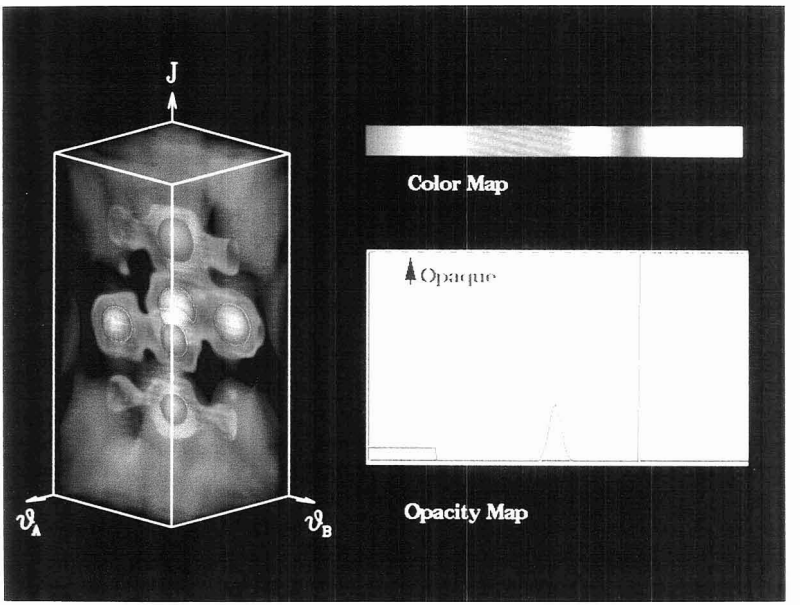

Figure 8. Calculated response function of the simulated spectrum from Figure 7 with overlap of two bond signals. A combination of color and opacity is used to show the nature of the agreement function. The six possible interpretations of the data as diagramed in Figure 6b can be clearly seen as well-resolved maxima of the agreement function. The data of Figure 7 has been transformed such that the alternative interpretations are readily apparent, and the S/N of this display is nearly 1 order of magnitude better than that in Figure 7.

Table I. Coefficients of Correlation between Model Parameters for Bond 2–3 in 1,1-Dimethyltetralin

	I_1	I_2	I_3	I_4	ν_A	ν_B	ϕ_A	ϕ_B	ϕ_{DQ}	$T_{2,A}^{SQ}$	$T_{2,B}^{SQ}$	J
J	0.001	0.000	0.000	0.000	0.005	0.003	0.000	0.000	0.000	−0.001	0.000	1.000
$T_{2,B}^{SQ}$	0.000	0.000	**−0.585**	**−0.583**	0.000	0.007	0.000	−0.005	0.000	0.000	1.000	
$T_{2,A}^{SQ}$	**−0.596**	**−0.603**	0.000	0.000	0.017	0.000	−0.012	0.000	0.000	1.000		
ϕ_{DQ}	0.000	0.000	0.001	0.000	−0.026	−0.043	0.019	0.030	1.000			
ϕ_B	0.000	0.000	0.017	−0.015	0.000	**−0.714**	0.000	1.000				
ϕ_A	0.016	−0.009	0.000	0.000	**−0.728**	0.000	1.000					
ν_B	0.000	0.000	−0.013	0.009	0.000	1.000						
ν_A	−0.014	0.005	0.000	0.000	1.000							
I_4	0.000	0.000	**0.338**	1.000								
I_3	0.000	0.000	1.000									
I_2	**0.357**	1.000										
I_1	1.000											

two doublets, one must conclude that the pattern is a misinterpretation because all four transitions of a bond pattern must have exactly the same DQ frequency. The Lorentzian line width in the DQ direction, T_2^{DQ}, is approximately 1 Hz, considerably less than the usual digital resolution of about 80 Hz in the DQ direction, and no attempt is made to regress this parameter because the line width is dominated by the sinc contribution. However, with higher spectral resolution, T_2^{DQ} might need to be given more attention.

Having excluded T_A^{DQ}, T_A^{SQ}, ν_{DQ}, and T_2^{DQ}, the remaining 12 model parameters can be obtained from the nonlinear regression and the following discussion will focus on the question of how accurately these 12 values can be determined from the 2D dataset as a function of the rms S/N. Some of these values can also be derived from prior knowledge with comparable precision, and earlier knowledge accumulated from the analysis of bond patterns can be used to simplify subsequent analyses. Various methods for using this prior knowledge to reduce substantially the computational burden of the analysis will be discussed below.

The determination of initial parameter estimates for the model equation, the optimization of these estimates in a nonlinear regression analysis, and the calculation of the variance–covariance matrix, **C**, from partial derivatives of the model with respect to each of the adjustable parameters were described previously.[8] From the variance–covariance matrix, the correlation of the determined parameter values can be estimated from

$$r(x_i,x_j) = \frac{\mathbf{C}_{ij}}{\sqrt{\mathbf{C}_{ii}\mathbf{C}_{jj}}} \tag{8}$$

The spectrum and simulation of bond 2–3 in 1,1-dimethyltetralin were shown above in Figures 2 and 3. Table I lists the corresponding correlation coefficients $r(x_i,x_j)$ calculated by eq 8 for the determined parameter values. No pair of parameters in the model is correlated above 0.8 or below −0.8, confirming that the 12 remaining parameters are independently determined by the experimental data. The highest correlation coefficients in Table I are shown in a bold font and can be found (1) between shift frequencies and their corresponding phase values (ν_A with ϕ_A and ν_B with ϕ_B), (2) between intensity parameters of a doublet and the corresponding relaxation times (I_1, I_2 with $T_{2,A}^{SQ}$ and I_3, I_4 with

$T_{2,B}^{SQ}$), and (3) between the intensity of one line of a doublet and the other line of the same doublet (I_1 with I_2 and I_3 with I_4). This last correlation is due to high correlation of each line to their common relaxation parameters and to the partial overlap of their dispersive signal tails as shown in the imaginary/imaginary part of the spectral region in Figure 3. By locking highly correlated parameter values to one another or to a specific value, the speed of convergence of the nonlinear regression analysis is improved, and the uncertainty in the remaining determined parameter values is reduced.

In addition to the estimation of parameter values and correlations, the data analysis also provides a confidence limit for every parameter. Assuming that the response surface is nearly quadratic in the vicinity of the best-fit parameter values, an estimate of the marginal standard deviation in parameter x_i is obtained from the diagonal elements of the variance–covariance matrix, **C**, by

$$\sigma(x_i) = \sqrt{\mathbf{C}_{ii}} \tag{9}$$

These values, easily calculated, are used extensively for the automated bond detection as described later.

The modeling of the data was introduced to summarize the information contained in a spectral region in a way that is fairly independent of spectral resolution and allows one to decide whether or not this region contains a bond pattern. Based on the supposition that a fit of the model to a sufficiently strong bond signal will lead to well-defined parameter values, the precision of parameters will be used as a criterion for bond existence. The parameter precision measures how closely the outcomes of multiple measurements cluster about the mean value of a specified parameter and indicates how well this parameter value is determined by the data. The precision implies repeatability of the observation and does not necessarily imply accuracy.[21]

For 1D spectra a relationship describing the precision of fitted parameters as a function of the S/N was published by Posener[22] and identical expressions have been applied by Marshall and Verdun[23]

$$P(i) = c(i)\sqrt{K}(\mathrm{S/N}) \tag{10}$$

where $c(i)$ is a constant that depends upon the line shape (Gaussian, Lorentzian, sinc, etc.) and the kind of parameter to be determined and K is the number of data points per line width at half height. Posener defined the parameter precision $P(i)$ in eq 10 to be the reciprocal of the relative standard deviation or in case of frequency parameters as the ratio of line width to the frequency standard deviation. In the present work Posener's definition is extended to include phase parameters. Phase angles can be assumed to lie between zero and 2π since they only influence the signal shape through sine and cosine functions (see equation 3), and the average phase angle is used to determine the parameter precision. The following definitions are used:

$$P(I_i) = \frac{I_i}{\sigma(I_i)} \quad P(T_i) = \frac{T_i}{\sigma(T_i)} \quad P(\phi_i) = \frac{\pi}{\sigma(\phi_i)} \tag{11}$$

$$P(J) = \frac{\Delta\nu_{1/2}}{\sigma(J)} \quad P(\nu_i) = \frac{\Delta\nu_{1/2}}{\sigma(\nu_i)}$$

where $\Delta\nu_{1/2}$ is the line width at half height and σ is the determined standard deviation of the corresponding parameter.

In the following discussion, the influence of S/N on these parameter precisions will be examined. The factors associated with K and c are assumed to constitute a simple constant of proportionality. The influence of K, however, is important in that the digital resolution chosen for manual interpretation of spectra might not be optimal for automated interpretation. One Monte Carlo simulation, described later, corroborates the dependence of the parameter precision on the digital resolution as given in eq 10.

The covariance matrix, **C**, provides unbiased estimates of the correlations and marginal standard deviations of the parameters only when the response surface is quadratic in all the parameters. While this condition strictly holds only when the model equation is linear in the fitting parameters, it is a reasonable approximation in some region of parameter space about the best-fit point. Equations 8 and 9 are valid even for a nonlinear model if the errors are small enough. Of course, if the residuals show a systematic departure from the model, then the covariance matrix will not yield good estimates of the errors, and the model must be expanded to account for the factors that produce the systematic residuals. To explore these questions for a given nonlinear model, one would like to repeat an experiment many times and examine the distribution of the residuals. Unfortunately, the acquisition time of one or more days per spectrum renders this approach impractical for the 2D INADEQUATE experiment.

As an alternative way to explore the effects of random noise, different samples of pseudorandom noise may be added to a simulated spectrum, and then subject such datasets to the same analysis as experimental data. This procedure is often referred to as a Monte Carlo simulation.[24] From comparison of experimental and simulated spectral regions (e.g., see Figures 2–5) it is clear that the model equation approximates the experimental spectral pattern rather well, so it is reasonable to presume that systematic contributions to the residuals are negligible. To confirm that the distribution of noise in an experimental spectrum is normal, the distribution of amplitudes in the cholesterol dataset was computed. Since the contribution from NMR signals is negligible over the entire dataset, the distribution accurately characterizes the noise. The agreement between the best-fit Gaussian distribution with zero mean and the experimentally determined intensity distribution is excellent, and, hence, it is presumed for the Monte Carlo simulations that the noise in these spectra is normally distributed. Using the best-fit parameter values, multiple datasets were simulated by calculation of the bond pattern and by adding noise calculated by a normally distributed pseudorandom number generator, and these datasets were used to replace repetitive measurements. Each of these simulated datasets is regressed and analyzed exactly like measured data. The deviations of the estimated parameters obtained in this manner yield error values from which one can construct a distribution. This method has been used previously in the context of 1D spectroscopy.[23,25]

A problem arises in the determination of the S/N for spectra with essentially sinc line shapes. The S/N is specified as the ratio of maximum height of a well-phased line to the standard deviation of the noise. The standard deviation for the noise can be easily determined, but the line shape in the DQ direction is to a good approximation a sinc function due to the extreme underdigitization in this dimension. Figure 9 shows a perfectly phased 1D sinc function digitized in various ways. The light line shows a continuous pure absorption mode sinc functions on the left half of the figure and a pure

(21) Deutsch, R. *Estimation Theory*; Prentice-Hall: London, 1965; p 154.
(22) Posener, D. W. *J. Magn. Reson.* **1974**, *14*, 121.
(23) Marshall, A. G.; Verdun, F. R. *Fourier Transforms in NMR, Optical, and Mass Spectrometry*; Elsevier: Amsterdam, 1990, p 150.
(24) Press, W. H.; Flannery, B. P.; Teukolsky, S. A.; Vetterling, W. T. *Numerical Recipes. The Art of Scientific Computing*; Cambridge University: Cambridge, 1987; p 531.
(25) Chen, L.; Cottrell, C. E.; Marshall, A. G. *Chemom. Intell. Lab. Syst.* **1986**, *1*, 51.

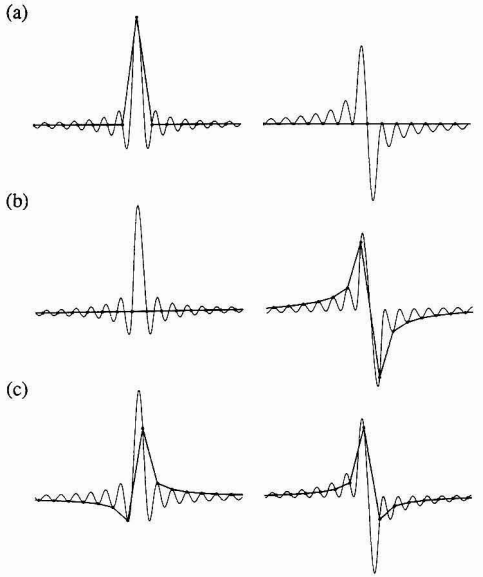

Figure 9. Digitization of a sinc function. In each case the same sinc function is shown as a light line with the pure absorption component on the left and the pure dispersion component on the right. In a the transition frequency falls on a digitization point; in b it falls halfway between two digitization points; and c is a case between a and b. The heavy lines show what a spectroscopist sees when the data points are simply connected by straight lines. Note, the signal can completely disappear in one or the other of the components of the spectrum. Furthermore, c shows that the signal can appear to have badly misadjusted phase when, in fact, it does not.

dispersion mode sinc function on the right side. Depending on the relative position of the transition frequency of the signal with respect to the digitization points, the observed signal in the absorption mode spectrum (bold line) can be a maximum, similar to the behavior of a Lorentzian line (Figure 9a); zero everywhere (Figure 9b); or an intermediate case (Figure 9c). Even though the spectrum is perfectly phased an intermediate case may appear to be poorly phased. Fortunately, the underdigitization does not influence the computerized analysis as long as all quadrants of the dataset are used in the regression analysis and the model equation contains the sinc contribution to the lineshape. The 2D line shape is simply the product of two 1D line shapes (see eq 1), so the 2D line shape exhibits corresponding behavior. In the numerical analysis used here no attempts are made to phase the data; the phase of the spectrum is simply a parameter to be determined. The signal used to compute the S/N is the maximum absolute value amplitude of the unphased simulated pattern in all four quadrants. Automated phase correction of these 2D spectra, however, is necessary to linearize the determination of the sum-of-square residuals for response surface mapping. A general technique for automated phase correction of n-dimensional spectra has been developed.[26] The approach is demonstrated in the application paper[20] and will be discussed in detail in a subsequent publication.

The following Monte Carlo simulations demonstrate the implication of various S/N values. The parameter values, for the Monte Carlo simulations, are taken again from the best-fit values of bond 2–3 in 1,1-dimethyltetralin shown in Figures 2 and 3. Figure 10 shows the simulated imaginary/real dataset in the region where the strongest signal components of this bond pattern appear with varying amounts of normally distributed noise to produce S/N of (a) 20, (b), 10, (c) 5, and (d) 2.5. In each case the best-fit is shown below the corresponding spectrum. Note, there are no readily apparent differences among any of the best-fit spectra. A spectroscopist could readily identify all four signals at S/N = 20 but would encounter problems at S/N = 10 with no hope of identifying the complete bond pattern at the lower S/N levels. In contrast, the computerized analysis can identify the pattern at all S/N levels shown with only minor deviations of the determined parameter values from the values used in the Monte Carlo simulations. Thus, qualitatively, the technique detects bonds better than would a spectroscopist. The remainder of this paper is devoted to quantifying the reliability with which the method will detect bonds.

To determine the distributions of errors in the various parameters and how they affect the ability to detect bonds, 1000 spectra, each with a different noise sample, were simulated and analyzed. The computational requirements for these Monte Carlo simulations are similar to the analysis of 1000 experimental fitting windows and take between 1 h and several days depending on the parameters to be optimized, the response surface mapping used, and the number of points in the fitting window. At each S/N level, the standard deviation of each parameter was calculated from the 1000 simulations, and the parameter precisions were determined using eq 11. The resulting data are plotted in Figure 11 versus S/N. As predicted by eq 10, the parameter precision is proportional to the S/N. The DQ phase angle, ϕ_{DQ}, precision is twice that of the SQ phase angles because the former is determined by all four transitions of the AB pattern, whereas the latter two phases rely on data from only one of the doublets. Parameter precisions of the coupling constant and of the chemical shift frequencies are similar. The relaxation time precision shows a slightly nonlinear behavior at the rms S/N ratio of 2.5 where the parameter precision begins to decrease more rapidly than expected. At this S/N level, this relaxation parameter is no longer well determined by the data. The next section discusses how to avoid this and related problems.

PARAMETER ESTIMATION

While nonlinear regression analysis is normally used to determine accurate parameter values from the data, it should be remembered that the primary goal for this work is to decide whether or not a given fitting window contains a bond signal. Hence, the goal is to obtain the best possible discrimination between noise-related and bond-related patterns, while achieving an acceptable run time for CCBOND consistent with the size of the dataset and the n^2 time complexity of the algorithm for n identified 1D resonances.

One of the most time-consuming steps in the extraction of bond information from the 2D INADEQUATE spectrum is associated with the response surface mapping of the 3D parameter space. This step is required to detect all possible valid interpretations of the data, especially in a region where bond patterns can overlap. When it is possible to linearize the regression required for each grid point during this mapping step, one may replace the iterative nonlinear regression analysis by a straightforward and much faster linear regression. In the accompanying application paper[20] the nonlinear approach to extraction of bond information is demonstrated using a sample of bistramide A.[27] In addition, the linearized approach to mapping the response surface in conjunction

(26) Dunkel, R. U.S. Patent Application No. 675,401.

(27) Foster, M. P.; Mayne, C. L.; Dunkel, R.; Pugmire, R. J.; Grant, D. M.; Kornprobst, J.-M.; Verbist, J.-F.; Biard, J.-F.; Ireland, C. M. *J. Am. Chem. Soc.* **1992**, *114*, 1110.

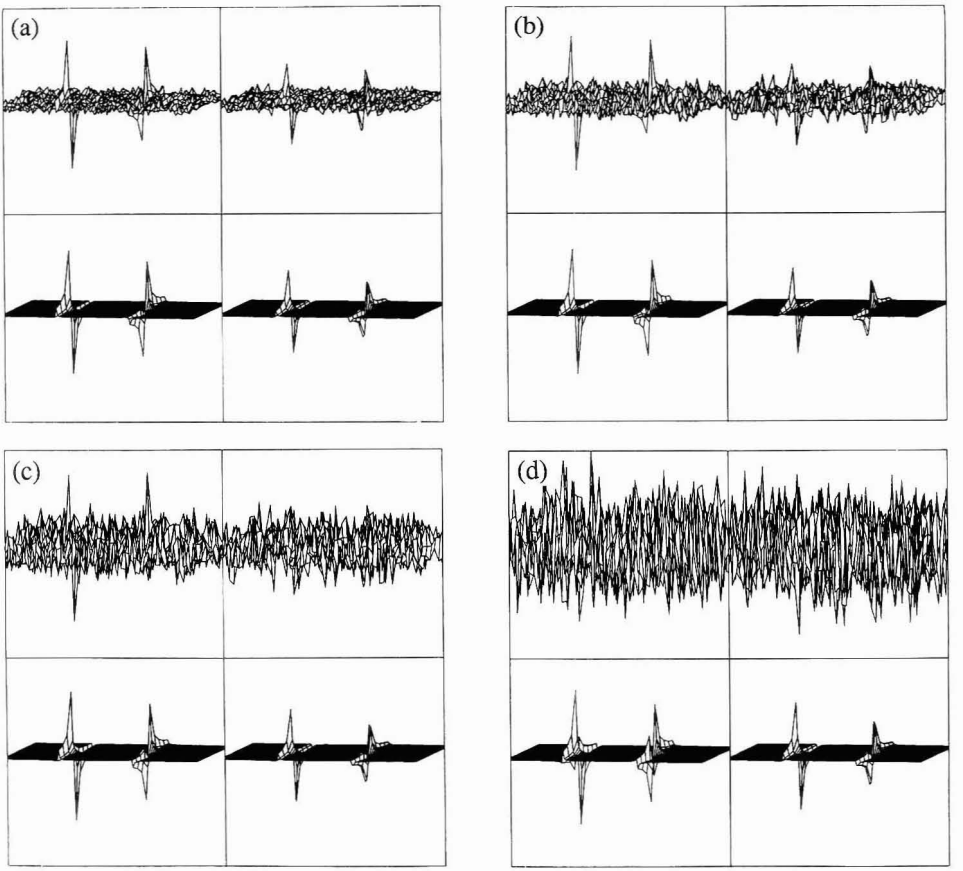

Figure 10. Fitting of simulated spectra with varying S/N. In each case the upper plot shows the real-real part of the hypercomplex spectrum and the lower plot shows the best-fit. Each successive case shows decreasing S/N, (a) 20, (b) 10, (c) 5, and (d) 2.5. There is no appreciable difference in the best-fit spectral patterns even at the lowest S/N where the signals are essentially obscured by the noise.

with a nonlinear refinement of identified local minima is demonstrated using a cholesterol sample.

The model equation has 16 parameters, three of which (T_A^{DQ}, T_A^{SQ}, and T_2^{DQ}) are sufficiently accurately known that they need no further adjustment. The double quantum frequency is subject to a constraint ($\nu_{DQ} = \nu_A + \nu_B$) so that normally it need not be treated as an independent parameter. The remaining 12 parameters may in part be locked to initial values or regressed during either the mapping or the final optimization stages. Obviously as many parameters as possible should be locked to increase the computational efficiency. Locking those parameter values that are strongly correlated to other parameters obviously proves to be very beneficial. Failure to do this adversely affects the run time of the regression analysis, and the precision is seriously degraded for parameters which are highly correlated. Table II records the parameter precisions as determined from 1000 Monte Carlo simulations for various combinations of locked and regressed parameters. In the language of nonlinear regression analysis each of these combinations constitutes a different model, as they are designated here, even though the functional form of the model is never changed. The parameter values underlying these simulations are I_1 = 65.227, I_2 = 64.960, I_3 = 58.135, I_4 = 59.336, J = 32.708 Hz, ν_A = 39.353 ppm, ν_B = 19.734 ppm, $T_{2,A}^{SQ}$ = 0.6544 s, $T_{2,B}^{SQ}$ = 0.4817 s, ϕ_{DQ} = −0.4479 radians, ϕ_A = −0.2829 radians, and ϕ_B = −0.4914 radians.

Model 1. The first column of Table II, designated model 1, contains the most general model where all 12 parameter values are regressed. The recorded values are the slopes of the lines in Figure 11 corresponding to the factor $c(i)\sqrt{K}$ in eq 10. Since the parameter values used to make the simulation stem from an experimental bond pattern with small differences in the four intensity values, the resulting parameter precisions also show slight differences for the four transitions.

Model 2. Model 2 in Table II locks both relaxation times in the shift direction ($T_{2,A}^{SQ}$, $T_{2,B}^{SQ}$). Figure 11 shows that these parameters cannot be determined reliably at low S/N since the parameter precision actually decreases even more rapidly than eq 10 predicts. Furthermore, Table I indicates strong correlations of these relaxation parameters to the corresponding intensity parameters. The values of these effective relaxation parameters are determined mainly by the lifetime of the corresponding excited spin states and by dephasing due to magnet inhomogeneity. It is conceivable that the values of these relaxation parameters determined

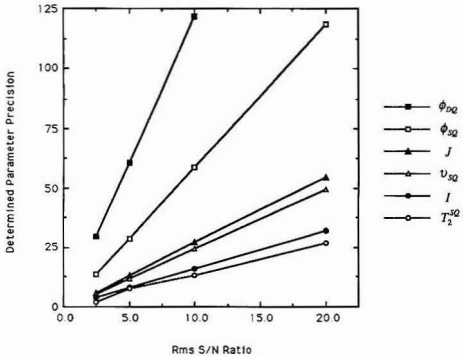

Figure 11. The parameter precisions determined for bond 2–3 in 1,1-dimethyltetralin by Monte Carlo simulation using 1000 different noise samples. The precision is directly proportional to the spectral S/N except, for the lowest S/N, the relaxation time in shift direction, T_2^{SQ}, cannot be reliably determined from the data as shown by the rapid nonlinear decrease in parameter precision.

from the 1D spectrum would be slightly larger than those characterizing the 2D spectrum since adjacent ^{13}C nuclei provide an additional relaxation pathway. However, Figure 12 shows a strong correlation between relaxation times determined for all bonds of 1,1-dimethyltetralin and the corresponding relaxation times determined from the 1D spectrum. The error bars shown are tilted so that the horizontal and vertical projections for each data point are an interval of plus or minus one marginal standard deviation calculated from eq 9 for the 1D and the 2D parameters, respectively. Encouragingly, these data correspond reasonably well to a line of slope one. Considering the 2D relaxation times are determined from a high S/N spectrum, the marginal standard deviation decreases in proportion to the inverse of the S/N ratio (eqs 10 and 11), and relaxation times above 0.5 s in the 2D spectrum correspond to a line width less than the digital resolution. Thus, locking the transverse relaxation times in low S/N spectra to the values extracted from the 1D spectrum is more than justified. The slopes, $c(i)\sqrt{K}$, for eq 10 are given in Table II for the 10 parameters specified by model 2.

Model 3. In model 3 of Table II I_1 is locked to I_2 and I_3 is locked to I_4. Ideally the intensity parameters I_1, I_2, I_3, and I_4 would all be identical, but modest spectral distortions arise because of differences in line widths and resonance offset effects from the pulse sequence. Locking I_1 to I_2 and I_3 to I_4 has been justified in the cases we have studied. For example, Figure 13 shows excellent correlation of determined intensities for A1 to A2 and for B1 to B2 transitions in all the bond signals in 1,1-dimethyltetralin. Again, the values of $c(i)\sqrt{K}$ are given in Table II for the eight parameter values specified by model 3.

Model 4. The only high correlations remaining among the parameters of model 3 are between the chemical shift frequencies and the corresponding phase values. Model 4 in Table II locks all three phase values to predetermined phase functions. The two chemical shift frequencies cannot be estimated sufficiently accurately from the 1D data due to isotope shifts as discussed above. Further, the phases in the 1D spectrum fail to correlate well with those in the 2D spectrum due to differences between the two pulse sequences. There is no prior knowledge on the variation of phase angle with frequency in the DQ direction. However, it has been found experimentally that phase and frequency correlate within a given spectrum, and an automatic phasing routine has been developed.[26] Where other methods have failed, the automated phasing program works well independent of line width and even at extremely low S/N. The accuracy obtained is well above that achievable with manual phasing.[9] The method is also not subject to the problems introduced by truncation of the FID. This phasing method is explained and demonstrated in the accompanying application paper.[20]

The initial autophasing step is very important since the phase parameters are nonlinear parameters and the only ones left to impact the time-consuming mapping step as explained above. Thus, a sufficiently accurate estimate of phase as a function of frequency allows one to map all $n(n-1)/2$ bond regions with linear rather than nonlinear methods. The 2D line shape of a transition is a product of two 1D line shapes (eq 1), each of which is only influenced by the phase parameter associated with the corresponding axis (eq 3). The needed approximate dependence of the shift phase on the shift frequency and of the DQ phase on the DQ frequency can be obtained from a few nonlinearly analyzed bond signals in a time insignificant compared to the nonlinear analysis of all fitting windows. Judicious choice of a few fitting windows to be analyzed nonlinearly yields sufficient data to permit the remaining fitting windows to be analyzed linearly. The values of $c(i)\sqrt{K}$ are given in Table II for the five parameter values of model 4 assuming that all other model parameters may be set to appropriate values.

Model 5. In model 5 the number of parameters has been reduced finally to four by locking the four intensities, I_1, I_2, I_3, and I_4, to a single value. This final simplification presumes that it is sufficient to determine only one overall intensity parameter for all four transitions of the AB spin system. Figure 14 shows the correlation of the best-fit intensity of B to A transitions. The observed deviations from a linear correlation, well above the experimental uncertainties in the intensities, are probably caused by instrumental artifacts such as variations in the distances from the carrier frequency and in the line widths. However, there is a sufficiently clear correlation between the A and B intensities, so that in low S/N spectra where the errors are much larger and the only objective is to detect whether or not a bond signal is present, these differences of intensity between A and B transitions usually can be ignored. The final modification of the parameterization leaves the model dependent on the single remaining intensity parameter during the mapping step, since the nonlinear two chemical shifts and the coupling constant are locked to grid values. Optimization of the intensity parameter for each point of the grid can be computed rapidly since no iteration is required for the linear regression. Let S_i be the experimental amplitude of the ith point in a spectrum of n points and IT_i the amplitude of the corresponding point in the simulated spectrum. The sum-of-square residuals is then given by

$$\chi^2(I) = \sum_{i=1}^{n} (S_i - IT_i)^2 \tag{12}$$

Differentiating (12) with respect to I, setting the right-hand side equal to zero, and solving for I then gives the optimum value of I as

$$I_{opt} = \sum_{i=1}^{n} S_i T_i \Big/ \sum_{i=1}^{n} T_i^2 \tag{13}$$

Use of (13) permits mapping of the response surface for the other three variables to be accomplished with reasonable computing resources. Model 5 in Table II contains the $c(i)\sqrt{K}$ values for the remaining intensity value, coupling constant, and the two chemical shifts. Using the methodology developed thus far, the question can now be addressed as to

Table II. Comparison of Parameter Precisions $c(i)\sqrt{K}$ Determined by Monte Carlo Simulation of 1000 Experiments under Different Conditions

	model 1	model 2	model 3	model 4	model 5
$P(I_1)$	1.78	2.27	3.21	3.15	3.97
$P(I_2)$	1.73	2.19			
$P(I_3)$	1.39	1.68	2.40	2.45	
$P(I_4)$	1.42	1.76			
$P(J)$	2.75	2.77	2.77	2.85	2.84
$P(\nu_A)$	2.91	2.92	2.90	4.28	4.28
$P(\nu_B)$	2.21	2.23	2.23	3.37	3.37
$P(T_{2,A}{}^{SQ})$	1.40				
$P(T_{2,B}{}^{SQ})$	1.20				
$P(\phi_{DQ})$	12.14	12.16	12.15		
$P(\phi_A)$	6.87	6.88	6.89		
$P(\phi_B)$	5.10	5.13	5.14		

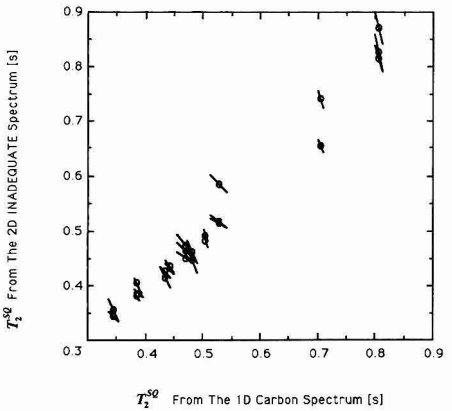

Figure 12. Correlation of transverse relaxation times in the chemical shift direction determined from bond signals in the 2D INADEQUATE spectrum versus those determined from the 1D carbon spectrum for the 1,1-dimethyltetralin spectrum. Experimental values are shown as circles with an error bar such that the projection onto each axis reflects the parameter value plus or minus one marginal standard deviation. The plot shows a direct correlation consistent with the errors. This justifies locking these parameters to the values obtained from the high S/N 1D spectrum during regression of 2D data where the S/N is much lower.

what is the lowest S/N at which bonds can be reliably detected?

DETECTION LIMIT

The previous section described a method for detecting bond patterns by mapping a response surface for only three parameters: the coupling constant and the two chemical shifts. All other parameters of the model are held constant at values obtained either from constraints on the fit or from prior knowledge except that the overall intensity of the pattern is optimized at each grid point. The question now to be addressed is the following: what S/N level is required for reliable bond detection? A bond-related pattern can be expected to result in a much larger parameter precision than a noise-related pattern. The objective of this final section is to establish an adequate bond criterion based upon the determined intensity parameter precision or upon the lowest such value in case more than one intensity parameter is determined for a specific AB pattern. This leads naturally to a definition of the detection limit for the method based upon an intensity criterion. The five models discussed in the last section and specified in Table II are further examined here to illustrate the effect of locking parameter values on

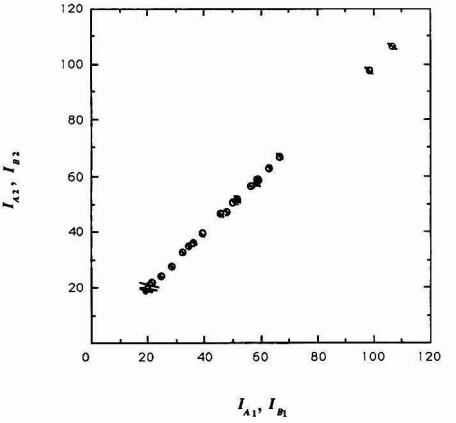

Figure 13. Comparison of determined intensities within each doublet of the AB spin systems in the 1,1-dimethyltetralin spectrum. Experimental values are shown as circles with an error bar such that the projection onto each axis reflects the parameter value plus or minus one marginal standard deviation. The bond patterns with severe second-order effects have the lowest intensity values and largest errors because these patterns are weak and have much lower S/N. Note also that the model is parameterized so that the two transitions of the A or B doublets should ideally have equal intensity parameters, even when severe second-order effects are present. The plot shows a direct correlation consistent with the errors justifying the locking of these two intensity parameters together for regression.

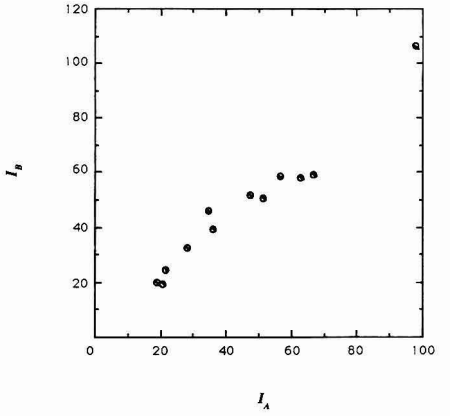

Figure 14. Comparison of the determined intensity parameter for the B and A doublets of the AB spin systems in the 1,1-dimethyltetralin spectrum. Experimental values are shown as circles with an error bar such that the projection onto each axis reflects the parameter value plus or minus one marginal standard deviation. The correlation of the determined intensity values is much poorer than would be expected based on the errors in the determined parameters. The correlation is sufficient to justify locking the parameters together for detecting bonds in low S/N spectra, but this constraint must be used with caution.

the chosen bond criterion. The use of models 2 and 5 for the structure elucidation of bioorganic molecules is illustrated further in the accompanying application paper.[20] Model 5 will be given special attention because of its high sensitivity and computational efficiency.

All parameter precisions shown in Table II were calculated using the standard deviations from the Monte Carlo simulations mentioned above. At the same time the average marginal standard deviations, calculated using eq 9, were

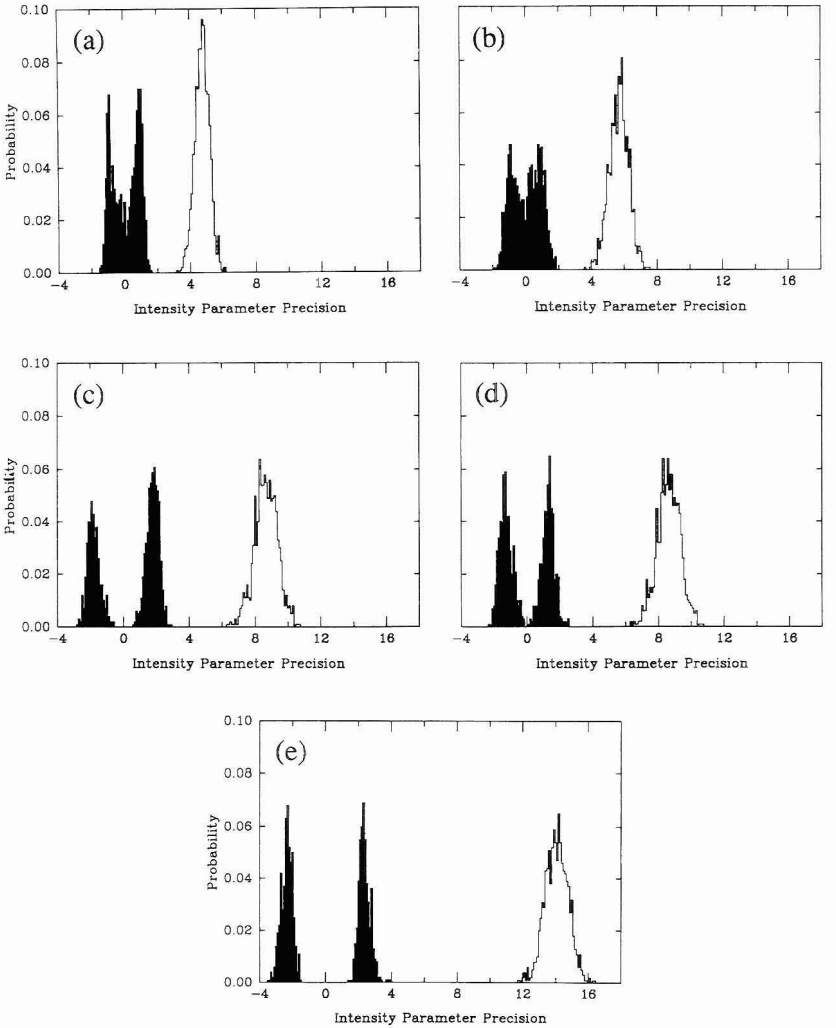

Figure 15. Distribution of intensity parameter precisions determined from simulated spectra. The white distribution corresponds to simulated spectra containing bond signals at a S/N of 5, while the black distribution is derived from datasets containing only noise. Each distribution is based on 1000 simulations using the parameter values of the 2-3 bond in 1,1-dimethyltetralin. The five plots, a–e, correspond to models 1–5, respectively, as discussed in the text and shown in Table II.

determined for each model. These values were found to be uniformly higher, by 11–53%, than the values determined from the simulations. Hence, the error values calculated from eq 9 are considered to be conservative estimates of the uncertainties in the parameter values and are used for all routine applications of CCBOND.

To be useful, a bond-detection algorithm must have high reliability. In the following discussion a probability of at least 99.9% for correctly identifying a bond pattern is considered satisfactory. This same level of reliability is required for rejecting a dataset involving only random noise. Error distributions based on at least 1000 Monte Carlo simulations are required to approximate this high level of reliability. The distribution of errors for datasets containing only noise depends somewhat on the surface mapping techniques employed. For all spectra in the application paper[20] and for all Monte Carlo simulations in this paper, 10 points distributed over a region of ±6.5 Hz for the coupling constant and 3 points distributed over ±1.5 Hz for each of the chemical shift dimensions are mapped for each fitting window. Figure 15 shows bar charts indicating the distributions of intensity parameter precision for each of the five models using a S/N of five. The determined parameter precisions for noise only datasets (black bars) and noise plus bond pattern datasets (white bars) is based on 1000 Monte Carlo simulation for each distribution.

All the noise-only distributions are bimodal because, in underdigitized spectra such as those used here, a slight shift in parameter values will locate a noise excursion that gives some agreement with the model, and because the probability is small that no such noise excursion exists in the dataset. Indeed, numerous local maxima of the agreement function

will exist, and the program will find the global maximum so long as the grid density used for response surface mapping is high enough for the digital resolution employed. Negative parameter precisions in the noise-only simulations result from negative-determined intensities that are not excluded by the model and can be found in noise even though they have no physical meaning for a correctly phased spectrum.

As in the preceding discussion, the parameter values used for simulating the datasets are the determined best-fit parameters of bond 2–3 in 1,1-dimethyltetralin. These values are also used as the initial estimates for the bond pattern search in both the noise-only and signal-containing datasets. As the parameterization of the model is progressively restricted by introducing more prior knowledge, an increase is realized in intensity precision for datasets containing bond patterns and in absolute precision for noise-only datasets. The only exception occurs when phase parameters are locked (compare parts c and d of Figure 15). This case hardly increases intensity precision since these parameters are not significantly correlated (see Table I). However, locking the phase parameters caused a significant decrease in intensity precision for pure noise datasets due to a reduction in noise patterns that are compatible with the model. If the distribution derived from pure noise does not overlap with that derived from noise plus signal, it is presumed, since the distributions shown are based on 1000 simulations, that a threshold value for intensity parameter precision can be chosen where bonds will be correctly detected at 99.9% confidence, and nonbonds will be rejected with the same confidence.

Figure 15a indicates that a S/N of 5 is close to the detection limit if all 12 parameters are optimized during an analysis of a fitting window. Slightly lower S/N values are satisfactory for the other models, but model 5 is clearly superior. Since the parameter precision is directly proportional to S/N, Figure 15e indicates that the S/N may be reduced by an additional factor of about 2 without producing overlap of the two distributions. Figure 16a presents simulations for a S/N of 2.5 and appears to establish this value as a suitable lower limit for the program's detection limit in its current state. The motivation for choosing parameter precisions instead of parameter values for the definition of bond criteria resides in the independence of precisions on spectral amplitude. The average parameter precision for detected bonds increases proportionally with the spectral rms S/N ratio, given by eq 10. The detection limit also can be influenced by other factors. For example, the influence of second-order quantum mechanical effects and lines of changing width compared to digital resolution are shown in Figure 16b,c. Figure 16b uses the strong second-order parameters (the ratio of chemical shift difference to coupling constant is 1.36) of the 6–7 bond of 1,1-dimethyltetralin with a S/N of 2.5.

The decrease in parameter precision for strongly coupled AB patterns arises mainly from the definition of S/N which is based on the height of the tallest line in the pattern. The INADEQUATE experiment is normally optimized for detection of patterns in the AX limit, but is far from optimum for strongly second-order AB patterns. Hence, the S/N of such patterns is usually significantly lower than for corresponding AX patterns, and the parameter precision decreases. The overall intensity of an AB pattern also decreases precipitously in an INADEQUATE experiment for chemical shift to coupling ratios below three; hence, the experimenter must be wary of concluding that a bond does not exist when none is detected in a spectrum of two carbons having chemical shifts that differ by less than three times the coupling constant. Figure 16c uses the same parameters as Figure 16a, but the digital resolution of the spectrum is doubled in both dimensions. The number of points within the half height contour of each 2D signal quadruples. According to eq 10, this increase of information should double the precision of parameter values determined from the expanded dataset thereby improving the detection limit by a factor of 2 corresponding to an S/N of 1.25.

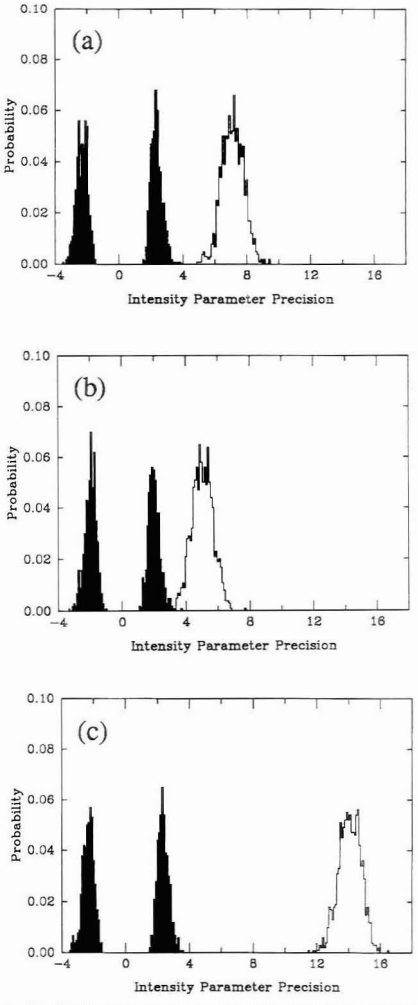

Figure 16. Distributions of intensity parameter precision as described in Figure 15 for model 5 at a S/N of 2.5. Shown are the distributions for (a) bond 2–3 with weak second order effects, (b) bond 6–7 with strong second-order effects, and (c) bond 2–3 again with the same parameter values but with twice the digital resolution in both spectral dimensions.

Several additional points are worth mentioning. By considering only a single fitting parameter for bond identification, in this case the overall intensity, one neglects information from the other parameters that could improve the detection limit. Bond identification should, in principle, be based upon the joint probability distribution of all adjusted parameter values; relevant studies on this issue are now in progress. All parameter precisions determined by Monte Carlo simulations assume that spectra contain only a signal

of the shape described by the model equation along with uncorrelated random noise. Several deviations from this assumption are known. First, about 3% of the total signal power not explained by the model in a spectral region consists of nonrandom residuals. Second, all signals coming from the probe of an NMR instrument are amplified before the signal is separated into the two quadrature components.[28] This introduces correlation of the noise between the real and imaginary parts of the hypercomplex dataset in the shift direction. Such correlations were not represented in the Monte Carlo simulation. Third, incompletely suppressed single quantum signals span the entire DQ-axis at the chemical shift frequency of each carbon, producing nonrandom residuals. Fourth, the first few points in the t_2 FIDs are frequently severely distorted due to experimental artifacts.[9] However, all of these effects have normally been controlled adequately compared to the experimental random noise relevant to this study, and artifacts in our results have yet to be encountered that exhibit such inconsistencies. Still, nonrandom components in the data other than those arising from the sought after bond can result in a false positive test. Chen et al.[25] compared error values calculated by both covariance matrix and Monte Carlo simulation with experimentally determined error values. For 1D proton NMR spectra of water, the precision of experimentally determined values in line positions was found to be five times lower than that predicted by uncertainties in the regression analysis. The other determined parameters show similar discrepancies. Their experimentally determined precisions show hardly any correlation with S/N and are probably dominated by other instrumental factors leading to nonreproducible results. The experimentalist must be constantly on guard for occurrences of this sort when using the type of analysis of experimental data described here.

SUMMARY AND CONCLUSIONS

Our former attempts at automated bond extraction from 2D INADEQUATE spectra were limited to spectra with sufficient S/N that the resonances could be readily observed by a spectroscopist, and the spectrum was phased manually. The bond extraction was reliable so long as the bond regions were free of overlapping signals and initial estimates of the coupling constant were sufficiently accurate. Any violation of these conditions could interfere with the program's ability to correctly detect bonds. Time domain truncation of the data also introduced severe problems that necessitated substantial line broadening to suppress the frequency domain truncation artifacts. The improvements described in this paper satisfactorily resolve these problems. The model has been extended to include all four quadrants of the hypercomplex spectrum, and truncation effects have been included in the model so that no line-broadening functions are required. The phase-sensitive model allows one to eliminate manual phase correction of spectra, and inclusion of all four quadrants of the hypercomplex data improves the detection limit of the method. Inclusion of all possible constraints and prior knowledge in the model extends the sensitivity of the method. Elimination of all manual manipulation of the data permits full advantage to be taken of the sensitivity of the nonlinear regression techniques to extend the bond detection limit of the method to S/N of 2.5, well below the level where manual data manipulation and interpretation is possible. The autophasing technique is not limited solely to use with 2D INADEQUATE spectra but may be naturally extended to phase correction of n-dimensional spectra. Details of such work will be published elsewhere.

Response surface mapping in a three-dimensional parameter space for every possible bond region is able to detect resolved bond patterns even in the presence of nearby local minima in the response surface and to identify possible alternative interpretations of the data in cases where overlapping bond patterns introduce ambiguities in the assignments of the spectral bond patterns.

Computer simulations have been used to explore the validity of the techniques and show that the program should perform reliably for S/N of 2.5 or more. The program has been used to interpret spectra obtained from as little as 20 μmol of complex organic molecules. These results are described in the accompanying paper.[20] The x-window version of the described software is commercially available for UNIX workstations through the Scientific Instrumentation Technology and Research Corp., P.O. Box 58072, Salt Lake City, UT 84158-0072.

ACKNOWLEDGMENT

Assistance from the following sources is gratefully acknowledged: Michael Pernice of the Utah Supercomputing Institute for pointing out the algebraic solution, eq 13, for determination of the optimum intensity; James A. Rose and Robert McDermott of the Utah Supercomputing Institute for assistance in rendering Figure 8; the Department of Computer Science supported by a visualization grant from IBM for the volume rendering software; the Utah Supercomputing Institute assisted in part by a grant from IBM for computing resources; the Deutsche Forschungsgemeinschaft (R.D.); NIH Grant GM 08521-31 (D.M.G.); and the Consortium for Fossil Fuel Liquefaction Science funded by DOE/PETC under Contract No. DE-FC22-90PC 90029 (R.J.P.).

RECEIVED for review March 5, 1992. Accepted August 6, 1992.

Registry No. Carbon-13, 14762-74-4.

(28) Shaw, D. *Fourier Transform N.M.R. Spectroscopy*, 2nd ed.; Elsevier: Amsterdam, 1984; p 150.

Applications of the Improved Computerized Analysis of 2D INADEQUATE Spectra

Reinhard Dunkel,[†] Charles L. Mayne,[†] Mark P. Foster,[‡] Chris M. Ireland,[‡] Du Li,[⊥] Noel L. Owen,[⊥] Ronald J. Pugmire,[§] and David M. Grant*,[†]

Departments of Chemistry, Medicinal Chemistry, and Fuels Engineering, University of Utah, Salt Lake City, Utah 84112, and Department of Chemistry, Brigham Young University, Provo, Utah 84602

This paper illustrates the use of the program CCBOND to determine the carbon skeletons of bioorganic molecules in low concentration samples. Discussed is the structure elucidation of bistramide A, a compound extracted from a Fijian *Lissoclinum* sp. and cholesterol in 71- and 20-μmol samples, respectively. The detection limit of the automated bond extraction is shown to be dramatically improved compared to the manual interpretation of 2D INADEQUATE spectra.

INTRODUCTION

A method for improving the computerized extraction of carbon–carbon bond data from 2D INADEQUATE spectra as well as a thorough treatment of detection limits and recognition of possible ambiguities in signal assignments is described in an accompanying paper.[1] The current paper describes the application of this method to two samples.

The first compound was a natural product, bistramide A, extracted from *Lissoclinum* sp. ascidian collected in Fijian waters. Despite the use of a rather large amount of material, 50 mg or 71 μmol, and extensive time averaging employed for the acquisition of the 2D INADEQUATE spectrum, manual interpretation of the data was marginal for most bonds and was not able to identify some crucial bonds. As this work involved correction of a previously published structure, the structural data had to be absolutely irrefutable. The details of the structure elucidation have been recently published in a communication.[2] The 2D INADEQUATE data, which played a crucial role in solving this structure, are discussed here as a typical example of the automated spectral analysis.

Cholesterol was selected as a second molecule to examine the lower limits of applicability of the method. Only 8 mg or 20 μmol of the compound were used. This molecule has sufficient structural complexity to test the methods employed and exhibits several features that illustrate the limitations of the method. The amount of compound and the length of time averaging were chosen to yield a spectrum that would be completely impossible either to phase manually or to distinguish visually its signals from the noise. Despite these obstacles, the program CCBOND extracted all but a few bonds from the spectrum. These bonds were not detected for fundamental reasons, to be discussed later, that may under certain conditions limit the impact of this method. They are presented to illustrate potential pitfalls in the use of the method. Nevertheless, these examples illustrate that the 2D INADEQUATE method can contribute substantially to the solution of actual structure elucidation problems even when sample quantities are limited to amounts commonly encountered in natural product research.

EXPERIMENTAL SECTION

The first compound, bistramide A ($C_{40}H_{68}N_2O_8$, MW 704), was extracted from *Lissoclinum* sp. collected at a depth of 35 ft in Fijian waters. From 104 g of the dried organism, 50 mg (71 μmol) of the purified sample was obtained and used for the structure elucidation. Further details of the sample preparation are given elsewhere.[2] The 2D INADEQUATE spectrum was obtained on a 500-MHz Varian Unity spectrometer using a 5-mm broadband probe with a one-turn observe coil. The $\pi/2$ pulse width was 8.2 μs, and the spectral width was 24 830 Hz (197.5 ppm) in both dimensions. For each of 512 increments of the double-quantum evolution time, 49 664 complex samples of the FID were acquired, and the process was repeated with the phase of the double-quantum preparation sequence shifted by $\pi/2$ to produce the hypercomplex dataset. Autoshimming of all z gradients was performed before each increment. A 2-s recycle time, equal to the longest carbon T_1, and 512 transients per increment were used resulting in an acquisition time of 12 days. Neither zero filling nor weighting of the time domain data was used in the subsequent data analysis.

The cholesterol ($C_{27}H_{45}O$, MW 386) consisted of 8 mg (20 μmol) of the compound as received from the vendor without further purification. The spectrum was obtained on a Varian VXR-500 spectrometer using a standard broadband probe with a two-turn observe coil. The $\pi/2$ pulse width was 9.3 μs, and the spectral width was 20 kHz (159 ppm) in both dimensions. For each of 207 increments of the double-quantum evolution time, 32 768 complex samples of the FID were acquired, and the process was repeated with the phase of the double-quantum preparation sequence shifted by $\pi/2$ to produce the hypercomplex dataset. A 10-s recycle time, equal to the longest carbon T_1, and 256 transients per increment were used resulting in an acquisition time of 6 days. The data set was zerofilled to the next power of two in the DQ dimension, but no weighting of the time domain data was used.

Both spectra were acquired using deuteriochloroform as the solvent and a solution volume of approximately 700 μL. The center resonance of the chloroform triplet was defined as 77 ppm and used to reference all chemical shifts to TMS. Broadband proton decoupling was achieved using WALTZ modulation of a 3-kHz H_2 field. The probe temperature was regulated at approximately 26 °C. The 2D INADEQUATE pulse sequence from Bax et al.[3,4] along with the extensions of Levitt and Ernst[5] was used to acquire hypercomplex data. The details of the pulse sequence have been given elsewhere.[6] The preparation of the double quantum coherence was optimized for J = 40 Hz. These

* To whom correspondence should be addressed.
† Department of Chemistry, University of Utah.
‡ Department of Medicinal Chemistry, University of Utah.
§ Department of Fuels Engineering, University of Utah.
⊥ Department of Chemistry, Brigham Young University.

(1) Dunkel, R.; Mayne, C. L.; Pugmire, R. J.; Grant, D. M. *Anal. Chem.*, preceding paper in this issue.
(2) Foster, M. P.; Mayne, C. L.; Dunkel, R.; Pugmire, R. J.; Grant, D. M.; Kornprobst, J.-M.; Verbist, J.-F.; Biard, J.-F.; Ireland, C. M. *J. Am. Chem. Soc.* **1992**, *114*, 1110.
(3) Bax, A.; Freeman, R.; Kempsell, S. P. *J. Am. Chem. Soc.* **1980**, *102*, 4849.
(4) Bax, A.; Freeman, R.; Frenkiel, T. A. *J. Am. Chem. Soc.* **1981**, *103*, 2102.
(5) Levitt, M. H.; Ernst, R. R. *Mol. Phys.* **1983**, *50* (5), 1109.
(6) Dunkel, R.; Mayne, C. L.; Curtis, J.; Pugmire, R. J.; Grant, D. M. *J. Magn. Reson.* **1990**, *90*, 290.

0003-2700/92/0364-3150$03.00/0

data were processed according to the prescription of States et al.[7] To assist the automated analysis of the low S/N 2D INADEQUATE spectra, a 1D proton-decoupled carbon spectrum was acquired in each case under the same experimental conditions as were used for acquiring the 2D data. The resonance frequencies, intensities, and relaxation times for all carbon resonances in the 1D spectrum provide initial parameter estimates for the analysis of the 2D spectrum.

RESULTS AND DISCUSSION

The Bistramide A Example. Proton spectra of the bistramide A sample contain severe signal overlap, especially in the methylene region, which may explain the erroneous assignments of carbon–carbon bonds published previously for bistramide A (alias bistratene A).[8] Even though more demanding in acquisition time than the plethora of techniques involving protons, a 2D INADEQUATE spectrum detects directly the carbon skeleton of the molecule. Despite the presence of an unusually high-digital resolution in the 2D spectrum and extensive time averaging intended to render the 2D INADEQUATE spectrum visually interpretable, several crucial bond signals could not be identified during an extensive manual examination of the acquired data set, and those bond patterns that could be visually identified were, for the most part, marginally identifiable. Previous work in the area of computerized analysis of such spectra[6] had revealed the possibility of dramatically increased sensitivity for computerized versus manual interpretation.[9] Therefore, the automated bond extraction method was applied to the bistramide A spectrum.

To obtain frequencies, intensities, phases and relaxation times of transitions of bistramide A, the 1D carbon spectrum was analyzed by the program PHASEIT,[10] and Figure 1 summarizes the results of the analysis. From top to bottom are shown (a) the experimental spectrum after automated correction, (b) the simulated spectrum calculated from the determined intensity, frequency, phase and relaxation parameters of each transition, and (c) the residual spectrum after subtracting b from a. Neglecting the three solvent signals near 77 ppm and the incompletely suppressed carrier signal in the center of the spectrum, 40 resonances remain each corresponding to just one carbon.[2] In contrast to the proton spectrum, even though the aliphatic region of the carbon spectrum is crowded, the increased dispersion of carbon chemical shifts combined with the simplification afforded by proton decoupling permits each carbon to be resolved. The analysis of the 1D carbon spectrum took 3 min and the 2D FFT 90 min. If not stated otherwise all timing information in this paper is given in wall-clock time for an IBM RS/6000-320 workstation. The parameter values obtained from PHASEIT are used for the analysis of 780 possible bond regions in the 388-MB 2D INADEQUATE data set. The analysis required 27 h on three IBM RS/6000-520 workstations running in parallel (79-h total CPU time). The program CCBOND was used with response surface mapping and detection of individual transitions corresponding to the set of operating parameters, model 2, described in ref 1. Bond criteria based upon (1) positive values of all intensity parameters, (2) a minimum intensity parameter precision of 2.5, (3) a maximum isotope shift of 3 Hz, and (4) a maximum deviation of the final coupling constant of 15 Hz from the initial estimate[6] were used.

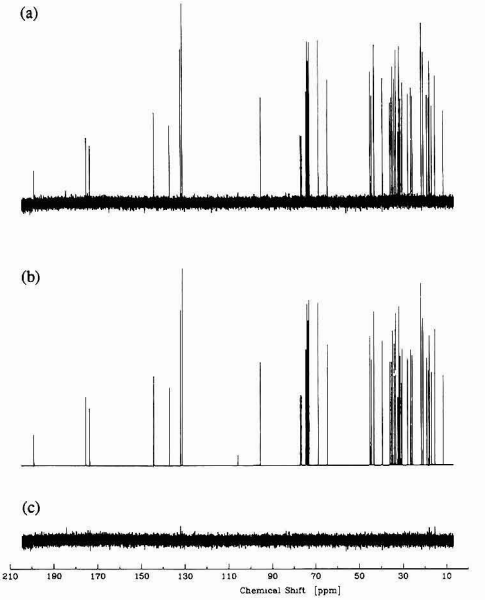

Figure 1. Results of the analysis of the 1D proton-decoupled carbon spectrum of bistramide A by program PHASEIT: (a) the experimental spectrum with phase and baseline automatically corrected, (b) the simulated spectrum calculated from determined parameter values, and (c) the residual spectrum, a minus b, showing that essentially all the nonrandom features of the spectrum are accurately simulated.

The automated analysis identified 35 bond signals, each with a unique assignment to a pair of carbon resonances. Several examples of fitting windows will now be presented to illustrate how the analysis proceeds. Figure 2 shows the response surface, as described in ref 1, of a fitting window corresponding to the chemical shifts in the 1D spectrum of two nonbonded carbons, i.e., the fitting window contains only noise. This figure shows the lack of any agreement between experimental data and simulated bond patterns depending upon a coupling constant, J, and both chemical shifts, ν_A and ν_B. The dimensions of the volume rendered are 6 Hz in the J axis and 3 Hz in the ν_A and ν_B axes. This particular fitting window was chosen as an example of a nonbond because it gave one of the highest intensity parameter precision values of any nonbond. Thus, this fitting window would be an example from the right-hand tail of the distribution of nonbonds shown in Figure 15b of ref 1. The featurelessness of this volume rendering is to be contrasted with the well defined patterns present in those of subsequent figures where bonds are known to exist. At the right side of Figure 2 are given the color and opacity maps used for all volume renderings of this paper.

The weakest confirmed carbon–carbon bond signal was detected between carbon atoms resonating at 173.32 and 32.35 ppm. The pulse sequence used to obtain this dataset was optimized for $J = 40$ Hz. However, this bond, with $J = 51.0$ Hz, deviates significantly from the optimum; thus, its signal was not well excited by the pulse sequence. Figures 3 and 4 show the real and imaginary parts of the unphased experimental, simulated, and residual data of this bond region. This bond signal is well below the noise level, and there would be

(7) States, D. J.; Haberkorn, R. A.; Ruben, D. J. *J. Magn. Reson.* **1982**, *48*, 286.

(8) (a) Bistramide A from *L. bistratum* collected in New Caledonia: Gouiffés, D.; Moreau, S.; Helbecque, N.; Bernier, J. L.; Hénichart, J. P.; Barbin, Y.; Laurent, D.; Verbist, J. F. *Tetrahedron* **1988**, *44*, 451. (b) Bistratene A from *L. bistratum* collected at the Great Barrier Reef: Degnan, B. M.; Hawkins, C. J.; Lavin, M. F.; McCaffrey, E. J.; Parry, D. L.; Watters, D. J. *J. Med. Chem.* **1989**, *32*, 1354.

(9) Dunkel, R. Ph.D. Thesis, University of Utah, December 1990.

(10) Dunkel, R. U.S. Patent Application No. 675,401.

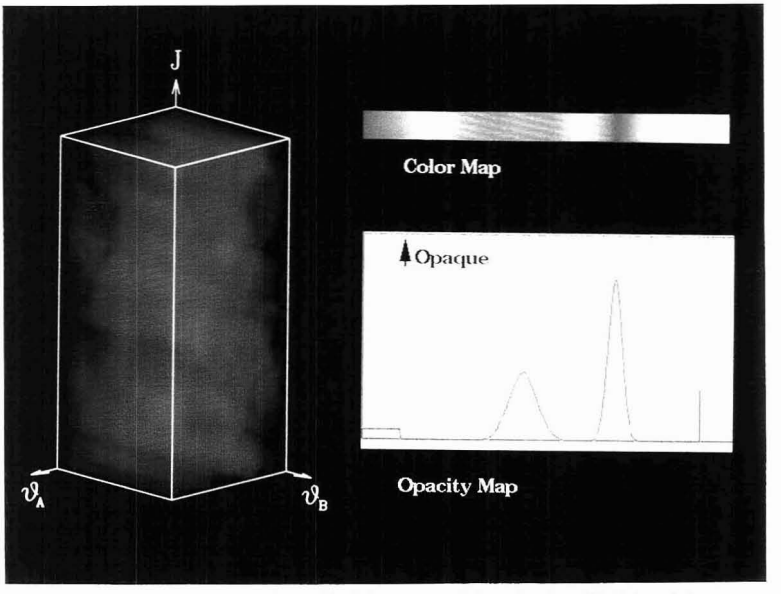

Figure 2. Response surface of a fitting window in the bistramide A data set containing only noise. This fitting window gave one of the highest intensity parameter precision values of any fitting window with only noise.

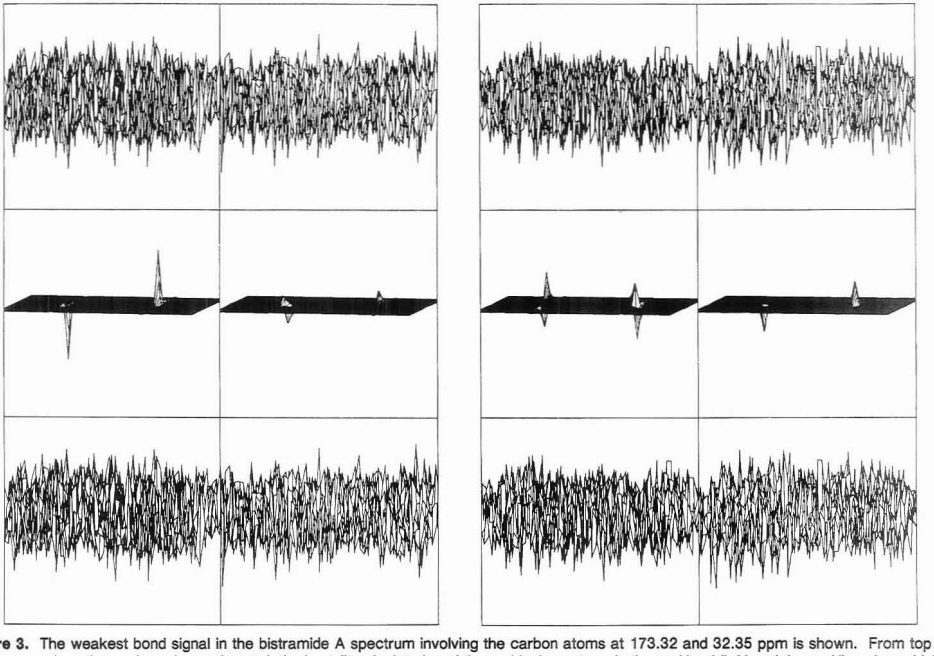

Figure 3. The weakest bond signal in the bistramide A spectrum involving the carbon atoms at 173.32 and 32.35 ppm is shown. From top to bottom are given the unphased experimental, the best-fit calculated, and the residual spectrum in the real/real (left) and the real/imaginary (right) data sets.

no hope of visually finding and identifying the pattern. Figure 5 presents the response surface of this spectral region on the left and the corresponding simulated response surface on the right. These two plots show that low S/N does influence the experimental response surface. However, the prior knowledge extracted from the 1D dataset and included in the construction of the mathematical model as well as the complete hypercomplex dataset allows this bond signal to be clearly

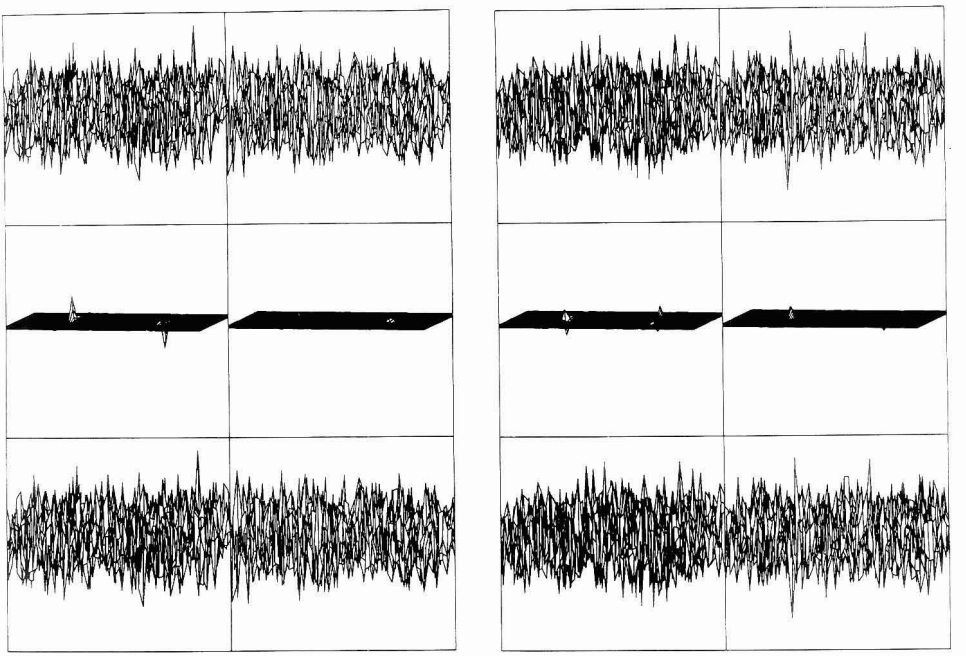

Figure 4. The weakest bond signal in the bistramide A spectrum involving the carbon atoms at 173.32 and 32.35 ppm is shown. From top to bottom are given the unphased experimental, the best-fit calculated and the residual spectrum in the imaginary/real (left) and the imaginary/imaginary (right) data sets.

differentiated from the noise only response surface given in Figure 2.

Figure 6 shows the bistramide A molecule with the detected 35 bond signals drawn in bold. The italicized numbers are the scalar coupling constants in hertz, and normal text is used for resonance frequencies from the 1D carbon spectrum in ppm from TMS. Five fragments of the carbon skeleton can be assembled from the analysis containing all carbon–carbon single bonds in the molecule. These fragments could have been further assembled by an additional 2D INADEQUATE experiment optimized for the detection of double bonds with coupling constants on the order of 70 Hz. However, sufficient information is available from other experiments to identify these bonds unambiguously, and a further 2D INADEQUATE experiment was not needed to prove the structure.[2]

The Cholesterol Example. The analysis of the 1D carbon spectrum of the 20-μmol cholesterol sample by the program PHASEIT took 3 min. Thirty resonances were identified and numerically characterized. Figure 7 shows (a) the automatically corrected experimental spectrum, (b) the simulated spectrum calculated from the determined parameter values, and (c) the residuals obtained by subtracting b from a. After elimination of the three solvent resonances near 77 ppm as well as an incompletely suppressed carrier glitch, which falls under the solvent resonances, one is left with 26 resonances to be used in the analysis of the 2D INADEQUATE spectrum. Figure 7 suggests that the signal at 31.93 ppm is actually an overlap of two carbon resonances, and as will be seen below, this ambiguity introduces problems in the structure elucidation. The 2D fast Fourier transform of the 2D dataset took 15 min.

In this example, involving a known compound, the data were acquired with minimal resolution as well as a S/N ratio barely above the detection limit of CCBOND to illustrate problems that can potentially arise in the elucidation of an unknown structure. The number of data points in the 2D INADEQUATE cholesterol dataset is about one-fourth that of the bistramide A spectrum discussed above, hence potentially reducing the sensitivity of the automated analysis by a factor of 2 (compare parts a and c of Figure 16 in ref 1). To maximize the performance of the program CCBOND for detection of weak bond signals, the most sensitive operational mode, referred to as model 5 in Table II of ref 1, was selected for the analysis of these data. During the mapping stage of the analysis of a bond region, only the overall intensity value is adjusted for every grid point while keeping all other parameters constant. After identification of the grid point or points corresponding to an optimum agreement between simulated and experimental spectral regions, the coupling constant and the two shift frequencies are also unlocked and regressed, using the parameter values corresponding to optimum grid points as initial values. These few nonlinear regressions determine the final optimum parameter values upon which the bond criteria are based, and these values are reported by the program CCBOND.

Use of model 5 achieves greater sensitivity than use of any of the other models (compare parts a–d with part e in Figure 15 of ref 1) but requires that the spectral phase be determined a priori. Use of model 5 also increases the speed of extracting bond information by about 1 order of magnitude by linearizing the regression during the time consuming mapping stage. A method for autophasing n-dimensional spectra[10] will be described in detail in a later publication. Briefly, however, the approach is to identify a few spectral signals and to determine their phases in each dimension by a nonlinear regression analysis. These phases are then further regressed with a model expressing phase as a function of frequency in each of the two dimensions. A simple linear model has proven adequate so far in our work. Once the parameters of this

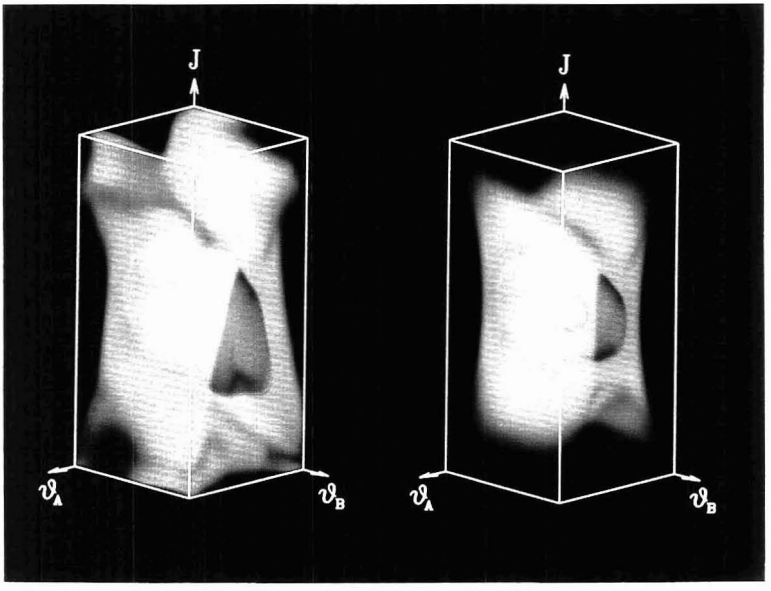

Figure 5. On the left is shown a volume rendering of the experimental response surface of the same spectral region as shown in Figures 3 and 4, and the weakest bond pattern in bistramide A. On the right is shown the corresponding simulated response surface. Contrasted with Figure 2, the positive bond test for this weakest of bond patterns is certainly justified.

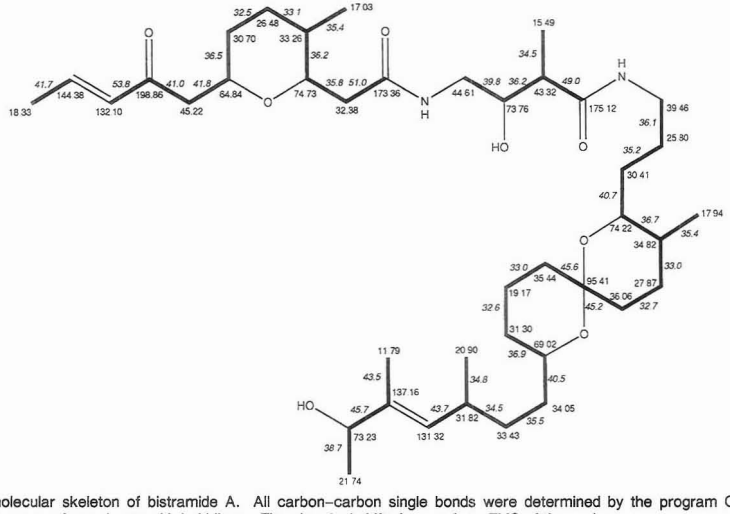

Figure 6. The molecular skeleton of bistramide A. All carbon–carbon single bonds were determined by the program CCBond from a 2D INADEQUATE data set and are shown with bold lines. The chemical shifts in ppm from TMS of the carbon resonances were determined from the 1D spectrum by the program PhaseIt. Italic numbers are coupling constants in hertz determined from the 2D data by the program CCBond.

model are determined sufficiently accurately, the phases for subsequent regressions are computed from the model. For the cholesterol sample nine detected bond patterns were used to determine the phase-frequency model as shown in Figures 8 and 9. This approach is somewhat analogous to phasing the data before subjecting them to the full spectral analysis.

From Figure 16a of ref 1, it is known that bonds with weak second-order effects ($\Delta\nu/J > 4$) produce, using model 5 at a S/N above 2.5, patterns with a detected intensity precision greater than 4 with at least 99.9% probability. Hence, the following bond criteria are chosen to establish bond identification: (1) the value of the intensity parameter must be positive, (2) the intensity parameter precision must be greater than 4, (3) the isotope shift must be less than 3 Hz, and (4) the value of the coupling constant must differ by less than 15 Hz from the initial estimate.

All 325 potential bond regions were evaluated under these conditions in 4 h and 30 min. This time is roughly equivalent

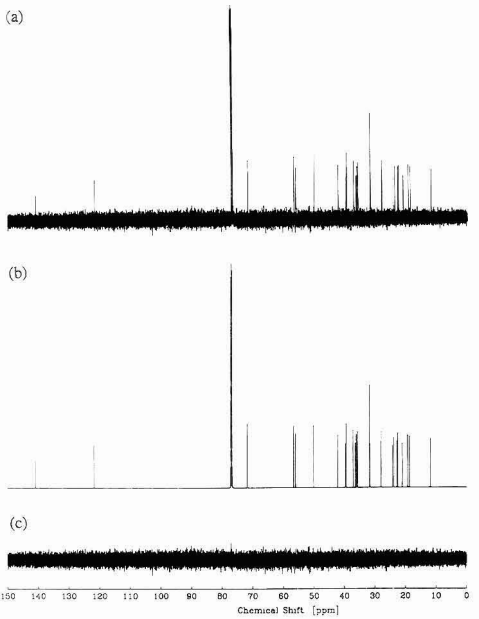

Figure 7. Results of the analysis of the 1D proton–decoupled carbon spectrum of cholesterol by the program PHASEIT: (a) the experimental spectrum with phase and baseline automatically corrected, (b) the simulated spectrum calculated from determined parameter values, and (c) the residual spectrum, a minus b.

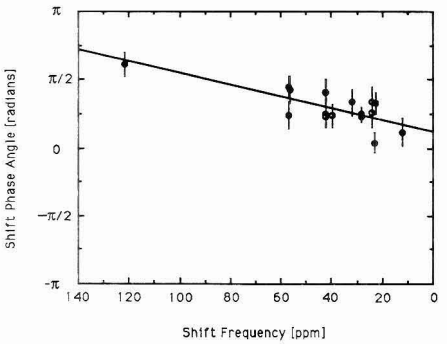

Figure 8. The weighted linear phase correction in the shift direction determined for the 2D INADEQUATE spectrum for the 20-μmol cholesterol sample by program CCBOND. The experimental points are the phase values in shift direction (ϕ_A and ϕ_B) shown as circles with an error bar corresponding to plus or minus one marginal standard deviation as determined by fitting the model equation described in the text to nine bond patterns identified during examination of possible bond regions.

to the time required to interpret manually a high S/N spectrum of this size and is negligible compared to the 2 orders of magnitude increase in acquisition time necessary to acquire a high S/N spectrum that could have been interpreted manually. The overall improvement in time and savings in spectrometer costs more than justifies the computational burden of automated interpretation. The program CCBOND reported that 34 of the 325 possible pairs of carbons in cholesterol produced a bond pattern in the 2D INADEQUATE spectrum. Only 8 of these 34 reported bonds occur in fitting windows that are totally free of overlap with fitting windows

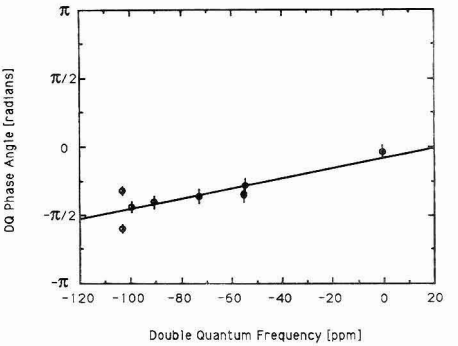

Figure 9. The weighted linear phase correction in the double quantum direction determined for the 2D INADEQUATE spectrum of cholesterol by program CCBOND. The experimental points are the phase values in the double quantum direction (ϕ_{DQ}) shown as circles with an error bar corresponding to plus or minus one marginal standard deviation as determined by fitting the model equation to nine bond patterns identified during examination of possible bond regions. The outliers at −103 ppm are due to the low digital resolution of the spectrum in the DQ direction that causes overlap of the signals from the bonds between the carbon at 28.02 ppm and the two methyl groups with resonances at 22.56 and 22.81 ppm.

from other reported bond patterns, a clear indication that a significantly higher spectral resolution in the DQ direction would have been preferable. The major sources of fitting window overlap are six reported bond patterns, each listed twice by CCBOND, one of each pair includes the carbon at 42.32 ppm and the other of each pair includes the carbon at 42.34 ppm in the 1D spectrum. The chemical shift difference of 2.5 Hz between these two carbons on a 500-MHz spectrometer is less than the maximum expected isotope shift of 3 Hz, and the duplication of these reported patterns simply indicates that these atoms are indistinguishable as far as assignment of the identified bond patterns is concerned. Either of these carbon atoms satisfy the bond criteria equally well for all six simulated patterns, and it remains unclear how to assign these six patterns to the two carbons. Thus, CCBOND produces an enumeration of all 12 possible interpretations, and the spectroscopist is left with the task of resolving the problem by bringing to bear additional information. For example, one might use an alternative solvent to increase the difference in chemical shift of the two carbons thereby removing the ambiguity; only a very small change in chemical shift would be required to render the data unambiguously interpretable.

While ref 1 compared mainly the analysis of pure noise spectral regions with those containing just one bond pattern, experimental spectra can contain regions with several overlapping bond patterns. Program CCLOGIC was written to summarize the output of CCBOND in the form of a connectivity table with indications of ambiguous signal assignments and of overlap between bond patterns that might cause a false positive bond test. Compared to the analysis of bistramide A, these problems in the analysis of the cholesterol spectrum are significantly increased due to reduced spectral resolution. Furthermore, use of model 5 in the fitting increases the difficulty of identifying cases where only three of the four lines in the pattern exist.

Three positive bond tests for the cholesterol spectrum were called into question because of overlap of fitting windows for both A and B transitions. Examination of these three regions reveals that only the pattern involving carbons at 28.02 and 24.29 ppm shows significant signal overlap for all four transitions. For the other two cases, even though the fitting

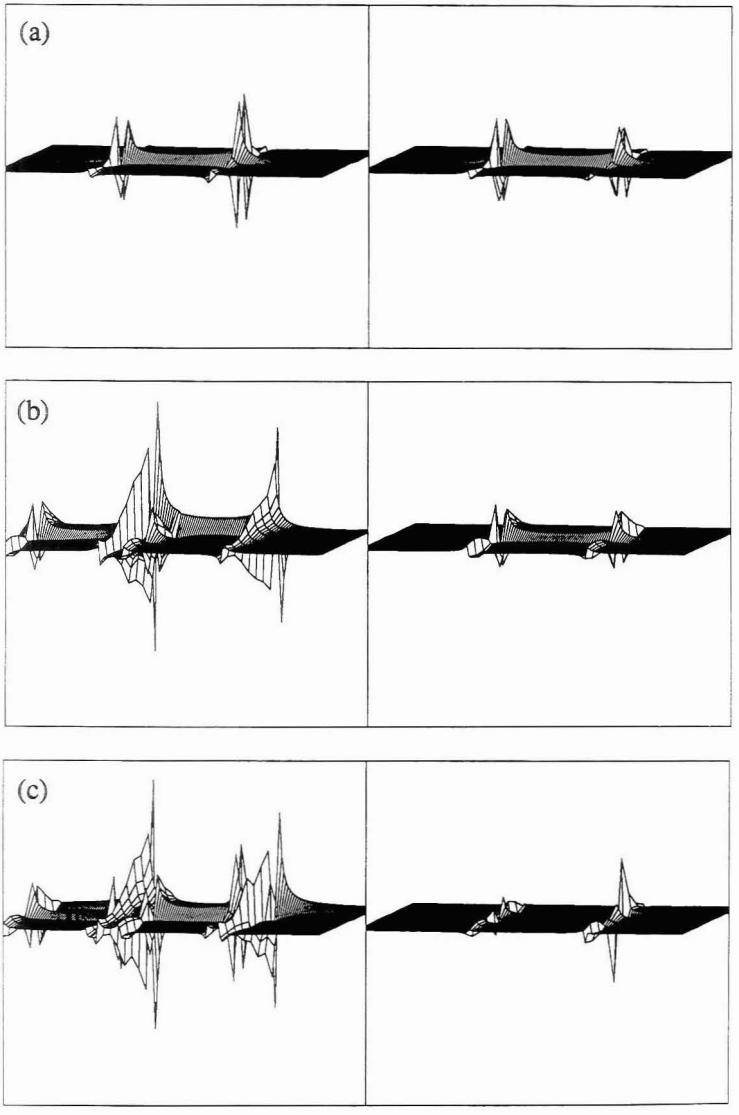

Figure 10. The fitting window of a spectral pattern that caused a false positive indication of a bond between the carbons at 28.02 and 24.29 ppm in the 20-μmol cholesterol spectrum. The figure illustrates (a) the simulated prospective bond signal, (b) a simulation of the three bond signals (28.01 bonded to 22.81, 28.01 bonded to 22.56, and 24.30 bonded to 28.23 ppm) overlapping the false one, and (c) the difference b minus a. Because of extreme underdigitization in the DQ direction, these three patterns overlap the fitting window in such a way that all the intensity attributed to the false bond is drawn from these overlapping signals.

windows overlap, there is sufficient independent data so that ambiguous interpretations are not produced. Figure 10 examines the problem bond between the carbons at 28.02 and 24.29 ppm. Using the best-fit parameter values for the various overlapping patterns Figure 10 shows (a) a simulation of the bond in question, (b) a simulation of the three other bond patterns significantly influencing this fitting window, and (c) the difference between the two, b minus a. Of course, the actual experimental data could not be used in this figure because of the very low S/N. The dispersive signal components best illustrate the extreme degree of signal overlap. The left half of Figure 10b, the A part of the fitting window, is composed of the A part of the spectrum from three bond patterns. At the left edge of the window is the A1 transition of the bond between carbons at 28.23 and 24.30 ppm. In the center is an overlap of the A2 transition of this same bond with the A1 transitions of bond patterns between the carbons at 28.02 and 22.81 ppm and between carbons at 28.02 and 22.56 ppm. The right side contains an overlap of the A2 transitions of these last two bonds. The right half of Figure

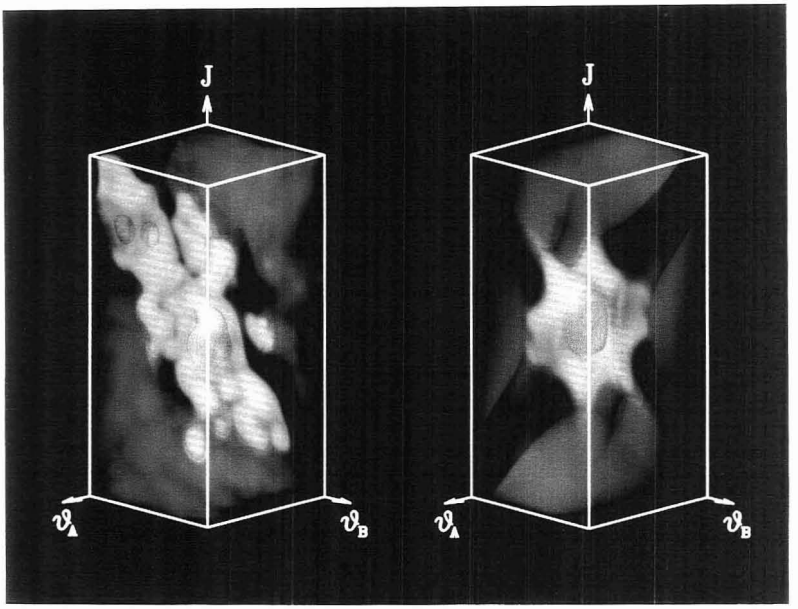

Figure 11. On the left is shown the experimental response surface corresponding to the false bond case described in Figure 10, and on the right is shown the response surface that would be expected for such a bond. The severe distortions and the poor agreement between experimental and simulated patterns allow one to suspect the misinterpretation of the experimental pattern.

10b, the B part of the fitting window, contains the B doublet of the bond pattern between carbons at 28.23 and 24.30 ppm. Since every transition of the prospective bond overlaps with transitions of other bond patterns, there is no independent evidence that this bond signal really exists.

Figure 11 shows a better way to examine this overlap problem. On the left is shown the actual response surface, while on the right is shown the response surface expected from an isolated bond with appropriate parameters. The correspondence between the two surfaces is poor, and nearby maxima exist which cannot be excluded from consideration. The assumption of an isolated AB spin system used to derive the bond criteria is clearly violated. Furthermore, the prospective pattern has a parameter precision of 4.1, barely above the threshold for bond detection, and is by far the weakest pattern found in the cholesterol spectrum. In fact, this pattern does not correspond to a legitimate bond in cholesterol. This example serves to emphasize when the program gives a warning of problems that the results of the automated analysis must be interpreted with care. Problems of this sort can be ameliorated by acquiring the data with higher digital resolution in the DQ direction.

Figure 12 shows the real/real part of the spectrum of the weakest bond signal detected in the cholesterol sample. This bond connects the carbons resonating at 140.77 and 42.32 ppm. Model 3 was used for the last step in the fitting for this bond so that all phase values as well as all four intensity parameters were optimized along with the coupling constant and both chemical shifts. In this manner the signal intensities detectable with the model equation are faithfully reproduced. The experimental data set was automatically phase corrected based upon the determined best-fit phase parameters so that the spectrum shown is in pure absorption mode. Figure 12a is the experimental spectrum, part b is the simulated spectrum, and part c is the residual spectrum. It becomes immediately obvious that manual interpretation of even the well-phased spectrum would be impossible. Figure 13 shows a volume rendering of expected, on the right, and experimental, on the left, response surfaces. Even though significant differences between the simulated and experimental response surfaces are evident, the features in the experimental response surface are clearly nonrandom in contrast to Figure 2, and the area of high agreement is well localized in contrast to Figure 11.

Assembly of molecular fragments[11] and enumeration of the possible candidate structures from the connectivity table generated by program CCLOGIC can be done by programs such as CASE,[12-14] CHEMICS,[15,16] and GENOA,[17] but so far we have done this step manually. Either approach requires additional information to complete the structure elucidation. In the case of cholesterol it is instructive to discuss the kind of additional information needed to complete the carbon skeleton in addition to that obtained from the analysis of the 2D INADEQUATE spectrum.

As with the bistramide A sample, the double bond between the resonances with chemical shifts of 140.77 and 121.72 ppm was not detected. Such carbon–carbon double bonds exhibit coupling constants around 68 Hz,[18] and since the pulse sequence was optimized to detect single bonds (J = 40 Hz),

(11) Gray, N. A. B. *Computer-Assisted Structure Elucidation*; John Wiley & Sons: New York, 1986; Chapter VII.
(12) Christie, B. D.; Munk, M. E. *J. Chem. Inf. Comput. Sci.* **1988**, *28*, 87.
(13) Christie, B. D.; Munk, M. E. *Anal. Chim. Acta* **1987**, *200*, 347.
(14) Munk, M. E.; Shelley, C. A.; Woodruff, H. B.; Trulson, M. O. *Fresenius' Z. Anal. Chem.* **1982**, *313*, 473.
(15) Funatsu, K.; Susuta, Y.; Sasaki, S. I. *J. Chem. Inf. Comput. Sci.* **1989**, *29*, 6.
(16) Funatsu, K.; Miyabayashi, N.; Sasaki, S. I. *J. Chem. Inf. Comput. Sci.* **1988**, *28*, 18.
(17) Lindley, M. R.; Shoolery, J. N.; Smith, D. H.; Djerassi, C. *Org. Magn. Reson.* **1983**, *21* (7), 405.
(18) Wray, V. Carbon–Carbon Coupling Constants: A Compilation of Data and a Practical Guide. *Progr. NMR Spectrosc.* **1979**, *13*, 184.

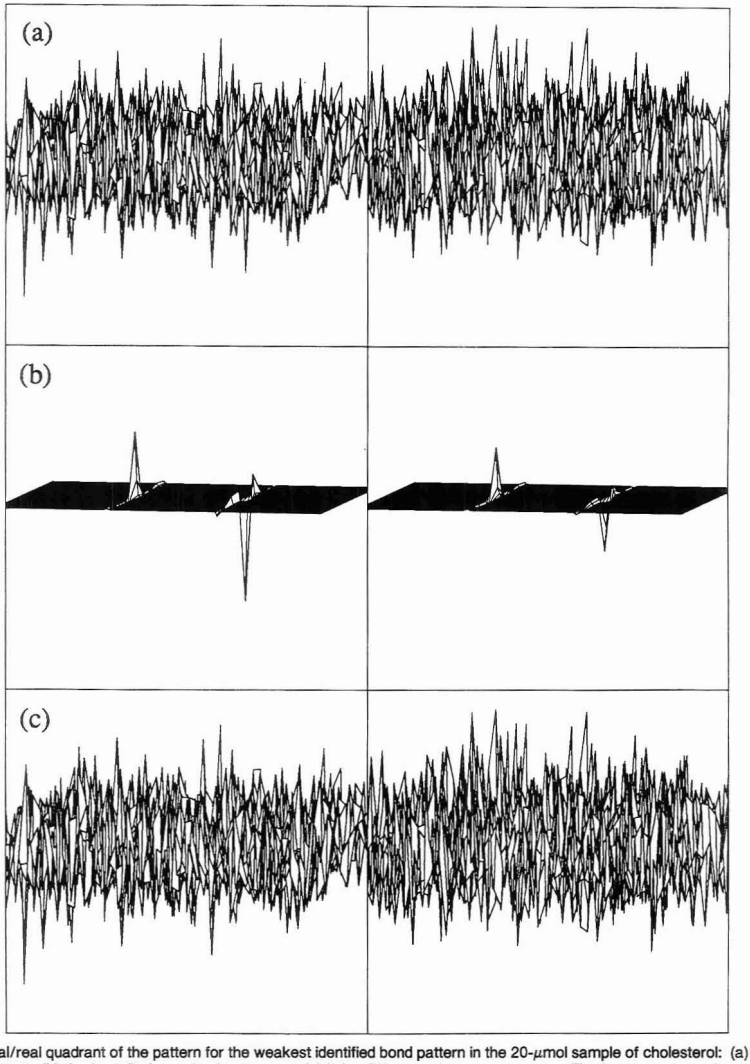

Figure 12. The real/real quadrant of the pattern for the weakest identified bond pattern in the 20-μmol sample of cholesterol: (a) the autophased experimental spectrum, (b) the best-fit determined pattern, and (c) the difference between the two. The bond connects the carbon at 140.77 to the one at 42.32 ppm. Clearly the experimental data is uninterpretable visually.

these bonds fail to appear in the spectrum. To remedy this problem would require the experiment to be repeated with optimization for the detection of sp^2–sp^2 bonds. As these two chemical shifts are characteristic of either alkenes or aromatic compounds the characteristic shifts for the two carbons suggest the presence of an alkene pair even though the bond was not detected in the spectrum. Numerous circumstances in an unknown sample can combine so that a particular bond is not observed, and interferences from such negative data must be made with great caution.

The carbon resonance at 31.92 ppm in the 1D spectrum is an overlap of two magnetically equivalent carbon atoms that are not resolved on a 500-MHz spectrometer. When the surrounding structure is assembled clearly this is a case of accidental magnetic equivalence and is not due to molecular symmetry. The actual bond between these two carbon atoms forms an A_2 spin system and, consequently, is undetected in the 2D INADEQUATE spectrum. Use of a different solvent or a shift reagent may separate such resonances and resolve this problem.

While the bond signal between carbon resonances at 36.52 and 37.27 ppm with prominent second-order multiplet intensity distortion ($\Delta\nu/J \approx 2.8$) was observed without undue difficulties, the bond between resonances at 35.79 and 36.21 ppm was undetected due to the severe second order effects ($\Delta\nu/J \approx 1.5$). This result is expected based on the Monte Carlo simulations shown in Figure 16a compared to that of Figure 16b of ref 1. Severely second-order AB patterns, with lower intensities in the outer two lines, require higher S/N than do AX patterns to obtain reliable bond detection. This

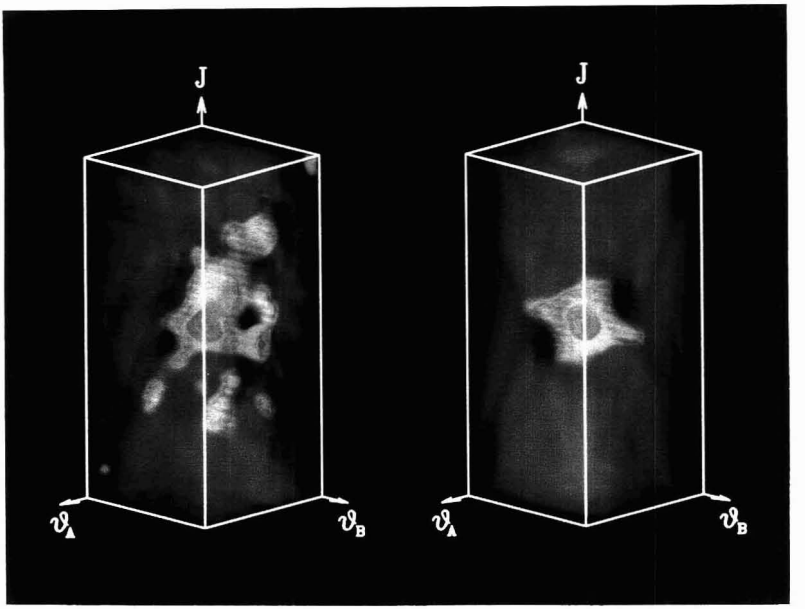

Figure 13. On the left is shown the experimental and on the right the simulated response surfaces for the data shown in Figure 12. Note that the experimental pattern is better localized and agrees fairly well with the simulation in contrast to the case shown in Figure 11.

problem is aggravated by three additional effects: (1) Severely second-order patterns give lower signal intensities than do AX patterns. The pulse sequence could be optimized to give somewhat better performance for cases[19] where $\Delta\nu/J < 3$, but this would lower the threshold at which the problem becomes intractable only slightly and would require acquisition of a new 2D data set. No matter what measures are taken, as the spin system approaches the A_2 limiting case, bond detection becomes impossible. (2) The phase in the DQ direction of AB patterns with severe second-order effects does not follow the linear relation to frequency used for other patterns.[9] Thus, it becomes more difficult to use models with predetermined phases. (3) Due to weak A_1 and B_1 outer transitions the coupling constant is highly correlated with both chemical shifts. This slows the convergence of the nonlinear regression analysis. The agreement between simulated and experimental data for the bond between carbons at 35.79 and 36.21 ppm can be substantially improved by allowing the DQ phase to be adjusted during the nonlinear regression analysis. However, a probability of 99.9% for bond detection is not achievable for this spectral pattern.

Figure 14 summarizes the structural information obtained for cholesterol from the 2D INADEQUATE data and the 1D carbon spectrum. The chemical shifts reported are those from the 1D spectrum and the coupling constants are those determined from the 2D spectrum. The determined average marginal standard deviation is 0.137 Hz for the reported coupling constants and 2.3×10^{-4} ppm for the transition frequencies. All detected bonds are shown as bold lines in Figure 14, and dashed lines are used for the bonds to carbons at 42.32 and 42.34 ppm as a result of the ambiguities encountered in the assignment discussed above. Light lines are used for the double bond since it was not observed. The coupling constant for the double bond is about 71 Hz, a value

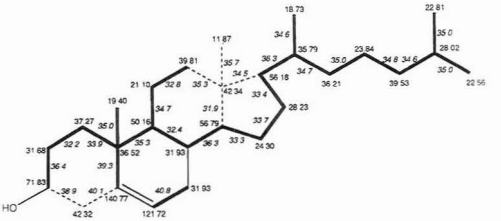

Figure 14. The carbon skeleton of cholesterol from 20 μmol of compound. The chemical shifts of the carbon resonances were determined from the 1D spectrum in ppm from TMS, and the italic numbers are the coupling constants in hertz obtained from the 2D INADEQUATE spectrum. Dashed lines are used for bond signals that were detected, but assignment of the bond to a unique pair of carbon resonances was ambiguous. Bold lines are used for all other detected bonds. Light lines are used for bonds that were not detected. The text discusses the experimental limitations leading to these uncertainties.

determined for a cholesterol derivative.[20] A light line is also used for the bond that is unobserved because of an accidental magnetic equivalence of the two carbons at 31.93 ppm. The bond between carbons at 35.79 and 36.21 ppm has severe second-order effects that prevent reliable detection. The value of the coupling constant of this AB pattern was determined independently to be $J = 34.7$ Hz from a 120-mg sample of cholesterol.

It is instructive to consider what additional data would be needed, as a minimum, to complete the cholesterol structure determination. The presence of the double bond can reliably be infered from the chemical shifts of the carbons, and the anomalously high chemical shift of the carbon at 71.83 ppm in an aliphatic ring indicates the presence of some functionality. A high-resolution mass spectrum would give a reliable molecular formula confirming the hydroxyl on the carbon at

(19) Bax, A.; Freeman, R. *J. Magn. Reson.* **1980**, *41*, 507.

(20) Wray, V. Carbon–Carbon Coupling Constants: A Compilation of Data and a Practical Guide. *Progr. NMR Spectrosc.* **1979**, *13*, 233.

71.83 ppm and ensuring that there are no additional oxygens or other heteroatoms in the molecule. A DEPT experiment would establish the number of directly bonded protons for each carbon. At this point each of the carbons at 31.93 ppm has only one unsatisfied bond. No additional bonds were detected to either of them, and none of the possible bonds to other carbons with unsatisfied valences would produce a strongly second-order case that might not be detected. In conditions such as this it may be safe to assume that such carbons are bonded to each other. At this point it is known that the carbon at 42.32 ppm has two unsatisfied valences and the one at 42.34 ppm has four. All six of the required bonds were detected. The only question is how they should be distributed. There are 15 possible isomers consistent with the constraints. Some experimentation with models leads to the conclusion that only the structure of Figure 14 is reasonable. All the others yield highly strained ring systems or systems uncharacteristic of natural products. The only remaining uncertain bonds are on the carbons at 35.79 and 36.21 ppm, so these two carbons must be bonded to each other. Recall that there is evidence for a bond between these two carbons, although not at the level of certainty we have chosen as our standard. The first assignment of the carbon resonances in cholesterol was done by Reich et al.[21] using data obtained with a frequency sweep cw spectrometer at 15.1 MHz. Some corrections in the assignment were made later, and the results of Figure 14 agree with this more recent work.[22]

SUMMARY AND CONCLUSIONS

In this paper it has been demonstrated that 2D INADEQUATE data sets with rms S/N as low as 2.5 can be successfully analyzed which extends the realm of applicability of this powerful technique to about 20 μmol of the unknown compound. Computer automated methods for extracting carbon–carbon bond information from the spectrum and constructing the carbon skeletons of molecules have been established, and a program called CCBOND implementing these techniques has been written and is described in ref 1. Two examples of the use of the program (cholesterol and bistramide A) are discussed in detail in this paper. At this S/N no cases were encountered where noise was interpreted as a bond. Some bonds characterized by highly second-order spin systems were not detected satisfactorily, and cases were encountered where a bond could not be unambiguously assigned to one or the other of the two carbons differing in chemical shift by less than 3 Hz. However, most of the carbon–carbon bonds in both examples were correctly detected, and with minimal additional information, the complete structure of the molecule could be inferred.

Computer automation removes the need to search visually through a 2D INADEQUATE spectrum to find the connectivity information. Indeed, at the lowest S/N levels tested, the computer program performed reliably while experienced spectroscopists were unable to detect the signals. We estimate that the program works reliably at a S/N about 1 order of magnitude lower than that required for reliable manual interpretation. Although the computation necessary to analyze the data required many hours on powerful workstations, enhancement of S/N by time averaging of signals would have required about 2 orders of magnitude more spectrometer time in addition to the spectroscopist's time to interpret the spectra manually. Thus, it is economically advantageous to trade computation time for spectrometer acquisition time. In fact, most modern high-field spectrometers include good computer workstations as part of the system, so that the computation required can be accomplished in the background while other acquisition tasks are in progress. Because of the very low sensitivity of the INADEQUATE experiment, the automated method is preferable even when a millimolar quantity of an unknown is available and a satisfactory solvent can be found. For samples of less than a few hundred micromoles there is no efficient alternative to the computer-automated techniques.

The 2D INADEQUATE experiment has some fundamental limitations: (1) Only bond patterns with a limited range of coupling constants can be observed in one spectrum. (2) Bonds between carbons with identical chemical shifts cannot be detected. (3) Bonds between carbons where the chemical shifts differ by less than about twice the carbon–carbon coupling constant are detected considerably less reliably than are bonds between carbons with greater separation. (4) If a given carbon is bonded to one of two or more other carbons differing in chemical shift by less than about 3 Hz, it is impossible to determine which of this group is actually bonded to the first. The computer program detects and catalogues all these possible ambiguous interpretations of the data for further scrutiny by the spectroscopist.

Besides automating the spectral analysis, CCBOND is also an interactive tool that provides the spectroscopist with a unique "filter" through which to view 2D INADEQUATE data in a three-dimensional parameter space. This display on color graphics workstations not only shows a considerably increased S/N ratio compared to normal 2D spectral data but also reduces the subjective elements associated with bond identification. The method also systematizes and simplifies the interpretation of the data, especially in cases where overlapping bond patterns introduce ambiguities into the interpretation.

With the achieved improvement in detection limit using program CCBOND, it now becomes feasible to use the powerful 2D INADEQUATE technique for structure elucidation of small samples in a routine fashion as long as attention is paid to the limitations mentioned above. The x-window version of the described software is commercially available for UNIX workstations through the Scientific Instrumentation Technology and Research Corp., P.O. Box 58072, Salt Lake City, UT 84158-0072.

ACKNOWLEDGMENT

Assistance from the following sources is gratefully acknowledged: James A. Rose and Robert McDermott of the University of Utah Visualization Laboratory for assistance in rendering Figures 2, 5, 11, and 13 and the Department of Computer Science supported by a visualization grant from IBM for the volume rendering software; the University of Utah Visualization Laboratory under a grant from IBM for computing resources; the Deutsche Forschungsgemeinschaft (R.D.); NIH Grants GM 08521 (D.M.G.), CA 36622 (C.M.I.), CA 01179 (C.M.I.); and the Consortium for Fossil Fuel Liquefaction Science funded by DOE/PETC under contract No. DE-FC22-90PC 90029 (R.J.P.).

Received for review March 5, 1992. Accepted August 6, 1992.

Registry No. Bistramide A, 115566-02-4; Cholesterol, 57-88-5.

(21) Reich, H. J.; Jautelat, M.; Messe, M. T.; Weigert, F. J.; Roberts, J. D. *J. Am. Chem. Soc.* **1969**, *91*, 7445.
(22) Blunt, J. W.; Stothers, J. B. *Org. Magn. Reson.* **1977**, *9* (8), 439.

Quantitative Determination of Sulfonated Aliphatic and Aromatic Surfactants in Sewage Sludge by Ion-Pair/Supercritical Fluid Extraction and Derivatization Gas Chromatography/Mass Spectrometry

Jennifer A. Field,*,†,‡ David J. Miller,§ Thomas M. Field,† Steven B. Hawthorne,§ and Walter Giger†

Swiss Federal Institute for Water Resources and Water Pollution Control (EAWAG), CH-8600 Dübendorf, Switzerland, and Energy and Environmental Research Center, University of North Dakota, Grand Forks, North Dakota 58202

Secondary alkanesulfonate (SAS) and linear alkylbenzenesulfonate (LAS) surfactants were quantitatively (>90%) extracted from sewage sludges as their tetrabutylammonium ion pairs using 400 atm of supercritical CO_2 for 5 min of static extraction followed by 10 min of dynamic extraction at 80 °C. Ion pairs of SAS and LAS quantitatively formed butyl esters in the injection port of the gas chromatograph and were determined by gas chromatography/mass spectrometry without class fractionation of the sewage sludge extracts. Concentrations of SAS and LAS in sludges from five different sewage treatment plants ranged from 0.27 to 0.80 g/kg of dry sewage sluge and from 3.83 to 7.51 g/kg, respectively. Good reproducibility was achieved with RSDs of typically 5% for replicate extractions and analyses. Homologue and isomer distributions of SAS in sewage sludge indicated an enrichment of the more hydrophobic components in sewage sludge during sewage treatment.

INTRODUCTION

Supercritical fluid extraction (SFE) has gained attention as a viable technique for combining derivatization reactions with extraction for the determination of polar and ionic organic compounds in solid samples. Coupling derivatization reactions with sample extraction and concentration reduces sample handling and analysis time. Hawthorne et al.[1] reported SFE of polar analytes (e.g., 2,4-dichlorophenoxyacetic acid, phospholipid-derived fatty acids, and phenols) using trimethylphenylammonium hydroxide as an ion pair and methylating reagent. Hills et al.[2] combined silylation reactions with SFE for extracting oxalic acid, dicarboxylic acids, and alcohols from roasted coffee.

Important classes of amphiphilic compounds used in laundry and cleaning products are linear alkylbenzenesulfonate (LAS) surfactants with 1.8×10^6 tons consumed worldwide in 1987.[3] Although it has been shown that LAS removal from the aqueous phase varies from 80 to 98% depending on the type of sewage treatment,[4] LAS generally accumulates in sewage sludges.[5–8] Concentrations of LAS in sewage sludge and sediment have been determined using various extraction methods including refluxing in methanol,[8] sonication using methanol,[9] and ion-pair extraction using methylene blue.[6] It also has been shown that LAS is quantitatively extracted from sewage sludge using SFE with methanol as modifier.[10]

Secondary alkanesulfonates (SAS) are surfactants with a European SAS production capacity of approximately 1.5×10^5 tons/year[11] and are potentially present in sewage sludge and extractable using LAS extraction methods. LAS can be determined using HPLC with UV absorption[12] or fluorescence[13–15] detection, but SAS lack a chromophore and is therefore not amenable to HPLC methods using photometric detectors. Because SAS and LAS are ionic, nonvolatile analytes, derivatization is required prior to their determination by GC.

Previously reported derivatization procedures for LAS, including formation of sulfonyl chlorides,[6,16–18] methyl esters,[16,18–21] and trifluoroethyl esters,[9,22] are not directly amenable for coupling with extraction techniques and typically require multiple preparative steps and the use of hazardous reagents (e.g. diazomethane). However, Heywood et al.[19] reported high-temperature esterification of ρ-dodecylbenzenesulfonic acid from its tetramethylammonium ion-pair form. As previously reported,[1] ion-pair extraction under

† Swiss Federal Institute for Water Resources and Water Pollution Control.

‡ Current address: Department of Agricultural Chemistry, Oregon State University, Corvallis, OR 97331.

§ Energy and Environmental Research Center.

(1) Hawthorne, S. B.; Miller, D. J.; Nivens, D. E.; White, D. C. *Anal. Chem.* **1992**, *64*, 405–412.
(2) Hills, J. W.; Hill, H. H.; Maeda, T. *Anal. Chem.* **1992**, *63*, 2152–2155.
(3) Berth, P.; Jeschke, P. *Tenside, Surfactants, Deterg.* **1989**, *26*, 75–79.
(4) Rapaport, R. A.; Eckhoff, W. S. *Environ. Toxicol. Chem.* **1990**, *9*, 1245–1257.
(5) McEvoy, J.; Giger, W. *Naturwissenschaften* **1985**, *72*, 429–431.
(6) McEvoy, J.; Giger, W. *Environ. Sci. Technol.* **1986**, *20*, 376–383.
(7) Giger, W.; Alder, A. C.; Brunner, P.; Marcómini, A.; Siegrist, H. *Tenside Surfactants Deterg.* **1989**, *26*, 95–100.
(8) Matthijs, E.; DeHenau, H. *Tenside, Surfactants, Deterg.* **1987**, *4*, 193–199.
(9) Trehy, M.; Gledhill, W. E.; Orth, R. G. *Anal. Chem.* **1990**, *62*, 2581–2586.
(10) Hawthorne, S. B.; Miller, D. J.; Walker, D. D.; Whittington, D. E.; Moore, B. L. *J. Chromatogr.* **1991**, *541*, 185–194.
(11) Personal communication, Hüls AG, Marl, Germany, 1991.
(12) Marcomini, A.; Giger, W. *Anal. Chem.* **1987**, *59*, 1709–1715.
(13) Castles, M. A.; Moore, B. L.; Ward, S. R. *Anal. Chem.* **1989**, *61*, 2534–2540.
(14) Nakae, A.; Tsuji, K.; Yamanaka, M. *Anal. Chem.* **1980**, *52*, 2275–2277.
(15) Kikuchi, M.; Tokai, A.; Yoshida, T. *Water Res.* **1986**, *20*, 643–650.
(16) Parsons, J. S. *J. Gas Chromatogr.* **1967**, May, 254–256.
(17) Watanabe, S.; Nukiyama, M.; Takagi, F.; Lida, K.; Kaise, T.; Wada, Y. *J. Food Hyg. Soc. Jpn.* **1975**, *16*, 212–217.
(18) Hon-nami, H.; Hanya, T. *J. Chromatogr.* **1978**, *161*, 205–212.
(19) Heywood, A.; Mathias, A.; Williams, A. E. *Anal. Chem.* **1970**, *42*, 1272–1273.
(20) Imaida, M.; Sumimoto, T.; Yada, M.; Yoshida, M.; Koyama, K.; Kunita, N. *J. Food Hyg. Soc. Jpn.* **1975**, *16*, 218–224.
(21) Kirkland, J. J. *Anal. Chem.* **1960**, *32*, 1388–1393.
(22) Field, J. A.; Leenheer, J. A.; Thorn, K. A.; Barber, L.; Rostad, C. E.; Macalady, D. L.; Daniel, S. R. *J. Contam. Hydrol.* **1992**, *9*, 55–78.

0003-2700/92/0364-3161$03.00/0

SFE conditions using tetraalkylammonium ion-pair reagents can be coupled with ion-pair derivatization, thereby minimizing analysts exposure to hazardous reagents as well as reducing the number of sample preparation steps and time.

This paper describes an ion-pair/SFE and injection-port derivatization method for determining SAS and LAS in sewage sludges. SAS and LAS are coextracted from sewage sludge and unambiguously determined by gas chromatography/mass spectrometry (GC/MS) without class fractionation of the SFE extract. The ion-pair/SFE method presented in this paper reduces total sample preparation and analysis time to less than 1 h.

EXPERIMENTAL SECTION

Samples. Three anaerobically stabilized sewage sludges and two fresh (untreated) sludges were collected from mechanical–biological sewage treatment plants in the area of Zürich, Switzerland. Sewage sludge samples were dried at 80 °C for 72 h, finely ground, and stored in amber bottles.

Chemicals and Reagents. Commercial mixtures of SAS (Hostapur 60; Hoechst AG, Frankfurt, Germany) and LAS (Dobane 113; Shell) were obtained through the Lever Co. (Port Sunlight, England) for use as standards. Primary alkanesulfonates (C_{12}-SAS and C_{18}-SAS) were purchased from Lancaster Synthesis Ltd. (Lancaster, England) for use as SAS surrogates and 4-octylbenzenesulfonic acid (C_8-LAS) was purchased from Aldrich Chemical (Milwaukee, WI). The C_{12}-SAS, C_{18}-SAS, and C_8-LAS surrogates were chosen for this study because they do not occur in commercial SAS and LAS mixtures and are therefore suitable for evaluating the efficiency of SAS and LAS extraction and alkylation.

Reagent grade ion-pair reagents were prepared as 0.5 M methanolic solutions except where noted. Reagents tested included tetrabutylammonium hydrogen sulfate (TBA; Aldrich Chemical), tetraethylammonium hydrogen sulfate (TEA; Fluka AG, Buchs, Switzerland), tetramethylammonium hydrogen sulfate (TMA; Aldrich Chemical), trimethylphenylammonium hydroxide (0.2 M) (TMPA; Pierce, Rockford, IL), and (trifluoromethyl)phenylammonium hydroxide (0.2 M) (TFMPA; Alltech, Deerfield, IL).

A preliminary survey of ion-pair reagents was first conducted to determine the most efficient reagent for ion-pair extraction and derivatization of SAS using water as the sample matrix. Reagent evaluation based on liquid–liquid extraction of aqueous SAS standard solutions was performed at room temperature by adding 0.5 mL of each 0.5 M ion-pair reagent to separate vials containing 3 mL of 15 μg/mL C_{12}-SAS standard. Standard solutions were extracted a total of three times with 2 mL of chloroform by shaking for 30 s. The chloroform extracts were combined and concentrated to 1 mL under nitrogen. Samples for this preliminary investigation of ion-pair reagents were analyzed using a Hewlett Packard Model 5890 GC equipped with a HP-5 column (20-m × 0.2-mm × 0.17-μm film thickness; Hewlett-Packard) with flame ionization detection (FID). Injection conditions included a split ratio of 1:15, a glass inlet liner packed with silanized glass wool, and an inlet injection temperature of 300 °C. The GC oven was ramped from an initial temperature of 100 to 250 °C at 10 °C/min.

Ion-Pair/Supercritical Fluid Extraction. All extractions were performed using an ISCO 260D pump and SFX 210 extractor (Lincoln, NE) and SFC grade CO_2 (Scott Specialty Gases, Plumsteadville, PA). Lengths (10 cm) of 30–32-μm-i.d. fused silica (Polymicro Technologies, Phoenix, AZ) were attached to the extractor outlet and used to obtain dynamic extraction flow rates of 0.7–0.9 mL/min measured as liquid CO_2 flow at the pump. Extracts were collected by placing the end of the restrictor in 3–4 mL of chloroform. Chloroform was periodically added to the collection vials to compensate for evaporative losses during the extraction. During the dynamic extraction step, the restrictor was constantly warmed with a heat gun to maintain constant flow by minimizing restrictor plugging.

Ion-pair/SFE, a two-step procedure, was applied using a static extraction step during which an ion-pair reagent is permitted to mix with the sewage sludge sample under supercritical conditions, followed by a dynamic extraction step to recover the extracted analytes. Unless otherwise noted, the following procedures were used for extracting sewage sludges under ion-pair/SFE conditions. First, a 0.45-μm glass-fiber filter (Gelman Sciences, Ann Arbor, MI) was placed over the outlet frit of a 2.5-mL ISCO extraction cell end cap to minimize restrictor plugging by the finely ground sewage sludge. The extraction cell body was attached and dry sewage sludge (100 mg) was then weighed directly into the cell followed by addition of 25 μL of 2 μg/mL each SAS and LAS surrogates and 1 mL of ion-pair reagent. Finally, the cell was placed into the extractor (maintained at 80 °C) and immediately pressurized to 400 atm of CO_2 for 5 min of static extraction by opening the inlet valve and keeping the exit valve closed. After 5 min, the exit valve was opened for 10 min of dynamic extraction. The cell was removed from the extractor and allowed to cool to room temperature. Second and third extractions were conducted by adding additional SAS and LAS surrogates and 1 mL of ion-pair reagent to the cooled cell and repeating the extraction procedure. Sewage sludge extracts were concentrated to ca. 1 mL under a gentle stream of nitrogen and transferred to GC autosampler vials. The sewage sludge extracts required no additional fractionation or cleanup steps prior to GC/MS analysis.

Conventional Liquid Solvent Extraction of Sewage Sludge. Liquid solvent extraction of sewage sludge using 0.02 M TBA in methanol was performed using a sewage sludge collected from the Zürich–Glatt sewage treatment plant. Three 100-mg samples of sewage sludge were weighed into 15-mL glass vials with Teflon-lined screw caps. TBA (5 mL) was added to each vial, and the mixtures were sonicated for 30 min at room temperature. The vials were centrifuged for 10 min, after which the methanol supernatant was decanted. Each sewage sludge sample was extracted a total of three times by adding 5 mL of fresh TBA prior to each extraction. The three extracts for each sewage sludge sample were combined, spiked with SAS and LAS surrogates, and concentrated to approximately 0.5 mL for GC/MS analysis.

Gas Chromatography/Mass Spectrometry. Gas chromatographic separations were performed with a Hewlett-Packard Model 5890 GC equipped with a HP-5 column (20-m × 0.2-mm i.d. × 0.33-μm film thickness; Hewlett-Packard) with helium as carrier gas. For SAS and LAS determinations, the oven was ramped at 10 °C/min from an initial temperature of 110 to 220 °C, followed by a second ramp of 6 °C/min to 300 °C where the temperature was held for 3 min. Injection-port conditions for SAS and LAS included a split ratio of 1:7, an injector temperature of 300 °C, and a glass inlet liner with a plug of silanized glass wool. Inlet liners were routinely replaced every 20–25 injections. Each sewage sludge extract injection was followed by a 1-μL injection of TFMPA to minimize any potential sample carryover into the next injected sample. For TFMPA injections the GC oven was ramped at 20 °C/min from 110 to 300 °C. Mass spectral detection was performed with a Hewlett-Packard 5971A mass-selective detector with electron impact ionization (70 eV). The mass spectrometer was operated in both full scan (50–400 amu) and in selected ion mode (SIM) using a dwell time of 50 ms for each mass.

GC/MS Quantitation of SAS and LAS. Commercial preparations of Hostapur 60 and Dobane 113 were used to construct SAS and LAS quantitation curves, respectively. Glass vials containing aqueous solutions of 50–1000 μg of SAS and from 500 to 1500 μg of LAS were each spiked with 50 μg each of C_{12}-SAS, C_{18}-SAS, and C_8-LAS. To each vial, 0.5 mL of 0.5 M TBA in methanol was added and shaken to allow ion-pair formation. Each sample was then extracted a total three times with 2 mL of chloroform each for 30 s. The chloroform extracts were combined and evaporated to 0.5 mL.

For quantitation, the peak areas of the ($[M - 138]^{+\cdot}$) ions at m/z 196, 210, 224, and 238 corresponding to the C_{14}-, C_{15}-, C_{16}-, and C_{17}-SAS homologues, respectively, were ratioed to the area of the ($[M - 138]^{+\cdot}$) ion at m/z 168 of the C_{12}-SAS surrogate. The correlation between peak area and total SAS concentration was determined by linear regression, typically with $r^2 = 0.997$. SAS homologue distributions were determined by summing all isomers for each homologue and calculating their percent of the total. Quantitation of LAS was based on the sum of the ion currents corresponding to m/z 91, 171, and 185. A LAS quantitation curve

Table I. Relative Efficiency of C_{12}-SAS Derivatization

ion-pair reagents[a]	alkyl group added by reagent	% SAS retained by the inlet liner[b]
TBA	butyl	nd
TEA	ethyl	40
TMA	methyl	50
TFMPA	methyl	20
TMPA	methyl	10

[a] TBA: tetrabutylammonium hydrogen sulfate. TEA: tetraethylammonium hydrogen sulfate. TMA: tetramethylammonium hydrogen sulfate. TFMPA: (trifluoromethyl)phenylammonium hydroxide. TMPA: trimethylphenylammonium hydroxide. [b] % SAS retained by the inlet liner is determined by comparing the peak area in the first injection to that observed for a subsequent injection of 1 μL of TFMPA. nd: not detected.

was constructed by ratioing the area of the LAS standard to that of the C_8-LAS surrogate. The correlation between total LAS and C_8-LAS surrogate peak area and total LAS concentration was determined by linear regression, typically with $r^2 = 0.994$.

High-Performance Liquid Chromatography. HPLC with fluorescence detection was used to independently determine whether alkylation occurred under SFE or injection-port conditions. The butyl ester of the C_8-LAS surrogate (C_8-LAS-Bu) was prepared by an alternative method to ion-pair derivatization by first converting C_8-LAS to its sulfonyl chloride derivative with phosphorus pentachloride, followed by substitution to the butyl ester using butanol. Formation of C_8-LAS-Bu was verified by GC/MS. Prederivatized C_8-LAS-Bu was then spiked into extracts of both a LAS commercial mixture, extracted from water at room temperature, and a sewage sludge extracted under ion-pair/SFE conditions. Underivatized C_8-LAS surrogate had been added to each sample prior to extraction. Extracts were analyzed by HPLC before and after spiking with C_8-LAS-Bu.

HPLC separations were performed with a liquid chromatograph (Hewlett-Packard 1090) equipped with a dual grating fluorescence spectrophotometer (Hewlett-Packard 1046A). The fluorescence detector was operated at an excitation wavelength of 225 and an emission wavelength of 295 nm, with a spectral band-pass of 2 nm. The volume of the detector flow cell was 5 μL. For reversed-phase separations, a Hypersil ODS (120-mm × 2.1-mm i.d.) column (Hewlett-Packard) was operated at ambient temperature with a flow rate of 0.4 mL/min. Gradient elution was performed with a binary solution of methanol and 0.1 M ammonium acetate buffer (pH 6.5) using a linear gradient from 35/65 methanol/buffer to 90/10 methanol/buffer in 25 min. One minute of 35/65 methanol/buffer was used to reestablish initial conditions.

RESULTS AND DISCUSSION

Ion-Pair Reagent Evaluation. Ion-pair reagents served two purposes in this study. First, ion-pair reagents enhanced the extraction of sulfonated surfactants into supercritical CO_2 by decreasing their polarity. Second, surfactant ion pairs underwent derivatization in the GC injection port to form sulfonate alkyl esters. Since different ion-pair derivatization reagents were available and since derivatization efficiency may depend upon the reagent selected, ion-pair reagents were evaluated for their reaction with SAS to form alkyl esters under injection-port conditions (Table I). Of the five reagents tested, only TBA indicated no retention of SAS by the inlet liner. In addition, SAS butyl esters formed quantitatively from SAS ion pairs with TBA under injection-port conditions, as demonstrated by the fact that the peak area for the C_{12}-SAS surrogate was between 90 and 107% of the predicted response.

Gas Chromatography/Mass Spectrometry of SAS and LAS. Mass spectral fragmentation (Figure 1A) for SAS under electron impact ionization was consistent with fragmentation

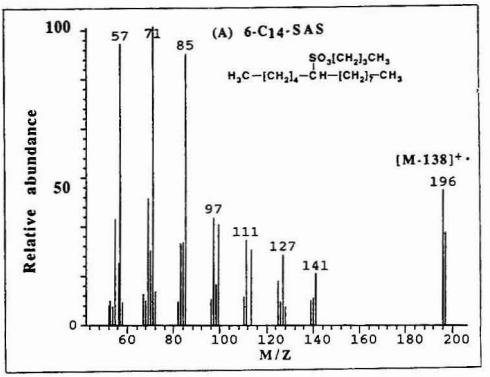

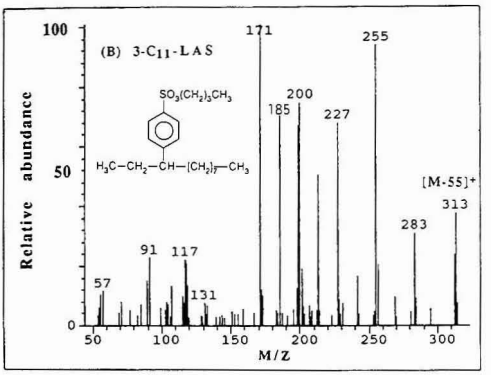

Figure 1. Mass spectra of (A) 6-C_{14}-SAS and (B) 3-C_{11}-LAS.

previously reported for alkyl esters of alkane sulfonates.[23] Although the commercial SAS standard was reported to contain mono-, di-, and polysulfonates, only monosulfonated SAS were detected using GC/MS. All SAS components give an intense homologue-specific ion of ($[M - 138]^{\cdot+}$), corresponding to the loss of $HSO_3C_4H_9$ (sulfonate butyl ester). Therefore, the ($[M - 138]^{\cdot+}$) ions of m/z 168, 196, 210, 224, and 238 were used for quantitating the C_{12}-SAS surrogate, native C_{14}-SAS, C_{15}-SAS, C_{16}-SAS, and C_{17}-SAS, respectively. Since preliminary work indicated that C_{13}-SAS and C_{18}-SAS, found at trace levels in the SAS commercial mixture, were not detectable in sewage sludge extracts; their ($[M - 138]^{\cdot+}$) ions were excluded from subsequent analyses.

Electron impact ionization spectra of LAS were characteristic of the aromatic nature of LAS (Figure 1) with intense peaks typically at m/z 91 (tropylium ion) or m/z 171 or 185, corresponding to $C_nH_{2n}C_6H_4SO_3H$ where $n = 1$ or 2.[24] For purposes of locating individual LAS homologues and their isomers, the $[M - 55]^+$ ions of m/z 299, 313, 327, and 341 arising from the loss of C_4H_7, were characteristic of C_{10}-LAS, C_{11}-LAS, C_{12}-LAS, and C_{13}-LAS, respectively. The sum of the LAS ions at m/z 91, 171, and 185 were used for quantitating the C_8-LAS surrogate and native C_{10}–C_{14}-LAS in ion-pair/SFE extracts of sewage sludge.

Total ion current chromatograms for extracts of sewage sludge demonstrated the complexity of the sample extracted

(23) Truce, W. E.; Campbell, R. W.; Madding, G. D. *J. Org. Chem.* **1967**, *32*, 308–317.
(24) Agozzino, P.; Ceraulo, L.; Ferrugia, M.; Caponetti, E.; Intravaia, F.; Triolo, R. *J. Colloid Interface Sci.* **1986**, 26–31.

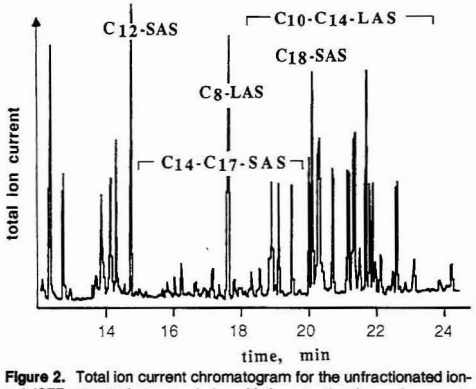

Figure 2. Total ion current chromatogram for the unfractionated ion-pair/SFE extract of sewage sludge with the retention times of surrogate and native SAS and LAS indicated.

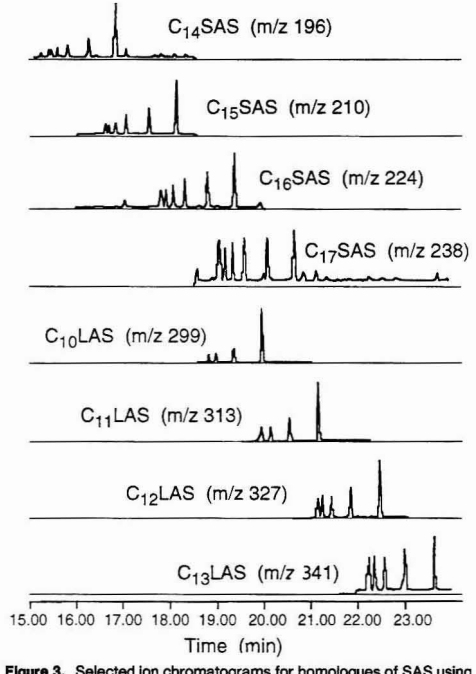

Figure 3. Selected ion chromatograms for homologues of SAS using $[M - 138]^{+\cdot+}$ ions at *m/z* 196, 210, 224, and 238 and of LAS using $[M - 55]^{+}$ ions at *m/z* 299, 313, 327, and 341 in an unfractionated ion-pair/SFE extract of sewage sludge.

by ion-pair/SFE (Figure 2). Owing to their high concentrations in sewage sludge, LAS peaks were observed in the full scan chromatogram of the unfractionated sewage sludge extract. Although native SAS were not easily distinguished from the many other components in the total ion chromatogram, selected ion monitoring (SIM) yielded relatively simple chromatograms for both SAS and LAS (Figure 3). Although SAS and LAS overlap in retention time, SAS and LAS were easily distinguished from one another and from other matrix components using SIM analysis without class fractionation of the ion-pair/SFE extract.

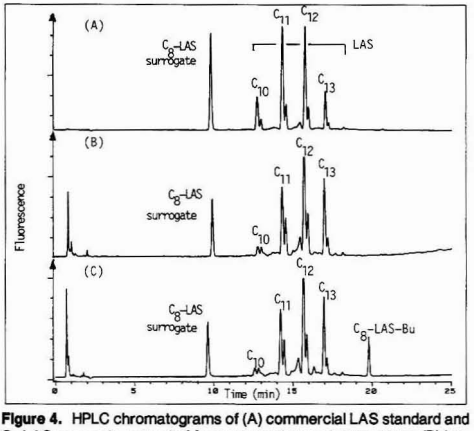

Figure 4. HPLC chromatograms of (A) commercial LAS standard and C_8-LAS surrogate extracted from water at room temperature, (B) ion-pair/SFE extract of sewage sludge with C_8-LAS and native LAS indicated, and (C) ion-pair/SFE extract of sewage spiked with C_8-LAS-Bu. For chromatographic conditions see the Experimental Section.

Table II. Effect of Sample Size and Support Material on Native SAS Recovery from Sewage Sludge[a]

sample size, mg	sample support	% SAS recovery extract 1	extract 2	extract 3
250	filter	92	5	3
100	filter	93	5	2
50	filter	92	5	3
100	glass wool	75	19	6
50	glass wool	75	18	7

[a] Recoveries based on three sequential extractions of sewage sludge from the Zürich–Glatt sewage treatment plant where 100% recovery is defined as the sum of three sequential extractions.

Verification of Ion Pairs in Ion-Pair/SFE Extracts Using HPLC. HPLC with fluorescence detection was used to determine whether alkylation occurred already under ion-pair/SFE conditions in the SFE apparatus or later in the GC injection port. The HPLC chromatogram (Figure 4A) of a commercial C_{10}–C_{14}-LAS mixture and C_8-LAS surrogate ion pairs, extracted from water using TBA in liquid methanol at room temperature, showed typical reversed-phase chromatographic behavior. The selected conditions for HPLC separation of LAS resulted only in partial separation of the C_{10}–C_{13}-LAS isomers (Figure 4). Retention times identical to that of the commercial LAS extract were observed for the C_8-LAS surrogate and native LAS in a HPLC chromatogram for an unspiked ion-pair/SFE sewage sludge extract (Figure 4B), demonstrating that LAS ion pairs are present in SFE extracts. Further evidence that ion-pair/SFE extracts contain ion pairs and not butyl esters was shown by spiking the ion-pair/SFE extract with prederivatized C_8-LAS-Bu. The C_8-LAS-Bu was detected as a later-eluting peak (Figure 4C), compared to the C_8-LAS ion pair, further indicating that the butyl ester of C_8-LAS is chromatographically different from the ion pair. Having shown that C_8-LAS exists as an ion pair in the ion-pair/SFE extract and not as a butyl ester proves that derivatization occurs under the high-temperature conditions of the GC injection port and not in the SFE extraction apparatus.

Ion-Pair/Supercritical Fluid Extraction of Sewage Sludge. Initial experiments were performed to demonstrate ion-pair formation and extraction under SFE conditions using surrogates spiked onto sand, a relatively simple sample matrix.

Table III. Recovery of SAS and LAS from Sewage Sludges

sewage treatment plant[a]	% SAS recovery		
	extract 1	extract 2	extract 3
Glatt	93	5	2
Seegräben	94	5	1
Niederglatt	89	9	2
Stäfa-uetikon	91	7	2
Opfikon	90	7	3
	% LAS recovery		
sewage treatment plant	extract 1	extract 2	extract 3
Glatt	91	6	3
Seegräben	91	8	1
Niederglatt	86	10	4

[a] Sewage treatment plants in the Zürich area. The area of three sequential extractions is defined as 100% recovery.

Table IV. Concentration of SAS and LAS in Sewage Sludge

sewage treatment plant	concn, g/kg of dry sludge[a]	
	SAS	LAS
(A) Zürich-Glatt[b]	0.76 ± 0.02	5.54 ± 0.06
(B) Zürich-Glatt[b]	0.80 ± 0.05[c]	5.39 ± 0.11[c]
(C) Opfikon-Kloten[b]	0.80 ± 0.04	7.51 ± 0.23
(D) Niederglatt[b]	0.27 ± 0.01	3.98 ± 0.25
(E) Seegräben[d]	0.37 ± 0.01	3.83 ± 0.31
(F) Stäfa-uetikon[d]	0.51 ± 0.02	4.90 ± 0.26

[a] Concentrations determined from four replicate samples except for B and F with three replicate samples. [b] Anaerobically stabilized sewage sludge. [c] Determined by liquid solvent extraction. [d] Fresh sewage sludge.

The SAS surrogates spiked onto sea sand were recovered quantitatively (>97%) using TBA as an ion-pair reagent under SFE conditions of 150 °C with 30-min static followed by 15-min dynamic extraction times. In a separate experiment, quantitative recovery (93–94%) of SAS and LAS surrogates, spiked onto 250 mg of sewage sludge instead of sea sand, demonstrated quantitative ion-pair formation and extraction from sewage sludge, a complex organic-rich matrix.

Because spiking solid samples with surrogate standards is potentially problematic, two separate sets of experiments were conducted in order to validate the use of surrogate standards for quantitating native SAS and LAS in sewage sludge extracts. First, exhaustive extraction of native SAS and LAS was determined by ratioing the total amount of native analyte recovered in sequential extractions to the C_{12}-SAS and C_8-LAS surrogate standards, which were shown to be quantitatively recovered in a single extraction. Second, the total concentrations of native SAS and LAS determined by ion-pair/SFE were compared directly with those obtained by liquid ion-pair extraction. For both methods, C_{12}-SAS and C_8-LAS were used as surrogate internal standards.

The dependence of native SAS recovery from sewage sludge on extraction temperature was investigated by varying the extractor temperature between 150 and 80 °C. Although no dependence on recovery with temperature was observed, the use of lower temperatures was more convenient with less time required to cool the extraction cells to room temperature in between additions of TBA. In addition, no change in the recovery of native SAS was observed by decreasing the static extraction time from 30 to 5 min or the dynamic extraction time from 15 to 10 min. Therefore, an extraction temperature of 80 °C and a 5-min static extraction followed by a 10-mim dynamic extraction were used as standard conditions for ion-pair/SFE.

Table V. Distributions of SAS Homologues for Sewage Sludges and a Commercial Product

sewage treatment plant	SAS homologue distribution[a]			
	C_{14}	C_{15}	C_{16}	C_{17}
Zürich-Glatt[b]	19 ± 1.5	35 ± 0.3	30 ± 1.0	17 ± 0.5
Zürich-Glatt[c]	15 ± 0.1	34 ± 0.3	32 ± 0.1	19 ± 0.3
Opfikon-Kloten[b]	18 ± 1.8	34 ± 0.9	31 ± 0.6	18 ± 0.3
Niederglatt[b]	19 ± 1.6	31 ± 1.2	28 ± 0.6	22 ± 1.1
Seegräben[b]	20 ± 1.0	35 ± 0.8	28 ± 0.6	16 ± 0.8
Stäfa-uetikon[b]	20 ± 1.0	37 ± 0.7	28 ± 0.4	15 ± 0.6
commercial product (Hostapur 60)[c]	40 ± 0.3	32 ± 0.2	19 ± 0.2	9 ± 0.2

[a] As percent of total SAS. [b] Determined from ion-pair/SFE. [c] Determined from liquid solvent extraction.

Since methanol-modified CO_2 is known to extract LAS from sewage sludge,[10] the recovery of native SAS from sewage sludge extracted under supercritical fluid conditions using TBA was compared to that extracted using methanol. Two 100-mg samples of sewage sludge were extracted under standard conditions with either 1 mL of pure methanol or 1 mL of 0.5 M TBA in methanol added to the extraction cell containing sewage sludge. The methanol-only extract was analyzed by adding TBA prior to GC/MS analysis. The advantage of ion-pair/SFE extraction over that using only the methanol modifier was demonstrated by a 2.5-fold increae in the amount of native SAS extracted from sewage sludge samples using ion-pair reagent (TBA) compared to that extracted using only methanol.

To investigate the dependence of native SAS recovery on sample size and the number of extractions required for quantitative recovery, three samples each of 50, 100, and 250 mg of sewage sludge from the Zürich–Glatt sewage treatment plant were extracted using three sequential extractions under standard ion-pair/SFE conditions. Recoveries of native SAS from all three sample sizes were essentially identical (e.g., 92–93%, 5–6%, and 2–3% for the first, second, and third extractions, respectively (Table II)). Consistent recovery of >92% in the first extract indicated that only one extraction was required for essentially quantitative extraction of native SAS from sewage sludge, regardless of sample size. Since no dependence of recovery on sample size was observed, 100 mg was arbitrarily selected for subsequent extractions.

The effect of support material covering the extraction cell outlet frit on native SAS recovery and overall extraction performance was tested by replacing the 0.45-μm glass-fiber filter with a plug of silanized glass wool. Decreased dynamic extraction flow rates and restrictor blocking occurred frequently when using glass wool, suggesting incomplete retention of sewage sludge particles inside the extraction cell. In addition, native SAS recovery from sewage sludge supported by glass wool decreased to 75% in the first extract compared to 92% using the glass-fiber filter (Table II) so the filter was used as the sample support for all subsequent extractions.

The ability of the ion-pair/SFE method to quantitatively extract SAS and LAS from different types of sewage sludges also was tested by performing three sequential extractions each on four additional sewage sludges collected from sewage treatment plants in the region around Zürich (Table III). Native SAS recovery varied in the first extract between 89 and 94% with an additional 5–9% and 1–3% in the second and third extracts, respectively. Sewage sludge extracts from three of the samples were also analyzed for LAS. Between 86 and 91% of native LAS was recovered in the first extract followed by an additional 6–10% in the second extract and 1–4% in the third extract. Consistent recovery of ≥89% for SAS and ≥86% for LAS in the first extract indicated that

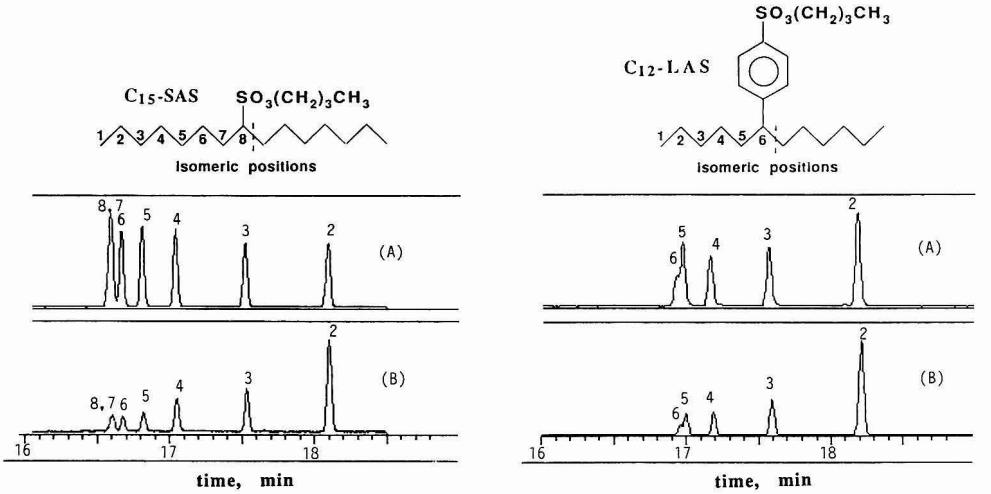

Figure 5. Selected ion chromatograms for C_{15}-SAS (*m/z* 210) and C_{12}-LAS (*m/z* 327) isomers in (A) standard commercial mixtures and in (B) an ion-pair/SFE extract of a sewage sludge.

only a single extraction was required for the reproducible and quantitative recovery of SAS and LAS from different sludges.

Quantitative of SAS and LAS in Sewage Sludge. Concentrations of SAS and LAS in sewage sludge were determined from the extraction and analysis of four replicates of each sewage sludge sample extracted by ion-pair/SFE (Table IV). Concentrations of SAS in the five sewage sludge samples ranged from 0.27 to 0.80 g/kg and LAS concentrations ranged between 3.83 and 7.51 g/kg. The method gave good relative standard deviations (typically 5%) for both SAS and LAS. The reproducibility of the injection-port derivatization, calculated from four replicate injections of a single sewage sludge extract, gave a relative standard deviation of <1% for both SAS and LAS. However, when samples of very high concentrations preceded samples containing low levels of SAS and LAS, traces of SAS were observed in the sample of low concentration but could be eliminated by changing the inlet liner.

Concentrations of LAS found in sewage sludge using ion-pair/SFE and injection-port derivatization are comparable to those previously reported for sludges collected from municipal sewage treatment plants in Switzerland,[5,6] Germany,[8] and the United States.[4] Ion-pair/SFE was further validated by comparing SAS and LAS concentrations in sewage sludge from the Zürich–Glatt treatment plant using a conventional liquid solvent extraction with TBA as the ion-pair reagent as described above (Table IV). The concentration of SAS in sewage sludge, obtained by liquid solvent extraction, was 0.76 g/kg compared to 0.80 g/kg by ion-pair/SFE. Liquid solvent extraction gave a LAS concentration of 5.39 g/kg compared to 5.54 g/kg obtained by ion-pair/SFE. Excellent agreement between SAS and LAS concentrations in sewage sludge determined by the two methods proved that ion-pair/SFE is quantitative while requiring only 15 min for complete extraction. In contrast, the time needed to prepare sewage sludge extracts using conventional liquid solvent extraction was a minimum of 2 h.

Homologue and Isomer Distributions for SAS in Sewage Sludge. Quantitative information on the homologue and isomer composition of SAS mixtures in sewage sludge also was available by integrating the individual SAS peaks shown in Figure 3. Homologue distributions were determined for each sewage sludge by summing the individual isomers for C_{14}–C_{17} homologues of SAS. Table V also gives the homologue distribution determined for the commercial SAS standard. Unfortunately, no published information on the homologue composition of the commercial SAS standard was available. However, comparison of SAS homologue distributions for sewage sludge and the commercial mixture demonstrated a relative enrichment of the longer-chain SAS homologues by sewage sludge (Table V). As shown in Figure 5, isomers with the sulfonic acid group located near the middle of the alkyl chain (internal isomer) elute first followed by those with the sulfonic acid group attached to the end of the chain (external isomers). Selected ion chromatograms of C_{15}-SAS and C_{12}-LAS for sewage sludge both gave isomeric patterns that demonstrated a relative enrichment of the more hydrophobic (external) isomers relative to the standard mixture (Figure 5). Selective enrichment of the more hydrophobic homologues and isomers of LAS has been previously reported for sewage sludges[6] and sediments.[25]

CONCLUSIONS

Ion-pair/SFE and injection-port derivatization is a simple, fast, and quantitative alternative for determining both aliphatic and aromatic sulfonated surfactants in sewage sludge by GC/MS. Although SAS lack a chromophore necessary for selective and sensitive detection by HPLC, they can be determined in the presence of aromatic surfactants (LAS) without prior class fractionation or sample cleanup of sewage sludge extracts using GC/MS. Ion-pair/SFE improves upon a previous SFE method[10] for extracting LAS from sewage sludge by reducing the total extraction time from 30 to 15 min. In addition, ion-pair/SFE does not require modification of existing instrumentation or a second pump for delivering a high percent of methanol modifier. Ion-pair derivatization requires a minimum number of preparative steps and does not involve hazardous reagents. Although this report illustrates ion-pair/SFE for sulfonated surfactants, it can be applied to other sulfonated chemicals. Ongoing work in our

(25) Hand, V. C.; Williams, G. K. *Environ. Sci. Technol.* **1987**, *21*, 370–373.

laboratories indicates that sulfonated stilbene and biphenyl derivatives, used as optical brighteners in laundry detergents, are also present in the ion-pair/SFE extracts of sewage sludge. By combining ion-pair extraction with derivatization, the number of analytes that can be determined simultaneously is increased while the time and cost of sample extraction and analysis is reduced.

ACKNOWLEDGMENT

This work is part of a cooperative research project between the Commission for the Promotion of Scientific Research, Swiss Department of Public Economy, Lever AG, Switzerland, and Carlo-Erba SA, Switzerland. As partners in the Rhine Basin Program, we gratefully acknowledge the donation of the GC/MS equipment by the Hewlett Packard Co. Additional support came from Umweltbundesamt, Berlin, Shell Development Corp. (Houston, TX) and the U.S. Department of Energy. We thank Thomas Poiger for providing the HPLC chromatograms. Sewage sludges were collected by the sewage treatment plant operators in the region of Zürich, Switzerland.

RECEIVED for review May 20, 1992. Accepted September 14, 1992.

Enantiomer Separation of Chlordane Components and Metabolites Using Chiral High-Resolution Gas Chromatography and Detection by Mass Spectrometric Techniques

Hans-Rudolf Buser* and Markus D. Müller

Swiss Federal Research Station, CH-8820 Wädenswil, Switzerland

Octa- and nonachlordanes, oxychlordane, and heptachlor *exo*- and *endo*-epoxide were analyzed using achiral and chiral high-resolution gas chromatography (HRGC) and detection by electron ionization (EI) and electron-capture, negative ionization mass spectrometry (ECNI MS). Two β-cyclodextrin (β-CD) derivatives were used as chiral selectors and dissolved in a polysiloxane stationary phase (PS086). Silylated β-CD (BSCD) showed increased enantiomer resolution compared to permethylated β-CD (PMCD); however, BSCD was less suitable for the analysis of a technical chlordane mixture because of coelution of enantiomers of different major octachlordanes. Chiral HRGC and MS were then applied to the analysis of aquatic vertebrate species and human adipose tissue. All chiral synthetic reference compounds and the chiral components in technical chlordane showed enantiomeric ratios of approximately 1:1, but significantly different ratios of some of these components were observed in the biological samples. In some cases different enantiomers of the same compound were predominating in different species, although the compounds presumably originate from the same original source. Whereas differences in enantiomeric composition of some octachlordanes were detected previously in the aquatic samples, such differences were now also detected for the metabolic products, oxychlordane and heptachlor *exo*-epoxide. These changes are most likely caused by enantioselective biological processes and not by abiotic processes in the environment. Although enantiomeric ratios can be determined without the availability of individual enantiomers, it is shown that they may be affected by the presence of chiral or achiral interferents.

INTRODUCTION

Chlordane, formerly one of the most widely used pesticides, consists of a series of different congeners and isomers.[1-3] It belongs into the group of chlorinated hydrocarbons. Chlordane and some metabolites are very persistent and therefore ubiquitous environmental contaminants.[4-7] Not surprisingly, it can now be found in specimens at all trophic levels, generally together with many other halogenated compounds like the polychlorobiphenyls (PCBs), polychloronaphthalenes (PCNs), polychloroterphenyls (PCTs), polychlorodioxins and dibenzofurans, toxaphenes, DDT (1,1,1-trichloro-2,2-bis(4-chlorophenyl)ethane), and related compounds. Whereas most of these halogenated hydrocarbons are achiral, several chlordane components, including the two main components, *cis*- and *trans*-chlordane (structures, see Chart I), are chiral and thus exist as two enantiomers (optical isomers).

In the course of biological transformation and environmental degradation, drastic changes in congener and isomer composition of chlordane components in biota were observed, and minor components of the technical mixture became predominant in some biological samples.[5,6,8] Biological transformation of chiral compounds can be stereoselective, and uptake, metabolism, and excretion of enantiomers may thus be very different.[8-11] Therefore, the enantiomeric composition of chiral compounds may be changed in these processes. Metabolites of chiral compounds often are chiral, and even metabolites of achiral compounds may be chiral if chiral reagents or catalysts (enzymes) are involved. For instance, *trans*-nonachlor (structure see Chart I), another major constituent of technical chlordane, is achiral (prochiral), and replacement of a chlorine substituent by another atom or group can lead to a chiral compound. Oxychlordane, the key metabolite of chlordane,[4] is chiral (the structures of the two enantiomers are shown in Chart II). It was previously reported that both *cis*- and *trans*-chlordane in pigs would lead to oxychlordane but to the racemate in the former and to an optically active form in the latter case,[12] although the exact enantiomeric composition remained unknown. Therefore, achiral analyses of chiral compounds will give only partial information, and chiral analysis is required for a full understanding of the biological behavior of such compounds. Nevertheless, so far little has been done on optical isomerism and enantiomer composition of chlordane components.

In a previous study we reported on the successful application of chiral high-resolution gas chromatography (HRGC) and electron-capture, negative ionization mass spectrometry (ECNI MS) toward the enantioselective determination of chiral octa- and nonachlordanes in a technical chlordane mixture and in a small number of aquatic environmental samples.[8] Several chiral chlordane components were separated into pairs of enantiomers, and significant differences in the enantiomer composition between the technical mixture and these environmental samples were observed. However,

(1) WHO/IARC. *Occupational Exposures in Insecticide Application, and some Pesticides*; IARC Monographs on the Evaluation of Carcinogenic Risks to Humans, Volume 53; World Health Organization, International Agency for Research on Cancer: Lyon, 1991; pp 115–177.
(2) Savage, E. P. *Rev. Environ. Contam. Toxicol.* **1989**, *110*, 117.
(3) Dearth, M. A.; Hites, R. A. *Environ. Sci. Technol.* **1991**, *25*, 245–254.
(4) Nomeir, A. A.; Hajjar, N. P. *Rev. Environ. Contam. Toxicol.* **1987**, *100*, 1–22.
(5) Norstrom, R. J.; Simon, M.; Muir, D. C. G.; Schweinsburg, R. E. *Environ. Sci. Technol.* **1988**, *22*, 1063–1071.
(6) Muir, D. C. G.; Norstrom, R. J.; Simon, M. *Environ. Sci. Technol.* **1988**, *22*, 1071–1079.
(7) Dearth, M. A.; Hites, R. A. *Environ. Sci. Technol.* **1991**, *25*, 1279–1284.
(8) Buser, H. R.; Müller, M. D.; Rappe, C. *Environ. Sci. Technol.* **1992**, *26*, 1533–1540.
(9) Ariens, E. J., van Rensen, J. J. S., Welling, W., Eds. *Stereoselectivity of Pesticides, Biological and Chemical Problems*; Chemicals in Agriculture Volume 1; Elsevier: Amsterdam, 1988.
(10) Bartels, M. J.; Smith, F. A. *Drug Metab. Dispos.* **1989**, *17*, 286.
(11) Müller, M. D.; Schlabach, M.; Oehme, M. *Environ. Sci. Technol.* **1992**, *26*, 566–569.
(12) Schwemmer, B.; Cochrane, W. P.; Polen, P. B. *Science* **1970**, *169*, 1087.

0003-2700/92/0364-3168$03.00/0

Chart I. Structures of Some Chlordane Components and Metabolites[a]

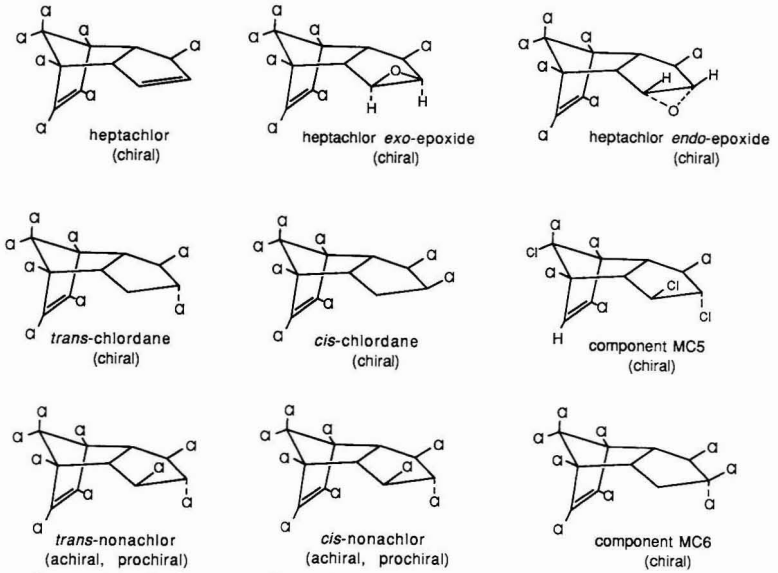

[a] Chiral compounds: structure of only one enantiomer shown.

Chart II. Structures of the Two Enantiomers of Oxychlordane

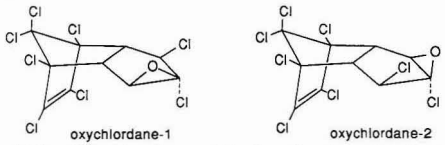

[a] Arbitrarily assigned as oxychlordane-1 and oxychlordane-2; mirror plane perpendicular through C_2 and C_8.

some compounds were still not enantiomerically resolved or their chirality remained unknown. Particularly, the chiral metabolites oxychlordane and heptachlor *exo*-epoxide, the latter a metabolite of heptachlor (structures see Chart I), were not resolved by our technique, although these compounds were resolved using another separation system.[13]

In the present paper, we report more detailed information on the chromatographic behavior and the enantiomer separation of chiral chlordane components and metabolites and mass spectrometric techniques for the selective detection of these compounds. The enantiomer separation of additional components is reported. Chiral HRGC in combination with MS was then applied to the analysis of tissue extracts of aquatic vertebrate species and a human tissue extract. Specific analytical problems encountered in this type of analysis are described and remedies suggested. Again significant differences in enantiomer composition of some of these environmental contaminants were observed, and we show that different enantiomers of the same compound may predominate in different species. The results further document the application and potentialities of chiral HRGC in environmental analyses.

EXPERIMENTAL SECTION

Materials and Reference Compounds. *cis*-Chlordane, *trans*-chlordane, *cis*- and *trans*-nonachlor, heptachlor, heptachlor *exo*- and *endo*-epoxide, and oxychlordane were from Dr. Ehrenstorfer, GmbH Augsburg, FRG; a technical chlordane was obtained in the 1950s from Maag Ltd., Dielsdorf, Switzerland. This particular sample has been archived in Wädenswil and was previously analyzed;[8] it was now used for comparative analyses. Solutions of the reference compounds and the technical chlordane mixture in toluene (1–10 ng/μL) were prepared and used for analysis.

The silicon compounds used for the preparation of the capillary columns were from the following sources: 1,3-diphenyl-1,1,3,3-tetramethyldisilazane and *N*-(*tert*-butyldimethylsilyl)-*N*-methyltrifluoroacetamide from Fluka, Buchs, Switzerland, and PS086, an OH-terminated dimethylpolysiloxane containing 12–15% diphenylsiloxane groups, methyltriethoxysilane, and 1,3,5-trimethyl-1,3,5-triphenylcyclotrisiloxane from Petrarch Systems, Bristol, PA. β-Cyclodextrin (β-CD) and permethylated β-CD (PMCD) were from Fluka and Sigma (Buchs, Switzerland), respectively; (*tert*-butyldimethylsilyl)-β-CD (BSCD) was prepared according to ref 14.

Preparation of Biological Samples. Herring oil and tissues of a salmon, a seal, and a penguin were examined. The samples were the same as those described in a previous study.[8] The herring oil was prepared from herring (*Clupea harengus*) collected from the Gulf of Bothnia. The salmon muscle tissue was from a female salmon (*Salmo salar*) caught in the Ume river at Stornorrfors, Sweden. The seal sample was a composite of liver tissue of adult grey seal (*Halichoerus grypus*) collected from the Baltic Sea along the Swedish southeastern coast line. The penguin tissue was from an juvenile Adelaide penguin (*Pygoscelis adelis*) found dead on Ross Island, Antarctica. In addition to these aquatic samples, human adipose tissue of a male American was analyzed.

The samples were extracted and the extracts cleaned up at the Institute of Environmental Chemistry, University of Umeå, Sweden.[15] Briefly, the tissues (approximately 20 g) were homogenized with Na_2SO_4 and extracted with dichloromethane/

(13) König, W. A.; Icheln, D.; Rung, T.; Pfaffenberger, B.; Ludwig, P.; Hühnerfuss, H. *J. High Resolut. Chromatogr. Chromatogr. Commun.* **1991**, *14*, 530–536.

(14) Blum, W.; Aichholz, R. *J. High Resolut. Chromatogr. Chromatogr. Commun.* **1990**, *13*, 515–518.

(15) Zook, D. R.; Buser, H. R.; Olsson, M.; Bergqvist, P. A.; Rappe, C., submitted to *Ambio*.

Table I. Ions Monitored (m/z Values) in SIM Experiments for Chlordane Components and Metabolites

compds	ECNI (ions monitored)	EI (ions monitored)
octachlordanes	405.798 $(M)^{\cdot-}$	
($C_{10}H_6Cl_8$)	407.795 $(M + 2)^{\cdot-}$	
	409.792 $(M + 4)^{\cdot-}$	
nonachlordanes	439.759 $(M)^{\cdot-}$	
($C_{10}H_5Cl_9$)	441.756 $(M + 2)^{\cdot-}$	
	443.753 $(M + 4)^{\cdot-}$	
oxychlordane	419.777 $(M)^{\cdot-}$	384.808 $(M - Cl)^+$
($C_{10}H_4Cl_8O$)	421.774 $(M + 2)^{\cdot-}$	386.805 $(M + 2 - Cl)^+$
	423.771 $(M + 4)^{\cdot-}$	421.774 $(M + 2)^{\cdot+}$
heptachlor *exo*- and	385.816 $(M)^{\cdot-}$	350.847 $(M - Cl)^+$
endo-epoxide	387.813 $(M + 2)^{\cdot-}$	352.844 $(M + 2 - Cl)^+$
($C_{10}H_5Cl_7O$)	389.810 $(M + 4)^{\cdot-}$	354.841 $(M + 4 - Cl)^+$
		387.813 $(M + 2)^{\cdot+}$

n-hexane (1:1). Lipid removal was effected by polyethylene film dialysis followed by gel permeation chromatography using Biobeads SX3. The eluate was then fractionated using florisil chromatography. In this scheme, the chlordane components including oxychlordane were found to elute into fraction 2 (15% dichloromethane/*n*-hexane). Heptachlor *exo*-epoxide is more polar[5,6] and was eluted into fraction 3 (50% dichloromethane/*n*-hexane). The human adipose tissue (approximately 2 g) was extracted as above but not subjected to this florisil cleanup. Procedural blanks showed no detectable quantities of the analytes under investigation. Aliquots of 2 μL corresponding to 200–400 mg of tissue were used for analysis, or smaller sample aliquots if required.

HRGC-MS Analysis. A VG Tribrid double-focusing magnetic sector hybrid mass spectrometer (VG Analytical Ltd., Manchester, England) was used for analyte detection and identification. The ion source was operated in either the electron ionization (EI, 70 eV, 180 °C) or ECNI (50 eV, 140 °C) mode. A modified chemical ionization source (courtesy Harry Seed, VG Analytical) was used in these ECNI experiments. This source allowed the use of neat argon as a buffer gas ((0.5–1) $\times 10^{-4}$ mbar, as measured by the ion gauge). Initially, some experiments were carried out using argon/10% methane and carbon dioxide as buffer gases. Comparable results were obtained but the use of argon showed the least background signals, and argon was later used exclusively.

Full-scan mass spectra (m/z 50–500, 1.16 s/scan, resolution $M/\Delta M = 500$) were recorded for analyte identification in the technical chlordane mixture and in all biological samples. Analyses were then repeated with selected-ion monitoring (SIM) for increased sensitivity and optimal enantiomer/isomer separation (faster cycle times; 0.50 s/scan; see Table I). The ions chosen were not necessarily the most intense in the ECNI and EI mass spectra but those expected to show least interference from other compounds. A lock-mass of 451.974 (ECNI) or 413.978 (EI) from perfluorotributylamine was used in the SIM experiments. Concentrations in the biological samples were estimated from SIM chromatograms in comparison to those of known quantities of the reference compounds.

All samples were comparatively analyzed using an achiral and two chiral HRGC column systems. The glass capillary HRGC columns used were (1) a 20-m column coated with a 0.2-μm film of neat PS086, thermally cross-linked;[16] (2) a 20-m column coated with a 0.2-μm film of PS086 containing 10% (w/w) PMCD as chiral selector and 0.5% methyltriethoxysilane as cross-linker; and (3) a 16-m column coated with a 0.2-μm film of PS086 containing 30% BSCD as chiral selector and 0.5% methyltriethoxysilane as cross-linker. The glass capillary columns were made from 0.3-mm-i.d. Duran glass and leached and persilylated prior to coating.[16] Initially, a commercial 25-m SE54 fused silica column was also used.

The achiral PS086 and the chiral PS086/BSCD HRGC columns were temperature programmed as follows: 100 °C, 2-min isothermal, 20 °C/min to 140 °C, then at 3 °C/min to 250 °C, followed by an isothermal hold at this temperature. The chiral PS086/PMCD HRGC column was operated at a lower intermediate temperature (120 °C) and a slower programming rate (2 °C/min) for increased enantiomer resolution. All samples (2 μL in toluene) were on-column injected at 100 °C. Data acquisition and retention time measurements were started at 140 °C (PS086 and PS086/BSCD) or 120 °C (PS086/PMCD). Retention indexes (RI) were calculated relative to *n*-alkanes (C_{12}–C_{26}; RI 1200–2600), co-injected with the samples; linear interpolation was used in the temperature-programmed runs. Enantiomeric ratios (ER) were defined as ER = p_1/p_2, whereby p_1 and p_2 = peak areas of the earlier- and later-eluting enantiomers, respectively. Enantiomer resolution (R) was defined as $R = (t_2 - t_1)/(w_1 + w_2)$, whereby t_1 and t_2 = retention times of earlier- and later-eluting enantiomers, respectively, and w_1 and w_2 = peak widths at half-height of earlier- and later-eluting enantiomers, respectively.

Compound Identification. In addition to the reference compounds available, other chlordane compounds, in particular components MC4, MC5, MC6 (also known as nonachlor III), and MC7 (Miyazaki compounds, ref 17), and U82[3,7,18] were identified in the technical chlordane mixture and then assigned in the environmental samples using published retention data (retention indexes), in particular the data reported by Dearth and Hites.[3] These identifications were done initially on the SE54 HRGC column. Compound identifications were supported from full-scan mass spectra (molecular ions, number of Cl atoms, and fragmentation patterns).

RESULTS AND DISCUSSION

Isomer and Enantiomer Separation of Chlordane Components and Metabolites. Technical chlordane consists of a complex mixture of primarily hepta-, octa-, and nonachlorinated, tricyclic compounds. It is prepared by the Diels–Alder reaction of hexachlorocyclopentadiene and cyclopentadiene leading to chlordene, which is then further chlorinated. The main constituents in technical chlordane are *cis*- and *trans*-chlordane, and *trans*-nonachlor (structures see Chart I). These products are of the 6 + 2 and 6 + 3 substitution type.[3,19] There are a number of additional components present in technical chlordane, some of which are of the 5 + 2 (heptachloro) and 5 + 3 (octachloro) substitution type, and some have even more complex structures resulting from rearrangement reactions.[3] The compounds from technical chlordane considered in our study are primarily the octa- and the nonachlordanes, and they are of the 5 + 3, 6 + 2, and 6 + 3 substitution type (see Chart I for some structures). The carbon skeleton of all these compounds has an endo configuration.

Also considered in this study were heptachlor, an unsaturated constituent of technical chlordane and an insecticide of its own,[1,3] oxychlordane, and heptachlor *exo*- and *endo*-epoxide (structures, see Charts I and II). Oxychlordane is the principal mammalian metabolite of *cis*- and *trans*-chlordane and of nonachlors;[4] it is an important environmental contaminant. The epoxy ring in oxychlordane has the exo configuration (structure, see Chart II). Heptachlor *exo*-epoxide, often just referred as heptachlor epoxide, is the main metabolite of heptachlor.[4] These oxygenated compounds are usually not present in the technical chlordane mixture.

cis-Chlordane and *trans*-chlordane, and components MC5, MC6, heptachlor, heptachlor *exo*- and *endo*-epoxide, and oxychlordane all are chiral; *cis*- and *trans*-nonachlor are both achiral but can be considered as prochiral.[20] Component U82, a 5 + 3 type octachlordane of unknown configuration, is shown in this study to be chiral (see below). Components MC5,

(16) Blum, W. *J. High Resolut. Chromatogr. Chromatogr. Commun.* **1985**, *8*, 719.

(17) Miyazaki, T.; Yamagishi, T.; Matsumoto, M. *Arch. Environ. Contam. Toxicol.* **1985**, *14*, 475–483.

(18) Dearth, M. A.; Hites, R. A. *Environ. Sci. Technol.* **1991**, *25*, 1125–1128.

(19) Sittig, M. *Pesticide Manufacturing and Toxic Materials Control Encyclopedia*; Noyes Data Corporation: Park Ridge, NJ, 1980.

(20) March, J. *Advanced Organic Chemistry*, 3rd ed.; John Wiley and Sons: New York, 1985; pp 82–140.

Table II. Retention Indexes of Some Chlordane and Reference Compounds on an Achiral (PS086) and Two Chiral (PS086/PMCD and PS086/BSCD) Column Systems[a]

compounds[b]	PS086	PS086/ PMCD	PS086/ BSCD
U82-1	2104	2096	2127
U82-2			2132
MC5-1	2208	2218	2257
MC5-2		2223	2295
trans-chlordane-1	2184	2188	2292
trans-chlordane-2		2193	2310
cis-chlordane-1	2215	2208	2294
cis-chlordane-2		2211	2301
MC6-1	2188	2174	2264
MC6-2			2275
trans-nonachlor	2210	2204	2238
cis-nonachlor	2365	2373	2391
heptachlor *exo*-epoxide-1	2136	2135	2266
heptachlor *exo*-epoxide-2			2277
heptachlor *endo*-epoxide-1	2149	2153	2219
heptachlor *endo*-epoxide-2			2229
oxychlordane-1	2126	2119	2226
oxychlordane-2			2235
heptachlor-1/2[c]	1970	1961	2056
DDE	2279	2286	2247
aldrin	2032	2015	2141
dieldrin	2265	2265	2455

[a] Also included are DDE, aldrin and dieldrin as achiral retention markers. [b] Annexes-1 and -2 denote first- and later-eluting enantiomer on each column; enantiomers not necessarily the same on the two chiral columns. [c] The two enantiomers are not separated.

MC6, and U82 were not available as individual reference compounds but were present in the technical chlordane mixture.

All synthetic reference compounds and the technical chlordane mixture were analyzed on the achiral PS086 and on the two chiral HRGC column systems. In Table II we list the RI values observed. Also included in the list are the retention indexes of 1,1-bis(4-chlorophenyl)-2,2-dichloroethane (DDE), aldrin, and dieldrin as further achiral reference compounds. As expected single peaks were observed for all compounds on the achiral PS086 HRGC column (data not shown), but both chiral columns showed separation of some chiral compounds into pairs of enantiomers. Previously, PS086/PMCD showed enantiomer resolution of *cis*- and *trans*–chlordane, and of some additional octachlordanes (see Figure 3, ref 8). However, PS086/PMCD did not enantiomerically resolve other chiral compounds, like component MC6, heptachlor, heptachlor *exo*- and *endo*-epoxide, and oxychlordane.

PS086/BSCD now showed the separation of several additional chiral compounds into pairs of enantiomers, including heptachlor *exo*- and *endo*-epoxide, and oxychlordane whereas heptachlor still remained unresolved. The enantiomeric resolutions obtained were better than on PS086/PMCD. Excluding heptachlor (not enantiomerically resolved), the enantiomeric ratios of all synthetic chiral reference compounds were close to the theoretical value of 1.00. The enantiomeric ratios determined showed good reproducibility (1–2% standard deviation at 95% confidence interval), as shown in previous studies.[8,11]

A comparison of the RI values listed in Table II revealed similar values (±17 RI units) for the reference compounds on PS086 and PS086/PMCD, although the elution order of component MC5 and *cis*-chlordane is reversed on these two columns. In contrast, the RI values on PS086/BSCD are generally higher (23–190 RI units) than those on PS086, indicating a changed polarity of this column, not unexpected because it contained a higher proportion (30%) of the more polar β-CD derivative. Retention index differences (ΔRI) among enantiomers were up to 38 RI units on PS086/BSCD,

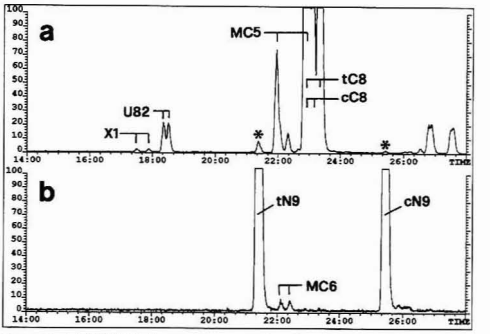

Figure 1. ECNI SIM chromatograms showing elution of (a) octachlordanes (*m/z* 410) and (b) nonachlordanes (*m/z* 444), respectively, in the technical chlordane mixture using the chiral PS086/BSCD HRGC column. Signals for *cis*- and *trans*-nonachlor are marked by asterisks in chromatogram a. Abbreviations: cC8 and tC8 for *cis*- and *trans*-chlordane, cN9 and tN9 for *cis*- and *trans*-nonachlor, others see text. Several octachlordanes not assigned using this column.

but only up to 5 RI units on PS086/PMCD (data for heptachlor not considered). The data in Table II indicate that RI differences (ΔRI) of 3–10 RI units are required for successful enantiomer resolution. The elution order of enantiomers is not necessarily the same on chiral columns with different β-CD derivatives,[21] and therefore it remained unknown whether the elution order of enantiomers is the same on both of our chiral columns. The enantiomer resolution for a given ΔRI value is better on the PD086/PMCD column because this column was longer and slower temperature programmed.

In Figure 1 ECNI SIM chromatograms (*m/z* 410 and 444) show the elution of octa- and nonachlordanes in the technical chlordane mixture on the chiral PS086/BSCD HRGC column; the same sample was previously analyzed on the achiral PS086 and the chiral PS086/PMCD HRGC column (see Figures 2 and 3, ref 8). As shown in Figure 1, the unknown components X_1 and U82, and component MC6, previously not enantiomerically resolved, are now also separated into pairs of enantiomers. The enantiomeric ratios of these chiral compounds are close to the theoretical value of 1.00, as previously observed for the other chiral components in this technical mixture. Also noticeable is the increased enantiomer resolution of component MC5 (ΔRI = 38 RI units), the two enantiomers being assigned with the aid of the environmental samples (see below). Some minor octachlordanes (components MC4 and MC7) could not be assigned on this column because individual reference compounds were not available; however, these compounds were previously assigned on PS086 and PS086/PMCD.[8]

A potential problem previously pointed out with chiral HRGC is coelution of the later-eluting enantiomer of one isomer with the earlier-eluting enantiomer of another, later-eluting isomer, although the isomers are well separated by achiral HRGC. This phenomen can actually be observed in Figure 1, where the later-eluting enantiomer of component MC5 (MC5-2) is coeluting with the first-eluting enantiomers of *trans*-chlordane (*trans*-chlordane-1) and *cis*-chlordane (*cis*-chlordane-1) (RI values 2295, 2292, and 2294, respectively, see Table II). All three compounds are easily separable by achiral HRGC (see Figure 2, ref 8). On PS086/BSCD, coelution or near coelution of other components is more of a problem than on the other two columns. In this way, the enantiomers of MC6 and heptachlor *exo*-epoxide, and enantiomers of oxychlordane and heptachlor *endo*-epoxide, practically coelute as can be seen from the data in Table II.

(21) Armstrong, D. W.; Li, W. Y.; Pitha, J. *Anal. Chem.* **1990**, *62*, 217.

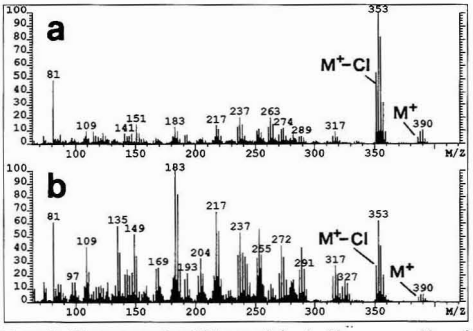

Figure 2. EI mass spectra of (a) racemic heptachlor *exo*-epoxide and (b) racemic heptachlor *endo*-epoxide. For both compounds, $M^{\cdot+}$ = *m/z* 386, Cl_7.

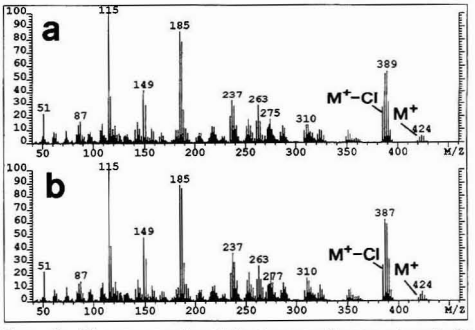

Figure 3. EI mass spectra of the two enantiomers of synthetic oxychlordane ($M^{\cdot+}$ = *m/z* 420, Cl_8) separated on PS086/BSCD: (a) oxychlordane-1 (earlier-eluting), (b) oxychlordane-2 (later-eluting enantiomer). Absolute configurations not known. Note that mass spectra are virtually identical.

In many instances, this problem can be circumvented by a selective detection of these compounds using MS techniques. Due to the similarity of the mass spectra, however, this is not possible in the case of the octachlordanes. Although PS086/BSCD shows the best enantiomer resolution of all components when injected individually, coelution of the above enantiomers makes enantioselective determinations of these major chlordane components impossible, and for that purpose the chiral PS086/PMCD column is more suitable.

Selective Detection of Chlordane Compounds Using Various Mass Spectrometric Techniques. EI and ECNI MS are extensively used for the detection of chlorinated hydrocarbons. In particular, ECNI MS has become an important tool for screening of environmental contaminants and their metabolites, due to its potential for increased sensitivity and selectivity toward organochlorine compounds and its virtual transparency to many otherwise interfering compounds. Particularly, the heptachlorinated and higher-chlorinated compounds considered in this study are expected to show high sensitivity in ECNI MS.

Selective detection of analytes in environmental samples is important since many other compounds are often present in the fractions analyzed despite the sophisticated cleanup methods used. Coelution of analytes with interferents is particularly a problem with chiral HRGC, since the number of compounds (enantiomers/isomers) which have to be considered is increased (up to 2-fold) but chromatographic performance (theoretical or effective plate numbers) in general is the same as in achiral HRGC. Therefore, the possibility for interference is increased, and selective detection is of particular importance in chiral HRGC. In the present study, both EI and ECNI were used for selective detection of the chlordane compounds.

EI and ECNI mass spectra of chlordane components have been described,[3,22,23] although mass spectra of individual enantiomers so far have hardly been reported. Whereas the mass spectra of isomers may differ significantly, those of enantiomers should be identical. As examples, we show in Figure 2a,b the EI mass spectra of racemic heptachlor *exo*- and *endo*-epoxide and in Figure 3a,b those of the two enantiomers of oxychlordane. Whereas the EI mass spectra of heptachlor *exo*- and *endo*-epoxide differ significantly, those of the two enantiomers of oxychlordane are virtually identical, and the minor differences observed are likely from small variations in the instrumental conditions. Similarily, almost identical EI and ECNI mass spectra were observed for the enantiomers of the other synthetic chiral reference compounds. EI and ECNI MS can distinguish among some isomers, e.g. between heptachlor *exo*- and *endo*-epoxide and among 5 + 3 and 6 + 2 type octachlordanes and generally easily among (chloro) homologs. However, both techniques cannot distinguish among enantiomers, and enantiomer assignment therefore must be derived from (chiral) chromatographic data.

The SIM responses of enantiomers, both in EI and ECNI MS, are identical, and therefore individual standards of enantiomers are not required for precise determinations of enantiomeric ratios and compositions. However, enantiomer detection must be highly selective since other compounds (achiral or chiral) may mimick the presence of one or the other enantiomer. In ECNI MS, interference can also attenuate signal intensity, because electron-capturing compounds may deplete the ion source of the limited number of thermalized electrons. Furthermore, the presence of larger quantities of other chlorinated compounds can lead to the formation of Cl^- and then to adduct ion formation $(M + Cl)^-$ resulting in too low signals for the ions monitored. Coeluting components may thus easily affect the signals for one or the other enantiomer and thus change the enantiomeric ratios observed. Therefore, the absence of major interferents has to be ensured, preferably by aquisition of full-scan mass spectra. In principle, the enantiomeric ratios are independent of recovery efficiency since no chiral reagents or materials are involved in extraction and cleanup, and chemical and physical properties of enantiomers are identical.

Analysis of Biological Environmental Samples. Chiral HRGC with EI and ECNI MS detection were applied to the analysis of the aquatic environmental samples and a human tissue extract. Of particular interest were oxychlordane and heptachlor *exo*-epoxide, metabolic products of technical chlordane, and so far never enantioselectively determined in such samples.

In Figure 4a–d we show ECNI SIM chromatograms (*m/z* 424) for oxychlordane in four biological samples using PS086/BSCD. Whereas achiral HRGC showed single peaks (data not shown), the chromatograms now show the separation of oxychlordane into a pair of enantiomers and document the presence of both enantiomers in these biological samples with the first-eluting enantiomer (oxychlordane-1) being somewhat more abundant. The enantiomeric ratios observed in these biological samples are clearly different from 1.00 but surprisingly similar (1.3–1.6) in all the species, although the total concentrations of oxychlordane in these species varied. The total concentrations of oxychlordane were estimated at 2 (herring), 5 (salmon), 60 (seal), 80 (penguin), and 40 ng/g (human tissue).

(22) Stemmler, E. A.; Hites, R. A. *Anal. Chem.* **1985**, *57*, 684–692.
(23) Ribick, M. A.; Zajicek, J. *Chemosphere* **1983**, *12*, 1229–1242.

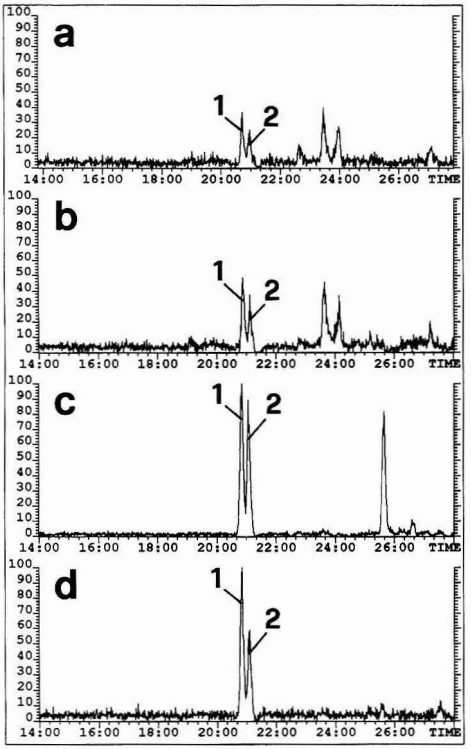

Figure 4. ECNI SIM chromatograms (m/z 424) showing the presence of oxychlordane in extracts of (a) Baltic herring, (b) Baltic salmon, (c) Baltic grey seal, and (d) in a human adipose tissue. Note the presence of both enantiomers in enantiomeric ratios clearly different from 1.00. Peak identifications: 1 = oxychlordane-1, 2 = oxychlordane-2.

Full-scan mass spectra confirmed the presence of oxychlordane in these samples. In Figure 5a–d we show EI and ECNI mass spectra of both oxychlordane enantiomers in the penguin tissue using PS086/BSCD. The mass spectra indicate the presence of additional components, coeluting with these enantiomers. The EI mass spectra of oxychlordane-1 (Figure 5a) and oxychlordane-2 (Figure 5b) show the presence of DDE ($M^{\bullet+}$ = m/z 316) and *trans*-nonachlor ($M^{\bullet+}$ = m/z 440), respectively. The ECNI mass spectrum of oxychlordane-2 (Figure 5d) also shows the presence of *trans*-nonachlor, whereas DDE does not respond under these conditions.

Whereas the presence of interferents in this case did not disturb mass spectrometric identification, it can significantly alter chromatographic performance of the chiral columns and hence enantiomer resolution. This reversible, novel phenomen is illustrated in Figure 6 for oxychlordane. The chromatograms of the penguin and seal tissue extracts show almost complete separation ($R \approx 0.9$) of the two enantiomers (see Figure 4c for seal and Figure 6a for penguin) when analyzed on PS086/BSCD and injecting sufficiently small (25-mg) sample aliquots, but the chromatograms in Figure 6b,c show significant deterioration of enantiomer resolution ($R \approx 0.5$ and $R \approx 0.2$, respectively) when larger (200-mg) sample aliquot were injected. Apparently, the presence of larger amounts of DDE and *trans*-nonachlor in these samples are the cause for a significant loss in enantiomer resolution, presumably by saturating the chiral selector in the stationary phase; the presence of nonvolatile lipid material in the samples would cause irreversible loss of resolution. Apparently, complexation and saturation of the chiral selector can be caused by achiral interferents, in agreement with results from complexation experiments in the liquid phase under non-gas chromatographic conditions.[24] The chromatograms clearly show, contrary to expectations, that the α-ratio (a measure for enantiomer selectivity) is reduced although the apparent column efficiency increased (narrower peak width, higher effective plate numbers). The latter is likely caused by a chromatographic focusing effect due to the presence of larger quantities of these coeluting components and comparable to a cosolvent effect[25] whereby the analyte and the interferant (cosolvent) have similar or equal retention times. The observed enantiomeric ratio of a chiral compound may thus differ from the real ratio in the sample, and deviations thus can be caused not only by nonselective detection (see above) but also by chromatographic effects. A solution to the latter problem is the analysis of sufficiently small sample aliquots. This, however, also mandates that MS detection be at the highest sensitivity.

It can be speculated that the chiral selector (BSCD or PMCD) forms a one-to-one guest–host complex with the analyte or an interferent.[25] The amount of chiral selector in our thin-film, narrow-bore HRGC columns is small and on the order of 0.4 and 1.2 mg or 0.28 and 0.34 μmol of PMCD (molecular weight, MW $\approx$ 1430) and BSCD (MW $\approx$ 3530), respectively, assuming fully derivatized products. The amount of chiral selector within the length of column corresponding to the height-equivalent of one effective plate is thus 5.6 and 6.8 pmol (N_{eff} = 50 000). Assuming the separation process to take place in one or a few effective plates at a time, and with MW's = 400–500 for the compounds of interest, the expected sample capacities of our chiral HRGC columns are in the low nanogram range.

Heptachlor *exo*-epoxide was detected in the Baltic aquatic samples and in the human adipose tissue; the corresponding fraction of the penguin tissue was not available for this analysis. In Figure 7a–d, EI SIM chromatograms (m/z 353) show the elution of heptachlor *exo*-epoxide in these samples using PS086/BSCD. Both enantiomers are present in all the samples and their separation is clearly demonstrated. However, there are significant differences in the enantiomeric composition. Whereas the later-eluting enantiomer (heptachlor *exo*-epoxide-2) is more abundant in the aquatic species, heptachlor *exo*-epoxide-1 is more prevalent in the human tissue. The two fish species, herring and salmon, show a very similar enantiomeric composition; the seal tissue shows a much higher enantiomeric excess of heptachlor *exo*-epoxide-2, indicating a more stereoselective uptake or formation of this metabolite by the warm-blooded seal. The total concentrations of heptachlor *exo*-epoxide were estimated at 2 (herring), 5 (salmon), 10 (seal), and 20 ng/g (human tissue); heptachlor *endo*-epoxide was not detected in these samples.

The aquatic samples were further examined for the presence of octa- and nonachlordanes. Previously, several octachlordanes were separated into enantiomers on PS086/PMCD but component U82 and MC6, a chiral nonachlor, eluted as single peaks (see Figure 3, ref 8). The presence of octa- and nonachlordanes was now confirmed on PS086/BSCD. In Figure 8a–h we show ECNI SIM chromatograms (m/z 410 and 444) of the same samples. As observed with the technical mixture (see Figure 1a), component U82 is now clearly separated into enantiomers. Whereas the enantiomeric ratio of this component in the technical mixture and in the two fish species is 1:1 (see Figures 1a and 8a,b), clearly different ratios are observed in both of the warm-blooded species, seal and penguin (see Figure 8c,d respectively). Interestingly, the

(24) Bender, M. L.; Komiyama, M. *Cyclodextrin Chemistry*; Springer-Verlag: Berlin, 1978; pp 10–27.

(25) Grob, K.; Müller, E. *J. High Resolut. Chromatogr. Chromatogr. Commun.* **1988**, *11*, 388–394.

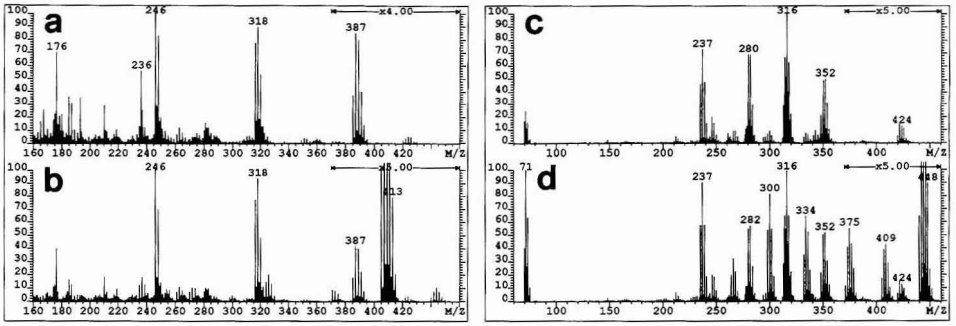

Figure 5. EI and ECNI mass spectra of the two enantiomers of oxychlordane identified in Antarctic penguin. (a, c) EI and ECNI mass spectra of oxychlordane-1, respectively. (b, d) EI and ECNI mass spectra of oxychlordane-2, respectively. Note coelution of DDE (EI, $M^{\cdot+}$ = *m/z* 316, Cl_4, $(M - Cl_2)^{\cdot+}$ = *m/z* 246; no detection in ECNI) with oxychlordane-1, and of *trans*-nonachlor (EI, $M^{\cdot+}$ = *m/z* 440, Cl_9, $(M - Cl)^+$ = *m/z* 405; ECNI, $M^{\cdot-}$ = *m/z* 440, Cl_9) with oxychlordane-2.

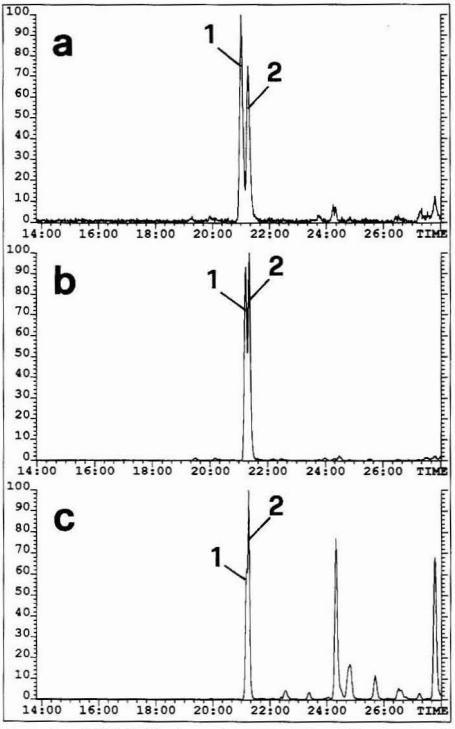

Figure 6. ECNI SIM chromatograms (*m/z* 424) showing the deterioration of enantiomer resolution for oxychlordane in the presence of increasing amounts of coeluting interferents (DDE, nonachlor). (a, b) Injection of small (25-mg) and larger (200-mg) aliquots of extract of Antarctic penguin, respectively. (c) Injection of a larger (200-mg) aliquot of extract of Baltic seal. Peak identifications: 1 = oxychlordane-1, 2 = oxychlordane-2.

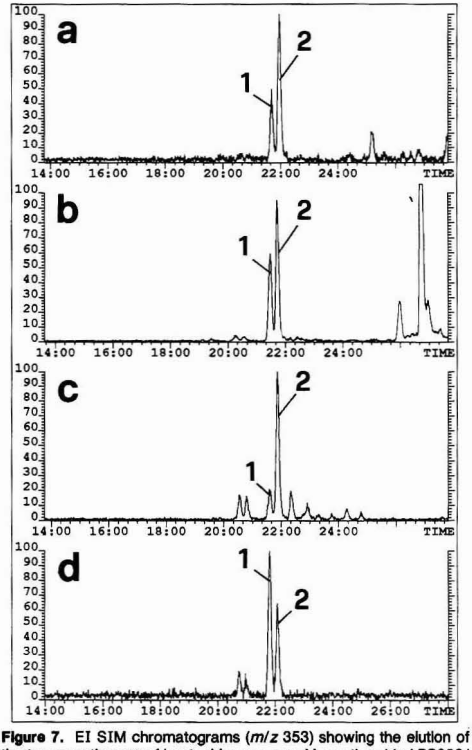

Figure 7. EI SIM chromatograms (*m/z* 353) showing the elution of the two enantiomers of heptachlor *exo*-epoxide on the chiral PS086/BSCD HRGC column in aquatic species from the Baltic and a human adipose tissue. (a) Baltic herring, (b) Baltic salmon, (c) Baltic seal, and (d) human adipose tissue. Peak identifications: 1 = heptachlor *exo*-epoxide-1, 2 = heptachlor *exo*-epoxide-2.

first-eluting enantiomer (U82-1) is clearly dominating in seal, whereas the later-eluting enantiomer (U82-2) is more prevalent in penguin. The chromatogram in Figure 8d shows the enhanced enantiomer separation of component MC5 on this chiral column. In case of the nonachlors (see Figures 8e–h), component MC6 shows enantiomeric ratios of around 1:1 in all aquatic species; *cis*-nonachlor and *trans*-nonachlor are achiral and, as expected, elute as single peaks. The presence of additional peaks in the ECNI SIM chromatogram (*m/z* 410) for octachlordanes (see Figure 8a–d) are due to PCBs, particularily octachlorobiphenyls, and toxaphenes.

CONCLUSIONS

The enantiomer separation of several chiral chlordane components as well as the oxygenated metabolites oxychlordane and heptachlor *exo*-epoxide was accomplished by chiral

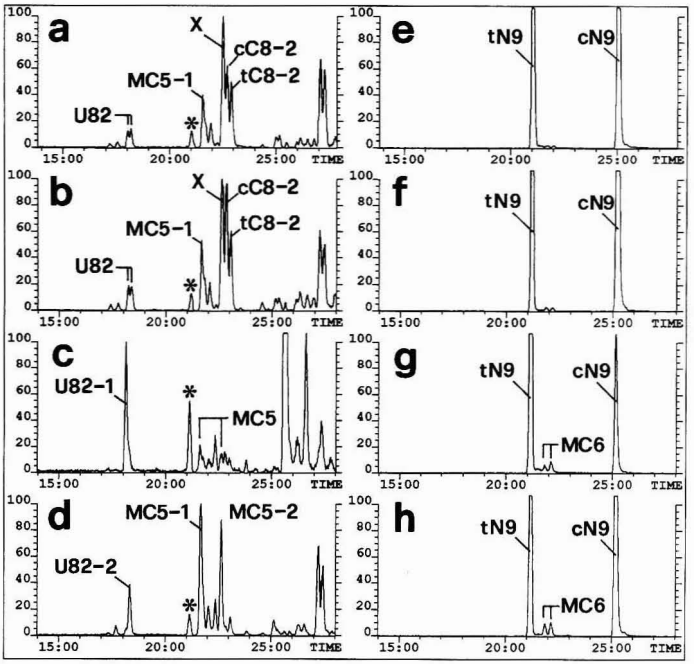

Figure 8. ECNI SIM chromatograms showing elution of (a–d) octachlordanes (*m/z* 410) and (e–h) nonachlordanes (*m/z* 444) on the chiral PS086/BSCD HRGC column in (a, e) Baltic herring, (b, f) Baltic salmon, (c, g) Baltic grey seal, and (d, h) Antarctic penguin. Abbreviations, see Figure 1 and text. Signal for *trans*-nonachlor marked by asterisks in chromatograms a–d. Peak marked by X comprized of *trans*-chlordane-1, *cis*-chlordane-1, and MC5-2.

HRGC. Two β-CD derivatives (BSCD and PMCD) were used as chiral selectors. Addition of these chiral selectors to the polysiloxane stationary phase (PS086) changed the polarity and thus the isomer elution profiles of the columns. Enantiomer resolution was dependent on the chiral selector and varied among different analytes; it was generally best using the silylated derivative (BSCD). However, the permethylated derivative (PMCD) showed a better selectivity toward the separation of the enantiomers of the major chlordane components in the technical chlordane mixture, like *cis*- and *trans*-chlordane and component MC5. Absolute configurations of the enantiomers thus separated, however, still remain unknown.

Enantiomers have largely the same chemical and physical properties and therefore the same response using MS detection techniques. Enantiomeric ratios can be determined without the availability of the individual enantiomers, as long as the enantiomers are sufficiently resolved and detection is selective. However, when analyzing biological and environmental samples the presence of interferents may cause problems. Coeluting components, present in the extracts despite sophisticated cleanup procedures, may lead to difficulties in the determination of precise ratios due to the chromatographic effects and detection problems outlined. Generally, these problems are not encountered when analyzing pure reference compounds. A further problem demonstrated was the coelution of enantiomers of different isomers in chiral HRGC (e.g. *trans*-chlordane-1, *cis*-chlordane-1, and MC5-2 on PS086/BSCD) although the isomers were resolved using achiral HRGC.

Chiral HRGC revealed significant deviations in the enantiomeric composition of chlordane components in the environmental biological samples. Whereas we have previously detected some deviations in major and minor chlordane components,[8] we now detected such differences also in the metabolic products of chlordane, heptachlor *exo*-epoxide and oxychlordane. We show that in all the species analyzed both enantiomers of these metabolites are present. We further show that one or the other enantiomer of a particular chiral compound (e.g. component U82) may predominate in different species, although the original source (technical chlordane) presumably is the same. We found that in general the enantiomeric ratios deviate more in aquatic species at higher trophic level. These changed enantiomeric compositions must be due to enantioselective biological processes and cannot be due to abiotic processes, as we have pointed out previously.[8] The results further document the importance of chiral analyses in environmental studies of chiral pollutants.

ACKNOWLEDGMENT

We thank C. Rappe, Institute of Environmental Chemistry, University of Umeå, Umeå, Sweden, and his staff for discussions and making the environmental biological and the human tissue extracts available for analysis. We thank Ad de Jong, National Institute of Public Health and Environmental Protection, Bilthoven, The Netherlands, and H. Seed, VG Analytical, Manchester, England, for discussions and for suggesting construction of a modified ECNI ion source.

RECEIVED for review May 27, 1992. Accepted September 29, 1992.

Determination of Heavy Metals by Thin-Layer Chromatography–Square-Wave Anodic Stripping Voltammetry

Joseph H. Aldstadt and Howard D. Dewald*

Department of Chemistry, Clippinger Laboratories, Ohio University, Athens, Ohio 45701-2979

A square-wave anodic stripping voltammetric method is described for low parts per million determination of heavy metals separated by thin-layer chromatography (TLC). Heavy metal samples are separated on carboxymethyl cellulose TLC plates and detected by anodic stripping voltammetry (ASV) using a cellulose dialysis membrane-covered mercury film electrode (CM-MFE) placed directly on the TLC plate surface in a thin film of supporting electrolyte solution. The fast scan rates possible in square-wave voltammetry during the stripping step eliminate the need to deoxygenate the sample. Results are presented for a mixture of Pb(II), Cd(II), Cu(II), and Zn(II). Calibration curves for Pb(II) were linear over the range 10–500 ng, with a relative standard deviation of the peak current over a set of eight separate 100-ng Pb(II) samples of 16%.

INTRODUCTION

Anodic stripping voltammetry (ASV) is a powerful technique for rapidly measuring trace levels of heavy metals, especially in conjunction with modern pulse voltammetric techniques that discriminate double-layer charging currents from Faradaic currents.[1] The application of ASV to analytes in complex sample matrices can be complicated by several factors, particularly the adsorption of interfering components to the electrode surface. A gradual loss of electrode activity ("poisoning") by the adsorption of proteins and surfactants or the accumulation of reaction products can be observed when ASV is used in determinations of heavy metals in complex mixtures. Mercury electrode surfaces in particular are poisoned readily by humic acids, which are usually present in samples of environmental origin.[2,3] In addition to these adsorptive interferences, the presence of overlapping peaks in mixtures containing several electroactive components can also hinder the successful application of ASV.

The coupling of electrochemical techniques to various column liquid chromatographic (LC–EC) techniques has proven to be an effective way of preventing adsorptive interferences and separating electroactive components.[4] In addition to LC–EC, chemically-modified electrodes have been used to improve ASV selectivity. Efforts have been reported with Nafion perfluorosulfonate resin films,[5–7] cellulose acetate films,[8] and cellulose dialysis membrane-covered electrodes.[9,10] These membranes serve to control access to the mercury film. Furthermore, the presence of overlapping peaks in mixtures can be addressed by using a mercury film electrode (MFE), which has the highest resolving power of the electrodes used in ASV.[1,9]

Koval reported recently the novel application of in situ voltammetric detection for thin-layer (or planar) liquid chromatography (TLC).[11] Low-nanogram levels of *p*-anisidine and *p*-phenetidine were identified by square-wave voltammetry (SWV) using a Pt disk microelectrode after development on silica gel TLC plates, with linearity observed over several orders of magnitude. We demonstrate here the feasibility of using of a cellulose acetate membrane-covered mercury film electrode (CM-MFE) to determine Pb(II), Cd(II), Cu(II), and Zn(II) by themselves and in mixtures by in situ ASV after separation on carboxymethyl cellulose (CMC) TLC plates.

EXPERIMENTAL SECTION

Apparatus. Thin-layer chromatography (TLC) was performed in a 10- x 10-cm saturated (sandwich) vertical development chamber, fabricated in-house using Macor (a machinable ceramic material). The sandwich or "S-chamber" provides more reproducible chromatographic conditions.[12]

A glassy carbon disk working electrode (3-mm diameter) and Ag|AgCl (3 M NaCl) reference electrode (Model RE-1) were obtained from Bioanalytical Systems (West Lafayette, IN), while a Pt disk auxiliary electrode (0.25-mm diameter) was fabricated as described by Koval et al.[13] ASV was conducted on a Bioanalytical Systems Model 100A electrochemical analyzer (West Lafayette, IN) using Osteryoung square-wave anodic stripping voltammetry (SWASV), primarily because the fast scan rates attainable obviate the need to deoxygenate the sample. As Wojciechowski and Balcerzak point out,[14] SWV scan rates in excess of 40 mV/s allow stripping to be completed before a significant amount of dissolved oxygen can reach the electrode surface and oxidize the amalgam. Solution purging is not only time-consuming in any ASV measurement but also impractical for the in situ method developed here.

TLC-SWASV. The apparatus used is shown in Figure 1. A Nylon "canopy" (15-mm height, 22-mm i.d., 24-mm o.d.) was machined with three holes symmetrically arranged for the electrode insertions, as well as a small (<0.5-mm i.d.) hole for venting (i.e., to relieve pressure during supporting electrolyte addition). Two small three-pronged laboratory clamps were used to secure the canopy over the TLC plate.

Reagents and TLC Supplies. All chemicals were of ACS reagent grade or better. All reagents were prepared in water than was de-ionized and then doubly-distilled. Heavy metal standards (nitrate salts) were prepared volumetrically from atomic absorption standards (Fisher Scientific, Pittsburgh, PA).

(1) Wang, J. *Stripping Analysis*; VCH: Deerfield Beach, FL, 1985.
(2) Batley, G. E.; Florence, T. M. *J. Electroanal. Chem. Interfacial Electrochem.* **1976**, *72*, 121–126.
(3) Wang, J.; Luo, D. B. *Talanta* **1984**, *31*, 703–707.
(4) Kissinger, P. T.; Heineman, W. R. *Laboratory Techniques in Electroanalytical Chemistry*; Marcel Dekker: New York, NY, 1984; Chapter 22.
(5) Hoyer, B.; Florence, T. M.; Batley, G. E. *Anal. Chem.* **1987**, *59*, 1608–1614.
(6) Hoyer, B.; Florence, T. M. *Anal. Chem.* **1987**, *59*, 2839–2842.
(7) Morrison, G. M. P.; Florence, T. M. *Electroanalysis (N.Y.)* **1989**, *1*, 485–491.
(8) Wang, J.; Hutchins-Kumar, L. D. *Anal. Chem.* **1986**, *58*, 402–407.
(9) Stewart, E. E.; Smart, R. B. *Anal. Chem.* **1984**, *56*, 1131–1135.
(10) Smart, R. B.; Stewart, E. E. *Environ. Sci. Technol.* **1985**, *19*, 137–140.
(11) Brown, G. N.; Birks, J. W.; Koval, C. A. *Anal. Lett.* **1989**, *22*, 507–518.
(12) Geiss, F. *Fundamentals of Thin-Layer Chromatography (Planar Chromatography)*; Alfred Hüthig Verlag: Heidelberg, Germany, 1987.
(13) Koval, C. A.; Austermann, R. L.; Turner, J. A.; Parkinson, B. A. *J. Electrochem. Soc.* **1985**, *132*, 613–623.
(14) Wojciechowski, M.; Balcerzak, J. *Anal. Chem.* **1990**, *62*, 1325–1331.

0003-2700/92/0364-3176$03.00/0

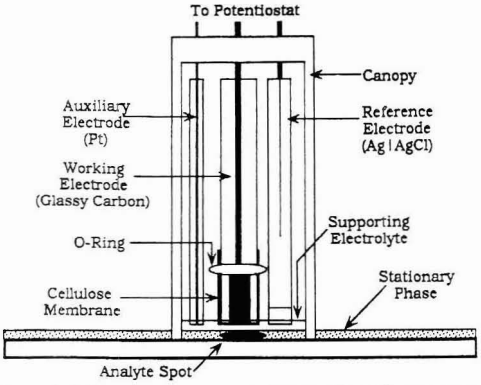

Figure 1. Schematic cross-sectional view of the TLC–ASV apparatus.

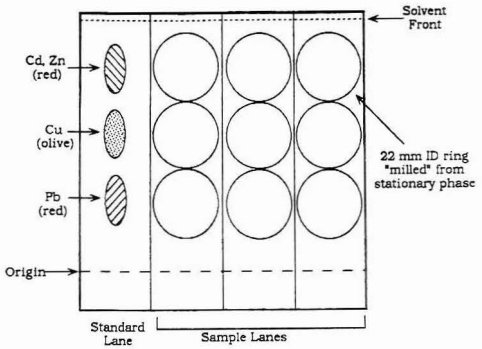

Figure 2. Schematic representation of a developed TLC plate (10 × 10 cm). The color of the dithizonate complex of the metal is indicated. Typical dimensions of the spots were 15 × 5 mm.

A pH between 2 and 3 was maintained in order to prevent the formation of metal hydroxides. Dithizone (Eastman Kodak, Rochester, NY) was repurified and then dissolved in chloroform as a 0.10% (w/v) solution.[15]

Nafion 117, a perfluorosulfonate cation-exchange resin, was obtained from Aldrich (Milwaukee, WI) as a 5% (w/v) solution in a mixture of lower aliphatic alcohols and 10% (v/v) water. Spectrum Spectra/Por 6 cellulose acetate dialysis membranes (28-μm thickness) with a nominal molecular weight cutoff of 3500 were obtained from Fisher Scientific (Pittsburgh, PA).

Whatman polyester-backed carboxymethyl cellulose (CMC) plates (100-μm thickness) were obtained from VWR Scientific (Cleveland, OH).

Procedures. *Container Cleaning.* Heavy metal reagent solutions were stored in polyethylene containers that had been soaked with 0.1 M HNO_3 for at least 1 week.

TLC Procedure. The procedure of Cozzi et al. for the separation of metals on CMC was modified to use 0.60 M acetic acid/0.60 M sodium acetate as the mobile phase.[16] Four samples (0.5–1.0 μL) were applied to separate manually-scored lanes on the TLC plates using plastic Eppendorf pipets (Brinkmann, Westbury, NY) or glass Nanopipettes (Analtech, Newark, DE). Following a 25-min chromatographic development time, a standard lane was excised and analyte spot(s) were identified with 0.10% (w/v) dithizone in chloroform followed by 10% (v/v) NH_4OH using a glass atomizing sprayer. The location of samples in adjacent lanes was based on the retardation factors (R_f) determined from dithizone identification of the standards, as depicted in Figure 2. The visual detection limit using dithizone was approximately 100 ng for each analyte.

Electrode Polishing. The working and auxiliary electrodes were polished on a felt pad daily before use with 0.5-μm γ-Al_2O_3 (Buehler Ltd., Lake Bluff, IL).

NC-MFE Preparation. Nafion-coated mercury film electrodes (NC-MFE) were prepared as described by Hoyer and co-workers.[5] Nafion 117 was diluted with absolute ethanol to 0.24% (w/v), and 10 μL was applied to the polished working electrode surface to cast the film. The electrode was covered for 1 h to allow dust-free evaporation and then dried in the warm air stream (~50 °C) of a heat gun for 1 min. NC-MFE's prepared in this manner correspond to the "thick" width used by Hoyer et al.,[5] with an approximate electrode coverage of 1.2 $\mu g/mm^2$. Best results were obtained when the Nafion-coated electrode was equilibrated prior to MFE preparation for at least 12 h in a 10 mM HNO_3/10 mM KNO_3 solution. This proved to be a critical step—the influence of Nafion film swelling on membrane transport efficiency is well-documented.[17,18]

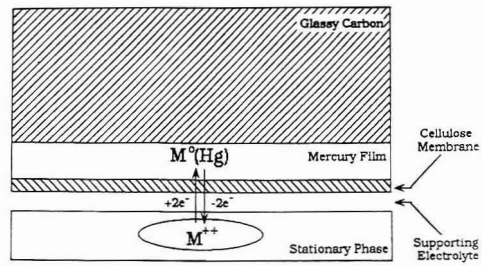

Figure 3. Apparent diffusion of metal cations from the TLC stationary phase to the MFE depicted schematically. Approximate thicknesses are 0.010, 28, and 100 μm for the MFE, CM, and stationary phase, respectively.

CM-MFE Preparation. The CM-MFE was prepared daily and stored as described by Stewart and Smart.[9] Spectra/Por 6 cellulose dialysis membranes were heated for 20 min at 70 °C in reagent water, followed by 48 h in reagent water to remove traces of the sodium azide preservative. To prevent degradation by cellulytic microbes, the tubing was transferred to freshly boiled water daily. Stock dialysis membranes (i.e., unwashed) were refrigerated per the manufacturer's instructions. A silicone rubber O-ring was used to hold the membrane (~1 cm^2) in place on the end of the working electrode. Care must be exercised such that the membrane is neither stretched nor allowed to dry out.[19]

MFE Preparation. MFE's were prepared in solution ex situ from 1.0 mM $Hg(NO_3)_2$ in 10 mM KNO_3/10 mM HNO_3 for 10 min at −1.000 V (all potentials are vs a Ag|AgCl (3 M NaCl) reference electrode). The mercury film was prepared under a N_2(g) blanket to improve its uniformity.[14] The supporting electrolyte (10 mM KNO_3/10 mM HNO_3) also included 0.1 mM $Hg(NO_3)_2$ to help maintain the mercury film during the measurement. Best results were obtained by electrically preconditioning the CM-MFE in a deaerated 10 mM KNO_3/10 mM HNO_3 solution by cycling the potential between +100 and −1000 mV for eight cycles (each of 2-min duration) immediately following MFE preparation. The estimated MFE thickness is 100 Å.

SWASV. The following conditions were typically used for on-plate measurements: initial (deposition) potential of −1.100 V; final potential of +0.100 V; deposition time of 30–60 s; quiet time of 0 s; square-wave amplitude of 25 mV; frequency of 25 Hz; potential step of 4 mV—thus the scan rate was 100 mV/s.

TLC–SWASV. A schematic of the apparent transport process is depicted in Figure 3. The TLC–SWASV experimental procedure is as follows: (1) after chromatography, the plate is

(15) Marr, I. L.; Cresser, M. S. *Environmental Chemical Analysis*; International Textbook Co.: New York, 1983; p 139.
(16) Cozzi, D.; Desideri, P. G.; Lepri, L. *J. Chromatogr.* **1969**, *42*, 532–540.
(17) Yeo, R. S.; Chan, S. F.; Lee, J. *J. Membr. Sci.* **1981**, *9*, 273–283.
(18) Moore, R. B., III; Martin, C. R. *Macromolecules* **1988**, *21*, 1334–1339.
(19) Kesting, R. E. *Synthetic Polymer Membranes*, 2nd ed.; Wiley-Interscience: New York, 1985; Chapter 4.

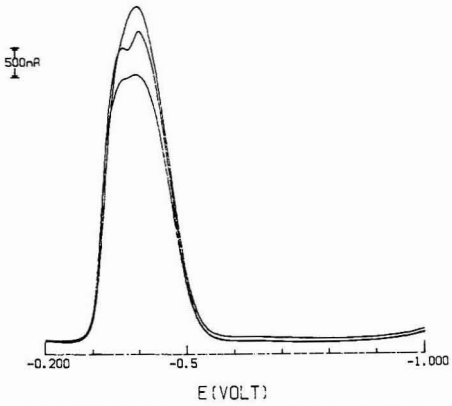

Figure 4. Example of SWASV using the NC-MFE on a CMC TLC plate. Pb(II) measured in triplicate (200-ng sample) reveals a gradually increasing current response and distortion of the peak shape.

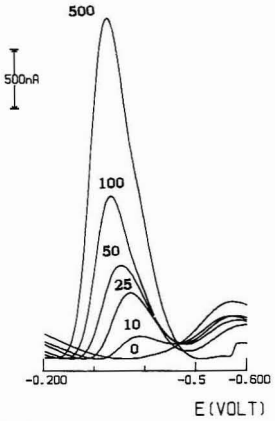

Figure 5. Calibration standards for on-plate SWASV of Pb(II) using the CM-MFE. Pb(II) was applied as 0-, 10-, 25-, 50-, 100-, and 500-ng samples. Each sample was measured in triplicate.

dried at room temperature; (2) on the basis of the standard's R_f, analyte spots are isolated using a milling device (22-mm i.d., 24-mm o.d.) to remove the stationary phase around the spot as depicted in Figure 2; (3) a cylindrical Nylon canopy (15-mm height, 22-mm i.d., 24-mm o.d.) containing the three electrodes (arranged symmetrically within it) is clamped over the spot, such that the edges of the canopy fit securely within the milled ring; (4) 600 μL of supporting electrolyte is immediately added through a port in the top of the canopy to form a shallow (~0.4-mm) film across the plate surface that is confined by the canopy; (5) the ASV measurement is made in quadruplicate (3–6 min/sample). In this way, the measurement is made directly on the TLC plate. Approximately 20-fold analyte losses were observed as a result of chromatographic development, in basic agreement with Koval's estimate for their voltammetric method.[11] Between samples the working electrode is rinsed in deoxygenated 10 mM KNO_3 and polarized in solution under a N_2(g) blanket to +100 mV (by cycling the BAS 100A "step" function between +99 and +100 mV indefinitely).

RESULTS AND DISCUSSION

Nafion-Modified Electrodes. Initial characterization of Nafion-coated (NC) polymer-modified MFE's was performed using Pb(II) standards applied to CMC TLC plates without chromatographic development. Heavy metal standards (10 μL) were applied to CMC and allowed to air dry. Figure 4 shows a typical voltammogram using a NC-MFE. Three disadvantages in using the NC-MFE on-plate were observed. First, Nafion's ability to preconcentrate cations proved to be impractical. A stable peak current signal could only be obtained after at least six measurements. Supporting electrolyte (blank) samples revealed a high background signal which increased with coating thickness. Furthermore, when samples over a range of concentrations were analyzed in random order, the peak current signal for a given sample was proportional to that of the previous spiked sample (i.e., hysteresis). Second, the variability of measurements on successive days was very high, as the reproducibility in casting a fresh Nafion coating each day by the evaporative procedure was poor. In fact, roughly half of the NC-MFE's yielded erratic responses following MFE preparation and were not used further. Finally and most importantly, although NC-MFE's have been successfully used for solution-phase ASV measurements,[5-7] the Nafion films used in this work were too thin to protect the MFE from abrasive contact with the TLC stationary phase surface. The prospect of having to prepare a fresh MFE after each sample was unattractive from the standpoint of sample throughput. Attempts to design an electrode housing for a bare MFE that would prevent abrasive damage (e.g., use of spacers) were unsuccessful, apparently because the distance from the working electrode to the TLC stationary phase was much greater than the diffusion layer.

Cellulose-Modified Electrodes. Voltammograms obtained using a CM-MFE on a CMC TLC plate are shown in Figure 5. Several improvements compared to the NC-MFE results became evident. First, preparation of the CM-MFE is simple. Working electrodes can be prepared quickly on the day of use since membrane equilibration is not required for each electrode. Second, the background signal is low, as cellulose does not preconcentrate cations as significantly as Nafion. Cellulose is less specific than Nafion, which is an important consideration analytically as rapid diffusion across the membrane minimizes sample carryover as well as shortens the analysis time. Although a delay in reaching the maximum current response was observed, the signal stabilizes quickly (usually by the third replicate of a given sample). Furthermore, a useful diagnostic was that peak currents above ~4 μA were indicative of an overloaded MFE, as distorted peaks (very broad with "jagged" crests) were consequently observed. A slight positive drift in the peak potential was observed for NC- and CM-MFE's, though this usually stabilized by the second replicate of a given sample for the CM-MFE's. Third, the peaks are narrower than those obtained with the NC-MFE which again suggests less restricted ion transport through the membrane. Fourth, the membranes protect the MFE from abrasive contact with the TLC surface during the course of the day.

The relative standard deviation (RSD) for eight separate 100-ng samples (10 μL of 10 ppm) of Pb(II) spotted on CMC was 15.9%—by comparison, a bare glassy carbon electrode in solution (250 ppb) exhibited a RSD of 4.00%. Calibration curves for Pb(II) applied to the surface were linear from approximately 10 to 400 ng. For a series of calibration standards (e.g., Figure 5), each sample was measured in triplicate and the third measurement was plotted. For example, four separate calibration curves over a period of several weeks yielded an overall least-squares linear fit of y (μA) = 0.007 19 ± 0.004 12 (μA/ng) + 0.211 ± 0.253 (μA); correlation coefficient, $r = 0.976 \pm 0.0258$. Thus in qualitative terms, the variability in the slope and intercept values illustrates the high day-to-day variability of the CM-MFE calibration curves, while the low variability in the correlation

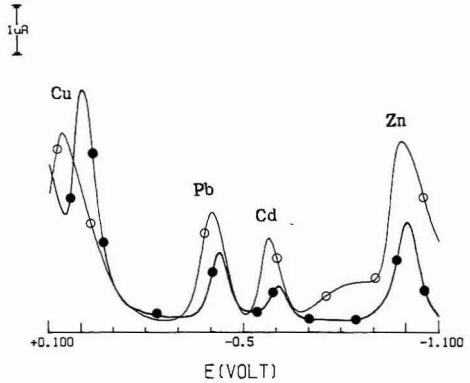

Figure 6. On-plate (O) and solution (●) SWASV of a four-component mixture using the CM-MFE. The solution concentrations were 3.00 ppm Zn(II), 0.250 ppm Cd(II), 0.250 ppm Pb(II), and 0.500 ppm Cu(II), while a 10-μL sample containing 100 ppm Zn(II), 10 ppm Cd(II), 10 ppm Pb(II), and 20 ppm Cu(II) was applied to the TLC plate.

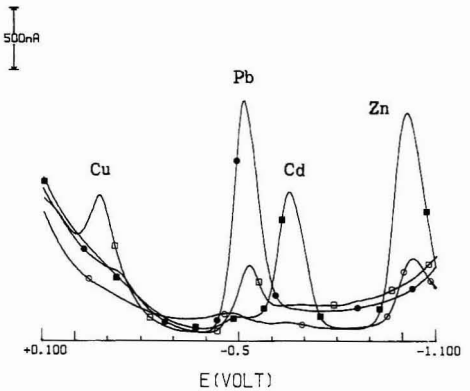

Figure 7. On-plate SWASV of a four-component mixture after chromatographic development using the CM-MFE. Voltammograms from the origin (O), Cu (□), Pb (●), and Cd/Zn (■) region of the TLC plate (as shown in Figure 2) are overlaid on the same potential axis.

coefficient shows that CM-MFE's prepared for a given day possessed good linearity.

ASV Determination in Mixtures by Carboxymethyl Cellulose TLC. A mixture containing Cu(II), Pb(II), Cd(II), and Zn(II) in reagent water was applied (1 μL) to carboxymethyl cellulose TLC plates (250 ng/analyte) and developed. The R_f zones were lead (0.30–0.48), copper (0.51–0.70), and zinc/cadmium (0.73–0.86). The TLC spots "tailed" slightly more in a multicomponent mixture, and the R_f values increased by ~10% compared to the values observed for single component determinations. It is important to note that the origin is well-separated from the heavy metals—that is, where most potentially interfering organic substances would remain under these chromatographic conditions.

Figure 6 shows voltammograms comparing the four-component mixture on-plate (i.e., undeveloped) to a qualitatively identical mixture in solution, using the same CM-MFE. The peak resolution does not degrade noticeably, and only minor drift in peak potentials was observed. Voltammograms from each of the chromatographic zones given above (origin, Pb, Cu, and Zn/Cd) are superimposed on the same potential axis in Figure 7, using a CM-MFE after development of the four-component mixture. Only minor carryover is apparent: some Pb(II) was observed in the Cu(II) zone, while Zn(II) was found at the origin. Intermetallic compounds of Cu(II), particularly of Cu(II)–Zn(II) and Cu(II)–Cd(II), can be signficant problems in ASV.[1] The separation of Cu(II) from Zn(II) and Cd(II) in the method reported here reduces this phenomenon to a negligible level. Although Cd(II) and Zn(II) coelute, they are resolved by the inherent electrochemical selectivity of SWASV.

CONCLUSIONS

There are few quantitative detection methods in TLC and even fewer that are electrochemical in nature. Work using amperometric detection[20,21] and voltammetric detection[11,22] are the only other reports of electrochemical detection in TLC that could be identified in the literature, although the isolation of specific regions of various surfaces to perform diverse electrochemical measurements has been the subject of recent efforts in several laboratories.[23–25]

The accurate measurement of free metal ion concentration is important in environmental, forensic, and clinical applications. This technique is simpler than atomic spectroscopic methods and potentially more powerful than the basic ASV technique; thus it may hold promise for field laboratory use, e.g., trace metals in hazardous waste samples. While the MFE is known for its stability and ease of preparation and usage, the cellulose dialysis membranes used in this study also possess many attractive features. These membranes are chemically inert, nonelectroactive, hydrophilic, and insoluble in water—ideal properties for an electrode membrane material. A highly variable film casting procedure is not needed to prepare the working electrode—the cellulose membranes are in fact quite easy to handle. Furthermore, the cellulose membranes are nontoxic, inexpensive, and widely available.

Work is in progress to modify the experimental configuration by using an array of ultramicroelectrodes, as the accuracy of working electrode placement is a major source of variability in the present system (variability of electrode placement was revealed by staining samples with dithizone *after* the ASV measurement). The methodology will also be optimized, especially the sensitivity (deposition time and volume of supporting electrolyte within the canopy), and the apparatus will be minaturized to increase the sample throughput. Finally, potentiometric stripping analysis is being explored as an alternative to SWASV because it not only also allows one to forego sample deoxygenation but also may possess selectivity and sensitivity advantages.

ACKNOWLEDGMENT

Mr. Dewey King is gratefully acknowledged for the fabrication of the TLC chamber, milling device, and electrode canopy. This work was supported in part by a John Houk Memorial Research Grant to J.H.A. and the Research Challenge Program at Ohio University. Presented in part at the 43rd Pittsburgh Conference and Exposition on Analytical Chemistry and Applied Spectroscopy, New Orleans, LA, March 1992.

RECEIVED for review June 10, 1992. Accepted October 12, 1992.

(20) Di Stefano, V.; Marini, P. *Analyst (London)* **1973**, *98*, 251–256.
(21) Bochkov, A. S. *J. Liq. Chromatogr.* **1982**, *5*, 1567–1572.
(22) Ostrovidov, E. A. *Zavod. Lab.* **1984**, *50*, 15–16; Chem. Abstr. **1985**, *102*, 71822e.
(23) Howard, J. N.; Koval, C. A. *Anal. Chem.* **1991**, *63*, 2777–2786.
(24) Unwin, P. R.; Bard, A. J. *Anal. Chem.* **1992**, *64*, 113–119.
(25) Fritsch-Faules, I.; Faulkner, L. R. *Anal. Chem.* **1992**, *64*, 1118–1127.

Stable Films of Cationic Surfactants and Phthalocyaninetetrasulfonate Catalysts

Naifei Hu,† David J. Howe, Maryam F. Ahmadi, and James F. Rusling*

Department of Chemistry, Box U-60, University of Connecticut, Storrs, Connecticut 06269-3060

Films made from cationic surfactants and well-retained redox catalysts were investigated. Full loading of metal phthalocyaninetetrasulfonates ($MPcTS^{4-}$) into water-insoluble dialkyldimethylammonium surfactants by ion exchange from aqueous solutions yielded coatings on electrodes that retain these catalyst ions for 1–2 weeks in electrolyte solutions. In contrast, partly loaded films lost most $MPcTS^{4-}$ ions in a few hours. All films showed gel-to-liquid crystal phase transitions at temperatures characteristic of surfactant bilayers. Cross-sectional views by SEM showed layers of 0.1–0.2 μm, as well as some disordered regions. Each larger layer is probably made up of stacks of many molecular bilayers. Retention of $MPcTS^{4-}$ ions seems related to their dimerization. Dimers of $MPcTS^{4-}$ associated with ammonium head groups may cross-link adjacent surfactant bilayers. The $MPcTS^{4-}$ ions that enhance stability in these films are also good redox catalysts.

INTRODUCTION

Films of water-insoluble surfactants[1] can be prepared by casting their solutions onto a solid support and evaporating the organic solvent. Casting offers a simple means to prepare relatively thick multiple bilayer surfactant films compared to the reliable but tedious Langmuir–Blodgett film transfer.[2] Surfactant bilayer films intercalated between clay layers[3] or linear ionic polymers,[4,5] as well as films of polymerized surfactants,[4d–f] have also been prepared by casting. The surfactants used typically have two or three hydrocarbon chains of 12 or more carbons. They do not form micelles which would tend to dissolve the films in water.

Permeability of cast surfactant films is controlled by their phase. Neutral, water-soluble solutes pass through films that are in the liquid crystal state, but permeability is turned off when the films are brought to the solid-like gel phase.[3–5] Results of X-ray diffraction and electron microscopy, as well as phase transitions for surfactant films at temperatures close to those of bilayer vesicle suspensions of the same surfactants, have been used to propose multiple bilayer structures.[1,3–6]

Stable, ordered surfactant films have a wide range of potential applications. Possibilities include membranes with controllable permeability,[3–6] coatings for piezoelectric[6] or amperometric sensors,[9] and kinetic control of catalytic chemical or electrochemical reactions.[7–9] Surfactant molecules in these films are arranged in bilayers resembling those of lipid membranes in living cells. Thus, additional applications include biomembrane-like supports for ordering biological macromolecules[1d–f] and inorganic complexes[1c,g] and for designing systems with vectorial electron transport.[10]

We are currently evaluating insoluble surfactant films containing redox mediators for electrochemical catalysis, specifically for dehalogenations of organohalide pollutants.[8] Films of didodecyl- and dioctadecyldimethylammonium bromide (DDAB and DODAB) cast onto pyrolytic graphite electrodes readily incorporated multivalent anions from solution. When used in aqueous solutions, these films excluded hydrophilic multivalent cations but were able to preconcentrate hydrophobic ions and neutral molecules.[7] Thus, such films should be useful in exerting selectivity and control of catalytic reactions.

Anionic redox catalysts can be introduced into liquid crystalline DDAB and DODAB films on electrodes by ion exchange from aqueous solutions. Anionic macrocyclic complexes such as metal phthalocyaninetetrasulfonates have a wide range of catalytic activity.[11] Films incorporating such complexes catalyzed dehalogenation of organohalide pollutants, converting vicinal dibromides to olefins and trichloroacetic acid to acetic acid.[8] Clay–surfactant composite films containing neutral metal phthalocyanines catalyzed similar reductions.[9] Charge transport rates are much better for both types of films in liquid crystal phases than in solid-like gel states. Gel-to-liquid crystal phase transitions were detected by voltammetry and differential scanning calorimetry.[7–9]

Composite clay–surfactant films containing metal phthalocyanines showed excellent stability, retaining catalytic activity for 1 month or more.[9] However, maintenance of stable amounts of anionic catalysts in pure DDAB and DODAB films depends strongly on the type of anion incorporated. Hexacyanoferrate(4-) ion and cobalt(III) corrinhexacarboxylate are readily incorporated into DDAB and DODAB films. However, when films loaded with these anions are placed in a solution containing only supporting electrolyte, 50–75% of these electroactive anions are leached out in several hours.[8,9]

† Permanent address: Beijing Normal University, Beijing, China.

(1) (a) Nakashima, N.; Ando, R.; Kunitake, T. *Chem. Lett.* **1983**, 1577–1580. (b) Kunitake, T.; Shimomura, M.; Kajiyama, T.; Harada, A.; Okuyama, K.; Takayanagi, M. *Thin Solid Films* **1984**, *121*, L89–91. (c) Ishikawa, Y.; Kunitake, T. *J. Am. Chem. Soc.* **1986**, *108*, 8300–8302. (d) Hamachi, I.; Noda, S.; Kunitake, M.; Hamachi, I.; Honda, T.; Noda, S.; Kunitake, T. *J. Am. Chem. Soc.* **1990**, *112*, 6744–6745. (e) Hamachi, I.; Honda, T.; Noda, S.; Kunitake, T. *Chem. Lett.* **1991**, 1121–1124. (f) Hamachi, I.; Noda, S.; Kunitake, T. *J. Am. Chem. Soc.* **1991**, *113*, 9625–9630. (g) Ishikawa, Y.; Kunitake, T. *J. Am. Chem. Soc.* **1991**, *113*, 621–630.

(2) Fendler, J. H. *Membrane Mimetic Chemistry*; Wiley: New York, 1982.

(3) Okahata, Y.; Shimizu, A. *Langmuir* **1989**, *5*, 954–959.

(4) (a) Shimomura, M.; Kunitake, T. *Polym. J.* **1984**, *16*, 187–190. (b) Kunitake, T.; Tsuge, A.; Nakashima, N. *Chem. Lett.* **1984**, 1783–1786. (c) Nakashima, N.; Kunitake, M.; Kunitake, T.; Tone, S.; Kajiyama, T. *Macromolecules* **1985**, *18*, 1515–1516. (d) Higashi, N.; Kajiyama, T.; Kunitake, T.; Prass, W.; Ringsdorf, H.; Takahara, A. *Macromolecules* **1987**, *20*, 29–33. (e) Nakashima, N.; Eda, H.; Kunitake, M.; Manabe, O.; Nakano, K. *J. Chem. Soc., Chem. Commun.* **1990**, 443–444. (f) Kunitake, T. *Polym. J.* **1991**, *23*, 613–618.

(5) (a) Okahata, Y.; Enna, G.; Taguchi, K.; Seki, T. *J. Am. Chem. Soc.* **1985**, *107*, 5300–5301. (b) Okahata, Y.; Enna, G. *J. Phys. Chem.* **1988**, *92*, 4546–4551. (c) Okahata, Y.; Enna, G.; Takenouchi, K. *J. Chem. Soc., Perkin Trans. 2* **1989**, 835–843.

(6) Okahata, Y.; Ebato, H. *Anal. Chem.* **1991**, *63*, 203–207.

(7) Rusling, J. F.; Zhang, H. *Langmuir* **1991**, *7*, 1791–1796.

(8) Rusling, J. F.; Hu, N.; Zhang, H.; Howe, D.; Miaw, C.-L.; Couture, E. In *Electrochemistry in Microheterogeneous Fluids*; Mackay, R. A., Texter, J., Eds.; VCH Publishers: New York, 1992.

(9) Hu, N.; Rusling, J. F. *Anal. Chem.* **1991**, *63*, 2163–2168.

(10) Gratzel, M. *Heterogeneous Photochemical Electron Transfer*; CRC Press: Boca Raton, FL, 1989.

(11) Moser, F. H.; Thomas, A. L. *The Phthalocyanines*; CRC Press: Boca Raton, FL, 1983; Vol. I, pp 79–100.

0003-2700/92/0364-3180$03.00/0

On the other hand, when sufficient metal phthalocyanine-tetrasulfonates ($MPcTS^{4-}$) are incorporated, DDAB films retain most of these catalytic anions for 10 days or more in 0.1 M KBr solutions.[8]

In this paper, we present results of differential scanning calorimetry, molecular spectroscopy, voltammetry, and scanning electron microscopy (SEM) with energy-dispersive X-ray (EDX) analysis which provide insight into the structure and causes of stability of cationic surfactant films containing metal phthalocyaninetetrasulfonates. Absorbance spectra suggest that dimerization of metal phthalocyaninetetrasulfonates[12] contributes to the remarkable stability of catalytic films containing these complexes. These films are microscopically ordered in multiple bilayers of surfactants, but are macroscopically heterogeneous.

EXPERIMENTAL SECTION

Chemicals and Solutions. Didodecyldimethylammonium bromide (DDAB) and dioctadecyldimethylammonium bromide (DODAB) were 99+% from Eastman Kodak. Cetyltrimethylammonium bromide (CTAB, hexadecyltrimethylammonium bromide) was Fisher certified (99.8%). Copper phthalocyanine-3,4′,4″,4‴-tetrasulfonic acid and nickel phthalocyaninetetrasulfonic acid (mixture of isomers) were obtained as tetrasodium salts from Aldrich. All other chemicals were reagent grade.

Apparatus and Procedures. A Bioanalytical Systems BAS-100 and PARC Model 273 electrochemistry system were used for cyclic voltammetry (CV). The working electrode was a basal plane pyrolytic graphite (HPG-99, Union Carbide) disk (geometric $A = 0.2\ cm^2$). Electrodes were prepared by sealing pyrolytic graphite (PG) disks into the large end of a polypropylene pipette tip as described previously[9] or by sealing to a glass tube with heat shrinkable tubing. Electrodes were abraded with 600-grit SiC paper on a metallographic polishing wheel prior to coating with surfactant. Two film thicknesses were used. PG electrodes were coated by pipeting 20 μL of 0.1 M solution of DDAB in chloroform (thick film) or 6 μL of 0.01 M solution of DDAB (thin film) onto PG disks. Chloroform was allowed to evaporate for 24 h after fitting a small bottle tightly over the electrode to serve as a closed evaporation chamber. Coated electrodes were subsequently cured for at least 24 h in air.

This method gave reasonably uniform and reproducible coatings as evaluated by light microscopy, SEM, and CV of incorporated ferrocyanide and $MPcTS^{4-}$ ions. Approximate film thicknesses estimated from geometric factors[7] and confirmed by SEM cross-sectional views were 1–2 μm for thin films and 30–50 μm for thick films. Thin DDAB films were used for most of the electrochemical experiments.

The three electrode cell for CV studies included the surfactant-coated PG working electrode, a platinum wire counter electrode, and a saturated calomel electrode (SCE) or a Ag/AgBr wire as reference. In 0.1 M KBr, the Ag/AgBr reference half-cell had a potential of 0.086 V vs SCE. The ohmic drop of cells was compensated ≥90% by the electrochemical analyzers; the typical uncompensated resistance was 10–20 Ω. Experiments were thermostated at 25.0 ± 0.1 °C. All solutions were purged with purified nitrogen to remove oxygen before voltammetry.

Absorption spectroscopy was done using either a Perkin-Elmer Model λ3B or a Milton Roy Spectronic 3000 Array UV–vis spectrophotometer. Films were deposited as above onto glass microscope slides at a sufficient thickness to give measurable absorbance. These films were equilibrated with aqueous 0.1 M KBr solutions containing 0.5 mM of the metal phthalocyanine-tetrasulfonates ($MPcTS^{4-}$). Films were removed from these solutions, dipped in pure water several times, and then placed in the spectrometer to obtain the spectra.

Scanning electron microscopy (SEM) and energy-dispersive X-ray analysis (EDX) were done with an Amray 1810 microscope using a tungsten filament as the electron source. DDAB films for SEM/EDX analysis were coated onto PG electrodes using the same method as for voltammetry. The entire electrode assembly could be attached to the mounting stage of the SEM with electrical connection through the electrode lead wire. Prior to analysis by SEM, 5 nm of gold was coated onto samples with a Model SC 500 sputter coater (Bio-Rad).

For cross-sectional SEM views, coatings were cast onto very thin disks of pyrolytic graphite and freeze-fractured after immersion in liquid nitrogen. EDX was done using a Phillips North American EDAX Model PV-9800 system. The beam diameter for spot analyses was 2 μm. Sensitivity factors provided with system software were used to convert counts to relative atom percent.

Differential scanning calorimetry was done with a Perkin-Elmer Model DSC 7 calorimeter calibrated with water (0.0 °C) and indium (156.6 °C). Thick DDAB films (5–10 mg) were prepared as above on PG electrodes and equilibrated until steady-state CVs were obtained. The films were kept in solution until immediately before the DSC run and then scraped off of the PG into aluminum sample pans which were then crimped shut. Samples were held at −30 °C for 10 min and then scanned at 10 °C min^{-1} to 0.0 °C, where they were held for 10 min. Analytical scans at 10 °C min^{-1} were subsequently initiated. Phase transitions are reported as onset temperatures of peaks in the thermograms.

Table I. Phase-Transition Temperatures (°C)

sample	diff scanning calorimetry: this work	diff scanning calorimetry: lit. [ref]	voltammetry prev work [ref]
dry DDAB powder[a]	55		
wet DDAB powder[b]	10		
aqueous DDAB dispersion[c]	15	10 [3], <5 [14a]	
DDAB films[d]	10, 12		
+ $NiPcTS^{4-}$	16, 17		10 [8]
+ $CuPcTS^{4-}$	16, 17		
+ $Fe(CN)_6^{4-}$	16		9 [7]
aqueous DODAB dispersion[c]		44 [4a], >50 [14a]	
DODAB films[d]			
+ $NiPcTS^{4-}$			38 [8]
+ $CuPcTS^{4-}$			41 [8]
+ $Fe(CN)_6^{4-}$			52 [8]

[a] Dried in a vacuum over $CaSO_4$ dessicant for 2 days. [b] Stored in a closed chamber with saturated water vapor for several days. [c] 10 mM aqueous solution sonicated for 4 at 50 °C. [d] After full equilibration in solution of 0.1 M KBr or 0.1 M KBr + 1 mM of ion stated. Duplicate values are for separate films.

RESULTS

Calorimetry. Previous work showed that gel-to-liquid crystal phase transitions measured for surfactant films by differential scanning calorimetry (DSC) corresponded to breaks in cyclic voltammetric peak current vs temperature curves.[7-9] More extensive calorimetric studies are reported herein.

A phase transition at 55 °C was observed for dry DDAB powder (Table I). When the powder was allowed to equilibrate with saturated water vapor under ambient temperature, a transition (T_c) was observed at 10 °C with no peak at 55 °C. The 10 °C transition most likely corresponds to the so called Lam_2 phase, a lamellar liquid crystal system observed[13] when there is about 7–11% water present in DDAB. An aqueous

(12) (a) Schelly, Z. A.; Farina, R. D.; Eyring, E. M. *J. Phys. Chem.* **1970**, *74*, 617–620. (b) Schelly, Z. A.; Harward, D. J.; Hemmes, P.; Eyring, E. M. *J. Phys. Chem.* **1970**, *74*, 3040–3042. (c) Gruen, L. C.; Blagrove, R. J. *Aust. J. Chem.* **1972**, *25*, 2553–2558; **1973**, *26*, 319–323. (d) Boyd, P. D. W.; Smith, T. D. *J. Chem. Soc., Dalton Trans.* **1972**, 839–843. (e) Farina, R. D.; Halko, D. J.; Swinehard, J. H. *J. Phys. Chem.* **1972**, *76*, 2343–2348. (f) Abel, E. W.; Pratt, J. M.; Whelan, R. *J. Chem. Soc., Dalton Trans.* **1976**, 509–514. (g) Yang, Y.; Ward, J. R.; Seiders, R. P. *Inorg. Chem.* **1985**, *24*, 1765–1769.

(13) Fontell, K.; Ceglie, A.; Lindman, B.; Ninham, B. *Acta Chem. Scand.* **1986**, *A40*, 247–256.

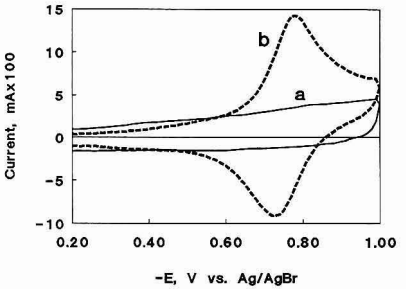

Figure 1. Cyclic voltammograms at 0.10 V s^{-1}: (a) at bare PG electrode in 0.1 M KBr/0.2 mM $NiPcTS^{4-}$; (b) DDAB-coated PG fully loaded with $NiPcTS^{4-}$ in 0.1 KBr with no $NiPcTS^{4-}$ in solution.

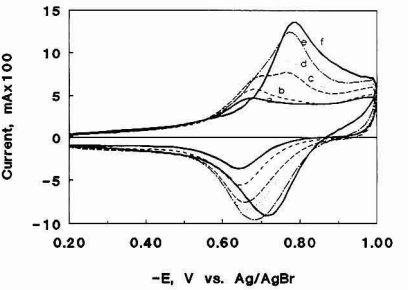

Figure 2. Series of cyclic voltammograms at 0.10 V s^{-1} in 0.1 M KBr showing uptake of $NiPcTS^{4-}$ by a DDAB film from its 0.2 mM solution during continuous scanning after (a) 1, (b) 3, (c) 8, (d) 10, (e) 18, and (f) 48 min.

sonicated dispersion of DDAB gave a T_c of 15 °C, slightly larger than values previously reported for sonicated vesicle dispersions,[13] but similar to that reported for the lamellar liquid crystal phase Lam_1 observed at low DDAB concentrations in water.[14]

Similar DSC behavior for dry dioctadecyldimethylammonium chloride (DODAC) has also been found. A gel-to-liquid crystal transition at 52 °C was observed only after addition of sufficient water and persisted between 9 and 86% water.[15] This higher value of T_c is consistent with the longer chain length compared to DDAB and is similar to that reported for DODAB (Table I), despite the difference in anion.

Films of DDAB fully loaded with $MPcTS^{4-}$ or ferrocyanide ions showed phase transitions by DSC and CV at similar temperatures (Table I) to those of cast DDAB films containing Br^- ions and the Lam_1 and Lam_2 phases. Data for DODAB support similar conclusions.

Electrochemistry. Voltammetry was done at 25 °C with DDAB films in a lamellar liquid crystal state. Films were loaded with $MPcTS^{4-}$ ions by placing freshly prepared DDAB-coated electrodes into 0.2–1.0 mM $MPcTSNa_4$/0.1 M KBr solutions and scanning repeatedly over the potential range of the first CV peak, usually −0.2 to −1 V. Full incorporation of $MPcTS^{4-}$ ions into DDAB films, as detected by reproducible CVs, occurs in about 30 min for thin films. Loading also occurs without scanning, but at a slightly slower rate.

In water, $MPcTS^{4-}$ ions are heavily aggregated,[12] and only very small, broad irreversible CV peaks are observed at PG electrodes.[16] When DDAB films fully loaded with $MPcTS^{4-}$ ions are rinsed with water and placed into 0.1 M KBr without $MPcTS^{4-}$, chemically reversible cyclic voltammograms (Figure 1) are observed. At 100 mV s^{-1}, the first cathodic peak for $NiPcTS^{4-}$ is at −0.75 V vs Ag/AgBr and that of $CuPcTS^{4-}$ is at −0.4 V. These cathodic peak potentials are similar to those reported for the one-electron $M(II)PcTS^{4-}/M(II)PcTS^{5-}$ redox couples in noncoordinating organic solvents.[17]

As discussed below, these fully loaded films have excellent stability in water. When DDAB films fully loaded with $MPcTS^{4-}$ were sonicated for several seconds in chloroform, the solvent took on the characteristic color of the $MPcTS^{4-}$. Since $MPcTSNa_4$ is completely insoluble in chloroform, this suggests that the $MPcTS^{4-}$ removed from the electrode was associated with surfactant head groups. Moreover, no CV peaks were observed after returning the chloroform-washed electrodes to 0.5 mM $MPcTS^{4-}$/0.1 M KBr. Chloroform apparently solubilizes most of the electroactive $MPcTS^{4-}$ from the electrode. As mentioned, diffusion-controlled peaks of $MPcTS^{4-}$ are difficult to detect in water on bare PG (cf. Figure 1a).

Scan rate studies were done on thin films fully loaded with $NiPcTS^{4-}$ and $CuPcTS^{4-}$ ions. Peak current vs scan rate (ν) plots were linear only at $\nu < 3$ mV s^{-1}, where nearly symmetric peaks were observed. Between 0.06 and 10 V s^{-1}, the peak had the characteristic unsymmetrical diffusion-controlled shape (Figure 1) and cathodic peak currents were proportional to $\nu^{1/2}$. Cathodic and anodic peak currents were equal throughout this range of scan rates. These observations are consistent with the CV behavior expected[18] for an electroactive species confined to a relatively thick film on an electrode surface.

Symmetric CV peaks found at very low scan rates suggested that nearly all the electroactive material was reduced at the cathodic end of these scans. Integration under this one-electron cathodic peak gives the charge (Q) proportional to the so-called surface concentration of electroactive material (Γ_o), given by[18]

$$\Gamma_o = Q/FA$$

where A is the area of the electrode and F is Faraday's constant.

Surface concentrations for thin films were estimated in two different ways: (1) integration of the cathodic CV at 1 mV s^{-1} and (2) integration of scans made at 6 mV s^{-1} through the potential range of the peak, but stopped and held at a potential corresponding to about 60% of peak current on the negative side of the peak for 600 s. The latter method might measure charge from $MPcTS^{4-}$ monomers slowly dissociated from dimers in the film. Results of these two experiments were in good agreement and consistently gave surface concentrations of $(4–5) \times 10^{-8}$ mol cm^{-2} for the two $MPcTS^{4-}$ ions. Using the average of these surface concentrations and 1.5 μm for the estimated film thickness to obtain film volume, we estimate a concentration of about 0.3 M for the electroactive species in fully loaded thin films.

The CVs show interesting changes as the film is loaded by repetitive scanning in $MPcTS^{4-}$ solutions. Shortly after a freshly prepared thin film DDAB–PG electrode is placed into aqueous 0.2 mM $NiPcTS^{4-}$, a reversible CV is observed with cathodic peak potential of −0.67 V (Figure 2a). With

(14) Evans, D. F.; Mitchell, D. J.; Ninham, B. W. *J. Phys. Chem.* **1986**, *90*, 2817–2825.
(15) Komada, M.; Kuwabara, M.; Seki, S. *Thermochim. Acta* **1981**, *50*, 81–91.
(16) Zevecic, S.; Simic-Glavaski, B.; Yeager, E.; Lever, A. B. P.; Minor, P. C. *J. Electroanal. Chem. Interfacial Electrochem.* **1985**, *196*, 339–358 and references therein.
(17) Lever, A. B. P.; Licoccia, S.; Magnell, K.; Minor, P. C. *Advances in Chemistry Series No. 201*; American Chemical Society: Washington, DC, 1982; pp 237–251.
(18) Murray, R. W. In *Electroanalytical Chemistry*; Bard, A. J., Ed.; Marcel Dekker: New York, 1984; Vol. 13, pp 191–368.

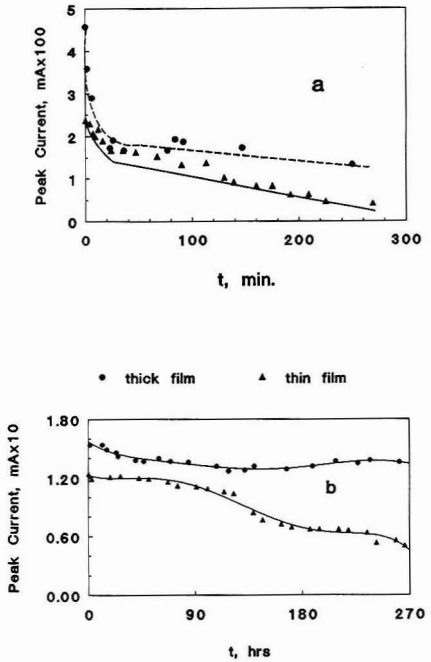

Figure 3. Influence of time in a 0.1 M KBr solution on cathodic voltammetric peak current of DDAB films at 0.10 V s^{-1}: (a) loaded with $NiPcTS^{4-}$ by continuous CV cycling for 5 min; (b) fully loaded with $NiPcTS^{4-}$. Note time scale of minutes in a and hours in b. (Lines drawn arbitrarily.)

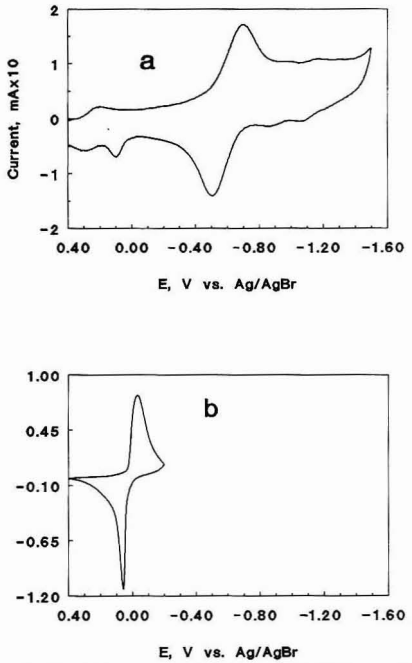

Figure 4. Cyclic voltammograms at 0.10 V s^{-1} of DDAB-coated PG electrodes: (a) film fully loaded with $CuPcTS^{4-}$, used for several days in 0.1 M KBr solutions, then scanned after 3 h in 5 mM $K_4Fe(CN)_6$/0.1 M KBr; (b) fresh DDAB film on PG electrode fully equilibrated with 5 mM $K_4Fe(CN)_6$/0.1 M KBr. Note different current scales in a and b.

increasing time, during which repetitive scanning was done, both cathodic and anodic peaks shift negative. Between 7 and 10 min, a new, slightly more negative cathodic peak (Figure 2c,d) grows in and replaces the original peak. The cathodic peak potential shifts negative to about −0.78 V in the first 20 min and then remains nearly constant. The overall potential shift during loading was typically −110 mV. The anodic peaks shift comparably. A steady-state CV is reached after about 30 min of scanning, after which the CV remains constant with time (Figure 2g). Similar results were obtained when incorporating $CuPcTS^{4-}$.

An increase in rigidity of the films was also observed upon loading them with $MPcTS^{4-}$. DDAB films soaked in aqueous solutions are soft and malleable. Fully loaded films are rather brittle, and pieces can be chipped away from the PG surface with a spatula.

Retention of incorporated $MPcTS^{4-}$ ions in DDAB films depends strongly on the amount of loading. In thick films that were removed from solution before full loading was reached (cf. Figure 2a–c), washed, and placed in fresh 0.1 M KBr, about 75% of the $MPcTS^{4-}$ is lost to the solution within several hours (Figure 3a). Thin films show a more gradual decay, but show a 75% loss in about 3 h. In contrast, fully loaded films have much smaller rates of decrease in CV currents over 270 h in 0.1 M KBr. Thus, a sufficiently large concentration of incorporated $MPcTS^{4-}$ produces films that retain $MPcTS^{4-}$ quite effectively.

Ion-exchange properties of films fully loaded with $MPcTS^{4-}$ are different from the original films containing Br^- ions. For example, when a DDAB film loaded with $CuPcTS^{4-}$ and used for several days was placed in 5 mM ferrocyanide/0.1 M KBr, a quite small sharp oxidation peak for ferrocyanide was found at 0.1 V (Figure 4a), even after 2.5 h of soaking and intermittent CV scans. (An additional small oxidation peak near 0.3 V is probably caused by diffusion of ferrocyanide to small uncoated sites on this electrode.) In contrast, a fresh DDAB film loaded in 5 mM ferrocyanide for about 30 min gave a nearly symmetric oxidation peak at 0.05 V that was about 100 times larger (Figure 4b) than on the DDAB–$CuPcTS^{4-}$ electrode.

Molecular Spectroscopy. Electronic absorption spectra of $MPcTS^{4-}$ ions give characteristic peaks for dimers in the visible region.[12] This is illustrated by spectra of $CuPcTS^{4-}$ in water (Figure 5). Peaks at 668 nm correspond to the monomer, and those at 630 nm are for dimers. Similar results were obtained in water for $NiPcTS^{4-}$. These spectra show that $MPcTS^{4-}$ ions are heavily dimerized in water even at quite low concentrations. Analyses of A (668 nm) vs concentration data with the appropriate Beer's law models[19] were consistent with monomer–dimer equilibrium between 0.3 and 5 μM $MPcTS^{4-}$, as reported previously.[12]

DDAB films fully equilibrated with $MPcTS^{4-}$ solutions, removed from solution, and washed with water (Figure 6) had relatively small dimer peaks. Their spectra suggested similar degrees of dimerization in equilibrated films and in aqueous solutions with concentrations of 0.3 μM, assuming that extinction coefficients are similar in the two media. Also, spectra of 1 μM $MPcTS^{4-}$ in 0.1 M micellar solutions of cetyltrimethylammonium bromide showed only a monomer peak, with no evidence for dimerization.

Spectra of films soaked in $MPcTS^{4-}$ solutions for different times were also measured. The ratio of monomer to dimer peak absorbance decreased with time, reaching a constant value of 1.3–1.5 in <10 min (Figure 7).

(19) Rusling, J. F. *CRC Crit. Rev. Anal. Chem.* **1989**, *21*, 49–81.

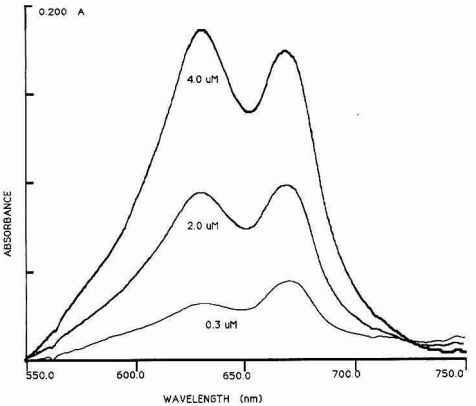

Figure 5. Visible absorbance spectra of $CuPcTS^{4-}$ in water.

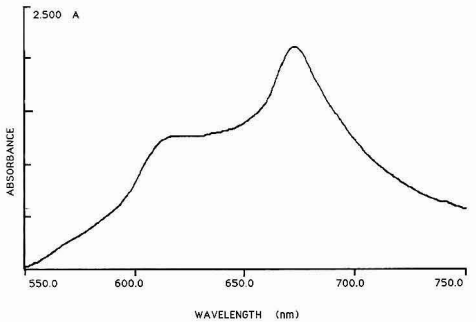

Figure 6. Visible absorbance spectrum of DDAB film fully equilibrated with aqueous 0.2 mM $CuPcTS^{4-}$.

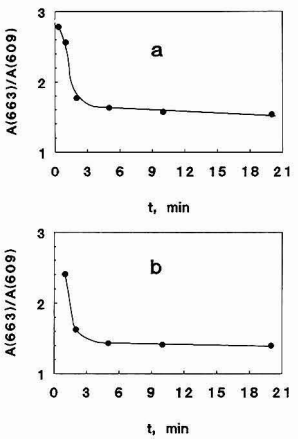

Figure 7. Influence of equilibration time with 0.2 mM $MPcTS^{4-}$/0.1 M KBr solutions on ratio of monomer/dimer absorbance peaks for DDAB films: (a) $NiPcTS^{4-}$; (b) $CuPcTS^{4-}$.

Microscopy and EDX. Top-view appearances were very different for freshly cast films and films that had been soaked in aqueous solutions. SEM and EDX are reported only for films that had been treated with aqueous solutions to be more relevant to conditions of use in catalysis. Light microscopy and SEM (Figure 8a) showed that the films had similar rough surfaces with or without $MPcTS^{4-}$ incorporated.

SEM cross-sectional views after freeze-fracture showed regions with wavy, layered structures (Figure 8b,c). These were similar for films with and without $MPcTS^{4-}$ incorporated. However, distinct regions featuring a nonlayered appearance were also observed in the same samples. In the example shown, the latter region appears rather amorphous and includes some needle-like structures (Figure 8d).

EDX spot analysis provided semiquantitative information on elemental concentrations. Since the sampling depth of EDX is on the order of 1 μm, these studies were done on thick films (30–50 μm) with and without $MPcTS^{4-}$ incorporated. The only element detected for DDAB films without incorporated foreign ions was Br. After overnight equilibration of films with 0.5 mM $MPcTS^{4-}$/0.1 M KBr, the Br peak was almost completely gone.

Elemental signals were monitored by EDX at six spots on equilibrated films (Table II). The number of counts per unit time for the central metal ions should give an estimate of relative $MPcTS^{4-}$ concentrations at different locations in the films. Considering the reproducibility of about 10–15% for EDX, the data for Cu, in particular, could be construed as suggesting some degree of heterogeneity.

As mentioned above, only trace amounts of Br were detected in samples equilibrated with $MPcTS^{4-}$ solutions. However, significant K was found. The K/S ratio is consistent with <1 K^+ ion for each $MPcTS^{4-}$ (Table II). However, M/S ratios are larger than expected. This may result from inaccurate sensitivity factors caused by a sample matrix effect. Nevertheless, it is likely that some K^+ ions are associated with sulfonate groups of the $MPcTS^{4-}$ ions in the films.

DISCUSSION

DSC results (Table I) show that water is necessary to observe T_c values for DDAB at less than ambient temperature, indicating that water influences the gel-to-liquid crystal phase transition. T_c values of the DDAB films are roughly similar to those of Lam_1 and Lam_2 phases irrespective of the incorporated ion. The effects of these transitions are also seen as breaks in cyclic voltammetric peak current vs temperature data[7,8] for incorporated electroactive ions (Table I). Similarities in T_c values for films and known bilayer systems of the same surfactants suggest that the films contain surfactant bilayers.

Why do fully loaded films retain $MPcTS^{4-}$, while partly loaded films undergo rapid loss of these ions in supporting electrolyte solutions? Changes in visible spectra of $MPcTS^{4-}$ as the films are loaded are consistent with an increasing degree of dimerization of $MPcTS^{4-}$. An increased fraction of dimer upon loading is clearly seen in the visible spectra as the growth of the peak between 600 and 620 nm. At low loadings, where this peak is not present, $MPcTS^{4-}$ ions can be rapidly exchanged out of the film in a few hours in electrolyte solutions. When the dimer peak is present, $MPcTS^{4-}$ ions are retained for many days. Also, ferrocyanide and cobalt(III) corrinhexacarboxylate ions, which do not dimerize, can be replaced in several hours in fully loaded DDAB films.[8] We conclude that dimerization is important for good retention of $MPcTS^{4-}$ in the films.

Comparison of spectra (Figures 6 and 7) shows that fully loaded films have about the same degree of dimerization of $MPcTS^{4-}$ as 0.3 μM aqueous solutions. This is remarkable in view of the fact that these films contain about 0.3 M $MPcTS^{4-}$. The relatively low fraction of dimers in the films and in aqueous micellar CTAB solutions may be explained by a strong interaction between the sulfonates of the macrocyclic catalysts and cationic head groups of the sur-

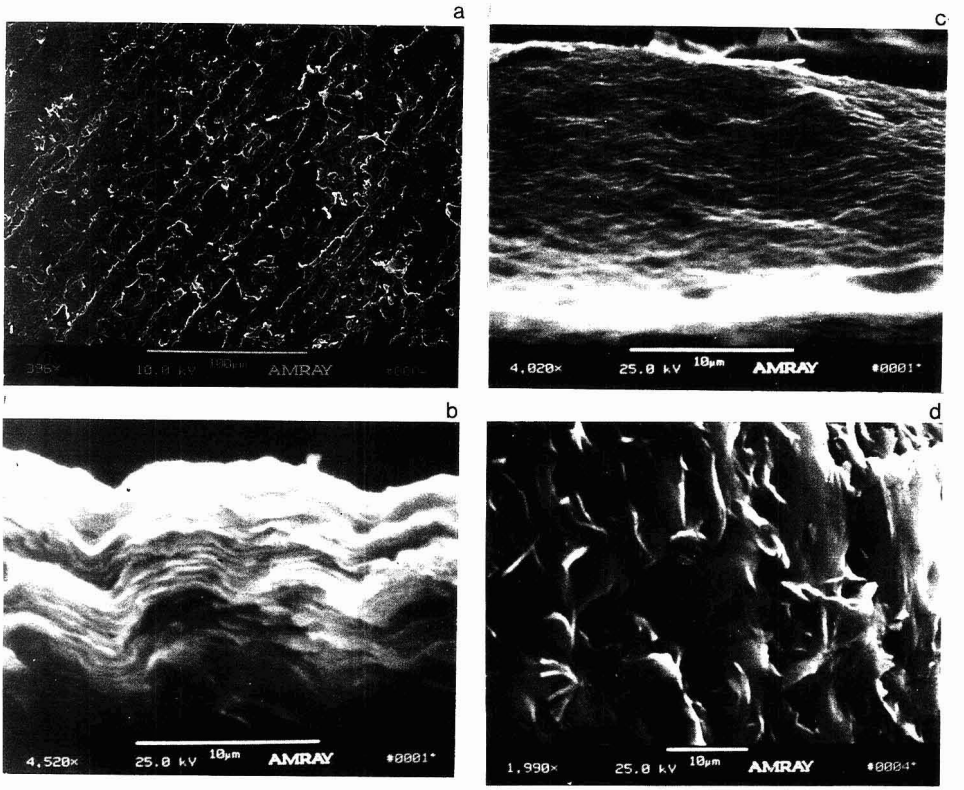

Figure 8. Top view SEM image (a) of DDAB film equilibrated with 0.1 M KBr/0.2 mM $NiPcTS^{4-}$. Cross-sectional SEM images (b–d) of freeze-fractured DDAB films after equilibration in solution with (b) $CuPcTS^{4-}$, layered region; (c) $NiPcTS^{4-}$, layered region; and (d) $NiPcTS^{4-}$, nonlayered region.

Table II. Energy Dispersive X-ray Spot Analyses of Films

NiPcTS/DDAB spot no.	Ni counts	CuPcTS/DDAB spot no.	Cu counts
1	3230	1	5372
2	3324	2	5545
3	2245	3	4695
4	2280	4	4812
5	2721	5	11724
6	2208	6	7996
mean ± s (rsd)	2668 ± 508 (±19%)	mean ± s (rsd)	6691 ± 2742 (±41%)
apparent av atomic ratios[a]			
Ni/S = 0.45 ± 0.12		Cu/S = 0.32 ± 0.03	
K/Ni = 0.33 ± 0.09		K/Cu = 0.49 ± 0.10	
K/S = 0.16 ± 0.02		K/S = 0.16 ± 0.03	

[a] Average ± s for six spots.

factants in micelles and bilayers. This interaction may cause $MPcTS^{4-}$ ions to lie flat on the bilayer surfaces. This is consistent with recent results of Ishikawa and Kunitake, who used ESR anisotropy to show that metal macrocyclic complexes such as porphyrins and phthalocyanines with four symmetrically attached sulfonate groups are inserted in orientations parallel to the plane of the head groups in bilayers of ammonium surfactants.[1g]

Previous investigators of $MPcTS^{4-}$ dimers in water proposed face-to-face orientations.[12] Once the concentration of $MPcTS^{4-}$ in the film becomes large enough, flat orientations on bilayer surfaces may facilitate dimerization between $MPcTS^{4-}$ ions on adjacent bilayers, cross-linking pairs of bilayers. However, at smaller concentrations in the film, $MPcTS^{4-}$ ions on bilayer surfaces would tend to be isolated from one another.

The influence of dimerization on shifts in CV peak potentials upon loading the films were explored with digital simulations.[20] To pick the range of kinetic constants, we used published data on the dimerization kinetics.[12a,b,e,h] For example, for $Co(II)PcTS^{4-}$ in water at 58 °C, dimerization rate constant[12a] k_f was 600 M^{-1} s^{-1}, and the dissociation rate constant $k_r = 0.003$ s^{-1}. Simulations of CVs were done for two mechanisms featuring reversible one-electron transfer (ET) to the phthalocyanine and electoinactive dimers: (i) dimerization preceding ET, and (ii) dimerization preceding and following ET. Values of k_f of 600, 3000, and 30000 M^{-1} s^{-1} were used with a series of k_r values from 0.003 to 300 s^{-1}. Results showed that cathodic potential shifts >20 mV could not be achieved without changes to sigmoid cathodic wave shapes for any combination of rate constants. Since diffusion-like peak shapes are always found in the films at 0.10 V s^{-1}, dimerization is unlikely to be the full cause of the observed potential shifts upon loading. Simulations showed that less than 20 mV of the observed 110-mV shift in cathodic peak potential (cf. Figure 2) could be explained by dimerization. Other factors that may contribute to the potential shift include

(20) Gosser, D. K.; Zhang, F. *Talanta* **1991**, *38*, 715–722.

a change in the microenvironment of $MPcTS^{4-}$, also suggested by the increase in film rigidity, and a change in axial ligation.[17]

SEM and EDX analyses are consistent with some disorder in the bulk structure of the films. A significant fraction of cross sections were observed as stacked wavy layers of thickness 0.1–0.2 μm. Each of these relatively thick layers may be associated with stacks of many individual 3-nm-thick surfactant bilayers. This was confirmed for several composite surfactant films by comparing SEM cross sections with molecularly resolved transmission electron microscopy[5b,c] and X-ray diffraction.[3-5] This multibilayer structure is consistent with the observation of gel-to-liquid crystal phase transitions characteristic of other bilayer systems of the same surfactants. However, portions of the cross sections also had a more amorphous, unlayered appearance. The presence of bilayers in these regions cannot be confirmed by SEM because of the lack of molecular resolution. However, tubular myelin figures proposed to contain concentric bilayers form when dry DDAB films are swelled with water.[21] Similar myelin figures were observed by light microscopy on the top of thick DDAB films when soaked in 0.1 M KBr. The amorphous parts of the films found by SEM might possibly be related to such bilayer-containing structures.

Water wets abraded PG disks prepared for film casting, as well as DDAB/$MPcTS^{4-}$ films, indicating that these surfaces are hydrophilic. Carbon surfaces contain considerable oxygen (8–25%) present in various functional groups,[22-24] which is the probable cause of the polar nature of the surface. In addition, surface-enhanced Raman studies of amphiphilic alkylammonium ions adsorbed on rough Ag electrodes indicated that head down orientations predominated at full coverage over a wide potential range, even positive of the point of zero charge.[25] These observations would support the likelihood of an average head down orientation for the first surfactant layer next to the PG surface.

Detection of K in the films by EDX, but only trace Br, suggests that a small fraction of the sulfonate groups of $MPcTS^{4-}$ are associated with K^+ ions rather than ammonium head groups.

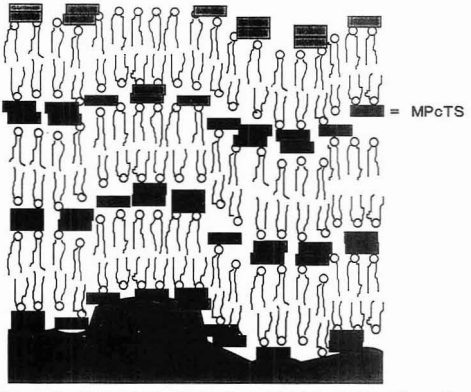

Figure 9. Conceptual, idealized model of a small portion of a dialkyldimethylammonium film on PG stabilized by $MPcTS^{4-}$ ions.

In summary, films of dialkyldimethylammonium surfactants in the liquid crystal phase incorporate large concentrations of $MPcTS^{4-}$ ions, yielding stable electroactive films on electrodes. Stability is associated with dimerization of $MPcTS^{4-}$ ions, which may cross-link adjacent surfactant bilayers. Stacked surfactant bilayers seem to be the major feature of the supramolecular structure (Figure 9), although some disorder was found on the micrometer scale. The multiple bilayer structure is consistent with proposed structures of cationic surfactant films stabilized by clay colloids and linear anionic polymers.[1,3-5] However, in the present case, the stabilizing agent is also a redox catalyst.

ACKNOWLEDGMENT

This work was supported by U.S. PHS Grant No. ES03154 from NIH awarded by the National Institute of Environmental Health Sciences. The authors thank Yanfei Shen for help with EDX and SEM analyses.

RECEIVED for review July 16, 1992. Accepted September 29, 1992.

(21) Shchipunov, Y. A.; Maslennikova, I. G.; Kolpakov, A. F.; Schumilina, E. V. *Bioelectrochem. Bioenerg.* **1989**, *22*, 45–56.
(22) Kamau, G. N.; Willis, W. S.; Rusling, J. F. *Anal. Chem.* **1985**, *57*, 545–551.
(23) Kamau, G. N. *Anal. Chim. Acta* **1988**, *207*, 1–16 and references therein.
(24) Rusling, J. F.; Zhang, H.; Willis, W. S. *Anal. Chim. Acta* **1990**, *235*, 307–315.
(25) Sun, S.; Birke, R. L.; Lombardi, J. R. *J. Phys. Chem.* **1990**, *94*, 2005–2010.

CORRESPONDENCE

Determination of Mercury(II) in Dithizone-Impregnated Latex Microparticles by Photochromism-Induced Photoacoustic Spectroscopy

V. A. VanderNoot and E. P. C. Lai*

Centre for Analytical and Environmental Chemistry, Ottawa-Carleton Chemistry Institute, Department of Chemistry, Carleton University, Ottawa, Ontario, Canada K1S 5B6

The determination of trace levels of toxic heavy metals continues to represent an important area of analytical chemistry. Mercury has been determined over the years in trace levels by reaction with the ligand phenylazothioformic acid 2-phenylhydrazide, more commonly known as dithizone.[1] Dithizone forms complexes with many heavy metals of which a number are photochromic. Photochromism refers to the reversible color change that the compounds undergo on exposure to visible light. Analysis of these photochromic species by photoacoustic spectroscopy (PAS) has been quite successful. The method is sensitive and is quite specific for mercury if samples are prepared in solid films; no other heavy metal complexes with dithizone exhibit photochromism in the solid state.[2] Frequently however, the preparation of solid samples can be somewhat time-consuming. In this work, a novel technique is presented in which aqueous Hg(II) is sequestered into small uniform polystyrene latex microparticles which are previously impregnated with dithizone. The particles can then be easily turned into a solid sample suitable for photochromism-induced photoacoustic spectroscopy (PCPAS) analysis by simple filtration onto commercially available small-pore membrane filters. The method is fast, simple, and has the potential for simultaneous quantification and clean-up of Hg(II) in environmental waters.

Much work has been carried out to make use of the very regular surfaces of latex microparticles.[3] The particles have recently been used as a support on which silver needles were grown for surface-enhanced raman spectroscopy.[4] Many substances have been adsorbed onto the surfaces of microparticles, not the least of which being immunoglobulins for the now well-established latex immunoassay agglutination tests.[5] The technique for dyeing microparticles has been well established, and particles are available in a variety of colors, usually to aid in visual determination of agglutination assays. Fluorescent dyes have also been used for a number of spectroscopic techniques. In these cases the dye has been shown to be deep in the interior of the particle and does not alter the surface chemistry.[6] A number of iron(III) complexes have been recently incorporated into sodium dodecyl sulfate micelles and studied spectroscopically,[7] but these were limited to the case of the continuous phase being aqueous. This work is the first example reported in the literature, to the authors' knowledge, of an analytical reagent being put inside a latex microparticle. The reagent-impregnated microparticles are stable in aqueous suspension and can be removed from the aqueous phase along with the Hg(II) for analysis under ambient conditions. Additionally, the potential for a variety of organic complexing agents being incorporated in microspheres to create tailor-made reagents for toxic clean-up is great.

EXPERIMENTAL SECTION

Latex Microparticles and Dithizone. Polystyrene latex microparticles were obtained from Seradyn (Indianapolis, IN) in a range of particle diameters from 0.204 to 0.944 μm. The particles were of uniform size distribution and very regular in appearance. Standard suspensions were prepared by simple dilution of the 15% (w/w) stocks with 18-MΩ deionized water. These suspensions were stored at room temperature. Unless otherwise specified, all analyses were carried out using the smallest diameter, 0.204 μm. Dithizone was purified by Irving's method, and the purified dithizone solution in spectroscopic grade CCl_4 was stored under a layer of 1 N H_2SO_4 in the dark. Solutions stored this way keep very well.[8]

Reagent Impregnation and Hg(II) Extraction. In a small vial, 50 μL of 0.01% (w/v) dithizone (H_2Dz) solution in CCl_4 was added to 900 μL of deionized water. The H_2Dz was extracted into the aqueous phase by addition of 10 μL of 25% (v/v) NH_4OH followed by gentle shaking. The CCl_4 layer was carefully removed after all traces of the green H_2Dz were gone. A 100-μL aliquot of 0.2% (w/w) latex microparticle suspension was added, and the suspension, a soft orange-yellow color, was acidified with 10 μL of 3% (v/v) H_2SO_4 as the pH needed to drive H_2Dz into the microparticles is below 6. The resulting green suspension of H_2Dz-impregnated latex microparticles (see Figure 1) was added to 1.0-mL Hg(II) samples in 100-μL aliquots. This volume contained sufficient H_2Dz to completely complex the most concentrated standard plus a modest excess. The samples were filtered through 0.1-μm pore size filters (Nuclepore, Toronto, ON, Canada) which were then removed from the filter housing and allowed to air dry before analysis.

PCPAS Measurement. The schematic diagram of the PCPAS system is illustrated in Figure 2. The excitation source was an argon ion-pumped dye laser (Spectra-Physics 164 and 375B, Mountainview, CA). The output beam from the dye laser, 605 nm in wavelength and typically 90 mW in power, was directed through a window into the photoacoustic cell after being mechanically chopped at 200 Hz. The samples (membrane filters supporting latex microparticles) were placed directly into the

* Author to whom all correspondence should be addressed.

(1) Sandell, E. B.; Onishi, H. *Colorimetric Determination of Traces of Metals*, 4th ed.; Wiley-Interscience: New York, 1978; p 391.
(2) Chen, N.; Guo, R.; Lai, E. P. C. *Anal. Chem.* **1988**, *60*, 2435–39.
(3) Pelton, R. *NATO ASI Series, Ser. C 303* (Scientific Methods for the Study of Polymer Colloids and Their Applications) **1990**, 493–516.
(4) Wachter, E. A.; Moore, A. K.; Haas, J. W., III. *Vibr. Spectrosc.* **1992**, *3*, 73–78.
(5) Masson, P. L.; Cambiaso, C. L.; Collet-Cassart, D.; Magnusson, C. G. M.; Richards, C. B.; Sindic, C. J. M. *Methods Enzymol.* **1981**, *74*, 106–139.
(6) Bangs, L. B. *Uniform Latex Microparticles*; Seradyn Inc.: Indianapolis, 1984; Chapter VII.
(7) Mazumdar, S. *J. Chem. Soc. Dalton Trans.* **1991**, 2091–6.
(8) Irving, H. M. N. H. *Dithizone*; The Chemical Society: London, 1977; Chapter 8.

0003-2700/92/0364-3187$03.00/0

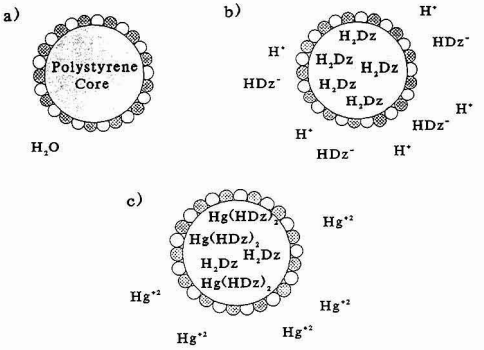

Figure 1. Schematic showing the impregnation and extraction processes. (a) Representation of a latex microparticle; open circles are SO_3^- functional groups from the surfactant used in the original production of the latex microparticles; shaded circles are SO_4^- groups resulting from the termination of the styrene polymerization steps in the microparticle core. (b) Representation showing dithizone in the process of transferring into the microparticle center at solution pH ≤ 6. (c) Representation showing Hg^{2+} in the process of complexing with H_2Dz in the interior of the microparticle.

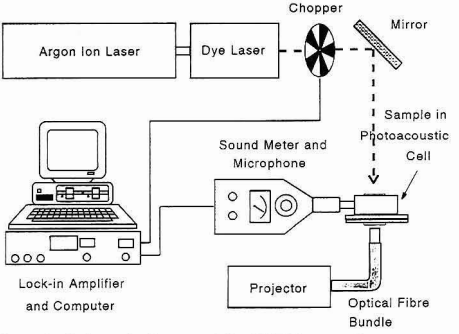

Figure 2. Schematic diagram of the PCPAS apparatus.

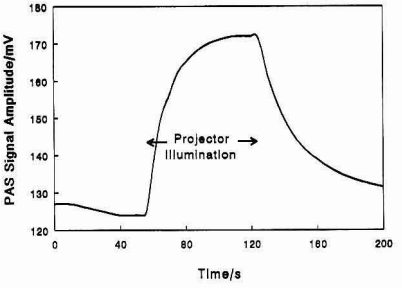

Figure 3. Typical PCPAS signal for Hg(II) dithizonate in latex microparticles. The signal rises abruptly when exposed to visible illumination from the projector source due to higher absorptivity of the blue excited-state complex at the wavelength of 605 nm.

gas-tight cell which was fitted to a condenser microphone and a sound meter which contained a preamplifier and an octave filter set (Brüel and Kjaer 4144 and 2209, Pte. Claire, PQ, Canada). The baseline PAS signal from the sample (see Figure 3) was first recorded using a lock-in amplifier (Stanford Research SR510, Sunnyvale, CA). Then the sample was illuminated by the light of an 80-W projector lamp focused into an optical fiber bundle. The optical fiber bundle was brought close to the photoacoustic cell and directed onto the sample through the back window. The PAS signal was again recorded for sufficient time to achieve a steady-state signal. The absolute difference in the signal voltages, the PCPAS signal amplitude, was taken as an indication of the amount of Hg(II) present in the sample.

Interference from other heavy metals was examined by preparation of mixed metal standards. The dithizone present in the 100-μL aliquot remained in excess of the total amount of extractable metals. These samples were analyzed in the same way as described above.

RESULTS AND DISCUSSION

The chemistry of the H_2Dz-impregnated latex microparticles preparation and Hg(II) extraction is very interesting. It is not clear yet how H_2Dz, and then Hg(II), is transported into the microparticle center. These solid particles of polystyrene, with a rigid structure allowing them to be filtered while retaining their shape, possess a negatively charged surface due to residual surfactant from their production. It is unlikely, then, that H_2Dz adsorbs onto the surface at any time to be followed by seepage into the microparticle interior. It may be that the presence of residual CCl_4 facilitates the transfer of H_2Dz in a manner similar to the procedure involved with dyeing the particles. In dyeing particles, the particles are initially swollen with a dye solution in a solvent for polystyrene, such as CCl_4. The solvent is then carefully boiled off, trapping the dye inside the latex.[6] Although very little CCl_4 (50 μL) was involved in the H_2Dz-impregnation step, the transport process might be analogous since the latex volume itself was quite small. The particles were hence slightly swollen by the organic solvent, allowing enough fluidity or flexibility to the structure to allow transfer of H_2Dz across the interface.

The pH of the extraction is generally important to achieve quantitative results. As illustrated in eq 1, a large H_2Dz concentration will tend to drive the reaction toward completion. Sigmoid curves of the percentage extraction of

$$M^{n+} + nH_2Dz(org) \rightleftarrows M(HDz)_n(org) + nH^+ \quad (1)$$

primary dithizonates into a solution of 10^{-5} M H_2Dz in a suitable organic solvent reach 100% above pH 4 while the extraction drops to zero below pH 3. Lower concentrations of H_2Dz in the organic phase exaggerate the curves and push them to higher pH regions; a 10^{-8} M solution will require a pH of 8 to achieve quantitative extraction.[9] In this work, the concentration of H_2Dz was essentially constant at approximately 2% (w/w) in the latex. This represented a larger concentration of H_2Dz in the latex phase compared to solution-phase extractions which are typically carried out in the 10^{-7} to 10^{-5} M range. Hence, the control of pH was less critical and a pH of ca. 6 was maintained in the extraction vessel to ensure quantification. The extraction was assumed to be complete after 15 min of occasional shaking, although the reaction was seen to be much faster in those samples concentrated enough to observe the color change visually. The quantification was ascertained by reanalyzing the filtrate from aqueous samples after the primary reaction and filtration. The data verified that extraction efficiency was greater than 99% for 50 and 100 ng Hg(II) in aqueous samples under the given experimental conditions.

Photoacoustic analysis of Hg(II) dithizonate-impregnated latex microparticles was straightforward. The presence of essentially nonabsorbing latex polystyrene surrounding the analyte species did not complicate the issue of signal generation appreciably at a chopping frequency of 200 Hz.

(9) Irving, H. M. N. H. *Dithizone*; The Chemical Society: London, 1977; Chapter 5.

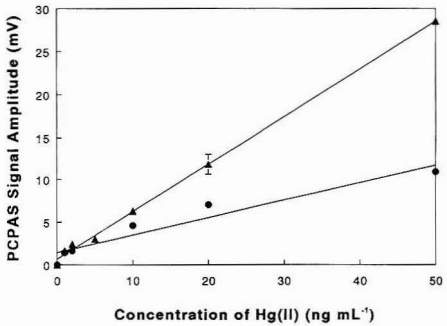

Figure 4. Analytical calibration curve for Hg(II) dithizonate in latex microparticles. The error bar shows the typical standard deviation of replicate samples. Triangles represent data taken from samples impregnated into 0.204-μm spheres while the circles are data from 0.944-μm spheres.

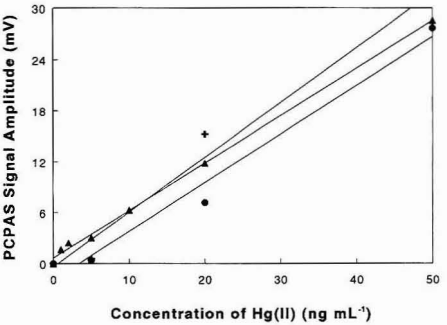

Figure 5. Calibration for Hg(II) (▲) and for mixed metal standards containing equal quantities of Hg(II) and Ag(I) (●) and Zn(II) (+).

Calibration curves of latex microparticles dyed dark blue with Sudan Black (Seradyn, Inc.) showed a linear response with quantity as expected. The calibration curve for the determination of Hg(II) using 0.204-μm microparticles is shown in the upper trace of Figure 4. The current detection limit, determined at twice the standard deviation of the blank, is 500 pg (in a 1.0-mL aqueous sample) or 3 pmol of mercury. It should be noted that the actual amount of Hg(II) being sampled by the excitation beam, and thus generating the signal, is about 1%, or 5 pg, of the total amount of Hg(II) in the microparticles trapped on the filter surface. A 10-fold improvement in the detection limit, from 500 to 50 pg, was conveniently achievable simply by reducing the filtration area from the current commercially available size of 130 mm^2 to 13 mm^2. Samples prepared in this manner did generate measurable signals for 50-pg Hg(II) standards, with a signal-to-noise ratio of 2.

Given that H_2Dz does not exhibit any appreciable photochromism at the excitation wavelength of 605 nm, excess H_2Dz in the microparticles did not add to the observed PCPAS signal amplitude. The amount of residual H_2Dz in each sample varied roughly inversely with the concentration of the standard. This meant that, since H_2Dz absorbed at this wavelength, the baseline signal amplitude did necessarily vary from sample to sample, but since it was only the photochromism-induced signal change that was taken as a measure of mercury content, it did not represent a problem to the analysis. Nevertheless, the excess H_2Dz produced a background PAS signal which, if large enough, could limit the sensitivity range used on the sound meter. It appeared possible to remove some of the excess dithizone from the microparticles by addition of NH_4OH to bring the pH to 9 after complexation with Hg(II) was complete. In most cases, however, the excess of dithizone was modest and did not affect the analysis to any significant extent.

The lower trace of Figure 4 shows the resulting calibration curve when 0.944-μm microparticles were used for the extraction. There did not appear to be any difference in the amount of H_2Dz that could be sequestered into equal volumes of particles of different sizes. Since the surface area to volume ratio did not seem to affect the impregnation, it was confirmed that H_2Dz, and hence Hg(II), was being transferred into the interior of the latex and not being adsorbed onto the surface. The calibration results did show enhanced detection sensitivity when smaller particles (0.204 μm) were used to collect Hg(II). This was undoubtedly due to a combination of factors, including optical shielding of the interior of the larger particles (0.944 μm) which inhibited the photochromic activity and higher surface area of the smaller particles which lead to more efficient transfer of heat to the gas in the photoacoustic cell.

In the present experimental setup, the projector illumination entered the PAS cell through the back window. While this simple design avoided interference with the incident laser beam, it had a tendency to limit the intensity of projector light reaching the sample as the original filters were a mixed esters/cellulose acetate type and were strongly scattering. The useful dynamic range of PCPAS analysis was drastically improved by changing to Nuclepore filters, which were a polycarbonate type and were much more transparent to visible light (average absorbance in the visible range = 0.75). The new filters allowed more than enough light to reach the samples to ensure that small variations in projector intensity did not affect the generation of excited state Hg(II) dithizonate (i.e. the PAS signal vs light intensity is flat). Additionally, the switch served to improve the ease of filtration. The polycarbonate pores are formed by nuclear bombardment followed by etching leaving a clear channel; the cellulose acetate filters are of the tortuous path type. The result was less back-pressure allowing larger volumes of dilute samples to be extracted for preconcentration of Hg(II). Many tens of milliliters of dilute solutions can be incorporated into very small quantities of latex; a 50-mL volume of 50 ppb Hg(II) will only require ca. 300 μg of dithizone-impregnated latex.

The selectivity of the PCPAS determination for Hg(II) was quite good using the latex microparticles as it is in other solid sample preparations of $Hg(HDz)_2$. Samples of Ag(I) and Zn(II) dithizonates showed only small PCPAS signals at the excitation wavelength of 605 nm even at very high concentrations. Comparable quantities of either Ag(I) or Zn(II) in a standard of Hg(II) did not add appreciably to the measured PCPAS signal amplitude for Hg(II) as shown in Figure 5. Note that the slopes of these calibration curves were esentially the same; the variation from curve to curve was due to slight variations in the preparation of dithizone-impregnated latex microparticles. This variation usually will not affect a calibration series from the same preparation.

The presence of interfering heavy metals becomes a problem, however, if the total amount of extractable metals is in excess of the amount of H_2Dz introduced to the sample. There will be competition between the metals for extraction into the latex microparticles under this circumstance. A smaller overall PCPAS signal for $Hg(HDz)_2$ will be produced since some Hg(II) ions will remain in the aqueous phase and be washed away with the filtrate. If large amounts of other heavy metals are suspected, a larger amount of H_2Dz-impregnated latex microparticles will be needed. This may generate smaller PCPAS signals for Hg(II) as a result of the inner filter effect of the nonphotochromic, but absorbing, interfering metal dithizonates. Again, the use of stronger

projector illumination to induce photochromism should surmount the difficulty. Besides, intentionally swamping the latex microparticles with heavy metals will help remove any excess H_2Dz after extraction of Hg(II) from a sample solution, resulting in a lower background signal, providing that the choice of added metal does not interfere spectrally.

CONCLUSIONS

A novel technique has been demonstrated for the determination of mercury at picomole levels in aqueous samples. The extraction of Hg(II) into H_2Dz-impregnated latex microparticles is both rapid and quantitative. PCPAS detection for $Hg(HDz)_2$ in these particles remains selective over other toxic heavy metals, and the sensitivity of the technique is good for environmental analysis.

Since there is a noticeable color change of the H_2Dz-impregnated latex microparticles upon reaction with heavy metals (regardless of PCPAS detection ability), a packed column of the microparticles can be applied to water streams as a visual indicator for heavy metals contamination. Additionally, the latex microparticles are a potential tool for water clean-up as they can be collected easily on a membrane filter for safe disposal after quantitative removal of the heavy metals. It remains to be seen, however, whether it will be possible to successfully scale the method up to meet environmental needs.

ACKNOWLEDGMENT

This work was funded by the Natural Sciences and Engineering Research Council of Canada. A GR-5 grant from the Faculty of Graduate Studies and Research, Carleton University, is gratefully acknowledged.

RECEIVED for review June 29, 1992. Accepted September 18, 1992.

Registry No. Mercury, 7439-97-6; dithizone, 60-10-6; polysytrene, 9003-53-6; water, 7732-18-5.

Selective Surface Acoustic Wave-Based Organophosphonate Chemical Sensor Employing a Self-Assembled Composite Monolayer: A New Paradigm for Sensor Design

Larry J. Kepley and Richard M. Crooks*

Department of Chemistry, University of New Mexico, Albuquerque, New Mexico 87131

Antonio J. Ricco*

Microsensor Department 1315, Sandia National Laboratories, Albuquerque, New Mexico 87185

INTRODUCTION

We report the first example of a chemical sensor that derives a degree of selectivity, sensitivity, reversibility, and durability from a rationally designed, composite monolayer consisting of simple molecular components. This approach to sensor design has a number of advantages, including (1) prediction of sensor response based on known bulk-phase intermolecular interactions, (2) rapid response times resulting from ultrathin coatings, and (3) simplicity of fabrication. In this correspondence we show how each of these desirable characteristics results from simple sequential self-assembly chemistry.

Chemical sensors usually consist of a chemically sensitive coating supported by an inert physical transducer.[1] Because the exact nature of the intermolecular interactions between the coating and the target analyte are often ambiguous, the design of selective sensor coatings is based largely on trial and error. A more appealing approach to sensor fabrication relies upon rational design based on known, bulk-phase interactions between the analyte and the selective coating. Three elegant examples that employ this design strategy have recently been reported, and they serve to summarize the state of the art.[2–4] Although all three are viable, these sensing schemes suffer from various practical difficulties. For example, all rely on complex and difficult-to-synthesize molecules.

The device described in this report derives its selectivity, reversibility, and durability from a simple, self-assembled monolayer and its sensitivity from a mass-sensitive surface acoustic wave (SAW) device. The coating design takes advantage of the interaction between organophosphonate nerve-agent simulants and a composite monolayer, consisting of Cu^{2+} tethered to the SAW device by an ordered, carboxylate-terminated *n*-alkanethiol monolayer. The rationale for this design is that Cu^{2+} and some of its chelates are hydrolysis catalysts for certain nerve agents.[5] Thus, a surface layer of coordinatively unsaturated Cu^{2+} might be expected to provide selective and reversible binding sites for organophosphonates. The general approach is illustrated in Chart I, where the analyte (D) is the nerve-agent simulant diisopropyl methylphosphonate (DIMP).

The selective coating responds proportionally and reversibly to DIMP, in a manner readily distinguishable from its response to common organic solvents and water. Moreover, the sensor is both sensitive and durable.

The details of organomercaptan self-assembly on Au, Ag, and Cu substrates have been widely studied and will not be recapitulated here, except to note that, under certain conditions, highly ordered monolayers of organomercaptans spontaneously adsorb onto Au surfaces from the vapor phase[6] and from solution.[7] Carboxylic acid-terminated monolayers are more disordered than methyl-terminated *n*-alkanethiols, and they undergo extensive intramonolayer hydrogen bonding.[6c,7b,c,8] For the purposes of this preliminary report, it is sufficient to visualize the organomercaptan monolayer acting only as scaffolding for the Cu^{2+} surface.

Chart I

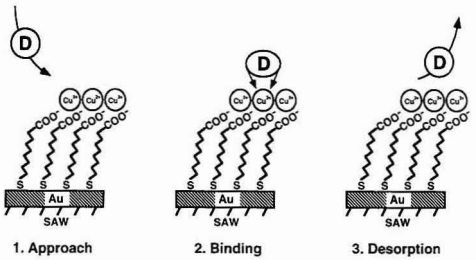

A number of transducers have been used as platforms for sensing organophosphorus compounds.[9–12] We have used SAW devices because of their extreme mass sensitivity.[1,13–15] Because of their high operating frequency and confinement of the acoustic wave energy to within one wavelength of the surface, the SAW devices we used are sensitive to the presence of as little as 100 pg/cm^2 of surface adsorbates (ca. 1.5×10^{-3} monolayers of DIMP).[1,16] In the uncomplicated case, the velocity of the SAW is perturbed in direct proportion to adsorbed mass-per-area, which is measured as a shift in the

* To whom correspondence should be addressed.

(1) Hughes, R. C.; Ricco, A. J.; Butler, M. A.; Martin, S. J. *Science* **1991**, *254*, 74.
(2) Ebersole, R. C.; Miller, J. A.; Moran, J. R.; Ward, M. D. *J. Am. Chem. Soc.* **1990**, *112*, 3239.
(3) Mirkin, C. A.; Wrighton, M. S. *J. Am. Chem. Soc.* **1990**, *112*, 8596.
(4) Steinberg, S.; Rubinstein, I. *Langmuir* **1992**, *8*, 1183.
(5) Wagner-Jauregg, T.; Hackley, B. E., Jr.; Lies, T. A.; Owens, O. O.; Proper, R. *J. Am. Chem. Soc.* **1955**, *77*, 922.
(6) (a) Thomas, R. C.; Sun, L.; Crooks, R. M.; Ricco, A. J. *Langmuir* **1991**, *7*, 620. (b) Sun, L.; Thomas, R. C.; Crooks, R. M.; Ricco, A. J. *J. Am. Chem. Soc.* **1991**, *113*, 8550. (c) Sun, L.; Kepley, L. J.; Crooks, R. M. *Langmuir* **1992**, *8*, 2101.
(7) (a) Nuzzo, R. G.; Allara, D. L. *J. Am. Chem. Soc.* **1983**, *105*, 4481. (b) Bain, C. D.; Troughton, E. B.; Tao, Y.-T.; Evall, J.; Whitesides, G. M.; Nuzzo, R. G. *J. Am. Chem. Soc.* **1989**, *111*, 321 and references therein. (c) Chidsey, C. E. D.; Loiacono, D. N. *Langmuir* **1990**, *6*, 682 and references therein.
(8) (a) Nuzzo, R. G.; Dubois, L. H.; Allara, D. L. *J. Am. Chem. Soc.* **1990**, *112*, 558. (b) Ihs, A.; Liedberg, B. *J. Colloid Interface Sci.* **1991**, *144*, 282.
(9) Nieuwenhuizen, M. S.; Barendsz, A. W. *Int. J. Environ. Anal. Chem.* **1987**, *29*, 105.
(10) (a) Grate, J. W.; Klusty, M.; Barger, W. R.; Snow, A. W. *Anal. Chem.* **1990**, *62*, 1927. (b) Grate, J. W.; Klusty, M.; McGill, R. A.; Abraham, M. H.; Whiting, G.; Andonian-Haftvan, J. *Anal. Chem.* **1992**, *64*, 610–624.
(11) Kolesar, E. S., Jr.; Walser, R. M. *Anal. Chem.* **1988**, *60*, 1731.
(12) Butler, M. A.; Ricco, A. *J. Anal. Chem.* **1992**, *64*, 1851.
(13) Ricco, A. J.; Frye, G. C.; Martin, S. J. *Langmuir* **1989**, *5*, 273.
(14) Wohltjen, H. *Sens. Actuators* **1984**, *5*, 307.
(15) Wenzel, S. W.; White, R. M. *Appl. Phys. Lett.* **1989**, *54*, 1976.
(16) The frequency shift corresponding to one monolayer of DIMP was calculated from eq 1 and the density of bulk liquid DIMP. Substrate surface roughness was not taken into account, but previous studies have shown roughness factors to be about 1.5–2.1 (see ref 6a).

0003-2700/92/0364-3191$03.00/0

oscillation frequency of the device when it is used as the feedback element of an appropriate oscillator circuit.[13] In real systems, such as those described here, the SAW velocity may also be affected by changes in the mechanical properties of the coating.[6a,10b,17]

EXPERIMENTAL SECTION

Chemicals. The following chemicals were used as received: diisopropyl methylphosphonate, DIMP (98%, Alfa), dimethyl methylphosphonate, DMMP (Aldrich), 11-mercaptoundecanoic acid, MUA (Aldrich); $Cu(ClO_4)_2{\cdot}6H_2O$ (98%, Aldrich); absolute ethanol, EtOH (Midwest Grain Products); H_2SO_4 (J. T. Baker); H_2O_2 (30%, J. T. Baker). Water was purified with a Milli-Q (Millipore) deionization system or was double distilled. For vapor testing, a number of reagent-grade solvents were used as received. The vapor pressure of a sample of fractionally distilled DIMP, measured using the Knudsen effusion method, was found to be 0.7 ± 0.3 mmHg at 25 °C.

Substrate Preparation. Au-coated substrates were cleaned in freshly prepared "piranha" solution (**Caution**: "Piranha" solution, 1:3 H_2O_2:H_2SO_4, reacts violently with many organic materials and should be used with extreme care, and it should not be stored in sealed containers) for about 10 s, rinsed with deionized water, and dried under N_2 gas. The freshly cleaned Au substrates were immersed in a 1 mM MUA/EtOH solution for 8–12 h, rinsed with EtOH and water, then immersed in a 2 mM $Cu(ClO_4)_2{\cdot}6H_2O$/EtOH solution for 5–10 min to yield the composite monolayer depicted in Chart I. Best results were obtained when all of these procedures were performed in inert-atmosphere glovebags.

FTIR–External Reflection Spectroscopy (FTIR–ERS). Polished Si (100) wafers (1.3- × 2.5-cm) were coated by electron-beam evaporation of 300 Å of Ti and 2000 Å of Au and then modified as described above. Measurements were made using a Digilab FTS-40 FTIR spectrometer equipped with a Harrick Scientific Seagull reflection accessory and a liquid N_2-cooled MCT detector. All spectra were obtained using p-polarized light incident on the substrate at 85° from the surface normal. Each spectrum is the sum of 256 individual spectra, acquired over the course of 3.5 min.

SAW Experiments. SAW devices (98-MHz) on ST-quartz with Al or Au-on-Cr transducers were designed at Sandia National Laboratories (SNL) and fabricated by SNL or Crystal Technologies, Inc. (Palo Alto, CA). In the active surface region between the transducers, 2000 Å of Au was either electron-beam evaporated over a Ti adhesion layer or thermally evaporated over a Cr adhesion layer. Composite monolayers were prepared according to the procedure described above. Experiments were conducted at 25 °C.

SAW experiments were performed according to previously described procedures.[6a,b,13] DIMP, DMMP, organic solvents, and water were entrained in a stream of high-purity N_2 using gas washing bottles. Vapor-saturated streams were diluted as necessary with pure N_2 to give desired concentrations. The relationship between the changes in frequency (Δf) and mass-per-area (m_A) is given by eq 1. Here, κ is the fraction of the

$$\Delta f/f_o = -\kappa c_m f_o m_A \quad (1)$$

center-to-center distance between the transducers covered by the Au film. In the present case, its value is 0.57. The mass sensitivity, c_m, is 1.33 $cm^2/(g\ MHz)$ for ST-quartz; f_o is the oscillator frequency.

Ellipsometric Experiments. The substrates prepared for FTIR–ERS measurements were also used for ellipsometric thickness measurements. The method used for determining film thickness has been described previously.[6a] The value used for the refractive index of the films was 1.50.

RESULTS AND DISCUSSION

The formation of a carboxylate/Cu^{2+}-terminated monolayer, such as that illustrated in Chart I, was confirmed by FTIR–ERS, X-ray photoelectron spectroscopy (XPS), and

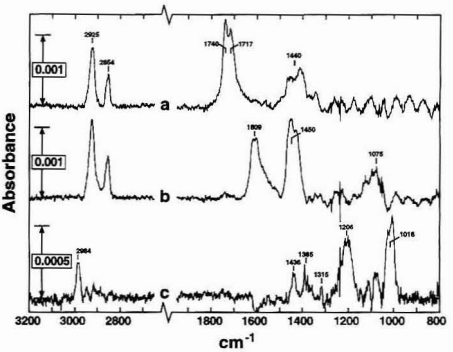

Figure 1. FTIR–ERS spectra of (a) a monolayer of the acid form of MUA confined to a Au substrate, (b) the carboxylate form of a MUA monolayer complexed to Cu^{2+}, and (c) DIMP adsorbed to a Cu^{2+}/carboxylate-terminated monolayer.

ellipsometry. Figure 1a shows the FTIR–ERS spectrum for a monolayer of the protonated form of MUA prior to Cu^{2+} adsorption. The asymmetric and symmetric methylene stretching frequencies at 2925 and 2854 cm^{-1}, respectively, are typical for a monolayer of acid-terminated *n*-alkanethiols and indicate liquidlike packing of the methylene chains.[6c,7b,c,8a] The carbonyl stretching peaks at 1740 and 1717 cm^{-1} indicate that the acid groups are protonated and present as a mixture of free monomers and laterally hydrogen-bonded dimers, respectively.[6c,7b,c,8] Figure 1b was obtained after immersing the acid-terminated surface in a dilute Cu^{2+}/EtOH solution. The methylene stretching region is essentially identical to that shown in Figure 1a, but significant changes are apparent in the carbonyl stretching region. The peaks for the carbonyl stretch have disappeared, and two new absorbances, which represent the asymmetric and symmetric C–O stretches of the carboxylate groups, are present at about 1609 and 1450 cm^{-1}, respectively. These peaks strongly suggest that the surface has been deprotonated and is complexed to Cu^{2+}.[8b,18]

A prominent Cu 2p doublet in the XPS spectrum of the composite monolayer confirms the presence of Cu^{2+} on the monolayer surface. Film thicknesses calculated from ellipsometric data verify that only a single composite monolayer is generally present on the Au surface prior to analyte exposure.

Figure 1c shows the difference spectrum obtained by subtracting Figure 1b from a spectrum recorded 2–5 min after exposing the composite monolayer to DIMP/N_2 vapor for 20 min. Several peaks characteristic of DIMP are present: the P—O stretch at 1016 cm^{-1}; the hydrogen-bonded P=O stretch at 1206 cm^{-1}; the symmetric deformation of the P-bound CH_3 groups at 1315 cm^{-1}; the resonance-split symmetric deformation of the isopropyl methyl groups centered at 1385 cm^{-1}; and the asymmetric C—H stretch of the isopropyl methyl groups centered at 2984 cm^{-1}.[18] Unfortunately, these data do not conclusively prove the phosphonate interacts with the unsaturated Cu^{2+} sites, although they are not inconsistent with this hypothesis. The frequencies and magnitudes of the peaks in Figure 1c do conclusively demonstrate that, under these conditions,[19] approximately one monolayer of DIMP adsorbs onto the carboxylate/Cu^{2+} surface.

Figure 2 shows the SAW response for a MUA/Cu^{2+}-modified SAW device upon exposure to pure N_2 and mixed DIMP/N_2

(17) Martin, S. J.; Frye, G. C. *Appl. Phys. Lett.* **1990**, *57*, 1867.

(18) Bellamy, L. J. The *Infra-red Spectra of Complex Molecules*; Wiley: New York, 1975.

(19) FTIR–ERS experiments were performed ex situ, and as a result, there is significant DIMP desorption from the substrate prior to spectral acquisition. In situ SAW experiments discussed later in the text indicate multilayer DIMP adsorption.

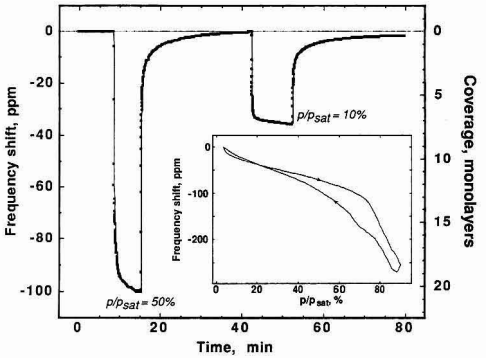

Figure 2. Response of a Cu^{2+}/MUA-modified SAW device to 50%- and 10%-DIMP-saturated N_2 vapor streams. Inset: Frequency shift of the same device as a function of the gas-phase concentration of DIMP. The isotherm was obtained over the course of 2 h.

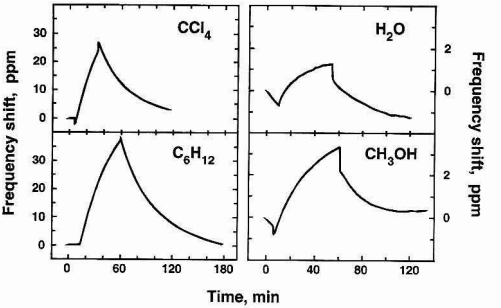

Figure 3. Plots of frequency shift versus time for a MUA/Cu^{2+}-coated SAW device exposed to flowing N_2 streams of pure vapor-phase solvents. Shortly after $t = 0$ min, the sensor was exposed to a 10% solvent-saturated stream of N_2. All solvents caused positive frequency shifts, in contradistinction to the negative frequency shifts obtained for DIMP and DMMP. Nonpolar solvents resulted in a substantially larger response than polar solvents, suggesting that interactions with the hydrocarbon chains of the MUA monolayer are important.

vapor streams. Between 0 and 8 min the sensor was exposed to pure N_2. These data were used to establish a linear correction for a very slight baseline drift of 0.07 ppm/min. Between 8 and 15 min, the sensor was exposed to 50%-saturated DIMP vapor in N_2. Between 15 and 42 min the sensor was again exposed to pure N_2, and then between 42 and 52 min it was exposed to 10%-saturated DIMP. Several points are worth noting. First, the negative frequency shifts, which correspond to a mass loading of about 20 and 6 monolayers[16] of DIMP for 50% and 10% DIMP streams, respectively, are approximately proportional to the partial pressure of DIMP. Second, the sensor has rapid response time: for 10% saturated DIMP, 90% of the maximum frequency shift is attained in 35 s. Third, DIMP reversibly binds to the chemically sensitive surface: when the 50%-saturated stream is replaced by pure N_2, 90% of the DIMP desorbs in just over 2 min. Similar responses have also been obtained for DMMP. The sort of response illustrated in Figure 2 was obtained consistently over a period of several months, during which the sensor was repeatedly exposed to a range of common organic solvents and the laboratory ambient.

There are two nearly linear regions in the complete adsorption isotherm for the DIMP sensor, as shown in the inset of Figure 2, suggesting two simple, single-energy equilibrium constants relating gas-phase to surface-adsorbed DIMP concentrations. We are able to detect DIMP at concentrations as low as 100 ppb.

Useful chemical sensors must be selective as well as reversible and sensitive. To investigate selectivity, we exposed the sensor used to obtain the data shown in Figure 2 to 10%-saturated streams of polar and nonpolar solvents (Figure 3). The frequency shifts observed for these vapors, and for several other common organic solvents, are all in the opposite direction to the shifts resulting from DIMP or DMMP exposure. Also, the sensor responds much more slowly to water and the organic solvents than to the organophosphonates. These data demonstrate this sensor's selectivity for organophosphonates relative to typical interferants, though the sensor response to ligands likely to strongly coordinate the Cu^{2+} remains to be examined.

It is somewhat surprising that positive frequency shifts result from exposure of the device to common organic solvents. Since no mass loss is apparent after N_2 purging, we conclude that the positive frequency shifts correspond to changes in the viscoelastic properties of the film.[6a,10b,17] Anecdotal support for this conclusion is provided by the small magnitude of the shifts for polar molecules compared to the shifts for nonpolar molecules. We speculate that the solvents insert between the methylene chains of the MUA monolayer, most likely at defects which must occur at boundaries between adjacent Au crystallites, effectively stiffening the film. Such an effect would be most pronounced for nonpolar solvents, consistent with our data. We are presently investigating this interesting result.

As control experiments, SAW devices having bare quartz, bare Au, and Cu^{2+}-free MUA self-assembled films were examined. Quartz and Au surfaces yielded measurable response to DIMP, but in both cases, a significant fraction of the response was irreversible, irreproducible, and apparently dependent on surface cleanliness. Moreover, responses to organic solvents were not generally distinguishable from responses to DIMP in these control experiments, since all frequency shifts were negative. The Cu^{2+}-free MUA films gave responses similar to those of the Cu^{2+}-terminated films, including positive frequency shifts for organic solvents, but the repeatability and reversibility of the DIMP responses were inferior to those of the Cu^{2+}-terminated films.

CONCLUSIONS

The most important result of this study is that straightforward self-assembly chemistry can be used to fabricate surfaces that are chemically sensitive to important analytes. This implies that rational development of selective coatings need not involve tedious synthesis of complex and fragile "active sites". Moreover, since this sensor is based on a simple monolayer, rapid responses are obtained. Finally, we have demonstrated that this simple fabrication procedure incorporates all of the essential features of an ideal sensor: (1) it is selective for organophosphonates; (2) it is sensitive to 100 ppb of an important nerve-gas simulant; (3) it provides a reversible and proportional response to target analytes; (4) it is durable for periods of months.

ACKNOWLEDGMENT

The excellent technical assistance of Barbara L. Wampler (SNL) is gratefully acknowledged. Valuable technical discussions with R. C. Hughes (SNL) and Li Sun (UNM) are also acknowledged. This work is supported by the National Science Foundation (Grant No. CHE-90146566) and the U.S. DOE (Contract No. DE-AC04-76DP00789).

RECEIVED for review June 11, 1992. Accepted September 24, 1992.

Attomole Level Capillary Electrophoresis–Mass Spectrometric Protein Analysis Using 5-μm-i.d. Capillaries

Jon H. Wahl, David R. Goodlett, Harold R. Udseth, and Richard D. Smith*

Chemical Methods and Separations Group, Chemical Sciences Department, Pacific Northwest Laboratory, Richland, Washington 99352

There is a strong interest in the development of analytical techniques with enhanced sensitivity for biochemical applications, because in many cases sample size is limited or obtained at great effort and expense. This enhanced sensitivity is beneficial for all applications, but for large biopolymers (proteins, DNA segments, and larger carbohydrates), the difficulties and analytical demands increase significantly. Some of the most exciting and demanding applications require methods capable of analyses that are on the single-cell level,[1] where the maximum amounts of components would typically be in the attomole range, and that extend down to zeptomoles (10^{-21} mol) and below. In general, analytical methods being developed for such applications are more useful when they combine a separation method with a sensitive, selective, and broadly applicable detection method.

In this regime of ultrasensitive analysis and, in particular, for biopolymer characterization, mass spectrometry (MS) has not generally been considered sufficiently sensitive when compared with techniques such as laser-induced fluorescence[2-4] and electrochemical detection.[5] Indeed, Dovichi,[2] Zare,[3] Guzman,[4] and their respective co-workers, among others, have successfully demonstrated capillary electrophoresis (CE) of fluorescently labeled compounds at the low-zeptomole level. These detection methods have provided the most impressive sensitivities yet demonstrated using CE, but application is restricted and information for compound identification is generally limited due to a reliance on electrophoretic mobilities. The attraction of MS detection is that accurate molecular weight information and component identification can be performed, even for proteins,[6] and techniques for obtaining structural information based upon tandem methods are being currently extended to larger molecules.[6-9]

With the recent dramatic developments in ionization techniques, the primary limitation for the use of mass spectrometry is due to sensitivity constraints. For electrospray ionization (ESI) sensitivity generally decreases as molecular weight increases,[9] an observation largely attributable to the increased extent of charging and broader charge state distribution for large molecules. Previous work by Thibault and co-workers,[10] Moseley et al.,[11] and this laboratory[12] have generally used sample sizes on the order of 100 fmol and larger to obtain mass spectra of proteins with sufficient quality for precise molecular weight measurements.

In this correspondence we report the use of chemically modified 5-μm-i.d. capillaries for CE–MS of proteins. We have found that the use of small inner diameter capillaries results in greatly improved sensitivity in CE–ESI/MS, an approximately 25–50-fold improvement, for the detection of attomole quantities of injected protein. Previously, Moseley et al.[13,14] have demonstrated femtomole level detection for peptide separation using approximately 15-μm-i.d. capillaries where a continuous-flow fast atom bombardment interface was utilized, but the choice of capillary i.d. was largely dictated by their interface design, no particular sensitivity advantage related to capillary i.d. was suggested, and the ionization method used is inappropriate for proteins. To our knowledge this report demonstrates the first attomole range CE–MS results for proteins and, in particular, the first obtained with scanning MS detection.

EXPERIMENTAL SECTION

The CE instrument used for this work is constructed at our laboratory and is interfaced to a modifed Sciex TAGA 6000E triple-quadrupole mass spectrometer as previously described.[12] The electrospray interface utilized a coaxial sheath flow of 75% methanol–24% water–1% acetic acid. The sheath liquid establishes electrical contact with the CE capillary terminus and defines the CE electric field strength.[15] The sheath liquid is delivered by a Harvard syringe pump at approximately 2 μL/min and assists in stabilization of the electrospray signal.[15] The electrospray is established using approximately a +4-kV gradient between the capillary terminus and the MS sampling orifice.

Separations of a 30 μM protein mixture containing aprotinin (6.5 kDa) cytochrome *c* (12 kDa), myoglobin (17 kDa), and carbonic anhydrase (29 kDa) (Sigma, St. Louis, MO) in doubly-distilled deionized water are conducted in 100-cm-long, 50-μm- and 5-μm-i.d., nominally 150-μm-o.d. fused-silica capillaries (Polymicro Technologies, Phoenix AZ). About 1 cm of the fused-silica capillary terminus was stripped of its polyimide coating and is etched with 40% hydrofluoric acid to form a tapered tip. The inner walls of the capillaries are chemically modified with aminopropylsilane, in a manner similar to that described by Bruin et al.[16] and as demonstrated previously by Lukacs.[17] A 0.01 M acetic acid solution, pH = 3.4, buffer was used. Because of the very low ionic strength of this acetic acid buffer system, any extracapillary broadening to the solute zone due to Joule heating during the separation is assumed negligible for both the capillary diameters. This aminopropylsilane surface modification and the acidic buffer system give rise to a net positive surface charge to the inner walls of the capillaries and an electroosmotic flow in

(1) Kennedy, R. T.; Oates, M. D.; Cooper, B. R.; Nicherson, B.; Jorgenson, J. W. *Science* **1989**, *246*, 57.
(2) Cheng, T. F.; Dovichi, N. J. *Science* **1988**, *242*, 562.
(3) Sweedler, J. V.; Shear, J. B.; Fishman, H. A.; Zare, R. N. *Anal. Chem.* **1991**, *63*, 496.
(4) Hernandez, L.; Escalana, J.; Joshi, N.; Guzman, N. *J. Chromatog.* **1991**, *559*, 183.
(5) Wallingford, R. A.; Ewing, A. G. *Anal. Chem.* **1989**, *61*, 98.
(6) Smith, R. D.; Loo, J. A.; Edmonds, C. G.; Barinaga, C. J.; Udseth, H. R. *Anal. Chem.* **1990**, *62*, 882.
(7) Smith, R. D.; Fields, S. M.; Loo, J. A.; Barinaga, C. J.; Udseth, H. R.; Edmonds, C. G. *Electrophoresis* **1990**, *11*, 709.
(8) Smith, R. D.; Loo, J. A.; Barinaga, C. J.; Edmonds, C. G.; Udseth, H. R. *J. Chromatog.* **1989**, *480*, 211.
(9) Smith, R. D.; Loo, J. A.; Edmonds, C. G.; Barinaga, C. J.; Udseth, H. R. *J. Chromatog.* **1990**, *516*, 157.
(10) Thibault, P.; Paris, C.; Pleasance, S. *Rapid Commun. Mass Spectrom.* **1991**, *5*, 484.
(11) Moseley, M. A.; Jorgenson, J. W.; Shabanowitz, J.; Hunt, D. F.; Tomer, K. B. *J. Am. Soc. Mass Spectrom.* **1992**, *3*, 289.
(12) Smith, R. D.; Udseth, H. R.; Barinaga, C. J.; Edmonds, C. G. *J. Chromatog.* **1991**, *559*, 197.
(13) Moseley, M. A.; Deterding, L. J.; Tomer, K. B.; Jorgenson, J. W. *J. Chromatogr.* **1989**, *481*, 197.
(14) Moseley, M. A.; Deterding, L. J.; Tomer, K. B.; Jorgenson, J. W. *J. Chromatogr.* **1990**, *516*, 167.
(15) Smith, R. D.; Olivares, J. A.; Nguyen, N. T.; Udseth, H. R. *Anal. Chem.* **1988**, *60*, 436.
(16) Bruin, G. L. M.; Huisden, R.; Kraak, J. C.; Poppe, H. *J. Chromatogr.* **1989**, *480*, 339.
(17) Lukacs, K. D. *Diss. Abstr. Int., C* **1983**, *44*, 3766.

0003-2700/92/0364-3194$03.00/0

the opposite direction compared to uncoated fused-silica capillaries. The CE voltage is approximately −26 kV, resulting in a CE gradient of −300 V cm^{-1} with the electrospray voltage at the capillary terminus at +4 kV. CE currents are approximately 1.1 μA for the 50-μm-i.d. capillary and less than 60 nA for the 5-μm-i.d. capillary. Electrokinetic injection was conducted at −5 kV for approximately 3 s and was used for all separations, and the amount injected, Q, is determined with the following equation:

$$Q = \mu_{app} E \pi r^2 C_A t_{inj} \quad (1)$$

where μ_{app} is the apparent solute mobility, E is the applied field strength, r is the inner radius of the capillary, C_A is the solute concentration, and t_{inj} is the injection time. The injection conditions (i.e., t_{inj}) were adjusted somewhat for the two capillary diameters to account for differences due to migration velocities arising from differences in electroosmotic flow rates, so that a factor of 100 less sample was injected onto the 5-μm capillary (neglecting the small errors indicated by the different analyte migration rates).

RESULTS AND DISCUSSION

Our expectation in beginning this study was that smaller CE currents (i.e., comparable or smaller than the ESI current) would provide a situation where ESI efficiency would increase. A general observation from our experiments is that the sensitivity in CE–MS generally improves with the use of smaller i.d. capillaries. For larger i.d. capillaries the CE currents greatly exceed the maximum electrospray ion currents, where CE currents are commonly greater than 1 μA, and ESI currents are typically between 0.1 and 0.5 μA.[6] Smaller diameter capillaries incur smaller CE currents that provide a better match to the ESI current. Thus, the efficiency of the ESI process may increase as the capillary i.d. decreases, other conditions being constant. Consequently, solute sensitivity may also increase as the capillary i.d. decreases. The increase in sensitivity observed in this study, however, is even greater than predicted. Other factors also appear to contribute to the sensitivity enhancement obtained using small-i.d. capillaries.

Although there are increased difficulties using small-i.d. capillaries, primarily due to plugging of the capillary, the MS interfacing methods remained reliable throughout the study. One concern relevant to the interface was that incomplete mixing between the CE buffer system and the sheath liquid would cause a decrease in analyte ion current (because the analyte would then be present in only a fraction of the electrospray droplets). Observation of the terminus of an uncoated fused-silica capillary of small i.d., squarely cut with the polyimide coating intact, showed that the electrospray could emanate from both the outer diameter and near the inner diameter of the capillary. Points of electrospray emanation were observed to move rapidly, and apparently in a random manner, between various sites on the capillary terminus. We believe that such a mode of operation may degrade signal stability and sensitivity because electrosprays emanating from the capillary outer diameter likely contain less analyte. For this reason the capillary terminus was etched, as described in the Experimental Section. A tapered capillary terminus should allow liquid to flow to the conical apex and provide more effective mixing between the CE effluent and sheath liquid for the small i.d. capillaries.

The results of our initial separations with proteins are shown in Figure 1, where the total ion current electropherograms obtained for the protein mixture using the 50-μm- (top) and the 5-μm-i.d. (bottom) capillaries are illustrated on the same absolute scale. In both experiments, the mass spectrometer is scanning from m/z 600 to 1200 in 2 m/z steps at 1.5 s/scan. The surface treatment for the 5-μm capillary appears less homogeneous on the basis of the slower electroosmotic flow

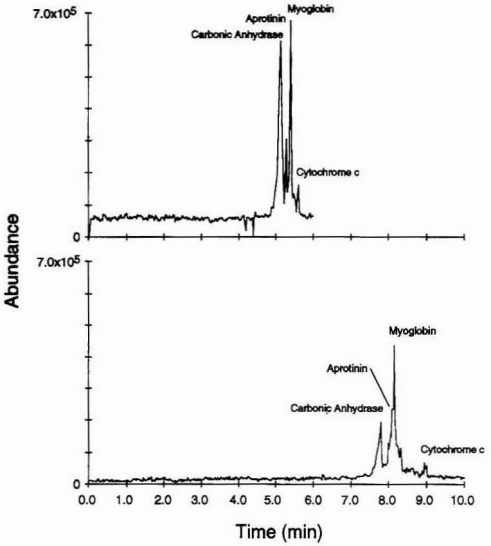

Figure 1. Total ion current electropherograms obtained for the 30 μM protein mixture containing carbonic anhydrase, aprotinin, myoglobin, and cytochrome *c* using 500-μm- (top) and 5-μm-i.d. (bottom) capillaries. Injected amounts were 60 fmol of protein for the 50-μm-i.d. capillary and 600 amol of protein for the 5-μm capillary by electrokinetic injection. Comparison of the two electropherograms shows only 2–4-fold difference in signal intensity. Experimental conditions: 100-cm capillary length; 0.01 M acetic acid buffer solution, pH = 3.4; electric field, −300 V cm^{-1}; MS scanning conditions, m/z 600–1200 in 2 m/z steps at 1.5 s/scan.

rates observed, presumably due to less effective surface coverage for the smaller capillaries. The electrokinetic injection method delivered approximately 60 fmol of protein onto the 50-μm-i.d. capillary and 600 amol of protein onto the 5-μm capillary. This corresponds to a 100-fold difference in the injected sample amount between the two capillaries; however, comparison of the two electropherograms shown in Figure 1 illustrates only a 2–4-fold difference in signal intensity. Consequently, this corresponds to a gain in sensitivity of 25–50, which is far outside the day to day variation in instrumental response (a factor of approximately 2). The changes in relative migration rates and the failure to gain in separation efficiency suggests that sample interactions with capillary surface are contributing.

The mass spectra obtained for the 600 amol of protein injection into the 5-μm-i.d. capillary are shown in Figure 2 and are of sufficient quality to determine the molecular weight to approximately 0.03% for most components. To our knowledge these are the first subfemtomole level CE–MS results for proteins obtained while a relatively broad m/z range is scanned. These results clearly indicate that CE–MS of proteins is feasible at subfemtomole levels and that sensitivity for the selected ion monitoring (SIM) mode of operation should easily extend to the low-attomole range for the proteins studied (generally a sensitivity improvement of 10–100 is noted for SIM relative to scanning detection). In addition, the distribution of ESI signal due to the multiplicity of charge states (observed for the higher molecular weight proteins) suggests that even greater sensitivity should be obtainable for smaller singly charged species.[9] It is also important to realize that the sensitivity gain obtained in this work would not be realized if one injected 600 amol into the large i.d. capillary due to the constant ESI contribution from buffer components. A detailed study is in progress aimed at

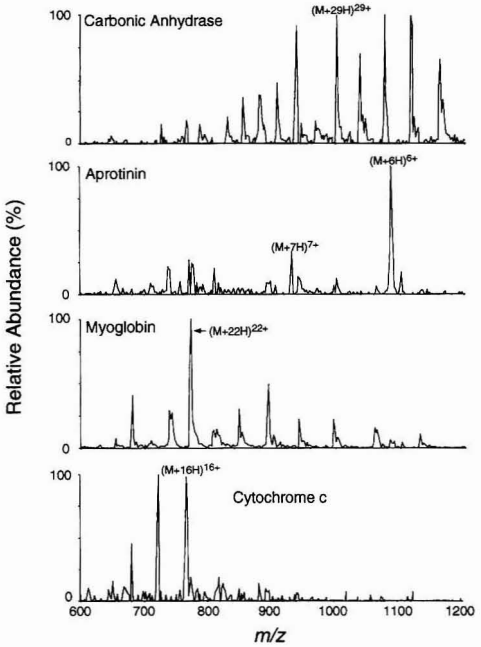

Figure 2. Mass spectra obtained from the individual solute zones for 600 amol of protein injected using the 5-μm-i.d. capillary shown in Figure 1 (bottom). Experimental conditions are given in Figure 1.

more fully determining the relationship of sensitivity, injection size, and capillary diameter.

The high sensitivity demonstrated by this work utilizing a conventional scanning quadrupole mass spectrometer might initially be surprising. We have previously estimated overall transport efficiency of ions from the ESI source to the MS detector as $\sim 10^{-4}$ for conventional ESI currents. Thus, 600 amol of protein would correspond to only $\sim 4 \times 10^4$ ions reaching the detector during peak elution without mass analysis (i.e., transmission of all ions through the quadrupole filter). (Due to the pulse counting detection used in this work, background is negligible over the m/z range of interest, allowing low-signal levels to be reliably measured.) Due to "scanning" the quadrupole mass filter in discrete steps, only about 10^2 counts/protein would be expected to be recorded during peak elution. In fact, the detected signals are intact between 1 and 2 orders of magnitude greater than expected on the basis of this simple estimate. For example analysis of the raw spectra shows that a total of about 5000 discrete ion counts contribute to the mass spectra during elution of carbonic anhydrase. Clearly, the detected signals are much more intense than expected on the basis of the above assumptions. While we have not completely explored all the phenomena possibly contributing to our obervations, we believe that the sampling efficiency for protein ions to be substantially better than 10^{-4}. Possible reasons for this improved performance include (a) an expected enrichment for massive ions relative to light ions for MS transmission due to beam dynamic effects and (b) a reduction in space charge expansion of the electrospray plume due to a reduced ESI current with the smaller i.d. capillary. Preliminary studies at out laboratory suggest that the latter can account for as much as a 10^2 gain in transmission efficiency. Further studies are in progress aimed at quantifying the various contributions to the observed performance and to extend these gains.

These results represent an encouraging initial step toward the longer range goal of ultrasensitive protein analysis at low-attomole and subattomole levels, although a number of problems remain to be addressed. For example, the techniques used to surface modify small-i.d. capillaries needs to be improved to provide more uniform surfaces and enhanced separation quality. Improved procedures for sample and buffer preparation are also needed to prevent capillary plugging, a fairly common occurrence with small-i.d. capillaries. In addition, the ESI interface sensitivity may be further improved because the efficiency of ion transport from the ESI source, which is at atmospheric pressure, to the MS detector remains low.[6] Sensitivity for broad m/z range detection can be further improved by the use of array detectors and, potentially, with ion trapping[18] and time-of-flight[19] mass spectrometers. These developments may also mitigate the somewhat reduced dynamic range resulting from the smaller ESI currents with very small diameter capillaries (a factor of <4 in the present study). Finally, the ancillary sample-handling methods needed to more fully exploit attomole level detection require significant attention. A coalescence of these methods is potentially useful for CE–MS at zeptomole levels.

ACKNOWLEDGMENT

This research was supported by internal exploratory research and the Director, Office of Health and Environmental Research, U.S. Department of Energy. Pacific Northwest Laboratory is operated by Battelle Memorial Institute for the U.S. Department of Energy, through Contract DE-AC06-76RLO 1830.

(18) Cox, K. A.; Williams, J. D.; Cooks, R. G.; Kaiser, R. E., Jr. *Biol. Mass Spectrom.* **1992**, *21*, 226.
(19) Lee, M. L.; Liv, Z.; Wu, M.; Lee, E. D. Presented at Pittcon '92, March 9–13, 1992, New Orleans, LA; Abstract 667.

RECEIVED for review June 30, 1992. Accepted September 15, 1992.

TECHNICAL NOTES

Thermospray–Microatomizer Interface for the Determination of Trace Cadmium and Cadmium–Metallothioneins in Biological Samples with Flow Injection– and High-Performance Liquid Chromatography–Atomic Absorption Spectrometry

K. A. High, R. Azani, A. F. Fazekas, Z. A. Chee, and J. S. Blais*

McGill University, Macdonald Campus, Department of Food Science and Agricultural Chemistry, 21,111 Lakeshore Road, Ste-Anne-de-Bellevue, Quebec, Canada H9X 3V9

INTRODUCTION

Metal-induced, sulfhydryl-rich polypeptides found in plants (phytochelatins)[1] and animals (metallothioneins)[2] have been been described as sequesters and detoxifiers of toxic heavy metal ions (Hg, Cd) as well as major players in the homeostatic control of the essential metals Zn and Cu. Metallothioneins (MTs) have been used as a bioindicator of heavy metal induced stress because they tightly bind the metals (groups IIA and IIB) which induce their biosynthesis.[3] An excess of metal-binding capacity due to MTs has been observed in both animal and fish tissues as a result of metal- or drug-induced stress.[4–7] Although this overproduction of available coordination thiol sites may be desirable in terms of transient resistance to heavy metals,[5] the sequestration of essential metallic cations may account for noxious side effects.[4,7] Recently, the developmental toxicity of urethane has been attributed to an alteration of embryonic Zn status due to urethane-induced MTs in maternal liver.[7]

As the most extensively studied component of metallobiochemistry, thiolic metal-binding proteins have been preferentially determined by selective and sensitive analytical tools. Techniques providing limits of detection (LOD) in the picomolar range include radioimmunoassay, electrophoresis/silver staining, and polarography.[8] Extensive sample purification steps are required to achieve a high degree of selectivity. Since it provides two elements of specificity which attenuate the possibility of false positive or overestimated determinations, on-line coupling of HPLC to flame atomic absorption spectroscopy (AAS) detection represents a reliable metal speciation tool.[9] This technique has been used for the determination of MTs after saturation with various metallic cations.[8] However, the inefficient pneumatic nebulization and flame atomization processes resulted in relatively high LODs (nanomole range). For the determination of cadmium-saturated MTs, a modular thermospray/desolvation HPLC–flame AAS accessory improved the pneumatic nebulization efficiency to 100%, with signal enhancements of 7–8-fold.[10] However, the LOD for Cd (1.9 ng) was still much higher than the theoretical absolute value. The unavoidable limitations of high spectral background (low S/N ratio) and a short residence time of the atomic vapors in the air/acetylene flame, still remained.

We have shown previously that miniaturized thermochemical cells, used as HPLC–AAS interfaces, can provide LODs 100–200 times lower than those achieved with conventional flame AAS. Ionic organolead species, extracted from various environmental samples, were determined using a methanol-fueled thermospray–microatomizer interface[11] with LODs in the 1–5-ng range. In this simple quartz apparatus, the HPLC methanolic effluent (composition >60% methanol) was thermosprayed and vaporized in the presence of oxygen. The resulting microflame pyrolyzed organic species and atomized Pb which was transported in a vapors retainer tube mounted in the AAS optical beam. More recently, hydride-forming metalloids emerging from this pyrolytic flame were found to form hydride derivatives thermochemically upon addition of hydrogen to the gas stream.[12,13] The resulting hydrides of Se or As were channeled to a diffusion flame atomizer providing LODs between 5 and 25 ng. The microatomization approach was found to be very efficient for "volatile" heavy metals which form thermally unstable oxides and hydrides (Pb, Cd, Hg, etc.). The microflame which pyrolyzes molecular interferents to CO_2 and water vapors is positioned remotely from the AAS optical beam, virtually eliminating spectral interferences. Furthermore, the lower gas flow rates and the use of a vapors retainer tube increase the residence time of the analyte in the optical beam. In the first generation of these microatomizers, the HPLC mobile phase was used to fuel the pyrolytic flame, which caused severe limitations in flexibility.

In the present article we report a flexible microatomization interface fueled by hydrogen and capable of handling 100% aqueous HPLC mobile phases. This versatile interface allows HPLC–AAS coupling with most methods used for the separation of complex mixtures containing trace levels of volatile metallic elements. The system has been optimized for the detection of cadmium in mussels and animal tissues using flow injection (total and bound soluble Cd) or HPLC–AAS (Cd MTs) modes.

* To whom correspondence should be addressed.

(1) Grill, E.; Winnacker, E. L.; Zenk, M. H. *Methods Enzymol.* **1991**, *205*, 333–340.
(2) Bremner, I. *Methods Enzymol.* **1991**, *205*, 25–35.
(3) Klaverkamp, J. F.; Dutton, M. D.; Majewski, H. S.; Hunt, R. V.; Wesson, L. J. In *Metal Ecotoxicology*; Newman, M. C., and McIntosh, A. W., Eds.; Lewis Publishers: Chelsea, MN, 1991; pp 33–63.
(4) Torreblanca, A.; Del Ramo, J.; Sarkar, B. *Toxicology* **1992**, 167–174.
(5) McCarter, J. A.; Roch, M. *Comp. Biochem. Physiol.* **1983**, *74C*, 133–137.
(6) Petering, D. H.; Krezoski, S.; Villalobos, J.; Shaw, C. F.; Otvos, J. D. *Experimentia Suppl.* **1987**, *52*, 573–580.
(7) Daston, G. P.; Overmann, G. J.; Taubeneck, M. W.; Lehman-KcKeeman, L. D.; Roger, J. M.; Keen, C. L. *Toxicol. Appl. Pharmacol.* **1991**, *110*, 450–463.
(8) Summer, K. H.; Klein, D. *Methods Enzymol.* **1991**, *205*, 57–60.
(9) Ebdon, L., Hill, S., Ward, R. W. *Analyst (London)* **1987**, *112*, 1–16.
(10) Larsen, E. H.; Blais, J. S. Submitted for publication in *J. Anal. At. Spectrom.* 1992.
(11) Blais, J. S.; Marshall, W. D. *J. Anal. At. Spectrom.* **1989**, *4*, 271–277.
(12) Blais, J. S.; Momplaisir, G. M.; Marshall, W. D. *Anal. Chem.* **1990**, *62*, 1161–1166.
(13) Blais, J. S.; Huyhues-Despointes, A.; Marshall, W. D. *J. Anal. At. Spectrom.* **1991**, *6*, 225–232.

0003-2700/92/0364-3197$03.00/0

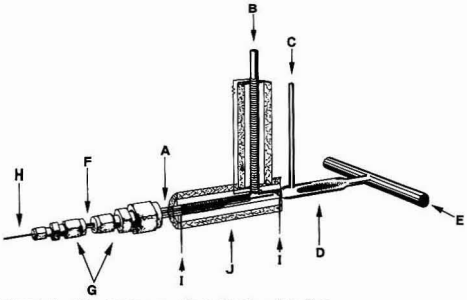

Figure 1. Thermospray–microatomizer interface.

EXPERIMENTAL SECTION

Instrumentation and Thermospray Microatomizer Interface. The mobile phase for flow injection (FI) and HPLC analyses was delivered (1 mL/min) by a dual-pump HPLC system (Gilson 305/306). The sample injection volume was 97 μL. Cadmium vapors produced in the microatomizer interface were detected by a double-beam atomic absorption spectrometer (Pye Unicam Model 1900) set at 228.9 nm. Absorbance/time data were collected at 10 Hz and integrated (JCL-6000 software, Jones Chromatography, Littleton, CO). Hydrogen and oxygen were delivered from calibrated flow meters (Model 802 with microvalves; Matheson Co., Toronto, ON).

The microatomizer interface, presented in Figure 1, was composed of quartz tubes which were connected together by glass blowing. The main body comprised a thermospray inlet tube (A, 4-mm i.d. × 6-mm o.d. × 10 cm), a hydrogen inlet (B, 4-mm i.d. × 6-mm o.d. × 10 cm) connected at a 90° angle, 7 cm from the inlet of tube A, a combustion chamber (D, 9-mm i.d. × 11-mm o.d. × 5 cm), a thin oxygen inlet tube (C, 2-mm i.d. × 3.2-mm o.d. × 6 cm) emerging at a 90° angle in the combustion chamber, and an atomic vapors retainer tube (E, 9-mm i.d. × 11-mm o.d. × 12 cm) positioned in the optical beam of the AAS instrument. A concentric guide tube (F, 2-mm i.d. × 3.2-mm o.d. × 10 cm) was inserted in the thermospray inlet tube via reducing Swagelok unions (G, 0.64–0.32 and 0.32–0.16 cm) fitted with Vespel ferrules. The outlet tip of this guide tube was constricted to 0.5–0.8-mm i.d. and positioned in the junction formed by the thermospray and hydrogen inlet tubes. During operation, the HPLC or flow injection liquid carrier was channeled through a short length of silica capillary tube (H, 50-μm i.d. × 15 cm; Chromatographic Specialties, Brockville, ON) which was centered in the thermospray inlet via the guide tube. This capillary was connected to the steel HPLC tubing from the injection valve by a 1.6–0.8-mm reducing union and a zero dead volume Vespel capillary ferrule (Chromatographic Specialties, Brockville, ON).

The thermospray and hydrogen inlet tubes were heated by a continuous thermoelectric wire (I, Kanthal A-1 wire, 4.53 Ω/m, 22-G diameter, Pyrodia Co., Montreal, PQ) wound tightly in 45 and 60 coils, respectively (plus 15 coils around the 2.4-cm length between the thermospray/hydrogen inlets intersection and the combustion chamber). The heater was embedded in refractive wool (Fiberfrax, The Carborundum Co., Niagara, NY) for thermal insulation and protection against corrosion from the ambient air. The heated sections were then encased with cylindrical pieces of firebrick of approximately 15-mm wall thickness (J). To circumvent short-circuits between coils, the resistive wire was surface-oxidized (red hot, 800–900 °C) for 15 min before embedding in refractive wool. The ac potential applied to the heater was controlled by a variable transformer (Variac) and monitored with a digital voltmeter. The vapors retainer tube (E) was mounted in a cylindrical aluminum casing (5-cm i.d.) and secured by firebrick disks and refractive wool at both ends. An additional support was positioned at the center of the encased thermospray tube assembly.

The interface was made operational as follows: (1) hydrogen was introduced at 1.7 L/min and ignited at both end of the vapors retainer tube; (2) the heating coils were then energized to 45 V (red hot, 800–900 °C); (3) a small flame spontaneously ignited in the combustion chamber upon addition of a gentle stream of oxygen (100 mL/min); (4) the silica capillary was then inserted in the Swagelok fitting assembly; (5) the oxygen flow was increased to 500 mL/min; (6) the solvent delivery system was *rapidly* adjusted to 1 mL/min and the capillary was *immediately* positioned in the thermospray inlet tube, approximately 1 cm from the combustion chamber. The thermosprayed HPLC mobile phase has a significant cooling effect which should be maintained at all times; operating the prescribed hydrogen/oxygen flame without liquid flow causes the quartz assembly to soften around the oxygen inlet tube. For the same reason, the silica capillary should not be inserted in the heated compartments without liquid flowing through. ***CAUTION***: Oxygen and hydrogen should never be allowed to flow simultaneously in the absence of a flame in the combustion chamber. Since uncontrolled ignition may shatter the chamber, the use of a face-shield is recommended during preliminary work. In step one, hydrogen escaping from the optical tube was ignited to avoid possible accumulation in the venting system. This flame was extinguished during operation. The interface was turned off using the reverse sequence.

Reagents and Standards. All chemicals used were of ACS reagent grade or better. Working solutions in the range 0.49–62.5 ng/mL of cadmium were made from 1000 μg/mL analytical grade stock solutions in dilute (0.5% v/v) nitric acid (Analytical Grade, BDH, Montreal, PQ). The same acidic solution was used as a carrier stream throughout all the FI experiments. Test mobile phases for HPLC consisted of aqueous solutions of Tris (2-amino-2-(hydroxymethyl)-1,3-propanediol) buffer (10–100 mM) adjusted to appropriate pHs with HCl (BDH, Montreal, PQ). Stock solutions of partially purified horse kidney metallothionein I and II isoforms (Sigma Chemical Co. St. Louis MI) were prepared in 10 mM Tris–HCl, pH 7.21, preserved with 0.02% (w/v) sodium azide.

High-Performance Liquid Chromatography of Metallothioneins. Horse kidney MTs I and II isoforms were separated isocratically (1 mL/min) in a weak anion-exchange column (SK-DEAE-5PW, 7.5 mm × 7.5 cm; Supelco Co. Bellefonte, PA) using 15 mM Tris–HCl, pH 7.21, as mobile phase. Both mobile phase and standards solvents were deoxygenated with helium. A mussel MT fraction was eluted isocratically with Tris–HCl (100 mM, pH 7.21, 1 mL/min).

Characterization/Optimization of the Interface. Hydrogen and oxygen flow rates were optimized as a function of AAS response (FI mode) to a standard (3 ng of Cd) or a biological sample (mussel extract) by multivariate factorial experiments (composite 2^2 designs). The effect of potential inteferents (glutathione, Cu, Zn) coinjected with 0.97 ng of Cd was assessed similarly using a composite 2^3 factorial design.[12] Nonspecific absorption from real samples was determined by comparing pure AAS signals with D_2 background corrected responses. Matrix effects were estimated by comparing standard addition calibrations of standard and mussel extract solutions. Five replicate standards (3 ng/mL) or sample solutions were spiked with increasing levels of standard (+2, +4, +6, +8, and +10 ng/mL) and analyzed in triplicate injections.

Preparation and Analysis of Cd-Contaminated Mussel Extracts. Freshwater mussels (*Elliptio complanata*) of similar size (68 ± 4 mm) were collected from a nonpolluted river, 80 km north of Montreal. The population (N = 45) was transferred to a tank of continuously oxygenated double-distilled water for a period of 1 month. During this period, the mussels expelled particulate matter from their siphon/gills system.[14] The population was then exposed to 100 μg/L Cd (as $CdCl_2$) for a period of 29 days. The Cd-spiked water was replaced daily in order to maintain a constant level of exposure. Random sampling (N = 3) was done every second day. Residual Cd in solution was removed by keeping the sampled mussel in double-distilled water for 24 h prior to analysis.

Analytical glassware was soaked in 10% nitric acid before use. Total mussel viscera was homogenized in 10 mL of Tris–HCl buffer (10 mM, pH 7.4, 0.02% w/v NaN_3 as antibacterial, 0.05 mM phenylmethanesulfonyl fluoride as proteases inhibitor) at

(14) Hemelradd, J.; Holwerda, D. A.; Zandee, D. I. *Arch. Environ. Toxicol.* **1986**, *15*, 1–7.

10 °C, with a Polytron homogenizer (20 000 rpm), and centrifuged for 20 min at 17000*g* (10 °C). The supernatants were decanted and diluted to 40 mL with buffer. Total Cd was determined by injecting 10-fold dilutions of these extracts in the FI–microatomizer-AAS system. An "unbound" Cd fraction was isolated by subjecting the extracts (1.5 mL) to ultrafiltration (1 kDa cutoff membrane) in micropartitioning units (Amicon, Danvers, MA) at 1.500*g* for 1.5 h. The ultrafiltrates were injected directly in the FI–AAS system. External calibration was corrected for matrix effect determined by standard addition.

Exploratory determinations of metallothionein-bound Cd were done by injecting selected extracts in the HPLC(DEAE)–microatomizer-AAS mode. Confirmation of the MT–Cd bands was obtained by analyzing the same extracts after thermocoagulation (20 min at 70 °C) and centrifugation (17000*g*).

RESULTS AND DISCUSSION

Performance of Microatomizer. In the first microatomizer design,[11] the thermosprayed HPLC methanolic mobile phase was used to support the pyrolytic flame. This resulted in a thorough premixing of analytes (alkylleads) with the fuel vapors before ignition. However, this approach was not compatible with aqueous samples and HPLC mobile phases. The present hydrogen-fueled microatomizer interface was designed in order to obtain full compatibility with aqueous systems.

Preliminary experiments demonstrated that the configuration of the thermospray/fuel/oxidant inlets was a critical aspect affecting the performance of the interface, especially when exposed to biological samples. Thermal atomization of cadmium, lead, and mercury from pure standard solutions could be achieved with various geometries in which O_2, H_2, and sample vapors were mixed simultaneously in concentric or cross-flow configurations. However, during the analysis of biological extracts, an inefficient premixing of HPLC effluent vapors with the fuel/oxidant mixture resulted in laminar flow systems in which a portion of the solvent vapors flew separately from the flame front. Under these conditions, organic interferents from the biological samples were not pyrolyzed completely, causing nonspecific absorption signals and/or memory effects. The design shown in Figure 1 represents the simplest configuration which provided the desired performance. The reproducibility of the response was dependent on a smooth thermospray effect. Since water was more difficult to thermospray than organic solvents, a two-stage heating process was developed. The liquid phase flowing through the silica capillary (Figure 1. H) was heated by conduction/radiation via thermoelectric elements coiled around the thermospray inlet tube (A). The last 1–1.5 cm of the capillary received an additional input of thermal energy by convection heating with hot hydrogen gas introduced from the heated fuel inlet tube (B). Under these conditions the fine aerosol emerging from the capillary was instantaneously converted to vapors which mixed with H_2 before reaching the combustion chamber (D). The small diameter of the oxygen inlet tube (C) maximized the linear velocity of the oxidant gas, which spontaneously ignited the fuel/aqueous vapors mixture in a homogeneous flame, with a characteristic jet sound.

The microatomizer interface was optimized in flow injection mode. The AAS response surface (to a Cd standard) as a function of hydrogen and oxygen flow rates is presented in Figure 2. The response areas were minimized when conditions promoted a relatively cool flame (fuel or oxidant deficiency). Intermediate flow rates exceeding the stoichiometric fuel/oxygen ratio resulted in maximum AAS signals. Optimum flow rates were determined as O_2 = 270 mL/min and H_2 = 1.2 L/min. The response to sequentially diluted Cd standard solutions (N = 4) is presented in Figure 3. The calibration

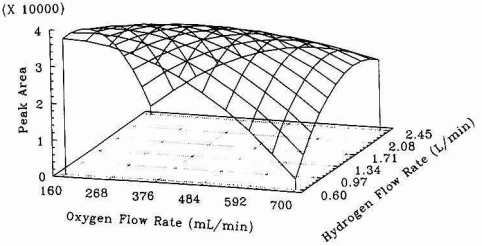

Figure 2. Surface predicting response (peak area) to 3 ng of Cd as a function of O_2 and H_2 flow rates, in the flow injection mode.

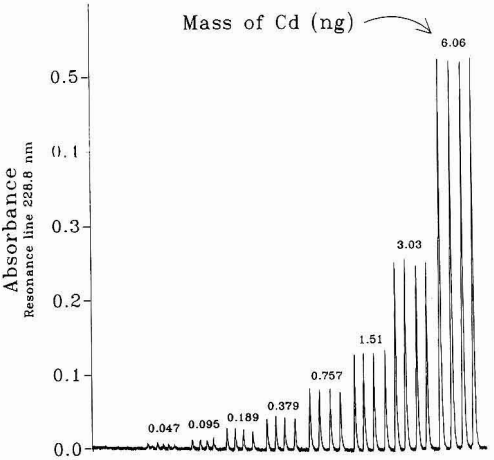

Figure 3. AAS responses to sequentially diluted Cd standards in the flow injection mode (N = 4).

model was linear over the studied range (r = 0.9981). The absolute limit of detection, determined as three relative standard derivations of the average background signal, was 71 pg.

Applications to biological samples demanded additional characterization studies on possible analytical interferents. As the interface was to be used in HPLC–AAS mode for the determination of sulfhydryl-rich polypeptides, we studied the effect of major components present in these complex analytes. MTs normally coordinate the essential metals Zn and Cu. Glutathione was used to mimic the high cysteine content and lack of aromatic amino acids in the primary structure of MTs. The surface response models predicting the matrix effect of large excesses of these species when coinjected with Cd (8.6 pmol) are presented in Figure 4. In the absence of cadmium, a nonspecific absorption signal was not observed at the highest levels of each interferent. In the absence of Cu or Zn, glutathione affected the atomization efficiency linearly to a maximum of 6.5% (34 884-fold molar excess relative to Cd). The formation of CdS during the combustion process may account for this effect, which diminished as the concentration of Zn or Cu in the sample was increased up to 174-fold molar excess. Copper and zinc appeared to quench the atomization process to maxima of 13% and 7%, respectively. Since the relative stoichiometry of Cd:Cu/Zn:amino acids in metallothioneins is not predicted to be higher than 1:10:100,[2] these potential interferents were not expected to significantly affect the response of MT-bound cadmium in HPLC bands.

The interface was then exposed to biological samples, in the flow injection mode. The soluble cadmium fraction from

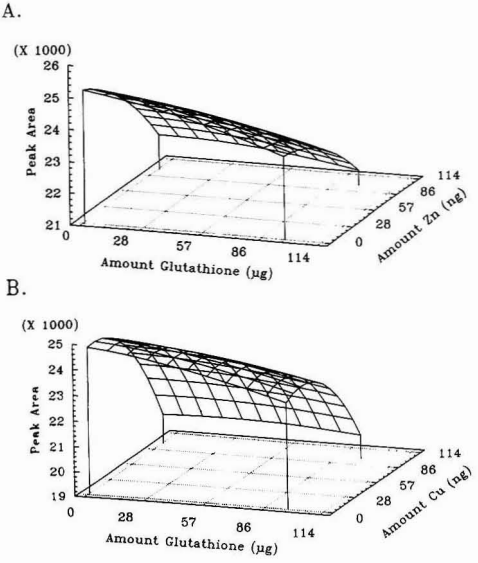

Figure 4. Surface responses to Cd (0.97 ng) coinjected with various amounts of (A) glutathione and Zn and (B) glutathione and Cu.

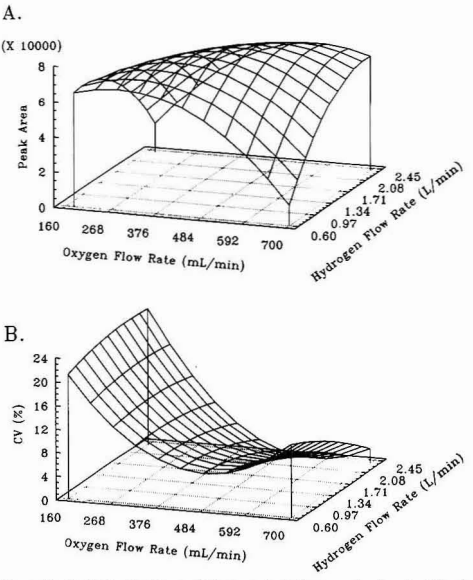

Figure 5. Optimization for cadmium analysis in mussel extracts. Effect of O_2 and H_2 flow rates on (A) peak area and (B) coefficient of variability (four replicate injections).

mussel tissues was prepared by homogenization in Tris–HCl buffer, centrifugation, and dilution (10-fold). Without the filtration effect of the HPLC column, considerable amounts of organic matter and metallic species were copyrolyzed with the analyte. Adjustment of the flame composition was required to reduce variations in performance. The effects of H_2/O_2 flow rates on AAS response and reproducibility (N = 4) with a mussel extract are presented in Figure 5. The level of cadmium in the sample aliquot was estimated at 6.2 ng (87 × LOD). The response to Cd (Figure 5A) was maximized using a more voluminous flame. As shown in Figure 5B the flame composition critically affected the reproducibility of the microatomization process. Low oxygen supply produced a cooler flame which did not pyrolyze the sample efficiently. A black deposit on the walls of the combustion chamber adsorbed the analyte, causing up to 23% variation in AAS response. The deposited cadmium was recovered as a sharp peak by increasing the H_2/O_2 flow rates. An excess of oxygen was also detrimental, presumably due to a combination of factors: (1) at low H_2 flow rates the flame was almost extinguished, and (2) at higher H_2 flow rates the tip of the flame reached the optical tube, decreasing the S/N ratio and affecting the precision of the integration algorithm. Optimal response and reproducibility were observed using a fuel-rich flame obtained with an intermediate oxygen flow rate and a relatively large hydrogen supply (550 mL/min and 2.3 L/min, respectively).

Validation of the AAS signal observed during flow injection of crude mussel extracts (N = 3) was done using D_2 background correction (for nonspecific absorption signal) and standard addition methods (for atomization quenching). The average ratio between total and background-corrected absorbances was 0.99 ± 0.036. Taking into account the relatively large volume of sample injected in the microatomizer (97 μL) and the crude composition of the mussel extracts, we concluded that nonspecific absorbance signals do not represent a significant source of error. The magnitude of interference to the cadmium atomization efficiency was evaluated by comparing the slopes of standard addition calibrations from a mussel extract and from a 3 ng/mL Cd standard. Both standard addition curves were linear (N = 5; r = 0.9886 and 0.9972, respectively). The slope of the sample calibration was reduced by 13.8% relative to that of the standard calibration, which reflected quenching of the atomization process. As with other atomic spectroscopy techniques, external calibration of the flow injection microatomizer AAS system should be used with precaution. For crude samples, standard addition appears to be the most appropriate calibration technique.

Characterization of the Soluble Cadmium Fraction in Mussel Tissues. The microatomizer interface was developed as a component of a routine analytical protocol for the study of heavy metals bioaccumulation in the fresh water mussel *E. complanata*. In a preliminary experiment aimed at optimizing this protocol, we exposed a mussel colony to 100 ng/mL Cd, sampled periodically (N = 3), and determined the soluble cadmium content in homogenates before and after ultrafiltration through a 1 kDa cutoff membrane (Figure 6). Cadmium levels were calculated by external standardization corrected for matrix effect (as determined by standard addition calibration). As observed previously in other *Unionidae* mussels,[14,15] soluble cadmium accumulated at a relatively constant rate and with significant biological variations during the 4-week exposure period. Most of this soluble Cd was bound to large biomolecules. Levels of "free cadmium" in ultrafiltrates remained essentially constant at 2–4% of soluble Cd. Given the relatively low Cd concentration and short exposure period, it is probable that a saturation of coordination sites in soluble proteins has not been achieved.

Determination of Metallothioneins. The microatomizer was applied to the determination of metallothioneins in the HPLC–AAS mode, using the standard DEAE ion-exchange method (Figures 7 and 8). Both MT-I and MT-II isoforms

(15) Hemelradd, J.; Holwerda, D. A.; Teerds, K. J.; Herwig, H. J.; Zandee, D. I. *Arch. Environ. Toxicol.* **1986**, *15*, 9–21.

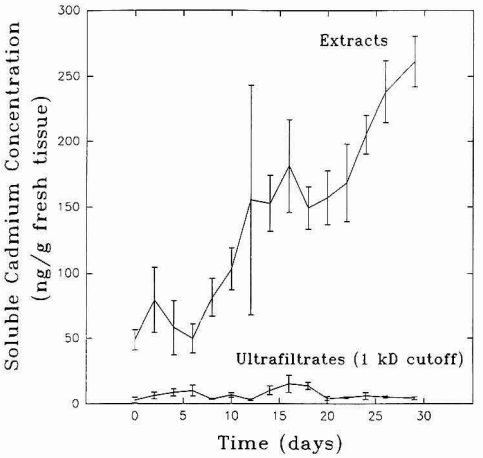

Figure 6. Level of souble bound (>1 kDa) and free cadmium in whole mussel tissues ($N = 3$) as a function of exposure time.

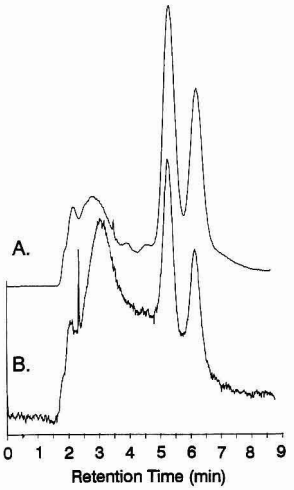

Figure 7. HPLC–microatomizer AAS chromatograms of a commercial horse kidney extract containing Cd- and Zn-MTs I and II isoforms: (A) 4.85-μg total proteins, with integrator gain set at 1; (B) 485-ng total proteins, with integrator gain set at 20. Chromatograms were obtained isocratically (15 mM Tris–HCl, pH 7.21).

from a crude commercial horse kidney extract were separated isocratically using a 15 mM Tris–HCl buffer (Figure 7). On the basis of the specifications of the supplier, the LOD for horse kidney MTs was estimated conservatively at 10–40 ng. The mussel extracts contained a single peak which was eluted using a stronger buffer (Tris–HCl, 100 mM). As this chromatographic band was recovered in solution after thorough thermocoagulation and centifugation of the extract (Figure 8A), we confirmed it as a metallothionein fraction.[8] Since the mussel population was intentionally exposed to cadmium under extreme starving conditions, cysteine and other amino acids required in the biosynthesis of MTs were limited to endogenous sources only. Whereas the concentration of soluble Cd increased 5-fold during the exposure, the magnitude of the cadmium-containing metallothionein peak only increased by a factor of 1.5 (Figure 8B), suggesting that a significant proportion of Cd was bound to other soluble

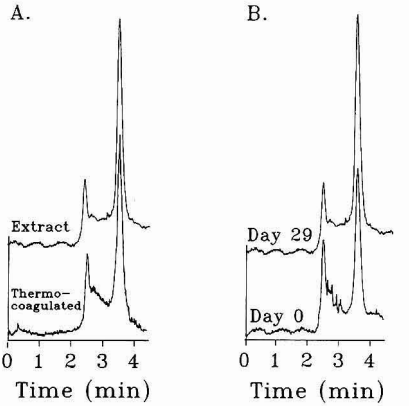

Figure 8. HPLC–microatomizer AAS chromatograms from (A) a mussel extract before and after a thermocoagulation/centrifugation treatment aimed at confirming the presence of a metallothioneins fraction and (B) extracts from mussels sampled at the beginning of the trial (control) and after 29 days of exposure to 100 μg/L Cd, in starving conditions.

proteins. We are currently exposing mussel colonies, fed with microplankton, in order to determine the biosynthesis rate of this metal-binding polypeptide fraction under environmentally relevant conditions. Calibration (as a function of AAS response to Cd) will be obtained via isolation of Cd-saturated MT and determination of its amino acid profile.

CONCLUSION

For the determination of cadmium in aqueous samples, the FI/HPLC–microatomizer AAS approach provided a unique combination of advantages over alternate techniques. While the microatomizer interface was constructed with inexpensive components, it effectively pyrolyzed organic interferents and provided a limit of detection for cadmium which was about 2.2 orders of magnitude lower than that observed with a conventional flame AAS detector, and 27-fold lower than that obtained with a thermospray-enhanced flame AAS system.[10] In HPLC–AAS mode, the detectability of Cd-containing MTs was improved by similar factors.

As reported previously,[11] continuous exposure to high concentrations of sodium (from HPLC buffers) promotes devitrification of the quartz combustion chamber and corrosion of the silica capillary used to thermospray the HPLC effluent. Further improvements to the physical strength of the interface will include the development of a ceramic combustion chamber and the use of a metallic thermospray capillary. The performance of the microatomizer in the determination of other volatile metals is currently being investigated.

ACKNOWLEDGMENT

The authors gratefully ackowledge financial support from the Natural Science and Engineering Research Council of Canada, the Fonds FCAR, and Fisheries and Oceans Canada.

RECEIVED for review May 27, 1992. Accepted September 18, 1992.

Determination of Ethers and Alcohols in Gasolines by Gas Chromatography/Fourier Transform Infrared Spectroscopy

John W. Diehl,* John W. Finkbeiner, and Frank P. DiSanzo

Mobil Research and Development Corporation, Paulsboro Research Laboratory, Paulsboro, New Jersey 08066

INTRODUCTION

In response to clean fuel legislation, research is underway in the petroleum industry to develop fuels which reduce vehicle exhaust emissions. Part of this effort is the addition of certain ethers and alcohols such as methyl *tert*-butyl ether (MTBE) and ethanol to gasolines. The capability of accurately measuring these compounds is important in maintaining minimum levels prescribed by law as well as optimum levels for engine performance. A number of techniques have been developed to determine ethers and alcohols such as ASTM D4815,[1] the oxygen specific FID (O-FID),[2] and atomic emission detection (AED).[3] All of these methods have had some problem such as hydrocarbon interference with D4815 and reliability with the O-FID and AED. This compound class has distinct absorbances in the mid-infrared.[4] Solution infrared spectroscopy cannot readily deal with mixtures of ethers and alcohols which can potentially occur by deliberate blending or from impurities in the feed ethers such as methanol, *tert*-butyl alcohol, and even *tert*-amyl methyl ether in the case of MTBE. Gas chromatography (GC), however, to first resolve the compounds followed by infrared spectroscopy addresses this problem. GC/Fourier transform infrared (FTIR) spectroscopy has already been demonstrated as a good quantitative tool for organic acids[5] and various pollutants.[6] The results of our investigation into the applicability of GC/FTIR for oxygenates in fuel are presented below.

EXPERIMENTAL SECTION

A Hewlett-Packard Model 5890 Series II GC/5965B IRD was configured as follows.

Column: J&W 60-m × 0.32-mm-i.d. 5.0-μm film DB-1. The column was connected to a 0.5-m section of J&W 0.53-mm-i.d. deactivated fused silica tubing with a Swagelok low dead volume $^1/_{16}$-in. union. This retention gap was installed in the injector to allow use of the HP 7673B autosampler.

Carrier: H_2, 42 cm/s set at 300 °C (approximately 20 psi).

Oven temperature program: 20 °C (0 min) 2 deg/min to 80 °C (0 min) 30 deg/min to 300 °C.

Injector: Cool on-column capillary injector with heater turned off. Injector temperature was approximately 5 °C higher than the oven temperature.

FTIR Spectrometer Parameters. *Detector*: wide band MCT (4000–550 cm^{-1}) (nominal $D^* = 1.0 \times 10^{10}$ $cm \cdot Hz^{0.5}/W$).

Light pipe temperature: 250 °C.

Transfer line temperature: 250 °C.

Resolution: 8 cm^{-1}.

Scan rate: six interferograms coadded for 1 spectrum per second.

Selective absorbance reconstructions: second difference reconstruction. Derivative function width = 75.[7,8] Table I contains the frequencies for each compound. These were the absorbance maxima in the region of interest ±4 cm^{-1}. A reference spectrum for each sample's reconstructions was obtained by averaging the spectra from 0.1 to 0.5 min run time. No analyte or gasoline component eluted during this retention time window.

Table I. Reconstruction Frequencies

compound	frequency range (cm^{-1})	compound	frequency range (cm^{-1})
methanol	1055–1063	diisopropyl ether	1122–1130
ethanol	1052–1060	isobutyl alcohol	1037–1045
2-propanol	1141–1149	ethyl *tert*-butyl ether	1199–1207
tert-butyl alcohol	1207–1215	1,2-dimethoxyethane (ISTD)	1123–1131
1-propanol	1056–1064	1-butanol	3665–3673
methyl *tert*-butyl ether	1205–1213	*tert*-amyl methyl ether	1185–1193
2-butanol	1128–1136		

Table II. Analyte Densities at 25 °C

compound	density (g/mL)	compound	density (g/mL)
methanol	0.781	2-butanol	0.787
ethanol	0.782	diisopropyl ether	0.717
2-propanol	0.771	isobutyl alcohol	0.788
tert-butyl alcohol	0.764	ethyl *tert*-butyl ether	0.737
1-propanol	0.791	1-butanol	0.792
methyl *tert*-butyl ether	0.733	*tert*-amyl methyl ether	0.768

Table III. Selectivities over Toluene

compound	selectivity	compound	selectivity
methanol	43	diisopropyl ether	>1000
ethanol	42	isobutyl alcohol	24
2-propanol	4	ethyl *tert*-butyl ether	152
tert-butyl alcohol	77	1,2-dimethoxyethane (ISTD)	>1000
1-propanol	22	1-butanol	143
methyl *tert*-butyl ether	124	*tert*-amyl methyl ether	119
2-butanol	>1000		

Pure ethers and alcohols were obtained from Aldrich Chemical Co. and Wiley Organics. Twenty calibration solutions were prepared in the 0–20 vol % range by pipetting and weighing aliquots in 1-mL increments of the analytes with 10 mL of 1,2-dimethoxyethane which was the internal standard (ISTD) and diluting to 100 mL with toluene. Multilevel calibration curves were developed on a weight/weight basis. Calibrations in a base fuel did not improve accuracy. Gasolines were analyzed by weighing the internal standard into a known volume and weight of sample and determining the weight of the ether or alcohol from the calibration curves. The volume percent was calculated by dividing the determined weight by the density of the compound of interest with this volume divided by the starting sample volume. Table II contains the densities used for these measurements. There were some small differences between the literature values and those measured in the laboratory.

(1) ASTM D4815-88.
(2) DiSanzo, F. P. *J. Chromatogr. Sci.* **1990**, *28*, 73–74.
(3) Slatkavitz, K. J.; Uden, P. C.; Barnes, R. M. *J. Chromatogr.* **1986**, *355*, 117.
(4) Silverstein, R. M.; Bassler, G. C. *Spectrometric Identification of Organic Compounds*, 2nd ed.; John Wiley & Sons, Inc.: New York, 1967.
(5) Olson, E. S.; Diehl, J. W.; Froehlich, M. L. *Anal. Chem.* **1988**, *60*, 1920–1924.
(6) Gurka, D. F.; Pyle, S. M. *Environ. Sci. Technol.* **1988**, *22*, 963–967.
(7) de Haseth, J. A.; Isenhour, T. L. Reconstruction of Gas Chromatograms from Interferometric Gas Chromatography/Infrared Spectrometry Data. *Anal. Chem.* **1977**, *49*, 49.
(8) Bowater, I. C.; Brown, R. S.; Cooper, J. R.; Wilkins, C. L. Maximum Absorbance Algorithm for Reconstruction of Gas Chromatograms from Gas Chromatograph/Infrared Spectrometry Data. *Anal. Chem.* **1986**, *58*, 2195.

0003-2700/92/0364-3202$03.00/0

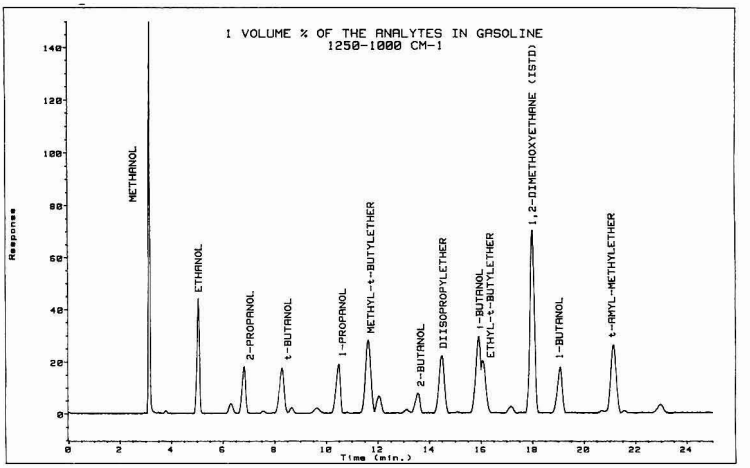

Figure 1. 1250–1000-cm^{-1} selective absorbance chromatogram of the analytes and ISTD at 1 volume % each in gasoline. Unlabeled peaks are from hydrocarbons.

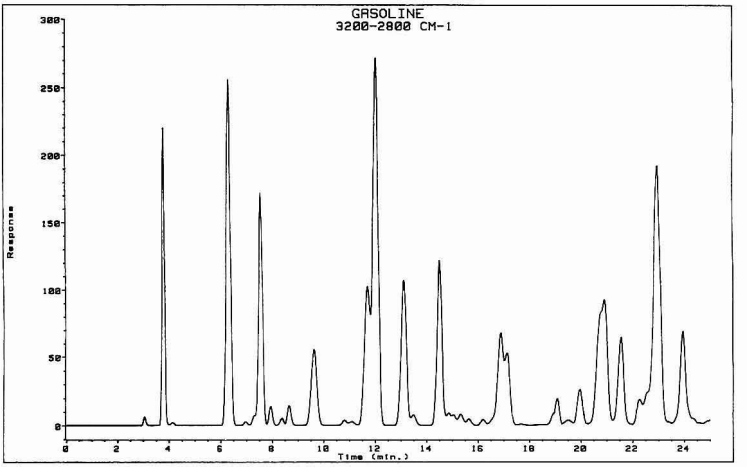

Figure 2. 3200–2800-cm^{-1} selective absorbance chromatogram of a typical gasoline highlighting the large number of coeluting and potentially interfering compounds.

RESULTS AND DISCUSSION

Figure 1 shows a GC/FTIR chromatogram of the analytes reconstructed from 1250 to 1000 cm^{-1}. Most analyses were performed in this C–O stretching region. All of the compounds were chromatographically well resolved except for isobutyl alcohol and ETBE. Better separation could have been obtained by starting at a lower oven temperature, but at a sacrifice of analysis time. The absorbance maxima of isobutyl alcohol and ETBE, 1041 and 1203 cm^{-1}, respectively, were sufficiently different that they were measurable even with coelution. Figure 2 shows a 3200–2800-cm^{-1} chromatogram of a typical gasoline which highlights the potential hydrocarbon interferences. Gasolines usually contain C4–C12 saturates and olefins and C6–C12 one- and two-ring aromatics all of which have strong absorbances in the 3200–2800-cm^{-1} spectral region. These classes also have some absorbance in the 1250–1000 cm^{-1} range resulting from methylene twisting and wagging, and aromatic C–H in-plane bending.[4] Of these, the aromatic absorption is the most intense. This can be seen in Figure 3 where the gasoline from Figure 2 was reconstructed between 1250 and 1000 cm^{-1}. Even though there are no ethers or alcohols in this fuel, a number of peaks can be seen. By GC/FID, 2-methylpentane which eluted at 12 min was about 5.5 wt % of the sample while benzene at 20.5 min was about 1.5 wt %, yet their peak areas in the 1250–1000-cm^{-1} region were approximately equal.

GC/FTIR was not found to be as selective over hydrocarbons as oxygen-specific detectors,[2,3] and Table III contains selectivities relative to toluene. These were calculated by dividing the chromatographic peak area of 1 volume % of an analyte at its respective selective wavelength reconstruction region by the chromatographic peak area of 1 volume % of toluene at the analyte's wavelength region. The selectivities ranged from 4 to >1000. Reconstructions at the narrow frequency ranges listed in Table II were necessary to completely eliminate coeluting hydrocarbon interferences. No background hydrocarbon signals were present in any selective absorbance reconstructions of a number of gasolines

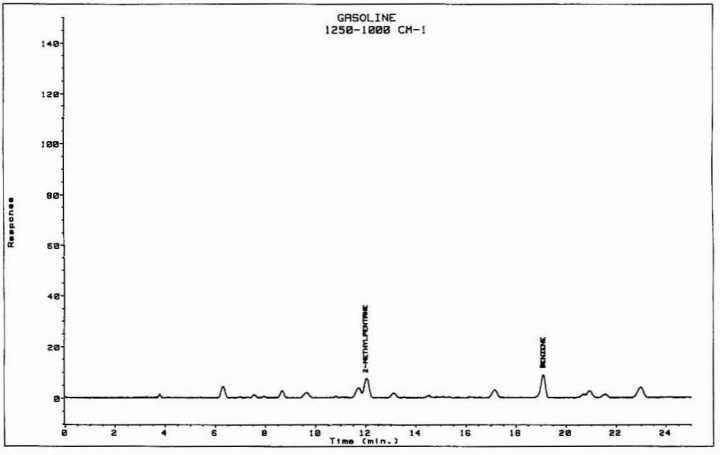

Figure 3. 1250–1000-cm^{-1} selective absorbance chromatogram of the same gasoline as in Figure 2 which shows that the gasoline hydrocarbons have some signal in the C–O stretching region.

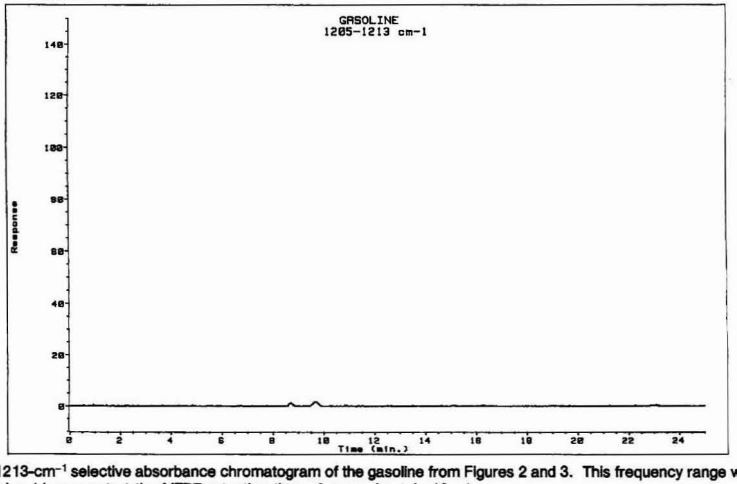

Figure 4. 1205–1213-cm^{-1} selective absorbance chromatogram of the gasoline from Figures 2 and 3. This frequency range was used for MTBE quantitation. No signal is present at the MTBE retention time of approximately 12 min.

and blending feeds. This can be seen in Figure 4 where a typical gasoline has been reconstructed at MTBE's frequency range of 1205–1213 cm^{-1}. No peak is evident at the MTBE retention time of 12 min. Figure 5 shows the 1205–1213-cm^{-1} chromatogram of the 1 volume % mixture from Figure 1. The narrow reconstruction frequency reduced the MTBE signal by approximately 50% compared to the wider range of 1250–1000 cm^{-1}. There was a problem in the case of 1-butanol's C–O stretching absorbance at 1042 cm^{-1}. This alcohol coeluted with benzene, a common component in gasolines typically found in the 1–2 wt % range. The selectivity of 1-butanol over benzene at 1042 cm^{-1} was only 3. 1-Butanol had to be analyzed at the O–H stretching frequency of 3669 cm^{-1} where the selectivity was 143. Since this is a weaker IR band the detection limit for this compound was 0.5 volume % compared to 0.1% for the other analytes.

Although no quantitation problems were encountered with the 12 compounds addressed here, this was definitely a situation where both gas chromatography and infrared spectroscopy were needed to ensure good analytical data. If other ethers or alcohols are to be determined, interference problems have to be addressed, especially if coelution with an aromatic hydrocarbon can occur.

All calibration curves were linear even up to 95 volume % with correlation coefficients >0.999. This was more in line with the results reported by Gurka and Pyle[6] than the nonlinear ones reported by Olson et al.[5] In the latter case, the analytes and their respective internal standards not only coeluted chromatographically but had relatively close C=O absorptions. This may explain the nonlinear calibrations.

All calibration curves were found to be stable for several months. Table IV contains precision and accuracy data for the analytes at the 5, 10, and 15 volume % levels in gasoline (7.7 mg/mL = approximately 1 volume %). The average relative standard deviation (RSD) ($n - 1$) was 0.3%, and the average percentage accuracy was 0.8%. The RSD with split injection was 1.0%, and on-column injection was definitely the more precise injection technique. There was some peak shape distortion with C4 alcohols above the 10% level apparently from overload of the 5.0-μm film column, and this

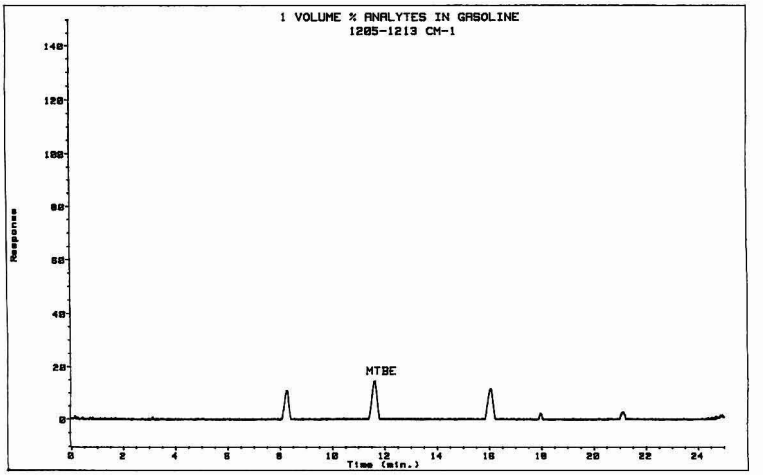

Figure 5. 1205–1213-cm^{-1} selective absorbance chromatogram of the 1 volume % analyte mixture from Figure 1. The narrow reconstruction frequency reduced the MTBE signal by approximately 50%.

Table IV. Precision and Accuracy Data[a]

compound	determined (mean mg/mL)	actual (mg/mL)	RSD ($n-1$)	% accuracy
methanol	39.11	39.14	0.5	0.1
ethanol	39.19	38.93	0.1	0.7
2-propanol	38.52	38.49	0.2	0.1
tert-butyl alcohol	36.85	37.45	0.3	1.6
1-propanol	39.58	39.43	0.2	0.4
methyl *tert*-butyl ether	36.50	36.91	0.4	1.1
2-butanol	39.18	39.18	0.4	0.1
diisopropyl ether	36.08	36.93	0.2	2.3
ether isobutyl alcohol	39.08	39.18	0.2	0.3
ethyl *tert*-butyl ether	36.50	36.04	0.4	1.3
1-butanol	38.42	39.41	0.3	2.0
tert-amyl methyl ether	38.15	38.52	0.4	1.0
methanol	84.25	82.67	0.2	1.9
ethanol	82.07	81.49	0.1	0.7
2-propanol	81.43	80.96	0.1	0.6
tert-butyl alcohol	78.21	78.50	0.5	0.4
1-propanol	83.76	82.67	0.2	1.3
methyl *tert*-butyl ether	74.33	74.22	0.3	0.1
2-butanol	83.75	82.07	0.3	1.5
diisopropyl ether	72.97	72.51	0.2	0.6
isobutyl alcohol	82.73	80.91	0.2	1.0
ethyl *tert*-butyl ether	73.24	73.94	0.1	1.0
1-butanol	82.29	83.70	0.2	1.0
tert-amyl methyl ether	76.13	77.05	0.1	1.2
methanol	118.16	117.83	0.3	0.3
ethanol	117.68	117.56	0.1	0.1
2-propanol	116.48	116.48	0.1	0.0
tert-butyl alcohol	112.98	114.52	0.2	1.3
1-propanol	119.06	119.11	0.3	0.0
methyl *tert*-butyl ether	110.62	110.86	0.8	0.2
2-butanol	119.43	119.31	0.5	0.1
diisopropyl ether	108.78	108.63	0.5	0.1
isobutyl alcohol	118.74	118.35	0.1	0.3
ethyl *tert*-butyl ether	109.84	111.17	0.6	1.2
1-butanol	118.03	120.06	0.6	1.7
tert-amyl methyl ether	113.79	115.63	0.6	1.6

[a] $n = 10$. 7.7 mg/mL = approximately 1 volume %.

had an adverse effect on accuracy. Accuracy was improved when these solutions were diluted 5:1 with toluene. Sample dilution was not normally performed because of analysis time requirements.

Table V. Analysis of Fuels

fuel	interlab[a] (volume %)	O-FID	GC/FTIR
A	MTBE 14.6 ± 0.3[b]	14.9[c]	14.4 ± 0.2[d]
B	MTBE 14.5 ± 0.9	15.1	14.6 ± 0.2
C	MTBE 13.9 ± 0.8	14.7	13.9 ± 0.2
D	MTBE 14.6 ± 0.8	14.8	14.8 ± 0.2
E	MTBE 15.2 ± 0.9	15.5	14.9 ± 0.2
F	ETOH 9.7 ± 0.6	9.8	9.0 ± 0.1
G	ETOH 9.7 ± 0.7	9.5	9.4 ± 0.1
H	ETOH 9.6 ± 0.5	9.9	9.3 ± 0.1
I	ETOH 9.6 ± 0.7	9.7	9.0 ± 0.1

[a] Mean of D4815 results from 7 to 9 participating laboratories. [b] Standard deviation, $2s$ = 95% confidence limit. [c] Precision data not available for O-FID. [d] From Table IV.

Table V shows the analyses of a number of test fuels compared to O-FID, and the mean of the results from 7 to 9 laboratories employing D4815. Although the GC/FTIR results seemed to be lower than those of the O-FID, all results were well within the precisions of the methods. The RSD's reported for D4815 ranged from 2 to 7%, which were much worse than the 0.1–0.8% reported here for GC/FTIR (Table IV). Precision data was not available for the O-FID.

CONCLUSION

GC/FTIR is definitely a precise and accurate technique for measuring C1–C4 alcohols and C5 and C6 ethers in gasolines. The use of the correct absorbance reconstruction frequencies gives good selectivity over hydrocarbons as well as very linear and stable calibration curves. These features should make it applicable to the analysis of other ethers and alcohols as well as other compound classes as long as possible chromatographic and spectroscopic interferences are kept in mind.

RECEIVED for review July 2, 1992. Accepted September 30, 1992.

Stripping Voltammetry of Reversible Redox Species by Self-Induced Redox Cycling

Tsutomu Horiuchi,* Osamu Niwa, Masao Morita, and Hisao Tabei

NTT Basic Research Laboratories, Nippon Telegraph and Telephone Corporation, Tokai, Ibaraki 319-11, Japan

INTRODUCTION

Voltammetry has been widely used to analyze electroactive species in solution because of its simplicity. However, the typical detection limits of cyclic and linear sweep voltammetry are in the micromolar range. At these concentrations it is difficult to detect the amounts of trace materials. Various pulse methods have been proposed to improve the sensitivity of voltammetry. Their use has a detection limit 1 or 2 orders of magnitude lower than that of cyclic or linear sweep voltammetry.[1,2]

Electrode miniaturization also improves the sensitivity. This is because a microelectrode has high mass transport density, small double layer capacitance, and low ohmic losses which result in a higher S/N ratio than that of a conventional size electrode.[3] We have reported that redox cycling on two closely spaced potentiostated microelectrodes increases the sensitivity of the reversible redox species and has been used to obtain a detection limit of 10^{-8} mol/dm^3.[4] However, the sensitivity of these methods is not as high as with the stripping analysis.

Stripping voltammetry has the lowest detection limit of the commonly used electroanalytical techniques.[1,2] It has been applied for the detection of metal ions and halides in water, foods, biological fluid, and environmental samples.[5–13] The detection limit of stripping voltammetry for heavy metal ions is from 10^{-10} to 10^{-11} mol/dm^3. Despite its high sensitivity, stripping voltammetry can only be used to detect a limited range of species, which includes some metal ions, halides, or adsorptive organic compounds, unless special techniques are employed such as electrode modification or the addition of ligands to form adsorptive complexes.[14–18] However, the experimental conditions for electrode modification or ligand formation must be optimized for individual samples in order to deposit them efficiently on the electrode surface.

Recently, we enhanced the limiting current by self-induced redox cycling at a closely spaced micro–macro twin electrode. This was achieved by applying potential only to the microelectrode.[19] Figure 1A shows the mechanism of self-induced redox cycling. When sufficient potential to electrolyze the redox species is applied to a microelectrode placed very close to a macroelectrode, the electroactive species produced on the former diffuses to the neighborhood of the latter. The oxidative reaction R → O is induced on the macroelectrode edge nearest to the microelectrode, and the reductive reaction O → R is induced on the far edge. The oxidized species produced at the macroelectrode edge nearest to the microelectrode diffuse back to the microelectrode and are reduced again; then self-induced redox cycling is established between the micro- and macroelectrodes. Since electrons produced in the electrochemical reaction on the nearest edge of the macroelectrode are consumed in the reverse electrochemical reaction on the far edge of the macroelectrode, the current flows from the far edge to the nearest edge.

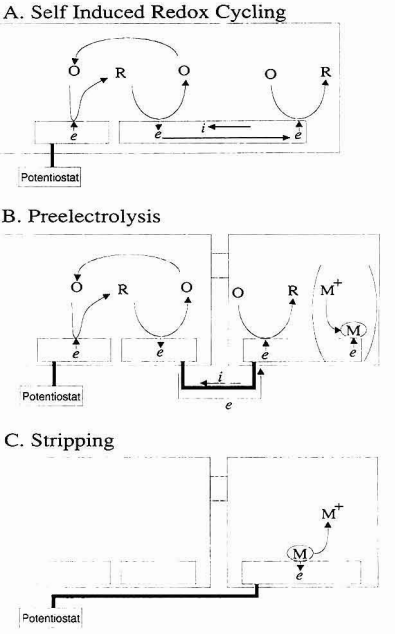

Figure 1. Schematic diagram of self-induced redox cycling and new stripping voltammetry. (A) Mechanism of self-induced redox cycling. Micro- and macroelectrodes were placed in the same cell. (B) Self-induced redox cycling in a two-cell system. A twin microelectrode was placed in one cell and a macroelectrode in the other cell. The two cells were connected by a salt bridge (hatched area). One electrode of the twin microelectrode was electrically connected to the macroelectrode. The preelectrolysis mechanism of the new stripping voltammetry is in parentheses. Preelectrolysis of the reversible species at the twin electrode induces the preconcentration of metal. (C) Metal stripping stage on the macroelectrode.

The self-induced redox cycling effect also occurred in a two cell-system as shown in Figure 1B. In order to construct a closely spaced microelectrode/macroelectrode pair, twin microelectrodes and a macroelectrode were placed in respective cells. One of the twin microelectrodes was connected to the macroelectrode by a lead. With this cell system, the charge produced by the self-induced redox cycling in the left cell is

(1) Bard, A. J.; Faulkner, L. R. *Electrochemical Methods*; John Wiley & Sons: New York, 1980.
(2) Kissinger, P. T.; Heineman, W. R. *Laboratory Techniques in Electroanalytical Chemistry*; Marcel Dekker, Inc.: New York, 1984.
(3) Fleishmann, M.; Pons, S.; Rolison, D. R.; Schmidt, P. P. *Ultramicroelectrodes*; Datatech Systems, Inc.: Morganton, NC, 1987.
(4) Niwa, O.; Morita, M.; Tabei, H. *Anal. Chem.* **1990**, *62*, 447.
(5) Florence, T. M. *J. Electroanal. Chem. Interfacial Electrochem.* **1972**, *35*, 237.
(6) Florence, T. M. *Anal. Chim. Acta* **1982**, *141*, 73.
(7) Anderson, L.; Jagner, D.; Josefson, M. *Anal. Chem.* **1982**, *54*, 1371.
(8) Sadana, R. S. *Anal. Chem.* **1983**, *55*, 304.
(9) Kinard, J. T. *Anal. Lett.* **1977**, *10* (14), 1147.
(10) Hu, A.; Dessy, R. E.; Graneil, A. *Anal. Chem.* **1983**, *55*, 320.
(11) Schieffer, G. W.; Blaedel, W. J. *Anal. Chem.* **1978**, *50*, 99.
(12) Figura, P.; McDuffie, B. *Anal. Chem.* **1979**, *51*, 120.
(13) van den Berg, C. M. G. *Anal. Lett.* **1984**, *17*, 2141.
(14) van den Berg, C. M. G.; Jacinto, G. S. *Anal. Chim. Acta* **1988**, *211*, 129.
(15) Wang, J.; Varughese, K. *Anal. Chim. Acta* **1987**, *199*, 185.
(16) Wang, J.; Farias, P. A. M.; Mahmoud, J. S. *Anal. Chim. Acta* **1985**, *171*, 215.
(17) van den Berg, C. M. G. *Analyst* **1989**, *114*, 1527.
(18) Moreira, J. C.; Zhao, R.; Fogg, A. G. *Analyst* **1990**, *115*, 1561.
(19) Horiuchi, T.; Niwa, O.; Morita, M.; Tabei, H. *J. Electrochem. Soc.* **1991**, *138*, 3549.

0003-2700/92/0364-3206$03.00/0

transmitted to the electrochemical reaction of a different species in the right cell.

We developed a new stripping method using this self-induced redox cycling effect in two cells which contain different electroactive species. The left cell is filled with a sample solution containing the redox species and the right cell is filled with an electrolyte containing metal ions. A twin microelectrode at which the redox cycling occurs and an electrode on which the metal ions can be deposited are placed in the left and right cells, respectively. At the preconcentration stage, the oxidative current of the redox species at the twin microelectrode in the left cell is transmitted to deposit metal ions on the electrode in the right cell (in parentheses of Figure 1B). After a fixed period of preelectrolysis, the quantity of metal ions deposited on the electrode in the right cell can be evaluated by conventional stripping voltammetry, which is measured by sweeping the potential of the macroelectrode (Figure 1C). Since the amount of metal deposited on the electrode in the right cell is related to the concentration of the redox species in the left cell, we can estimate the concentration from the large stripping peak of the metal. Highly sensitive detection of the redox species can be achieved by this combination of electrodes without directly preconcentrating the electroactive species on the electrode surface.

In this paper, we present the first example of a new stripping analysis of reversible redox species based on self-induced redox cycling with an interdigitated array (IDA) and a glassy carbon combination electrode.

EXPERIMENTAL SECTION

Electrodes. In this experiment, the combination electrode at which the self-induced redox cycling occurred, consisted of an interdigitated array electrode (IDA) and a glassy-carbon electrode (BAS, West Lafayette, IN). The IDA was used for the redox cycling, and the glassy-carbon electrode was used for metal ion deposition. The IDA electrode consisted of two series of finger electrodes. The finger widths and gaps were all 2 μm, and each finger was 2 mm long. The IDA consisted 750 pairs and was fabricated on a thermally oxidized silicon wafer by photolithographic, lift off, and dry etching techniques, as described elsewhere.[20-22] The diameter of the glassy-carbon electrode was 3 mm. The reference and auxiliary electrodes were a Ag/AgCl electrode (BAS, West Lafayette, IN) and a platinum wire, respectively.

Chemicals and Apparatus. Potassium nitrate (Wako Chemicals, Osaka, Japan), Ruthenium(III) hexaammine chloride ($[Ru(NH_3)_6]Cl_3$, ruthenium hexaammine) (Johnson Matthey/Alfa Products, Ward Hill, MA), pH 4.0 standard buffer solution (0.05 mol/dm^3 potassium hydrogen phthalate) (Nakarai Chemicals LTD, Kyoto, Japan), and silver nitrate (Kanto Chemicals, Kyoto, Japan) were used as purchased.

Electrochemical measurements were performed using a twin potentiostate HECS 990 (Huso, Kanagawa, Japan), a potential sweep unit 175 (Princeton Applied Research, Princeton, NJ), and an $X-Y$ recorder 3025 (Yokogawa Denki, Tokyo, Japan). A magnetic stirrer PC-351 (Iwaki Glass, Tokyo, Japan) was used to stir the electrolyte.

Cells. Figure 2 shows a schematic diagram of the measurement system. Two small glass cells were connected by a salt bridge. A 0.05 mol/dm^3 standard buffer solution containing 1 μmol/dm^3 ruthenium hexaammine was used in the left cell. A 0.1 mol/dm^3 potassium nitrate solution containing 1 μmol/dm^3 silver nitrate was used in the right cell. The salt bridge was made of a glass tube, whose interior diameter was 5 mm. A Vycor disk, G0070 (Princeton Applied Research, Princeton, NJ), was connected to each end of the glass tube with Teflon heat-shrink tubing. The electrolyte in the salt bridge was saturated potassium nitrate solution.

(20) Sanderson, D. G.; Anderson, L. B. *Anal. Chem.* **1985**, *57*, 2388.
(21) Aoki, K.; Morita, M.; Niwa, O.; Tabei, H. *J. Electroanal. Chem. Interfacial Electrochem.* **1988**, *256*, 269.
(22) Niwa, O.; Morita, M.; Tabei, H. *J. Electroanal. Chem. Interfacial Electrochem.* **1989**, *267*, 291.

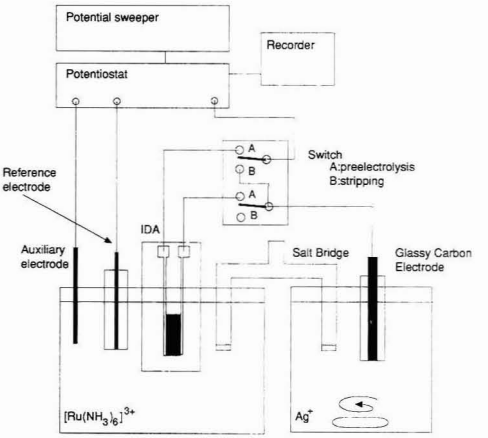

Figure 2. Schematic diagram of the measurement system.

A reference electrode, auxiliary electrode, and IDA working electrode were placed in the left cell, and the glassy-carbon electrode was placed in the right cell. The reference and auxiliary electrodes were directly connected to the potentiostat. The working electrode terminal of the potentiostate, the two terminals of the IDA working electrode, and the glassy-carbon electrode were connected to a switch box. When the switch was in the A position, one working electrode of IDA was connected to the potentiostat and the other working electrode was connected to the glassy-carbon electrode. In position B, the glassy-carbon electrode was directly connected to the potentiostat.

Procedures. As with the conventional stripping method, our new method requires preelectrolysis and then stripping. During preelectrolysis, the switch in Figure 2 was in position A and one working electrode of the IDA was potentiostated at −0.4 V. The electrolyte solution was stirred with the magnetic stirrer during preelectrolysis in the right cell. After 10 min of preelectrolysis, stirring was stopped and the solution was left for 10 s. During stripping, the switch was moved to position B and immediately the potential of the glassy-carbon electrode began to be swept from −0.4 V to +0.5 V at a scan rate of 20 mV/s.

In addition, cyclic voltammetry was performed on the IDA electrode by potentiostating both finger sets of the IDA without connecting the glassy-carbon electrode. One finger set of the IDA electrode was fixed at 0 V, and the other was swept at the same scan rate as that of the stripping voltammetry in order to compare this current with the peak current obtained by the new stripping method.

RESULTS AND DISCUSSION

The redox potential of the ruthenium hexaammine was −0.2 V in a pH 4.0 standard buffer solution. The stripping peak of silver on the glassy-carbon electrode in potassium nitrate solution was 0.35 V, which was measured with the conventional stripping method.

When one finger set of the IDA electrode in the standard buffer containing oxidized ruthenium hexaammine was connected to the glassy-carbon electrode in the silver nitrate solution of the other cell, no ruthenium hexaammine oxidation or silver ion deposition took place in spite of the redox potential difference between ruthenium hexaammine and the silver ions. This is because there was no reduced species in either cell. When the electrode of the IDA which was not connected to the carbon electrode was potentiostated at below the redox potential of the ruthenium hexaammine, we observed a steady-state current flowing from the glassy-carbon electrode to the IDA. This current flow indicates that the reduced ruthenium hexaammine is oxidized at the IDA and the electrons generated in this reaction are consumed by the reductive reaction on the glassy-carbon electrode. It also

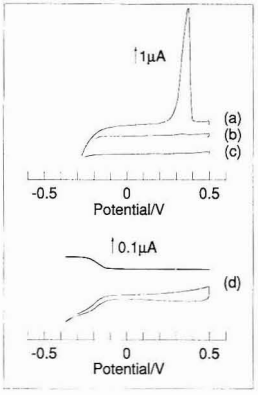

Figure 3. New stripping voltammogram of the 1 μmol/dm³ ruthenium hexaammine at a sweep rate of 20 mV/s compared to the cyclic voltammogram of the same species at an interdigitated array electrode (IDA): (a) result of the new stripping method. (b) IDA working electrode potentiostated at 0 V during preelectrolysis (other experimental conditions were the same as those in (a)); (c) no ruthenium hexaammine in the electrolyte (other experimental conditions were the same as those in (a)); (d) cyclic voltammograms in twin potentiostated mode.

suggests that self-induced redox cycling occurs on the IDA. Since the electroactive species in the other cell consists only of silver ions which can easily be reduced by the redox potential of ruthenium hexaammine, silver ions should be deposited accompanied by ruthenium hexaammine oxidation.

In Figure 3, (a) shows the result of the new stripping method applied to 1 μmol/dm³ ruthenium hexaammine by sweeping the glassy-carbon electrode potential from −0.3 to +0.5 V after 10 min of preelectrolysis. The potential of one of the IDA electrodes was fixed at −0.4 V during preelectrolysis. A large silver stripping peak with a magnitude of 7.1 μA was obtained at 0.35 V, indicating that silver ion deposition actually took place accompanied by the electrolysis of ruthenium hexaammine. (b) in Figure 3 is also the result of the new stripping volammetry of ruthenium hexaammine while one electrode of the IDA was potentiostated at 0 V during the 10-min preelectrolysis period. Other experimental conditions were the same as those for (a). No stripping peak was observed in this experiment. Since the preelectrolysis electrode of the IDA was potentiostated above the redox potential of ruthenium hexaammine, no reduced ruthenium hexaammine was produced in the left cell. As a result, no silver ions were deposited on the glassy-carbon electrode because there was no electron supply from the finger set electrode of the IDA connected to the glassy-carbon electrode. The voltammogram shown by (c) in Figure 3 was obtained by the same experiment as that shown by (a) without ruthenium hexaammine. There was also no stripping peak observed in this experiment, because no redox reaction took place on the IDA electrode due to the absence of ruthenium hexaammine. These results indicate that the deposition of silver on the glassy-carbon electrode occurred only as a result of the charge arising from the redox reaction of ruthenium hexaammine.

(d) in Figure 3 shows the cyclic voltammogram of 1 μmol/dm³ ruthenium hexaammine in the twin potentiostated mode in the left cell when the glassy-carbon electrode was not connected. The IDA cathode was swept from −0.4 to +0.5 V at a sweep rate of 20 mV/s. The anode was fixed at 0 V. The oxidative limiting current of ruthenium hexaammine is much clearer than the reductive limiting current because of the absence of charging current and residual current from the dissolved oxygen or hydrogen ions caused by the potential scan. The observed limiting current was 0.09 μA, which agreed well with the calculated value.[21]

As with the oxidative current of the IDA in the twin mode ((d) in Figure 3), the oxidative current generated by self-induced redox cycling on the combination electrode also contains much less interference or charging current than that observed at the potentiostated finger set of the IDA. As a result of this noise reduction effect at the IDA during preelectrolysis, this new stripping method has the potential to achieve high sensitivity with an excellent signal to noise ratio. It was also confirmed that this method can be used to determine reversible redox species which cannot be preconcentrated by conventional stripping analysis.

The peak height obtained by this new stripping method was 7.1 μA, which is 79 times higher than that obtained from a cyclic voltammogram ((d) in Figure 3) at the IDA. Furthermore, the limiting current observed in the cyclic voltammogram at the IDA was already amplified by the redox cycling. The peak current of a cyclic voltammogram obtained at a single working electrode was reduced to about one-tenth that at a twin potentiostated IDA at a sweep rate of 20 mV/s. Therefore the detected signal with the new stripping method was about 790 times larger than with conventional electrochemical detection with a single electrode.

The peak area of (a) in Figure 3 was calculated to be about 23.2 μC by converting the horizontal axis to the time dimension. On the other hand, the total charge in preelectrolysis was 54 μC, which is calculated by assuming that the steady-state current whose magnitude was 0.09 μA continued to flow for 10 min. From these results, the Coulomb efficiency for conversion from ruthenium hexaammine oxidation to silver deposition was estimated to be more than 43%.

The detection limit of this measurement system was 10 nmol/dm³. The linear relationship between the stripping peak height and the sample concentration was maintained in the 10–100 nmol/dm³ range. A higher silver ion concentration than the redox species and a small glassy-carbon electrode will be effective for achieving higher sensitivity. The higher concentration will increase the Coulomb efficiency during the preelectrolysis stage and result in a large stripping peak. The small glassy-carbon electrode will reduce the charging current during the stripping stage and flatten the baseline of the voltammogram.

CONCLUSION

A new stripping method for reversible species which cannot be preconcentrated on the electrode as in the conventional stripping method was developed by combining a closely spaced twin microelectrode and an electrode capable of depositing metal ions. An interdigitated array (IDA) electrode in a solution of the reversible redox species was used as the twin microelectrode, one finger set of which was connected to a glassy-carbon electrode in another solution containing metal ions. The glassy-carbon electrode was used because metal ions can be deposited on it. The preelectrolysis of the reversible species at one finger set of the IDA induced a reversible reaction at the other finger set, and the charge produced by this reverse reaction was transmitted to deposit metal ions on the glassy-carbon electrode. By measurement of the current from dissolution of the metal ions, a highly amplified signal was obtained which is related to the concentration of the reversible species.

This method will be very useful for analyzing trace amounts of reversible redox species.

RECEIVED for review May 27, 1992. Accepted August 24, 1992.

Registry No. Carbon, 7440-44-0; ruthenium(III) hexaammine, 18943-33-4; silver, 7440-22-4.

AUTHOR INDEX

AUTHOR INDEX

KEYWORD INDEX

A-PAGE INDEX

A/C Interface

Analytical Approach

Focus

Instrumentation

Report

Analytical CHEMISTRY

VOLUME 64, 1992
January–March
ANCHAM
ISSN 0003-2700

Published by the American Chemical Society, 1155 Sixteenth St., N.W., Washington, D.C. 20036

January 1	1–112	1 A–62 A
January 15	113–240	63 A–114 A
February 1	241–336	115 A–242 A
February 15	337–464	243 A–294 A
March 1	465–576	295 A–362 A
March 15	577–704	363 A–410 A
April 1	705–832	411 A–462 A
April 15	833–976	463 A–502 A
May 1	977–1076	503 A–550 A
May 15	1077–1204	551 A–598 A
June 1	1205–1316	599 A–646 A
June 15	Fundamental Reviews 1 R–514 R	
July 1	1317–1508	647 A–694 A
July 15	1509–1636	695 A–744 A
August 1	1637–1748	745 A–800 A
August 15	LabGuide 1 G–322 G	
September 1	1749–2020	801 A–852 A
September 15	2021–2200	853 A–900 A
October 1	2201–2312	901 A–948 A
October 15	2313–2472	949 A–992 A
November 1	2473–2664	993 A–1048 A
November 15	2665–2888	1049 A–1096 A
December 1	2889–3068	1097 A–1401 A
December 15	3069–3260	1141 A–1180 A

Analytical CHEMISTRY

VOLUME 64, 1992
April–June
ANCHAM
ISSN 0003-2700

Published by the American Chemical Society, 1155 Sixteenth St., N.W., Washington, D.C. 20036

January 1	1–112	1 A–62 A
January 15	113–240	63 A–114 A
February 1	241–336	115 A–242 A
February 15	337–464	243 A–294 A
March 1	465–576	295 A–362 A
March 15	577–704	363 A–410 A
April 1	705–832	411 A–462 A
April 15	833–976	463 A–502 A
May 1	977–1076	503 A–550 A
May 15	1077–1204	551 A–598 A
June 1	1205–1316	599 A–646 A
June 15	Fundamental Reviews 1 R–514 R	
July 1	1317–1508	647 A–694 A
July 15	1509–1636	695 A–744 A
August 1	1637–1748	745 A–800 A
August 15	LabGuide 1 G–322 G	
September 1	1749–2020	801 A–852 A
September 15	2021–2200	853 A–900 A
October 1	2201–2312	901 A–948 A
October 15	2313–2472	949 A–992 A
November 1	2473–2664	993 A–1048 A
November 15	2665–2888	1049 A–1096 A
December 1	2889–3068	1097 A–1401 A
December 15	3069–3260	1141 A–1180 A

Analytical CHEMISTRY

VOLUME 64, 1992
July–September
ANCHAM
ISSN 0003-2700

Published by the American Chemical Society, 1155 Sixteenth St., N.W., Washington, D.C. 20036

January 1	1–112	1 A–62 A
January 15	113–240	63 A–114 A
February 1	241–336	115 A–242 A
February 15	337–464	243 A–294 A
March 1	465–576	295 A–362 A
March 15	577–704	363 A–410 A
April 1	705–832	411 A–462 A
April 15	833–976	463 A–502 A
May 1	977–1076	503 A–550 A
May 15	1077–1204	551 A–598 A
June 1	1205–1316	599 A–646 A
June 15	Fundamental Reviews 1 R–514 R	
July 1	1317–1508	647 A–694 A
July 15	1509–1636	695 A–744 A
August 1	1637–1748	745 A–800 A
August 15	LabGuide 1 G–322 G	
September 1	1749–2020	801 A–852 A
September 15	2021–2200	853 A–900 A
October 1	2201–2312	901 A–948 A
October 15	2313–2472	949 A–992 A
November 1	2473–2664	993 A–1048 A
November 15	2665–2888	1049 A–1096 A
December 1	2889–3068	1097 A–1401 A
December 15	3069–3260	1141 A–1180 A

Analytical CHEMISTRY

VOLUME 64, 1992
October–December
ANCHAM
ISSN 0003-2700

Published by the American Chemical Society, 1155 Sixteenth St., N.W., Washington, D.C. 20036

January 1	1–112	1 A–62 A
January 15	113–240	63 A–114 A
February 1	241–336	115 A–242 A
February 15	337–464	243 A–294 A
March 1	465–576	295 A–362 A
March 15	577–704	363 A–410 A
April 1	705–832	411 A–462 A
April 15	833–976	463 A–502 A
May 1	977–1076	503 A–550 A
May 15	1077–1204	551 A–598 A
June 1	1205–1316	599 A–646 A
June 15	Fundamental Reviews 1 R–514 R	
July 1	1317–1508	647 A–694 A
July 15	1509–1636	695 A–744 A
August 1	1637–1748	745 A–800 A
August 15	LabGuide 1 G–322 G	
September 1	1749–2020	801 A–852 A
September 15	2021–2200	853 A–900 A
October 1	2201–2312	901 A–948 A
October 15	2313–2472	949 A–992 A
November 1	2473–2664	993 A–1048 A
November 15	2665–2888	1049 A–1096 A
December 1	2889–3068	1097 A–1401 A
December 15	3069–3260	1141 A–1180 A

To See How Powerful Your PC Can Be, Kick In The Turbo.

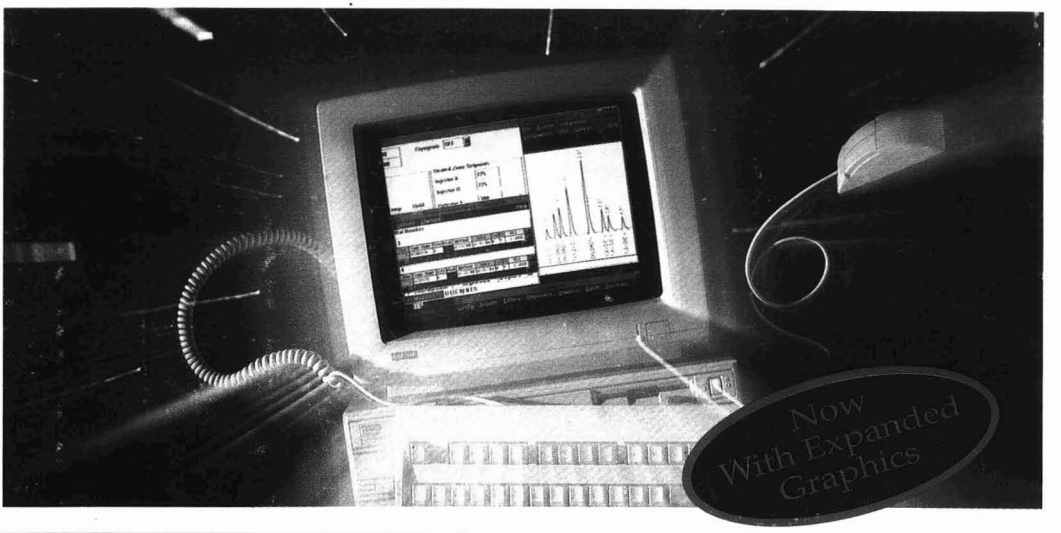

TURBOCHROM 3

PE Nelson's Turbochrom 3 has more horsepower than anything else in its class.

It's a PC-based chromatography workstation that represents a whole new concept. An architecture of buffered interfaces, multi-vendor connectivity, and expandability that allows maximum use of your existing resources.

Automation, validation, communication, and productivity are the driving forces.

Speed, high performance, and safety are the standard features.

And just wait until you see the extras:

❶ The Series 900 Buffered A/D interfaces let you collect data from up to 15 GC's and LC's of any make simultaneously, freeing your PC to do other jobs. And a unique buffering RAM protects that valuable data from computer failures, lockups, or rebooting.

❷ The Series 600 LINK Module provides two-way digital communication between PC and supported GC, giving you a single, totally integrated method for instrument control and data acquisition. LINK allows single-point control of the entire chromatographic process. And easier validation later.

❸ The Series 500 Interface Validation Module and accompanying software let you test each interface in your lab for linearity, gain, and gain error, ensuring conversion integrity and GLP compliance.

❹ Turbochrom 3 keeps the road ahead clear by providing a solid growth path for the future of your lab, adding more GC's and LC's, networking — all the way to SQL*LIMS connectivity.

❺ PE Nelson furthers its reputation as the industry standard in chromatography data handling by designing Turbochrom 3 to run in the industry-standard Microsoft Windows 3.1 environment. This easy-to-use, visual operation will not only increase your productivity now, it will ensure it for years to come.

Keep your lab out in front. Take advantage of all the power in your PC. Kick in the Turbo.

For more information, contact PE Nelson or your local Perkin-Elmer office. For product literature in the U.S., call **1-800-762-4000.**

PE NELSON

10040 Bubb Road, Cupertino, CA 95014. PE Nelson is a division of The Perkin-Elmer Corporation.

CIRCLE 88 FOR INFORMATION ONLY.
CIRCLE 89 FOR SALES CALL